AD-A170 797 PROCEEDINGS OF THE TOPICAL MEETING ON THE MICROPHYSICS OF SURFACES BEAMS A.. (U) OPTICAL SOCIETY OF AMERICA WASHINGTON D C J W QUINN 18 DEC 85 AFOSR-TR-86-0469 1/3

UNCLASSIFIED AFOSR-85-0018 F/G 7/4 NL

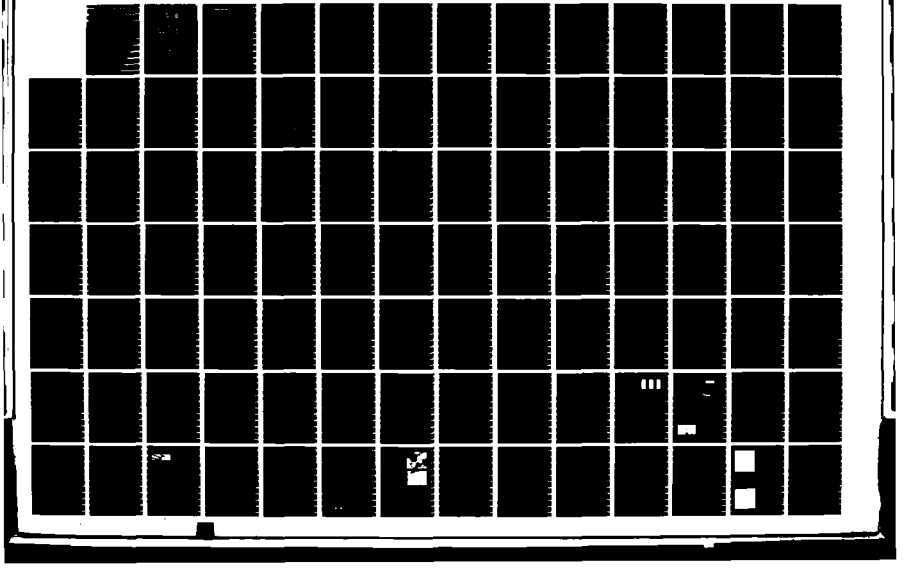

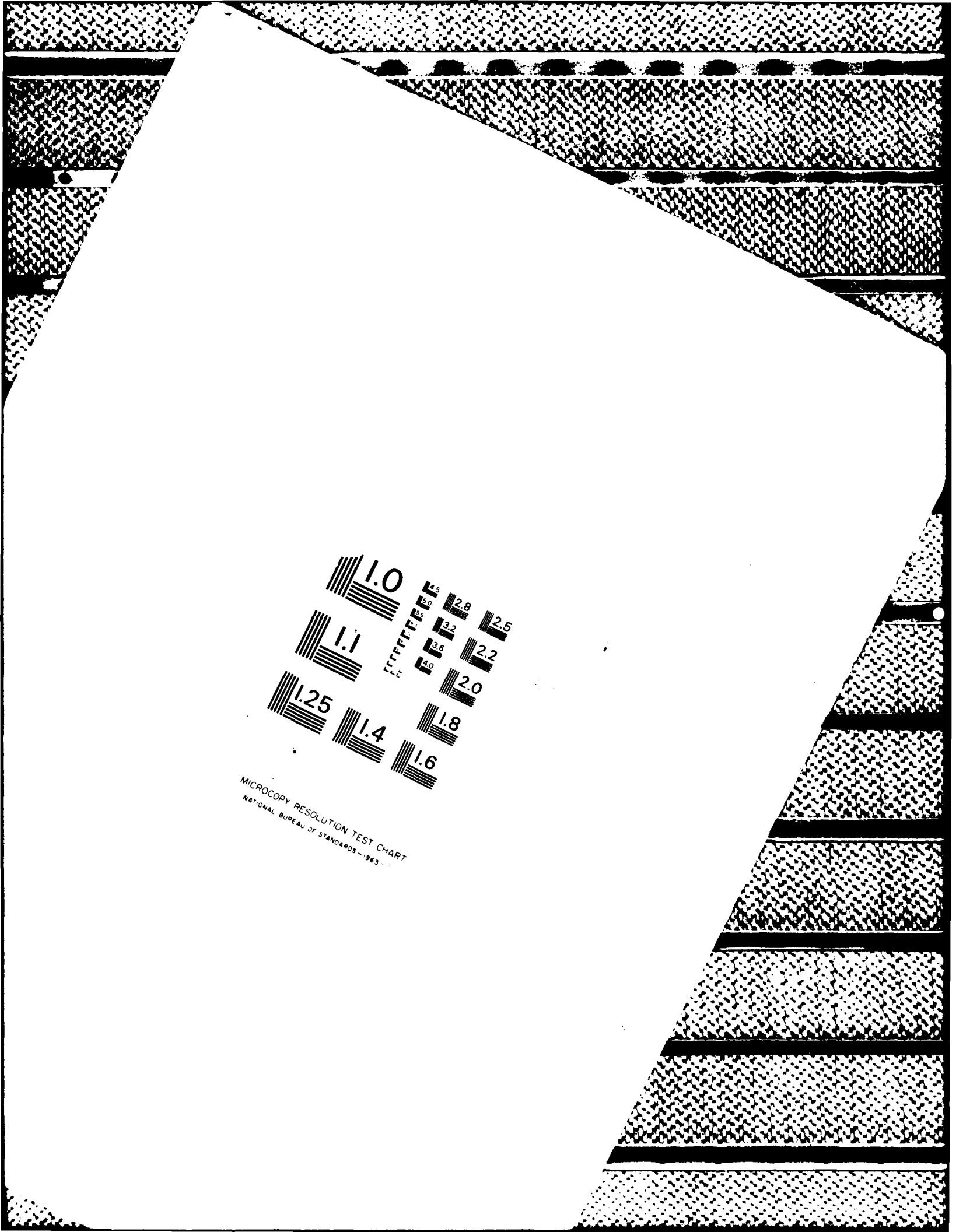
1.0
1.1
1.25
1.4
1.6
1.8
2.0
2.2
2.5
2.8
3.2
3.6
4.0
4.5
5.0
5.6
MICROCOPY RESOLUTION TEST CHART
NATIONAL BUREAU OF STANDARDS - 1963

(1)

PROCEEDINGS

TOPICAL MEETING ON THE MICROPHYSICS OF SURFACES, BEAMS, AND ADSORBATES

D. J. Ehrlich and T. J. Chuang, Editors

1985

●

AVS

[redacted]

AFOSR-TR 86-0469

1985 TOPICAL MEETING ON MICROPHYSICS...
REGISTRATION LIST

LASTNAME	FIRSTNAM	ORGANIZA	ADDRESS1	ADDRESS2	MAILCODE	COUNTRY
AGRAWALLA	BIJAY S.	UNIVERSITY OF S. CALIFORNIA	UNIVERSITY PK DRB-17-1112	LOS ANGELES, CA	90089	USA
AL-JUMAILY	GHANIM A.	UNIVERSITY OF NEW MEXICO		ALBUQUERQUE, NM	87131	USA
ALLEN	SUSAN D.	UNIVERSITY OF S. CALIFORNIA	UNIVERSITY PK DRB-17-1112	LOS ANGELES, CA	90089	USA
ANDERSON	WALLACE E.	LOS ALAMOS NATIONAL LAB	MS E-511 GROUP MS7-13	LOS ALAMOS, NM	87545	USA
ASPNES	D. E.	BELL COMMUNICATIONS RES.	600 MOUNTAIN AVENUE	MURRAY HILL, NJ	07974	USA
AVOURIS	PHAEDON	IBM WATSON RESEARCH CENTER	PO BOX 218	YORKTOWN HGTS, NY	10598	USA
BALOOCH	MEHDI M.	UNIVERSITY OF CALIFORNIA		BERKELEY, CA.	94720	USA
BENSON	RICHARD C.	JHU APPLIED PHYSICS LAB.	JOHNS HOPKINS ROAD	LAUREL, MD	20707	USA
BERI	AVINASH C.	UNIVERSITY OF ROCHESTER	RIVER CAMPUS	ROCHESTER, NY	14627	USA
BJORKHOLM	JOHN E.	AT&T BELL LABS	ROOM 4B-423	HOLMDEL, NJ	07733	USA
BOGHOSIAN	CHARLES	US ARMY RESEARCH OFFICE	PO BOX 12211	RES. TRI. PARK, NC	27712	USA
BOYER	KIRK	TEKTRONIX, INC.	P.O.BOX 500 MS 50-324	BEAVERTON, OR	97077	USA
BRUECK	STEVE	MIT LINCOLN LABORATORY	PO BOX 73	LEXINGTON, MA	02173	USA
CAMPION	ALAN	UNIVERSITY OF TEXAS		AUSTIN, TEXAS	78712	USA
CARLETON	KAREN L.	UNIVERSITY OF COLORADO	JILA	BOULDER, CO.	80309	USA
CHUANG	TUNG J.	IBM RESEARCH LABS	5600 COTTLE ROAD K33/281	SAN JOSE, CA.	95193	USA
CLAWSON	ARTHUR R.	NAVAL OCEAN SYSTEMS CENTER	CODE 561	SAN DIEGO, CA	92152	USA
DOMANN	FRED E.	UNIVERSITY OF WISCONSIN	PLATTEVILLLE-DEPT OF PHY.	PLATTEVILLE, WI	53818	USA
DRAKE	MIKE	EXXON RESEARCH		CLINTON, NJ	08801	USA
DREYFUS	RUSSELL W.	IBM WATSON RESEARCH CENTER	PO BOX 218	YORKTOWN HGTS, NY	10598	USA
EHRLICH	DAN	MIT LINCOLN LABORATORY	PO BOX 73, C-174	LEXINGTON, MA	02173	USA
ERMAN	MARKO	L. E. P.	3 AVENUE DESCARTES	LIMEIL-BREVANNE	94450	FRANCE
EWBANK	DALE E.	GOULD-AMI SEMICONDUCTORS	3800 HOMESTEAD RD.	SANTA CLARA, CA.	95051	USA
FALT	ROBERT M.	TEXAS INSTRUMENTS		DALLAS, TX	75265	USA
FIGUEIRA	JOSEPH	LOS ALAMOS NATIONAL LAB.	PO BOX 1663	LOS ALAMOS, NM	87545	USA
FLAMM	DANIEL L.	AT&T BELL LABORATORIES	6E-216	MURRAY HILL, NJ	07974	USA
GARRISON	BARBARA J.	PENNSYLVANIA STATE UNIVERS.	152 DAVEY LABORATORY	UNIVERSITY PK, PA	16802	USA
GILLILAND	JOHN W.	CORNING GLASS WORKS	SULLIVAN PARK-PR-1-1	CORNING, NY	14831	USA
GILLIS	H.P.	HUGHES RESEARCH LABS	3011 MALIBU CANYON RD.	MALIBU, CA.	90265	USA
GREENE	JOE	UNIVERSITY OF ILLINOIS	CSL 1101 WEST SPRINGFIELD	URBANA, IL	61820	USA
GUENTHER	ARTHUR H.	AIR FORCE WEAPONS LAB		KIRTLAND AFB, NM	87117	USA
HAIGH	JOHN	BRITISH TELECOM RESEARCH		IPSWICH	IP5 7RE	ENGLAND
HALL	RICHARD B.	EXXON RESEARCH & ENGINEERIN	RT. 22E	ANNANDALE, NJ	08801	USA
HAMILTON	JOHN C.	SANDIA NATIONAL LABORATORY		LIVERMORE, CA	94550	USA
HEILWEIL	EDWIN J.	NATL. BUREAU OF STANDARDS	DIVISION B-268	GAITHERSBURG, MD	20899	USA
HEINZ	TONY F.	IBM WATSON RESEARCH CENTER	PO BOX 218	YORKTOWN HTS, NY	10598	USA
HETHERINGTON	WILLIAM M	UNIVERSITY OF ARIZONA	DEPT. OF CHEMISTRY	TUCSON, AZ.	85721	USA
HIGASHI	GREGG S.	AT&T BELL LABORATORIES	600 MOUNTAIN AVENUE	MURRAY HILL, NJ	07974	USA
HIROSE	MASATAKA	HIROSHIMA UNIVERSITY	SAIJOH-CHO	HIGASHIHIROSHIMA	724	JAPAN
HOFFMAN	FRIEDERICH M.	EXXON CORPORATE RESEARCH	CLINTON TOWNSHIP	ANNANDALE, NJ	08801	USA
HOLM	RONALD T.	NAVAL RESEARCH LABS		WASHINGTON, DC	20375	USA
HORIIKE	YASUHIRO Y.	TOSHIBA VLSI RES. CENTER	1-KOMUKAI-TOSHIBACHO SAIWA	KAWASAKI	210	JAPAN
HUSINSKY	WOLFGANG	TECH. UNIVERSITAET WIEN	INST. F. ALLGEM. PHYSIK	WIEN		AUSTRIA
IRVINE	STUART J.	R.S.R.E.	ST ANDREWS ROAD-MALVERN	WORCESTERSHIRE	WR143PS	ENGLAND
JACKSON	WILLIAM M.	HOWARD UNIVERSITY	GLASER CHEMISTRY	WASHINGTON, DC	20016	USA
JEDRZEJEK	CZESLAW	TEXAS A & M UNIVERSITY	PHYSICS DEPARTMENT	COLLEGE STN, TX	77843	USA
JETTE	NORMAN	JHU APPLIED PHYSICS LAB.	JOHNS HOPKINS ROAD	LAUREL, MD	20707	USA
KAPLAN	RAY	NAVAL RESEARCH LAB		WASHINGTON, DC	20375	USA
KAWATE	YOSHIO	KOBE STEEL, ASADA RES. LAB.	53-3 AZA-MARUYAMA, GOMO	NADA-KU, KOBE	657	JAPAN
KESTER	JOHN J.	DOW CHEMICAL COMPANY	BUILDING 1776	MIDLAND, MI	48640	USA
KING	KEVIN K.	UNIVERSITY OF ILLINOIS	607 E. HEALEY	CHAMPAIGN, IL	61820	USA
KLAFTER	JOSEPH	EXXON RESEARCH		ANNANDALE, NJ	08801	USA
KOWALCZYK	STEVEN P.	ROCKWELL INTERNATIONAL	P.O. BOX 1085	THOUSAND OAKS, CA	91360	USA
KROGH	OLE D.	TEGAL CORPORATION	11 DIGITAL DRIVE	NOVATO, CA	94947	USA
LAMBERT	DAVID K.	GENERAL MOTORS RES. LAB.	PHYSICS DEPT.	WARREN, MI	48077	USA

1985 TOPICAL MEETING ON MICROPHYSICS...
REGISTRATION LIST

LASTNAME	FIRSTNAM	ORGANIZA	ADDRESS1	ADDRESS2	MAILCODE	COUNTRY
LANE	ANDREW. P.	TEXAS INSTRUMENTS	ROUTE 2. BOX 653	WESTMINSTER. TX	75096	USA
LIAO	PAUL F.	BELL COMMUNICATIONS RESEARC	4E218	HOLMDEL. NJ	07733	USA
LIU	YUNG S.	G.E. RESEARCH CENTER		SCHENECTADY. NY	12301	USA
LOEWENSTEIN	LEE M.	TEXAS INSTRUMENTS. INC.	P.O. BOX 225936. MS 147	DALLAS. TEXAS	75265	USA
LOPEZ-RIOS	TOMAS F.	UNIVERSITE P.M. CURIE PARIS	14 PLACE JUSSIEU	PARIS		FRANCE
LOUDIANA	MICHAEL A.	BOEING AEROSPACE COMPANY	P.O. BOX 3999 MS 8K-16	SEATTLE. WASH.	98031	USA
MARINERO	ERNESTO E.	IBM RESEARCH LABORATORY	5600 COTTLE ROAD	SAN JOSE. CA	95193	USA
MAYER	THOMAS M.	UNIV.OF NORTH CAROLINA	DEPARTMENT OF CHEMISTRY	CHAPEL HILL. NC	27514	USA
MISEWICH	JAMES A.	IBM WATSON RESEARCH CENTER	PO BOX 218	YORKTOWN HGHTS. NY	10598	USA
MORSE	PATRICIA L.	AIR FORCE WEAPONS LAB	OPTICAL COMPONENTS DIV.	KIRTLAND AFB. NM	87117	USA
MYERS	LEE E.	AFOSR	AFOSR/NC	BOLLING AFB. DC	20332	USA
NARBUT	MARTHA	HEWLETT-PACKARD LABORATOR.	640 PAGE MILL ROAD	PALO ALTO. CA	94304	USA
OLSON	WILLIAM M.	LOS ALAMOS NATIONAL LAB	MST-13 E511	LOS ALAMOS. N.M.	87545	USA
OLSON	RAD W.	IBM	P.O. BOX 218	YORKTOWN HGTS. NY	10598	USA
OSGOOD	RICHARD M.	COLUMBIA UNIVERSITY	RADIATION LABORATORY	NEW YORK. NY	10027	USA
PAMLER	WERNER	IBM RESEARCH LABORATORY	5600 COTTLE ROAD	SAN JOSE. CA	95193	USA
PEASE	FABIAN R.	STANFORD UNIVERSITY	MCCULLOUGH 204	STANFORD. CA	94305	USA
PEERCY	PAUL S.	SANDIA NATIONAL LABORATORY		ALBUQUERQUE. NM	87185	USA
PETELIN	ANDREW N.	FUSION SYSTEMS. INC.	7600 STANDISH PLACE	ROCKVILLE. MD	20855	USA
PONS	STANLEY	UNIVERSITY OF UTAH	DEPARTMENT OF CHEMISTRY	SALT LAKE CITY. UT	84112	USA
REINECK	STEFAN R.	LEYBOLD-HERAEUS	1876 HARTOG DRIVE	SAN JOSE. CA	95131	USA
RILEY	MERLE E.	SANDIA NATIONAL LABORATORY		ALBUQUERQUE. NM	87185	USA
RITCHIE	GEORGE W.	RIDER COLLEGE		LAWRENCEVILLE. NJ	08648	USA
SANDERS	FRANS H.	PHILIPS RESEARCH LABS.	PROF. HOLSTLN	EINDHOVEN	5600 JA	NETHERLANDS
SCOLES	KEVIN J.	DREXEL UNIVERSITY	32ND & CHESNUT STREETS	PHILADELPHIA. PA	19104	USA
SHE	CHIAO-YAO	UNIVERSITY OF MARYLAND	LAB. FOR PHYSICAL SCIENCE	COLLEGE PARK. MD	20740	USA
SHEN	Y. R.	UNIVERSITY OF CALIFORNIA	DEPARTMENT OF PHYSICS	BERKELEY. CA	94720	USA
SQUIRE	DAVID W.	NAVAL RESEARCH LABORATORY	CODE 6105 CHEMISTRY DIV	WASHINGTON. DC	20375	USA
SRINIVASAN	SRI R.	IBM WATSON RESEARCH CENTER	PO BOX 218	YORKTOWN HGTS. NY	10598	USA
STOFFEL	NED G.	BELL COMMUNICATIONS RES.	600 MOUNTAIN AVENUE	MURRAY HILL. NJ	07974	USA
SUNDERLAND	ROBERT. J.	DOUGLAS AIRCRAFT	3855 LAKEWOOD BLVD. MS 1-3	LONG BEACH. CA	90846	USA
TACHI	SHINICHI	UNIVERSITY OF HOUSTON	DEPARTMENT OF CHEMISTRY	HOUSTON. TX	77004	USA
TAYLOR	THOMAS N.	LOS ALAMOS NATIONAL LAB.	MS-6738. GROUP CHM-2	LOS ALAMOS. NM.	87545	USA
TOLK	NORMAN H.	VANDERBILT UNIVERSITY	DEPT. OF PHYSICS & ASTRON.	NASHVILLE. TN	37235	USA
TSAO	JEFFREY Y.	SANDIA NATIONAL LABS.		ALBUQUERQUE. NM	87185	USA
TSONG	TIEN T.	PENNSYLVANIA STATE UNIVER	104 DAVEY LAB	UNIVERSITY PK. PA	16802	USA
VOSS	DAVID F.	NAVAL RESEARCH LABORATORY	CODE 6510	WASHINGTON. DC	20375	USA
WAGNER	JOHN J.	EASTMAN KODAK CO.	RESEARCH LABS 81-510	ROCHESTER. NY	14580	USA
WALKUP	ROBERT E.	IBM RESEARCH CENTER	P.O. BOX 218	YORKTOWN HGTS. NY	10598	USA
WALTHER	HERBERT	MPI FOR QUANTUMOPTICS	FORSCHUNGSGELANDE	GARCHING	8046	WEST GERMAN
WASS	BECKY G.	UNIVERSITY OF COLORADO	3850 PASEO DEL PRADO #35	BOULDER. CO.	80301	USA
WEST	PAUL E.	AEROJET ELECTROSYSTEMS	PO BOX 296	AZUSA. CA	91702	USA
WINTERS	HAROLD F.	IBM RESEARCH LABORATORY	5600 COTTLE ROAD	SAN JOSE. CA	95193	USA
WITTIG	CURT	UNIVERSITY OF S. CALIFORNIA	CHEMISTRY DEPARTMENT	LOS ANGELES. CA	90089	USA
WOKAUN	ALEXANDER J.	SWISS FED. INST. OF TECH.	UNIVERSTRASSE 22	ZURICH	8092	SWITZERLAND
WOLF	EDWARD D.	CORNELL UNIVERSITY	NATIONAL SUBMICRON FACILIT	ITHACA. NY	14853	USA
YAMASHITA	KEN	NIPPON SHEET GLASS	5-4 TOKODAI. TOYOSATO	IBARAKI-KEN	300-26	JAPAN
ZAPMANI	HAMID	COLORADO STATE UNIVERSITY	EE DEPARTMENT	FORT COLLINS. CO	80523	USA
ZEIGER	HERBERT J.	MIT LINCOLN LABORATORY	P.O. BOX 73	LEXINGTON. MA	02173	USA

Proceedings of the
Topical Meeting on the Microphysics of Surfaces, Beams, and Adsorbates

4–6 February 1985
La Fonda Hotel
Santa Fe, New Mexico

Cosponsored by
Air Force Office of Scientific Research
American Vacuum Society
Optical Society of America

Co-Editors for the Proceedings:
D. J. Ehrlich
T. J. Chuang

Published for the American Vacuum Society by
the American Institute of Physics, New York, 1985

Library of Congress Catalog Number: 85-72737

International Standard Book Number: 0-88318-481-8

Published by the American Institute of Physics
335 East 45th Street, New York, New York 10017

Printed in the United States of America

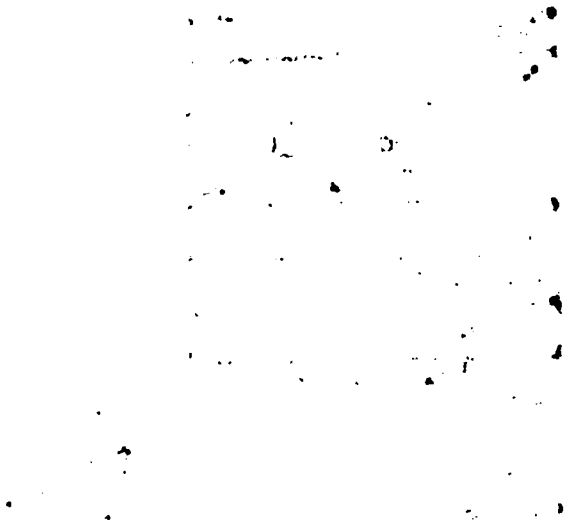

The Proceedings are published in both the 1985 September/October issue of the

Journal of Vacuum Science and Technology B, Vol. 3, No. 5 and in a special casebound edition available to participants

PROGRAM COMMITTEE

Proceedings of the Topical Meeting on the Microphysics of Surfaces, Beams, and Adsorbates

(continued)

(continued)

PREFACE

The first Topical Meeting on the Microphysics of Surfaces, Beams, and Adsorbates was held at the La Fonda Hotel, Santa Fe, New Mexico, February 4–6, 1985. The emphasis was the fundamental science of surface reactions initiated by laser-, electron-, and ion-beam irradiation, in combination with the relevant interactions of beams with surfaces and adsorbates. The Meeting was cosponsored by the Air Force Office of Scientific Research, the American Vacuum Society, and the Optical Society of America. The format of the meeting was a three-day program (single sessions) that consisted of a combination of invited, contributed, and posted papers. Afternoons were unscheduled to allow unstructured dialogue among the participants. The next Microphysics will be held in February 1987.

A large number of people contributed to the success of the first Microphysics Meeting. Barbara Hicks, Calva Lotridge, and Jarus Quinn of the OSA National Headquarters deserve particular thanks for the primary burden of organizing the Meeting. These people guided a 14-month process culminating in the conference itself. The Program Committee consisted of D. E. Aspnes, J. W. Coburn, I. Hayashi, K. L. Kompa, P. F. Liao, R. M. Osgood, and R. N. Zare, all of whom made critical suggestions regarding the technical program. The session presiders, Joe Greene, Dan Flamm, Steve Brueck, Kurt Wittig, Fabian Pease, Paul Liao, Dave Aspnes, Paul Peercy, and Ed Wolfe are specially thanked for their role in stimulating active discussion throughout the three days.

In addition, several people have generously given essential assistance in the preparation of this Proceedings volume. Principal among these are Jean O'Hare and Becky Gates. Finally, thanks are expressed to Howard Schlossberg of the AFOSR for his support and guidance.

D. J. Ehrlich
T. J. Chuang
Proceedings Editors

Summary Abstract: Ion-enhanced processes in etching of silicon

T. M. Mayer, M. S. Ameen, E. L. Barish, T. Mizutani,[a] and D. J. Vitkavage
Department of Chemistry, University of North Carolina, Chapel Hill, North Carolina 27514

(Received 18 March 1985; accepted 21 May 1985)

In the past two years considerable progress has been made in understanding the fundamental nature of the plasma-surface interaction in plasma-assisted etching processes. Simulation of the plasma environment by well controlled beam techniques and application of analytical tools capable of dynamic observation of the etching process have made these advances possible.

There are a number of basic questions about the etching process that cannot easily be studied in the plasma environment that have spurred this work. First is the identity of the etch products that are desorbed or ejected from the surface in an etching reaction, second is the role of energetic ion bombardment in promoting formation or removal of products, and third is the chemical and physical structure of the altered surface layer that is exposed to the plasma. Of course all of these questions are intimately related, and advances in the understanding of one contributes to the understanding of the entire phenomenon.

For a number of years the focus of most fundamental work on mechanisms of etching processes was the reactions of F atoms (or XeF_2) with silicon and other materials. Winters, Coburn, Chuang, and co-workers[1] have contributed most of this work. Recently, other groups have focused more heavily on the technologically important reactions of chlorine with silicon, gallium arsenide, aluminum, and other metallizations.[2-5] From the recognition that simultaneous ion bombardment of the substrate along with chemical reaction to form volatile products is responsible for the anisotropic nature of many etching processes, experiments have most often been designed to elucidate some aspect of ion impact phenomena.

What is now clear is that the importance of ion bombardment in formation and removal of etch products is in inverse proportion to the reactivity of the etch gas with the material (assuming the final product is volatile). Thus F has been found to be capable of extensive spontaneous reaction with Si to form SiF_2, SiF_3, and SiF_4 product species, involving substantial disruption of the Si lattice and breaking of Si–Si bonds. For highly fluorinated surfaces, ion bombardment seems to cause further reaction, likely by the disproportionation reaction $2SiF_3 \rightarrow SiF_4 + SiF_2$ and copious liberation of SiF_4 etch products. Trapping of SiF_4 in the fluorinated surface layer has also been observed,[6] and is probably liberated readily by ion bombardment. Qualitatively similar results have been obtained with $W + XeF_2$, $Cu + Cl_2$, and $Al + Cl_2$. The characteristic feature of these processes is extensive spontaneous reaction with the substrate, resulting in substrate–substrate bond breaking, and incorporation of etch gases into subsurface material layers.

A quite different qualitative picture has emerged for the interaction of chlorine with silicon. The Si–Cl bond being 2–3 eV less strong than the Si–F bond, considerably less energy is liberated upon adsorption and reaction with the surface. In addition, a substantial potential barrier (~ 13 eV) apparently exists for penetration of the Si lattice by a Cl atom. This is compared to a barrier of about 1 eV for F atom penetration.[7] Extensive *spontaneous* formation of $SiCl_2$, $SiCl_3$, and $SiCl_4$ species probably does not occur, and the spontaneous interaction consists mainly of chemisorption of Cl to the surface, forming rather weak Si–Cl surface bonds.[8] At room temperature significant removal of surface material only occurs with simultaneous energetic ion bombardment of the surface, indicating a crucial role for ion bombardment in promoting the etch process.

We have made extensive investigations of the sputtering of chlorinated silicon surfaces by Auger, secondary ion mass spectroscopy (SIMS), and ISS techniques.[2(b)-2(d)] The dependence of the removal yield of various species from the surface on ion bombardment conditions can give much information on the nature of surface species, and the mechanisms of product formation and removal. Removal yields of chlorine and silicon from a silicon surface as a function of ion angle of incidence is shown in Fig. 1 for Si sputtered by 1 keV Ar^+, adsorbed Cl sputtered by 1 keV Ne^+, and Si sputtered by 1.2 keV Cl^+ in the presence of neutral Cl_2. Si (Ar^+) and Cl (Ne^+) show behavior characteristic of a collisional sputtering process. The Cl yield at grazing angles is seen to be many times the Si yield, indicating removal of a weakly bound atom adsorbed on top of the surface. The Si (Cl^+/Cl_2) yield shows an anomalous maximum yield at normal incidence,

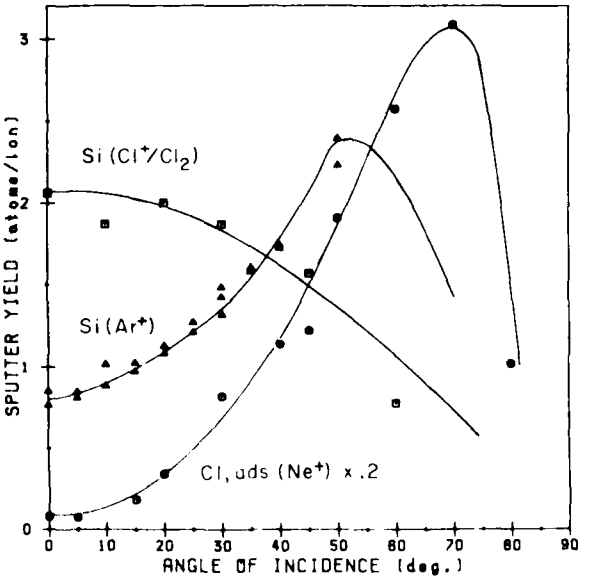

FIG. 1. Sputtering yields as a function of ion angle of incidence of (a) Si/Cl/Cl$_2$, 1.2 keV [Ref. 2(a)], (b) single crystal Si by Ar$^+$, 1 keV [Ref. 2(c)], (c) adsorbed Cl by Ne$^+$, 1 keV [Ref. 2(d)].

 0734-211X/85/051373-03$01.00

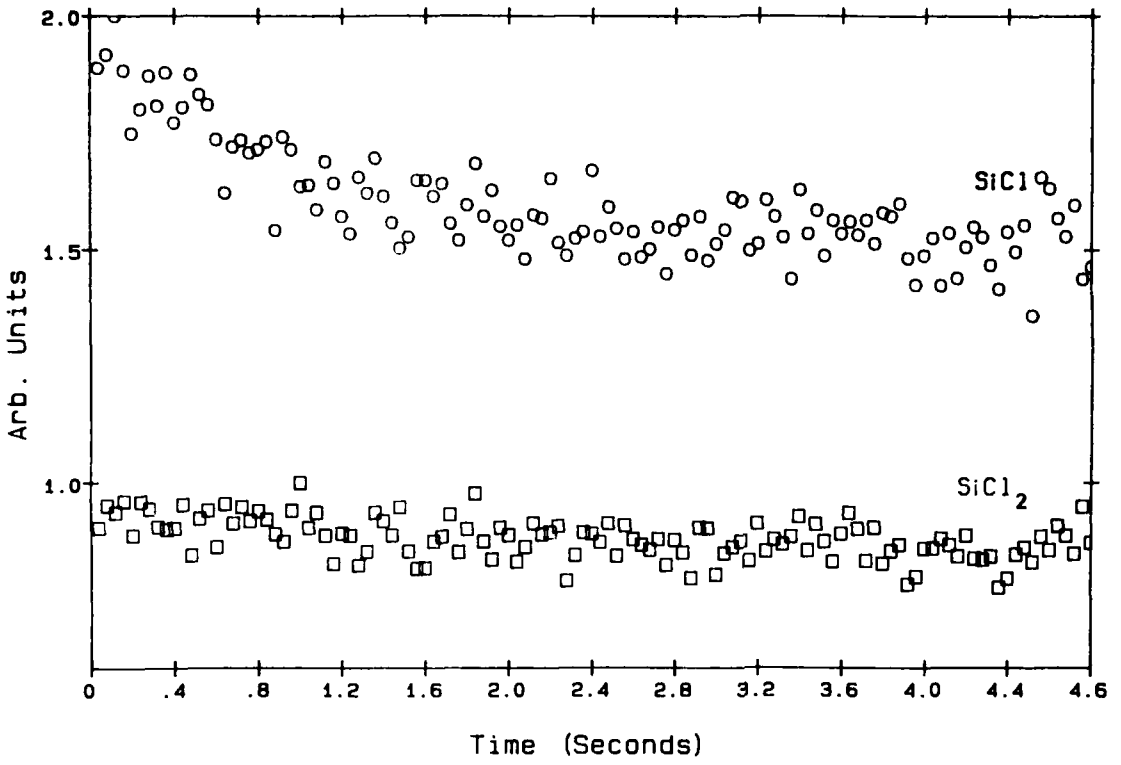

FIG. 2. SiCl and $SiCl_2$ neutral product fluxes as a function of time after surface exposure to 1 keV Ar^+ bombardment.

which is enhanced by a factor of 3–5 over the Si (Ar^+) yield. The total Cl yield is minimum at this point, and if one assumes that each Si atom ejected from the surface is bound to Cl then the average stoichiometry of the etch products is about $SiCl_{1.5}$.[2(d)]

These results have led to a number of suggestions and further measurements of product ejection and surface modification by ion bombardment. Product fluxes measured by mass spectrometry have tended to support the overall mass balance suggested above, in that SiCl is the most abundant product observed under similar conditions, with much smaller amounts of $SiCl_{2,3,4}$.[4,5] Kinetic energy distributions of the products suggest that a collisional process is responsible for ejecting species from the surface; however, the products exhibit a very low binding energy to the surface.[5] These phenomena are perhaps best explained by a mechanism which involves production of product molecules via mixing processes during the course of a collision cascade, with efficient ejection from the surface of newly synthesized species, rather than liberation of preexisting adsorbed or trapped molecules.

A mechanism of this sort would be expected to exhibit features characteristic of an ion mixing process, namely scrambling of chemical composition in the layer affected by the collision cascade. The removal yield of Si should correlate with the extent of cascade mixing of etch gases into the surface of the material. We have made Rutherford backscattering and SIMS measurements of implanted ion concentrations, incorporation of adsorbed etch gases via ion mixing, and Si crystal damage produced by ion impact. These measurements show maximum surface alteration at ion incidence normal to the surface, as expected.[2(e)]

Synthesis of complex products, such as $SiCl_2$ or $SiCl_4$, via a cascade mixing process should be sensitive particularly to the amount of Cl incorporated into the subsurface silicon layers, while SiCl production may simply represent the amount of Cl available at the surface at the end of the collision cascade. We can see evidence for this in the fluxes of SiCl and $SiCl_2$ observed liberated from the surface as a function of time after the fully chlorinated surface is exposed to the ion beam. This is shown in Fig. 2. The SiCl flux decays to a steady state value, directly proportional to the instantaneous surface concentration of Cl, measured by ISS. The $SiCl_2$ flux on the other hand does not decay with surface Cl concentration, but remains constant with perhaps a discernible rise time. Incorporation of Cl into subsurface layers by ion mixing, balanced by reemission of material by sputtering is expected to yield results of this type. We are attempting to model this behavior more quantitatively.

These results seem to be general to a variety of etch processes and materials. They also demonstrate a very symbiotic relationship between the well known sputtering phenomenon and less well understood chemical reactivity of semiconductor surfaces. The collisional processes leading to surface modification play an activating role in stimulating chemical reactions that lead to volatile product formation.

In summary, our studies of sputtering of silicon surfaces in the presence of reactive chlorine has led to a more complete understanding of a class of plasma assisted etching processes that rely on energetic ion bombardment for stimulation of the etching reaction. We have shown that extensive compositional and structure modification of the surface occurs

upon exposure of the surface to a plasma, and that this modification may be responsible for the formation and liberation of volatile etch products.

[a]Permanent address: Hitachi Central Research Labs, Kokubunji, Tokyo 185, Japan.

[1](a) Y.Y. Tu, T. J. Chuang, H. F. Winters, Phys. Rev. B **23**, 823 (1981); (b) T. J. Chuang, J. Appl. Phys. **51**, 2614 (1980); (c) U. Gerlach-Meyer. J. W. Coburn, and E. Kay, Surf. Sci. **103**, 177 (1981); (d) J. W. Coburn, H. F. Winters, and T. J. Chuang, J. Appl. Phys. **48**, 3532 (1979); (e) H. F. Winters, J. Vac. Sci. Technol. B **1**, 927 (1983).

[2](a) T. M. Mayer, R. A. Barker, and L. J. Whitman, J. Vac. Sci. Technol. **18**, 349 (1981); (b) R. A. Barker, T. M. Mayer, and W. C. Pearson, J. Vac. Sci. Technol. B **1**, 37 (1983); (c) D. J. Vitkavage, M. S. Ameen, and T. M. Mayer, J. Vac. Sci. Technol. A **2**, 492 (1984); (d) E. L. Barish, D. J. Vitkavage, and T. M. Mayer, J. Appl. Phys. **57** 1336, (1985); (e) T. Mizutani, C. J. Dale, W. K. Chu, and T. M. Mayer, Nucl. Instrum. Methods B (1985) (*in press*).

[3](a)S. G. McNevin, G. E. Becker, J. Vac. Sci. Technol B **3**, 485 (1985); (b) J. Vac. Sci. Technol. A **3**, 880 (1985).

[4]R. A. Rosen and H. H. Sawin, Appl. Phys. Lett. **45**, 860 (1984).

[5](a) A. W. Kolfschoten. R. A. Haring, A. Haring, A. E. DeVries, J. Appl. Phys. **55**, 3813 (1984); (b) F. H. M. Sanders, A. W. Kolfschoten, J. Dieleman, R. A. Haring, A. Haring, and A. E. DeVries, J. Vac. Sci. Technol. A **2**, 487 (1984).

[6]F. R. McFeely, J. Vac. Sci. Technol. A **3**, 879 (1985).

[7]M. Seel and P. S. Bagus, Phys. Rev. B **28**, 2023 (1983).

[8]J. E. Rowe, G. Margaritondo, and S. B. Christman, Phys. Rev. B **16**, 1518 (1977); M. Schluter, J. E. Rowe, S. P. Weeks, and S. B. Christman, J. Vac. Sci. Technol. **16**, 615 (1979).

Plasma-assisted etching mechanisms: The implications of reaction probability and halogen coverage

Harold F. Winters and J. W. Coburn
IBM Research Laboratory, San Jose, California 95193

(Received 18 March 1985; accepted 4 June 1985)

Evidence is presented which indicates that the way in which energetic ion bombardment accelerates the etching of Si in a fluorine environment is by a direct acceleration of the product formation step and not by damage-enhanced chemistry. The use of fluorine coverage to characterize the etching process is discussed in detail and the assumption that the etch rate of Si can be decoupled into a spontaneous and an ion-assisted contribution is questioned. Finally, examples of the influence of ion bombardment on Al(100)–Cl_2, Cu(100)–Cl_2 at 310 °C, and Nb–XeF_2 are used to emphasize that some of the conclusions reached for the Si–XeF_2 system are not generally applicable to all gas–solid combinations.

I. INTRODUCTION

Early studies of the plasma-assisted etching of various solids[1-3] showed the importance of energetic ion bombardment in accelerating the chemical etch rate in reactive gas glow discharges. This phenomenon, which is often referred to as chemical sputtering,[3,4] is generally believed to be responsible for the etching directionality obtainable in plasma-assisted etching systems. Subsequently, chemical sputtering has been studied in various directed beam simulations of the reactive gas discharge environment. It is apparent that in order for an etching process to occur, several sequential steps must take place[5]:

Step A: *Adsorption and /or reaction*. The chemically reactive gas phase species must form a chemical bond with the surface being etched. For example, $SiF_x(s) + F(g) \rightarrow SiF_{x+1}(s)$. [$x = 0$–3, where (s) and (g) represent surface and gas phase, respectively.]

Step B: *Product molecule formation*. [The details of how this process takes place are not clear but must involve a penetration of the halogens[6] into the solid lattice, probably by field-assisted mechanisms.[7] An example of the final step in product molecule formation for Si etching would be $SiF_3(s) + F \rightarrow SiF_4(s)$.]

Step C: *Product molecule desorption*. [Etching requires that the product molecule be volatile; e.g., $SiF_4(s) \rightarrow SiF_4(g)$.]

There are many examples of gas–surface reactions whose rates are increased by energetic particle bombardment. Ion bombardment is the dominant form of energetic particle bombardment in plasma-assisted etching systems and, even though electrons and photons are known to accelerate gas–surface reactions,[8,9] the present discussion will be limited to the effects of positive ion bombardment. Examples of systems in which substantial etch rate enhancements caused by energetic positive ion bombardment have been seen are Si–F, Si_3N_4–F, SiO_2–F, SiC–F, Si–Cl, C–F, C–O, W–F. The phenomenon is not general in that the etch rate of Al exposed to Cl_2 at room temperature has been shown to be independent of ion bombardment.[10] The Al–Cl_2 system and the Cu–Cl_2 system, which show a large ion-induced suppression of the etch rate, will be discussed later in this paper.

It is apparent that, if the etch rate is increased by energetic ion bombardment, the rates of each of the three steps of etching described above must also increase. However, it is not immediately apparent which of these three steps is *directly* accelerated by energetic ion bombardment. Consider the three possibilities: (A) Ion bombardment directly increases the reaction probability causing an increase in the halogen coverage which, in turn, accelerates the product formation and desorption steps; (B) ion bombardment directly increases the product formation step; the product volatility allows the product desorption step to keep up, resulting in a decrease in the halogen surface coverage which, in turn, causes an increase in the reaction probability (i.e., more clean surface exposed); (C) ion bombardment directly increases the product desorption step decreasing the surface concentration of product which then allows the preceding steps to proceed at a faster rate (assuming that neither of the steps A or B are rate limiting).

Each of these three possibilities has been supported in the literature using the Si–F system as an example: Donnelly and Flamm[11,12] suggest that step A is directly increased by ion bombardment via surface damage; the present authors[4,13-16] suggest that step B is directly increased via ion-assisted product formation or chemical sputtering; and Dieleman and Sanders[17] suggest that step C is directly enhanced via sputtering and/or detrapping. The present paper will describe recent experiments directed towards clarifying this situation and will approach the question from the point of view of the reaction probability and the relevance of halogen coverage. Most of the data presented initially will be for the Si–F system but results from other chemical systems will be discussed later in the paper.

II. EXPERIMENTAL APPARATUS

Most of the experimental data presented in this paper were obtained using a modulated beam mass spectrometric etch product monitoring system which has been described in detail previously.[18] This is a bakable UHV system in which atomically clean, usually single crystal, surfaces can be exposed to well-defined fluxes of chemically reactive neutral species (e.g., XeF_2, Cl_2) and energetic ion beams (e.g., 2 keV Ar^+). A small sample of the etch product evolved from the etched surface is modulated with a mechanical chopper and detected with a quadrupole mass spectrometer. The vacuum chamber containing the mass spectrometer is isolated from

 0734-211X/85/051376-08$01.00

the sample by two stages of differential pumping and a liquid nitrogen-cooled baffle. The sample can be heated[19] in the etching position and Auger analysis of the sample can be carried out away from the etching position.

This arrangement allows the detection of the primary etch products evolved from the surface without any gas phase or wall collisions. In addition, those incident reactive neutral species which are reflected from the sample surface can also be monitored, thus allowing a direct determination of the reaction probability. For a detailed discussion see Ref. 18. (The term reaction probability is defined here as the probability that an incident gas phase species forms a chemical bond with the surface species. This is often referred to as the sticking coefficient. The back reaction, where chemically bonded species react to re-form the incident gaseous species, is assumed to be negligibly small.)

In this work, as in previous studies,[4,13,14] XeF_2 gas will be used as a source of reactive fluorine. The results obtained with XeF_2 cannot be *quantitatively* extended to F atoms, as has been pointed out,[20,21] but we believe the phenomena of major importance in the Si–XeF_2 system will also be of major importance in the Si–F system.

III. RESULTS AND DISCUSSION

A. Influence of energetic ion bombardment on the reaction probability for XeF_2 on Si

As was mentioned earlier, the fact that ion bombardment of a Si surface during exposure to XeF_2 causes a large increase in the etch rate requires in turn a similar increase in the reaction probability. A direct measurement of this is presented in Fig. 1, which shows the intensity of XeF_2 reflected from a Si(100) surface with and without 2 keV Ar^+ ion bombardment. Without ion bombardment, essentially all the XeF_2 is reflected from this sample (reaction probability is close to zero) whereas with ion bombardment no reflected XeF_2 can be seen (reaction probability ~ 1).

There are several ways in which one can explain the fact that energetic ion bombardment results in an increase in the reaction probability for XeF_2 on Si. Some of these processes can be thought of as direct effects in that they could result in a larger coverage of fluorine on the Si surface. These include the previously mentioned damage mechanism,[11,12] ion-induced reordering of the surface structure, ion-induced dissociation of physisorbed XeF_2[22] and the sputter removal of surface contaminants. In contrast, the reaction probability can also be increased indirectly by accelerating subsequent surface chemical processes which will cause a decrease in the halogen coverage (e.g., product formation and/or product desorption). In a large number of gas–surface systems a decrease in the gas coverage is accompanied by an increase in the reaction probability.

Considerable insight as to the importance of these various possibilities can be derived from a sequential exposure of a surface to fluxes of ions and reactive neutral species. For example, the sequence of fluorination of the Si surface followed by ion bombardment (in the absence of incident gas phase XeF_2) provides a condition where no physisorbed XeF_2 can be present on the surface, and, if the etch yield is measured during the ion bombardment, a measure of the efficiency of the ion bombardment for decreasing the fluorine coverage can be obtained. This measurement has been carried out using quartz crystal microbalance methods in a separate system[13,14] and the result is shown in Fig. 2. This figure is a plot of the mass removed per incident 1 keV Ar^+ ion following a large exposure (adequate to cause spontaneous etching) of an amorphous Si thin film to F_2. Note that at the onset of ion bombardment (high F coverage) the mass yield is in excess of 3000 amu/ion which is equivalent to about 30 SiF_4 molecules/ion. This large yield is comparable to the yields observed during simultaneous exposure of the Si surface to the ion beam and a XeF_2 flux[4,13] and has been obtained under conditions where no physisorbed species were on surface and where no effects of ion bombardment were present. (The ion dose required to measure the first yield point was less than about 2×10^{12} 1 keV Ar^+

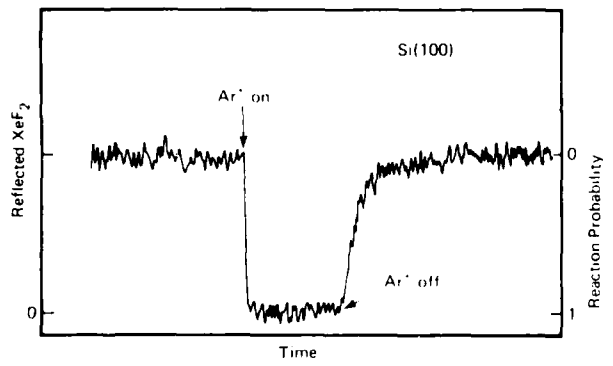

FIG. 1. The intensity of reflected XeF_2 molecules from a Si(100) surface as influenced by a 2 keV Ar^+ ion beam. Ar^+ current density $\sim 3.8\,\mu A/cm^2$, XeF_2 flux $\sim 3\times10^{13}$ mol/cm^2 s (estimated).

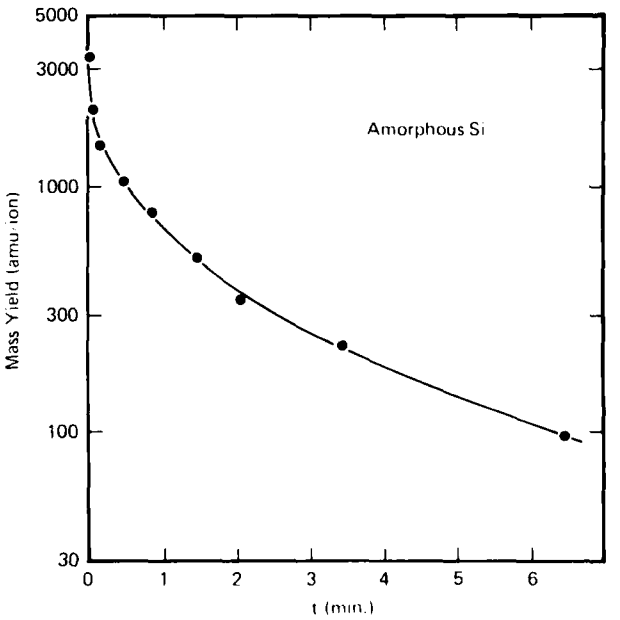

FIG. 2. The mass yield per 1 keV Ar^+ ion, determined using quartz microbalance methods, as a function of the time of ion bombardment from an amorphous Si thin film which had been previously exposed to a large dose of F_2 gas. No F_2 was present in the system during this measurement. Ar^+ current density $= 1.0\,\mu A/cm^2$.

ions/cm^2 and the Si was etched during the preceding F_2 exposure to remove any consequences of prior ion bombardment.)

The results of a second sequential experiment carried out in the modulated molecular beam system using a Si(100) single crystal sample are shown in Fig. 3. In this experiment, during the time $t < 200$ s, the Si was exposed to an XeF_2 flux only. At $t = 200$ s the XeF_2 flux was terminated leaving a fluorinated surface with no ion-induced damage. At $t = 400$ s a 2 keV Ar^+ beam was turned on causing a burst of SiF_4 to be formed and desorbed from the fluorinated surface. This type of burst is generally much larger than observed from this particular sample. At $t = 600$ s the ion beam was turned off and the XeF_2 turned on in as rapid a fashion as possible ($\sim$1 s delay). At this point the Si surface has been exposed to 5×10^{15} ions/cm^2 of 2 keV Ar^+ and is heavily damaged. However, the etch rate of this damaged surface as judged by the SiF_3^+ peak intensity at $t > 600$ s is not larger; in fact, it is smaller than the etch rate of the undamaged surface ($0 < t < 200$ s). Now at $t = 940$ s the 2 keV Ar^+ beam is switched on while continuing the XeF_2 exposure. Note that the etch rate increases immediately to a large value. The ion dose required to obtain this rapid increase is less than 3×10^{13} 2 keV Ar^+ ions/cm^2; a dose which is not expected to cause significant lattice damage. Finally at $t = 1140$ s the ion beam is turned off (the XeF_2 flux is left on) and the etch rate drops very rapidly to the value observed initially ($0 < t < 200$ s). If damage were important at $t = 1140$ s, one would expect a slower decrease in the etch rate as the damaged layer is etched away, as has been reported previously for the W(111)–XeF_2 system.[23]

Whereas repetitive measurements, under identical conditions, of the phenomena shown in Fig. 3 were very reproducible, subsequent measurements on different samples with minor apparatus changes showed some distinct differences. For almost all situations, the etch rate at $t = 600$ s was smaller than it was at 200 s. However, for some samples the rate would increase in the period between 600 and 800 s so that it became larger than at 200 s. Moreover, the rate decrease at 1140 s would sometimes exhibit a significant tail. These differences, which can be interpreted in terms of subsurface damage effects, synergistic effects involving lattice damage and sorbed fluorine, or possible reordering of the lattice structure, are not dominant as is demonstrated using direct measurements of the reaction probability as shown in Fig. 4.

Figure 4 is a plot of the reflected XeF_2 intensity from Si(100), first without ion bombardment ($150 < t < 300$ s), then with 2 keV Ar^+ bombardment ($300 < t < 450$ s) and finally without the ion beam again ($t > 450$ s). The XeF_2 intensity reflected from SiO_2, which is not etched by XeF_2,[20,21,24] is included ($0 < t < 150$ s) as a reference for unity reflection or zero reaction probability (for a description of the experiment see Ref. 18). This result should be compared with Fig. 1. Figures 1 and 3 were recorded on the same sample and the following differences can be seen: (a) The reaction probability for XeF_2 on undamaged Si(100) is significantly greater than zero in Fig. 4, whereas in Fig. 1 the reaction probability was essentially zero within the accuracy of this measurement. (b) The reaction probability following the ion bombardment (in Fig. 4) is slightly larger than before ion bombardment and tends to increase slightly ($t > 450$ s). Note in Fig. 1 the reaction probability returned to zero quite rapidly after the ion bombardment was stopped. The reason for the differences between Figs. 1 and 4 is not known and further work is planned to clarify this situation. However, these effects are small compared to the direct effect of ion bombardment during which the reaction probability goes to one (reflection coefficient is zero) in both Figs. 1 and 4. Thus the conclusions which are drawn from these sequential experiments are valid in general for this Si(100)–XeF_2 system and are not influenced by the unexplained differences between Figs. 1 and 4. Similar results have also been observed for a variety of Si(100) and Si(111) crystals with different doping levels.

These conclusions are (a) The enhanced Si etching caused

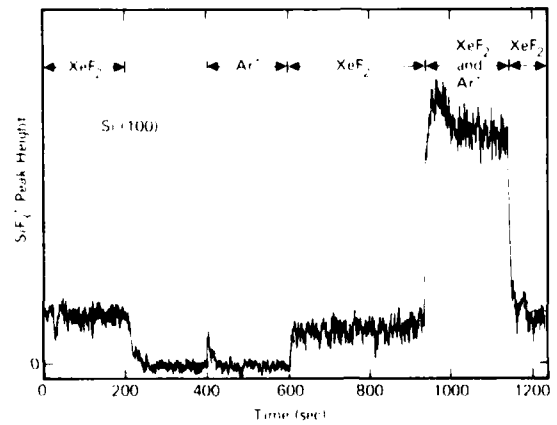

FIG. 3. The SiF_3^+ signal (indicative of SiF_4 etch product) monitored by modulated beam mass spectrometry, during sequential exposure of Si(100) to XeF_2 neutral molecules and 2 keV Ar^+ ions. Ar^+ current density ~ 3.8 μA/cm^2, XeF_2 flux $\sim 1.3\times10^{15}$ mol/cm^2 s (estimated). This Si(100) crystal is identical to that used for Fig. 1.

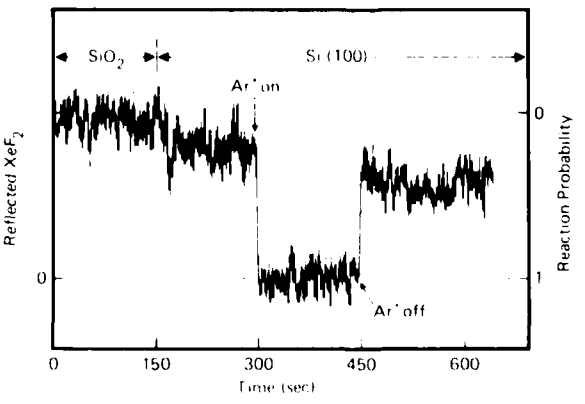

FIG. 4. The intensity of reflected XeF_2 molecules from a Si(100) surface as influenced by a 2 keV Ar^+ ion beam. The intensity of XeF_2 reflected from a SiO_2 surface is included as a reference for total reflection. The sample used in this measurement was a different Si(100) crystal than that used in Fig. 1 but with no known differences (see text for discussion). XeF_2 flux $\sim 1.4\times10^{15}$ mol/cm^2 s (estimated). Reflected XeF_2 was determined from the intensity of the XeF_2^+ peak.

by energetic ion bombardment in the presence of a flux of XeF_2 cannot be explained in terms of surface damage to the Si or ion-induced reordering of the Si surface. Even in the case of W where damage-enhanced chemistry has been clearly seen,[23] the enhancement of etching caused by ion bombardment cannot be attributed to surface damage under most conditions. (b) No significant impurities were seen with Auger spectroscopy at any stage of the experimental sequences in Figs. 3 and 4, and therefore the ion-enhanced etching cannot be attributed to the sputter removal of impurity species. (c) The ion-impact-induced dissociation of physisorbed XeF_2[22] is rejected as a major factor because (i) the very high etch yields (i.e., ~ 20 Si atoms removed per ion requiring > 50 F atoms) cannot be accounted for with such a mechanism; (ii) no Xe was ever detected on the surface with Auger spectroscopy during XeF_2 etching conditions[24]; (iii) the ion etch yield on a prefluorinated surface is very large (Fig. 2) and no physisorbed species are present in this situation.

Therefore the large increase in the reaction probability for XeF_2 on Si(100) caused by energetic ion bombardment as illustrated in Figs. 1 and 4 must be attributed to a reduction in the fluorine coverage caused by an ion-induced acceleration of the product formation–product desorption steps. Moreover, arguments presented previously indicate that the product desorption step is not rate limiting. In other words, neither physical sputtering nor detrapping is the dominant factor in the ion-enhanced chemistry involving fluorine and silicon.

A measurement of the dependence of the reaction probability for XeF_2 on Si(100) as a function of coverage can be derived from the data presented in the time interval $100 < t < 200$ s in Fig. 5. Figure 5 is a plot of the reflected XeF_2 signal versus the time after the XeF_2 gas flux is turned on at $t = 100$ s. The upper trace (a) is for a fully fluorinated surface on which the reaction probability for XeF_2 is essentially zero [this data was recorded using the Si(100) sample used in Figs. 1 and 3]. The lower plot (b) is for a Si(100) surface previously cleaned by 2 keV Ar^+ bombardment and therefore heavily damaged. The shape of the "reaction probability-coverage curve" derived from the difference in these curves is shown in curve (a) in Fig. 6 where the uncertainty in the absolute XeF_2 flux precludes a quantitative assignment of coverage. This result in Fig. 6 is consistent with the notion that a decrease in fluorine coverage induced by ion bombardment will cause an increase in the reaction probability and therefore an increase in the etch rate.

It should be noted that curve (a) was obtained on a damaged surface and nothing has been shown here which would require that the *low coverage* reaction probability is not influenced by damage. For example, curve (b) is a hypothetical result for a damage-free surface. Our data has been concerned with the high coverage, spontaneous etching region where damage does not appear to play a dominant role. It would seem possible that the damaged surface condition could have some relevance in practical reactive ion etching environments where energetic ion bombardment of the wafer surface is occurring.

Finally, chemisorption has generally been believed to proceed through precursors (i.e., mobile species which are weakly bound to the surface) when the sticking probability is found to be relatively independent of coverage near the origin. This behavior is clearly demonstrated in Fig. 6 and therefore it is reasonable to assume that XeF_2 is first adsorbed into a weakly bound, mobile state after which it dissociates and becomes chemisorbed.

B. Fluorine coverage during the etching of Si and its implications

There is limited direct experimental verification of the conclusion reached above that ion bombardment of a Si surface exposed to XeF_2 causes a decrease in the fluorine surface coverage. Efforts to monitor the fluorine coverage during etching with Auger spectroscopy in this laboratory have been hindered by electron-stimulated reactions and desorption. However, Barker *et al.*[25] have monitored the chlorine concentration on Si during exposure to Cl_2 and energetic argon ions. Their data show a strong decrease in the Cl coverage with increasing ion-to-neutral flux ratio. This result is consistent with the discussion of the preceding section.

Many of the phenomena and parameters in both plasma-assisted etching and the beam studies can be unified *qualita-*

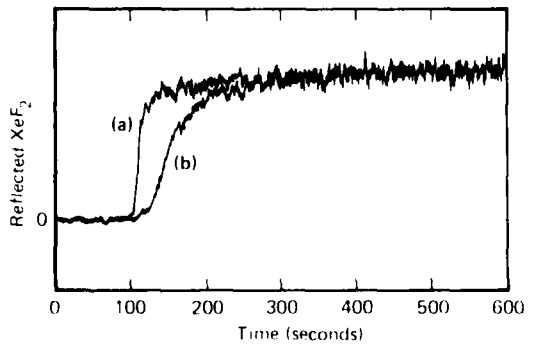

FIG. 5. The intensity of reflected XeF_2 molecules as a function of time from (a) Si(100) which was previously fluorinated; (b) the same Si(100) crystal but after cleaning with 2 keV Ar^+ ion bombardment. The XeF_2 flux was initiated at $t = 100$ s.

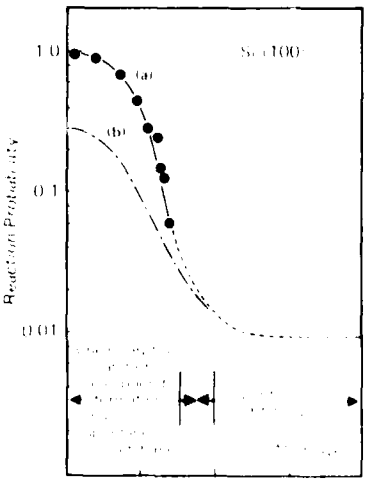

FIG. 6. The reaction probability for XeF_2 on Si(100) as a function of fluorine coverage. Curve (a) was obtained from the data of Fig. 5. Curve (b) was a hypothetical result for a damage-free surface which may differ from the damaged surface data [curve (a)] in the low coverage region. The XeF_2 flux uncertainty precludes quantitation of the coverage scale but the data points are believed to extend to at least one monolayer.

tively by introducing fluorine coverage as a generalizing parameter. This concept is illustrated in Fig. 7. The labels on the coverage axis are intended only as a *qualitative guide*. The coverage is to be thought of as a time-averaged coverage in that the coverage is decreased locally by an ion impact and builds up prior to the arrival of the next ion. Thus clearly the average coverage is determined by the ion-to-neutral flux ratio as shown by Barker *et al.*[25] The values of the coverage at which the transitions occur in this figure are not well known but there is some significance to the placement of these shaded transition regions in Fig. 7. For example, the analysis of fluorinated Si surfaces[26,27] (in the absence of the fluorinating flux) shows clearly that more than a monolayer of fluorine can be present with no spontaneous etching. In contrast, ion-induced volatile product formation is expected to occur at average coverages significantly less than a monolayer (note that the coverage at the time of an individual ion impact will be larger than the average coverage). Some measurements supporting this conclusion have been presented previously.[14] As another example of the significance of shaded areas, physical sputtering will be dominant only at very low average coverages (i.e., very large energetic ion/neutral flux ratios).

The fact that the average fluorine coverage on Si during ion-assisted etching can be less than the coverage required for spontaneous etching contradicts an assumption made often[4,13,28] in the determination of the ion-assisted component of the etch rate. It is usually assumed that the "Total Etch Rate" = "Spontaneous Etch Rate" + "Ion-assisted Etch Rate" where the total etch rate is measured with ion bombardment and neutral species incident simultaneously and the spontaneous etch rate is measured with only the neutral species arriving at the surface. It is our contention that these phenomena cannot be rigorously decoupled in this way in that the spontaneous etch rate, measured in the absence of ion bombardment, is a high coverage etch rate whereas the coverage prevailing during the total etch rate measurement may be much less. If this were the case, the spontaneous etch rate could be zero during ion bombardment.

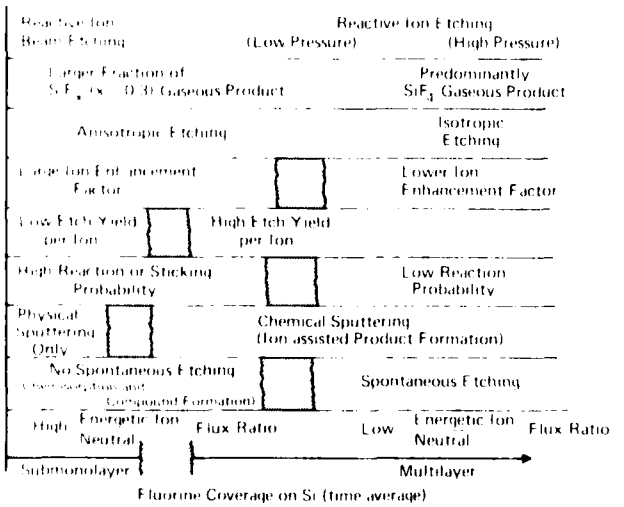

FIG. 7. The qualitative behavior of various parameters and processes in the ion-assisted etching of Si as a function of fluorine coverage. All transition regions are only approximate. This figure summarizes the authors' view as to a framework for interpreting a large quantity of etching data.

The dependence of reaction probability on coverage was discussed in connection with Fig. 6. The etch yield per ion will vary from a sputtering yield at very low coverage to the very large yield shown in Fig. 2 for a surface containing fluorine in the multilayer regime. The yield as a function of coverage in the lower coverage regimes has been presented previously.[14] The ion enhancement factor is defined as the etch rate with ion bombardment divided by the etch rate without ion bombardment (spontaneous etch rate) and will approach unity as the neutral flux becomes very large compared to the ion flux. For example, when a microscopic region of the surface suffers an energetic ion impact, the fluorine coverage in this small area will be depleted by the ion-induced formation of volatile product (SiF_4). The critical factor is the time required for this small region to refluorinate relative to the time of the next ion impact. When this refluorination time is very short compared to the mean time between ion impacts in this microscopic area, the average fluorine coverage will be large, and spontaneous etching will be dominant. In the Si–F system the neutral flux of F atoms (or XeF_2) must be very much larger (three or four orders of magnitude) than the ion flux (assuming ion energies are at least several hundreds of eV) if the spontaneous etch rate is to become approximately equal to the etch rate with ion bombardment. This is a result of the very large etch yields (~ 30 Si atoms/ion corresponding to about 100 F atoms/ion for 1 keV Ar^+ ions) and the low reaction probability for fluorine-containing species on fully fluorinated Si surfaces.[29]

It is clear that anisotropic etching can be obtained in the Si–XeF_2 system via ion-enhanced gas–surface chemistry if the ion-to-neutral flux ratio is large enough.[30] It is our contention that this conclusion can be extended to the Si–F system in a qualitative way. This extension has been criticized in the literature.[20,21] However, it is not clear as to what extent ion-enhanced gas–surface chemistry of the Si–F system is responsible for the etching directionality which is obtained in a real reactive gas glow discharge etching system. The reason for this uncertainty is that in most plasma environments, in addition to the etching species, there is a flux of condensible species incident on the wafer surface. Often these species are unsaturated halocarbon radicals (e.g., CF_2) created by dissociation of the discharge gas and which lead to the deposition of polymeric material on surfaces.[31] If the discharge gas does not contain carbon (e.g., SF_6, NF_3), these same species can be created by the dissociation of the products of photoresist etching. These condensing species are effectively removed from the bottom of an etched feature (presumably by ion-enhanced gas–surface chemistry of the CF_x–F system) but tend to block the etching of sidewalls.[32] It is very difficult, in real plasma systems, to be sure that such a blocking action is not contributing in some way to directional etching.

Finally, it is apparent that the nature of the primary etch product will depend on the fluorine coverage, ranging from predominantly elemental Si in the zero and very low coverage range where physical sputtering is the major erosion pro-

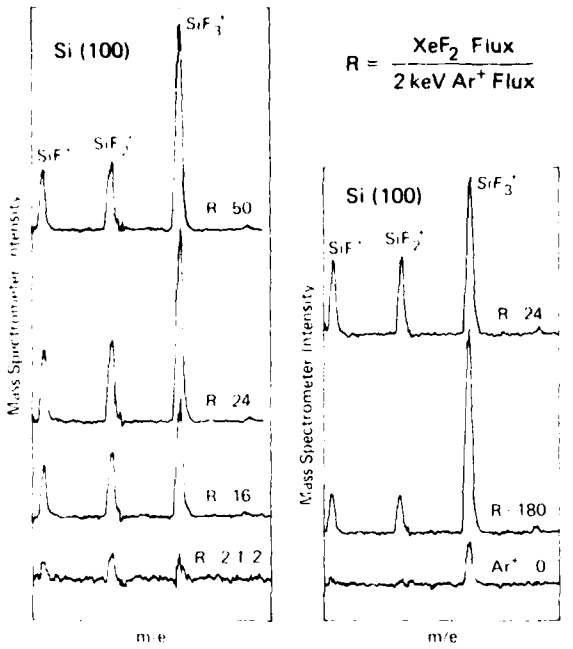

FIG. 8. Product distribution as measured with molecular beam mass spectrometry during the ion-assisted etching of Si(100) with XeF_2 and 2 keV Ar^+ ions for several values of the XeF_2/Ar^+ flux ratio. The approximate XeF_2/Ar^+ flux ratios are indicated on the right of each curve. Ionizing electron energy = 30 eV.

cess to predominantly SiF_4 at high coverages. Figure 8 shows product mass spectra obtained with modulated beam mass spectrometry in the Si–XeF_2 system for several values of the XeF_2-to-Ar^+ flux ratio. These results are combined with some other data in Fig. 9 to show the dependence of product stoichiometry on this incident flux ratio. In Figs. 8 and 9, the SiF_3^+ peak is representative of SiF_4 etch product, the SiF_2^+ peak is representative of SiF_2 etch product, and the SiF^+ peak is formed from both SiF and SiF_2 etch products.

C. Influence of ion bombardment on the etching of other gas–solid systems

As was mentioned in the Introduction, not all gas–solid systems show an increase in the etch rate when ion bombardment is superimposed on a purely chemical etching process. Smith and Bruce[10] showed that ion bombardment did not influence the etch rate of clean Al exposed to the effluent of a Cl_2 plasma. Furthermore, these workers showed that Cl_2 molecules alone (i.e., with no plasma) etch aluminum effectively. The etch product which is evolved from aluminum exposed to Cl_2 at room temperature is primarily Al_2Cl_6.[18] In Fig. 10, this Al_2Cl_6 etch product is monitored with our modulated beam mass spectrometer system as an Al(100) single crystal is exposed to sequential fluxes of Cl_2 neutral molecules and 2 keV Ar^+ ions (this sequential procedure is identical to that shown in Fig. 3 for the Si–XeF_2 system). In Fig. 10, note that, at $t = 800$ s when the Ar^+ beam is turned on in the presence of the Cl_2 flux, the $Al_2Cl_5^+$ peak intensity decreases slightly. Moreover, a complete mass spectrum taken under these conditions indicates no significant enhancement for any etch product. Much larger ion-induced suppression of the etch rate has been observed in this Al(100)–Cl_2 system when the Ar^+/Cl_2 flux ratio is increased. Among the possible interpretations, the decrease in the $Al_2Cl_5^+$ signal in the time interval $800 < t < 1000$ s in Fig. 10 could be caused by an increase in the velocity of the desorbed product species. The sensitivity of the ionization chamber of the mass spectrometer depends on the reciprocal of the particle velocity and it has been shown[33] that, for the Si–XeF_2 system, a fraction of the product species have velocity distributions similar to those found for weakly bound sputtered species. Our views as to the implications of this observation with regard to the relative importance of chemical sputtering, physical sputtering, and damage-enhanced chemistry have been discussed previously.[16]

Another system in which ion bombardment suppresses the etch rate is the Cu–Cl_2 system at temperatures above about 175 °C. In the temperature range $175\ °C < T < 600\ °C$, the dominant etch product evolved when Cu is exposed to Cl_2 is the trimer Cu_3Cl_3.[34] When a Cu(100) crystal at 310 °C is subjected to sequential fluxes of Cl_2 and Ar^+, the intensity of the $Cu_3Cl_3^+$ signal responds as shown in Fig. 11. Note the very large suppression in the time interval $800 < t < 1020$ s as the Ar^+ ion beam is superimposed on the Cl_2 flux. As was the case for the Al(100) crystal, no new product species were observed during this simultaneous exposure to both Cl_2 and

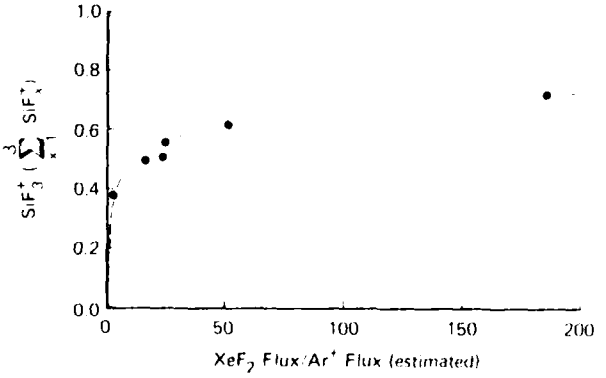

FIG. 9. The product distribution evolved during ion-assisted etching of Si(100) with XeF_2 molecules and 2 keV Ar^+ ions as a function of the estimated XeF_2/Ar^+ flux ratio. The data from Fig. 8 is included in this plot.

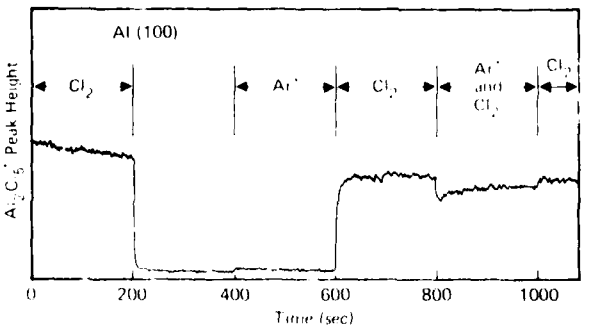

FIG. 10. The $Al_2Cl_5^+$ peak height, monitored by molecular beam mass spectrometry, during sequential exposure of Al(100) to Cl_2 molecules and 2 keV Ar^+ ions (Ar^+ current density = 4 $\mu A/cm^2$, Cl_2 flux = 2×10^{14} mol/cm^2 s (estimated)).

Ar^+ and therefore the ion bombardment has decreased the etch rate as shown in Fig. 11. This decrease is considered to be much too large to be accounted for by changes in the product velocity distribution.

Two possible reasons for this ion-induced suppression of the chemical etching of Cu by Cl_2 can be suggested: (i) The ion beam decreases the surface concentration of chlorine by sputtering chlorine atoms or molecules from the surface to the point where there is insufficient chlorine to form the volatile Cu_3Cl_3 species, or (ii) the ion bombardment dissociates either the trimer itself before it desorbs from the surface, or precursors to the formation of the trimer (e.g., the Cu_2Cl_2 dimer).

The effects of ion bombardment on the etching of polycrystalline Nb by XeF_2 has also been studied with molecular beam mass spectrometry. XeF_2 etches Nb spontaneously at room temperature and the dominant etch product is NbF_5.[18] Electron impact ionization of NbF_5 produces a large NbF_4^+ peak with various other smaller fragments. In this work the NbF^+ peak was used as a monitor of NbF_5 because of a mass interference between NbF_4^+ and $^{131}XeF_2^+$. The results of exposing a polycrystalline Nb surface to sequential fluxes of XeF_2 gas and Ar^+ ions are shown in Fig. 12. The two curves in Fig. 12 are for different fluxes of the XeF_2 gas (i.e., different values of the ion-to-neutral flux ratio) and, in the time interval $800 < t < 1000$ s, a small ion-induced etch rate enhancement is seen with a large XeF_2 flux (lower curve), whereas the ion bombardment clearly decreases the NbF^+ peak in the low XeF_2 flux case (upper curve). This decrease in the NbF^+ signal with ion bombardment ($800 < t < 1000$ s) could be, all or in part, a result of an increase in the product energy distribution. The relatively small ion enhancement (lower curve in Fig. 12, $800 < t < 1000$ s) is consistent with the directly measured reaction probability of about 0.7 on a fully fluorinated Nb surface,[18] i.e., a large increase in the steady state etch rate due to ion bombardment is impossible when the reaction probability in the absence of ion bombardment is already large. The long transient decay of the etch product after the termination of the XeF_2 flux ($200 < t < 400$ s) is a real effect which has been discussed previously.[18]

The relative importance of ion-assisted product formation or chemical sputtering can be derived from Figs. 3 and 10–12

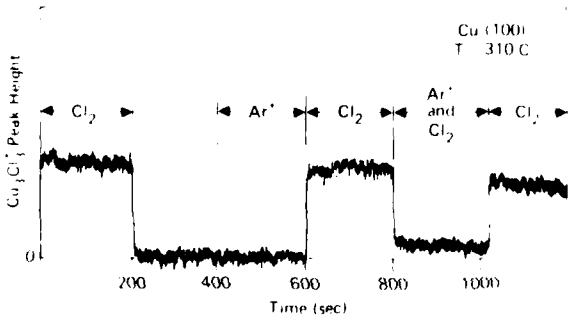

FIG. 11. The $Cu_3Cl_3^+$ peak evolved from a Cu(100) surface at $T = 310$ °C during sequential exposures to Cl_2 neutrals and 2 keV Ar^+ ions. Ar^+ current density $\sim 3.2\ \mu A/cm^2$, Cl_2 flux $\sim 7.2 \times 10^{14}$ mol cm^{-2} s (estimated)

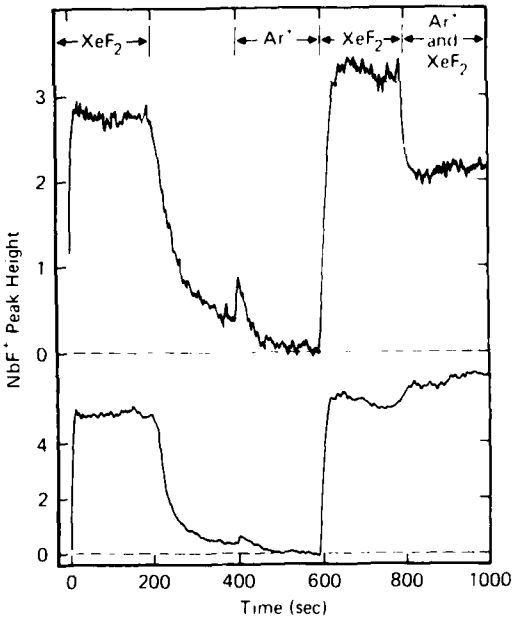

FIG. 12. The NbF^+ peak (used to monitor the NbF_5 etch product) evolved from a polycrystalline Nb surface during sequential exposures to XeF_2 molecules and 2 keV Ar^+ ions. Ar^+ current density (upper curve) $\sim 10\ \mu A/cm^2$, (lower curve) $\sim 10\ \mu A/cm^2$, XeF_2 flux (upper curve) $\sim 4 \times 10^{14}$ mol/cm^2 s; (lower curve) $\sim 2 \times 10^{15}$ mol/cm^2 s.

by comparing the product intensities when ion bombardment is initiated on a surface which has been previously exposed to a halogen flux (i.e., at $t = 400$ s in these four figures). Note that for Si (Fig. 3) and for Nb (Fig. 12) there is an easily observable burst of desorbed product at $t = 400$ s. In the Al case (Fig. 10) the desorbed product is barely observable, whereas for Cu (Fig. 11) no evidence of desorbed product can be seen.

Finally the importance of surface damage in the chemical etching process for these four materials' systems can be assessed by comparing the product intensity from a damage-free surface ($t < 200$ s in Figs. 3 and 10–12) to the product intensity when a heavily damaged surface is exposed to the flux of etching species ($t > 600$ s in Figs. 3 and 10–12). No significant difference in the intensity of the product species can be seen for Si(111), Al(100), Cu(100) or polycrystalline Nb. Previously a large effect of damage was seen with W(111) exposed to XeF_2.[17]

IV. SUMMARY AND CONCLUSIONS

Experimental results are presented which lead to the conclusion that the ion-bombardment-induced enhancement of the etch rate of Si exposed to fluorine is a result of a decrease in the fluorine coverage on the Si surface caused by ion-assisted product formation. Some subtle effects possibly attributable to surface damage were seen but these effects were never dominant. The importance of the fluorine coverage in ion-assisted etching is emphasized and a qualitative discussion is presented relating fluorine coverage to characteristics of the ion-assisted etching process such as ion etch yield, reaction probability, and product stoichiometry. In this con-

nection, a concern is expressed regarding the suitability of the assumption that the total etch rate can be expressed as a sum of a spontaneous etch rate and an ionic contribution. It is our contention that ion-assisted formation of a weakly bound product is the process directly accelerated by ion bombardment in the Si–F system. The weakly bound product desorbs thus producing etching. The entire process is often called chemical sputtering. The factors to be considered in distinguishing physical sputtering and chemical sputtering have been discussed previously.[16] Finally, it is emphasized that these conclusions are not readily extended to other chemical systems and some examples are given.

ACKNOWLEDGMENTS

The authors are very appreciative of the valuable technical skills of D. A. Pearson and R. W. Sadowski which were required in order that this work could be accomplished. Continuing valuable discussions with colleagues E. Kay, T. J. Chuang, P. S. Bagus, and F. A. Houle are gratefully acknowledged.

[1]N. Hosokawa, R. Matsuzaki, and T Asamaki, Jpn. J. Appl. Phys., Suppl. 2, Pt. 1, 435 (1974).
[2]G. C. Schwartz, L. B. Zielinski, and T. Schopen, in *Etching*, edited by M. J. Rand and H. G. Hughes, Electrochemical Society Symposium Series (Princeton, New Jersey, 1976), p. 122.
[3]L. Holland and S. M. Ojha, Vacuum **26**, 53 (1976).
[4]Y.-Y. Tu, T. J. Chuang, and H. F. Winters, Phys. Rev. B **23**, 823 (1981).
[5]H. F. Winters, J. Appl. Phys. **49**, 5165 (1978).
[6]P. S. Bagus, presented at Symposium: Plasma Synthesis and Etching of Electronic Materials, November 1984, Boston, Massachusetts, Materials Research Society Proceedings, p. 179; M. Seel and P. S. Bagus, Phys. Rev. B **28**, 2023 (1983).
[7]H. F. Winters, J. W. Coburn, and T. J. Chuang, J. Vac. Sci. Technol. B **1**, 469 (1983).
[8]J. W. Coburn and H. F. Winters, J. Appl. Phys. **50**, 3189 (1979).
[9]T. J. Chuang, Surf. Sci. Rep. **3**, 1 (1983); M. Sekine, H. Okano, and Y. Horiike, in *Proceedings of the Fifth Symposium on Dry Processes*, Tokyo, Japan, 1983 (Institute of Electrical Engineers of Japan, Tokyo, 1983), p. 97; F. A. Houle, J. Chem. Phys. **80**, 4851 (1984).
[10]D. L. Smith and R. H. Bruce, J. Electrochem. Soc. **129**, 2045 (1982).
[11]V. M. Donnelly and D. L. Flamm, Solid State Technol. **24** (4), 161 (1981).
[12]D. L. Flamm and V. M. Donnelly, Plasma Chem. Plasma Process **1**, 317 (1981).
[13]U. Gerlach-Meyer, J. W. Coburn, and E. Kay, Surf. Sci. **103**, 177 (1981).
[14]E.-A. Knabbe, J. W. Coburn, and E. Kay, Surf. Sci. **123**, 427 (1982).
[15]J. W. Coburn, Vacuum **34**, 157 (1984).
[16]J. W. Coburn and H. F. Winters, Appl. Surf. Sci. **22/23**, 63 (1985).
[17]J. Dieleman and F. H. M. Sanders, Solid State Technol. **27** (4), 191 (1984).
[18]H. F. Winters, J. Vac. Sci. Technol. B **3**, 9 (1985).
[19]H. F. Winters, J. Schlaegel, and D. Horne, J. Vac. Sci. Technol. **15**, 1605 (1978).
[20]D. L. Flamm, D. E. Ibbotson, J. A. Mucha, and V. M. Donnelly, Solid State Technol. **26** (4), 117 (1983).
[21]D. E. Ibbotson, D. L. Flamm, J. A. Mucha, and V. M. Donnelly, Appl. Phys. Lett. **44**, 1129 (1984).
[22]U. Gerlach-Meyer, Surf. Sci. **103**, 524 (1981).
[23]H. F. Winters, J. Vac. Sci. Technol. A **3**, 700 (1985).
[24]H. F. Winters and J. W. Coburn, Appl. Phys. Lett. **34**, 70 (1979).
[25]R. A. Barker, T. M. Mayer, and W. C. Pearson, J. Vac. Sci. Technol. B **1**, 37 (1983).
[26]T. J. Chuang, J. Appl. Phys. **51**, 2614 (1980).
[27]F. R. McFeely, J. F. Morar, N. D. Shinn, G. Landgren, and F. J. Himpsel, Phys. Rev. B **30**, 764 (1984).
[28]Y. H. Lee and M.-M. Chen, J. Appl. Phys. **54**, 5966 (1983).
[29]D. L. Flamm, V. M. Donnelly, and J. A. Mucha, J. Appl. Phys. **52**, 3633 (1981).
[30]J. D. Chinn, I. Adesida, and E. D. Wolf, Appl. Phys. Lett. **43**, 185 (1983).
[31]M. M. Millard and E. Kay, J. Electrochem. Soc. **129**, 160 (1982).
[32]J. W. Coburn and H. F. Winters, J. Vac. Sci. Technol. **16**, 391 (1979); P. M. Schaible and G. C. Schwartz, *ibid.* **16**, 377 (1979).
[33]R. A. Haring, A. Haring, F. W. Saris, and A. E. deVries, Appl. Phys. Lett. **41**, 174 (1982).
[34]H. F. Winters, J. Vac. Sci. Technol. A **3**, 786 (1985).

Studies on the mechanism of chemical sputtering of silicon by simultaneous exposure to Cl_2 and low-energy Ar^+ ions

J. Dieleman, F. H. M. Sanders, A. W. Kolfschoten, and P.C. Zalm
Philips Research Laboratories, 5600 JA Eindhoven, The Netherlands

A. E. de Vries and A. Haring
FOM-Institute for Atomic and Molecular Physics, 1098 SJ Amsterdam, The Netherlands

(Received 18 March 1985; accepted 21 May 1985)

The sputtering yield of Si when bombarded with a flux ϕ_{Ar^+} of low-energy Ar^+ ions may be enhanced a few times when the Si surface is exposed simultaneously to Cl_2 fluxes ϕ_{Cl_2} about one order of magnitude larger than ϕ_{Ar^+}. The mechanism of this synergistic etching has been studied, using mass spectroscopy and time-of-flight techniques, for a ϕ_{Ar^+} of about 5×10^{14} Ar^+ $cm^{-2}s^{-1}$ at Ar^+ ion energies (E_p) from 0.25 to 5 keV, Cl_2 fluxes between 10^{15} and 5×10^{16} Cl_2 $cm^{-2}s^{-1}$ and T in the range 300–625 K. As has been shown previously [J. Vac. Sci. Technol. A 2, 487 (1984)] the main products of the synergistic reaction are atomic Si and Cl and molecular SiCl and $SiCl_2$; the kinetic energy distributions of the molecular products consist of two parts, a Maxwell–Boltzmann and a collision cascade-like distribution. The Maxwell–Boltzmann part decreases relative to the collision cascade-like part when T and/or E_p are increased and/or ϕ_{Cl_2} is decreased. At the same time the collision cascade-like part shifts to higher kinetic energies. These observations and the dependence of the relative contributions of the various products on ϕ_{Cl_2}, T, and E_p can be understood from the Ar^+ ion-induced amorphization and Ar^+ ion-induced mixing of adsorbed Cl into the top atomic layers of the Si, in which the molecular products SiCl and $SiCl_2$ are formed and also trapped, without further chemical binding to the surrounding bulk network; and for higher T also by the competition between the thermal reaction, yielding $SiCl_4$ (and $SiCl_2$), and synergistic etching. The yields of the molecular products SiCl and $SiCl_2$ show an increase relative to atomic Si and their binding energies are reduced when ϕ_{Cl_2} is enhanced and/or E_p and/or T are decreased. It is suggested that this is due to an increasing concentration of Cl ion mixed into the top atomic layers of the Si. The experiments also suggest that the binding energy of atomic Si decreases systematically with increasing Cl concentration in the Si. The results show that the etching of Si with Cl_2 under simultaneous Ar^+ ion bombardment is not due to stimulation of the thermal reaction but to chemically enhanced physical sputtering.

I. INTRODUCTION

In the last few years several aspects of the etching of Si by simultaneous exposure to low-energy ion bombardment and Cl_2 have been studied. The aim of these studies was to try to understand the basic mechanisms involved in anisotropic plasma etching with the aid of plasmas containing Cl_2. Bombardment with low-energy noble gas ions during Cl_2 exposure (in particular Ar^+) has attracted the most attention.

Gerlach-Meyer *et al.*[1] observed that the sputtering yield (in Si atoms removed per incoming ion) of vacuum-deposited amorphous Si for perpendicular bombardment with ion beams of Ar^+, Ne^+, or He^+, with energy $E_p = 1$ keV and fluxes $\phi_{Ar^+,Ne^+,He^+} = 3$–$6\times10^{13}$ ions $cm^{-2}s^{-1}$, is enhanced with factors of 5, 4.3, and 13.6, respectively, when the Si is exposed simultaneously to a beam of Cl_2, $\phi_{Cl_2} = 6\times10^{16}$ Cl_2 $cm^{-2}s^{-1}$, at 45° to the surface normal. At this high ϕ_{Cl_2} the yield enhancement is approximately saturated. Although no systematic and quantitative study of the etch products was made, it was suggested that the role of ion bombardment is (a) ion-bombardment induced formation of $SiCl_4$ by the intense short-lived pulse of phonon energy imparted to the surface and near-surface atoms by the ion-surface collision; (b) physical sputtering of $SiCl_x$ ($x = 0$–3), and (c) possibly ion-induced desorption of $SiCl_4$. In view of the relatively low enhancement, physical sputtering (b) is considered to be relatively important. An explanation for the higher enhancement factor for He^+ has not been given. In a subsequent paper[2], Gerlach-Meyer proposed a model in which the enhanced sputter yield is ascribed to excitation of surface SiCl by the ion impact and subsequent reaction with physisorbed chlorine. However, in view of the Si temperature used (viz. 300 K) and the fact that physisorption energies are often at most a few tenths of an eV, the steady state concentration of physisorbed chlorine is (in all probability) too low to make this the main model explaining the enhancement.[3] Okano and Horiike[4] found that exposure of Si to $\phi_{Ar^+} \simeq 3\times10^{15}$ Ar^+ $cm^{-2}s^{-1}$ at $E_p = 0.35$ keV concurrent with $\phi_{Cl_2} \simeq 10^{17}$ Cl_2 $cm^{-2}s^{-1}$ enhanced the sputter yields as compared to purely Ar^+ sputtering. Besides the angular dependence of the etch rate was changed profoundly.

Mayer *et al.*[5,6] monitored the amount of Cl present in the topmost atomic layers of Si, during simultaneous ion bombardment with $\phi_{Ar^+} = 6\times10^{13}$–$3\times10^{15}$ Ar^+ $cm^{-2}s^{-1}$ at $E_p = 0.6$ keV and exposure to $\phi_{Cl_2} = 0$ to 6×10^{16} Cl_2 $cm^{-2}s^{-1}$, by Auger electron spectroscopy (AES). To explain their observations they assumed that the removal of species from the surface can be treated as a per ion event. Further assumptions were that the sticking probability s at

 0734-211X/85/051384-09$01.00

zero coverage is about 0.3 and decreases in proportion to $(1-\theta)$, where θ is the fractional coverage, and that saturation coverage corresponds to 10^{15} Cl cm^{-2}. It is also presumed that Si leaves the surface as Si and $SiCl_4$. With these and other assumptions it appeared that at $\phi_{Cl_2} = 3\times10^{16}$ Cl_2cm^{-2} s^{-1}, θ ranges from 0.8 to 0.2 when ϕ_{Ar^+} is changed from 3×10^{14} to 2×10^{15} Ar^+ cm^{-2} s^{-1}, respectively. For ratios of the product $sx\phi_{Cl_2}/\phi_{Ar^+}$ of 10 to 10^2, θ is relatively insensitive to an increase of E_p. For $\phi_{Ar^+} \simeq 10^{15}$ Ar^+ cm^{-2} s^{-1} an enhancement of about two times is observed when ϕ_{Cl_2} is increased from zero to 6×10^{16} Cl_2 cm^{-2} s^{-1}. In view of the above assumptions the model can only be considered as indicating trends. In agreement with Okano and Horiike[4] the angular dependence of the etch rate is observed to be markedly changed when an Ar^+ ion-bombarded surface is simultaneously exposed to high fluxes of Cl_2. For a possible explanation of the latter phenomenon, reference is made to the fact that ion bombardment can cause considerable lattice disorder in the surface region.

Until recently, no studies had been made on the nature of the products of the reaction of Si with Cl_2 under concurrent Ar^+ ion bombardment [Si(Cl_2, Ar^+)], and on their kinetic energy distributions (EDC). These are indispensable data for developing a more solid qualitative and quantitative model for this synergistic reaction. Last year these data were collected from studies on the Si(Cl_2, Ar^+) reaction for E_p equal to or larger than 1 keV using mass spectroscopy and time-of-flight (TOF) techniques.[7] The main products are found to be atomic Si and Cl and molecular SiCl and $SiCl_2$. For a temperature of 300 K, $\phi_{Ar^+} \simeq 5\times10^{14}$ Ar^+ cm^{-2} s^{-1} at $E_p = 1$ keV and $\phi_{Cl_2} \simeq 5\times10^{16}$ Cl_2 cm^{-2} s^{-1}, the amount of molecular products SiCl and $SiCl_2$ is of the same order of magnitude as that of atomic Si. The EDCs of the molecular products consist of two parts, one of which can be described by a Maxwell–Boltzmann (M–B) distribution at approximately target temperature and the other by a collision cascade-like (C-C) distribution with an average binding energy $[U_0]$[8] of a few tenths of an eV. At $\phi_{Cl_2} \simeq 5\times10^{16}$ Cl_2 cm^{-2} s^{-1} the latter contribution comprises more than 80% of the molecules produced. Thus it appears that under these conditions the main fraction of the molecular products is due to chemically enhanced physical sputtering and not to stimulation of the thermal reaction path leading to $SiCl_4$ and/or $SiCl_2$ by ion bombardment, as has been suggested strongly for the Si(XeF_2, Ar^+) reaction[9–11] and also for Si(Cl_2, Ar^+).[12] We have pointed out that modification of the topmost atomic layers of the Si by ion-bombardment-induced amorphization and incorporation of significant quantities of Cl might play a dominant role in the reaction mechanisms.[7]

Since ion energies in many plasma etch processes are lower than 1 keV[13] we performed studies on Si(Cl_2, Ar^+) for values of E_p substantially below 1 keV. This paper presents data on the effects of varying the value of E_p between 0.25 and 3 keV, that of T between 300 and 625 K and that of ϕ_{Cl_2} between 10^{15} and 5×10^{16} Cl_2 cm^{-2} s^{-1} on the EDCs of the molecular products SiCl and $SiCl_2$ and on the relative contribution of the various products to the removal of Si. On the basis of these and other results a more refined model of the Si(Cl_2, Ar^+) reaction will be developed and presented.

II. EXPERIMENTAL

The experimental setup is shown schematically in Fig. 1. A Si target, the temperature of which can be varied between 300 and 1000 K, is sprayed continuously with a beam of Cl_2 with a flux that can be chosen in the range of $\phi_{Cl_2} = 5\times10^{14}$–$5\times10^{16}$ Cl_2 cm^{-2} s^{-1}. A mass-selected Ar^+ ion beam with $E_p = 0.25$–6 keV and a flux of 2 to 5×10^{14} Ar^+ cm^{-2} s^{-1}, respectively, strikes the target at an angle of 60° to the normal. Neutral products leaving the target perpendicularly within a solid angle of 10^{-4} sr are mass-analyzed by a quadrupole filter. As has been resumed in the introduction, the neutral molecular products $SiCl_2$ and SiCl are hardly fragmented in the ionization chamber of the mass spectrometer. This means that the effects of E_p, T, and ϕ_{Cl_2} on the behavior of the neutral products $SiCl_2$, SiCl, Si, Cl, and Ar can be inferred from the influence of these parameters on the corresponding ion fluxes in the mass spectrometer. To determine the relative contribution of the various neutral products, the measured ion fluxes should be corrected for, e.g., the differences in transmission of the quadrupole filter for the various ions and the cross section for electron impact ionization. The latter depends, among other things, on the velocity distribution with which the neutrals traverse the ionization chamber. As our interest is focused here on the relative change in the contribution of the various neutral products, only certain velocity distribution corrections will

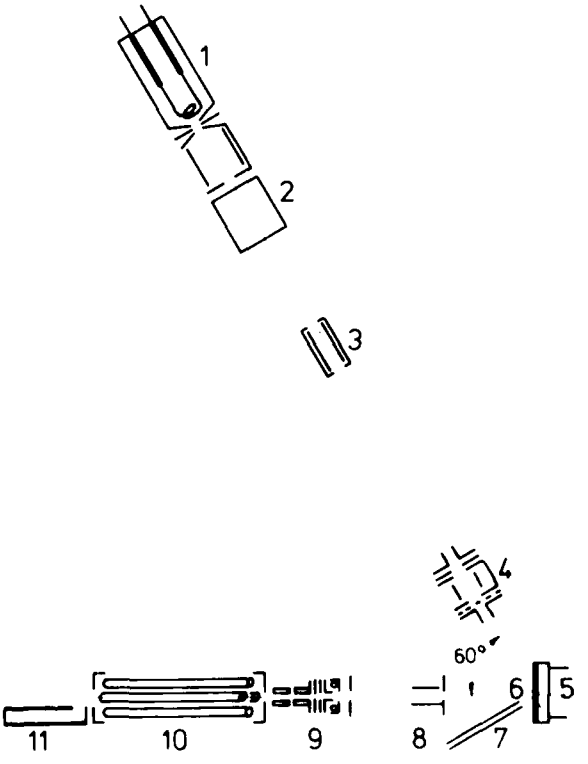

FIG. 1. Schematic, not to scale, experimental setup: (1) Ar^+ ion source, (2) Wien filter, (3) electronic beam modulator, (4) decelerator, (5) oven annex target holder, (6) Si target, (7) Cl_2 gas inlet, (8) diaphragm and deflection plates, (9) ionizer, (10) quadrupole mass filter, and (11) magnetic electron multiplier

be indicated. By electronically chopping the Ar^+ ion beam at 5 Hz and using lock-in techniques at the mass spectrometer, background contributions are reduced. All experiments described below were performed in steady-state conditions, i.e., with large fluences. TOF distributions of the neutrals produced by the $Si(Cl_2, Ar^+)$ reaction were measured by a correlation method[14] and corresponding EDCs were computed.[8] A more detailed description of the apparatus will be published separately.[15,16] The experimental setup allows discrimination between ion bombardment-induced and thermal reactions. This paper will deal with the ion bombardment induced ones. Secondary ions leaving the Si target are prevented from entering the mass spectrometer by a set of deflection plates (see Fig. 1).

III. RESULTS

A. EDCs of the products as a function of E_p, ϕ_{Cl_2}, and T

In our earlier paper[7] in which we discussed the dependence of the EDCs of Ar, SiCl, and $SiCl_2$ on T in the range between 300 and 800 K and on E_p for 1 and 3 keV at constant $\phi_{Cl_2} = 5\times10^{16}$ Cl_2 cm^{-2} s^{-1}, the results were illustrated with figures for $SiCl_2$. The effects were qualitatively the same for both SiCl and $SiCl_2$. As this is also observed for the lower E_p values used in the present investigation we will restrict most of the discussion to the results obtained for SiCl and illustrate them with figures for this neutral product.

Two typical examples of the effect of changing E_p and T are illustrated in Figs. 2 and 3, respectively. Figure 2 illustrates the changes in the EDC of the neutral product SiCl when E_p is increased from 0.25 to 5 keV at constant $\phi_{Cl_2} = 5\times10^{16}$ Cl_2 cm^{-2} s^{-1} and $T = 300$ K. Increasing T at constant E_p and ϕ_{Cl_2} or decreasing ϕ_{Cl_2} at constant E_p and T has similar effects. How large the changes are when both E_p and T are increased simultaneously from 0.25 to 3 keV and from 300 to 625 K, respectively, at $\phi_{Cl_2} = 5\times10^{16}$ Cl_2 cm^{-2} s^{-1}, is illustrated in Fig. 3. Generally, the effect of increasing E_p or T and decreasing ϕ_{Cl_2} is a relative increase of the C-C contribution with respect to the M–B part. At the same time the former contribution continuously shifts to higher kinetic energies and the high-energy cutoff steepens. Enhancement of T causes a corresponding shift of the M–B part to higher kinetic energies. Figure 3 shows a feature typical of conditions with low ϕ_{Cl_2}, high E_p, and T (viz. the development of a hump at higher kinetic energies).

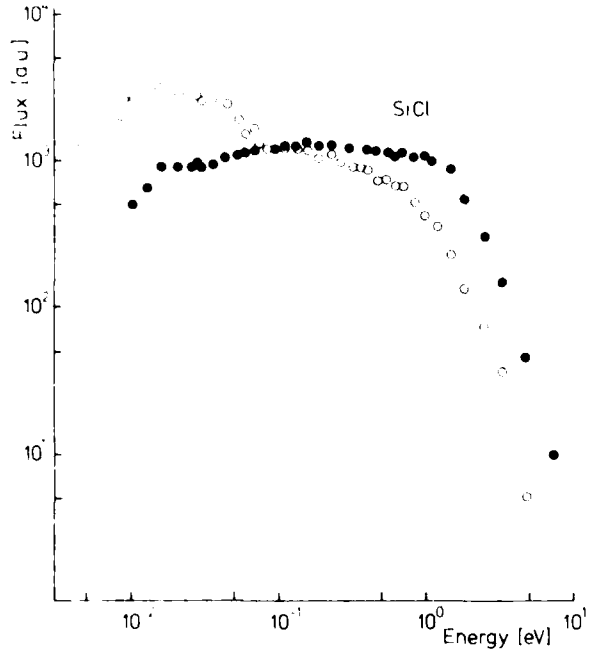

FIG. 2. Kinetic energy distribution curves (EDCs) of SiCl ($m/e = 63$) from the $Si(Cl_2, Ar^+)$ reaction at $\phi_{Cl_2} = 5\times10^{16}$ Cl_2 cm^{-2} s^{-1}, $T = 300$ K. (○) $E_p = 0.25$ keV, (●) $E_p = 5$ keV. The relative vertical position of the curves is arbitrary. The particle flux is given in arbitrary units.

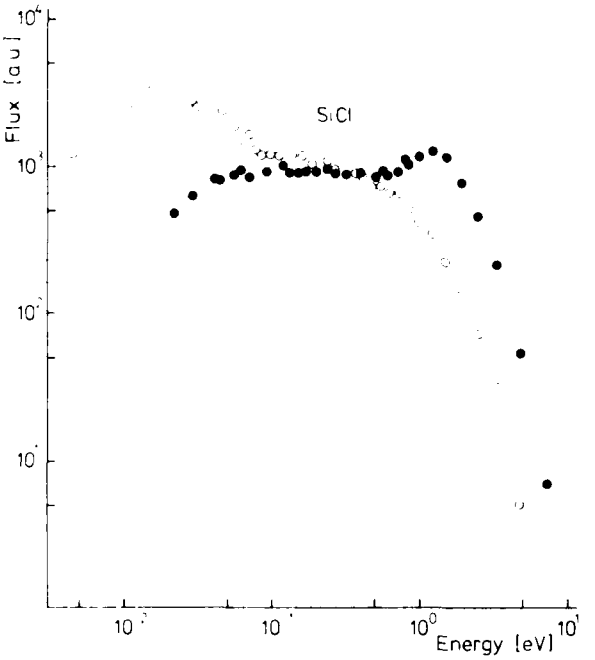

FIG. 3. Kinetic energy distributions (EDCs) of SiCl ($m/e = 63$) from the $Si(Cl_2, Ar^+)$ reaction at $\phi_{Cl_2} = 5\times10^{16}$ Cl_2 cm^{-2} s^{-1}. (○) $E_p = 0.25$ keV, $T = 300$ K, (●) $E_p = 3$ keV, $T = 625$ K. The relative vertical position of the curves is arbitrary.

As mentioned before, the behavior of $SiCl_2$ is similar to that of SiCl and will not be discussed here in further detail. For Si we have measured the EDC for $E_p = 3$ keV and $\phi_{Cl_2} = 0$ or 5×10^{16} Cl_2 cm^{-2} s^{-1} combined with $T = 300$ or 800 K, respectively. For pure Ar^+ bombardment the EDC is approximated well by a collision cascade with $U_0 = 7.8$ eV. When Cl_2 is added no significant signal is observed above the noise level at kinetic energies below 1 eV. The EDC indicates a shift to kinetic energies lower than without Cl_2 added. The EDC of Cl centers around a binding energy of about 2 eV.

Although Figs. 2 and 3 clearly show the qualitative effects of changing the value of E_p on the EDCs of SiCl, especially on the relative changes of the M–B and C–C parts, it is not straightforward to derive (semi) quantitative information

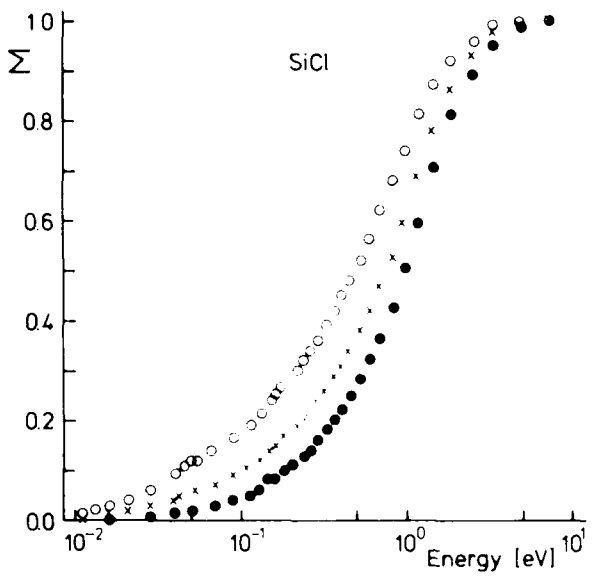

FIG. 4. Total number of SiCl (m/e = 63) particles, $\Sigma = \int_0^E \phi(E)\,dE / \int_0^{E_{max}} \phi(E)\,dE$, from the $SiCl_2$-Ar^+ reaction at $\phi_{Cl_2} = 5 \times 10^{16}$ Cl_2 cm^{-2} s^{-1}, T = 300 K. (○) E_p = 0.25 keV, (×) E_p = 2 keV, (●) E_p = 5 keV.

from it. To demonstrate this, Figs. 4 and 5 give the data of Figs. 2 and 3 in the form of

$$\int_0^E \phi(E)\,dE \Big/ \int_0^{E_{max}} \phi(E)\,dE,$$

where E_{max} is the maximum kinetic energy possible and $\phi(E)\,dE$ the flux of particles in the kinetic energy interval between E and $E + dE$. It follows that for $E_p = 0.25$ keV, $\phi_{Cl_2} = 5 \times 10^{16}$ Cl_2 cm^{-2} s^{-1} and $T = 300$ K the C-C part comprises more than 80% of the sputtered SiCl molecules. For $E_p = 5$ keV, $\phi_{Cl_2} = 5 \times 10^{16}$ Cl_2 cm^{-2} s^{-1} and $T = 300$ K, as well as for $E_p = 3$ keV, $\phi_{Cl_2} = 5 \times 10^{16}$ Cl_2 cm^{-2} s^{-1} and $T = 625$ K, these contributions have increased to more than 95%. Table I gives the M–B contribution as well as the mean kinetic energy for $\phi_{Cl_2} = 5 \times 10^{16}$ Cl_2 cm^{-2} s^{-1} and $T = 300$ K as a function of E_p, and for $E_p = 0.5$ keV, $\phi_{Cl_2} = 5 \times 10^{16}$ Cl_2 cm^{-2} s^{-1} as a function of T. The results in this table clearly indicate that down to the lowest E_p and T value and up to the highest ϕ_{Cl_2} the C-C part is by far the largest contribution.

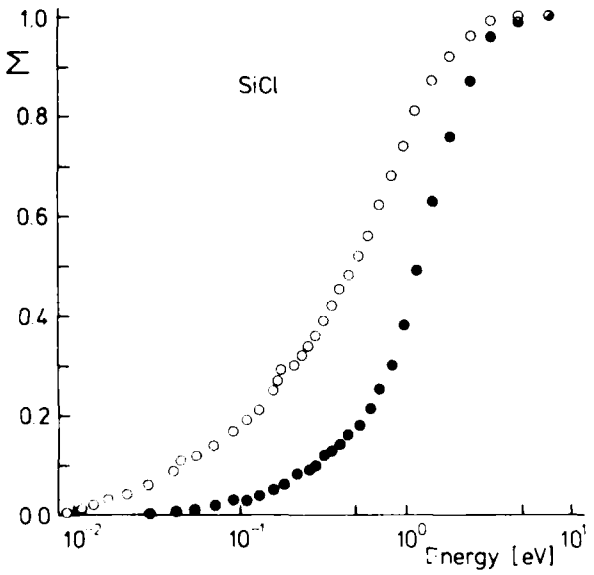

FIG. 5. Total number of SiCl (m/e = 63) particles, $\Sigma = \int_0^E \phi(E)\,dE / \int_0^{E_{max}} \phi(E)\,dE$, from the $SiCl_2$-Ar^+ reaction at conditions as given in Fig. 3.

TABLE I. Relative contribution of the Maxwell–Boltzmann part in the kinetic energy distribution of SiCl (m/e = 63) and the mean kinetic energy as a function of E_p at constant ϕ_{Cl_2} and T (left part) and as a function of T at constant E_p and Cl_2 (right part). $\phi_{Cl_2} = 5 \times 10^{16}$ Cl_2 cm^{-2} s^{-1}.

T = 300 K			E_p = 0.5 keV		
E_p keV	M–B %	mean energy eV	T K	M–B %	mean energy eV
0.25	16	0.76	300	18	0.75
0.5	18	0.75	450	11	1.18
0.75	17	0.87	625	10	1.32
1.0	15	0.94			
1.5	13	0.93			
2.0	11	0.99			
3.0	8	1.10			
5.0	6	1.31			

The mean kinetic energy of the SiCl neutrals belonging to the C-C part increases and their M–B contribution decreases considerably and continuously with increasing E_p, T, and decreasing ϕ_{Cl_2}. In the framework of the collision-cascade model an increase in mean kinetic energy also means an increase in binding energy U_0. In our experiments, the binding energies for SiCl, determined according to this model, range from about 0.25 to about 0.5 eV.

B. Yields of Ar, Si, Cl, SiCl, and $SiCl_2$ as a function of E_p, ϕ_{Cl_2}, and T

Currents of Ar^+, Si^+, Cl^+, $SiCl^+$, and $SiCl_2^+$ have been measured as a function of E_p, ϕ_{Cl_2}, and T for the ranges E_p = 0.25–3 keV, $\phi_{Cl_2} = 10^{15}$–5×10^{16} Cl_2 cm^{-2} s^{-1} and for T = 300–625 K. For illustration some of these data are given in Table II. The numbers of this table have not been corrected for the dependence of the kinetic energy on E_p, ϕ_{Cl_2}, and T. However, these corrections are relatively small. For example, the multiplication factors for $SiCl^+$ are given in Table III with E_p = 0.25 keV, $\phi_{Cl_2} = 5 \times 10^{16}$ Cl_2 cm^{-2} s^{-1} and T = 300 K as the reference. Similar corrections are applicable to the other ion signals. Comparison of the data given in Table II with the corrections shown in Table III indicates that the data of Table II can be used right away for discussing trends in the dependence of the abundance of the neutral products of E_p, ϕ_{Cl_2}, and T.

It appears that the yield of Ar is about proportional to $E_p^{1/2}$ and almost independent of ϕ_{Cl_2} and T. The yields of Ar provide a check on the consistency of the yield measurements. At $\phi_{Cl_2} = 5 \times 10^{16}$ Cl_2 cm^{-2} s^{-1} and T = 625 K the yield of Si increases more rapidly with E_p than the yield of

TABLE II. Yields of the products of the Si(Cl_2, Ar^+) reaction as a function of E_p, ϕ_{Cl_2}, and T. The data are given in counts/s. $\phi_{Ar^+} = 5\times10^{14}$ Ar^+ cm^{-2} s^{-1}. The numbers given have not been corrected for differences in kinetic energy.

E_p keV	Ar^+	Si^+	Cl^+	$SiCl^+$	$SiCl_2^+$	Ar^+	Si^+	Cl^+	$SiCl^+$	$SiCl_2^+$
	5×10^{16} Cl_2 cm^{-2} s^{-1}, 300 K					5×10^{16} Cl_2 cm^{-2} s^{-1}, 625 K				
0.25	560	420	730	1540	430	470	210	...	620	90
0.5	660	480	680	1690	490	580	440	170	850	120
1.0	1080	570	640	2810	750	1160	720	520	1540	200
3.0	1430	1540	1480	3200	730	1460	1910	750	2140	310
	1×10^{15} Cl_2 cm^{-2} s^{-1}, 300K					1×10^{15} Cl_2 cm^{-2} s^{-1}, 625 K				
0.25	500	180	420	650	130	480	200	150	290	40
0.5	660	260	440	840	180	...	...	...	...	...
1.0	1090	440	...	1410	280	1050	400	310	520	70
3.0	...	...	...	...	...	1860	1100	310	400	40

Ar, the increase being especially large when E_p is increased from 1 to 3 keV. While at $\phi_{Cl_2} = 5\times10^{16}$ Cl_2 cm^{-2} s^{-1} the yield of Si decreases for $E_p = 0.25$ and 0.5 keV when T is increased from 300 to 625 K, this yield shows enhancements for $E_p = 1$ and 3 keV. When ϕ_{Cl_2} is decreased from 5×10^{16} Cl_2 cm^{-2} s^{-1} to 10^{15} Cl_2 cm^{-2} s^{-1} the yield of Si is systematically reduced. The few data points of $\phi_{Cl_2} = 10^{15}$ Cl_2 cm^{-2} s^{-1} suggest that for this ϕ_{Cl_2} the yield of Si is hardly dependent on T. The yields of Cl, SiCl, and $SiCl_2$ decrease with increasing T and decreasing ϕ_{Cl_2}, and increase with E_p except at high E_p values combined with high T and low ϕ_{Cl_2}. The yield of $SiCl_2$ decreases more strongly with increasing T and decreasing ϕ_{Cl_2} than the yield of SiCl. At constant T and ϕ_{Cl_2} the ratio of the yields of $SiCl_2$ and SiCl is almost independent of E_p, except at 3 keV where a decrease in this ratio is observed.

C. Summary of experimental results

The experimental results for the products of the synergistic Si (Cl_2, Ar^+) reaction can be summarized as follows:

(1) For SiCl and $SiCl_2$ the M–B contribution decreases relative to the C-C contribution when E_p and/or T increases, and/or ϕ_{Cl_2} decreases. Even at the lowest E_p and T and the highest ϕ_{Cl_2} the C-C part comprises more than 80% of the molecular products. For Ar too, a decrease of the low-energy contribution is found when ϕ_{Cl_2} is reduced.

TABLE III. Multiplication factors for the ion currents of $SiCl^+$ given in Table II. The experiment with E_p = 0.25 keV, ϕ_{Cl_2} = 5×10^{16} Cl_2 cm^{-2} s^{-1}, T = 300 K is taken as the reference

E_p in keV	Cl_2 in Cl_2 cm^{-2} s^{-1}	T in K	Multiplication factor
0.25 + 3	5×10^{16}	300	1.3
0.25	5×10^{16}	300 + 625	1.3
0.25	5×10^{16} + 10^{15}	300	1.1
0.25 + 3	5×10^{16} + 10^{15}	300	1.3
0.25 + 3	5×10^{16}	300 + 625	1.4
0.25	5×10^{16} + 10^{15}	300 + 625	1.4
0.25 + 3	5×10^{16} + 10^{15}	300 + 625	1.5

(2) When E_p and/or T increases, and/or ϕ_{Cl_2} decreases, the C-C part of the EDCs of SiCl and $SiCl_2$ shifts to higher E and the high-energy cutoff steepens. For Ar and Si a reduction of ϕ_{Cl_2} shifts the EDCs to higher kinetic energies.

(3) The yield of Ar is almost independent of T and ϕ_{Cl_2}. That of Si increases with ϕ_{Cl_2} and E_p, T has a complicated effect. The yields Cl, SiCl, and $SiCl_2$ decrease with increasing T and with decreasing ϕ_{Cl_2}; the yields of Cl and $SiCl_2$ decrease more strongly than that of SiCl. The yields of SiCl and $SiCl_2$ increase with increasing E_p except at high values of E_p combined with high T and low ϕ_{Cl_2}.

IV. DISCUSSION

A. Ion-bombardment-induced damage and mixing

In this section part of the physics known about damage and mixing introduced into Si by ion impact will be recapitulated to serve as an introduction to the damage and mixing[17-19] to be expected for Si(Cl_2, Ar^+).

An energetic Ar^+ ion hitting a solid Si surface will deposit its energy in a so-called collision cascade. Between the impact on the surface and the moment it comes to rest at its implantation depth after about 10^{-12} s, an Ar^+ ion with an energy of about 1 keV loses about 80% of its energy by displacing atoms from the host matrix and 20% by electronic and vibrational excitation of the impact area. A very small part of the energy deposited is used for sputtering.

The number of displaced atoms per Ar^+ ion is roughly proportional to the Ar^+ ion energy E_p, a few tens to a few hundreds of displaced atoms for $E_p = 0.25$ or 3 keV, respectively. The displacements can occur to a depth corresponding to a few times the projected range R_p of the Ar^+ ions and roughly in a cylinder the dimensions of which increase with E_p. For perpendicular ion bombardment at $E_p = 0.25$ keV the calculated value of R_p is 15 ± 5 Å and that of the cylinder radius about 5 Å, while at $E_p = 3$ keV these numbers are 60 ± 20 Å and 30 Å, respectively.[20] Since high-angle, low-energy recoils are most probable, a substantial fraction of the energy is deposited in displacements in the very first atomic layers at the surface. These displacements correspond to the

production of large quantities of unbound Si atoms. Just after the end of the collision cascade, the region where the energy of the incoming Ar^+ ion has been deposited is very reactive and "hot". After that a relaxation period with a duration of approximately 10^{-11} s follows in which a number of processes occur. One of these processes is the ion-bombardment-enhanced diffusion of interstitial Si atoms to deep into the bulk, about two to three times deeper than the depth of the heavily damaged layer. Another important process is the ion-bombardment-enhanced diffusion of species adsorbed on the surface into the top atomic layers of the Si. In principle a third process, viz. the ion-bombardment-enhanced segregation of bulk species, is also possible. And of course unbound Si and in-diffused "adsorbates" will bind again to the bulk atoms or to other unbound atoms. It appears that ion bombardment of Si with an adsorbate layer on top with energetic Ar^+ ions results in an amorphous top layer in which part of the adsorbate may be mixed. This layer contains implanted Ar atoms. But it may also contain molecules, resulting from the formation of a bond between interstitial atoms, which have no chemical bond to the bulk network.

To illustrate the possible importance of ion-bombardment-enhanced diffusion of adsorbates into the bulk of the top film, experimental and calculated results for recoil implantation may be cited.[21,22] For $E_p = 20$ keV recoil implantation contributes only a fraction to the ion-beam mixing process. For example, Wach and Wittmaack[22] observed that the mixing efficiency of an oxygen adsorbate on Si for bombardment with 20 keV Xe^+ ions was one to two oxygen atoms per incoming Xe^+ ion. This can only be explained by assuming that the diffusion of oxygen from the adsorbate layer into the Si is greatly enhanced by the Xe^+ impact. Naturally, the relative importance of recoil mixing will increase for decreasing E_p, but also at lower energy ion-bombardment-enhanced diffusion of adsorbates into the bulk will remain a most important process.

B. Ar^+ ion-bombardment-induced damage and mixing for $Si(Cl_2, Ar^+)$

The review of ion-bombardment-induced damage and mixing given in the preceding section shows that species chemisorbed on the surface may be mixed quite efficiently into the uppermost layers of a substrate. It is self-evident that the degree of coverage of the surface with chemisorbed species will very much determine the quantitative effect. For the specific case of chlorine chemisorbed on single crystalline Si, Florio and Robertson[23] have found that the sticking probability of Cl_2 is about 0.1 in the temperature range from 300 to 650 K. Besides they have shown that, under these conditions, the saturation coverage corresponds to a very important fraction of a monolayer. Data about the coverage under ion bombardment can be derived from a paper of Gerlach-Meyer *et al.*[1] and can be taken from the work of Mayer *et al.*[5,6] The former authors found that the etch rate of amorphous Si for $\phi_{Ar^+} = 3\times10^{13}$ Ar^+ cm^{-2} s^{-1} at $E_p = 1$ keV and $T = 300$ K, approximately saturated when ϕ_{Cl_2} was enhanced from 0 to 5×10^{15} to 10^{16} Cl_2 cm^{-2} s^{-1}, while the latter authors concluded that for $\phi_{Cl_2} = 3\times10^{16}$ Cl_2 cm^{-2} s^{-1} the Cl coverage decreases by a factor of 4 when ϕ_{Ar^+} is increased from 3×10^{14} to 2×10^{15} Ar^+ cm^{-2} s^{-1} at $E_p = 0.6$ keV and $T = 300$ K. Both groups conclude that the Cl coverage is close to saturation when $\phi_{Cl_2}/\phi_{Ar^+} \gtrsim 10^2$.

In the present work the parameter values range from those for which saturation coverage may be expected, viz. $\phi_{Ar^+} = 5\times10^{14}$ Ar^+ cm^{-2} s^{-1} at $E_p = 0.25$–1 keV, $T = 300$ K and $\phi_{Cl_2} = 5\times10^{16}$ Cl_2 cm^{-2} s^{-1}, to values for which the Cl coverage will be far below saturation. Ar^+ bombardment of Si covered with chemisorbed Cl will, of course, cause sputtering, but also displace Si and Cl atoms, producing many unbound atoms. In the relaxation process following displacements, the diffusion of Cl into Si may be enhanced. The unbound atoms may bind again to the lattice forming an amorphous, solid mixture of Si and Cl, but some of them will bind to one another without being bound to the bulk network. The latter particles may be locked up into voids in the amorphous top layers in the form of, e.g., SiCl and $SiCl_2$.

C. Yields as a function of E_p, ϕ_{Cl_2}, and T

The results for the yields of Cl, SiCl, and $SiCl_2$ as a function of E_p, ϕ_{Cl_2}, and T (as given in Table II) are in agreement with the picture of Ar^+ ion-bombardment-induced damage and mixing for $Si(Cl_2, Ar^+)$ described in Sec. IV B. The yields of Cl, SiCl, and $SiCl_2$ decrease with decreasing ϕ_{Cl_2} and increasing T. As discussed in the preceding section the dependence on ϕ_{Cl_2} can be related to a reduction of the Cl coverage of the Si surface, and so too, therefore, to the amount of Cl mixed into that part of the top atomic layers of the Si from which Cl, SiCl, and $SiCl_2$ are sputtered. The reduction of these yields with increasing T stems from two effects. One is the reduced Cl coverage and the other the increase of the concurrent thermal reaction. The competition with the thermal reaction means that, in steady state, especially when E_p is low, the uppermost layers of the Si from which the Cl, SiCl, and $SiCl_2$ are sputtered, will be less mixed with Cl. That the thermal reaction is indeed important at $T \approx 625$ K is substantiated by the observation that at $\phi_{Cl_2} = 5\times10^{16}$ Cl_2 cm^{-2} s^{-1} the reduction in Ar^+ ion-bombardment-induced yields of SiCl and $SiCl_2$ with T is much larger for, e.g., $E_p = 0.25$ keV than for $E_p = 3$ keV.

The stronger decrease in the yield of $SiCl_2$ with decreasing ϕ_{Cl_2} and increasing T as compared to the decrease in the yield of SiCl is consistent with the process proposed for formation of void SiCl and $SiCl_2$ molecules as sketched in Sec. IV B. If these molecules are indeed formed from unbound atoms produced by the Ar^+ ion impact, the concentration of void SiCl molecules is linearly dependent on the concentration of unbound Cl atoms, whereas the concentration of void $SiCl_2$ molecules is proportional to the square of this concentration.

The increase of the yields of these products with E_p, except for low ϕ_{Cl_2} combined with high T, indicates that a large amount of Cl is mixed into the uppermost atomic layers of the Si. When this is true indeed, the density of Si atoms in this part decreases substantially. If the binding energy of Si atoms were not influenced by the mixing with Cl, a decrease

in the yield of Si would be expected when ϕ_{Cl_2} is enhanced from 10^{15} to 5×10^{16} Cl_2 cm^{-2} s^{-1}. In fact, however, an increase is observed, except for $E_p = 0.25$ keV at $T = 625$ K. The unequivocal conclusion that can be drawn from these observations is that the mixing of Cl into the top atomic layers of the Si decreases the binding energy of the atomic Si bound to the Si network. The effect of the enhanced thermal reaction at $T = 625$ K, for $\phi_{Cl_2} = 5\times10^{16}$ Cl_2 cm^{-2} s^{-1} and $E_p = 0.25$ keV, as compared to $T = 300$ K is to reduce the yield of Si to a value also observed for $\phi_{Cl_2} = 10^{15}$ Cl_2 cm^{-2} s^{-1} and $E_p = 0.25$ keV at $T = 300$ or 625 K. This observation is, again, consistent with a steady state in which the topmost atomic layers are less mixed with Cl, a conclusion also drawn above from the results for the yield at Cl, SiCl, and $SiCl_2$.

D. Origin of the M–B and C-C parts of the EDCs of SiCl and $SiCl_2$; effects of E_p, ϕ_{Cl_2}, and T

A crucial test on the extent of ion beam mixing of Cl adsorbed on Si into the uppermost atomic layers of the Si would be an *in situ* analysis of the composition of these layers by ESCA or similar surface-sensitive analysis techniques. Thus far, no such measurements have been reported. However, recent Rutherford backscattering spectroscopy (RBS) work of Mizutani *et al.*[24] provides some evidence for ion beam mixing of Cl into the topmost atomic layers of Si for chlorinated Si surfaces bombarded with 1 keV Ar^+ ions. Besides our results also give indications that Cl is indeed ion beam mixed into the Si. For example, assume with Sigmund[25] that the Cl adsorbed on the very surface lowers the surface barrier U_0 and that this is the sole, or main, reason for the reduction in the binding energies of SiCl and $SiCl_2$ molecules. This cannot be the only, or main, reason, because Gerlach-Meyer *et al.*[1] and Mayer *et al.*[5,6] have shown that for $\phi_{Cl_2} = 5\times10^{16}$ Cl_2 cm^{-2} s^{-1} and simultaneously $\phi_{Cl_2}/\phi_{Ar^+} \gtrsim 10^2$, the surface coverage is saturated, and this coverage is independent of the Ar^+ ion energy up to 1 keV.[6] Now, in Table I the mean kinetic energy of SiCl is given for just this value of ϕ_{Cl_2} and of ϕ_{Cl_2}/ϕ_{Ar^+} as a function of E_p from 0.25 to 5 keV. It appears that this mean kinetic energy is obviously dependent on E_p, which leads to the conclusion that the kinetic energies and thus the derived binding energies are for an important part determined by mixing of Cl into the bulk of the Si. Naturally, the Cl adsorbed on the surface will influence atoms and molecules present in the immediate neighborhood, i.e., bond to them or adjacent.

Within the framework of the statistical mechanism for sputtering of diatomic and triatomic molecules bound to the network of a bulk material[26] the probability for sputtering of diatomic or triatomic molecules from a bulk composed of Si and Cl, with comparable atomic masses, is of the order of a percent for diatomic molecules and of a promille for triatomic molecules. Since we have found that the yields of the molecular products SiCl and $SiCl_2$ are comparable to those of atomic Si, evidently, in our case, the statistical mechanism is not applicable. Another important observation is that the binding energies derived from the EDCs of SiCl and $SiCl_2$, which lie between 0.25 and 0.50 eV, tell us that these molecules are sputtered from the bulk and not from the very surface. Molecules with binding energies in this range have too high a desorption rate at $T = 300$ K or higher to have a significant surface concentration. Since the chemical binding energy of SiCl- or $SiCl_2$-fragments to the bulk network via Si–Si backbonds will certainly be higher than 1 eV, it also follows that these fragments cannot be bound to the bulk network via normal chemical bonds, but should be present as void molecules with only physical interaction with the surrounding internal surface. Their possible formation by ion beam mixing processes has been described in a preceding section. Further support for the importance of the ion-beam mixing process can be derived from the observation of Gerlach-Meyer *et al.*[1] that simultaneous exposure of Si to Cl_2 during sputtering with Ar^+, Ne^+, and He^+ gives a much larger enhancement of the yield for He^+ (13.6) than for Ar^+ or Ne^+ (5 or 4.3, respectively). The latter results are consistent with the relatively large contribution of bond breaking for low mass projectiles.[25]

A low estimate for the amount of Cl ion beam mixed into the topmost atomic layers of the Si can be derived from a comparison between the yield of sputtered Cl with that of SiCl and $SiCl_2$ for conditions of surface Cl saturation coverage, i.e., $\phi_{Cl_2} = 5\times10^{16}$ Cl_2 cm^{-2} s^{-1} and $T = 300$ K as a function of E_p (see Table II). If we take the numbers for $SiCl_2$ as the basis, the numbers for SiCl and Cl have to be multiplied by roughly 1.5 and 9, respectively. These correction factors are derived from the differences in geometrical dimensions and in mean kinetic energies. Now, if we assume for the moment that the Cl atoms are sputtered solely from the very surface, this means that, under the conditions specified, the uppermost atomic layers of the Si, from which the SiCl and $SiCl_2$ molecules are sputtered, contain at least an amount of Cl incorporated equivalent to about 50% of the surface saturation coverage of Cl. Since Cl atoms will also be sputtered from Cl incorporated in the bulk, this is a rough lower estimate. It compares surprisingly well with the rough estimate of Mizutani *et al.*[24] Of course, the amount of Cl ion beam mixed into the Si top will decrease to lower values of ϕ_{Cl_2} where saturation coverage is no longer reached.

As remarked before in Sec. IV B, ion bombardment of crystalline Si with (noble gas) ions produces an amorphous Si top film with a thickness corresponding to a few times the projected range of the ions. In addition considerable quantities of ions are implanted. For noble gas ion bombardment the implanted region will show a certain porosity. The ion beam mixing of large amounts of Cl into the topmost layers of this amorphous Si film has some additional consequences for their structure. If we call the amorphous Si a super cross-linked Si polymer, the effect of the ion-beam bombardment enhanced diffusion of Cl from the very surface into the topmost atomic layers will be a drastic reduction of the cross linking. As a result a large amount of new Cl-covered surface is formed in these top atomic layers of the Si. This Cl-covered new surface resides in the top of the amorphous surface film and will show an enhanced porosity as compared to the case of pure Ar^+ sputtering of Si. This new surface will also be connected for a large fraction to the geometrical surface.

It is difficult to imagine that molecules locked up in a bulk network will stay intact when being sputtered. Two solu-

tions for this problem seem possible. One is that the molecules like SiCl and $SiCl_2$ are present in quite large concentrations just below the geometrical surface, surface-locked molecules, e.g., with one of the composing atoms locked up by network atoms. The other possible solution is the formation of large quantities of these molecules in the porous interior of the amorphous top film. Of course these molecules may both be locked up in the surface, including the new part of it, and be trapped in voids in the porous film. The observation that at $\phi_{Cl_2} = 5\times10^{16}$ Cl_2 cm^{-2} s^{-1} and $T = 300$ K the relative contributions of SiCl and $SiCl_2$ increase less rapidly with E_p than that of Si seems to point to an important contribution of surface-locked SiCl and $SiCl_2$, because at $E_p = 0.25$ keV most of the ion beam mixing occurs in a few atomic layers just below the very surface. That the SiCl and $SiCl_2$ locked up by the new surface in the porous top part or trapped in voids will also contribute can be derived from the effect of ϕ_{Cl_2} on the relative M–B contributions of Ar and SiCl. Typically the EDC of Ar sputtered from Si in the presence of $\phi_{Cl_2} = 5\times10^{16}$ Cl_2 cm^{-2} s^{-1} has a clearly enhanced contribution in the M–B region as compared to sputtering in the absence of Cl_2. Since the peak concentration of Ar will be located at the relatively deep implantation depth, this M–B part will, in all probability, be due to ion-bombardment enhanced diffusion from larger depths than in the case without Cl_2, because of the enhanced porosity of the Cl-mixed amorphous Si top film. Since the effects of ϕ_{Cl_2} variation on Ar and SiCl are very similar, it goes without saying that the M–B contribution in the EDC of SiCl is in all probability due to ion-bombardment enhanced diffusion from SiCl trapped in voids or locked up in the new surface. This also explains why the temperature of the M–B distribution follows the temperature of the substrate.

The shift to higher kinetic energies of the C-C part of the EDCs of SiCl and $SiCl_2$ with increasing E_p and for ϕ_{Cl_2} decreasing below values corresponding to a decreasing Cl coverage, is explained by assuming that the mixing of Cl into the uppermost atomic layers from which the products are sputtered, also decreases. The same holds true for the EDC of Si.

E. Consequences for anisotropic plasma etching

Since ion bombardment is a key component of anisotropic plasma etching, it is inevitably accompanied by ion-bombardment induced effects like implantation, amorphization, and ion-bombardment enhanced diffusion. For anisotropic plasma etching of compounds preferential sputtering and ion-bombardment induced segregation may add. And, last but not least, ion-bombardment induced mixing of adsorbates into the uppermost atomic layers of the material to be etched, must be considered. So, when using anisotropic plasma etching to transfer a pattern into a film, the underlying film or substrate will always be damaged due to the above-mentioned bombardment-induced effects. Damage and anisotropic plasma etching are undetachably connected. The depth of the damage can be derived from the literature on physical sputtering and on ion beam mixing.

The ion bombardment may have both negative and beneficial effects. Whereas, e.g., damage and ion beam mixing exert negative effects on the properties of the substrate, they play a crucial and beneficial role in patterning the film overhead. For the case under study, the ion-bombardment induced mixing of chemisorbed Cl into the topmost atomic layers of the Si causes two related beneficial effects. One is the reduction of the binding energy of the Si sputtered as atoms, causing one part of the etch rate enhancement. The other is the production of considerable quantities of void molecules SiCl and $SiCl_2$ with a very low binding energy, taking care of the other part of the increase in the etch rate. That the measurements described above are related to etch rate enhancement,[1,4–6] has been checked recently under the conditions of our experiments, by measuring the etch rate enhancement of the sputtering of Si by Ar^+ when the Si surface is exposed simultaneously to Cl_2.[27]

It may be surmised that effects of a similar nature as deduced from the experiments on the Si(Cl_2, Ar^+) system, also apply for many other anisotropic plasma etch processes.

V. SOME FINAL REMARKS

Although some studies have been made of the effect of the angle of incidence of the ion beam on the etch rate[4,5] and the damage and ion-bombardment induced mixing of Cl into Si,[24] as yet no detailed data are available on the influence of this parameter on the yields and EDCs of the products Si, SiCl, and $SiCl_2$. These data are essential for further support of the model presented. Also more quantitative, high-resolution *in situ*, analysis of the uppermost, modified, layers of the Si by XPS, medium ion energy RBS and the like are crucial to further test the above conclusions. Finally, a direct detection of void molecules in these top layers would provide the keystone for the model proposed.

ACKNOWLEDGMENTS

The authors are grateful to J. v. Laar, R. A. Haring, and D. J. Oostra for their support during part of this work. The experimental work has been performed at the FOM-Institute in Amsterdam. Thanks are due to Dr. F. W. Saris and Dr. J. Los for their interest and generous hospitality. This work was partly sponsored by FOM with financial support by ZWO.

[1] U. Gerlach-Meyer, J. W. Coburn, and E. Kay, Surf. Sci. **103**, 177 (1981).
[2] U. Gerlach-Meyer, Surf. Sci. **103**, 524 (1981).
[3] F. C. Tompkins, *Chemisorption of Gases on Metals* (Academic, London, 1978), p. 3.
[4] H. Okano and Y. Horiike, Jpn. J. Appl. Phys. **20**, 2429 (1981).
[5] T. M. Mayer and R. A. Barker, J. Vac. Sci. Technol. **21**, 757 (1981).
[6] R. A. Barker, T. M. Mayer, and W. C. Pearson, J. Vac. Sci. Technol. B **1**, 37 (1983).
[7] F. H. M. Sanders, A. W. Kolfschoten, J. Dieleman, R. A. Haring, A. Haring, and A. E. de Vries, J. Vac. Sci. Technol. A **2**, 487 (1984).
[8] M. W. Thompson and B. W. Farmery, Philos. Mag. **18**, 361 (1968).
[9] H. F. Winters, J. Vac. Sci. Technol. B **1**, 927 (1983).
[10] H. F. Winters and F. A. Houle, J. Appl. Phys. **54**, 1218 (1983).
[11] J. W. Coburn, E.-A. Knabbe, and E. Kay, J. Vac. Sci. Technol. **20**, 480 (1982).
[12] J. W. Coburn and H. F. Winters, J. Vac. Sci. Technol. **16**, 391 (1979).
[13] J. W. Coburn and H. F. Winters, Annu. Rev. Mater. Sci. **13**, 91 (1983).
[14] G. Comsa, R. David, and B. J. Schumacher, Rev. Sci. Instrum. **52**, 789 (1981).

[15]R. A. Haring, R. Pedrijs, D. J. Oostra, A. Haring, and A. E. de Vries, Nucl. Instrum. Methods B **5**, 476 (1984).
[16]R. A. Haring, R. Pedrijs, D. J. Oostra, A. Haring, and A. E. de Vries, Nucl. Instrum. Methods B **5**, 483 (1984).
[17]D. A. Thompson, Radiat. Eff. **56**, 105 (1981).
[18]S. Matteson and M-A. Nicolet, *Metastable Materials Formation by Ion Implantation*, edited by S. T. Picraux and W. J. Choyke (North-Holland, Amsterdam, 1982), p. 3.
[19]S. Matteson and M-A. Nicolet, Annu. Rev. Mater. Sci. **13**, 339 (1983).
[20]J. P. Biersack and J. F. Ziegler, in *Ion Implantation Techniques*, edited by H. Rijssel and H. Glawischnig (Springer, Berlin, 1932), p. 157.
[21]R. Kelly and J. B. Sanders, Surf. Sci. **57**, 143 (1976).
[22]W. Wach and K. Wittmaack, Nucl. Instrum. Methods **149**, 259 (1978).
[23]J. V. Florio and W. D. Robertson, Surf. Sci. **18**, 398 (1969).
[24]T. Mizutani, C. J. Dale, W. K. Chu, and T. M. Mayer, Nucl. Instrum. Methods B **7/8**, 825 (1985).
[25]P. Sigmund, in *Sputtering by Particle Bombardment I*, edited by R. Behrisch (Springer, Berlin, 1981), p. 9.
[26]W. Gerhard, Z. Phys. B **22**, 31 (1975).
[27]A. W. Kolfschoten, F. H. M. Sanders, P. Vischer, and P. C. Zalm (to be published).

Summary Abstract: Simultaneous exposure of SiO_2 and ThF_4 to XeF_2 and energetic electrons

M. A. Loudiana and J. T. Dickinson
Washington State University, Pullman, Washington 99163-2814

(Received 18 March 1985; accepted 21 May 1985)

I. INTRODUCTION

Radiation induced and enhanced etching of solid surfaces is an area of considerable current interest. In thin film fabrication technology, there is potential for the use of such etching in highly controlled and selective removal of metal, semiconductor, and insulating material from a surface. In an excimer laser, optical components may be simultaneously exposed to reactive chemical radicals, low energy ions, energetic electrons, as well as a large flux of UV photons. Thus, the lifetime of materials such as optical coatings depends strongly on radiation/reactive gas phenomena at surfaces. In this extended abstract we examine the effects of electron bombardment on thin films of ThF_4 and SiO_2 as well as exposure of these materials to a source of fluorine (XeF_2 or F_2) under various sequences of electron bombardment.

II. EXPERIMENTAL

The experiments were done in a stainless-steel ultrahigh vacuum (UHV) chamber equipped with an ion pump and cryopump, the latter being used to pump XeF_2 and F_2. XeF_2 was obtained from PCR Research Chemicals and vacuum distilled at -64 °C before use. The gas was introduced to the chamber through a narrow stainless-steel tube directed at the sample. Following determination of the conductance of the tube for the gases, measurement of the pressure behind the tube using a capacitance manometer allowed the flux to be calculated.

The chamber was equipped with a Varian Auger electron spectrometer with a cylindrical mirror analyzer (CMA) and a UTI 100C quadrupole mass spectrometer. Auger spectra were obtained with a 2 keV, 0.5 μA primary electron beam. The axial electron gun in the CMA was also used as an electron source during irradiation experiments.

Mass changes in the thin films were measured with a sensitive, thermally stabilized, 5-MHz quartz crystal microbalance. For this particular microbalance, an increase in the frequency of 1 Hz corresponds to a mass decrease of 1.26×10^{-8} g.[12] 1000 A ThF_4 and SiO_2 films were evaporated onto gold electrodes of microbalance crystals at the Naval Weapons Center and shipped under dry nitrogen to Washington State University. The thin films were transferred to the UHV system and used without cleaning.

III. RESULTS AND DISCUSSION

A. Effect of electron bombardment on ThF_4

ThF_4 rapidly loses mass during electron bombardment, as indicated by microbalance measurements. The microbalance measures the total mass loss which includes the total mass of ions and neutral particles. Simultaneous with this mass loss, the quadrupole mass spectrometer registered a substantial increase in the 38 amu (F_2) peak. Since the quadrupole is not in line of sight with the ThF_4 surface, due to wall collisions, it is unlikely that it would detect emitted atomic fluorine. Although no increase in the 19 amu (F) peak could be measured, there is a strong possibility that at least part, if not all, of the desorbing fluorine is atomic.

The surface composition was monitored with AES during an extensive exposure to 1 keV electrons and is plotted in Fig. 1. The fluorine concentration decreased from 75% to 50% during the first 0.01 C (3×10^{17} electrons/cm^2) of bombardment, with little change in fluorine concentration thereafter. The thorium concentration initially increased due to the loss of fluorine and then decreased as the film slowly adsorbs carbon and oxygen containing gases from the background. The sticking probability of the residual gases on the ThF_4 surface was found to increase considerably with electron bombardment, due to the removal of fluorine.

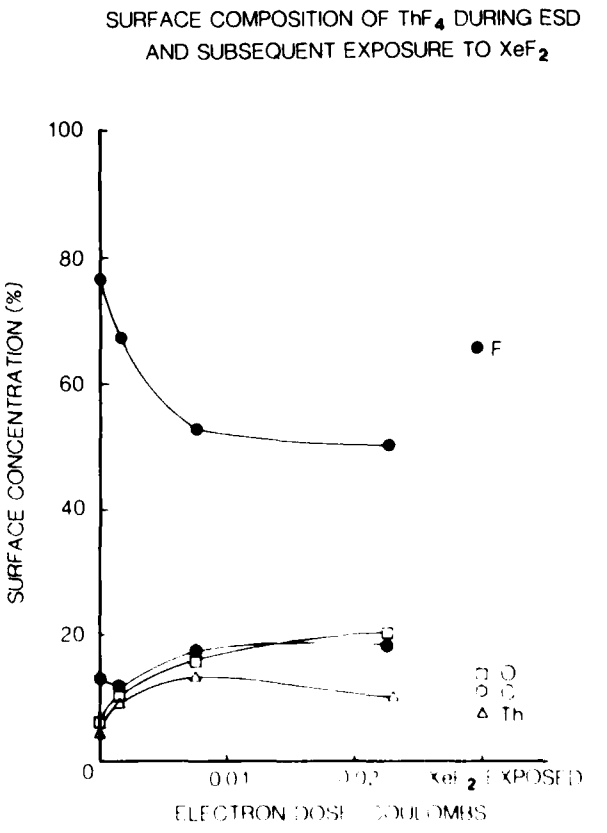

FIG. 1. Concentration of fluorine, oxygen, carbon, and thorium on the surface as determined by AES during electron stimulated desorption of ThF_4 with 1 keV electrons. Effect of XeF_2 exposure shown on right.

 0734-211X/85/051393-04$01.00

The damage caused by electron bombardment is not limited to the near surface layers. Microbalance measurements indicate that during extensive bombardment with a 1 keV, 50-μA electron beam, the fluorine loss was equivalent to all the fluorine contained in up to 27 monolayers of ThF_4. The damage actually extended much deeper than 27 monolayers since AES indicates that surface fluorine still remains after bombardment. This bulk damage was accompanied by a visible change in the ThF_4 film. The film developed a dark blue color where the electron beam was incident upon it. This blue color is due to bulk defects, or color centers, which presumably are associated with fluorine vacancies, although no information on ThF_4 color centers could be found in the literature. This blue color is visibly diminished after the film readsorbs a large amount of fluorine.

For a ThF_4 film to lose many monolayers of fluorine very quickly under electron bombardment in vacuum, electron bombardment must be stimulating the following processes: ThF_4 dissociation, fluorine bulk diffusion in the near surface layers, bulk-to-surface diffusion (surface segregation), and fluorine desorption. As we shall show, electron bombardment in the presence of XeF_2, under the appropriate conditions, can lead to the uptake of fluorine in ThF_4.

B. Exposure of electron damaged ThF_4 to XeF_2

When "virgin" ThF_4 is exposed to XeF_2, it slowly adsorbs a fraction of a monolayer of fluorine (typically 0.7 monolayer). The sticking probability is small and can vary considerably from one sample to the next due to surface contamination. Following exposure, Xe could not be detected with AES. The surface fluorine concentration was seen to rise by only about 5%, indicating that some of the adsorbed fluorine has diffused into the bulk.

We have found that a fluorine depleted ThF_4 film, produced by extended electron bombardment (such as shown in Fig. 1), readily adsorbs fluorine. When such a surface is exposed to XeF_2, microbalance data show that the surface rapidly gains a monolayer of fluorine with unity sticking probability. After one monolayer is adsorbed, the fluorine adsorption continues at a very slow rate with less than an additional monolayer adsorbed after several hours. The points plotted on the right-hand side of Fig. 1 show the increase in surface fluorine concentration which occurred after electron bombardment was stopped and the sample was exposed to XeF_2.

C. Simultaneous exposure of ThF_4 to electrons and XeF_2

When a ThF_4 surface is simultaneously exposed to XeF_2 and 1 keV electrons (50 μA), the film loses *less total fluorine than it would if the XeF_2 were not present*. Under the identical 1 keV electron beam used before, the maximum amount of fluorine a ThF_4 film lost when subjected to a flux of 1×10^{16} XeF_2 molecules/s was 13 equivalent monolayers, or less than half the mass loss when the XeF_2 was not present. Figure 2 shows the concentration of surface species as determined by AES during simultaneous exposure to XeF_2 and a 1-keV electron beam. Note the rapid initial loss of carbon and accompanying increase in the thorium concentration.

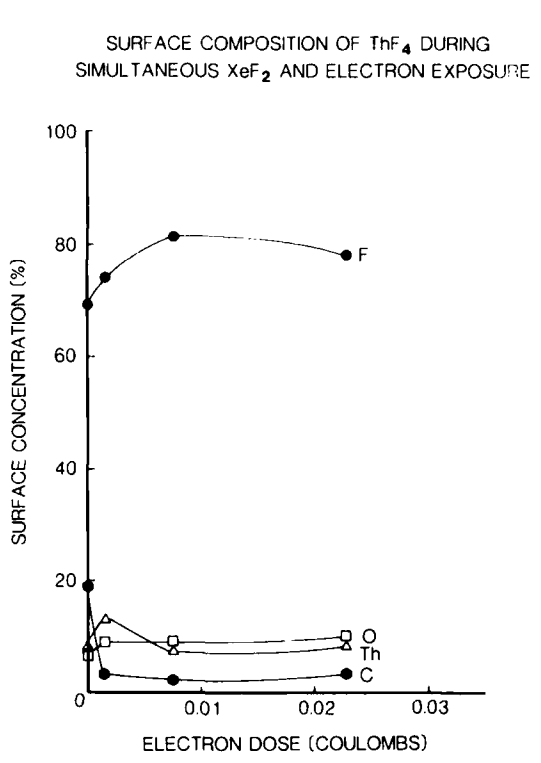

FIG. 2. Surface concentration of fluorine, oxygen, carbon, and thorium as determined by AES during simultaneous exposure of ThF_4 to 1 keV electrons and 3.5×10^{15} XeF_2 molecules/cm^2/s.

The fluorine concentration on the surface increases to 80% at a total electron dose of 0.008 C; further exposure led to a slow decrease in fluorine surface concentration.

ESD of fluorine from ThF_4 must still be occurring under these circumstances; however, an empty surface site is quickly filled from the gas phase. Electron stimulated diffusion of the near-surface fluorine results in a fluorine enriched surface. After some time, however, the bulk fluorine concentration decreases until a chemical equilibrium is established where fluorine is desorbed from the surface at the same rate as it is adsorbed from the gas phase. At low incident electron energies (< 150 eV) this chemical equilibrium is not estab-

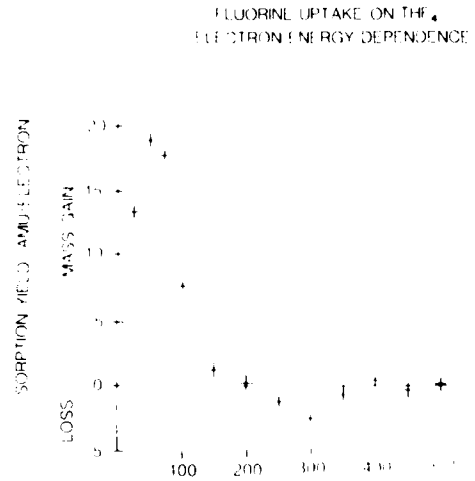

FIG. 3. Yield (mass change/electron current) dependence on electron energy during simultaneous exposure of ThF_4 to XeF_2 and electrons.

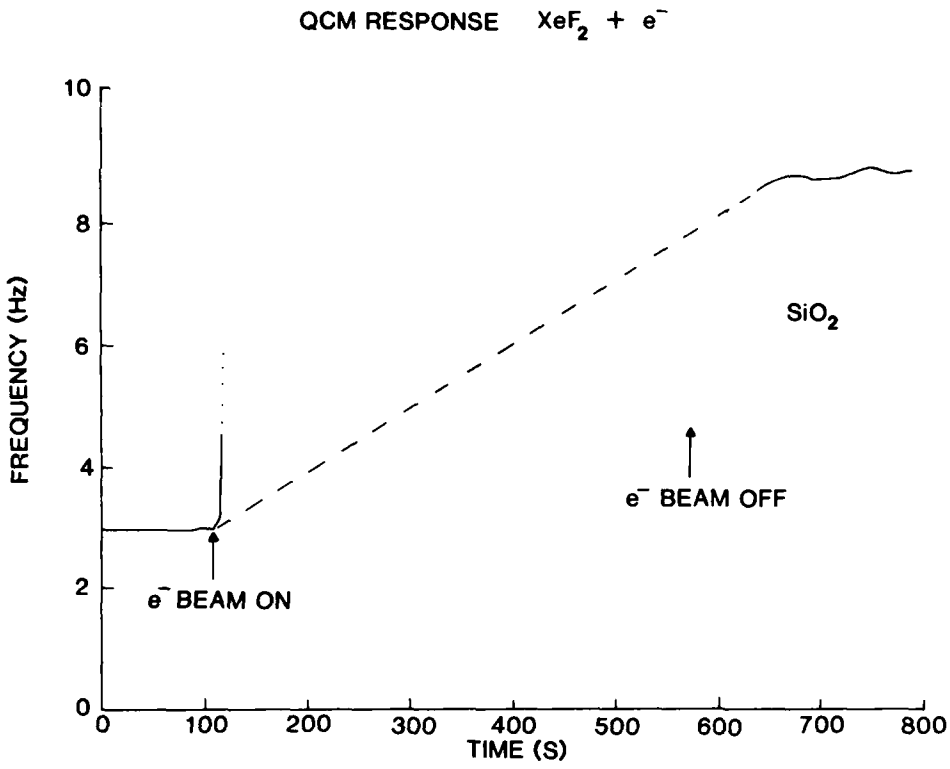

FIG. 4. Microbalance frequency vs time during simultaneous exposure of SiO_2 to XeF_2 and electrons at the time indicated.

lished for very long periods of time. During simultaneous bombardment with low energy electrons and XeF_2, the ThF_4 film gains mass at a steady rate depending on electron energy, XeF_2 flux, and electron flux.[3] After 2 h of bombardment with a 7 μA, 100-eV electron beam and 1×10^{16} XeF_2 molecules/s, the mass gain rate showed no change.

From our microbalance measurements we can calculate a "sorption yield" which is equal to the rate of mass gain/electron. Figure 3 shows the dependence of the sorption yield on incident electron energy measured by the microbalance during bombardment with 1 μA electron beams. The mass gain rate appears to peak at 50 eV, suggesting that this is the energy at which the diffusion of fluorine from the surface into the bulk is maximized. If at this energy the cross section for fluorine segregation into the bulk is a maximum, then the fluorine flow would be regulated at the surface by the incoming gas phase fluorine (XeF_2) and the electron current and not by the bulk concentration gradient. Field stimulated effects due to charging of the insulator surface may also play a role, since the secondary electron yield decreases at these low energies resulting in increased surface charging.

It should be noted that the results obtained with F_2 as a gas phase fluorine source were almost identical with those obtained with XeF_2 when care was taken to carefully match the fluxes for the two gases.[3]

D. Effect of electron bombardment on SiO_2

Microbalance measurements indicate that SiO_2 loses mass slowly during electron bombardment. A loss of oxygen during electron bombardment is indicated by AES. This is in agreement with the results of Carriere and co-workers.[4] Our results indicate that one monolayer of oxygen is desorbed by a 1 keV, 20-μA electron beam over a period of 36 min. An increase in the partial pressure of oxygen in the chamber could not be measured. This is not surprising considering the low electron stimulated desorption rate of oxygen from SiO_2. We saw *no* evidence of multilayer loss of oxygen from the SiO_2 films.

E. Exposure of electron damaged SiO_2 to XeF_2

Fluorine is adsorbed on fresh SiO_2 during exposure to XeF_2 or F_2 as indicated by AES. Microbalance measurements indicate that one monolayer of fluorine is adsorbed from XeF_2 or F_2 by SiO_2.[2] SiO_2 stops adsorbing fluorine after one monolayer as determined by both AES and crystal microbalance measurements.

We observed no spontaneous etching reaction between XeF_2 or F_2. Microbalance measurements indicate that an oxygen depleted SiO_2 surface (due to electron bombardment) increases mass when exposed to either XeF_2 or F_2 at the same rate as a virgin SiO_2 surface.

F. Simultaneous exposure of SiO_2 to electrons and XeF_2

As shown by Coburn and Winters,[5] an electron beam will etch SiO_2 in the presence of XeF_2. The microbalance results shown in Fig. 4 demonstrate the loss of mass from simultaneous bombardment of SiO_2 with a 1 keV, 20-μA electron beam and 1×10^{16} XeF_2 molecules/s. The large increase that occurs when the electron gun is allowed to hit the sample and the large decrease seen when it is turned off are due to thermal effects in the quartz crystal microbalance. Using the "before" and "after" values of the frequency, the rate of mass loss under these conditions is found to be 2.7×10^{-9} g/s (0.8 amu/electron). Our preliminary measurements indicate that this etch rate is linear in XeF_2 flux and electron current over a small range of the values given above.

acterization. High resolution is readily achieved; usually the spectral resolution is limited by the intrinsic width of the Raman bands from surface species. Easy access to the low frequency region allows observation of the motions of the adsorbed molecule relative to the surface. IR transmission measurements require a transparent support; this restriction does not apply to Raman spectroscopy as the scattered radiation is collected from the illuminated surface.

Surface Raman spectra may be interpreted at various levels. The high specificity of the vibrational frequencies may be used for fingerprint identification of the adsorbate composition. From a more detailed analysis of the observed frequencies one obtains information on the adsorption geometry, the surface–adsorbate bonding, and on structural changes within the adsorbed molecule (cf. Sec. V). Frequency analysis also yields information on the structures of reactive intermediates which exist only as surface species. The formation of such species plays a crucial role in catalytic reactions.

Raman scattering fulfills all the requirements mentioned above for *in situ* characterization: as an optical technique it is applicable in reactive or corrosive environments. Reactant and product gases above the surface at atmospheric pressures do not represent a problem; the technique can be made surface specific. These advantages of Raman spectroscopy have been recognized by researchers in heterogeneous catalysis for a long time. The crucial problem which prevented widespread application is sensitivity, as Raman scattering is an inherently weak process. Recently, advances have been made in two different directions which provide the necessary submonolayer sensitivity. The first improvement concerns multichannel detection technology. This approach, pioneered by Chang *et al.*,[11] has recently made it possible to detect monolayers of solid adsorbates on inert substrates.[12,13]

The second possibility to enhance sensitivity, which has been employed in this work, is the use of surface enhancement phenomena. The intensive experimental and theoretical activity which followed the discovery[14,15] of SERS has converged into a consensus that at least two mechanisms are contributing to the enhancement. As a series of reviews on the subject is available,[16–20] we shall restrict ourselves to listing the important effects. The first, electromagnetic enhancement contribution, is molecule independent and quite general in nature. On suitably roughened metallic surfaces, the adsorbed molecules experience local electromagnetic fields which are amplified compared to the incident laser field. This results in stronger excitation. When the molecule is radiating at the Raman-shifted frequency, the surface acts as an "antenna" and thus enhances the rate of emission. The field amplification is due to the so-called "lightning rod effect,"[21] and due to resonant excitation of localized or extended surface plasmons.[17,20] To support the enhancement, surface roughness on a well-defined size scale of 10–100 nm,[22–26] and a match between laser wavelength and the particle plasmon resonance frequency are required. Low loss metals can support large field amplifications; for this reason the noble metals Ag, Au, and Cu provide the strongest enhancements. The range of the enhancement is determined by the particle dimensions: it is strongest for the first adsorbed monolayer; several subsequent physisorbed layers experience weaker enhancements.

In contrast, the second, so-called "chemical" enhancement mechanism[18] is restricted to the first monolayer, as it requires electronic overlap between the substrate and the adsorbate. Resonant light-induced charge transfer processes appear to play a dominant role. This enhancement contribution is highly molecule specific, as it requires molecular donor or acceptor levels at suitable energies. It has been emphasized[18] that special adsorption sites ("adatoms") play an important role in this mechanism.

The relative importance of the two enhancement contributions will vary with the adsorbate. For the electromagnetic enhancement factor, reliable theoretical estimates are available.[24–26] They depend on the details of the surface structure; a factor of 10^4 is typical for a strongly enhancing Ag particle surface. The chemical enhancement factor may be 10^2 or larger for certain molecules (e.g., pyridine); most molecules for which this factor has been shown to exist contain a π electron system. While the chemical enhancement factor provides a substantial sensitivity increase in favorable cases, it can be less influenced by the experimenter. As we are aiming to develop surface enhanced Raman scattering into a more generally applicable analytical technique, our approach has been to maximize the electromagnetic enhancement contribution by designing optimum substrate preparation strategies.[27,28]

III. DEHYDROAMINATION REACTIONS ON COPPER

An example of practical importance has been chosen to test the utility of enhanced Raman scattering under conditions corresponding to catalytic operation. To obtain a realistic assessment, our guideline was to choose substrates and adsorbates according to their intrinsic interest for catalysis, rather than model compounds that give strong SERS enhancements.

The catalyzed process studied corresponds to the gross reaction[29]

$$R'\text{–}OH + NH_2\text{–}R \rightarrow R'\text{–}NH\text{–}R + H_2O\,, \qquad (1)$$

where R and R′ are aliphatic or aryl–alkyl organic residues. The product amines are large-scale industrial products used as fabric softeners, ore flotation agents, and additives in various products of petroleum refining. They are also important intermediates in the production of drugs, pesticides, and surfactants.

Copper has been found to be most suitable due to its high activity and selectivity to the desired amine.[30] High activities are also observed with cobalt and especially with nickel, but selectivities are relatively low. The high selectivity of copper is attributed to the fact that with copper virtually no C–C bond cleavage takes place under amination conditions.[31] In contrast, significant C–C bond cleavage (hydrogenolysis) is observed with nickel and cobalt.

The interactions of reactant and product amines with the metal surface play a decisive role for the activity, selectivity, and lifetime of the catalysts. Depending on these interactions the amines can undergo side reactions, such as disproportionations and hydrogenolysis.[32] These reactions lead to

both lower selectivity to the desired amine, and to catalyst deactivation by incorporation of nitrogen and carbon into the metal surface.[33] With copper only deactivation by surface nitride formation is observed, whereas with nickel and cobalt both nitride and carbide formation occurs. Deactivation by nitride formation can be completely prevented by adding hydrogen to the feed stream.[34] Hydrogen biases equilibria such as[33]

$$2\ NH_2\text{–}R + 3\ Me \rightarrow NH\text{–}R_2 + Me_3N + 3/2\ H_2\,, \qquad (2)$$

where Me represents the metal. It is evident from the above that the adsorption and desorption behavior of reactant and product amines is of crucial importance.

For these reasons, it is of high interest to obtain a detailed understanding of the bonding of the amine to the surface.[35] In a thorough study[29] of the mechanism of reaction (1), which has been termed "dehydroamination," a surface species of the form R–NH* was proposed, where * represents a surface site. The spectroscopic investigation described below is centered around determining the structure of this intermediate. Before discussing the results, the procedure employed to prepare copper surfaces suitable for enhanced Raman scattering is described.

IV. SUBSTRATE PREPARATION PROCEDURE

Surface enhancement depends critically on the creation of surface roughness; as mentioned above, particles in the 10–100 nm size range give strongest electromagnetic enhancement contributions. A variety of procedures is known to produce such roughness. Slow thermal evaporation of thin metal films onto cooled[36] or room temperature[37] substrates produces metal islands with typical dimensions of 5–50 nm, which yield quite strong enhancements in the case of Ag and Au. For the present investigation island films are less suitable as the islands change their shape and optical properties in the presence of surface-active adsorbents. Oxidation-reduction cycles on metal bars or foils[19] are another effective method for generating substrates providing strong surface enhancements. During reduction, the metal is redeposited in the form of globules or particles on the electrode. These protrusions are stochastically distributed over the surface and span a wide variety of sizes, a fraction of which fall into the range which is optimum for SERS. The chemical etching procedure described below is similar in this respect. For completeness we add that two procedures are known to date which produce particles that are uniform in size and shape. The first is angle evaporation of the metal onto a square array of posts, which is created by lithographic techniques on a dielectric substrate.[27,38] The second approach is evaporation of metal onto a surface consisting of tall SiO_2 needles, which are produced by plasma etching of a substrate using a random metallic mask.[28] The use of these substrates for catalytic studies is presently being pursued in our group.

The substrate preparation technique that was used to study adsorption of amines on copper involves the following steps.[19] Commercial copper foil of 0.1 mm thickness is sandblasted using SiO_2 powder. This treatment generates crater-shaped roughness on a relatively large size scale (typically 1 μm) which in itself does not lead to surface enhancement, but facilitates the following chemical etching step. The substrate is immersed into a vigorously stirred 2 M HNO_3 solution at room temperature, for about 2 min. This procedure creates a sponge-type surface with plentiful roughness features on the 10–100 nm size scale, as shown by electron micrographs. After the etch, the substrate is thoroughly rinsed with deionized water, dried with nitrogen, dip coated with the investigated liquid, and the excess liquid is blown off with nitrogen. The sample is then placed into a glass or quartz reactor, with a pool of liquid at the bottom. Adsorption/desorption equilibrium is established in a nitrogen atmosphere saturated with the vapor of the amine, before the optical measurements are begun.

V. BONDING OF TOLUIDINE ONTO COPPER

m-Toluidine (*m*-CH_3–C_6H_4–NH_2) was chosen as the first example to study the bonding of amines to copper catalyst surfaces. As mentioned above, our aim was to investigate the nature of the surface species R–NH* that plays an important role in the dehydroamination mechanism.[29] Two bonding models may be formulated (as illustrated in Fig. 1). In the first model, the amine looses a hydrogen atom and forms a (covalent) bond to the surface site. In the second picture, the amine bonds to the surface via the nitrogen lone pair.

To decide between the two models, we have based our argument on two pieces of evidence. (i) Raman spectra of model compounds (also shown in Fig. 1) were compared with the surface Raman spectrum of toluidine. Lithium *m*-toluidide corresponds to the model where a covalent bond between nitrogen and metal is formed. The toluidinium ion, where an additional proton is attached to the nitrogen lone pair, corresponds to the second picture above. (ii) A partial normal coordinate analysis was performed to interpret the frequencies seen in the toluidine surface spectrum.

Figure 2 shows Raman spectra of toluidine and of the model compounds. Trace (c) is the spectrum of the neat *m*-toluidine liquid; trace (b) is the SERS spectrum of the substance adsorbed on copper, in equilibrium with the saturated

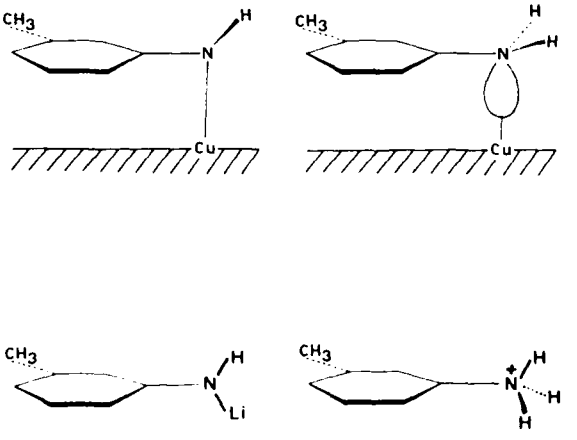

FIG. 1. Bonding of *m*-toluidine to a copper surface. The compound lithium toluidide (left) is a model for covalent bonding to the copper after dissociative loss of a hydrogen atom. The toluidinium ion (right) is a model for bonding to the surface via the nitrogen lone pair.

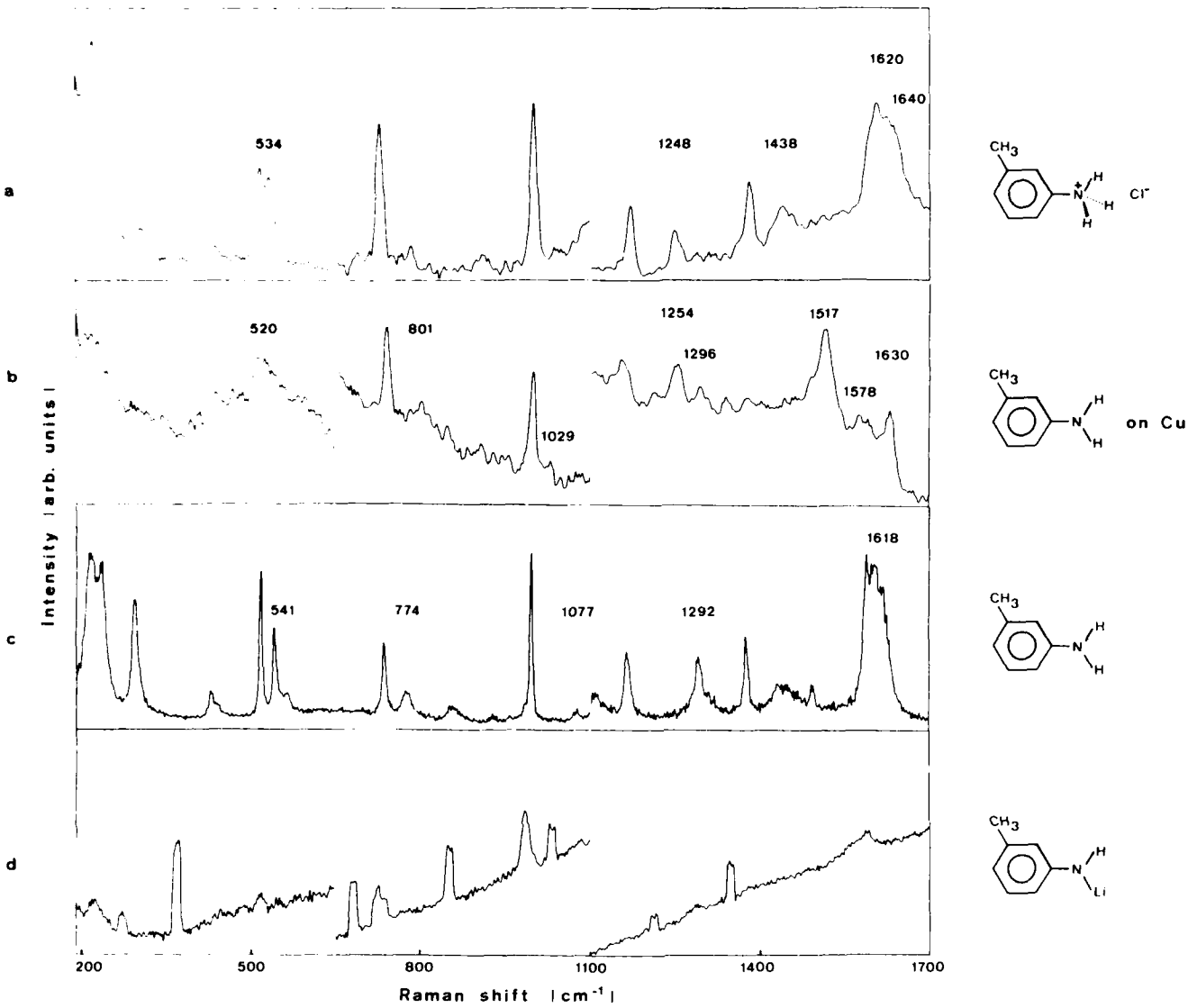

FIG. 2. Surface Raman spectrum of *m*-toluidine and spectra of model compounds. The enhanced Raman spectrum of toluidine excited with 10 mW from a DCM dye laser is shown in trace (b). Trace (c) is the Raman spectrum of neat *m*-toluidine liquid. The spectra of *m*-toluidinium chloride and of lithium toluidide are presented in traces (a) and (d), respectively. The breaks in the spectra at 650 and 1100 cm $^{-1}$ arise from different amounts of background subtracted for the low, medium, and high wave number regions.

vapor. Marked differences between the two spectra are clearly discernible. The highest frequency band of the 1600 cm $^{-1}$ region (observed at 1618 cm $^{-1}$ in the free molecule) is upshifted to 1630 cm $^{-1}$ in the surface spectrum. Another significant upshift is observed for the band at 1292 cm $^{-1}$. Importantly, the surface spectrum features an additional band at 1254 cm $^{-1}$, which is completely absent in the free molecule spectrum. In the torsional motion region above 500 cm $^{-1}$, the discrete spectrum of the free molecule merges into a broad band centered around 520 cm $^{-1}$, hinting to an inhomogeneous distribution for the hindered motions of the molecule on the surface.

It is illuminating to compare the surface spectrum [trace (b)] with the spectra of the model compounds. The Raman frequencies of lithium toluidide, while distinctly different from those of liquid toluidine, exhibit no apparent correlations with the surface spectrum. For toluidinium chloride [trace (a)], however, several remarkable similarities with the SERS spectrum of adsorbed toluidine are noted, e.g., an upshift of the highest-frequency band in the considered region, and the occurrence of a band around 1250 cm $^{-1}$. Thus the inspection of the model compound spectra appears to favor the second bonding model mentioned above, where the amino group retains both hydrogen atoms and bonds to the surface via the nitrogen lone pair.

This indication was confirmed by a partial normal coordinate analysis[35] of the frequencies in which the amino group is involved. The adsorbate was treated as a four-atom fragment Phe–NH_2, where Phe– was given the mass of a phenyl ring. The force constants within this fragment were adjusted to fit the relevant bands in the Raman spectrum of the free molecule, and were not further adjusted subsequently. For the molecule–surface complex, the geometry shown in Fig. 3 was adopted, where the value of 2 A for the copper–nitrogen

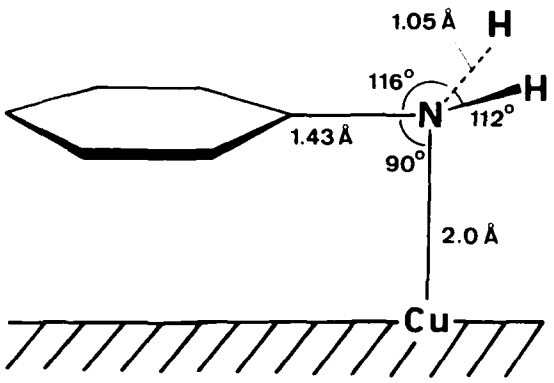

FIG. 3. Geometrical parameters of the phenyl–NH_2 fragment and of the surface complex used in the normal coordinate analysis (Ref. 35).

bond length is typical for nitrogen ligands in copper complexes. (The quality of the fit turns out to be relatively insensitive to this parameter.) Adjusting the Cu–N stretching and Cu–N–H, Cu–N–Phe bending force constants, a very satisfactory agreement with the observed frequencies in the SERS spectrum of adsorbed toluidine was obtained.[35] In particular, the upshifts of the two bands mentioned above and the additional vibration at 1254 cm^{-1} are well reproduced by the model; the latter is identified as a bending motion of the molecule relative to the surface. (Calculations using the same parameter set also identified the 1248 cm^{-1} band in the toluidinium spectrum as a doubly degenerate R–N–H bending mode.[35])

In conclusion, the evidence from the model compound spectra and from frequency analysis indicates that for room temperature adsorption, *m*-toluidine binds to the surface via the nitrogen lone pair, without N–H bond dissociation.

From the studies of amine adsorption we proceed to investigations of the dehydroamination catalytic system, represented by reaction (1) of Sec. III. For the bimolecular reaction (1), interpretation of the surface spectra is involved, due to the simultaneous presence of two reactants, at least one product, and of several intermediates on the surface. However, there exists an intramolecular variant[40] that produces cyclic amines from amino-alcohols; the prototype is the production of piperidine from 5-amino-pentanol. These reactions, as they start from only one reactant, are excellently suited for the application of SERS to study the mechanism and search for surface intermediates. Raman spectra of the reactants adsorbed on copper are presently being recorded.[41]

VI. SURFACE ENHANCEMENT ON INTERACTING METAL PARTICLE SURFACES

Progress in the analytical applications of SERS is intimately connected with our theoretical understanding of the enhancement mechanisms, which allows us to design substrates, and choose experimental parameters such that the enhancement is maximized. With this aim in mind, we have recently undertaken an analysis of the electromagnetic enhancement on surfaces that consist of interacting metal particles. It has long been observed experimentally[42] that the dipolar interactions between the metal particles in island films give rise to frequency shifts and broadening of the surface plasmon resonances, compared to those of an isolated particle. Recent experiments[27,28,38] have employed larger particles where in addition effects of finite particle size must be taken into account. The square arrays of uniformly shaped metal particles, first produced by Liao *et al.*,[27] require special attention due to the grating-type character of the surface, which gives rise to collective radiation phenomena. A general formalism that takes these effects into account, and models the retarded dipolar interactions between finitely sized particles, has recently been presented.[43]

Without giving a mathematical description, we show

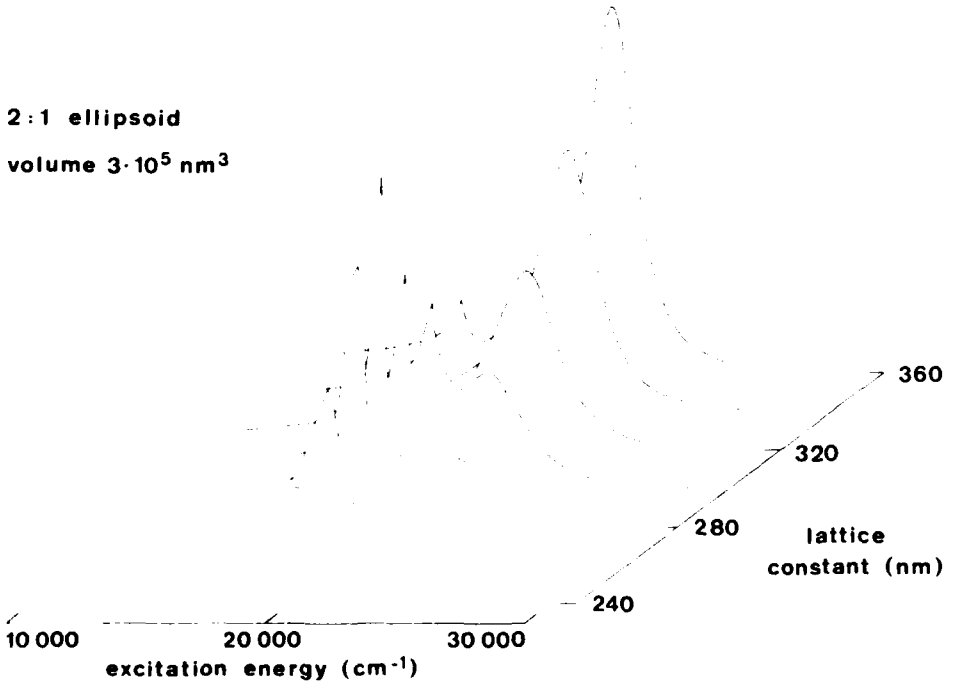

FIG. 4. Influence of dipolar interactions on surface enhancement. The local intensity enhancement (arbitrary units) at the tips of 2 : 1 ellipsoids of volume 3×10^5 nm^3 is plotted as a function of excitation energy. The particles are arranged on a square array of lattice constant *d* varying between 240 and 360 nm. The long axes of the particles are perpendicular to the plane of the array; the exciting laser is incident at an angle of 60°.

some consequences of the general results[43] for the wavelength dependence of the enhancement. Figure 4 shows, as a function of excitation energy, the local intensity enhancement on the tips of 2 : 1 ellipsoids, of constant volume $V = 3 \times 10^5\,\mathrm{nm}^3$, which are located on a square array. The lattice constant d of this array is contracted from 360 down to 240 nm. Three characteristic effects of the dipolar interactions are clearly visible in the figure.

(i) There is an overall decrease in the peak enhancement as the particles come closer together. This is due to collective radiation of the particle array, which increases with the square of the particles' area density, and reduces the enhancement due to radiation damping.

(ii) There is a "dip" in each curve, i.e., an energy for which the enhancement is essentially zero. It occurs when the grating order (n,m) = (−1,0) of the square array changes from radiating to evanescent character, i.e., is radiating at a grazing angle $\theta = -90°$ with respect to the surface normal. As elaborated in Ref. 43, for the particular incidence angle of 60° assumed in Fig. 4, this occurs for $1/\lambda = (1 + \sin 60°)^{-1}(1/d)$, i.e., the dip positions $(1/\lambda)_{\mathrm{dip}}$ follow a hyperbola when plotted as a function of lattice constant d.

(iii) On the high energy side of the "dip" the main effect of the dipolar interactions is damping; on the low energy side there is little damping but a strong red shift of the resonance position. This gives rise to the peculiar appearance of, e.g., the curve calculated for $d = 300$ nm. Here the dip occurs at an energy of 17 860 cm^{-1}. Following the wavelength dependence of the enhancement from the high energy side, we see the wings of a resonance curve which experiences progressively more damping as the dip position is approached. As soon as we have crossed beyond the critical energy at which the additional grating order stops radiating and becomes evanescent in character, the damping ceases, and strong red shifting sets in which "pulls the plasmon frequency into resonance," such that a sudden increase of the enhancement is observed. As we descend further to lower energies, the favorable red shift of the resonance frequency decreases in magnitude. Simultaneously the damping becomes stronger again, resulting in an overall rapid drop of the enhancement.

Summarizing we conclude that dipolar interactions have a profound influence on the resonance position and magnitude of the enhancement by a surface of interacting particles. Such effects, which have first been noticed on island films,[42] are even more important in several recent experiments[27,28,38] where particles of dimensions of 100 nm and above are employed. The consequences of these interactions will have to be taken into account when interpreting experimentally observed wavelength dependences, or calculating magnitudes of the electromagnetic enhancement contribution.

VII. CONCLUSIONS

Dehydroamination reactions on copper catalysts are being investigated with the aim of demonstrating the utility of surface-enhanced Raman scattering as an analytical tool in catalytic research. After discussing the information content and advantages of surface Raman spectroscopy, we have shown how surface enhancement techniques can be used in a catalytic environment to achieve the required submonolayer sensitivity. Present understanding of the size dependence of the enhancement, and of the influence of particle dipole interactions, has aided in the design of two substrate preparation procedures which result in strong enhancement: defined chemical etching of metal foils, and evaporation onto etched quartz substrates.[28] As a first application, the bonding of *m*-toluidine to a copper surface has been studied. On the basis of the surface Raman spectrum we were able to decide between two bonding models: Upon room temperature adsorption, toluidine binds to the surface via the nitrogen lone pair, without loss of hydrogen from the amino group.

Further studies will include intramolecular variants of the dehydroamination reaction at elevated temperatures, for various pressures and feed stream compositions.[41] With increasing detection sensitivity, applications of surface Raman spectroscopy to catalytically important metals which provide weaker enhancements will become possible. Work along these lines is in progress in our laboratories.

A final comment concerns the interesting question whether the surface sites observed by enhanced Raman spectroscopy are identical to those responsible for catalytic activity. This question is probably best answered by considering the three particle size ranges which are discernible based on their significantly different properties for catalysis.

(i) If we decrease the particle size starting from the bulk metal, structure sensitivity is expected to occur in the size range < 10 nm, where the statistics of the surface atoms change significantly.[44]

(ii) Electronic property changes are expected to influence surface reaction rates if the energy level spacing δ of the particle becomes larger than the thermal energy of the reactant. The level spacing δ is inversely proportional to the number N of metal atoms in the particle, and is approximately given by[45]

$$\delta \simeq 4\epsilon_F/(3N),$$

where ϵ_F denotes the Fermi energy of the metal. For Cu at room temperature, the criterion $\delta \simeq kT$ yields $N \simeq 240$, corresponding to a particle size of 2 nm as an upper limit.

Both the surface atom statistics and the changes in the electronic properties can influence the structure of the most abundant reaction intermediate (MARI).

This information answers the question concerning the connection between SERS and catalysis. As discussed in Sec. II (Refs. 22–26), the Raman enhancement is maximum for particles in the range 10–100 nm. From the catalytic standpoint this size range is equivalent to the bulk metal, and SERS will provide a spectroscopic image of the interaction of bulk metal with the adsorbates.

Two extensions are envisaged from this point. If we succeed in lowering the size range where SERS is observable substantially below 10 nm, changes in the detected adsorbate composition reflecting changes in the MARI due to structure sensitivity may become observable. The chemical enhancement mechanism which depends on dynamic charge transfer processes at specific defect sites (adatom clusters[18]) might be utilized to study the role of these sites as centers of catalytic activity.

ACKNOWLEDGMENTS

The authors would like to thank P. F. Liao for stimulating discussions. We are grateful to R. R. Ernst, W. Richarz, and U. P. Wild for their support and encouragement of this work, and thank U. P. Wild for the use of spectroscopic and computer equipment. Financial support by the Swiss National Science Foundation and the Branco Weiss Foundation is gratefully acknowledged.

[1]For a survey on the techniques with a view to catalytic applications, the reader is referred to the monograph *Characterization of Heterogeneous Catalysts*, edited by F. Delannay (Dekker, New York, 1984).
[2]*Characterization of Solid Surfaces*, edited by P. F. Kane and B. Larrabee (Plenum, New York 1976).
[3]A. Baiker, Int. Chem. Eng. **25**, 16, 30, 38 (1985).
[4]H. Ibach and D. L. Mills, *Electron Energy Loss Spectroscopy* (Academic, New York, 1982).
[5]*Vibrational Spectroscopies for Adsorbed Species*, edited by A. T. Bell and M. L. Hair, ACS Symposium Series (American Chemical Society, Washington, D.C., 1980), Vol. 137.
[6]F. Traeger, H. Coufal, and T. J. Chuang, Phys. Rev. Lett. **49**, 1720 (1982).
[7]J. Ducuing and N. Bloembergen, Phys. Rev. Lett. **10**, 474 (1963).
[8]C. K. Chen, A. R. B. de Castro, and Y. R. Shen, Phys. Rev. Lett. **46**, 145 (1981).
[9]A. Wokaun, J. G. Bergman, J. P. Heritage, A. M. Glass, P. F. Liao, and D. H. Olson, Phys. Rev. B **24**, 849 (1981).
[10]T. F. Heinz, M. M. T. Loy, and W. A. Thompson, J. Vac. Sci. Technol. B **3**, 1467 (1985); D. F. Voss, M. Nagumo, and L. S. Goldberg, *ibid.* (to be published); N. E. Van Wyck, E. W. Koenig, J. D. Byers, Z. Z. Ho, and W. M. Hetherington, *ibid.* (to be published).
[11]R. K. Chang and M. B. Long, in *Light Scattering in Solids*, edited by M. Cardona and G. Guentherodt (Springer, Berlin, 1982), Vol. 2, p. 179.
[12]A. Campion, J. K. Brown, and V. M. Grizzle, Surf. Sci. **115**, L153 (1982).
[13]J. C. Tsang, Ph. Avouris, and J. R. Kirtley, J. Chem. Phys. **79**, 493 (1983).
[14]M. Fleischmann, P. J. Hendra, and A. J. McQuillan, Chem. Phys. Lett. **26**, 163 (1974).
[15]D. L. Jeanmaire and R. P. Van Duyne, J. Electroanal. Chem. **84**, 1 (1977).
[16]R. P. Van Duyne, in *Chemical and Biochemical Applications of Lasers*, edited by C. B. Moore (Academic, New York, 1979), Vol. 4, p. 101.
[17]*Surface Enhanced Raman Scattering*, edited by R. K. Chang and T. E. Furtak (Plenum, New York, 1982).
[18]A. Otto, in *Light Scattering in Solids*, edited by M. Cardona (Springer, Berlin, 1983), Vol. 4, p. 289.
[19]R. K. Chang and B. L. Laube, Crit. Rev. Solid State Mater. Sci. **12**, 1 (1984).
[20]A. Wokaun, in *Solid State Physics*, edited by H. Ehrenreich, F. Seitz, and D. Turnbull (Academic, New York, 1984), Vol. 38, p. 223.
[21]J. I. Gersten, J. Chem. Phys. **72**, 5779 (1980); P. F. Liao and A. Wokaun, *ibid.* **76**, 751 (1982).
[22]M. Kerker, D. S. Wang, and H. Chew, Appl. Opt. **19**, 4159 (1980).
[23]A. Wokaun, J. P. Gordon, and P. F. Liao, Phys. Rev. Lett. **48**, 957 (1982).
[24]P. W. Barber, R. K. Chang, and H. Massoudi, Phys. Rev. B **27**, 7251 (1983).
[25]M. Meier and A. Wokaun, Opt. Lett. **8**, 581 (1983).
[26]E. J. Zeman and G. C. Schatz, in Proceedings of the 17th Jerusalem Symposium in Quantum Chemistry and Biochemistry, Reidel, 1984.
[27]P. F. Liao, J. G. Bergman, D. S. Chemla, A. Wokaun, J. Melngailis, A. M. Hawryluk, and N. P. Economou, Chem. Phys. Lett. **82**, 355 (1981).
[28]M. Meier, A. Wokaun, and T. Vo-Dinh, J. Phys. Chem. **89**, 1843 (1985).
[29]A. Baiker, W. Caprez, and W. L. Holstein, Ind. Eng. Chem. Prod. Res. Dev. **22**, 217 (1983).
[30]A. Baiker and W. Richarz, Ind. Eng. Chem. Prod. Res. Dev. **16**, 261 (1977).
[31]A. Baiker and W. Richarz, Helv. Chim. Acta **61**, 1169 (1978).
[32]J. Kijenski, J. Burger, and A. Baiker, Appl. Catal. **11**, 295 (1984).
[33]A. Baiker, D. Monti, and Y. Song Fan, J. Catal. **88**, 81 (1984).
[34]A. Baiker, Ind. Eng. Chem. Prod. Res. Dev. **20**, 615 (1981).
[35]A. Wokaun, A. Baiker, S. K. Miller, and W. Fluhr, J. Phys. Chem. **89**, 1910 (1985).
[36]T. H. Wood, D. A. Zwemer, C. V. Shank, and J. E. Rowe, Chem. Phys. Lett. **82**, 5 (1981).
[37]C. Y. Chen and E. Burstein, Bull. Am. Phys. Soc. **25**, 24 (1980); J. G. Bergman, D. S. Chemla, P. F. Liao, A. M. Glass, A. Pinczuk, R. M. Hart, and D. H. Olson, Opt. Lett. **6**, 33 (1981).
[38]H. W. Lehmann, R. Widmer, M. Ebnoether, A. Wokaun, M. Meier, and S. K. Miller, J. Vac. Sci. Technol. B **1**, 1207 (1983).
[39]S. K. Miller, A. Baiker, M. Meier, and A. Wokaun, J. Chem. Soc. Faraday Trans. 1 **80**, 1305 (1984).
[40]A. Baiker, A. Wokaun, W. Hammerschmidt, and W. Fluhr (to be published).
[41]W. Fluhr, K. Carron, A. Baiker, and A. Wokaun (to be published).
[42]T. Yamaguchi, S. Yoshida, and A. Kinbara, J. Opt. Soc. Am. **64**, 1563 (1974).
[43]M. Meier, A. Wokaun, and P. F. Liao, J. Opt. Soc. Am. B (in press).
[44]R. van Hardeveld and F. Hartog, Surf. Sci. **15**, 189 (1969).
[45]R. Kubo, J. Phys. Soc. Jpn. **17**, 975 (1962).

Normal (unenhanced) Raman spectroscopy of molecules adsorbed on surfaces

Alan Campion
Department of Chemistry, The University of Texas at Austin, Austin, Texas 78712

(Received 18 March 1985; accepted 21 May 1985)

Design considerations for a surface Raman spectrometer are reviewed. The behavior of the electromagnetic field near a conducting surface dictates the excitation and observation conditions for surface Raman spectroscopy; multichannel detection results in sufficient sensitivity to detect submonolayer quantities of material adsorbed on single crystal metal and semiconductor surfaces. Several examples, which illustrate the versatility of the technique, are presented.

I. INTRODUCTION

Optical techniques provide a powerful complement to the array of surface-sensitive electron spectroscopies available in surface science. Their power derives from their ability to study surface processes in the presence of a dense gas or liquid ambient phase, thus providing *in situ* process diagnostics. For surface chemical problems, which range from oxidation and corrosion electrochemistry to laser microchemistry of semiconductor surfaces, vibrational spectroscopies are particularly powerful since they provide high molecular specificity. Thus, it should be possible to unravel the mechanistic details of a surface chemical reaction by monitoring the intermediates present during a reaction.

Infrared reflection absorption spectroscopy is developing as a very powerful optical technique both for ultrahigh vacuum studies[1] and for studies of the electrochemical environment.[2] Raman spectroscopy is a promising alternative technique which offers some potential advantages including a wider spectral range, much higher spatial resolution, and perhaps greater sensitivity. The latter point needs to be emphasized, for it had long been thought that Raman spectroscopy of molecules adsorbed at low coverage on single crystal surfaces would require enhancement of the signal due either to resonance Raman scattering by the adsorbed molecule or to the surface-enhanced Raman (SERS) effect. The former case is molecule specific while the latter is substrate specific and thus neither is generally applicable.

We have improved the effective sensitivity of surface Raman spectroscopy so that it is now possible to record spectra of molecules adsorbed on low surface area substrates at submonolayer coverage. We achieved this sensitivity by designing a surface Raman spectrometer based upon the behavior of the electromagnetic field near conducting surfaces. These considerations required a certain geometry for optimum efficiency. In addition, multichannel detection provides a sufficient reduction in the time required to scan a spectrum to a few minutes, making it competitive with other techniques. In this article, I will describe the physical principles underlying the surface Raman experiment and provide several examples which illustrate its versatility.

II. EXPERIMENTAL CONSIDERATIONS

Achieving submonolayer sensitivity for surface Raman spectroscopy without enhancement requires attention to details of the experimental design, which arise from considerations of the behavior of the electromagnetic field near a conducting surface. Greenler and Slager[3] provided the first simple model with which to understand the surface Raman experiment. The electromagnetic field felt by a molecule near a surface is the sum of the incident laser field and that reflected by the substrate. Fresnel's equations are solved, using tabulated values of the substrate dielectric constant, to determine the magnitude and orientation of the local field as a function of incident angle and polarization. For most metals, the maximum local field is created by light incident near 60° to the surface normal and polarized parallel to the plane of incidence (p polarized). This geometry results in a slight amplification of the laser intensity by about a factor of 2.

The local electromagnetic field induces a dipole in the molecule which radiates. The orientation of the induced dipole depends upon the symmetry of the molecular vibration and the orientation of the molecular polarizability tensor in the surface frame of reference. In many cases the polarizibility tensor will be diagonal in the surface frame of reference which means that, for totally symmetric modes, the induced dipole will also be oriented along the surface normal. The angular distribution of the scattered radiation will be affected by the presence of the conducting surface. Greenler and Slager calculated the interference between directly emitted radiation and that suffering a single reflection from the surface, by the same procedure used for the incident field. Not surprisingly, the radiation is predicted to peak near 60° from the surface normal by symmetry, and its intensity is also enhanced by about a factor of 2.

These considerations dictate an optimum geometry for surface Raman experiments; excitation by a p-polarized laser incident at 60° and observation near 60°. I want to emphasize the latter point especially because it is not obvious intuitively. We have, in fact, measured the angular distribution of the scattered light[4] and found it to be in excellent agreement witht the predictions of Greenler and Slager. Even with the very fast (0.95) optics used in our experiment, the signal collected normal to the surface is down by about a factor of 5. The situation is much worse with slower optics, rendering the experiment essentially impossible using normal collection.

We have designed a surface Raman spectrometer based upon the model outlined above. Raman capabilities are easily added to an ultrahigh vacuum surface analysis chamber;

 0734-211X/85/051404-04$01.00

only two lenses are required: one to focus the incident laser and one to collimate the scattered radiation. Our ultrahigh vacuum chamber is equipped with low-energy electron diffraction (LEED), Auger electron spectroscopy (AES), and quadrupole mass spectrometry for surface analysis. We chose to make the plane of incidence and the scattering plane orthogonal to minimize difficulties with the specularly scattered beam. A standard high angle (71°) port was fitted with a 50-mm focal length lens to produce an elliptical spot on the sample whose dimensions are roughly $100 \times 300\,\mu$m. A special port was added in the horizontal plane oriented at 55° to the surface normal which contains a very small, very fast collection lens (D. O. Industries 2595; 25 mm $f/0.95$) which collimates the scattered light. A secondary focusing lens, which can be located anywhere in the collimated beam, is used to refocus the scattered light into a spectrograph, with proper f matching.

The scattered light is analyzed by either a single spectrograph, using a colored glass filter to reject the elastically scattered light, or a triple spectrograph. The former configuration is useful only for moderate to large wave number shifts (> 900 cm^{-1}) while the latter can be used down to at least 100 cm^{-1}. We use either a cooled, intensified vidicon (EG&G PARC 1254) or an intensified silicon photodiode array (EG&G PARC 1420) for multichannel detection either of which provides a multiplex advantage of about a factor of 500.

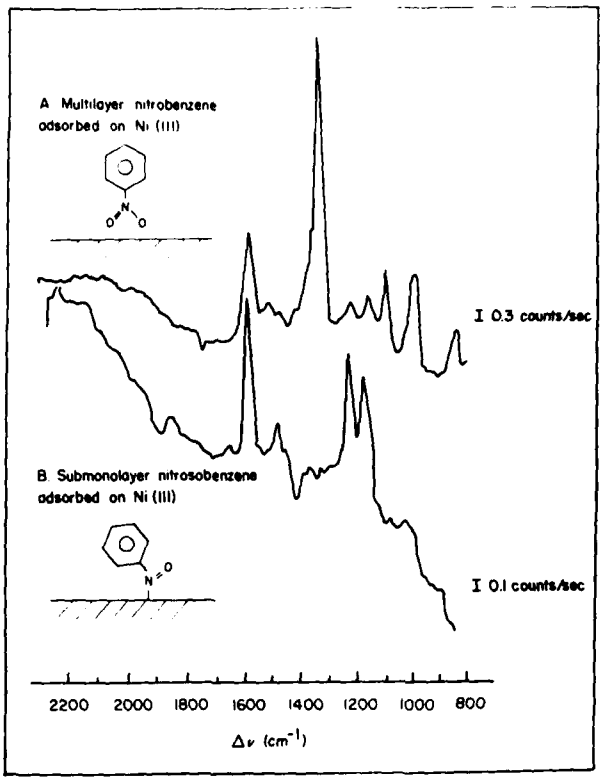

FIG. 1. Normal Raman spectrum of a very thin film (~ 5 nm) of nitrobenzene condensed on a Ni(111) surface at 100 K. 150 mW of 514.5-nm-laser power was used and the spectrum was integrated for 500 s. Normal Raman spectrum of less than a monolayer of nitrosobenzene adsorbed on Ni(111) at 100 K. The nitrosobenzene resulted from dissociative chemisorption of nitrobenzene. Conditions were the same as above except that the spectrum was integrated for 1000 s.

III. EXAMPLES AND APPLICATIONS

A. Nitrobenzene adsorption on Ni (111)

In this section I will discuss several examples that illustrate the versatility of the technique. The first example of a surface Raman spectrum without enhancement arose from a study of the adsorption of nitrobenzene on Ni (111).[5] This system was chosen because nitrobenzene has a well-known Raman scattering cross section and because nickel is too lossy to support the electromagnetic resonances thought to be largely responsible for surface-enhanced Raman scattering. In addition, since the surface was very flat, momentum conservation precluded the excitation of surface plasma resonances. The Raman spectrum of a very thin film (~ 5 nm) of nitrobenzene physically adsorbed on a Ni (111) surface is shown in Fig. 1. The spectrum is essentially identical to that of the liquid, as expected for a physisorbed system. This spectrum was acquired in less than 10 min with about 150 mW of laser power and clearly shows the enormous advantage offered by multichannel detection. Acquiring this spectrum, at the same signal-to-noise ratio would require several days using a conventional scanning instrument. Surface Raman spectroscopy is obviously an extremely promising tool for studying the structures of thin films, for example, photoresists, polymer coatings on electrode surfaces or other surface modifiers.

The adsorption of nitrobenzene on Ni (111) at submonolayer coverage produced the spectrum shown in Fig 1. The dramatic differences between the spectra strongly suggest that some chemical changes have occurred upon adsorption; in fact, the nitrobenzene adsorbs dissociatively to form nitrosobenzene and oxygen atoms, both of which are presumably bound to the surface. (X-ray photoelectron spectroscopy has detected the chemisorbed oxygen.[6]) This assignment was confirmed by adsorbing nitrosobenzene onto the surface, which resulted in the same spectrum.

B. Ethylene adsorption on Ag (110)

Ethylene is converted with high selectivity to ethylene oxide over supported silver catalysts.[7] In an effort to elucidate the mechanism of this industrially important reaction, we are conducting studies of ethylene oxidation over single crystal model catalysts at elevated pressures, the goal being to identify the reactive intermediates and correlate their concentrations with the rates and product distributions. As a first step towards that goal, we have taken the surface Raman spectrum of ethylene adsorbed on a Ag (110) surface at low temperature. It is known from high resolution electron energy loss spectroscopy (HREELS) that preadsorption of atomic oxygen on the surface greatly enhances the sticking coefficient of ethylene.[8] The HREELS studies did not detect any changes in the silver-oxygen mode upon ethylene chemisorption and suggested therefore that the ethylene was adsorbed on a silver atom. The apparent role of the oxygen is to make the silver more electropositive, and thus enhance the chemisorption of ethylene.

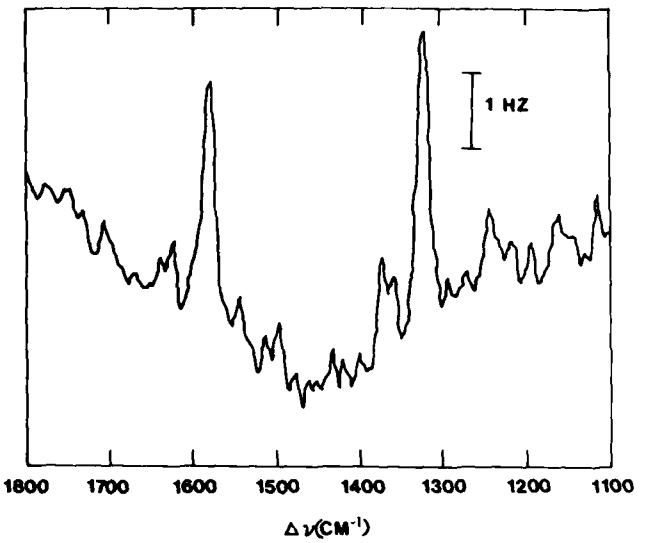

FIG. 2. Normal Raman spectrum of ethylene adsorbed on Ag(110) at 100 K. The silver surface was first dosed with oxygen at 300 K until a sharp 2×1 LEED pattern was achieved. Then 100 L (uncorrected) of ethylene was dosed resulting in half-monolayer coverage. 250 mW of 514.5-nm radiation was used for excitation and the spectrum was integrated for 1000 s.

Figure 2 shows the surface Raman spectrum (interestingly, the scattering is *not* enhanced on smooth silver) of ethylene adsorbed at half-monolayer coverage on a silver surface that had been predosed with oxygen. The C = C stretch and the symmetric C–H in plane bend are clearly observed at ~1580 and ~1320 cm^{-1}, respectively. These frequencies are about 20 cm^{-1} lower than in the gas phase, suggesting a very weak chemisorption interaction with the surface. The Raman spectrum confirms the HREELS results and is further evidence of the sensitivity of unenhanced surface Raman spectroscopy.

C. Acetonitrile adsorption on Si(100)

Unenhanced Raman spectroscopy offers great promise for studying chemical reactions occurring on semiconductor surfaces. The technique is especially appealing given the great current interest in using lasers to drive or control surface chemical processes related to microelectronic device fabrication. Since Raman spectroscopy is capable of extremely high spatial, as well as spectral, resolution the same laser can be used to initiate and monitor surface microchemistry. Alternatively, two-color experiments can be envisioned where two spatially coincident lasers of different frequencies and powers can be used for photolysis and Raman spectroscopy.

At first glance it might appear that Raman scattering by adsorbates on semiconductors would be overwhelmed by the bulk Raman scattering from the substrate. Our previous examples both involved face-centered cubic (fcc) metals, which have no Raman-active phonons. To determine the level of interference from substrate excitations, we have examined the Raman scattering from clean and adsorbate-covered silicon surfaces. The clean Si(100) surface (sputtered and annealed to give a 2×1 LEED pattern) shows the very strong one-phonon loss at 525 cm^{-1} and the much weaker two-phonon band at 1020 cm^{-1}.[9] Except for these two regions, the background scattering from the substrate is no worse than what we have observed from metals. Thus, we expect to have a large spectral window for studying adsorbates.

In our first attempt to study adsorption on silicon we have obtained the Raman spectrum of a few monolayers (50 L uncorrected exposure) of acetonitrile physically adsorbed on Si(100). The spectrum of the C–H stretching region is shown in Fig. 3. The excellent signal-to-noise ratio suggests strongly that we will be able to see submonolayer amounts of adsorbed molecules, with very low Raman cross sections (acetonitrile was chosen for this study because of its small

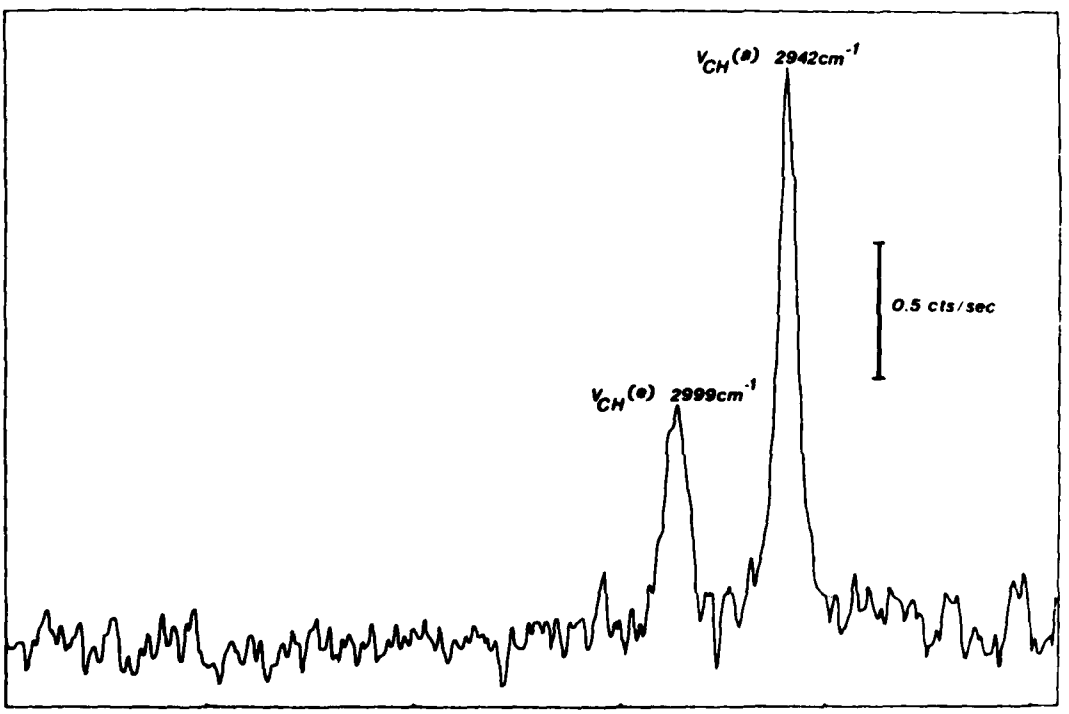

FIG. 3. Normal Raman spectrum of a very thin film (~5 nm) of acetonitrile adsorbed on Si(100) at 100 K. 50 mW of 457.9-nm radiation was used and the spectrum was integrated for 500 s.

Raman cross section). Because of the low reflectivity of silicon, sample heating is a bit more of a problem than for metals; we are redesigning our sample mount to alleviate this problem and bring our detectability into the submonolayer regime. These results, while preliminary, are very encouraging and point to the great potential Raman spectroscopy has for studying surface chemistry at semiconductors.

IV. CONCLUSIONS

We have shown that unenhanced surface Raman spectroscopy is a powerful new tool for investigating surface-mediated chemical processes. The method provides high spectral and spatial resolution, a wide spectral range, good sensitivity, and immunity to the presence of an ambient phase. Technological advances, which include more efficient collection of the scattered light, ultraviolet excitation, and the next generation of more sensitive (CCD-based) multichannel detectors can be expected to produce one to two orders of magnitude in increased sensitivity. A wide variety of applications is anticipated, including the study of molecules adsorbed on metal, semiconductor, and dielectric surfaces.

ACKNOWLEDGMENTS

The financial support of The Robert A. Welch Foundation, The Research Corporation, The National Science Foundation, The Camille and Henry Dreyfus Foundation, and The Alfred P. Sloan Foundation is gratefully acknowledged.

[1]F. M. Hoffmann, Surf. Sci. Rep. **3**, 107 (1983).
[2]J. W. Russell, M. Severson, K. Scanlon, J. Overend, and A. Bewick, J. Phys. Chem. **87**, 293 (1983).
[3]R. G. Greenler and T. L. Slager, Spectrochim. Acta Part A **29**, 193 (1973).
[4]D. R. Mullins and A. Campion, J. Phys. Chem. **88**, 8 (1984).
[5]A. Campion, J. K. Brown, and V. M. Grizzle, Surf. Sci. **115**, L153 (1982).
[6]K. Kishi, K. Chinomi, Y. Inoue, and S. Ikeda, J. Catal. **60**, 228 (1979).
[7]W. M. H. Sachtler, C. Backyx, and R. A. Van Santen, Cat. Rev. Sci. Eng. **23**, 127 (1981).
[8]C. Backyx, C. P. M. DeGroot, and P. Biloen, Appl. Surf. Sci. **6**, 256 (1980).
[9]P. A. Temple and C. E. Hathaway, Phys. Rev. B **7**, 3685 (1973).

Photodesorption and adsorbate–surface interactions stimulated by laser radiation

T. J. Chuang
IBM Research Laboratory, San Jose, California 95193

(Received 15 February 1985; accepted 23 April 1985)

Laser photons can interact with a gas-solid system to promote heterogeneous reactions and to stimulate desorption. In this paper, a review is given on desorption processes induced by photon radiation. This includes laser-induced thermal desorption and photodesorption by ultraviolet, visible, and infrared lasers. Relevant theories and recent experimental results are discussed with particular emphases on surface molecular dynamics and on assessing the quantum and the thermally assisted radiation effects.

I. INTRODUCTION

The study of photochemical interactions at gas-solid interfaces has emerged as a very interesting scientific discipline and many of the basic surface processes stimulated by photon radiation have been investigated or explored in recent years.[1] It is also well recognized that the photochemical techniques, in particular the utilization of lasers, may have a major impact in the processing of solid materials for microelectronic and micromechanical devices. These processes including laser-induced chemical etching,[2] chemical vapor deposition, and doping[3,4] seem to be applicable to a wide range of materials, whether they are metals, insulators, or semiconductors. The photon-induced or -enhanced interactions can be achieved by photoexcitation of molecules in the gas phase or the adsorbed states involving both electronic and vibrational activations. They can also be accomplished by photoirradiation of solid substrates to promote electronic and/or thermal excitations. When a photon beam is present on a solid surface, competitive processes between chemical reaction and desorption can take place. Even when a chemical reaction is enhanced by the photon radiation, the reaction product may be stimulated by the same light beam to desorb from the surface. Thus photodesorption can greatly affect surface chemistry and it should be considered as an integral part of the overall surface photochemical processes. In another aspect, photon-stimulated desorption (PSD), like the conventional thermal desorption spectroscopy (TDS), can be utilized to obtain kinetic information about surface interactions. In fact, as to be discussed in this paper, PSD by laser photons can provide much important insight into surface molecular dynamics not accessible by the conventional TDS method or other surface analytical techniques. In still another way, PSD measurements performed with a wavelength tunable light source can be a powerful spectroscopic technique for studying electronic and vibrational structures of adspecies. With a tunable laser, the spectroscopy can provide unsurpassed spectral resolutions. With these various aspects in mind, I shall attempt to review current as well as previous studies on photon-, in particular, laser-stimulated desorption and other surface chemical processes directly relevant to photodesorption. In this discussion, I shall confine the subject to desorption due to photochemical interactions and not include studies on the emission of neutral or charged particles from solids due essentially to a physical ablation effect by very high power lasers.

Before lasers are more widely used in desorption studies in recent years, photon-stimulated desorption (PSD) usually means desorption induced by x ray or relatively high energy (>10 eV) photons as opposed to electron-stimulated desorption (ESD) in contemporary literature.[5] Desorption induced by such high energy photons can involve core ionization[6] as well as valence excitation.[5(a)] Although the energy range (<8 eV) of laser photons discussed in this paper cannot induce core ionization by a single-photon absorption, valence excitation is possible by UV photons. Also at high laser power levels, multiphoton excitation and ionization are possible. Thus, we shall continue to use the term PSD in this general sense when UV or visible light beams are used. In the infrared range with the photon energy less than 1 eV, electronic excitation of the adsorbate-surface complex is not attainable by single photon absorption. Resonant excitation of surface vibrational modes, however, can lead to photodesorption.[1] This is a distinctive phenomenon and we shall call this IR laser-induced photodesorption as IRPD. In contrast to x-ray or other low intensity light sources, a laser beam can in many cases heat up a solid substrate and induce thermal desorption. Thus laser-induced thermal desorption (LITD), is an important part of laser radiation effects. In LITD, surface heating can be due to direct lattice phonon excitation or initial substrate electronic excitation which rapidly decays to phonon bath before desorption occurs. The characteristics of LITD are the lack of strong photon wavelength dependence and are governed by the absorptivity of the solid which generally has a rather broad absorption spectrum. For more than a decade, major studies on stimulated desorption by low energy photons have been centered around the subject of separating the quantum effects (i.e., desorption due to resonant electronic and vibrational excitations) and the thermal effects. While undoubtedly the differentiation between these two effects needs to be resolved, other aspects of the phenomena have to be closely examined. For applications, recent studies on PSD, IRPD, and LITD show that these photodesorption processes and techniques can indeed be utilized to probe the basic adsorbate-surface interactions.

 0734-211X/85/051408-13$01.00

II. LASER-INDUCED THERMAL DESORPTION (LITD)

LITD was demonstrated in a number of adsorbate-solid systems more than a decade ago.[7,8] The phenomenon and the technique have been further investigated in recent years and interesting applications have been found.[9-14] The unique features of the laser thermal desorption, as pointed out by Cowin *et al.*,[9] include the vast range of heating rates ranging from 10^5 to 10^{11} K/s, the easy control of heating period from 1 ms or longer to 1 ns or shorter, and such technical advantages as no need for a chopper for desorption velocity measurements, no special requirements for thermal or electrical properties of the sample or its shape, and the usually high signal-to-noise ratio allowing angular resolved measurements to be performed with high precision. The wide range of heating rates may allow one to examine desorption kinetics over a wide dynamic range and help to clarify the mechanisms for multistep reactions. It may also be possible to desorb chemical intermediates not detected by other methods. Therefore, the laser thermal desorption technique should be very useful for surface studies as well as be a powerful supplement to conventional thermal desorption and flash desorption methods. In the case of metals, the absorption of laser radiation by the conduction electrons of the substrates is rapidly transformed into lattice heating. For a laser pulse width of 10^{-9} s or longer, the ordinary bulk thermal conduction laws are applicable. Solution of the heat conduction equations for application to laser experiments were given by Ready[15] and Bechtel.[16] Specifically, Cowin *et al.* investigated deuterium atom-recombination desorption with a Q-switched Nd : glass laser at 1.06 μm with a pulse width of 30 ns irradiated on W surfaces covered with D atoms. D_2 desorption time-of-flight was measured with a differentially pumped mass spectrometer. The time-of-flight distributions were converted into velocity distributions and thermal energy distributions. The desorption flux was also determined as a function of angle from the surface normal. At low desorption fluxes, they observed Boltzmann velocity distributions for the desorbed particles. But at high molecular fluxes they detected a noncosine angular distribution and a seemingly non-Boltzmann behavior in the pulsed laser-induced desorption. But after careful model analyses, they attributed this observation to the effect of collisions between molecules after they left the metal surface. The authors concluded that the desorption of D_2 from tungsten at rates of 5×10^7 monolayers/s by the laser technique was governed by the same kinetics as obtained by extrapolating previous thermal desorption measurements made at a rate of about 10^5 or more slower.

Wedler and Ruhmann[10] performed a rather thorough LITD study of CO from Fe(110) surfaces. The time-dependent CO desorption signals were recorded by a mass spectrometer following a 30 ns Nd : glass laser pulse, and compared with the calculated desorption signal due to the temperature rise induced by the laser irradiation. The maximum amplitudes of the desorption signals were examined carefully as a function of the laser intensity and the CO coverage for both single pulses and sequences of laser pulses. For a monolayer of CO adsorbed on Fe, the threshold for laser-induced desorption was about 8 MW/cm^2 and at about 30 MW/cm^2 a saturation value was reached, corresponding to all the CO being desorbed by one pulse. There was also evidence to show that in the low temperature range, the translational temperature of desorbed molecules (T_d) followed a Maxwell-Boltzmann distribution identical to the maximum surface temperature (T_s). Above $T_s = 600$ K, T_d was found to be smaller than T_s. The experimental observations were analyzed successfully with the first order rate equation for desorption. A similar system CO desorption from a Cu(100) surface was studied by Burgess *et al.*[12,13] using a KrF excimer laser and a differentially pumped quadrupole mass analyzer. Time-of-flight spectra were obtained as a function of CO coverage, laser intensity, and initial surface temperature. The major findings were that Boltzmann distributions were obeyed for all coverages and for all incident laser power levels from the threshold for desorption near 6 MW/cm^2 up to 40 MW/cm^2, a region where all adsorbed molecules within the area of irradiation were desorbed with a single pulse. This was in contrast to that observed by Cowin *et al.*[9] in the D_2/W system where a Boltzmann distribution was detected only at low desorption fluxes. It was further found that the translational temperatures of the desorbed CO were always lower than the temperatures predicted from temperature-programmed thermal desorption or the calculated surface temperatures. The possibility of collisional cooling in the desorption process above the surface in causing this low translational temperature was ruled out.

From the experiments by Wedler, Burgess, and their coworkers[10,12] it seems that molecules desorbed by LITD can indeed have a lower translational temperature than the surface temperature raised by a laser pulse. The problem associated with such measurements is the difficulty to precisely determine the surface temperature experimentally during the laser pulse. Instead, one has to rely on the theoretical calculation based on the heat conduction equations including such parameters as optical absorptivity, thermal conductivity, and heat capacity of the solid. Although the conduction equations are well known[15,16] and the solutions can be obtained numerically, the uncertainties in the boundary conditions and the lack of complete knowledge on the optical and thermal parameters as a function of temperature have rendered the accurate determination of surface temperature difficult to accomplish. Even for a given set of parameters, different formulisms can also produce substantial variations in the calculated temperatures. Thus, before a reliable experimental method allowing a direct measurement of the surface temperature with time following a laser pulse is developed, this subject will remain somewhat controversial. Since the observed translational temperatures of CO in these prior experiments[10,12] appear to deviate rather substantially from the calculated surface temperatures, it seems appropriate to consider the cause of such low temperature behavior and to ask why the CO translational degrees of freedom are not in complete equilibrium with the surface heat bath when it desorbs. The possibilities suggested by Burgess *et al.*[12] were (1) energy transfer from the translational to internal degrees of freedom, and (2) near adiabatic desorption from the chemisorption surface potential, making the energy available to translational modes substantially reduced.

These possibilities can be easily resolved by using rare gas atoms in LITD experiments since these atoms do not have internal degrees of freedom and their surface potentials are rather shallow. We have recently carried out such experiments using Xe atoms adsorbed on a Cu surface[17] and exciting the surface with a XeCl excimer laser. An attempt is also made to determine the rise of surface temperature as a function of time following a laser pulse monitored by the pyroelectric calorimetry technique developed by Coufal.[18] Details of the results will be published elsewhere.[17] In a related theoretical study concerning thermal desorption, Tully[19] performed a classical trajectory calculation on the thermal desorption of Ar and Xe from a Pt(111) surface. It predicted that these atoms could desorb with mean energies considerably lower than $2k$ times the surface temperature. On the other hand, Gortel *et al.*[20] considered thermal desorption to be a nonequilibrium phenomenon and for He atoms thermally desorbed from graphite, sapphire, etc., solid surfaces the velocity distributions might not be Maxwellian. Furthermore, the translational temperature of the desorbed He could be hotter than the substrate temperature. Such desorption behavior was experimentally observed in H_2–Ni system.[21] From these various theoretical and experimental studies, it is clear that basic questions concerning energy equilibration and dynamic effects[22] in conventional thermal desorption are still not well resolved. LITD involving very short laser pulses and very high heating rates undoubtedly has made the situation even more complicated. Only further well-defined experiments can resolve the fundamental questions discussed above.

For applications, Viswanathan *et al.*[11] demonstrated that surface diffusion could be studied on macroscopic single crystals using the pulsed LITD technique. Specifically, they used a sequence of ArF laser pulses to deplete adsorbed CO from a small area on a Cu(100) surface and determined the rate of CO diffusion from the adjacent surface region which was not irradiated by the laser pulses. The diffusion coefficient for CO on copper at 140 K was measured to be about 3.5×10^{-6} cm^2/s and the activation energy was calculated to be about 2–3 kcal/mol, approximately the energy required to force CO out of its lowest energy adsorption sites into adjacent sites. In a different approach, Hall and DeSantolo[14] applied the LITD method as a probe for studying the reaction kinetics of CH_3OH decomposition on Ni surfaces. They found that with a conventional TDS at 15 K/s heating rate, CH_3OH could decompose into H_2 and CO before the molecule and the products were desorbed, whereas with LITD utilizing a pulsed Nd : YAG laser, CH_3OH could be desorbed intact. Therefore, by using the laser technique in conjunction with the programmed heating of the sample, they were able to determine the decomposition step which occurred at about 240 K. In addition, LITD desorption of CO from Ni was investigated. It was pointed out that spatial properties of the laser beam had to be included in order to interpret the experimental results correctly. This is an important consideration whenever a Gaussian or a nonuniform laser beam is used. From this point of view, an excimer laser capable of providing spatially uniform beam is more suitable for LITD studies.[13,17] It should also be mentioned that by varying the laser power (without changing the laser irradiation area), one should be able to change the laser heating rates by orders of magnitude in order to deduce the preexponential factor and the energy barrier for desorption independently and accurately. So far, this has not been demonstrated by the groups engaged in LITD studies. This is another fundamental problem that needs to be carefully examined.

III. PHOTODESORPTION BY INFRARED LASERS

Infrared laser-induced photodesorption (IRPD) due to resonant absorption of IR photons by adsorbed molecules performed under UHV conditions was first reported by Heidberg and his co-workers.[23,24] In 1978, they used a pulsed CO_2 laser to excite SF_6 molecules adsorbed on a NaCl surface at 67 K. At the laser intensity of about 11 MW/cm^2, molecular desorption was observed when the ν_3 mode of SF_6 was excited at 946 cm^{-1}.[23] At this laser intensity, however, desorption also occurred even when the laser was tuned off resonance from SF_6 vibrational bands. In this experiment, laser-induced thermal desorption seemed to overtake the resonant vibrational excitation effect. In subsequent studies performed on multilayers of CH_3F molecules adsorbed on a NaCl film at 70 K, they reported that desorption could take place when the ν_3 stretching mode of the molecule absorbed CO_2 laser photons in the 980–990 cm^{-1}[24(a)] or 970–985 cm^{-1}[24(b)] regions. The IR transmission spectrum of a solid CH_3F on NaCl was shown to have an absorption band centered around 995 cm^{-1} with a bandwidth of about 30 cm^{-1}. A further IR absorption study of the system revealed the coexistence of different adsorbed and physisorbed phases beside the presence of solid CH_3F at high exposures.[25] The observed bandwidth in the photodesorption spectrum was much narrower, i.e., about 10–15 cm^{-1}.[24(a)] The desorption yield (Y) dependence on the laser fluence (I) was found to be $Y\propto I^{2.8}$ and it was suggested that three photons might be involved in inducing the desorption. The photodesorption cross section was estimated to be about 2×10^{-19} cm^2,[26] only slightly smaller than the IR absorption cross section, i.e., a very high desorption quantum yield. This yield was obtained by firing a sequence of laser pulses, typically a few pulses, on the same sample spot until no desorption signal was detected by the mass spectrometer. It was then assumed that the laser-irradiated area was depleted of CH_3F molecules. No *in situ* surface analytical techniques were used to directly examine the solid surfaces before or after the laser irradiation. From our experiments on other molecule-surface systems (see examples in Ref. 1), it is observed that diminishing of desorption signals at a given laser intensity does not necessarily imply that the laser-irradiated area is depleted of adsorbed species. Therefore, it is not clear whether a very high desorption efficiency due to purely molecular vibrational excitation exists for the CH_3F–NaCl system. In the same experiments, the authors also reported that desorption of the first CH_3F layer chemisorbed on NaCl occurred at laser $\nu = 955$ cm^{-1}, whereas the physisorbed multilayer adsorbate desorbed at $\nu = 995$ cm^{-1}. Again, no direct determination of the surface coverage by *in situ* sur-

face analysis was carried out in these experiments. In a later study, Heidberg and Hussla[27] investigated the photodesorption behavior of a binary coadsorbate ($CH_3F + C_2H_6$) on a NaCl film with a similar apparatus. It was reported that CH_3F desorption took place when it was excited at 976 cm^{-1}, but no desorption of C_2H_6 molecules which did not absorb IR photons at this frequency was detected. It is not known whether the surface binding energies for the adsorbed CH_3F and C_2H_6 molecules are the same or not. Recently, Heidberg also reported photodesorption of CO from a NaCl surface[28] excited by IR pulses near 5 μm generated by frequency doubling of a pulsed CO_2 laser. From the sets of experiments reported by Heidberg *et al.*, it seems difficult to determine the true desorption quantum efficiency. It is also not easy to assess the relative importance between the thermally assisted process and the genuine quantum effects in the desorption following the initial absorption of IR laser photons by the adsorbed molecules.

The phenomenon of IR photodesorption was also investigated under UHV conditions by Chuang and Seki[1,29–32] with pyridine and deuterated-pyridine molecules adsorbed on a KCl, an Ag film, and on an Ag(110) crystal. These substrates were chosen because of the different optical and thermal properties in order to evaluate the various substrate heating effects. For example, KCl was highly transparent to the pulsed CO_2 laser beam in the 9–11 μm region, but it was a relatively poor thermal conductor. The polished Ag(110) crystal was highly reflective in the IR and was a very good thermal conductor. The thin Ag film (120 Å) deposited on a quartz substrate could absorb some CO_2 laser light because the optical absorption depth at 10 μm was greater than the film thickness and the underlying SiO_2 was opaque to the laser radiation. Its thermal conductivity was also poor because of the thin and discontinuous film. The pulsed laser could excite the symmetric ring mode (ν_9) of C_5D_5N and antisymmetric ring mode (ν_8) of C_5H_5N molecules. In addition to mass spectrometry, the molecule-surface systems were also analyzed with x-ray photoemission (XPS), thermal desorption (TDS), and in the case of C_5H_5N/Ag film, also with the surface-enhanced Raman scattering (SERS) in UHV chambers. The typical photodesorption yields (Y) of C_5H_5N desorbed from an Ag (film) surface determined by a mass spectrometer as a function of laser frequency (ν) and laser intensity (I) are displayed in Figs. 1 and 2. Figure 3 shows the change in the surface-enhanced Raman spectra for the C_5H_5N/Ag (film) system after irradiation by CO_2 laser pulses exciting the ν_8 mode of the adsorbed molecules. The major results obtained by Chuang and Seki in these prior studies may be summarized as follows: (1) Desorption due to resonant absorption of IR photons either by the ν_8 mode or the ν_9 mode of pyridine molecules could occur from both metallic and dielectric substrate surfaces. No clear mode selectivity in photodesorption was observed. (2) On metallic surfaces such as Ag, the desorption yields strongly depended on the polarization of the incident radiation. Namely, the *p*-polarized light at near grazing angle of incidence induced a much higher desorption yield than the *s*-polarized light consistent with the larger IR absorption factor for a vibrational dipole oscillating perpendicular to the surface. (3) The plot of

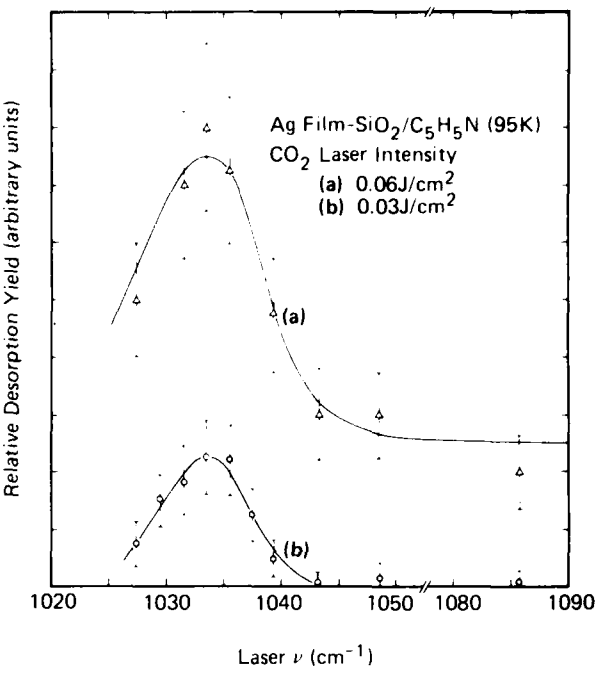

FIG. 1. Ag film (95 K)/C_5H_5N IR laser-stimulated pyridine desorption yields as a function of the laser frequency for the laser intensities at (a) 0.06 J/cm^2 and (b) 0.03 J/cm^2, at $\theta = 2$. The laser is *p* polarized and incident at 75° from surface normal. Each data point is an average of the mass peak heights due to 10 laser pulses (according to Chuang, Ref. 32).

ln Y vs ln I produced a slope greater than 2, suggesting that multiphoton absorption might be involved in the laser-induced desorption. A single CO_2 laser photon with 2.9 kcal/mol of energy certainly could not provide sufficient energy for breaking the surface bonds of the physisorbed molecules.

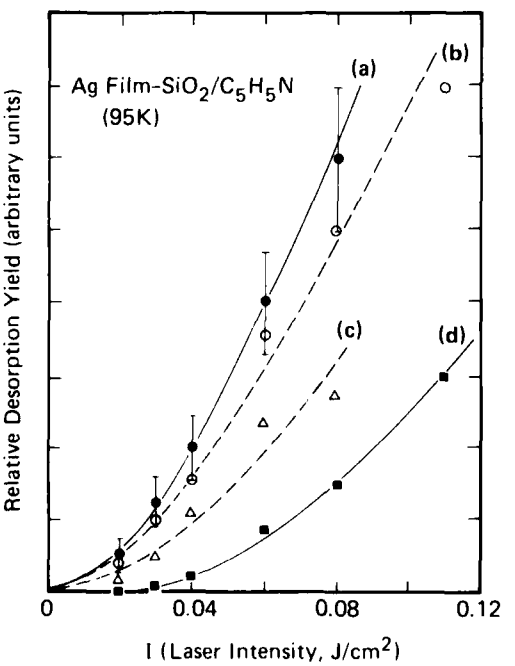

FIG. 2. Ag film (95 K)/C_5H_5N IR laser-stimulated desorption yields as a function of the laser intensity for ν at (a) 1033.5, (b) 1035.5, (c) 1039.4, and (d) 1085.8 cm^{-1}, all for surface coverage $\theta = 2$ (according to Ref. 32).

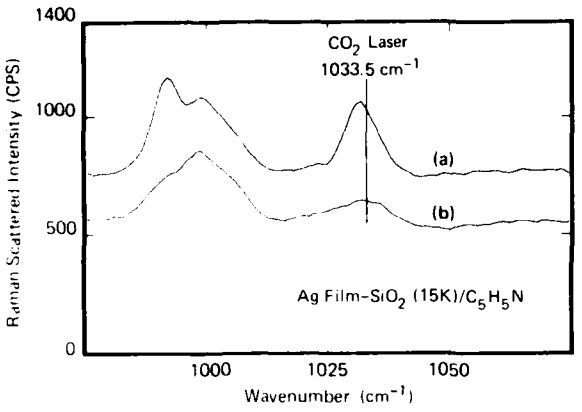

FIG. 3. Effect of CO_2 laser radiation at $\nu = 1033.5$ cm^{-1} and $I = 0.08$ J/cm^2 on the surface-enhanced Raman spectra of C_5H_5N on Ag island film at 15 K (a) before the laser irradiation and (b) after irradiation by 55 laser pulses (according to Seki and Chuang, Ref. 31).

(4) *Direct* laser-induced heating of the substrate was important even for such IR transparent material as KCl or IR reflective metal as a polished Ag crystal. This heating effect could account for the different desorption yields observed for the three different substrates. (5) In all cases studied, the desorption yields increased with the thickness of the adsorbed molecular layers. Apparently, absorption of IR photons did not directly lead to desorption. But rather, energy had to accumulate in the laser pulse width resulting in the local heating of the molecular layer as well as the underlying substrate, which eventually led to desorption of some weakly bound species. (6) The desorption quantum yield per absorbed IR photon was very small, very likely less than 10^{-3} and the photodesorption cross section was estimated to be less than 10^{-22} cm^2. A substantially higher desorption yield was obtained for pyridine adsorbed on the Ag film. The higher desorption yields were attributed mainly to the *direct* laser substrate heating effect which by a phonon-assisted process greatly reduced the activation barrier for desorption. (7) There was no clear isotope selectivity in the observed desorption. When C_5H_5N and C_5D_5N were coadsorbed on the surface and only one of the molecular species were excited by the IR laser, both isotope species could desorb with practically the same efficiency. The lack of appreciable molecular selectivity showed that photoexcited molecules did not desorb immediately and once the photon energy was absorbed by a molecule, it was quickly transferred to and shared with its neighboring molecules. It was suggested that rapid intermolecular vibrational energy transfer via dipole–dipole coupling could be responsible for the efficient energy delocalization process. Of course, very fast thermalization via electronic and/or phonon-mediated processes to create local heating could also be a major reason for the lack of molecular selectivity in desorption.

In about the same period when the experimental data became available, a number of theoretical studies also appeared. These included the work by Lin and George *et al.*,[33] Metiu and co-workers,[34] Gortel and Kreuzer *et al.*,[35,36] and Casassa *et al.*[37] Some of these studies and other theoretical considerations including the photoexcitation of the molecule-surface bonds and the possibilities of coherent and incoherent multiphoton excitation processes were discussed in the previous review (Ref. 1). In as far as relating the theoretical models to the experimental observations is concerned, the model suggested by Gortel, Kreuzer, and their coworkers[35] appears to be very relevant and conceptually useful. Basically, the processes involve the excitation of a molecular vibrational mode by a single-photon or multiphoton absorption. The photoactive mode usually has a much higher vibrational frequency than the modes directly associated with the molecule-surface bonds and it is generally considered to be decoupled from its interaction with the surface. Once excited, the vibrational energy can be transferred to energy levels in the molecule-surface potential via the bound state–bound state transitions with the transition probability $P_{i'i}^{v'v}$, following the notations used by Gortel, Kreuzer *et al.*,[35] where v and v' are the vibrational levels in the internal molecular mode and i and i' are the bound states in the surface potential. The process is followed by rapid thermalization of the levels in the surface potential via $P_{i'i}^{vv}$, and the decay of the surface energy into lattice phonons resulting in the heating of the solid. As mentioned earlier, we had called this process "*indirect* heating,"[1,32] while Gortel, Kreuzer *et al.* used the term "*resonant* heating."[35] If the rate of *indirect* or *resonant* heating is sufficiently rapid, it is then possible that the levels of excitation within the surface potential can be so high as to reach the desorption continuum and the molecule can depart from the surface with the probability $P_{ci}^{vv} > 0$, where c represents the level of desorption continuum. In the initial photoexcitation step, if the molecule can be pumped into such a high vibrational level that its total energy is degenerate with the continuum states of momentum, then tunneling from the vibrational level into these continuum states may occur via both elastic $Q_{ci}^{v'v}$ and inelastic $P_{ci}^{v'v}$ processes causing the molecular to desorb. The desorption resulting from these elastic[38] and inelastic[39] tunneling processes, the latter process being the bound state to continuum state transitions mediated by phonons, has been referred as genuine "photodesorption" due to resonant laser-molecule vibrational coupling.[35] In previous experimental and theoretical studies, it was generally considered that photodesorption via direct vibrational coupling and tunneling could be very important in the observed desorption phenomenon. In addition to giving the theoretical formula, Gortel *et al.* also performed a numerical calculation for the CH_3F–NaCl system assuming a harmonic molecular potential for the vibrational excitation by the laser beam. However, the calculated desorption rates were orders of magnitude higher than the experimental values obtained by Heidberg *et al.*[24,26] In addition to the basic photoexcitation, energy transfer, and tunneling processes described above, George and coworkers[33] also considered the effects of intramolecular vibrational energy transfer and relaxation on the desorption efficiency. For many molecule-solid systems, depending on the mode of excitation, these factors definitely have to be taken into account. However, regardless of the exact details of the energy flow through the internal molecular vibrational-rotational states and even coupling into other molecules, the essential question as far as desorption is concerned is still

related to the relative importance among the various coupling processes between the excited internal modes and the bound states as well as the continuum levels in the surface potential. Namely, what are the relative contributions of such processes as elastic and inelastic tunneling and the *indirect* or *resonant* heating to the IR excited desorption?

In another theoretical study, Wu *et al.*[40] used a macroscopic master equation approach to treat the photodesorption without having to follow the exact paths of the energy flow. They were able to show that for a two-level system involving single-photon absorption, the desorption yield would have an approximately linear dependence on the laser intensity (I), whereas for a multilevel system involving absorption of multiple (n) successive photons, the yield would be proportional to I^n. Furthermore, under the multiple photon excitation condition, the bandwidth of the desorption spectrum could be substantially narrower than the IR absorption spectrum. Using this approach, they were able to obtain the photodesorption spectrum and the desorption yield dependence on the laser intensity for the C_5H_5N/Ag system, in reasonably good agreement with those observed by Chuang and Seki[1,29,30,32] as shown in Figs. 1 and 2. The theoretical treatment as well as the numerical calculation were, however, also based on a harmonic molecular potential. Inclusion of the anharmonicity of the molecular vibration in the modeling for IRPD has now been considered by Jedrzejek.[41]

In order to further elucidate the basic processes involved in IRPD and, in particular, to assess the relative importance between the thermally assisted effects and the quantum effects, we have recently investigated NH_3, ND_3, and Xe systems neatly adsorbed or coadsorbed on a Cu(100), a NaCl (film), and an Ag(film) surface.[42–44] A tunable IR beam in the 2.5–4.2 μm range was used so that both single-photon and multiphoton excitation processes could be examined. In addition, time-of-flight mass spectrometry was employed to determine the velocity distribution of the photodesorbed molecules. The observed photodesorption yields of NH_3 adsorbed on Cu(100) at 90 K as a function of laser frequency and laser intensity at monolayer and multilayer coverages are shown in Figs. 4 and 5. Figure 6 shows the time-of-flight signals of NH_3 and ND_3 desorbed from Cu(100) when about two monolayers of the (1:1) molecular mixture adsorbed on the surface were excited by laser pulses at $\nu = 3370$ cm^{-1} which was absorbed by the stretching mode of NH_3. The lack of isotopic selectivity in IRPD is clearly evident even though only one of the adsorbed isotopic molecular species is vibrationally excited. The absence of molecular selectivity may be resulted from the very fast intermolecular energy transfer, but it may also be due to the electron and/or phonon-mediated thermal processes. The importance of the thermally assisted effect was illustrated in the experiment with a layer of Xe adsorbed on NH_3-covered Ag surfaces at 12 K. As displayed in Fig. 7, Xe atoms could also be desorbed when the underlying NH_3 molecules were excited. The results on ammonia system were very consistent with the major results obtained for the pyridine system studied earlier. The new results further revealed that both single-photon and multiphoton absorption could induce desorption. Although single-photon absorption might have a higher absorption cross section, it did not necessarily produce a higher desorption quantum yield. For NH_3/Cu(100), in fact a CO_2 laser could also excite the bending mode of NH_3 molecules and promote desorption via multiphoton absorption process.[45] The effect of electronic damping due to electron-hole pairs was further evaluated by model calculations following the approach developed by Gortel *et al.*[35] It was found that such damping effect played a major role in affecting the photodesorption yields from Cu and Ag surfaces.[46]

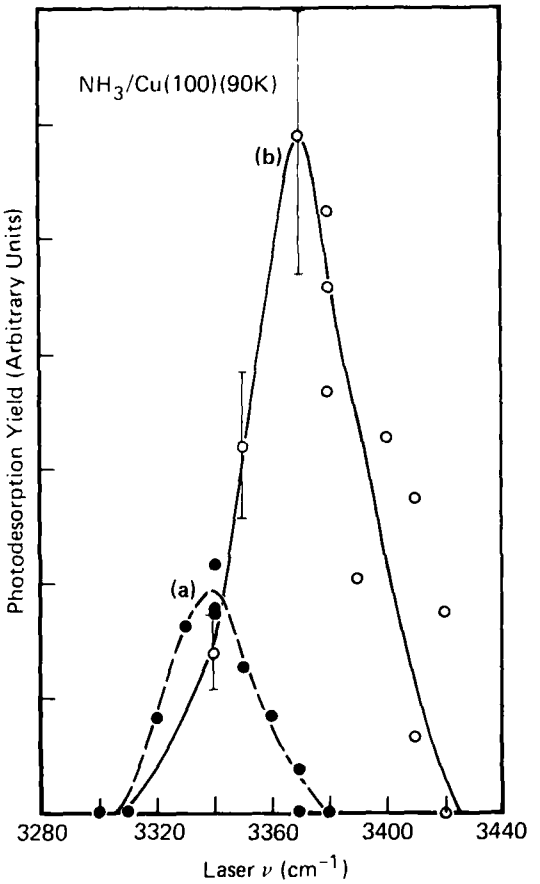

FIG. 4. IR photodesorption yields of NH_3 adsorbed on Cu(100) at 90 K as a function of laser frequency: (a) surface coverage about a monolayer, $\theta = 1$ and laser intensity, $I = 10$ mJ/cm^2; (b) multilayer coverage, $\theta = 3.4$ and $I = 10$ mJ/cm^2. The laser is p polarized and at 75° angle of incidence. Each data point is an average of mass spectrometer signals due to 20 laser pulses. Some typical error bars are also indicated. (Data according to Refs. 42 and 44 by Chuang *et al.*)

The observed translational temperature as determined from time-of-flight signals for NH_3 molecules desorbed from Cu(100) at or near a monolayer surface coverage was about 80 K $\pm$ 25 K and for the coverage of a few monolayers about 90 K $\pm$ 25 K. Experiments with conventional thermal desorption showed that a substantial amount of physisorbed NH_3 could desorb around 125 K even though the peak of the desorption signal appeared near 140 K. The original substrate temperature in the absence of laser radiation was 90 K and the direct laser-induced substrate heating could cause momentary increase in substrate temperature by about 10–15 K. This value was determined by increasing the laser intensity until thermal desorption induced by the IR pulse not

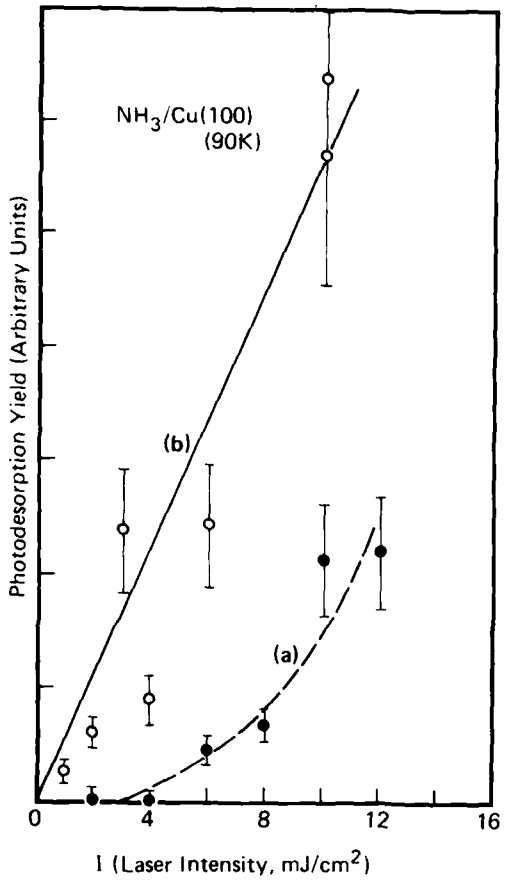

FIG. 5. Photodesorption yields of NH_3/Cu(100) at 90 K as a function of laser intensity: (a) $\theta = 1$, $\nu = 3340$ cm^{-1} and (b) $\theta = 3.4$, $\nu = 3370$ cm^{-1}, sampling average of 20 laser pulses. (Data according to Refs. 42 and 44.)

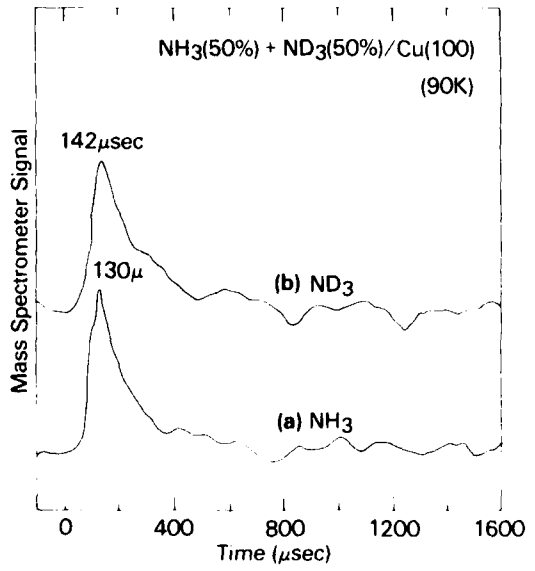

FIG. 6. TOF signals of NH_3 and ND_3 photodesorbed from Cu(100) at 90 K for a (1 : 1) mixture in the adsorbed phase: $\theta = 2.5$, $\nu = 3370$ cm^{-1}, and $I = 6$ mJ/cm^2, sampling average of 20 laser pulses. (Data according to Ref. 44.)

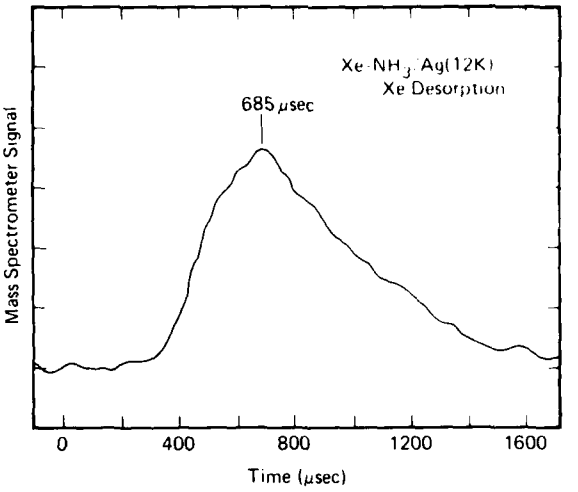

FIG. 7. TOF signal of Xe desorbed from Xe ($\theta = 2$), condensed on a NH_3 layer ($\theta = 2$), adsorbed on an Ag film at 12 K with an IR laser at $\nu = 3400$ cm^{-1}, and $I = 6$ mJ/cm^2. (Data according to Ref. 44.)

in resonance with NH_3 vibrational bands was observed. Thus, from purely thermal consideration, if resonant IR absorption could provide temporary localized heating by an additional 15–25 K via *indirect* (or "*resonant*") heating, then desorption of some physisorbed molecules due to the combined effect of *direct* and *indirect* heating could take place. This, however, cannot be entirely the case because if this resonantly excited thermal desorption were to occur, the *whole molecular layer in the laser-irradiated area would* reach this temperature due to the thermal conduction, and consequently, a rather large desorption signal should be observed. In fact, only a very small fraction of adsorbed molecules are photodesorbed in our experiments. Therefore, while the thermal contribution from the *direct* and *indirect* heating is definitely very important, the effect alone cannot explain the observed desorption phenomenon. From this consideration, it seems possible that the desorbing species may still be in internally excited states (vibrationally and/or rotationally excited) during the photoexcited desorption process. It should be very interesting to determine the internal energy distribution for the photodesorbed molecules. In addition, as in LITD, a lower translational temperature than the surface temperature raised by the IR laser pulses is also observed in IRPD. The reasons for causing such behavior, as discussed in the previous section, need to be further studied and understood.

From the results obtained for the pyridine and ammonia systems that we have investigated, the important surface processes involved in IRPD become quite clear, although a complete picture is still not available. Apparently the surface vibrational dipoles can provide a good medium for absorbing the incident IR photons when the light frequency is in resonance with the vibrational motion of the adsorbate. The absorbed photon energy is quickly transferred and shared with the surrounding molecules and surface atoms resulting in the local heating of the molecular layer and the substrate. This *indirect* (or *resonant*) heating in combination with the *direct* substrate heating can lead to desorption of some very weakly bound molecules during the laser pulse width, par-

ticularly if the molecules are also internally excited. The excited molecules or the excited internal modes (vibrational and/or rotational) may not be the original molecules or the original vibrational modes that absorb the IR photons. This internal excitation may be acquired via the rapid intra- and inter-molecular energy transfer processes from the initially photoexcited molecules. From the experimental results, we conclude that thermal activation is very important although the thermal process alone cannot account for all the major observations of the desorption phenomenon, in particular, the small desorption yields. We also conclude that pure quantum processes, such as the elastic and inelastic tunneling processes as discussed by Gortel *et al.*,[35] leading directly to molecular dissociation from the solid surface, cannot be by themselves very important. This is apparently true even for single-photon excitation in which the energy of the initially excited vibrational level is degenerate with levels in the desorption continuum. Instead, we believe that bound state to bound state transitions, i.e., both $P_{i,i}^{(1)}$ and $P_{i,i}^{(n)}$ processes, play essential roles in channeling the absorbed photon energy into the levels in the surface potential via electron or phonon-mediated steps resulting in the thermal excitation of the surface potential. This thermal excitation in the molecule-surface potential can enhance the desorption probability when the molecule is also internally excited or when it is coupled with the elastic and inelastic tunneling processes. Without the thermal activation of the surface potential, tunneling processes alone cannot be effective in inducing molecular desorption. It is interesting to note that the theoretical calculations performed by Gortel *et al.*[35] also illustrate the importance of the processes involving bound state to bound state transitions. In these calculations, it is shown that the photodesorption rate is drastically reduced if $P_{i,i}^{(1)}$ is set to 0.

As demonstrated in these studies, IRPD can indeed provide important information concerning the dynamic processes on solid surfaces. In addition, it can furnish useful spectroscopic information of surface adsorbates. In fact, IRPD can be considered as absorption-desorption spectroscopy quite similar to surface IR absorption-reflection (IRARS) and absorption-transmission (IRATS) spectroscopies. This is due to the fact that there is essentially no mode selectivity in IRPD[1-44] and the desorption yields depend mainly on the IR absorption cross sections associated with the various vibrational modes. Thus the vibrational structure can be resolved from the photodesorption spectrum as illustrated in the NH_3 system[40] where the symmetric and antisymmetric N-H stretching vibrations are well separated. Because of the inherently high spectral resolution ($\lesssim 1$ cm^{-1}) provided by the laser light source, IRPD can be developed as a spectroscopic technique for probing weakly bound surface species with a resolution not attainable by conventional IRARS or IRATS. It should be pointed out, however, unlike IRARS and IRATS involving single-photon absorption, IRPD can be due to either single-photon or multiphoton absorption. Namely, the photodesorption yield is not necessarily linearly dependent on the incident laser intensity. For molecular systems such as physisorbed NH_3 at more than one monolayer coverages, photodesorption can be induced by single-photon absorption[42-44] and the desorption spectrum is very similar to the linear IR absorption spectrum. But for a multiphoton excited photodesorption, the desorption spectrum can be substantially narrower than the absorption spectrum, as illustrated theoretically by Wu *et al.*[40]

Other IR laser-induced desorption studies include the work by Hess and co-workers,[47-49] Mercier,[50] and Allen *et al.*[51] Mashni and Hess[47] studied the CO_2 laser radiation effect on thick ($\sim 200\,\mu m$) methanol layers condensed on metal plates at 77 K in a high vacuum system. At the laser intensity in the 10^6–10^7 W/cm^2 region, the pulsed laser could induce desorption of ionic species when the laser frequency was in resonance with the vibrational band of the condensed solid. The laser method produced several high mass ions not found in electron-impact spectra. Desorption of neutral molecules were also detected by resonant IR absorption of CO_2 laser photons irradiated on a condensed CCl_4 and other molecular solids.[48,49] It was found that the desorption was due mainly to the resonant heating effect. The translational temperatures determined from the time-of-flight measurements coincided with the linear infrared absorption spectra. These are essentially bulk experiments, namely, the photons are absorbed by the bulk of the materials, although desorption takes place from the surface regions of the condensed solids. In a different experiment, Mercier[50] tried to perform a photodesorption experiment on CO chemisorbed on a Pd surface with a cw CO laser in the 1800–2000 cm^{-1} range. It was found that the only detectable laser-induced desorption was thermal in nature, originated from the radiative heating of the metal surface by the laser. This result is not surprising because the CO–Pd surface bond energy is rather high, ranging from 18–34 kcal/mol depending on the surface coverage. Thus, excitation by single-photon absorption of IR photons with 5.7 kcal/mol of photon energy is not expected to be effective for inducing the breaking of the strong surface bonds at relatively low laser intensities. Recently, Allen *et al.*[51] used pulsed HF and DF lasers at 2.8 and 3.7 μ to irradiate contaminated solid surfaces and found that both H_2O and hydrocarbon species could be desorbed by the IR laser pulses.

IV. PHOTODESORPTION BY UV AND VISIBLE LASERS

For PSD induced by UV and visible photons studied before 1980, the experiments and results were critically reviewed by Lichtman,[52] and Koel,[53] and their co-workers. The general conclusion was that for gas-metal systems such as CO on nickel and tungsten, the observed photodesorption was mainly thermal in nature. The quantum effect, if present at all, was very small with the quantum efficiency less than 10^{-8} molecules desorbed per photon, corresponding to a cross section of less than 10^{-22} cm^2. A noted exception was that reported by Kronauer and Menzel,[54] who studied CO desorption from tungsten surfaces and observed relatively high photon desorption yield for the photon wavelength below 300 nm. At $\lambda = 250$ nm (4.96 eV), they reported a quantum yield of 4×10^{-7} which was attributed to a quantum effect based on the careful compensation of photo-induced temperature increases. To account for this observed effect,

the authors proposed two possible mechanisms. The first mechanism involved the photon absorption by the metal resulting in the excitation of an electron from the conduction band to an unoccupied state above the Fermi energy. The excitation energy was then transferred to the adsorbate possibly via elastic electron tunneling through the surface barrier into an empty state of the adsorbate above the Fermi level. The threshold for such a process would be the minimum energy required to lift an electron from the top of the conduction band to the empty adsorbate level. The second mechanism involved the electronic excitation of the adsorbate-metal complex leading either directly to a repulsive or to a metastable state which could cross into a repulsive state. The state involved in the absorption of photons with 5 eV or less could not be derived from the slight perturbed molecular CO upon chemisorption, because the lowest excited state of CO lies 6 eV above the ground state. To account for the low threshold energy, the authors suggested that the CO–W surface bond formation might lead to new, low-lying unoccupied molecular orbitals. This mechanism is very similar to a mechanism proposed by Menzel and Gomer[55] and by Redhead[56] for interpreting electron-stimulated desorption. This is an important concept, whether or not it is directly applicable to CO desorption from tungsten observed by Kronauer *et al.* More specifically, the MGR model suggested a two-step mechanism which was started with an optical or electron-induced excitation, causing a Frank–Condon transition from the ground state of the adsorbate-substrate complex to a neutral or ionic antibonding state of the system. As a consequence of this excitation, the neutral or ionic particle would begin to move away from the metal surface. If deexcitation did not occur, either ions or neutrals could be desorbed. If, on the other hand, the excited state was recaptured by an electron tunneling to fill the orbital emptied by the initial excitation, the system would relax and no desorption would take place. Even if not applicable for CO on tungsten, this model may still be relevant to photodesorption in other gas-surface systems which have low-lying antibonding states that can be reached by UV-visible photons. As mentioned earlier, a different mechanism has been proposed by Knotek and Feibelman[11] for ESD involving core-hole excitation. This mechanism is not expected to be applicable to photodesorption in the low photon energy region (< 6 eV), unless very high level multiphoton excitation is involved. Another desorption mechanism for PSD and ESD was suggested by Antoniewicz[57] as a modification of the MGR[55,56] model. The essential feature of this proposal was the creation of an adsorbate ion in the initial electron or photon excitation process and that the repulsive portion of the ionic potential curve should lie closer to the surface than the repulsive portion of the neutral-surface bonding curve. Once the ion was created, it could be forced to move toward the substrate gaining kinetic energy and be neutralized. The neutralized particle would then be in a higher position on the repulsive part of the potential curve and desorption of the neutral species could subsequently take place. In a similar manner, the author also proposed a scheme for ion desorption. More detailed reviews of the MGR, Knotek–Feibelman, and Antoniewicz models in the context of PSD and ESD were recently given by Gomer and Menzel.[58] The applicability of these theories to photodesorption in the UV-visible spectral region remains to be tested. Photodesorption studies on oxide and sulfide semiconductor surfaces were also critically reviewed by Lichtman and Shapira.[52] Basically, it involved band gap excitation of the semiconductor and surface carbon impurities.

Since PSD and LITD are important surface processes involved in surface etching reactions enhanced or induced by UV-visible laser radiation,[2,59] we have also studied the photodesorption phenomenon. Two examples are given here, one involving a semiconductor and the other a metal system. The dark reaction and laser-enhanced etching of Si exposed to XeF_2 gas have been recently summarized by Chuang, Houle, Winters, and co-workers.[2,59–61] For PSD studies, we used both visible (at 532 nm from the second harmonic of a Q-switched Nd : YAG laser) and IR (at 10.6 μm of a TEA-CO_2 laser) light pulses. The former could excite the band gap of the semiconductor to generate electron-hole pairs, while the latter was less strongly absorbed by Si and could not excite the Si band gap by a single-photon absorption. With time-of-flight (TOF) mass spectroscopy, we found[59] that less F-coordinated species such as SiF, SiF_2, and even Si atoms were the dominant etching products when a fluorine-saturated Si surface was irradiated by 532 nm laser pulses. The typical TOF signals are displayed in Fig. 8. This result was in

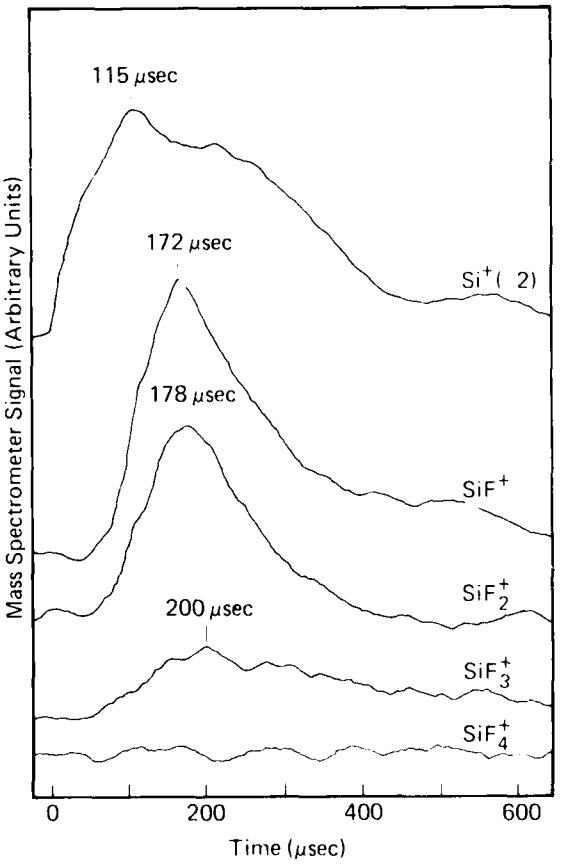

FIG. 8. TOF signals of SiF_3^+, SiF_2^+, SiF^+, and Si^+ detected by the mass spectrometer from XeF_2-exposed Si surface at 300 K, irradiated by 532 nm laser pulses at $I \sim 9$ MW/cm^2 on the surface; actual Si^+ signal a factor of 2 higher than other signals. (Data according to Ref. 59 by Chuang *et al.*)

great contrast to the dark reaction[61] or the etching enhanced by a relatively low power cw Ar^+ laser,[60] in which SiF_4 was detected to be the major reaction product. The translational temperatures of the photodesorbed SiF_x ($x \leqslant 3$) species were determined to be in the 400–560 K range at the laser fluence $F = 0.05\ J/cm^2$. These temperatures were substantially lower than the peak surface temperature estimated to be above 800 K due to the 6 ns laser pulse. By increasing the laser fluence above 0.1 J/cm^2 on the fluorinated Si, plasma formation giving rise to a characteristic optical emission from the surface and desorption of Si^+ and SiF^+ ions was observed. Some typical TOF spectra are shown in Fig. 9. The kinetic energies of the photodesorbed particles under this high power laser irradiation were quite high ($\gtrsim 0.4$ eV) and the translational "temperatures" (apparent departure from Boltzmann velocity distributions) were above 5000 K. It was further observed that the laser threshold for plasma generation was substantially reduced if a Si crystal was damaged due to either chemical etching or laser physical ablation. A similar although not identical etching behavior was found when the fluorinated Si was irradiated by CO_2 laser pulses. Figure 10 shows some of the TOF spectra for Si exposed to XeF_2 and irradiated at $F = 0.5\ J/cm^2$. Again, less F-coordinated SiF_x species and Si atoms were the major desorption

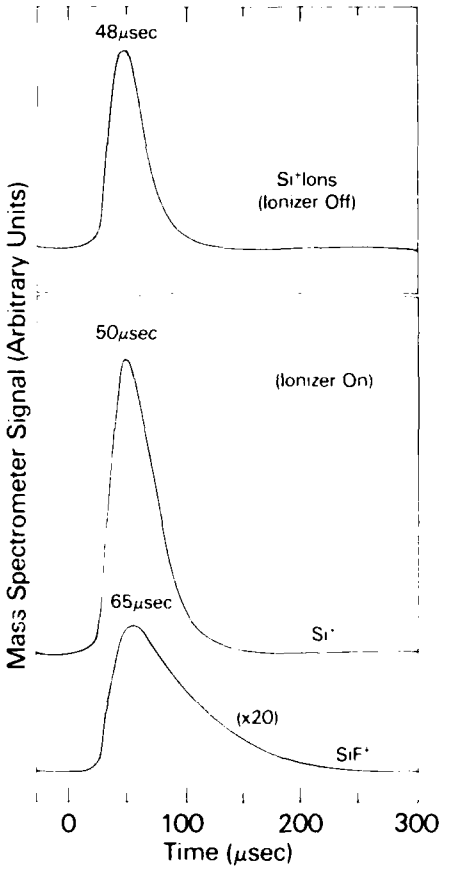

FIG. 9. TOF signals of SiF^+ and Si^+ detected by the mass spectrometer from XeF_2-exposed Si surface irradiated by 532 nm light pulses at $I = 18$ MW/cm^2, the top signal for Si^+ ions is detected by the mass spectrometer without using the ionizer. (Data according to Ref. 59.)

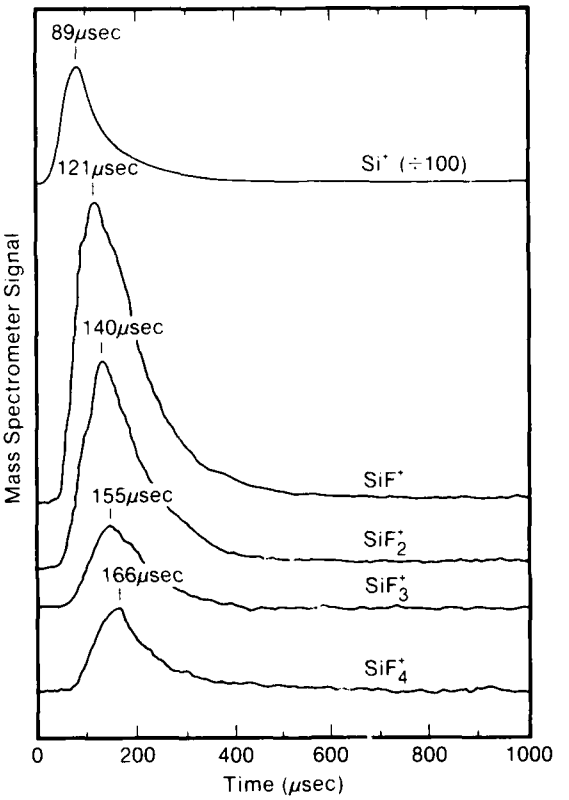

FIG. 10. TOF signals of species detected by the mass spectrometer from XeF_2-exposed Si surface at 300 K excited by CO_2 laser pulses at $I = 5$ MW/cm^2. (Data according to Ref. 59.)

products. Detailed comparison between Figs. 8 and 10 shows that IR excitation produces more SiF_4 than the visible laser pulses. The translational temperatures of the desorbed particles calculated from the TOF signals (Fig. 10) were in the 1000 K range. Clearly, a CO_2 laser could also produce a mass distribution very different from the thermal (dark) reaction even though the IR photons could not excite the Si band gap by a single photon absorption. It should be realized, however, that at this laser fluence (0.5 J/cm^2, 5 MW/cm^2) multiphoton absorption on Si substrate might be possible. In any event, apparently both the pulsed visible and IR lasers can enhance the Si etching reaction and produce etching products different from the thermal reaction. Furthermore, the translational temperatures of the laser-desorbed species may be quite different from the surface temperatures raised by the laser pulses. It is interesting to note that in a Ge–Br_2 etching reaction induced by 488 nm laser pulses performed by Davis *et al.*,[62] a significant deviation from a Maxwell–Boltzmann velocity distribution of the etching product ($GeBr_2$) has been detected. They, however, suggested that the etching reaction was basically thermally driven when Ge was heated by the laser to temperatures above the melting threshold of the solid. At the present time, the pulsed laser excitation effects and the cause for the deviation from the thermal or the Maxwell–Boltzmann behavior for both Si–XeF_2 and Ge–Br_2 reactions are still not completely clear. The nonthermal photon-enhanced etching reaction could be due to electronic excitation effects.

For PSD related etching reaction on metal surfaces, we

have recently investigated Ag–Cl_2 reaction induced by UV and visible laser light pulses.[59,63] From the extensive gas and surface analyses including XPS, AES, and TOF mass spectrometry, we concluded that the laser-gas-surface interaction steps took place as follows: (1) dark chlorine adsorption and diffusion in the period between laser pulses (and the extent of surface chlorination and diffusion depth depend on Cl_2 pressure and pulse repetition rate), (2) weakening of Ag–Ag bonds in the metal due to Cl penetration into the subsurface region, (3) laser excitation of the chlorinated surface via possibly electronic activation in addition to the thermal heating effects, and (4) desorption and ejection of Ag, Cl, AgCl, etc., particles by a laser pulse resulting in the etching of the solid. Among these interaction steps, processes (3) and (4) were most intriguing. For clarity, the typical TOF signals obtained with 532 nm pulses at 0.49 J/cm^2 are displayed in Fig. 11. The kinetic energies of the photodesorbed particles were determined to be 0.1, 2.9, and 4.7 eV, respectively, for the detected Cl, Ag, and AgCl species. Furthermore, the observed translational temperatures were not uniform and much higher than the estimated surface temperature (< 900 K) raised by the radiation or even higher than the boiling point of the metallic silver. Such behavior simply could not be explained based on the laser-induced surface heating effects. We therefore suggested[63] that electronic excitation mechanisms perhaps similar to MGR model[55,56] as discussed above might be involved in the photodesorption and etching reaction of metal-halogen systems, such as Ag–Cl_2. It should also be mentioned that electronic desorption mechanisms have been inferred in the "photon sputtering"[64–66] of dielectric materials such as alkali halides[64] and Al_2O_3.[67] Plasma formation is often observed from these solid surfaces irradiated by high power laser pulses. Since chemical etching of metals and semiconductors are usually achieved by relatively low power laser radiation without plasma formation, the nonthermal radiation effects of the chemical etching systems may be quite different from the electronic sputtering effects of dielectric materials.

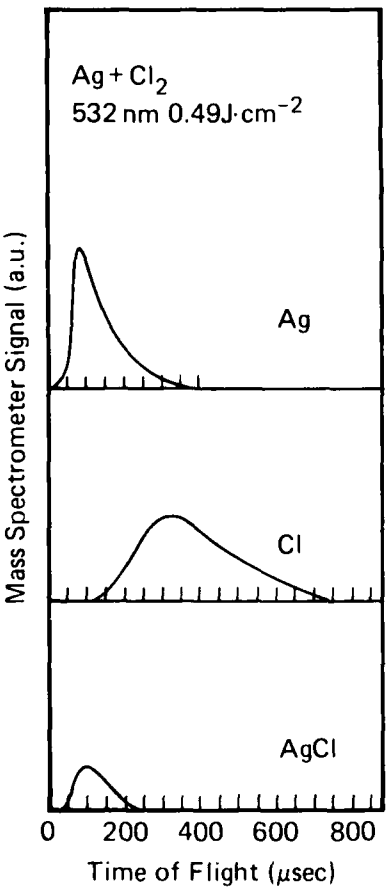

FIG. 11. TOF signals from a chlorinated Ag surface (1200 L of Cl_2 at 2×10^{-6} Torr) irradiated by 532 nm laser pulses. (Data according to Ref. 63.)

In a recent UV photodissociation and photodesorption study of adsorbed molecules, Bourdon *et al.*[68] observed that CH_3Br molecules could be photodesorbed from UV adsorption of a LiF crystal which was used as substrate. The photodesorption process was not simply due to heating of the crystal surface because the kinetic energy distribution of the desorbed molecules did not shift to higher energies when the laser power at either 222 or 308 nm was increased. For the desorption mechanism, the authors suggested that the pulsed photon energy was absorbed by the color centers of LiF causing a shock wave to pass through the crystal which resulted in the ejection of adsorbed surface species. This mechanism is naturally very different from PSD involving electronic transitions of the adsorbate-surface complex. In the same experiments, they also found that the adsorbed CH_3Br molecules could be photodissociated to produce CH_3 radicals which subsequently desorbed due to single-photon absorption of 222 nm light pulses. In contrast to the photodesorbed CH_3Br which possessed rather low kinetic energies (peak at 0.06 eV), CH_3 radicals were produced and desorbed with relatively high velocities (i.e. peak at 1.5 eV). Laser irradiation at 308 nm which was not absorbed by the absorbed CH_3Br molecules did not produce similar results. Studies of the CH_3 yields as a function of laser intensity and CH_3Br surface coverage further confirmed the photochemical effect on the LiF solid surfaces.

The effect of surface microstructure on photodesorption and surface photochemistry were also examined by a number of groups.[69–73] In the theoretical consideration, Nitzan and Brus[69] suggested that enhanced photon absorption and photochemistry could occur depending on the overlap between the molecular resonance and the excitable surface resonances, such as surface plasmons, which were determined by the dielectric function and the shape of the solid. The authors further demonstrated by calculation that for very fast reactions such as I_2 photodissociation on a silver sphere (~ 1000 Å in diameter), the absorption cross section and thus the photodissociation yield should be greatly enhanced by visible photons at 450 nm incident on the metal surface. Enhanced photofragmentation on rough metal surfaces indeed were observed in a number of systems.[70–72] Enhanced desorption from rough Ag surfaces was also reported,[73] although the demonstrated desorption efficiency did not show a strong dependence on the laser wavelength or the local electronic field strength at Ag island surfaces. Other

relevant work included the photodesorption of neutrals and ions from surfaces of molecular solids and molecules deposited as thin films on metal substrates irradiated by UV or visible lasers.[74,75] Again, the characteristics of the photodesorption could be quite nonthermal in nature.

Indeed, the diversity of experiments reported so far reveals the many facets of the electronically excited surface processes. There can be many mechanisms involved in the basic photon-molecule-surface interactions stimulated by UV and visible laser photons. With the advance of tunable UV and visible laser light sources, these surface processes including photodesorption can be fruitfully investigated in the years to come.

ACKNOWLEDGMENTS

The author wishes to thank Dr. Ingo Hussla and Dr. W. Sesselmann for their contribution to part of this work and for many helpful discussions.

[1]See the review by T. J. Chuang, Surf. Sci. Rep. **3**, 1 (1983).
[2]T. J. Chuang, J. Vac. Sci. Technol. **21**, 798 (1982); Mater. Res. Soc. Symp. Proc. **17**, 45 (1983); **29**, 185 (1984).
[3]D. J. Ehrlich and J. Y. Tsao, J. Vac. Sci. Technol. B **1**, 969 (1983).
[4]R. M. Osgood, Jr., Annu. Rev. Phys. Chem. **34**, 77 (1983).
[5]See, e.g., (a) D. Menzel, J. Vac. Sci. Technol. **20**, 538 (1982); (b) papers in *Desorption Induced by Electronic Transitions DIET I*, edited by N. H. Tolk, M. M. Traum, J. C. Tully, and T. E. Madey (Springer, Heidelberg, 1983).
[6]M. L. Knotek and P. J. Feibelman, Phys. Rev. Lett. **40**, 964 (1978); P. J. Feibelman and M. L. Knotek, Phys. Rev. B **18**, 6531 (1978).
[7]L. P. Levine, J. F. Ready, and E. Bernal, J. Appl. Phys. **38**, 331 (1967); J. M. Chen and C. C. Chang, *ibid.* **43**, 3884 (1972).
[8]G. Ertl and M. Neumann, Z. Naturforsch. Teil A **27**, 1607 (1972); K. Christmann, O. Schober, G. Ertl, and M. Neumann, J. Chem. Phys. **60**, 4528 (1974).
[9]J. P. Cowin, D. J. Auerbach, C. Becker, and L. Wharton, Surf. Sci. **78**, 545 (1978).
[10]G. Wedler and H. Ruhmann, Surf. Sci. **121**, 464 (1982).
[11]R. Viswanathan, D. R. Burgess, Jr., P. C. Stair, and E. Weitz, J. Vac. Sci. Technol. **20**, 605 (1982).
[12]D. Burgess, Jr., R. Viswanathan, I. Hussla, P. C. Stair, and E. Weitz, J. Chem. Phys. **79**, 5200 (1983).
[13]D. Burgess, Jr., I. Hussla, P. C. Stair, R. Viswanathan, and E. Weitz, Rev. Sci. Instrum. **55**, 1771 (1984).
[14]R. B. Hall and A. M. DeSantolo, Surf. Sci. **137**, 421 (1984).
[15]J. F. Ready, *Effects of High-Power Laser Radiation* (Academic, New York, 1971).
[16]J. H. Bechtel, J. Appl. Phys. **46**, 1585 (1975).
[17]I. Hussia, H. Coufal, F. Träger, and T. J. Chuang (to be published).
[18]H. Coufal, Appl. Phys. Lett. **44**, 59 (1984); H. Coufal and W. Lee, in *Laser Processing and Diagnostics*, edited by D. Bäuerle (Springer, Heidelberg, 1984), p. 25.
[19]J. C. Tully, Surf. Sci. **111**, 461 (1981).
[20]Z. W. Gortel, H. J. Kreuzer, M. Schäff, and G. Wedler, Surf. Sci. **134**, 577 (1983).
[21]A. E. Dabiri, T. J. Lee, and R. E. Stickney, Surf. Sci. **26**, 522 (1971).
[22]M. J. Cardillo and J. C. Tully, in *Dynamics on Surfaces*, edited by B. Pullman, J. Jortner, A. Nitzan, and B. Gerber (Reidel, Dordrecht, Holland, 1984), p. 169.
[23]J. Heidberg, H. Stein, A. Nestmann, E. Hoefs, and I. Hussla, in *Proceedings of the Materials Research Symposium on Laser-Solid Interactions and Laser Processing* (Boston, Massachusetts, 1978), edited by S. D. Ferris, H. J. Leamy, and J. M. Poate (American Institute of Physics, New York, 1979), p. 49.
[24](a) J. Heidberg, H. Stein, E. Riehl, and A. Nestmann, Z. Phys. Chem. (NF) **121**, 145 (1980); (b) J. Heidberg, H. Stein, and E. Riehl, in *Vibrations at Surfaces*, edited by R. Caudano, J.-M. Gilles, and A. A. Lucas (Plenum, New York, 1982), p. 17; also Surf. Sci. **126**, 183 (1983).
[25]J. Heidberg, I. Hussla, and Z. Szilagyi, J. Electron Spectrosc. Relat. Phenom. **30**, 53 (1983).
[26]J. Heidberg, H. Stein, and E. Riehl, Phys. Rev. Lett. **49**, 666 (1982).
[27]J. Heidberg and I. Hussla, J. Electron Spectrosc. Relat. Phenom. **29**, 105 (1983).
[28]J. Heidberg, presented at the International Symposium on Spectroscopic Studies of Adsorbates on Solid Surfaces, Nishinomiya, Japan, September 3–5, 1984 (to be published).
[29]T. J. Chuang, J. Chem. Phys. **76**, 3828 (1982).
[30]T. J. Chuang and H. Seki, Phys. Rev. Lett. **49**, 382 (1982).
[31]H. Seki and T. J. Chuang, Solid State Commun. **44**, 473 (1982).
[32]T. J. Chuang, J. Electron Spectrosc. Relat. Phenom. **29**, 125 (1983).
[33](a) J. Lin and T. F. George, Surf Sci. **100**, 381 (1980); J. Phys. Chem. **84**, 2957 (1980); Surf Sci. **115**, 569 (1982); (b) J. Lin, Ph.D. thesis, University of Rochester, 1980; (c) A. C. E..ri and T. F. George (to be published); (d) X.-Y. Huang, T. F. George, J.-M. Yuan, and L. M. Narducci, J. Phys. Chem. (in press).
[34](a) C. Jedrzejek, K. F. Freed, S. Efrima, and H. Metiu, Surf. Sci. **109**, 191 (1981); (b) G. Korzeniewski, E. Hood, and M. Metiu, J. Vac. Sci. Technol. **20**, 594 (1982).
[35]Z. W. Gortel, H. J. Kreuzer, P. Piercy, and R. Teshima, Phys. Rev. B **28**, 2119 (1983); *ibid.* B **27**, 5066 (1983).
[36]H. J. Kreuzer and Z. W. Gortel, Phys. Rev, B **29**, 6926 (1984).
[37]M. P. Casassa, F. G. Celii, and K. C. Janda, J. Chem. Phys. **76**, 5295 (1982); F. G. Celii, M. P. Casassa, and K. C. Janda, Surf. Sci. **141**, 169 (1984).
[38]D. Lucas and G. E. Ewing, Chem. Phys. **58**, 385 (1981).
[39]H. J. Kreuzer and D. N. Lowy, Chem. Phys. Lett. **78**, 50 (1981).
[40]G. S. Wu, B. Fain, A. R. Ziv, and S. H. Lin, Surf. Sci. **147**, 537 (1984).
[41]C. Jedrzejek, J. Vac. Sci. Technol. B **3**, 1431 (1985).
[42]T. J. Chuang and I. Hussla, Phys. Rev. Lett. **52**, 2045 (1984).
[43]T. J. Chuang and I. Hussla, in *Dynamics on Surfaces*, edited by B. Pullman, J. Jortner, A. Nitzan, and B. Gerber (Reidel, Dordrecht, Holland, 1984), p. 313.
[44]T. J. Chuang, H. Seki, and I. Hussla, Surf. Sci. **158**, 525 (1985).
[45]I. Hussla and T. J. Chuang, Ber. Bunsenges. Phys. Chem. **89**, 294 (1985).
[46]I. Hussla, H. Seki, T. J. Chuang, Z. W. Gortel, H. J. Kreuzer, and P. Piercy (to be published).
[47]M. Mashni and P. Hess, Chem. Phys. Lett. **77**, 541 (1981); Appl. Phys. B **29**, 205 (1982).
[48]B. Schäfer and P. Hess, Chem. Phys. Lett. **105**, 563 (1984).
[49]B. Schäfer, M. Buck, and P. Hess, Infrared Phys. (in press).
[50]J. Mercier, Ph.D. thesis, Cornell University, 1983.
[51]S. D. Allen, J. O. Porteus, and W. N. Faith, Appl. Phys. Lett. **41**, 416 (1984).
[52]D. Lichtman and Y. Shapira, CRC Crit. Rev. Solid State Mater. Sci. **8**, 93 (1978).
[53]B. E. Koel, J. M. White, J. L. Erskine, and P. R. Antoniewicz, in *Advances in Chemistry Series, No. 184* edited by M. S. Wrighton (American Chemical Society, Washington, D.C., 1980), p. 27.
[54]P. Kronauer and D. Menzel, in *Adsorption-Desorption Phenomena*, edited by F. Ricca (Academic, New York, 1972), p. 313.
[55]D. Menzel and R. Gomer, J. Chem. Phys. **41**, 3311 (1964).
[56]P. A. Redhead, Can. J. Phys. **42**, 886 (1964).
[57]P. R. Antoniewicz, Phys. Rev. B **21**, 3811 (1980).
[58](a) R. Gomer, in *Desorption Induced by Electronic Transitions DIET I*, edited by N. H. Tolk, M. M. Traum, J. C. Tully, and T. E. Madey (Springer, Heidelberg, 1983), p. 40; (b) D. Menzel, *ibid.*, p. 53.
[59]T. J. Chuang, I. Hussla, and W. Sesselmann, in *Laser Processing and Diagnostics*, edited by D. Bäuerle (Springer, Heidelberg, 1984), p. 300.
[60]F. A. Houle, J. Chem. Phys. **79**, 4237 (1983); **80**, 4851 (1984).
[61]Y. Y. Tu, T. J. Chuang, and H. F. Winters, Phys. Rev. B **23**, 823 (1981); H. F. Winters and F. A. Houle, J. Appl. Phys. **54**, 1218 (1983).
[62]G. P. Davis, C. A. Moore, and R. A. Gottscho, J. Appl. Phys. **56**, 1808 (1984).
[63]W. Sesselmann and T. J. Chuang, J. Vac. Sci. Technol. B **3**, 1507 (1985).
[64]P. D. Townsend, Surf. Sci. **90**, 256 (1979); and in *Sputtering in Particle*

Bombardment II, edited by R. Behrisch (Springer, Heidelberg, 1983), p. 147.
[65]M. Hanabusa, M. Suzuki, and S. Nishigaki, Appl. Phys. Lett. **38**, 385 (1981).
[66]N. Itoh and T. Nakayama, Phys. Lett. A **92**, 471 (1982); T. Nakayama and N. Itoh, Radiat. Eff. Lett. **67**, 129 (1982).
[67]I. E. Rothenberg and R. Kelly, Nucl. Instrum. Methods Phys. Res. B **1**, 291 (1984).
[68]E. B. D. Bourdon, J. P. Cowin, I. Harrison, J. C. Polanyi, J. Segner, C. D. Stanners, and P. A. Young, J. Phys. Chem. **88**, 6100 (1984).
[69]A. Nitzan and L. Brus, J. Chem. Phys. **75**, 2205 (1981); **74**, 5321 (1981).
[70]G. M. Goncher and C. B. Harris, J. Chem. Phys. **77**, 3767 (1982); G. M. Goncher, C. A. Parsons, and C. B. Harris, J. Phys. Chem. **88**, 4200 (1984).
[71]S. Garoff, D. A. Weitz, and M. S. Alvarez, Chem. Phys. Lett. **92**, 283 (1982).
[72]C. J. Chen and R. M. Osgood, Phys. Rev. Lett. **50**, 1705 (1983).
[73]R. A. Fletcher, I. Chabay, D. A. Weitz, and J. C. Chung, Chem. Phys. Lett. **104**, 615 (1984).
[74]V. S. Letokhov, V. G. Movshev, and S. V. Chekalin, Sov. Phys. JETP **54**, 257 (1981); V. S. Antonov, V. S. Letokhov, and A. N. Shibanov, Appl. Phys. **25**, 71 (1981).
[75]N. Nishi, H. Shinohara, and T. Okuyama, J. Chem. Phys. **80**, 3898 (1984).

In situ infrared spectroelectrochemistry

Carol Korzeniewski and Stanley Pons[a)]
Department of Chemistry, University of Utah, Salt Lake City, Utah 84112

(Received 15 February 1985; accepted 1 May 1985)

The vibrational spectrum of molecules at or near an electrode surface can be obtained using subtractively normalized interfacial Fourier transform infrared spectroscopy (SNIFTIRS) and electromodulated infrared spectroscopy (EMIRS). The large electric field existing at the electrode/solution interface is sufficient to induce dipole moments in highly polarizable molecules. The magnitude of the induced dipole moment is proportional to the electric field strength. As a result of this interaction some totally symmetric normal vibrations are made infrared active, and other bands appear in violation of the surface selection rule. This effect is known as the electrochemical Stark effect. Calculation of the expected absorption coefficients for the totally symmetric modes of adsorbed species gives values which are close to those observed experimentally. Experimental evidence of A_g mode activation of adsorbed pyrene is presented. The electric field dependence of the integrated absorption coefficient is demonstrated for acrylonitrile adsorbed on a gold electrode.

I. INTRODUCTION

In recent years several techniques have been developed for obtaining *in situ* the infrared spectra of species at the electrode–solution interface.[1,2] The vibrational spectra is strongly dependent upon the molecular orientation with respect to the electrode surface. Electromagnetic radiation polarized perpendicular to the metal surface (*s* polarized) undergoes a phase shift close to 180° for all angles of incidence resulting in a standing wave which has little amplitude at the metal surface. The electric vectors of light polarized parallel to the plane of incidence (*p* polarized) add constructively upon reflection at glancing angles giving rise to a sizable component of electric vector normal to the surface. Therefore, only molecules which have a component of their dipole moment normal to the surface are able to interact with electromagnetic radiation.

Since intense electric fields exist near electrode surfaces, it is possible for the electric field to interact with highly polarizable molecules. This interaction may distort the diffuse electron cloud inducing a dipole in the direction of the electric field. If the polarization of the infrared radiation is in the same direction as the induced dipole, the integrated absorption coefficient for the transition is proportional to the square of the electric field strength. Therefore, the electric field at the electrode surface may allow infrared activity for vibrations normally forbidden by symmetry or the surface selection rule. This effect is known as the electrochemical Stark effect.[6] Perturbation of vibrational spectra by strong electric fields was first predicted by Condon[3] and has been demonstrated in several systems.[4–6]

We report in this work a brief review and some new results that are related to the electrochemical Stark effect and vibronic activation of symmetric vibrational modes. The techniques used are modulated potential specular reflectance types that have recently been introduced to electrochemical science.

II. EXPERIMENTAL

Experiments were performed in a three-electrode thin-layer cell (Fig. 1). The working electrode consisted of an 8–10-mm-diam platinum or gold disk mounted on the end of a glass syringe barrel. The electrodes were polished to a mirror finish using alumina of decreasing sizes down to 0.05 μm, then positioned in the cell so as to trap a thin layer of solution between the metal surface and the single crystal silicon infrared transmission window. The cell was then mounted in the path of a focused infrared light beam such that the angle of incidence from the normal was slightly less than 70 °C.

Spectra were obtained using both subtractively normalized Fourier transform infrared spectroscopy (SNIFTIRS)[1] and electromodulated infrared spectroscopy (EMIRS).[7]

In the standard SNIFTIRS technique, interferograms are collected and coadded at each of two electrode potentials. After transformation of the interferograms to the frequency domain spectra, the two results are ratioed. The final spectrum represents the difference in the infrared vibrational structure of the interfacial region at the two potentials. If transmission notation is chosen for the display of the spectrum, then the result is in units of $1 + \Delta R/R$, where $\Delta R/R$, the normalized reflectivity, is composed of the difference in reflectivity of the surface region at the two potentials, and R is the reflectance of the electrode at the potential corresponding to the state used in the denominator of the original

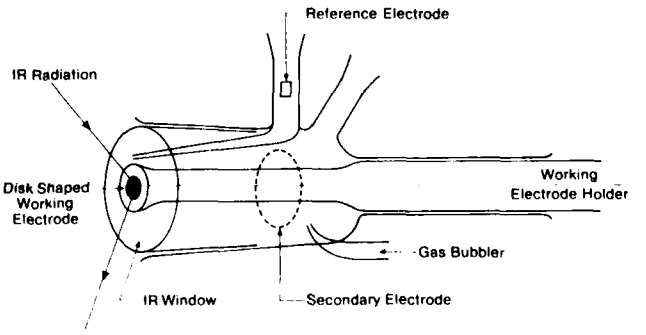

FIG. 1. Design of the thin layer spectroelectrochemical cell used for EMIRS and SNIFTIRS experiments.

 0734-211X/85/051421-04$01.00

ratio. At small values of ΔR compared to R, $\Delta R/R$ corresponds to the absorbance A.

In EMIRS, a high throughput dispersive monochromator is used. The potential at the electrode is rapidly modulated between the potentials of interest, thereby modulating the relative amounts of absorbing species in the interfacial region. This results in a small modulation of the reflectivity which is easily extracted by synchronous demodulation techniques. Details of both experimental techniques have been presented earlier.[1,7]

For cleaning cells, triply distilled water was used for steaming previously acid-cleaned cells. Aqueous solutions were prepared from recrystallized salts and triply distilled water. Acetonitrile (Burdick and Jackson, Muskegon, MI) was used as received. The water content was nominally $<0.01\%$. Organic substrates were obtained from Aldrich and used as received. Electrochemistry was controlled by a potentiostat and waveform generator (JAS Instrument Systems, Inc.) Cells and electrodes were also obtained from JAS.

Typically, spectra were obtained at an electrode potential where the species of interest was either not adsorbed or weakly adsorbed; and at a potential where the species was present on the electrode surface or interfacial region to a large extent. The values of these potentials can be obtained usually by conventional double layer capacitance measurements which can give quantitative values of the surface coverage and information on the thickness of the electrical double layer near the interface.

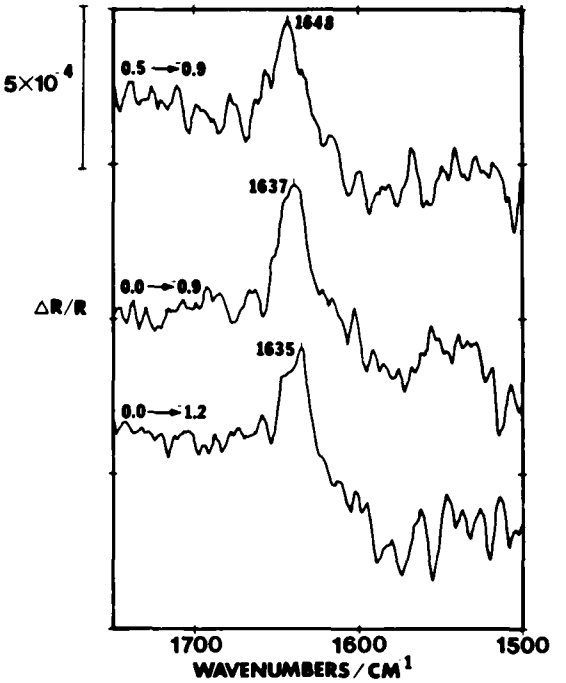

FIG. 2. SNIFTIRS difference spectrum of 0.5 mM pyrene at a platinum electrode in acetonitrile with 0.1 M tetra-*n*-butylammonium tetrafluoroborate (TBAF) as supporting electrolyte as a function of potential vs Ag/Ag$^+$.

III. RESULTS AND DISCUSSION

A. Calculation of B

In an experiment where the electric field ($\overline{E}_z$) is applied in a direction z, the induced dipole moment becomes

$$\mu_z = \alpha_{zz}\overline{E}_z,$$

where α_{zz} is the polarizability tensor. The integrated absorption coefficient is given by

$$B = \frac{2\pi^2\nu T}{\epsilon_0 hc}\,|\mu_{fi}|^2,$$

where μ_{fi} is the transition dipole matrix element, T is the number of absorbing molecules per unit area in the beam path, and all other constants have their usual meaning. In the presence of an external electric field the transition dipole matrix element can be expressed as the sum of the permanent dipole moment (μ_0) and the induced dipole moment (μ_z), where

$$\mu_0 = \Sigma_q \langle r\rangle.$$

Thus,

$$|\mu_{fi}| = \langle \Psi_{vf}|\,\mu_0 + \mu_z\,|\Psi_{vi}\rangle.$$

If the expression for μ_0 and μ_z are expanded in a Taylor series and the high order terms are neglected the integrated absorption coefficient becomes

$$B = \frac{2\pi^2\nu T}{\epsilon_0 hc}\,|\langle \Psi_{v_f}|\,\mu_0'|\Psi_{v_i}\rangle + E\,\langle \Psi_{v_f}|\alpha'|\Psi_{v_i}\rangle|^2,$$

where μ_0' and α' correspond to the change in the permanent dipole moment and polarizability with respect to a normal coordinate, respectively. We have calculated the absorption coefficient for the $C=C$ symmetric stretch of molecules adsorbed flat at an electrode surface. For these molecules μ_0 approaches zero and we are left with evaluating the remaining matrix element. Since the matrix elements $\langle \Psi_{v_f}|\alpha'|\Psi_{v_i}\rangle$ are not tabulated for molecules larger than diatomic, we have estimated this change to be of the same order of magnitude as the polarizability normal to the molecular axis, providing an upper bound value to the matrix element. The polarizabilities necessary for the calculation were taken from Ref. 11. The value of the absorption coefficient is calculated as a function of electric field strength and shown in Table I.

TABLE I. Predicted values for B.

E / V/m	$B/10^{-4}$ cm^{-1}				
	C_2H_4	Naphthalene	Anthracene	TCNQ	Pyrene
10^8		0.056	0.1	1.5	0.4
10^9	0.6	5.6	11	150	36
2×10^9	2.4	22	44	580	140
5×10^9	15	140	280	3 600	900
8×10^9	40	350	710	9 300	2 300
10^{10}	62	560	1 100	14 500	3 600

B. A_g mode activation

We have observed electric field activation of the totally symmetric A_g mode of pyrene at or near the surface of a platinum electrode. Figure 2 is the SNIFTIRS spectra of 0.5

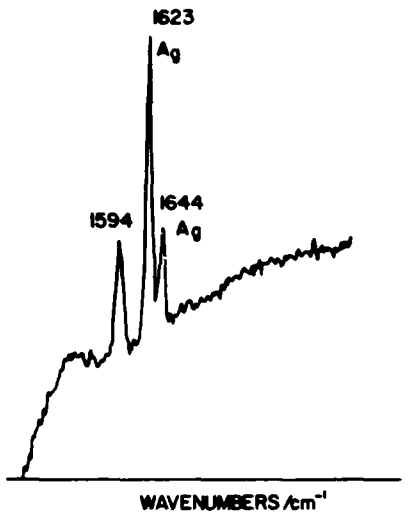

FIG. 3. Raman spectrum of pyrene in the region 1485–1800 cm $^{-1}$. Ag mode assignments taken from Ref. 8.

mM pyrene in acetonitrile. The limits of the modulation potential were set between $+0.5$ and -1.2 V vs Ag/Ag^+ where no electrochemical reaction was occurring. Therefore, the bands appearing in the difference spectra are due to the changing electric field rather than a chemical process. The band which occurs at $\sim 1640\ cm^{-1}$ corresponds to the totally symmetric (A_g) *C–C* stretching mode of pyrene. The Raman spectrum of pyrene was obtained in our labs and three bands were found in this frequency region (Fig. 3). The

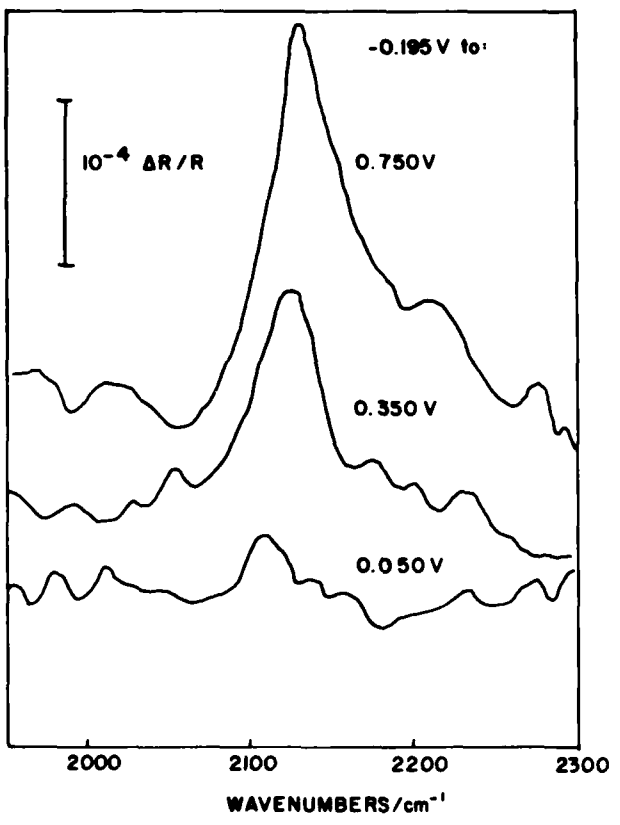

FIG. 4. EMIRS spectrum of 0.05 M acrylonitrile adsorbed at a gold electrode in 1 M H_2SO_4 as a function of potential vs SCE.

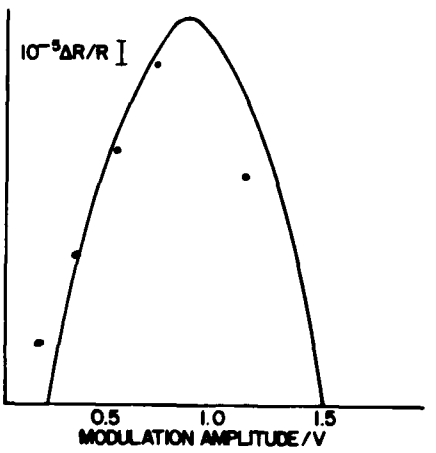

FIG. 5. Potential dependence of the intensity of the C≡N stretch band from adsorbed acrylonitrile. The dashed curve is calculated from the squared electric field dependence.

two bands at 1623 and 1644 cm^{-1} are assigned to the A_g *C–C* stretching mode of pyrene.[8] The positions of the activated band is very dependent on the potential, and is the subject of a forthcoming report.[10]

C. Electric field dependence of *B*

An example of the field dependence of band intensity of an adsorbed oscillator is demonstrated in the acrylonitrile system. Differential capacity measurements show that acrylonitrile is adsorbed on gold over a wide range of potentials ($+0.5$– -1.0 V vs SCE). Spectroscopic evidence indicates that the molecule is adsorbed flat and interacts with the surface via the conjugated π system.[9]

Figure 4 is the EMIRS spectra of acrylonitrile adsorbed on gold. The band at about 2130 cm^{-1} corresponds to the C≡N stretching mode of adsorbed acrylonitrile. The intensity of the band is about an order of magnitude weaker than expected for perpendicular adsorption, and is strongly potential dependent.[7] As the potential is made more positive the band intensity increases. Figure 5 shows the band intensity as a function of the amplitude of the potential modulation. If only desorption of acrylonitrile at higher potentials was occurring, the band intensity should increase over the entire potential range and a band of opposite sign corresponding to solution-free acrylonitrile should appear. However, as the modulation amplitude increases the band intensity increases, reaches a maximum, and begins to decrease. The observed spectra can be explained in terms of an electric field effect.

Since the potential dependence of the electric field at the electrode surface is unknown, it is difficult to test the exact field dependence of the intensity. However, there should be a maximum in band intensity when one of the modulation limits is at the potential point of zero charge at the interface. The dashed curve sketched in the figure is the theoretical curve predicted by the squared electric field dependence of intensity. The maximum in the curve appears at about $+0.7$ V vs SCE which is not an unreasonable position for the potential of zero field.

Also, the position of the band is not a linear function of

potential. In systems where perpendicular adsorption is certain, such as CO adsorbed on platinum and CN^- adsorbed on silver, band position is a linear function of potential.

Although the fit is only approximate it is sufficiently good to demonstrate the effect of strong electric fields on infrared spectra. Intense electric fields present near the electrode surface may interact with polarizable molecules and induce a dipole moment in the direction of the field which give rise to very weak absorptions. With refinements in the calculation it may be possible to use the electrochemical Stark effect to study the electric field intensity in the double layer region of the electrode.

ACKNOWLEDGMENT

We thank the Office of Naval Research for support of this work.

[a]To whom correspondence should be addressed.

[1]S. Pons, J. Electroanal. Chem. **150**, 495 (1983).
[2]A. Bewick, K. Kunimatsu, B. S. Pons, and J. W. Russell, J. Electronanal. Chem. **160**, 47 (1984).
[3]E. U. Condon, Phys. Rev. **41**, 759 (1932).
[4]M. F. Crawford and R. E. MacDonald, Can. J. Phys. **36**, 1022 (1958).
[5]E. D. Palik, R. T. Holm, A. Stella, and H. L. Hughes, J. Appl. Phys. **53**, 8454 (1982).
[6]C. Korzeniewski, R. B. Shirts, and S. Pons, J. Phys. Chem. **89**, 2297 (1985).
[7]A. Bewick and S. Pons, in *Advances in Infrared and Raman Spectroscopy*, edited by R. Hester and R. Clark (Hayden, London, 1985).
[8]A. Bree, R. A. Kydd, T. N. Misia, V. V. B. Vilkos, Spectrochim. Acta A **R7**, 2315 (1971).
[9]A. Bewick, C. Gibilaro, and S. Pons, Langmuir (submitted).
[10]C. Korzeniewski and S. Pons (in preparation).
[11]C_2H_4, naphthalene, anthracene: A. Chablo and A. Hinchliffe, Chem. Phys. Lett. **72**, 149 (1980). $TCNQ^-$: V. E. Klimenko, Ukr. Fiz. Zh. (Russ. Ed.) **23**, 1301 (1978), Chem. Abstr. **89**: 172337*u*. Pyrene: J. Waite, M. G. Papaduopoulos, and C. A. Nicolaides, J. Chem. Phys. **77**, 2536 (1982).

Formation of silicon and water cluster ions in pulsed-laser stimulated field desorption

T. T. Tsong
Physics Department, The Pennsylvania State University, University Park, Pennsylvania 16802

(Received 18 March 1985; accepted 21 May 1985)

Multiatom cluster ions of 3 to 16 atoms/cluster have been observed in pulsed-laser stimulated field desorption of silicon emitters. In a time-of-flight mass spectrum fine structures can be found in the mass line of every ion species, which are produced by isotope mixing in the clusters, and which will facilitate a correct identification of the charge state of the ions. The most abundant cluster ion species are Si_4^{2+}, Si_5^{2+}, and Si_6^{2+}. The numbers 4–6 may be called the magic numbers of the desorption process since they correspond to highly symmetric small units of atoms existing in Si surface layers. Most of the energy distributions of the ion species contain an exponentially decaying low energy tail which is produced by spontaneous dissociation of larger cluster ions, possibly due to photodissociation of larger cluster ions by the same laser pulses used for desorption. Water cluster ions of the form $(H_2O)_m H^+$ ($m = 1$–12) can be observed in pulsed-laser field desorption of "field condensed" water on a metal emitter surface. The appearance energy decreases monotonically with the cluster size, and also depends on the condition of the surface.

I. INTRODUCTION

Formation of microclusters of atoms and cluster ions has recently become a subject of considerable interest.[1–6] Topics actively pursued include magic and critical numbers, ionization energies and electronic energy levels, structures, and how cluster sizes are related to the substrate atomic structures, etc.

In low temperature field evaporation of solid emitters, ions formed are almost always multiply charged atomic ions. A small number of cluster ions have been occasionally observed, but the number is too small to render a systematic investigation possible.[7] With the observation of photon-stimulated field ion emission by laser pulses,[8] it is now possible to produce a good fraction of ions in the form of cluster ions in pulsed-laser stimulated field evaporation and field desorption.[5,6,9] Here, our result on Si-cluster[5,6] and water cluster ion formation will be summarized.[10]

II. EXPERIMENTAL METHODS

The instrument used in this study is the high mass and energy resolution pulsed-laser atom-probe field ion microscope[11] shown in Fig. 1. This system, when carefully operated under the condition without much photoexcitation,[6,12] is capable of determining the ionic mass to an accuracy of 0.0005 to 0.005 amu and the ion energy to an accuracy of better than five parts in 10^5.

In the silicon experiment,[5,6] a Si emitter is irradiated by nitrogen laser pulses of 300 ps width under an applied dc field of about 1.5 V/Å in 10^{-9}–10^{-10} Torr vacuum. Ions are collected one by one from a surface area of about 5 atom diam. Ionic masses and the kinetic energy of ions are calculated according to [6,12]

$$\frac{M}{n} = C\left(V_0 - \frac{\Delta E_c^{n+}}{ne}\right)(t_0 + \delta)^2, \tag{1}$$

and

$$E = neV_0 - \Delta E^{n+} = \frac{eM}{C(t+\delta)^2}, \tag{2}$$

where V_0 is the dc voltage, t_0 is the onset flight time, ΔE_c is the critical energy deficit of the ion species, $C \approx 0.010\,828\,35\ u/\mu s^2/kV$ is the flight path constant, $\delta = 26.4$ ns is the time delay constant, n is the charge state, M is the ionic mass in u (or amu), and t is the flight time of an ion. ΔE_c^{n+} is given by

$$\Delta E_c^{n+} = \Lambda + \sum_{i=1}^{n} I_i - n\phi_{AV} - Q \tag{3}$$

for $n+$ atomic ions where Λ is the sublimation energy, I_i is the ith ionization potential, ϕ_{AV} is the average work function of the flight tube, and Q is the activation energy of field desorption. For $n+$ cluster ions of m atoms, $\Delta E_c^{n+}(m)$ is given by[6]

$$\Delta E_c^{n+}(m) = m\Lambda + \sum_{i=1}^{n} I_i' - E_b(m) - n\phi_{AV} - Q, \tag{4}$$

where I_i' is the ith ionization energy of the cluster and $E_b(m)$ is the total binding energy or the total cohesive energy of the cluster. The kinetic energy of pulsed-laser field desorbed ions can exceed $neV_0 - \Delta E_c^{n+}$ if photoexcitation occurs. Photoexcitation effects tend to broaden the mass lines, which are also ion energy distributions, to the high energy side, and thus deteriorate the mass resolution of the system. However, the mass resolution of this system is still excellent even under such a circumstance.

It is relevant to consider here the condition for a material to favor field desorbing as a particular ion species. The image hump model[7] gives the desorbing field at very low temperature to be

$$F_c^{n+}(m) \approx [\Delta E_c^{n+}(m)]^2/n^3e^3. \tag{5}$$

The two sides are equal if no atomic tunneling occurs and if $T = 0$. For an ion species to be favored over another one, its $F_c^{n+}(m)$ or equivalently its $\Delta E_c^{n+}(m)/n^{3/2}$ should be comparable to or lower than that of the other ion species. A variety of ion species simultaneously present in a field desorption spectrum will indicate that the differences in the $\Delta E_c^{n+}(m)/n^{1/2}$ for all these ion species are not much greater

 0734-211X/85/051425-06$01.00

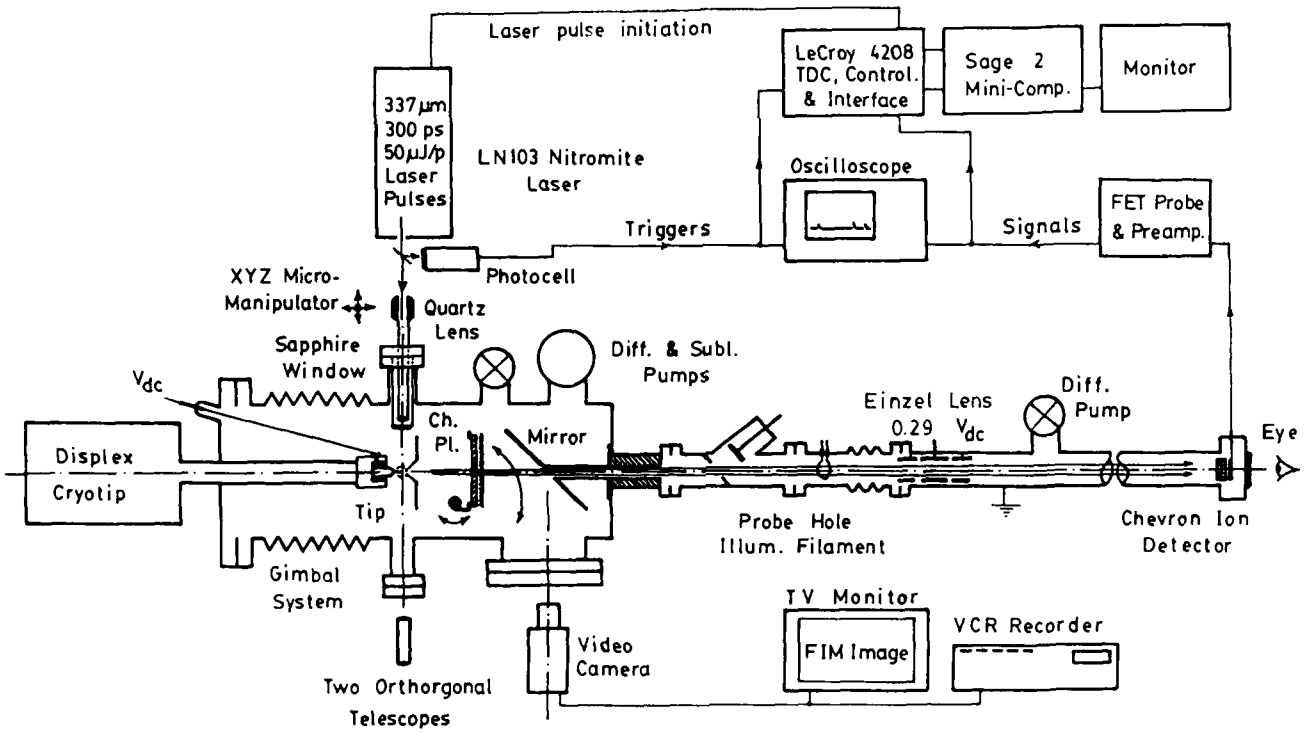

FIG. 1. Pulsed-laser TOF atom probe used in this study.

than kT, the thermal energy of the field desorption temperature. More precisely, if the differences in the activation energies of these ions species which are given by

$$Q_n(F) = \Delta E_c^{n+}(m) - (ne)^{3/2}F^{1/2}, \quad (6)$$

are not much greater than kT. This condition is apparently satisfied in field evaporation of silicon under intense laser irradiation where the surface temperature may arise to 1000 K or higher.

III. EXPERIMENTAL RESULTS AND DISCUSSIONS

A. Silicon clusters

In pulsed-laser field evaporation of Si emitters, only Si^{2+} can be observed if the laser power is sufficiently low and the dc field high. When the laser power is increased and the dc field is lowered, Si^+ and cluster ions of Si start to appear. In our experiment,[5,6] ~15% of ions are cluster ions which constitutes about 40% to 50% of all the field evaporated atoms since each cluster ion contains several atoms. The energy distributions as well as the mass lines of Si^{2+} are sharp without any low energy tail as shown in Fig. 2. This is not the case with Si^+ and Si-cluster ions, as shown in Figs. 3 and 4. For Si^+, in addition to the sharp main peak, there is a long, exponentially decaying low energy tail of an energy deficit of more than 200 eV. These low energy tails of Si^+ and cluster ions are produced by spontaneous dissociation of cluster ions. There are at least four possible mechanisms for this spontaneous dissociation to occur.

(1) Photodissociation by the laser pulses used for the field evaporation. A cluster ion desorbed by a laser pulse can still be dissociated by the same laser pulse.

(2) Electronic deexcitation of a cluster ion results in an excess vibrational energy of the cluster ion.

(3) For a cluster with three atoms or more, redistribution of vibrational energy of the cluster among the atoms can also result in dissociation of the cluster.

(4) Field dissociation, or dissociation by activating over an ionic potential barrier deformed by the applied field.

Our preliminary analysis indicates that dissociation of cluster ions within 100 ps or less of their formation is sufficient to explain the low energy tails we have observed. As Si^{2+} cannot be produced by dissociation, the mass lines of Si^{2+} should be sharp, as indeed observed experimentally. The low energy tails contain the dissociated Si_m^+ ions.

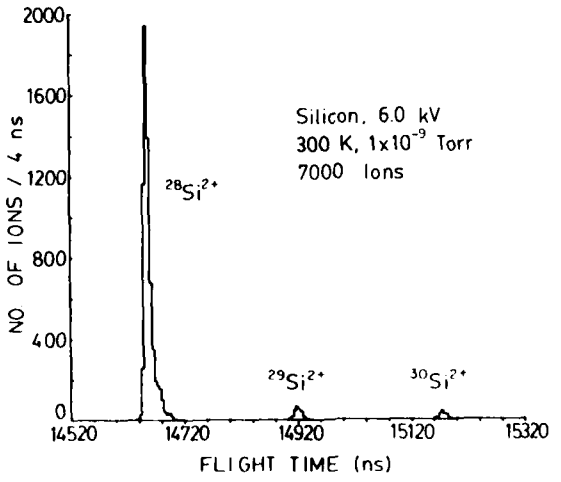

FIG. 2. Pulsed-laser stimulated field evaporation spectrum showing the sharply defined Si^{2+} mass lines of the three isotopes.

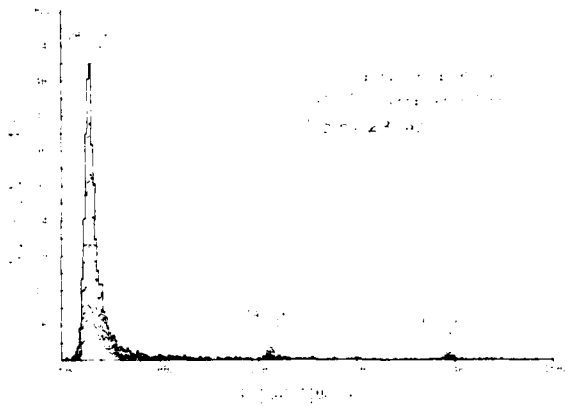

FIG. 3. Mass lines of Si^+ exhibit an exponentially decaying low energy tail, extending to over 200 eV in energy deficit. These low energy ions are produced by fragmentation of cluster ions, possibly by the desorbing laser pulses.

A unique feature of our cluster ion mass spectrum is the existence of fine structures as can be seen in Fig. 4. The fine structures arise from isotope mixing in the clusters. Since most of the fine structures show a mass difference of 1/2 u, the charge state of these ion species is identified as 2+. There is an exception, i.e., Si_4^+ where the fine structures show a mass difference of 1 u. The fractional abundance of each mass peak within an ion species due to isotope mixing can be calculated.[6] For example the fractional abundance of m-atom clusters with i ^{28}Si atoms and j ^{29}Si atoms and $(m-i-j)$ ^{30}Si atoms is given by the corresponding coefficient in the multinomial expansion,

$$[m!/i!\,j!(m-i-j)!]a^i b^j c^{(m-i-j)}, \tag{7}$$

where $a = 0.922$, $b = 0.047$, and $c = 0.031$ are, respectively, the fractional abundance of ^{28}Si, ^{29}Si, and ^{30}Si. In Table I, the fractional abundance of mass lines in ion species Si_4^{2+}, Si_5^{2+}, and Si_6^{2+} are listed. By comparing these values with the peak heights shown in Fig. 4, one can see that the calculated values agree with experimental values to within experimental uncertainties. Thus we are able to identify cluster ion species without uncertainties. This is important since, for example, Si_4^{2+} and Si_6^{2+} can be easily mistaken as Si_2^+ and Si_3^+. In most cluster ion studies, an ion species with a mass-to-charge ratio equal to an integral multiple of the atomic mass is almost always identified as singly charged ions.

With the cluster ion species now properly identified, it is now quite clear that the most abundant Si cluster ion species are Si_4^{2+}, Si_6^{2+}, $Si_5^{2+} \approx Si_4^+$, Si_3^{2+}, etc. The only 4+ ion which probably exists is Si_{13}^{4+}. It is interesting to note that 4–6 are the only highly symmetric small units of atoms existing in a Si lattice.[5] If we consider Si(111) layers, then 6 and 13 are the only highly symmetric "two-dimensional," small units of atoms in these layers. Thus 4–6 and 13 may be called the magic numbers in Si cluster formation by desorption from a Si surface. They reflect the two-dimensional atomic structures of the substrate surface where these cluster ions are desorbed. These magic numbers refer to the desorption process and they are different from the conventional "magic

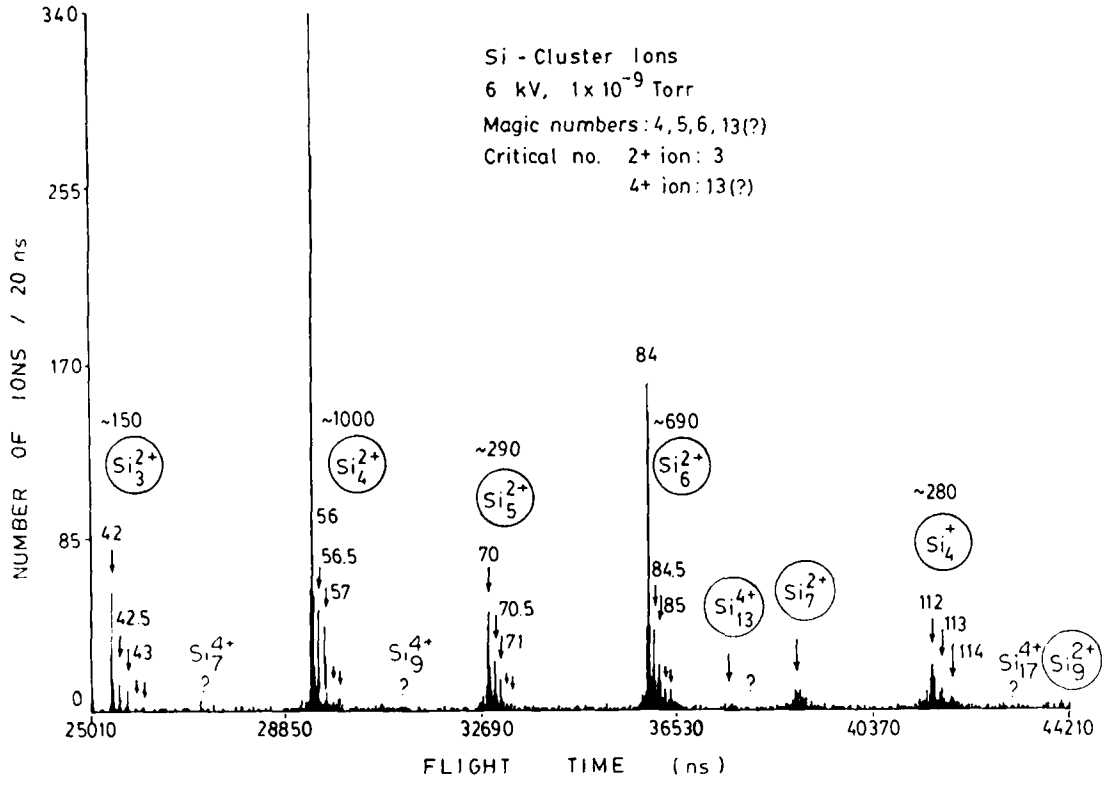

FIG. 4. Mass spectrum showing part of cluster ion species detected. Note the fine structures due to isotope mixing. From these fine structures, the charge state of each ion species can be correctly identified. The low energy tails contain dissociated singly charged ions.

TABLE I. Expected fractional abundance of various mass-to-charge ratios in Si cluster ion.

Ion species	Mass-to-charge ratios	Combinations of isotopes in a cluster	Fractional abundances (%)
Si_4^{2+}	56	4×28	72.3
	56.5	$3\times28+29$	14.7
	57	$2\times28+2\times29$, $3\times28+30$	10.8
	57.5	$2\times28+29+30$, $28+3\times29$	1.5
	58	$2\times28+2\times30$, $28+2\times29+30$, 4×29	0.6
Si_5^{2+}	70	5×28	66.6
	70.5	$4\times28+29$	17.0
	71	$3\times28+2\times29$, $4\times28+30$	12.9
	71.5	$2\times28+3\times29$, $3\times28+29+30$	2.4
	72	$28+4\times29$, $3\times28+2\times30$, $2\times28+2\times29+30$	0.9
Si_6^{2+}	84	6×28	61.4
	84.5	$5\times28+29$	18.8
	85	$4\times28+2\times29$, $5\times28+30$	14.8
	85.5	$4\times28+29+30$, $3\times28+3\times29$	3.3
	86	$4\times28+2\times30$, $2\times28+4\times29$, $3\times28+2\times29+30$	1.4

numbers" which refer to the sizes of the most stable clusters. Structures of these units of atoms are illustrated in Fig. 5. Our result, however, does not mean that the cluster, once desorbed from the surface, will maintain the same structure as in the lattice. In Fig. 6, possible structures of 4–6 atom clusters are shown.

Another result of interest is the smallest size of multiply charged cluster ions. This number is known as the critical number below which Coulomb repulsion will dissociate the cluster ion into smaller cluster ions.[2] Our critical number for 2+ ions is found to be as small as 3. In contrast, for metallic, ionic, and van der Waals cluster ions, the critical number is found to be ~30 or larger.[2] There are at least two reasons for this dramatic difference. First, while in other types of clusters atoms tend to stay as close together as possible to achieve the maximum binding, Si atoms tend to form covalent bonds and therefore do not have to stay very close from one another. The Coulomb repulsive force between the two charges is therefore much less strong. Second, in our time-of-flight measurement, if the lifetime of Si_3^{2+} is greater than the flight time in the acceleration section of the atom probe (which is only ~1.5 mm), then it will be detected as Si_3^{2+} even if it dissociates after it has left this acceleration section.[10] Thus as long as the life time of Si_3^{2+} ions is larger than 10^{-8} s, they will be detected as Si_3^{2+}. In many other types of experiments, a doubly charged ion will make many collisions with other particles before being mass analyzed. The term "critical number" of Coulomb explosion is vague at best in such an experiment since it does not reflect truly the energy difference between the cluster ion state and its dissociated state but rather the relative stability of cluster ions of different sizes and charge states.

Another interesting finding in our pulsed-laser field desorption study is that a large fraction of both atomic and cluster silicon ions has energy deficits less than those given by Eq. (4). These ions with excess energies are produced by a photoexcitation effect by the laser pulses.[6] Since our atom probe is also an ion energy analyzer of very high resolution,

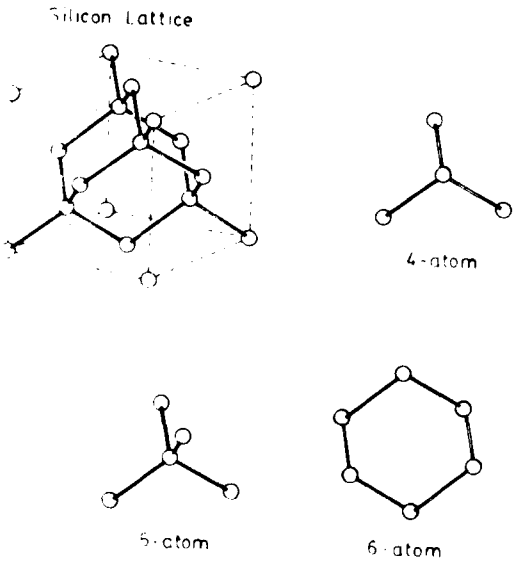

FIG. 5. Atomic structure of silicon and the small, symmetric units of atoms existing in the crystal.

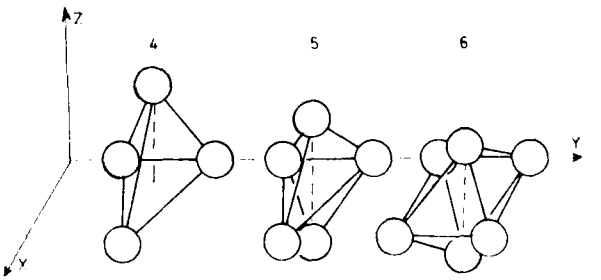

FIG. 6. Possible structures of small and highly stable silicon clusters.

TABLE II. Appearance energy of water clusters in eV.

	$(H_2O)_1H^+$	$(H_2O)_2H^+$	$(H_2O)_3H^+$	$(H_2O)_4H^+$	$(H_2O)_5H^+$	$(H_2O)_6H^+$	$(H_2O)_7H^+$	$(H_2O)_8H^+$	$(H_2O)_9H^+$
Data taken at 57 K	9.1 ± 0.3	7.6 ± 0.2	7.6 ± 0.2	7.3 ± 0.4	7.2 ± 0.2	7.2 ± 0.2	6.9 ± 0.6	6.9 ± 1.1	6.9 ± 0.5
Data taken at 150–250 K	10.5 ± 0.6	9.8 ± 0.4	9.2 ± 0.4	9.2 ± 0.2					
Data from Ref. 14	10.5 ± 0.2	10.4 ± 0.3							
Data from Ref. 13	8.8 ± 0.1	10.0 ± 0.1	11.5 ± 0.2	11.6 ± 0.3					

the energetics and detailed mechanisms of ion formation can be studied by measuring the ion energy distributions as have been reported recently.[6]

B. Water clusters

A thin layer of water will be "field condensed" on an emitter surface if the partial pressure of water is greater than 1×10^{-8} Torr. When the tip is kept at room temperature and the field is raised to 1.5 V/Å or higher, a blurred field ion image of the surface can usually be seen. If the field is sufficiently low, however, the field ionization ceases to be detectable. Pulsed-laser stimulated field desorption by time-of-flight analysis can then be carried out. At room temperature, H_2O^+, $(H_2O)H^+$, and O_2^+ can be detected at a field around 1.0–1.5 V/Å. This observation indicates that the first layer of the condensed water is dissociatively chemisorbed on the emitter surface (which is Rh). If the applied field is reduced, then $(H_2O)_2H^+$, etc., start to appear and H_2O^+ and O_2^+ disappear. The most abundant ion species as well as the relative abundance of various cluster ion species depends on the field strength, the partial pressure of water in the system and the pulsed-laser field desorption rate. If the emitter temperature is lowered to below 150 K, cluster ions of up to ~ 12 water molecules can be observed. H_2O^+ and O_2^+ and a small amount of $(H_2O)_m H_2^+$ can be observed if the emitter surface is not completely covered with ice. Once the surface is covered with a thin layer of ice, only $(H_2O)_m H^+$ can be observed. Two examples are shown in Figs. 7 and 8. The onset flight times of these cluster ions can be determined to an accuracy of $\pm$ 1–2 ns as shown in Fig. 9. From these onset flight times (t_o) the critical energy deficits of water cluster ions can be calculated according to

$$\Delta E_c = neV_o - \frac{eM}{C(t_o + \delta)^2}. \tag{8}$$

The appearance energy is simply the sum of ΔE_c and ϕ_{AV}, where ϕ_{AV} is the average work function of the flight tube. $\phi_{AV} = 4.5$ eV gives the best agreement of our measured appearance energies of inert gases with their ionization potentials. In field ionization of atomic and molecular gases involving no formation of new compounds, the appearance energy should be equal to the ionization energy as can be seen from Eq. (3) by taking $\Lambda = 0$, Q = 0, and n = 1. In the formation of $(H_2O)_m H^+$ ions, the appearance energies depend on the detailed atomic steps involved in the ion forma-

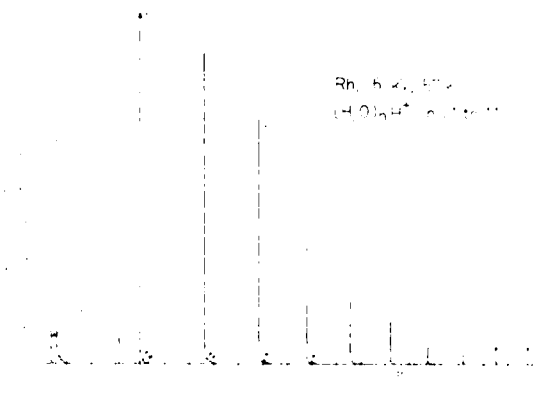

FIG. 7. Pulsed-laser field desorption mass spectrum of water taken when the Rh tip surface is not yet completely covered with ice. In addition to $(H_2O)_m H^+$ ions of $m = 1$–11, some H_3O^+, O_2^+, $(H_2O)_m H_2^+$, and $(H_2O)_m H_3^+$ ions are also observed.

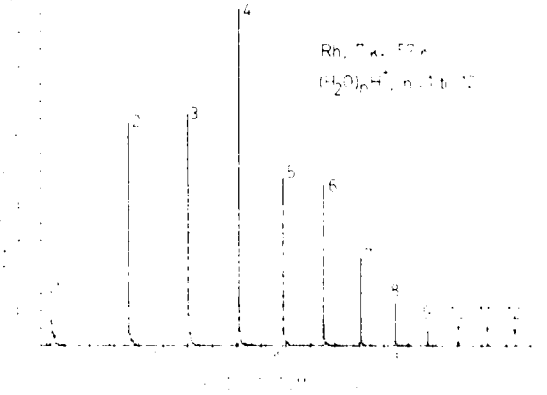

FIG. 8. When the Rh emitter surface is completely covered with a thin layer of ice, only $(H_2O)_m H^+$ ions of $m \sim$ 1–12 are observed. The ion species of maximum intensity (in this figure $m \sim 4$) shifts from a smaller cluster to a large one when the ice layer gets thicker.

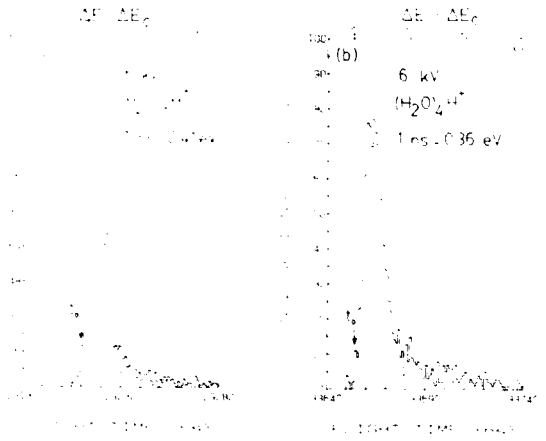

FIG. 9. Two examples of the energy distribution of water cluster ions. They all show a sharp onset and an exponentially decaying low energy tail, produced by dissociation of larger cluster ions.

tion near the surface. The appearance energies of water cluster ions we have measured are listed in Table I together with some other data[14,15] reported by others in field ionization of water using retarding potential analyzers. We are surprised to find that our measured appearance energies depend on the surface temperature. Also within the experimental uncertainty of our measurement (0.3–0.5 eV) the appearance energies decrease monotonically with the size of the cluster ions. In contrast, ionization energies of metal clusters decrease nonmonotonically with the cluster size to reach the value of the work function of the metal.[1]

ACKNOWLEDGMENTS

This work was supported by the National Science Foundation. The results reported here for water clusters is a joint work with Y. Liou of our laboratory; details of this work will be reported later.

[1] A. Herrmann, E. Schumacher, and L. Wäste, J. Chem. Phys. **68**, 2327 (1978).
[2] K. Sattler, J. Mühlbach, O. Echt, P. Pfau, and E. Rechnagel, Phys. Rev. Lett. **47**, 160 (1981).
[3] O. Echt, K. Sattler, and E. Recknagel, Phys. Lett. A **90**, 185 (1982).
[4] J. E. Campana, T. M. Barlak, R. J. Colton, J. J. DeCorpo, J. R. Wyatt, and B. I. Dunlap, Phys. Rev. Lett. **47**, 1046 (1981); R. J. Colton, Nucl. Instrum. Methods Phys. Res. **218**, 267 (1983).
[5] T. T. Tsong, Appl. Phys. Lett. **45**, 1149 (1984).
[6] T. T. Tsong, Phys. Rev. B **30**, 4946 (1984).
[7] E. W. Müller and T. T. Tsong, Prog. Surf. Sci. **4**, 1 (1973).
[8] T. T. Tsong, J. H. Block, M. Nagasaka, and B. Viswanathan, J. Chem. Phys. **65**, 2469 (1976); T. T. Tsong, Surf. Sci. **70**, 226 (1978).
[9] W. Drachsel, Th. Jentsch, and J. H. Block, *Proceedings of the 29th International Field Emission Symposium*, edited by H. O. Andren and H. Novden (Almqvist and Wiksell, Stockholm, 1982), p. 299; G. L. Kellogg, Appl. Surf. Sci. **11/12**, 186 (1982).
[10] T. T. Tsong and L. Liou, Phys. Rev. B (in press).
[11] T. T. Tsong, S. B. McLane, and T. J. Kinkus, Rev. Sci. Instrum. **53**, 1442 (1982).
[12] T. T. Tsong, Y. Liou, and S. B. McLane, Rev. Sci. Instrum. **55**, 1246 (1984).
[13] A. R. Anway, J. Chem. Phys. **50**, 2012 (1969).
[14] H. J. Heinen, F. W. Röllgen, and H. D. Beckey, Z. Naturforsch. Teil A **29**, 773 (1974).

Selective laser-stimulated desorption of molecules by internal vibration excitation

C. Jedrzejek[a)]
Department of Physics, Texas A&M University, College Station, Texas 77843

(Received 18 March 1985; accepted 21 May 1985)

The photodesorption model of Gortel, Kreuzer, and collaborators in which a laser is resonantly coupled to an internal vibration mode of an absorbed molecule is considered. The importance of including anharmonicity of the internal vibration and a broadening of energy levels of a zero-order Hamiltonian is demonstrated. A numerical calculation of the photodesorption as a function of a laser intensity is presented for a multilevel system of CH_3F on NaCl and compared with experimental data. In comparison to previous assumption of only harmonic motion for the internal vibration where the values of the laser fluences for laser-stimulated desorption are calculated to be too low, our results (saturation intensities $\sim 10^5$–10^6 W/cm^2) are in closer agreement with experiment.

I. INTRODUCTION

Infrared laser radiation can interact with an adsorbate covered solid surface through several mechanisms. The laser energy can be transferred (a) directly into the solid, (b) into an adsorbate–surface atom bond, or (c) into an internal vibrational mode of the adsorbed molecule. The first process heats the surface and leads to thermal desorption. The other two processes are resonant in character since only a single mode is initially excited. However, it is not well understood, in process (b), whether enough energy can be accumulated in a single mode to selectively break a bond. In case (c) the energy leaking out of the excited mode through various dissipative processes may either be transferred to the adsorbate–surface bond, resulting in desorption or it might heat the solid which leads to the desorption by resonant heating.[3–6]

Laser thermal desorption occurs when the laser intensities are in excess of $\sim 10^6$–10^7 W/cm^2.[1,2,6–9] It could be of great importance for technological applications if a low-power pulse, due to its coherence, could cause desorption. The direct excitation of the admolecule–surface bond is not effective because admolecule–surface energy levels are too broad and this leads to strong coupling to other modes and energy dissipation. For a model in which laser energy is directly deposited into a surface bond, Jedrzejek *et al.*[10] previously predicted a very high threshold laser intensity I_{LSD}, greater than 10^{10} W/cm^2 for CO/Cu. In that calculation the intrinsic width of the stretching vibration was assumed to be 100 cm^{-1}. It can also be shown that for smaller widths the threshold laser intensity should be much lower, because the dependence of the laser-stimulated desorption (LSD) rates on the width is dramatic.[11] So far, only a few experimental observations of resonant LSD have been reported and these, however, were for cases in which the laser energy was pumped into some internal vibrational mode of the adsorbed molecule. The experiments of Heidberg *et al.*[12,13] demonstrated the desorption of CH_3F from NaCl, whereas Chuang and Seki[8,9,14] showed the desorption of pyridine and deuterated pyridine from KCl and Ag. Both processes occurred at intensities $5\times(10^5$–$10^7)$ W/cm^2. Very recently Chuang and collaborators[6,15] obtained the experimental data for desorption of NH_3/ND_3 system from Cu(100) and Ag films. These latter experiments are also very useful, because they allow one to estimate the relative importance of quantum and thermal processes more reliably when compared to the information provided by earlier experiments.

Since LSD desorption is a complicated, many-body, quantum nonequilibrium phenomenon, the theory has to resort to rather drastic approximations from the outset. The method advanced mainly by George, Lin, and collaborators[16–19] and recently considered by Fain, Lin, and collaborators,[20,21] as well as Casassa *et al.*[22] reduces the desorption process to an effective-few-quantum-level dynamics. However, in this approach the multilevel aspect of the molecule "climbing the energy ladder" is lost. Also it is rather difficult to account for the broadening of the levels that is always present in the experiments. Therefore the "effective-few-quantum-levels" methods tend to overestimate the importance of coherence of the laser. This can lead to an overly optimistic prediction of the necessary intensity thresholds for LSD.[16,19] Another class of methods reduces the Liouville equation of the system dynamics to the master equation with the Markovian and random-phase approximations.[3–6,10] Though incapable of treating the coherent nature of laser radiation, the latter methods allow for much better correlation of theoretical parameters with the experimentally obtained binding energies. Finally, a third approach using classical stochastic equations has been widely used.[18,23–25] Obviously this last method is better suited for describing nonresonant laser-induced desorption rather than a selective desorption.

In this paper the Gortel, Kreuzer, and collaborators[3–5] model of photodesorption due to an internal vibrational mode excitation of the admolecule is considered. This model is effective for understanding the existing experimental data. It is shown, by including anharmonicity of the internal vibrational model with the accompanying broadening of the zero-order levels, as neglected by Gortel *et al.*,[3] that much larger threshold fluences for the desorption than previously predicted can be obtained. The theoretically calculated laser desorption rates are now in better agreement with experiment for CH_3F/NaCl system. The heating of the solid, an important limitation of this work, will be discussed elsewhere.

 0734-211X/85/051431-05$01.00

II. THE LSD MODEL BY EXCITATION OF INTERNAL VIBRATION MODE

In their fundamental work the Canadian group of Gortel, Kreuzer, and collaborators[3–5] proposed the resonant laser desorption model, including resonant heating, based on the coupling between admolecule–surface and internal vibrational modes. They successfully employed the concepts previously considered by George *et al.*[18] as well as by Lucas and Ewing.[26] The weakly bound adsorbate molecules can be described by a surface potential. Since typically the energy $\hbar\Omega$ of the vibrational mode of the molecule, to which the laser radiation is coupled, is much larger than the energy level differences of the binding potential, the two modes can be decoupled in the adiabatic approximation. The binding potential was assumed to be of the Morse form and the internal mode was modeled with a harmonic oscillator. Invoking a master equation approximation the time dependent average occupation functions obey the following equation:

$$\frac{d}{dt}n_i^v(t)=\sum_{v'=0}^{\infty}\sum_{i'=0}^{i_{\max}}[(\mathscr{L}_{ii'}^{vv'}+P_{ii'}^{vv'})n_{i'}^{v'}(t)-(\mathscr{L}_{i'i}^{v'v}+P_{i'i}^{v'v})n_i^v(t)]-\sum_{v'=0}^{\infty}(P_{ci}^{v'v}+Q_{ci}^{v'v})n_i^v(t). \tag{1}$$

Here i labels the states of the surface potential and v is the quantum number of the internal vibrational mode. In Eq. (1) $\mathscr{L}_{ii'}^{vv'}$ is the rate of vibration transitions due to the coupling of the molecular dipole moment to the laser radiation. $P_{ii'}^{vv'}$ is transition rate between the bound states induced by phonon absorption and emission calculated in the one-phonon approximation. The two terms $P_{ci}^{v'v}$ and $Q_{ci}^{v'v}$, responsible for desorption, are the rates of transitions from bound states to continuum, due to mediation by phonons and to the tunneling, respectively. After calculating the transition probabilities P, Q, and L in this work the rates of laser-induced desorption are calculated by the mean first-passage time method.[27] As can be inferred from Ref. 3, the difference between such calculated rates and the corresponding rates identified with the inverse of the smallest eigenvalue of the matrix associated with Eq. (1) is less than 1%. In the steady state the energy level occupation numbers obey the Maxwell–Boltzmann statistics:

$$n_i^v(t\leqslant 0)=A\exp(-\beta E_i^v). \tag{2}$$

This work is concerned with the effect of finite linewidths on the LSD rates. The width Γ_s of the stretching surface vibration is extremely important if the laser energy is pumped directly into an adsorbate–surface atom bond. For large Γ_s there are significant one-phonon mediated $P_{ii'}^{vv'}$ transitions even if the Debye energy is smaller than $E_i-E_{i'}$. Recently, with the use of the vibrational spectroscopy, the first accurate value of the intrinsic width Γ_s of the C–Ni stretching vibration for CO adsorbed on the Ni(100) surface was measured by Chiang *et al.*[28] to be 15 cm^{-1}. For the other systems it might be in the range 10–50 cm^{-1} and the calculated linewidths exhibit a linear variation with temperature, near room temperatures.[29] However, the laser detuning due to anharmonicity cannot be corrected by the width Γ_s in the lowest order perturbation theory.

When the laser energy is pumped into an internal vibration mode the relevant quantities against which the laser detuning should be measured are the width of internal vibration mode Γ_i (typically 3 cm^{-1})[30] and laser width Γ_l (up to 1 cm^{-1}).[6] To estimate the effect of the width let us consider the laser transition elements

$$\mathscr{L}_{ii'}^{vv'}=\delta_{ii'}(Q^2/4\pi^2\epsilon_0\mu c)\times\int d^2K\,d\kappa\,K^2n_r^2(K^2+\kappa^2)^{-1}\times(n_r^2+a^2+2a/n_r)^{-1}\{n_{em}(\mathbf{K},\kappa,II=p)v\delta_{v',v-1}+[n_{em}(\mathbf{K},\kappa,II=p)+1](v+1)\delta_{v',v+1}\}\times\delta[\Omega/c-(K^2+\kappa^2)^{1/2}], \tag{3}$$

with

$$a=\cos\theta_t/\cos\theta_i, \tag{4}$$

where θ_i is the angle between the incident laser beam and the normal, i.e., $\tan\theta_i=|\kappa|/|\mathbf{K}|$, and θ_t is the angle of the transmitted beam. Ω is the frequency distance between the two lowest vibrational levels. The phonon occupation numbers are given by

$$n_{em}(\mathbf{K},\kappa,II=p)+\frac{1}{2}=CI_0\frac{1}{2\pi}\frac{\Gamma_l}{(\Omega-\Omega_l)^2+\Gamma_l^2/4} \tag{5}$$

with

$$C=\frac{(2\pi)^3c^2}{(\hbar\Omega^3)}\frac{n_r^2+a^2+2a/n_r}{(n_r+a)^2}, \tag{6}$$

where $\Omega=c(K^2+\kappa^2)^{1/2}=ck$, Ω_l denotes the central frequency of the laser line, and I_0 is the intensity of the incoming beam far from the surface. For the finite-width levels of the zero-order Hamiltonian, the energetic delta function in Eq. (3) has to be replaced by

$$\Delta(k)=\frac{1}{2\pi}\frac{c\Gamma_i}{(\Omega-ck)^2+\Gamma_i^2/4}. \tag{7}$$

In this equation Δ denotes the difference between the centers of the two lowest vibrational levels. After substituting $\Delta(k)$ and $n_{em}(\mathbf{K},\kappa,II=p)+\frac{1}{2}$ into Eq. (3) and integrating over the angular variables one obtains

$$\mathscr{L}_{ii'}^{vv'}=\frac{2\pi Q^2}{\epsilon_0\mu c^2\hbar}\frac{n_r^2I_0\sin^2\theta_l}{(n_r+a)^2}[v\delta_{v',v-1}+(v+1)\delta_{v',v+1}]\delta_{ii'}\times\int_0^{\infty}\frac{dk}{k}\frac{1}{2\pi}\frac{c\Gamma_i}{(\Omega-ck)^2+\Gamma_i^2/4}\times\frac{1}{2\pi}\frac{\Gamma_l}{(\Omega_l-ck)^2+\Gamma_l^2/4}. \tag{8}$$

Note that due to the $1/k$ integrand dependence, to avoid nonphysical infrared infinity one of the Lorentzian functions in Eq. (8) has to have a very small width. More precisely, both delta functions cannot be replaced by Lorentzian functions without a regularization procedure.

In Ref. 3 it was assumed that $\Gamma_l\gg\Gamma_i$ by identifying Γ_i with Γ_m, the width due to quantum fluctuations of the electromagnetic vacuum. This essentially corresponds to ideally sharp energy levels of the zero-order Hamiltonian. In view of Ref. 3 the damping of the system is due to the interaction Hamiltonian in perturbation theory. It appears however, that the terms neglected in the zero-order Hamiltonian,

namely inhomogeneities in the system, anharmonicity of the solid, and internal vibrational modes, and coupling between the selected mode and the other vibrational and rotational modes of the system are much larger sources of damping. More realistically, $\Gamma_l \ll \Gamma_i$. With this assumption, the factor $I_0\tau_l = F$, the approximate fluence of the laser pulse, appearing in the final formula for the laser transition rate in Ref. 3,

$$\mathscr{L}_{ii'}^{vv'} = \frac{2\pi Q^2}{\epsilon_0 \mu c \hbar \Omega_l} \frac{n_r^2 \sin^2\theta_i}{\{n_r + [1+(1-n_r^{-2})\tan^2\theta_i]^{1/2}\}^2} \times (2I_0\tau_l/\pi)[v\delta_{v',v-1} + (v+1)\delta_{v',v+1}]\delta_{ii'}, \quad (9)$$

has to be replaced by

$$F = \frac{\Omega_l}{4\Omega} \frac{\Gamma_i \Gamma_l}{(\Omega - \Omega_l)^2 + \Gamma_i^2/4} I_0\tau_l, \quad (10)$$

where $\Omega - \Omega_l$ is the detuning frequency Δ_l and Γ_l is identified with the inverse of the laser pulse length. Typically with the laser pulse length $\tau_l = 2\times10^{-7}$ s and $\Gamma_i = 3$ cm^{-1} the required threshold laser intensity becomes four orders of magnitude larger compared to Ref. 3. Assuming $\Gamma_l = 1$ cm^{-1} will qualitatively give the same result. Rescaling the fluence axis with a factor $\sim 10^3$ due to exactly the same reasons as given here was already discussed by Kreuzer and Gortel.[5]

The new effects introduced in this work are anharmonicity of the internal vibration bond and detuning of the laser (when $\Omega \neq \Omega_l$) combined with the effect of finite linewidth Γ_i. The lifetimes and anharmonicities are treated here purely phenomenologically. It is assumed that the anharmonicity of the internal vibration bond only changes the separation between the subsequent vibrational levels. In Eq. (10) Ω is replaced by $\Omega_{vv'}$. Since in the LSD process only transitions between lowest vibrational levels are effective, the influence of anharmonicity on the matrix elements necessary to compute the radiative transition rates is neglected. Using the value of the detuning due to anharmonicity equal to 10 cm^{-1}, an additional order of magnitude larger threshold laser intensity is obtained as seen from Eq. (10). A larger detuning results in the correspondingly greater difference.

III. NUMERICAL CALCULATIONS OF LSD RATES

Numerical calculations were performed for CH_3F/NaCl with the following parameters of the Morse potential modeling and admolecule–surface bond:

$$V(r) = D(e^{-\alpha r} - 2e^{-2\alpha r}). \quad (11)$$

$D/kT = 2750$ K and the inverse range $\alpha^{-1} = 0.35$ Å. With the laser energy $\Omega = 1400$ K and the Debye energy $\omega_D = 281$ K, this choice represents the model presented in Fig. 4 in Ref. 3. The CH_3F molecule develops 23 bound states, the lowest of which are separated by the energy smaller than $\omega_D (E_1 - E_0 = 0.81\hbar\omega_D)$. It should be noted that with the use of Eq. (9) the laser transition rates for this system equal $\sim(2\text{–}8)\times10^{10} I_0\tau_l$.

The effect of the finite width of vibrational levels and anharmonicity is presented in Figs. 1–5 for the temperatures 50, 77, and 100 K. In all figures solid lines represent rescaled results of Ref. 3, where the truncated harmonic oscillator model for the internal molecular vibration is considered,

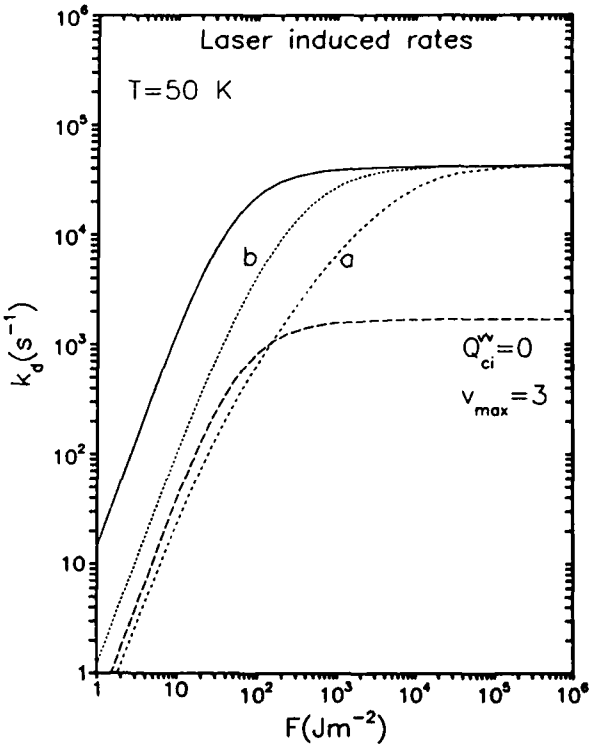

FIG. 1. Laser-stimulated desorption rates k_d for CH_3F on NaCl vs laser fluence F at $T = 50$ K. Solid line is the rescaled result of Ref. 3; broken line, the same result without elastic tunneling transition elements $Q_{ci}^{vv'}$. Dotted line (a) refers to the result with the included anharmonic defect, $\Delta\Omega = 10$ cm^{-1}; dotted line (b), as for line (a), plus the infrared laser shift equals 5 cm^{-1} assumed. The highest level retained in the truncated oscillator model is $v_{max} = 3$.

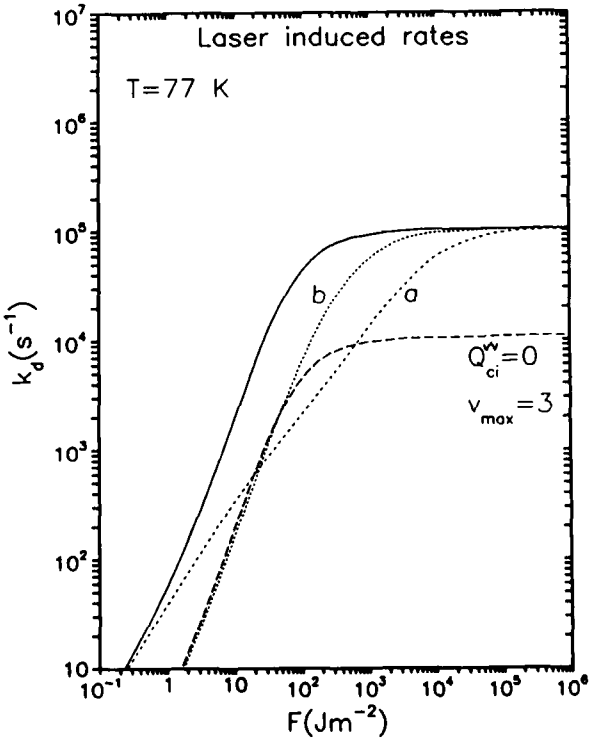

FIG. 2. LSD as in Fig. 1 but for $T = 77$ K.

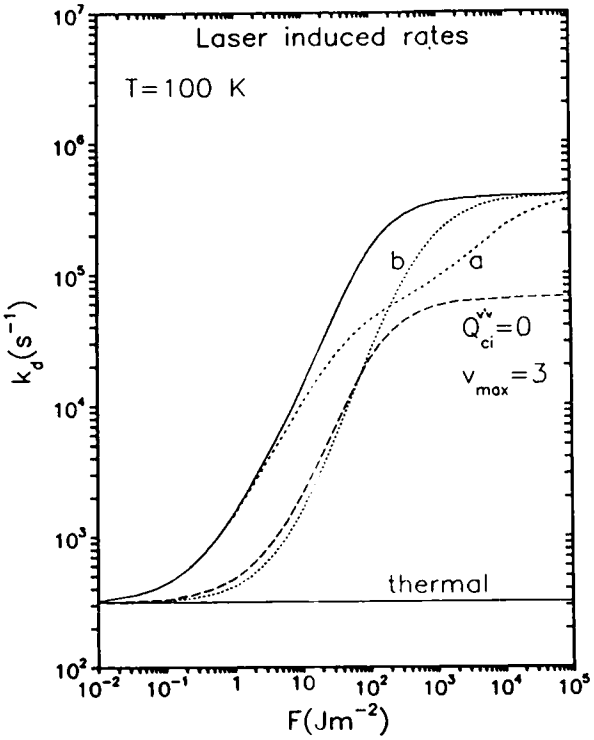

FIG. 3. LSD as in Fig. 1 but for $T = 100$ K.

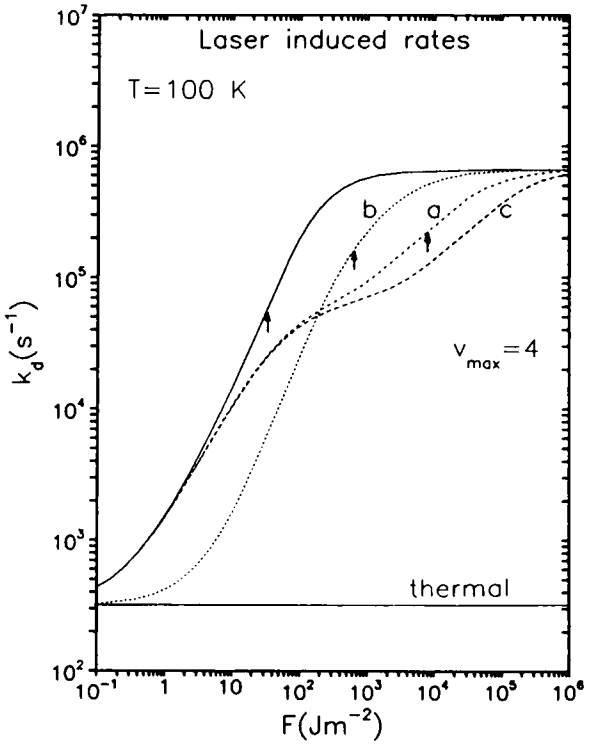

FIG. 5. LSD as in Fig. 4 but for $T = 100$ K.

only with $\Gamma_i \gg \Gamma_l$ and $\Gamma_i = 3\ \text{cm}^{-1}$ (no detuning and anharmonicity parameter). In Figs. 1–3 v_{max}, the highest level retained, equals 3. The broken lines in Figs. 1–3 refer to the same parameters as for the solid lines but with the transition

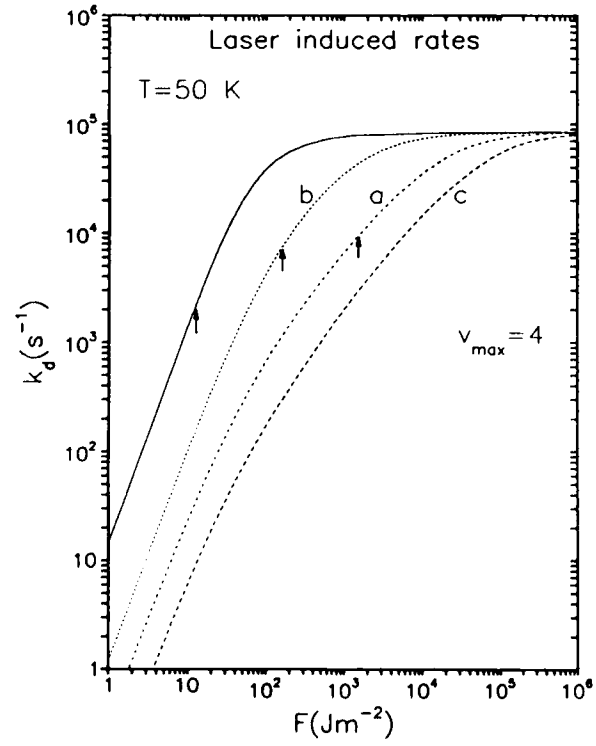

FIG. 4. LSD for $T = 50$ K but with $v_{max} = 4$. The meaning of curves (a) and (b) is the same as in Fig. 1. Curve (c) refers to the anharmonic defect $\Delta\Omega = 10\ \text{cm}^{-1}$. For fluences larger than these indicated by the arrows the rates for $v_{max} = 4$ becomes larger than the corresponding rates for $v_{max} = 3$.

elements $Q_{ci}^{v'v} = 0$ [see Eq. (1)]. The other two curves (a) and (b) include the anharmonic defect $\Delta\Omega = 10\ \text{cm}^{-1}$ meaning that if the laser frequency matches the energy difference between the two lowest vibrational levels then there are 10 and 20 cm^{-1} energy differences between the 1–2 and 2–3 transitions. In addition, for the curve (b) 5 cm^{-1} laser shift towards infrared is assumed. In order to understand the effect of anharmonicity and the additional laser detuning let us consider the following energy relations for the two lowest excited levels corresponding to (a) and (b) cases:

(a) $E_1 - E_0 = \hbar\Omega_l$ and $2\hbar\Omega_l - (E_2 - E_0) = 10\ \text{cm}^{-1}$,

(b) $E_1 - E_0 - \hbar\Omega_l = 5\ \text{cm}^{-1}$ and $(E_2 - E_0) = 2\hbar\Omega_l$.

Also note that the energy of the two-photon absorption is slightly larger than the admolecule–surface binding energy. Consequently, the following LSD mechanism is revealed. For low fluences the laser is effective only for increasing thermal desorption according to the following process: $(i,v) = (0,0) \rightarrow (0,1) \rightarrow (i_0,1) \rightarrow (c,0)$. Since the matching of the laser energy and the energy difference $E_1 - E_0$ is the most important factor, the rates corresponding to case (a) are larger than those corresponding to case (b). It should be explained that in Fig. 1 for $T = 50$ K the considered fluences are still too large to see this effect. For larger fluences more molecules are raised to the second and higher excited levels. Downward cascades of one-phonon transitions still bring most molecules to the ground state $(i,v) = (0,0)$. This loss mechanism which reduces LSD rates is called the resonant heating.[3,4] However, some molecules will desorb due to $(P_{c0}^{02} + Q_{c0}^{02})$ transitions after going through the sequence of the following steps $(i,v) = (0,0) \rightarrow (0,1) \rightarrow (0,2) \rightarrow (c,2)$. Matching the laser energy of two phonons with $E_2 - E_0$, the differ-

ence between the centers of the second excited and the ground state levels becomes increasingly important for higher fluences and therefore the rates corresponding to the (b) curves are larger than these for the (a) curves.

Increasing the number of retained levels does not change the rates at low fluences as displayed in Figs. 4 and 5 for $v_{max} = 4$. For fluences larger than these indicated by the arrows the rates for $v_{max} = 4$ become larger than the corresponding rates for $v_{max} = 3$. Dashed curves (a) and (b) have the same meaning as in Figs. 1–3. Dashed curve (c) corresponds to larger anharmonic defect, 20 cm^{-1}. Increasing v_{max} makes the saturation effect shift to larger fluences (i.e., such that they experimentally would cause vaporization of the surface). Dips in cases (b) and (c) for $T = 100$ K indicate the onset of stepwise saturation, a feature which is characteristic of larger anharmonicity. As seen from the figures, the threshold laser fluence is much closer to the experimental one, $F_l = 800$ J m^{-2} obtained by Heidberg *et al.*,[12,13] compared to the results of Ref. 3. The value of the desorption rates is still two orders of magnitude smaller than the experimental values,[12,13] however, the experimental values may reflect substantial errors.[6,9]

The results of this work signify the importance of anharmonicity and indicate that the rates calculated in Refs. 3–5 were overestimated. They also suggest the importance of resonant heating which might have been negligible for the threshold fluence $F = 10^{-2}$ J m^{-2}, but could be the dominant factor for four orders of magnitude larger fluences. Effectiveness of the resonant heating process is controlled by the efficiency with which the energy supplied by the laser to the absorbate can be transferred to the solid. This in turn depends on the phonon mediated deexcitation rates of vibrationally excited molecules, which are independent of the laser fluence only in linear (lowest order in perturbation theory) approximation. Consequently, if for the same LSD rate without including heating significantly larger laser intensity is required, nonlinear processes unaccounted in the original model[3–5] become very important. Notice that if such mechanisms are not introduced there is nothing in the theory which will predict laser ablation of the solid at a fluence $\sim 10^5$ J cm^{-2}. In view of this, the numerical results of Refs. 3–5 cannot be easily modified by simply rescaling the fluences. Since the calculations of heat transport in the solid were not performed in the present work, more decisive results can be obtained only where all these factors are accounted for: the linewidth of vibrational levels, anharmonicity of the internal vibration, and rise of the solid temperature upon the laser irradiation.

ACKNOWLEDGMENTS

The author thanks Dr. T. J. Chuang, Dr. J. Heidberg, Dr. Z. W. Gortel, and Dr. R. Viswanathan for numerous discussions, and a referee of this paper for elucidating comments which led to improvements. Dr. Z. Olejniczak's contribution to part of this work is gratefully acknowledged. This work was supported by R. A. Welch Foundation.

[a]On leave from Department of Physics, Jagellonian University, Kraków, Poland.
[1]J. P. Cowin, D. J. Auerbach, C. Becker, and L. Wharton, Surf. Sci. **78**, 545 (1978).
[2]G. Wedler and H. Ruhman, Surf. Sci. **121**, 464 (1982).
[3]Z. W. Gortel, H. J. Kreuzer, P. Piercy, and R. Teshima, Phys. Rev. B **27**, 5066 (1983).
[4]Z. W. Gortel, H. J. Kreuzer, P. Piercy, and R. Teshima, Phys. Rev. B **28**, 2119 (1983).
[5]H. J. Kreuzer and Z. W. Gortel, Phys. Rev. B **29**, 6926 (1984).
[6]I. Hussla, H. Seki, T. J. Chuang, Z. W. Gortel, H. J. Kreuzer, and P. Piercy (to be published).
[7]D. R. Burgess, Jr., R. Viswanathan, I. Hussla, P. C. Stair, and E. Weitz, J. Chem. Phys. **79**, 5200 (1983); D. R. Burgess, Jr., I. Hussla, R. Viswanathan, P. C. Stair, and E. Weitz, Rev. Sci. Instrum. **55**, 1771 (1984).
[8]T. J. Chuang, Surf. Sci. Rep. **3**, 1 (1983).
[9]T. J. Chuang, J. Vac. Sci. Technol. B **3**, 1408 (1985).
[10]C. Jedrzejek, K. F. Freed, S. Efrima, and H. Metiu, Surf. Sci. **109**, 191 (1981).
[11]C. Jedrzejek, in *Surface Studies with Laser*, Springer Series in *Chemical Physics*, edited by F. Aussenegg, A. Leitner, M. E. Lippitsch (Springer, Berlin, 1983), p. 230.
[12]J. Heidberg, H. Stein, E. Riehl, and A. Nestmann, Z. Phys. Chem. Naturforsch. **121**, 145 (1980).
[13]J. Heidberg, H. Stein, and E. Riehl, Phys. Rev. Lett. **49**, 666 (1982).
[14]T. J. Chuang and H. Seki, Phys. Rev. Lett. **49**, 382 (1982); T. J. Chuang, J. Electron Spectrosc. Relat. Phenom. **29**, 125 (1983).
[15]T. J. Chuang and I. Hussla, Phys. Rev. Lett. **52**, 2045 (1984).
[16]J. Lin and T. F. George, J. Chem. Phys. **72**, 2554 (1980); Phys. Rev. B **24**, 64 (1981).
[17]J. Lin, A. C. Beri, M. Hutchinson, W. C. Murphy, and T. F. George, Phys. Lett. A **79**, 233 (1980).
[18]T. F. George, J. Lin, A. C. Beri, and W. C. Murphy, Prog. Surf. Sci. **16**, 139 (1984).
[19]A. C. Beri and T. F. George, J. Vac. Sci. Technol. B **3**, 1529, (1985).
[20]B. Fain and S. H. Lin, Surf. Sci. **147**, 497 (1984).
[21]G. S. Wu, B. Fain, A. R. Ziv, and S. H. Lin, Surf. Sci. **147**, 537 (1984).
[22]M. P. Casassa, F. G. Celii, and K. C. Janda, J. Chem. Phys. **76**, 5295 (1982); F. G. Celii, M. P. Casassa, and K. C. Janda, Surf. Sci. **141**, 169 (1984).
[23]W. C. Murphy and T. F. George, Surf. Sci. **102**, L46 (1981); F. O. Goodman, *ibid.* **109**, 341 (1981); M. I. Riley and D. J. Diestler, J. Vac. Sci. Technol. B **3**, (to be published).
[24]J. Lin and T. F. George, Phys. Rev. B **24**, 64 (1981).
[25]R. R. Lucchese and J. C. Tully, J. Chem. Phys. **81**, 1631 (1984).
[26]D. Lucas and G. E. Ewing, Chem. Phys. **58**, 385 (1981).
[27]S. Efrima, C. Jedrzejek, K. F. Freed, and H. Metiu, J. Chem. Phys. **79**, 2436 (1983).
[28]S. Chiang, R. G. Tobin, P. L. Richards, and P. A. Thiel, Phys. Rev. Lett. **52**, 648 (1984).
[29]J. C. Ariyatsu, D. L. Mills, K. G. Lloyd, and J. Hemminger, Phys. Rev. B **30**, 507 (1984).
[30]S. Anderson and M. Person, Phys. Rev. B **24**, 3659 (1981); M. Person and S. Anderson, Surf. Sci. **117**, 352 (1982).

Technique for measuring surface diffusion by laser-beam-localized surface photochemistry[a)]

H. J. Zeiger, J. Y. Tsao,[b)] and D. J. Ehrlich
Lincoln Laboratory, Massachusetts Institute of Technology, Lexington, Massachusetts 02173-0073

(Received 18 March 1985; accepted 21 May 1985)

A technique is described for determining the surface diffusivity of a weakly bound adsorbate by measuring the kinetics of a spatially localized, laser-beam-driven surface photoreaction. The diffusivity is extracted from the experimental data by means of a Green's function integral technique. The solution is numerically integrated in order to calculate the spatial and temporal evolution of the surface-number-density of parent and product molecules. The new technique has been applied to experiments with tetraethyl lead molecules adsorbed on sapphire.

I. INTRODUCTION

Numerous techniques have been developed over the years for measuring surface-migration rates of adsorbed species.[1] Most of these techniques, however, are only applicable to observing the surface migration of strongly bound or robust adsorbates, such as atoms and some diatomic molecules. The techniques generally require ultrahigh vacuum systems, to eliminate probe-beam scattering and artifacts due to residual gases.

It is also important to develop techniques for observing the surface migration of weakly bound or fragile molecules. We briefly describe such a technique in this paper and discuss its application to a study of the surface migration of tetraethyllead (TEL) adsorbed on sapphire substrates. The details of the experiment and theoretical analysis will be published elsewhere.

The technique uses a tightly focused UV laser beam to drive a highly spatially localized photoreaction in an adsorbed molecular layer. This process creates a particle sink to which parent molecules must diffuse in order to sustain the reaction. The rate at which the reaction proceeds is then used as a sensitive measure of the surface-diffusion rate of the adsorbed parent molecules.

We briefly describe the experimental technique and results in Sec. II of this paper. A sketch of a mathematical model is given in Sec. III and its utilization to extract parameter values from the experimental data is discussed in Sec. IV.

II. EXPERIMENTAL TECHNIQUE AND RESULTS

The experimental technique is based on spatially localized UV-laser photodeposition,[2] a process in which molecules are photolyzed to form nonvolatile products confined to the focus of the incident laser beam. We will be concerned exclusively with adsorbed-phase-initiated photodeposition. It should be emphasized that for the present purpose the reaction mechanism is of secondary importance, since we are concerned only with kinetics, viz., the consumption rate of parent molecules.

The basic experimental geometry has been described previously.[3] Briefly, a few mW 257.2-nm laser beam was generated by frequency doubling an Ar^+ laser beam, and then focused by a high-power microscope onto a substrate mounted within a gas-containing vacuum cell. Spot diameters of 3 μm were typically used for these experiments. Just before each experiment the polished sapphire substrate surface was cleaned with acetone and methanol, then dipped for 20 s in a phosphoric acid bath.

The vacuum cell consisted of a small 1.8-cm-i.d. stainless-steel cylinder (internal volume and surface area of 1 cm^3 and 7.3 cm^2, respectively) and short stainless-steel sidearms (total internal volume and surface area of 1.2 cm^3 and 12.5 cm^2, respectively) that connected the cylinder, through 1-mm-diam orifices, to the main gas-flow control valves. The cell was pumped by a liquid-nitrogen trapped diffusion pump whose base vacuum was 10^{-6} Torr. The gases that were flowed through the cell were tetraethyllead (Alfa Products electronic grade), argon (Matheson 99.998% minimum purity) and helium (Matheson 99.995% minimum purity).

For controlled-temperature experiments the substrates were mounted on a small thermoelectric cooler/heater contained entirely within the vacuum cell. Within a limited temperature range (-30 to 50 °C) this low capacity but fast-response cooler/heater was found ideal for controlling the temperature of the low-thermal-mass substrates.

The kinetics of the photoreaction were studied by measuring the decrease in optical transmission of the 257.2-nm-laser beam due to photodeposition on the substrate. This decrease was found to be dominated by optical absorption rather than scattering or diffraction. The transmission was monitored by a UV photodiode, placed just beyond the vacuum cell, that had an aperture large enough to collect all the transmitted laser light. Each transmission trace was recorded and analyzed in real time by a microcomputer, which was also used to control a stage that automatically shifted the substrate between transmission traces and to synchronize the shuttering of the laser beam with the substrate motion.

We have found that during photodeposition from TEL the transmission decreases smoothly exponentially in time, indicating that early-time nucleation effects are unimportant and that the film thickness itself increases linearly with time. In practice, all the photodeposition rates described here were deduced by measuring the time, t_0, required for transmission to reach 70% of its initial value. This corresponds to about 20 molecular layers of deposit at Gaussian beam center, or about 10 layers of photodeposition for uniform deposition and illumination. The time average rates were defined as $1/t_0$.

 0734-211X/85/051436-05$01.00

The laser intensity dependence of the photodeposition rate was measured at a pressure of a few tenths of a Torr of TEL vapor. The linear dependence observed indicated that no depletion of adsorbed TEL occurred during growth at these pressures.

The equilibrium TEL coverage on the growth surface at high ambient TEL pressure is only about one monolayer. Therefore, as the adsorbed monolayers are consumed by photodeposition, they must be continually replenished during each transmission trace. The two possible sources for this replenishment are (1) adsorption of TEL from the ambient gas or (2) surface diffusion of TEL adsorbed on the surrounding area into the 7-μm^2 photodeposition zone. For the unambiguous observation of a surface-diffusion component, we have performed nonequilibrium experiments. In these experiments the system is first equilibrated at a TEL pressure sufficient to produce monolayer coverage on the sapphire substrate. The TEL vapor is then removed so quickly that a series of transmission measurements can be made before the TEL coverage on the substrate is reduced by desorption. To obtain reproducible measurements, an inert gas (Ar) purge procedure was adopted. In this procedure, the cell was first exposed to a saturation pressure ($\sim$0.27 Torr) of TEL, and successive transmission traces were recorded until the photodeposition rate reached a steady value. Then, while continuing to record transmission traces, the TEL reservoir was shut off, and Ar was flushed through the cell. All the measurements were taken in a flow-rate-independent regime (flow rate greater than 30 scc/min).

By analogy with all inhomogeneous reactions, two kinetic regimes can be expected for low ambient pressure experiments as a function of laser intensity. At sufficiently low laser intensities, the photodeposition will be reaction limited, and will depend linearly on laser intensity. At sufficiently high laser intensities, the photodeposition will be mass transport limited, and will not depend on laser power.

The intensity dependence of the rate immediately after the start of the purge is shown in Fig. 1. The low-intensity regime of Fig. 1, where photodeposition is reaction limited, was found difficult to resolve experimentally. The sharp saturation in rate at higher laser intensities, however, indicates that after the purge has begun, in this regime, photodeposition is mass transport limited. Consequently, the magnitude of the saturated photodeposition rate is a measure of the replenishment rate of photoreacted TEL by surface diffusion.

Finally, to gain insight into the temperature dependence of the surface diffusion and desorption rates, photodeposition rates vs time after start of purge were measured at various temperatures. Examples of these measurements are shown in Fig. 2. To avoid complications due to multilayer condensation at the lower temperatures, in all cases the initial dosing of the substrates with TEL was done at room temperature. The data shown in Fig. 2 were taken at high enough laser intensities that the photodeposition rates immediately after the start of the purge were mass transport limited. There is a clear dependence on temperature of the rate of adlayer desorption during the purge.

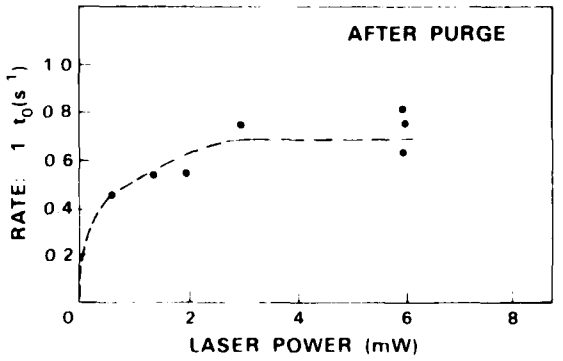

FIG. 1. Dependence of photodeposition rate $1/t_0$ on incident UV laser power immediately after start of purge. Ar flow rate was 60 scc/min.

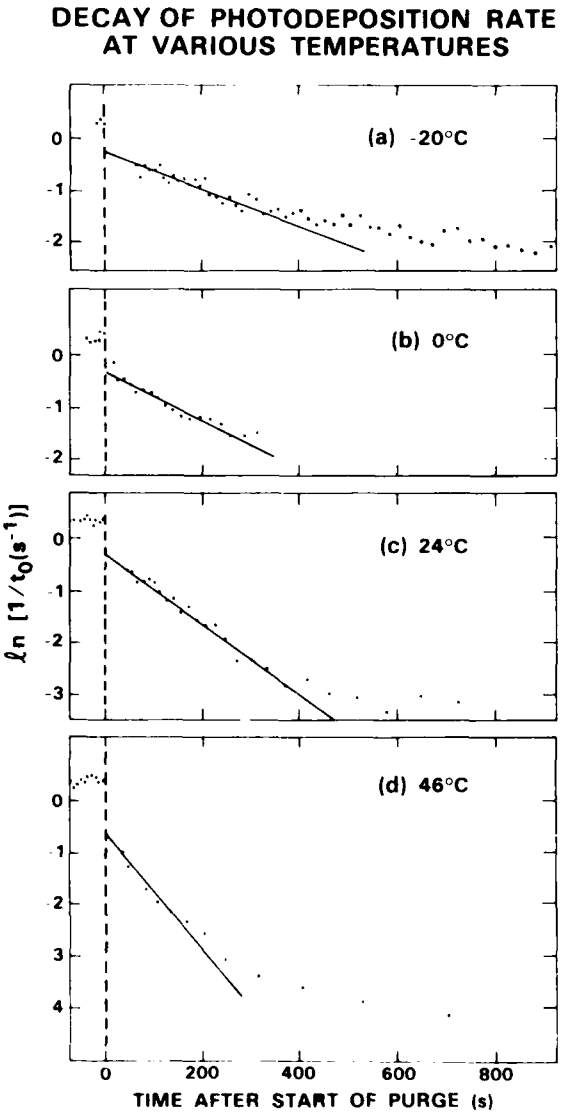

FIG. 2. Dependence of photodeposition rate $1/t_0$ on time after start of purge with flowing Ar. Substrate temperatures were (top to bottom) −20, 0, 24, and 46 °C. UV laser power incident on the surface was 0.6 mW.

III. MATHEMATICAL MODELING

In order to extract numerical estimates of parameters (particularly the surface diffusivity) from the results of Sec. II, a mathematical description of the system was formulated. In our experiment, the time evolution of the surface density is described by the partial differential equation:

$$\frac{\partial n(\mathbf{r},t)}{\partial t} = D\nabla^2 n(\mathbf{r},t) - An(\mathbf{r},t) + BP\,[n_{\max} - n(\mathbf{r},t)] - cI(\mathbf{r},t)n(\mathbf{r},t), \quad (1)$$

where $n(\mathbf{r},t)$, D, and A represent the surface density, the surface diffusivity, and the desorption rate of adsorbed parent molecules, respectively; $BP\,[n_{\max} - n(\mathbf{r},t)]$ represents a Langmuir-type adsorption term where P is the ambient pressure (assumed time independent) and $n_{\max}$ corresponds to monolayer coverage; $cI(\mathbf{r},t)$ is a photodeposition reaction rate proportional to the light intensity $I(\mathbf{r},t)$; and ∇^2 is the two-dimensional Laplacian. In this equation, we assume for tractability that D is everywhere constant, including the region of deposition.

To solve Eq. (1) we make use of a two-dimensional Green's function method. It is convenient to introduce normalized quantities, and, assuming the spatial light distribution is Gaussian and switched on at $t' = 0$ we find,

$$\mu(\rho,\tau) = e^{-\Gamma\tau} + \eta[1 - e^{-\Gamma\tau}] - \alpha\int\int_0^\tau \mu(\rho',\tau')\frac{\rho'}{(\tau-\tau')}e^{-(\rho^2+\rho'^2)/(\tau-\tau')} \times \mathscr{I}_0\left(\frac{2\rho\rho'}{\tau-\tau'}\right)e^{-\Gamma(\tau-\tau')}e^{-\beta\rho'^2}\,d\rho'\,d\tau', \quad (2)$$

where

$$\mu = n/n_0, \quad \rho = r/r_0, \quad \tau = 4Dt/r_0^2,$$
$$I(r) = I_0\exp[-\beta(r/r_0)^2] = I_0\exp(-\beta\rho^2), \quad (3)$$
$$\Gamma = \gamma r_0^2/4D = [A + BP]r_0^2/4D, \ \eta = n_{eq}/n_0$$

and

$$\alpha = cI_0 r_0^2/2D.$$

The parameters Γ and α are, respectively, the ambient-pressure-dependent rate at which surface-gas equilibration occurs, and the consumption rate by photolysis, both normalized to the surface-diffusion replenishment rate into a spot of Gaussian half-width r_0. $\gamma = A + BP$ is the equilibration rate for surface and gas phase molecules, and n_0 is the initial uniform value of n when the light is first switched on, and is not necessarily the equilibrium value, $n_{eq} = BPn_{\max}/\gamma$, at the ambient pressure. The parameter η is the ratio between the equilibrium coverage at pressure P and the actual (possibly nonequilibrium) coverage. $\mathscr{I}_0(x)$ is a modified Bessel function. For computational convenience we have introduced the geometrical scaling parameter β in Eq. (2), so that the Gaussian half-width of the beam is $r_0\beta^{-1/2}$. In all the calculations described here, we have made the choice $\beta = 4$. In the end, the parameter values extracted by comparing theory and experiment are independent of the choice of β.

In order to make a connection with the experimentally measured rates, Eq. (2) was solved in the following manner. For given values of η, α, and Γ the equation was solved for a discrete grid of ρ,ρ' for incrementally increasing values of τ. For each value of τ, a quantity $A(\rho,\tau)$ proportional to the deposited thickness at point ρ for a given illumination was computed numerically:

$$A(\rho,\tau) = \frac{\alpha}{2}\int_0^\tau \mu(\rho,\tau')d\tau'.$$

The experimental criterion for the rate $= 1/\tau_0$ is that when the illumination has been on for a time τ_0, the beam transmission $T(\tau_0)$ is 70%. But 70% transmission is known to be produced by the uniform deposition of approximately 10 monolayers of photodeposit. This leads to the definition of a transmission index:

$$\text{Index}(\tau) \equiv \frac{2\beta}{0.7}\int e^{-\beta\rho^2}\rho\exp\left[-0.036\left(\frac{n_0}{n_{\max}}\right)A(\rho,\tau)\right]d\rho. \quad (4)$$

Index(τ) was numerically calculated for each value of τ, and τ_0 was determined from the condition Index(τ_0) = 1.

IV. APPLICATION OF MODELING TO EXPERIMENTS

We first modelled experiments in which the initial coverage is a monolayer ($n_0/n_{\max} = 1$) for each transmission trace, but the ambient pressure may be different (i.e., Γ is different). We assumed that desorption is negligible on the time scale of the experiments ($\Gamma\tau_0 \ll 1$). In that case, we have for the first two terms in Eq. (2), $e^{-\Gamma\tau} + \eta[1 - e^{-\Gamma\tau}] \approx 1$. Thus, for $\Gamma\tau_0 \ll 1$, the result of an experiment with monolayer initial coverage and a nonequilibrium initial condition is the same as that given by Eq. (2) with monolayer initial coverage and the equilibrium initial condition $\eta = 1$.

We plotted values of $1/\tau_0$ as a function of the parameter α (proportional to the normalized laser intensity), for several values of Γ. The $1/\tau_0$ values were determined from Eq. (4) by the requirement that Index(τ_0) = 1, with the initial condition $(n_0/n_{\max}) = 1$. At high pressures ($\Gamma \gg 1$), the intensity dependence is linear, consistent with our data for $1/t_0$ vs light illumination before a purge. As the pressure is decreased ($\Gamma < 1$), the overall intensity dependence becomes more and more nonlinear. In the extreme case ($\Gamma \ll 1$) and at high intensities ($\alpha \gg 1$), the photodeposition rate shows a sharp saturation, consistent with the data in Fig. 1. From a comparison between the saturated value of $1/t_0$ shown in Fig. 1 and the saturated value of $1/\tau_0$ obtained for the $\Gamma \ll 1$ simulations, the magnitude of the surface diffusivity is estimated to be 3×10^{-7} cm^2/s. It should be pointed out that this is a much larger surface diffusivity than can be conveniently measured by previous techniques.

Figures 3 and 4 show the spatial profiles of the thickness of the photodeposit calculated for successive times during the photodeposition process in the low pressure regime. For the high laser intensity case ($\alpha = 25$), molecules are consumed rapidly in the vicinity of the rim of the laser spot, leading to a dip in deposition thickness near laser-beam center.

We next considered the case of purge experiments in which desorption is non-negligible between successive transmission traces, so that after the purge has begun, the initial coverage decreases. During a single transmission trace, how-

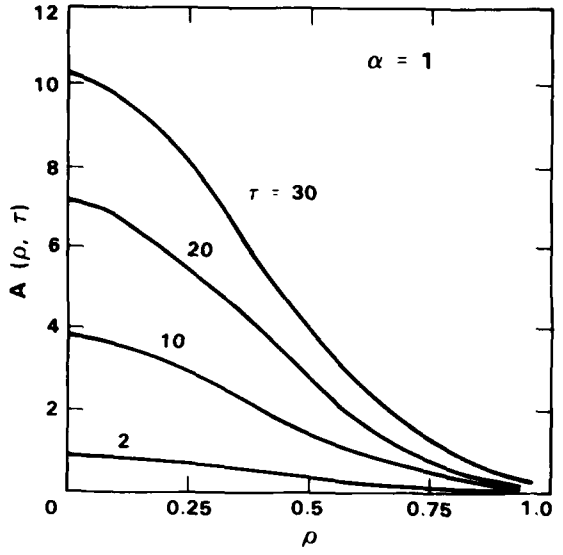

FIG. 3. Numerically calculated spatial profiles of normalized photodeposit thickness $A(\rho,\tau)$ for a photoreacting absorbed layer at a number of normalized times τ after a laser is switched on. ρ is the normalized radial distance from beam center, and the Gaussian half-width of the laser beam is at $\rho = 0.5$. The system is under low UV illumination ($\alpha = 1$).

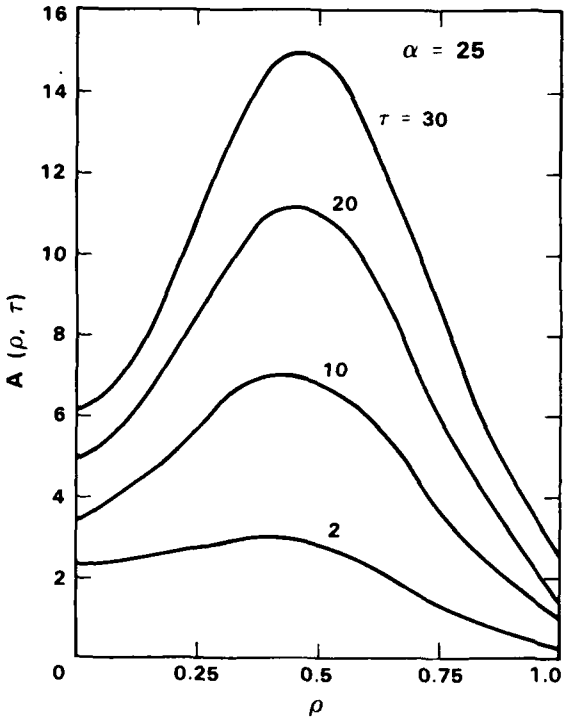

FIG. 4. Numerically calculated spatial profiles of normalized photodeposit thickness $A(\rho,\tau)$ for a photoreacting adsorbed layer at a number of normalized times τ after a laser is switched on. The system is under strong UV illumination and in the strongly diffusion limited regime ($\alpha = 25$).

ever, both adsorption and desorption are negligible ($\Gamma\tau_0 \ll 1$). For computational convenience, as in the case of monolayer coverage, we performed the equivalent calculations for $\eta = 1$.

As desorption proceeds, the coverage at a time τ_p after the beginning of the purge is given by $n_0 = n_{\max}\exp(-\Gamma\tau_p)$. Consequently, in evaluating Index(τ) during a transmission trace beginning at the time τ_p, the Index must be evaluated from Eq. (4) with $(n_0/n_{\max}) = \exp(-\Gamma\tau_p)$. Curves of $\ln(1/\tau_0)$ vs $\Gamma\tau_p$ obtained in this manner for $\Gamma \ll 1$ and a range of values of α are straight lines, consistent with the data of Fig. 2. The data in Fig. 2(c) indicate that the magnitude of the room-temperature (24 °C) desorption rate is $k_{\rm des} = 7\times10^3\ {\rm s}^{-1}$.

The temperature dependence of the desorption rate can be deduced from the rest of the data in Fig. 2, and a linear dependence of the logarithm of the decay rate on reciprocal absolute temperature is obtained, indicating that it may be fit to the classical transition state theory expression

$$k_{\rm des} = (k_{\rm attempt})\exp(-E_{\rm des}/kT), \tag{5}$$

where $k_{\rm attempt}$ and $E_{\rm des}$ are, respectively, the attempt frequency and activation energy for desorption. This fit yields values of $E_{\rm des} = 0.13$ eV and $k_{\rm attempt} = 1.3\ {\rm s}^{-1}$. Such an attempt frequency is extraordinarily low compared to the value $10^{12}\ {\rm s}^{-1}$ that is often assumed. One possibility is that the effective attempt frequency for such a large molecule is dominated by a large entropy barrier to desorption.[4] If we assume an expression of the form

$$k_{\rm des} = (k_0)\exp(S/k)\exp(E_{\rm des}/kT), \tag{6}$$

and fix $k_0 = 10^{12}\ {\rm s}^{-1}$, for $E_{\rm des} = 0.13$ eV the entropy barrier would have to be $S/k = -27$. Although such an entropy barrier is larger than any of which we are aware, it should be emphasized that measurements on the surface migration of large molecules such as TEL have heretofore been quite difficult.

V. CONCLUSION

We have investigated and carefully isolated the influence of surface transport on the kinetics of laser-beam-localized photochemistry in tetraethyl lead adsorbed on sapphire. A physical model has been numerically simulated, using an integral form of the diffusion equation, and compared to the data. The experimental technique is noteworthy in being applicable to weakly bound polyatomic molecules, which are prevalent in many technologically important surface chemical reactions.

ACKNOWLEDGMENTS

It is a pleasure to acknowledge J. H. C. Sedlacek, S. Fiorillo, B. E. Duquette, and D. J. Sullivan for technical assistance, B. J. Palm for computer simulations, P. M. Nitishin for scanning electron microscopy, and M. C. Finn for Auger spectroscopy. Special thanks are due to A. Strauss for a careful reading of the manuscript and many helpful comments and suggestions.

[a]This work was sponsored by the Department of the Air Force, in part under a specific program supported by the Air Force Office of Scientific Research, by the Defense Advanced Research Projects Agency and by the Army Research Office.

[b]Present address: Sandia National Laboratories, Albuquerque, NM 87185.

[1]G. Ehrlich and K. Stolt, Annu. Rev. Phys. Chem. **31**, 603 (1980).

[2]D. J. Ehrlich, R. M. Osgood, Jr., and T. F. Deutsch, J. Vac. Sci. Technol. **21**, 23 (1981).

[3]D. J. Ehrlich and J. Y. Tsao, J. Vac. Sci. Technol. B **1**, 969 (1983).

[4]D. A. Degras, in *Molecular Processes on Solid Surfaces*, edited by E. Drauglis, R. D. Gretz, and R. I. Jaffee (McGraw-Hill, New York, 1969), pp. 275–297.

Laser-induced selective deposition of micron-size structures on silicon

Y. S. Liu, C. P. Yakymyshyn, H. R. Philipp, H. S. Cole, and L. M. Levinson
General Electric Research and Development Center, Schenectady, New York 12301

(Received 18 March 1985; accepted 6 June 1985)

The feasibility of high speed direct writing of high resolution structures using a laser beam was demonstrated. Tungsten was selectively deposited on silicon via surface reduction reaction of tungsten hexafluoride. Fine lines of micron dimension with smooth surface morphology were fabricated using an argon laser at a writing speed of several cm per second. Compositions and structures of the micron-size lines, characterized using various microprobe analysis techniques including scanning Auger microprobe, Raman microprobe, and Rutherford microion-beam spectroscopy, are discussed.

I. INTRODUCTION

Recently, Ehrlich and Tsao reported the fabrication of submicron features sizes poly-Si lines by a pyrolytical process in $SiCl_4/H_2$ vapor using an argon laser beam.[1] Since the rate of chemical reactions depends nonlinearly upon the local temperature, the linewidth drawn was significantly narrower than the laser beam size. This result demonstrated the feasibility of writing submicron structures with a laser beam by taking the advantage of the nonreciprocity nature of the laser microchemical processing technique. The speeds for fabricating this kind of structure using this specific technique as well as other reported methods,[2,3] however, were limited to several tens to hundreds of microns per second.

In a separate work, these authors further studied the effect of geometrical scaling on chemical reaction rates in using lasers for fabricating microstructures.[4] It was shown that the reaction rate of a microchemical process induced by a focused laser beam can significantly exceed those of conventional diffusion-limited reactions for an extended heat source. The reaction rate in a heterogeneous reaction at a gas–solid interface is generally limited by the gas phase diffusion of reactants and products, and by reaction rates on the solid surface itself. The reactant flux channeled into the reaction zone increases as the dimension of the reacting area decreases to a value small compared with the gas diffusion distance due to the enhancement of mass transport via three-dimensional gas phase diffusion. In comparison, for a planar heated surface, the reaction flux at a high pressure is limited by one-dimensional gas phase diffusion. Several recent experiments have demonstrated this kind of enhanced reaction rates in laser-induced microchemical processing experiments, including laser etching of silicon in a chlorine gas[5] and the example cited above on laser-induced chemical vapor deposition of polysilicon.[1]

The purpose of the present work is to study the feasibility of high resolution direct writing at a high speed using laser-beam-induced microchemical processing.[6] In our present experiments, fine metal lines of micron dimension were selectively deposited on silicon via surface reduction of tungsten hexafluoride at room temperature using an argon laser with a focused spot size of about 20 μ. The nonlinearity exhibited by localization of heterogeneous surface reactions improved the writing resolution to a few microns, a value significantly smaller than the laser beam size.

In the following sections, we discuss the methods used for fabricating high resolution metal lines on silicon. Compositions and structures of the micron-size metal lines were characterized using various microprobe analysis techniques including scanning Auger microprobe, Raman microprobe, and Rutherford microion-beam spectroscopy. In addition, Raman spectra at 331 and 451 cm^{-1} were observed and identified, for the first time,[7] as the Raman lines from tungsten silicide formed directly by laser-induced chemical vapor deposition in a silicon and tungsten hexafluoride system.

II. EXPERIMENTAL

A. Apparatus

The experimental apparatus is shown schematically in Fig. 1. An argon laser (Spectra Physics, Model 171-08) was focused through a fused quartz window into a chemical vapor deposition reactor containing silicon samples. The focusing lens was an air-spaced three-element optics with a focal length of 20 mm. The power of the argon laser was computer controlled with a power stability better than 0.05 W over a power range varying from 3 to 10 W. The move-

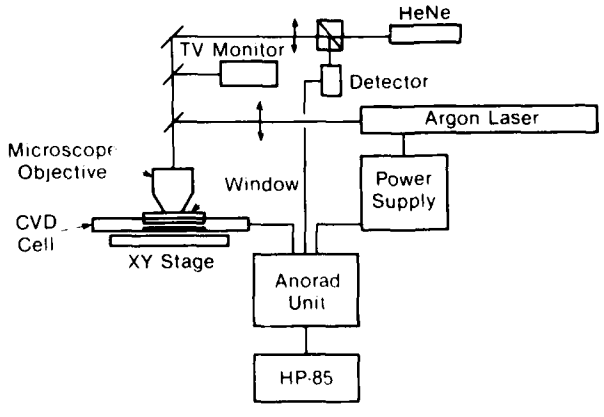

FIG. 1. A schematic of the experimental setup.

 0734-211X/85/051441-04$01.00

ment of the reaction cell, placed on top of a high resolution X–Y translational stage, was controlled by an optically encoded signal to give 1 μ resolution over the 4 in. translational distance at a traveling speed to 7 cm/s.

The reactor was baked prior to each run and was operated at room temperature during the deposition. During a typical run, a silicon sample, freshly cleaned in an HF solution to remove oxide, was immediately loaded into the reaction cell containing typical 50–100 Torr tungsten hexafluoride in 1 atm argon buffer gas.

In addition, a He–Ne laser probe beam, collimated through a 20× beam expander and propagating coaxially with the argon laser beam, was used for the beam alignment as well as for *in situ* monitoring the optical reflectivity during the deposition. The interference caused by the thin metal deposited layer provided a direct method of determining film thickness with a sensitivity to within 10 Å thickness on a silicon substrate. A silicon vidicon camera was used for process monitoring.

B. Chemical reactions

Tungsten hexafluoride and silicon systems were studied in the present experiments. Tungsten hexafluoride has been widely used as a source for tungsten deposition.[8,9] In a chemical vapor deposition (CVD) system containing only tungsten hexafluoride and silicon, tungsten is deposited by reduction of WF_6 on the silicon surface at a temperature of about 350 °C according to the following reaction:

$$2WF_6 + 3Si \rightarrow 2W + 3SiF_4. \quad (1)$$

This initial phase of the heterogeneous reduction reaction, however, is self-limiting to a tungsten thickness of 300–500 Å.[10] In a conventional thermal CVD system, hydrogen is frequently used to form thicker tungsten films by the reducing reaction

$$WF_6 + 3H_2 \rightarrow W + 6HF. \quad (2)$$

The reduction mechanism of WF_6 in the presence of hydrogen, described by Eq. (2), has been studied extensively.[11,12] The kinetics of the initial phase of surface reduction of WF_6 by silicon has been much less studied, however.

In a laser-beam-induced CVD process, the reaction typically takes place in an interaction period varying between several seconds to as short as milliseconds, determined by the scanning speed and the spot size of the laser beam. The deposition conditions would depend upon laser powers, scanning speeds, and the initial heterogeneous reduction reaction of WF_6 on the silicon surface. The present study focused only on the reaction described by Eq. (1), without the addition of hydrogen.

III. RESULTS AND DISCUSSIONS

Figure 2 shows a micrograph of typical line structures fabricated under three different laser power levels. The scanning speeds were held at a constant value of about 5 cm/s. The surface morphology of deposited tungsten was sensitive

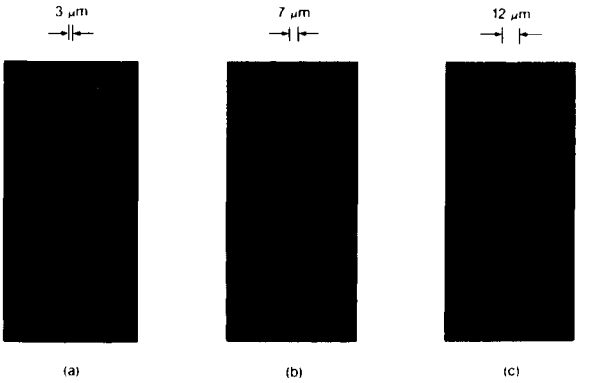

FIG. 2. Optical micrographs of typical line structures deposited under three different power levels: (a) 3 W, (b) 6 W, and (c) 9 W. The scanning speeds were about 7 cm/s.

to both laser power and to scanning speed. In these experiments, the samples were scanned at a speed to 7 cm/s and the reaction chamber contained 50 Torr tungsten hexafluoride in 1 atm argon buffer gas. The minimum linewidths observed were about 1 μ and were obtained using a 20 mm focal length lens. It is noted that, in comparison, high resolution lines reported by previous workers[1,4] were fabricated under an experimental condition in which much tighter focusing optics had to be used.

The deposition of tungsten in a WF_6–Si system is induced by reducing WF_6 on a silicon surface, and therefore is surface selective. This is demonstrated in Fig. 3 in which a silicon sample, first grown 2000 Å thermal oxide, was then patterned using a standard lithography method to remove oxide in certain areas. The sample was then placed inside the reaction cell and exposed to the argon laser beam in the presence of WF_6. The deposition of tungsten took place selectively on those areas exposed to the silicon surface, as shown in the figure. This kind of surface sensitive deposition is a very useful property for self-aligned metal deposition using lasers or other thermal deposition techniques.

The composition of the deposited lines was analyzed using Rutherford backscattering spectroscopy. The spectrometer was equipped with a 2 MeV focused He-ion source having a spatial resolution of about 1 μ. Figure 4 shows a typical spectrum when the microion beam was focused to an area near the center of a 10 μ deposited metal line, shown in the top photo of Fig. 4. Backscattered tungsten signals were also detected in the areas near the line edges, but reduced significantly in the regions beyond it.

The film thickness was estimated to be about 200 Å by monitoring the optical reflectivity during the deposition using a He–Ne laser probe beam. The reflectivity of thin tungsten films on silicon is thickness dependent due to interference effects between the tungsten–silicon interface. Using the known optical constants of tungten and silicon[13] at 632.8 nm, the reflectivity of 200 Å of tungsten on silicon is computed to be 0.59 compared to bare silicon surface of 0.36. The optical reflectivity measurement provides a direct *in situ* method for measuring the metal deposition rate, and thus enables one to measure rate constants for deposition. The technique is sensitive enough for resolving a tungsten film of

about 10 Å thickness on silicon.

The lateral distribution of tungsten across the laser-written lines was analyzed using a scanning Auger microprobe. The 5 keV electron beam with a spatial resolution less than 0.1 μ was scanned across a fabricated line. The linewidth measured from an optical microscope was 12 μ. The Auger signals from Si (92 eV) and W (169 eV) were detected, and results are shown in Fig. 5 (a) and (b), respectively. The tungsten distribution, as shown in the top curve, extends on both sides beyond the 12 μ linewidth, determined from the micrograph. Within the boundary of the line structure, however, the scanning Auger microprobe shows a depletion of tungsten. An analysis of silicon distribution shows no detectable silicon within a region of about 36 μ; outside this region, silicon Auger signals from the substrate were detected. Frequently, a sharp silicon signal, with a lateral width typically of 1–2 μ was observed at the center of the region where tungsten Auger signal was depleted.

One of the possible reasons for causing the depletion of tungsten in the center portion of the deposited lines was the formation of silicide.[14] Another possible reason would be the dissolution of silicon in tungsten. The search for a resolution of these identifications led us to the Raman microprobe examination of the deposited material. Previously, Raman scattering has been employed as a useful tool for surface structural analyses, and for detecting the formation and stoichiometric ratio of thermally produced silicides.[15,16] More recent work using Raman scattering has further indicated the technique is sensitive for identifying a PtSi thin film as thin as 10 Å.[17] Consequently, the Raman microprobe technique was ideally suitable for analyzing the structural information of thin metal structures of micron dimension.

Initially, a Raman spectrum of a large thermally annealed tungsten film on silicon was obtained as a reference spectrum since such a spectrum could not be found in the literature. The reference sample was prepared by a chemical vapor deposition of tungsten silicide from a tungsten hexafluoride and silane gas mixture. The resulting 0.2 μ tungsten film on silicon was annealed at 900 °C for 5 min prior to analysis. Rutherford backscattering spectroscopy and Auger analysis of the resulting sample showed the material to have the stoichiometric ratio of $WSi_{2.3}$. The sample was also examined by x-ray diffraction. The diffraction pat-

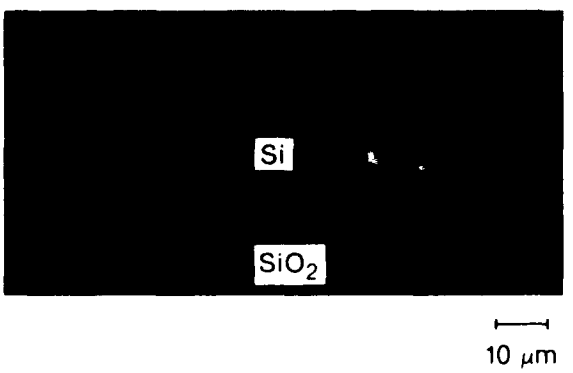

FIG. 3. Selective deposition of tungsten on a silicon surface patterned with oxide.

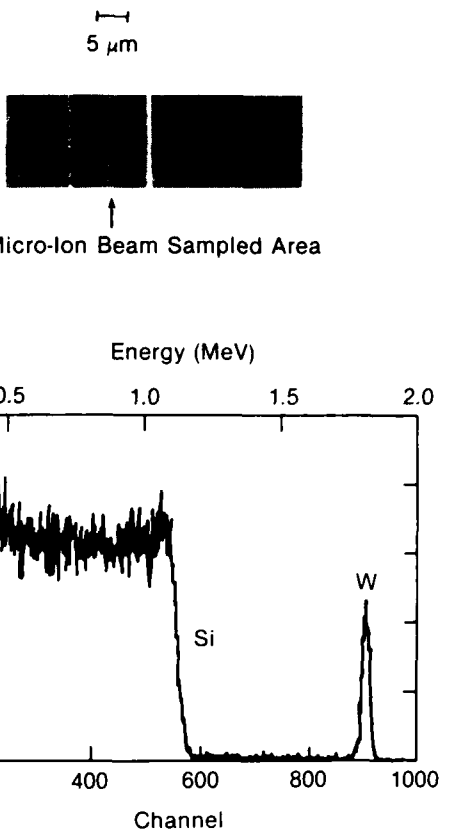

FIG. 4. Rutherford microion beam backscattering spectra from an area near the center portion of a 12 μ line deposited. The resolution of the focused ion beam (2 MeV He ion) was about 1 μ.

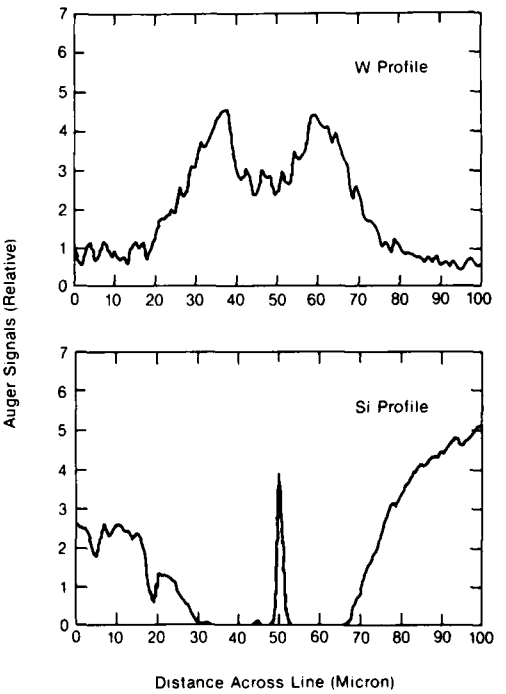

FIG. 5. The Auger signals from tungsten (top) and silicon (bottom) measured with a scanning Auger microprobe. The W (169 eV) and Si (92 eV) were measured when the electron beam was scanned across a 12 μ line structure fabricated. The electron beam had a spatial resolution less than 0.1 μ.

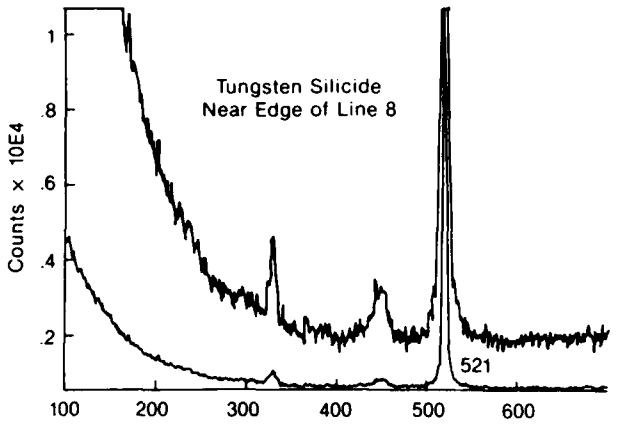

FIG. 6. The Raman signals observed when the probe beam was focused onto the center portion of a deposited line. Raman peaks at 331 and 451 cm^{-1} were identified as those from tungsten silicide. (Top trace was shown at 10× sensitivity.)

tern was found to correspond to the published data for WSi_2, thus establishing the sample used as the reference for the Raman analysis.

Raman spectra of the sample were taken on a Raman microprobe double-grating spectrometer (Ramanor U-1000, Instruments SA, Inc., Metuchen, New Jersey). The excitation argon laser at 514.5 nm was focused onto a spot about 1 μ through a microscope objective. Two peaks at 331 and 451 cm^{-1} were observed from an area near the center of the deposited line, as shown in Fig. 6. The sharp strong peak at 521 cm^{-1} was the Raman line from crystalline silicon. The Raman spectra taken were identical to those measured for the reference tungsten silicide sample which showed strong Raman peaks at 331 and 451 cm^{-1}. Much weaker signals at 520 cm^{-1}, due to silicon, were detected from the reference sample in which the depth of the silicide layer is sufficiently thick to block any Raman signals from the substrate. From these measurements, we concluded from the observed Raman microprobe analysis that the material of the deposited lines was tungsten silicide. No tungsten silicide Raman signals were observed from those regions outside the deposited lines. A detailed discussion on the Raman measurement was presented in Ref. 7.

IV. SUMMARY

In this paper, we demonstrated the feasibility of high speed writing of high resolution metal lines using a laser beam. Micron-size lines were obtained at a speed of several cm per second in a laser-beam-induced chemical vapor deposition system containing silicon and tungsten hexafluoride. In this approach, the heterogeneous surface reduction reaction of WF_6 by silicon was employed and gave a high writing speed. Results of several microprobe analyses, including Rutherford microion-beam backscattering spectroscopy, Raman microprobe analysis, and Auger microprobe spectroscopy, were discussed and characterization of surface morphology, compositions, and structures of the fine structures were presented in this paper.

ACKNOWLEDGMENTS

The authors wish to thank Dr. M. Burrell for performing excellent Auger analyses, and Dr. W. G. Morris and Prof. H. Bakhru for making the Rutherford microion-beam facility at the State University of New York at Albany, New York, available for the present experiments. Mr. R. Guida and Mr. P. Gallo's excellent technical assistance are also acknowledged.

[1] D. J. Ehrlich and J. Y. Tsao, Appl. Phys. Lett. **44**, 267 (1984).
[2] I. P. Herman, R. A. Hyde, B. M. McWilliams, A. H. Weisberg, and L. L. Wood, in *Laser Diagnostics and Photochemical Processing for Semiconductor Devices*, edited by R. M. Osgood, S. R. J. Brueck, and H. R. Schlossberg (North–Holland, Elsevier, New York, 1983), p. 9.
[3] D. Bauerle, in *Laser Diagnostics and Photochemical Processing for Semiconductor Devices*, edited by R. M. Osgood, S. R. J. Brueck, and H. R. Schlossberg (North–Holland, Elsevier, New York, 1983), p. 19.
[4] D. J. Ehrlich and J. Y. Tsao, in *Laser Diagnostics and Photochemical Processing for Semiconductor Devices*, edited by R. M. Osgood, S. R. J. Brueck, and H. R. Schlossberg (North–Holland, Elsevier, New York, 1983), p. 1.
[5] D. J. Ehrlich, R. M. Osgood, Jr., and T. F. Deutsch, Appl. Phys. Lett. **38**, 946 (1981).
[6] Y. S. Liu, C. P. Yakymyshyn, H. R. Philipp, H. S. Cole, and L. M. Levinson, in *Proceedings of the Laser Chemical Processing of Semiconductors*, edited by F. A. Houle, T. F. Deutsch, and R. M. Osgood (Materials Research Society, Pittsburgh, Pennsylvania, 1984), p. 73.
[7] P. J. Codella, Fran Adar, and Y. S. Liu, Appl. Phys. Lett. **46**, 1076 (1985).
[8] E. K. Broadbent and C. L. Ramiller, J. Electrochem. Soc. **131**, 1427 (1984).
[9] T. Moriya, S. Shima, Y. Hazuki, M. Chiba, and M. Kashiwagi, IEDM Tech. Dig. **1983**, 550.
[10] C. M. Melliar-Smith, A. C. Adams, R. H. Kaiser, and R. A. Kushner, J. Electrochem. Soc. **121**, 298 (1974).
[11] J. F. Berkeley, A. Brenner, and W. E. Reid, J. Electrochem. Soc. **114**, 701 (1967).
[12] W. A. Bryant, J. Electrochem. Soc. **125**, 1534 (1978).
[13] H. R. Phillip, J. Appl. Phys. **43**, 2835 (1972).
[14] S. P. Murarka, *Silicides for VLSI Applications* (Academic, New York, 1983).
[15] R. J. Nemanich, C. C. Tsai, and G. A. N. Connell, Phys. Rev. Lett. **44**, 273 (1980).
[16] R. J. Nemanich, M. J. Thompson, W. B. Jackson, C. C. Tsai, and B. L. Stafford, J. Vac. Sci. Technol. B **1**, 519 (1983).
[17] J. C. Tsang, Y. Tokota, R. Matz, and G. Rubloff, Appl. Phys. Lett. **44**, 4[illegible] (1984).

Characterization of photochemical processing

M. Hirose, S. Yokoyama, and Y. Yamakage
Department of Electrical Engineering, Hiroshima University, Higashihiroshima 724, Japan

(Received 18 March 1985; accepted 21 May 1985)

Thermally grown SiO_2 and crystalline GaAs surfaces exposed to an etching gas under an ArF excimer laser irradiation have been studied by *in situ* x-ray photoelectron spectroscopy (XPS). Reaction kinetics of photochemical etching and resulting products on the solid surfaces have been revealed from the chemical shifts of adsorbates and substrate atoms. Etching products in SiO_2/($NF_3 + H_2$) system are confirmed to be SiF_4, N_2O, and NO_2. For the etching of GaAs in HCl, $GaCl_3$ and $AsCl_3$ are found to be the most probable products in the gas phase.

I. INTRODUCTION

Recent progress in fabrication technology of submicron devices for very large scale integrated (VLSI) circuits is really remarkable and 4 Mbit dynamic random access memory (dRAM) will be realized in the near future. Beyond 4 Mbit dRAM, VLSI technology must encounter such a problem as ion bombardment damage of the active region of devices arising from the use of reactive plasmas, necessity of low-temperature oxidation, and demand to low-temperature doping. This implies that future VLSI technology needs some innovative processes to achieve silent chemical reactions at low temperature for etching, chemical vapor deposition (CVD), oxidation, and doping. In this sense photochemical process would be the most important candidate as a next generation VLSI fabrication technology.[1] Extensive studies on the photochemical etching of Si and SiO_2 have been carried out so far in several research groups and the reaction mechanism involved in the photoprocessing has been discussed.[2] For the purpose of wider applications of photochemical processing for VLSI, deep understanding of the reaction kinetics on the solid surface would be necessary. A possible approach to reveal the gas-solid interactions under laser irradiation is to employ *in situ* x-ray photoelectron spectroscopy (XPS),[3,4] which provides us with novel information on the chemical bonding features of the reacting surface.

In this paper, the reaction mechanism of laser-induced etching of SiO_2 in $NF_3 + H_2$ is discussed based on *in situ* XPS analysis. The similar method is also applied to the GaAs/HCl system. The result has clarified the time-dependent adsorbate-surface interactions during the course of photochemical etching.

II. EXPERIMENTAL

An ArF excimer laser light (193 nm in wavelength) from Lambda Physik EMG 103E with a pulse energy of 47 mJ/shot was irradiated at a repetition rate of 80 Hz onto a Si wafer covered with thermally grown SiO_2 with thicknesses of 10–300 nm or onto a 0.3-mm-thick quartz sheet in an NF_3 gas containing 0–4 mol % hydrogen. NF_3 gas has currently been used in the plasma etching of Si and SiO_2. A mixture of $H_2 + CF_4$ has also been employed for improving the etching selectivity of SiO_2 with respect to Si.[5,6] The etching rate of SiO_2 is significantly enhanced with increasing the hydrogen partial pressure and the SiO_2 etching rate becomes five times larger than Si. Without adding H_2, Si is etched faster than SiO_2. The absorption coefficient of NF_3 gas was measured to determine the optical absorption cross section σ at 193 nm irradiation as shown in Fig. 1. The result yields a value of $\sigma = 5.3 \times 10^{-21}$ cm^2. The oxide thickness on Si at each etching step was measured by the infrared absorption intensity of the Si-O stretching mode at 1060 cm^{-1} as well as by the multibeam interferometry. The x-ray photoelectron spectra of the phototreated SiO_2 were taken by using Shimadzu ESCA750H spectrometer, in which the specimen in the reaction chamber can be transferred to the ultrahigh vacuum (UHV) XPS chamber through the two gate valves immediately after the etching. The details of the equipment have been reported elsewhere.[4] The *in situ* infrared absorption spectra of the etching gas in the reaction chamber were also measured to identify the etching products in the gas phase.

As for GaAs etching, basically the same experimental technique as in the case of SiO_2 etching was used. *p*-type GaAs (100) crystal with a resistivity of 7.2×10^{-3} Ω cm has been etched in 5% HCl diluted with He at a temperature of 20 or 200 °C. The average etching rate was 23 nm/min at a laser power of 30–40 mJ/shot with a repetition frequency of 80 Hz.

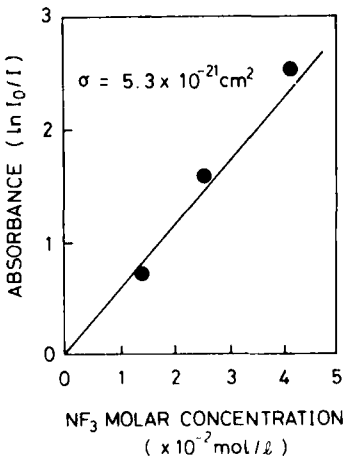

FIG. 1. Optical absorbance of NF_3 gas as a function of the molar concentration. I_0 and I refer to the incident laser light intensity and the transmitted intensity, respectively.

 0734-211X/85/051445-05$01.00

III. RESULTS AND DISCUSSION

A. SiO_2 etching

The etching rate of SiO_2 was measured for various configurations between incident laser beam and SiO_2 surface. Almost comparable etching rates were obtained for the normal and parallel incidence of laser beam to the sample surface. Also the measured etching rate is proportional to NF_3 gas pressure. Therefore, the etching rate is primarily controlled by the amount of reactive species created in the gas phase, in consistence with the result of Fig. 1 where a higher NF_3 concentration provides a larger amount of photodissociated radicals. It is found that when the SiO_2 surface is exposed to $NF_3 + H_2$ at low pressure ($NF_3 = 480$ Pa, $H_2 = 20$ Pa) for 60 s under laser irradiation, followed by photoprocessing at atmospheric pressure ($NF_3 = 9.8\times10^4$ Pa, $H_2 = 2.6\times10^3$ Pa), the photochemical etching reaction of SiO_2 promptly starts to proceed as shown in Fig. 2(a) where a Si(2*p*) signal from SiO_2 (~ 103.6 eV) becomes smaller with etching time. Contrary to this, without preirradiation at the low pressure the incubation time of more than 120 s is necessary for initiating the etching. In fact, as shown in Fig. 2 (b), Si(2*p*) signal intensity at 103.6 eV remains unchanged and no N(1*s*) signal is observed. Very small F(1*s*) peaks appear, but the intensity is hardly changed by laser irradiation. It is likely that in simple atmospheric pressure etching the reactive species on SiO_2 are frequently deexcited by the impinging flux of NF_3 and H_2 molecules and it takes a longer time to chemically activate the SiO_2 surface. Since the reaction system is static in the present experiment, the number of reactive species in the gas phase is accumulated with etching time and finally etching reactions take place irrespective of the low pressure pretreatment of the SiO_2 surface. The above interpretation is verified by the further examination of the XPS spectra of Si(2*p*), N(1*s*), and F(1*s*) signals from the phototreated SiO_2 surface. As illustrated in Fig. 2(a), the peak heights of N(1*s*) and F(1*s*) XPS signals arising from adsorbed nitrogen and fluorine radicals on SiO_2 are rapidly increased by the irradiation at low pressure (500 Pa in $NF_3 + H_2$), while under the irradiation at atmospheric pressure without low pressure preirradiation N(1*s*) signal does not appear even after the incubation time of more than 120 s [see Fig. 2(b)]. Very weak F(1*s*) peaks may originate in the adsorbed fluorine radicals on SiO_2 surface. Therefore it is suggested that laser irradiation in low pressure $NF_3 + H_2$ chemically activates the SiO_2 surface by the presence of reactive adsorbates such as nitrogen and fluorine radicals and the simple atmospheric pressure phototreatment deexcites the SiO_2 surface rather than chemically activates. Figure 2(a) also indicates that Si(2*p*) signal intensity from the SiO_2 layer (~ 103.6 eV) is progressively decreased through etching reaction and after the total phototreatment time of 150 s including low and atmospheric pressure processes, the residual oxide thickness is estimated to be about 1.5 nm from the XPS intensity ratio of Si(2*p*) in SiO_2 (~ 103.6 eV) to Si(2*p*) in the Si substrate (99.3 eV).[7] Initial oxide thickness was about 100 Å.

In order to assign the molecular structure of the etching surface, chemical shifts of Si(2*p*), F(1*s*), and N(1*s*) signals in Fig. 3 are examined based on the partial atomic charge model.[8] Regarding the chemical bonding between Si and F, measured and estimated chemical shifts of Si(2*p*) XPS signal are plotted against the electronegativity sum of O_mSiF_n molecules in Fig. 4, where the chemical shifts of Si(2*p*) for an adsorbed SiF_4 molecules is measured by Chuang,[8] and *m* and *n* denote the number of the nearest neighbor oxygen and fluorine bonds, respectively. Of course $m + n = 4$ must hold for satisfying the fourfold coordination of the silicon atom. Final chemical shift of Si(2*p*) in the present case is 0.8 eV (see Fig. 3), and the final position of the shifted Si(2*p*) peak in Fig. 4 is located at the middle of the peak energies corresponding to O_2SiF_2 and $OSiF_3$ molecules. If one assumes the equiva-

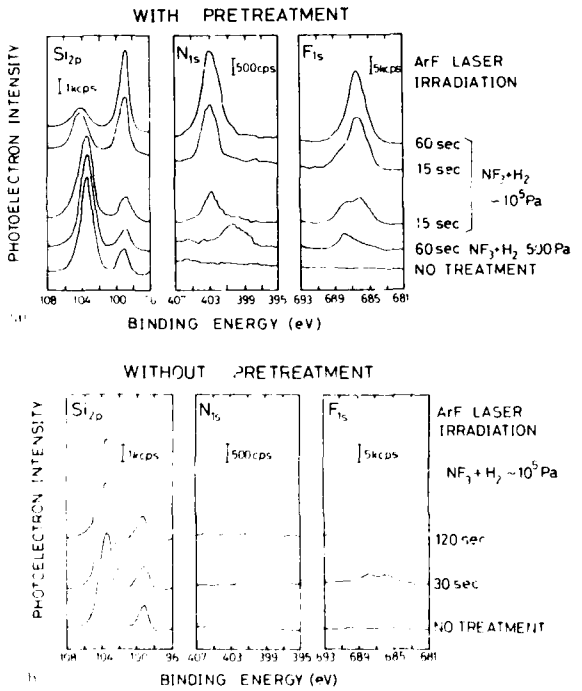

FIG. 2. (a) XPS spectra for Si(2*p*), N(1*s*), and F(1*s*) on SiO_2 surface photoprocessed in low pressure $NF_3 + H_2$ (500 Pa) for 60 s and subsequently in atmospheric pressure for 15 + 15 + 60 s. (b) XPS spectra of photoprocessed SiO_2 under the laser irradiation in atmospheric $NF_3 + H_2$ without low pressure (500 Pa) phototreatment.

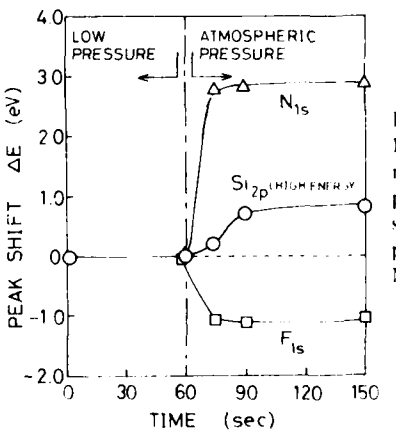

FIG. 3. Chemical shift of N(1*s*), Si(2*p*), and F(1*s*) signals during the course of pretreatment at low pressure and subsequent photoprocessing in atmospheric $NF_3 + H_2$.

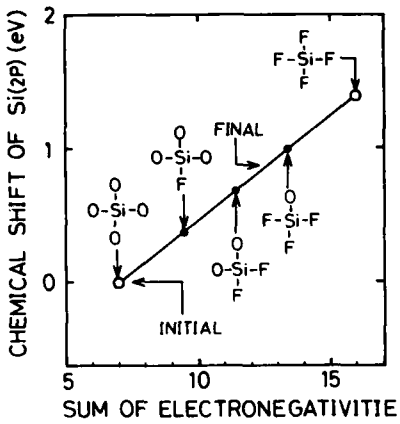

FIG. 4. Measured (open circle) and estimated (solid circle) chemical shifts of Si(2*p*) in O_m SiF_n molecules plotted against the electronegativity sum of the respective molecules.

lent coverage of O_2SiF_2 and $OSiF_3$ molecules on the etched surface layer, the Si(2*p*) XPS spectrum must exhibit a peak energy at the middle of the two peak energies for O_2SiF_2 and $OSiF_3$. The final product of the Si compound produced on SiO_2 is therefore thought to be volatile SiF_4. The chemical shift of F(1*s*) in Fig. 3 is consistent with the O_m SiF_n molecule formation because in the Si–F bond the fluorine atom has a partial negative charge with respect to silicon as a consequence of a larger electronegativity of F than that of Si.

As for nitrogen bonding, if there exist the surface NO bonds, the electron cloud of nitrogen moves to oxygen due to the smaller electronegativity of N than that of O, and hence the N(1*s*) signal shifts toward higher energy, being compatible with the result of Fig. 3. As shown in Fig. 5, adsorbed NO_2 and NO molecules on Ni exhibit similar XPS spectra[9] and the peak position of the N(1*s*) signal at 403 eV agrees well with the N(1*s*) peak on the etching surface. This suggests that NO and/or NO_2 bonds exist on the etched SiO_2 surface.

From the above result it is likely that the SiO_2 surface reacts with nitrogen and fluorine to form O_2SiF_2, $OSiF_3$, and NO and/or NO_2 molecular bonds. Therefore, the etching products such as SiF_4, N_2O, and NO_2 are inferred to desorb from the SiO_2 surface. This idea has been tested by infrared absorption measurements of the etching gas during the excimer laser irradiation. The gas cell consists of the Si IR windows and a stainless steel reaction chamber. The sample cell was filled with the etching gas. The excimer laser was irradiated onto the oxidized Si in the cell and the reference cell was evacuated. As shown in Fig. 6, the excimer laser irradiation induces new absorption peaks assigned as the stretching mode of N_2O and NO_2 at 2220 cm^{-1}, the stretching mode of NO_2 at 1620 cm^{-1} as well as the bending mode of SiF_4 at about 400 cm^{-1}. The stretching mode of SiF_4 appearing at 1010 cm^{-1} is not observable in Fig. 6 because of strong absorption of NF_3 gas, but clearly detected when the gas cell is pumped down to 500 Pa. Infrared absorption arising from the HF molecule could not be detected possibly due to its small IR sensitivity, but it is likely that HF molecules are produced in the etching system because of the high reactivity between NF_3 and H_2. Consequently, photochemical etching in $(NF_3 + H_2)/SiO_2$ system is inferred to occur through the following reaction:

$$SiO_2 + NF_3 + H_2 \xrightarrow{h\nu} SiF_4 + NO_2 + N_2O + HF. \quad (1)$$

Figures 7(a) and 7(b) are the cross-sectional view of the etched patterns of SiO_2 and Si, respectively. In SiO_2 etching by the use of Al multiple stripe pattern mask, reactive species isotropically attack the surface, resulting in the undercut below the mask. Contrary to this, anisotropic etching is accomplished in the case of Si crystal under similar etching conditions. In Fig. 7(b) the bright line is observable on the sidewall as well as on the bottom surface because there is a thin compound layer composed of Si, O, N, F, and C among which carbon might come from the reactor wall. The thin deposit can protect the sidewall from the etching species, while the deposit on the bottom surface does not act as a protective layer against etching species possibly because the normal incidence of laser light onto the surface enhances the diffusion of reactive species through the deposit. Roughness of the etched SiO_2 surface may be partly due to residual adsorbed water on the virgin surface which causes rapid reaction between HF and SiO_2.

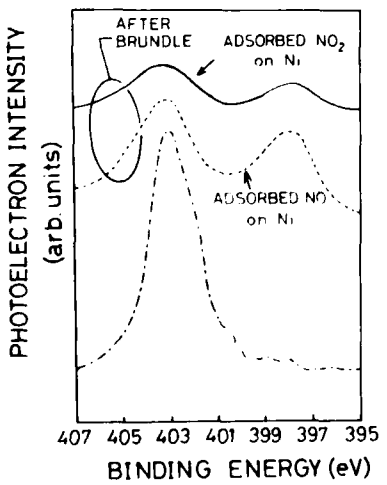

FIG. 5. Comparison of Si(2*p*) XPS spectra for N_2O and NO on Ni (Ref. 9) with the spectra for photochemically etched SiO_2 surface.

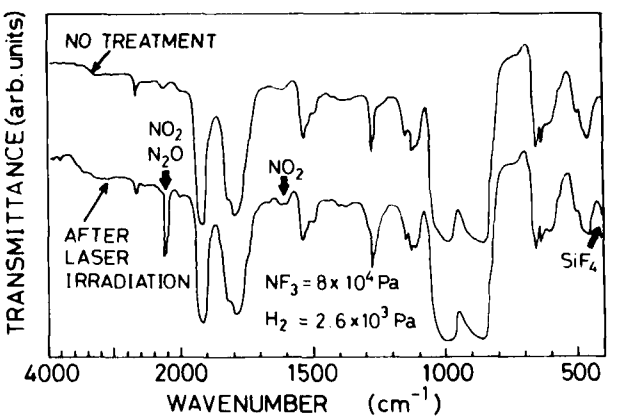

FIG. 6. Infrared absorption spectra of the etching gas ($NF_3 + H_2$) with and without laser irradiation.

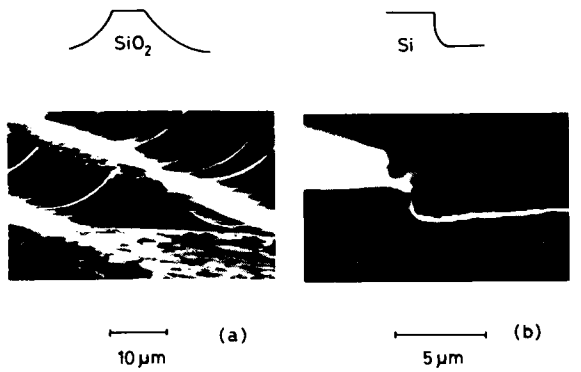

FIG. 7. Scanning electron micrograph (SEM) of photochemically etched (a) SiO_2 (quartz sheet) and (b) crystalline Si (100) using Al multistripe pattern.

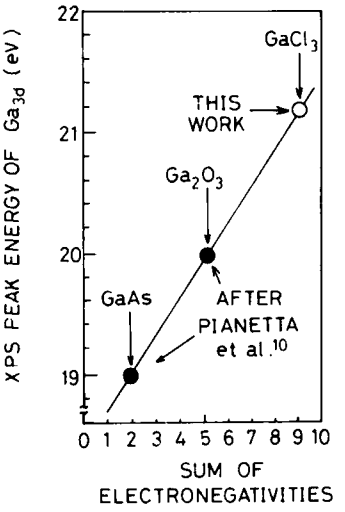

FIG. 9. Ga($3d$) XPS peak energy plotted as a function of electronegativity sum. Solid circles are experimentally determined. Peak energy of Ga($3d$) in $GaCl_3$ is estimated from sum of electronegativities.

B. GaAs etching

Figure 8 shows the typical XPS spectra taken for GaAs photochemically etched in HCl. In this case the substrate temperature was held near room temperature. A Ga($3d$) signal at 19.0 eV from the virgin surface originates in Ga in GaAs and the Ga($3d$) peak at 20.0 eV could be identified as a Ga_2O_3 compound.[10] The As($3d$) spectra are composed of a peak at 40.8 eV due to As in GaAs and at 44.0 eV arising from As in As_2O_3.[10] By exposing the GaAs surface to HCl under laser irradiation a new Ga($3d$) peak at 21.2 eV appears, being assigned as $GaCl_3$ by extrapolating a plot of the chemical shift vs electronegativity sum as shown in Fig. 9. Also, intense Cl($2p$) peaks at 199.5 eV ($j = 3/2$) and 200 eV ($j = 1/2$) are observed. An appreciable pileup of $GaCl_3$ adlayer on GaAs results in disappearance of As($3d$) signal. Since the integrated intensity ratio of Cl($2p$) to Ga($3d$) is about 2 : 1 and the escape depth of the Cl($2p$) photoelectron is smaller than that of Ga($3d$), the GaAs surface is thought to be covered with $GaCl_3$, whose thickness exceeds the escape depth of As($3d$) photoelectron. It is likely that the reaction products such as $GaCl_3$ remain on the etching surface due to the low vapor pressure, and probably created $AsCl_3$ easily evaporates from the surface because of the high vapor pressure. Formation of AsH_3 is less likely, because the bonding energy of H–H (104.2 kcal/mol) is significantly larger than that of As–H (58.6 kcal/mol) and H radicals recombine with each other to form H_2 molecules.

When a GaAs substrate is heated up to 200 °C, drastic change in the XPS spectra is observed as illustrated in Fig. 10. Now, no photoelectron signal from Cl($2p$) is observed and the Ga($3d$) peak arising from $GaCl_3$ is also absent, because the vapor pressure of $GaCl_3$ at 200 °C exceeds 1.01×10^5 Pa. Simple exposure of a GaAs virgin surface to HCl without laser irradiation causes a little increase in Ga($3d$) and As($3d$) signal intensities from GaAs. Excimer laser irradiation of more than 10 shots almost eliminates the Ga_2O_3 signal as well as As_2O_3,[11] indicating the efficient removal of the native oxide on GaAs as a consequence of photochemical etching. A little higher XPS peak energies assigned for Ga($3d$) and As($3d$) in Fig. 10 compared to those in

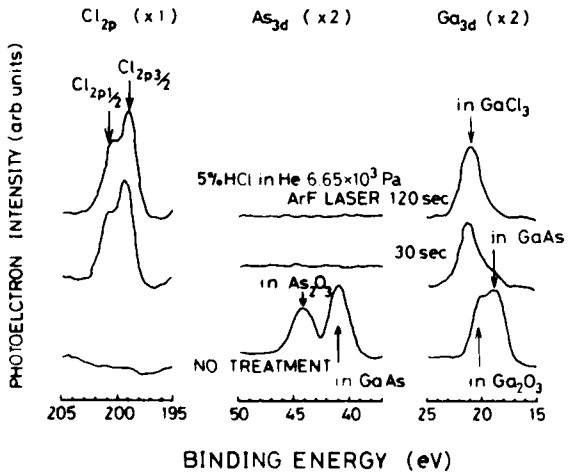

FIG. 8. XPS spectra of GaAs surface photochemically etched in 5% HCl with He at a pressure of 6.65×10^3 Pa.

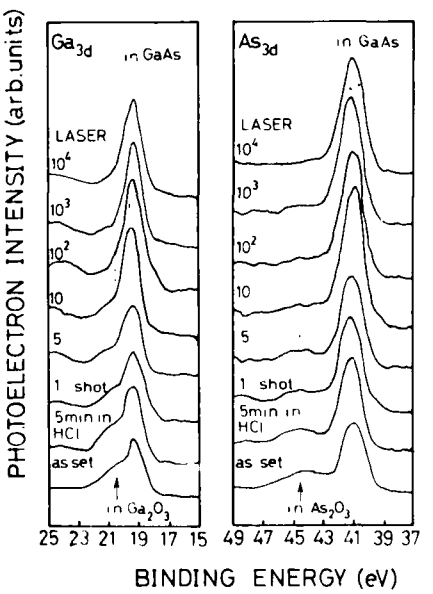

FIG. 10. 10 XPS spectra of photochemically etched GaAs surface at each step of laser irradiation. The substrate temperature is 200 °C. Gas pressure is 1.33×10^3 Pa.

Fig. 8 may be partly due to difference in the positions of the surface Fermi level of specimens held at different temperatures. From the above discussion, photochemical etching of GaAs is considered to proceed as follows:

$$GaAs + HCl \xrightarrow{h\nu} GaCl_3 + AsCl_3 + H_2. \quad (2)$$

IV. CONCLUSION

Reaction kinetics of photochemical etching and resulting products on the semiconductor surface have been revealed by *in situ* XPS measurements. In SiO_2 etching, major etching products emitted into the gas phase from the SiO_2 surface are also determined by combining the XPS data with the infrared absorption measurements of the etching gas. In GaAs etching main etching products are suggested from the XPS spectra depending on the substrate temperature. It is demonstrated that the XPS study is one of the powerful tools for diagnostics of photochemical processing.

[1]D. J. Ehrlich and J. Y. Tsao, *VLSI Electronics: Microstructure Science* (Academic, New York, 1983), Vol. 7, p. 129.
[2]T. J. Chuang, *Surface Science Reports*, (North-Holland, Amsterdam, 1983), Vol. 3, p. 1.
[3]C. R. Brundle, J. Vac. Sci. Technol. **13,** 301 (1976).
[4]S. Yokoyama, Y. Yamakage, and M. Hirose, in *Extended Abstracts of the 16th International Conference on Solid State Devices and Materials* (The Japan Society of Applied Physics, Kobe, Japan, 1984), p. 451.
[5]S. Nakayama, K. Tsuneto, A. Tasaka, T. Ohachi, D. Naito, and I. Taniguchi, in *Proceedings of the Second Symposium on Dry Processes* (The Institute of Electrical Engineers of Japan, Tokyo, 1980), p.115.
[6]R. A. H. Heinecke, Solid State Electron. **18,** 1146 (1975).
[7]S. I. Raider and R. Flitsch, IBM J. Res. Dev. **22,** 294 (1978).
[8]T. J. Chuang, J. Appl. Phys. **51,** 2614 (1980).
[9]C. R. Brundle, J. Vac. Sci. Technol. **13,** 301 (1976).
[10]P. Pianetta, I. Lindau, C. M. Garner, and W. E. Spicer, Phys. Rev. B **18,** 2792 (1978).
[11]P. A. Breeze, H. L. Hartnagel, and P. M. A. Sherwood, J. Electrochem. Soc. **127,** 454 (1980).

Photo-metal organic vapor phase epitaxy: A low temperature method for the growth of $Cd_xHg_{1-x}Te$

S. J. C. Irvine, J. Giess, J. B. Mullin, G. W. Blackmore, and O. D. Dosser
Royal Signals and Radar Establishment, St. Andrews Road, Malvern, Worcestershire WR14 3PS, United Kingdom

(Received 15 February 1985; accepted 23 April 1985)

A new epitaxial growth technique, photo-metal organic vapor phase epitaxy (photo-MOVPE), is described for the growth of $Cd_xHg_{1-x}Te$ (CMT). Ultraviolet radiation is used to decompose the metal-organics, diethyl-telluride (Et_2Te) and dimethyl-cadmium (Me_2Cd) on the substrate surface. Epitaxial HgTe can be grown at relatively low temperatures (200–300 °C) by a surface photosensitization reaction. However, the growth of CMT is only epitaxial if an inert carrier gas (He) is used instead of H_2. These results are described in terms of suppression of vapor phase nucleation while allowing surface nucleation to occur. Vapor phase nucleation results in the deposition of fine particles of CMT and can totally disrupt epitaxial growth. The growth rate dependence of CMT on CdTe substrate orientation is considered and compared with HgTe growth rates on the same orientations. These results show that surface kinetics can dominate the growth process, making it insensitive to vapor concentrations. Secondary ion mass spectrometry (SIMS) profiles through a CMT layer, grown at 250 °C, for the major elements, Cd, Hg, and Te, show an abrupt interface between the substrate and layer of less than 400 Å. Carbon impurity profiles through HgTe layers show that using the inert gas, carbon incorporation is no greater than for H_2 carrier gas. It is shown that carbon is not a major contaminant in the epitaxial HgTe and CMT layers, but may still be a problem at lower concentrations.

I. INTRODUCTION

The infrared detector material $Cd_xHg_{1-x}Te$ (CMT) has become the most widely used narrow gap semiconductor for photon detection in thermal imaging applications. However, this has proved to be a very difficult material to grow and fabricate into infrared detectors. This is because of high concentrations of electrically active Hg vacancies and rapid diffusion both for the major elements, Cd and Hg and for impurities/dopants during preparation. These problems can be more readily controlled by using relatively low temperatures for epitaxial growth of CMT and device fabrication. MOVPE is now a well-established technique for the preparation of CMT but due to the stability of the Te metal-organic, diethyltelluride (Et_2Te), growth below 400 °C is not practical.[1–3] At this temperature the Cd/Hg interdiffusion at a heterojunction interface is around 3000 Å for a typical growth time of 1 h and the equilibrium Hg vacancy concentration can be greater than 10^{17} cm^{-3}.

Molecular beam epitaxy (MBE) is capable of CMT growth at temperatures below 200 °C but the best crystallinity is obtained at this temperature or just above it.[4–6] Control at higher temperatures is difficult to achieve due to the need for a large, excess (noncongruent) Hg flux $\sim 10^{18}$ cm^{-2} s^{-1}. The regime of growth temperature between 200 and 300 °C is of considerable interest for CMT because the surface kinetics should allow good crystalline quality while maintaining sufficiently low temperatures to minimize interdiffusion and Hg vacancy concentration.

This paper describes a new technique (photo-MOVPE) for low temperature epitaxy which relies on nonthermal decomposition of metal-organic molecules by UV photolysis. Epitaxial growth of HgTe at temperatures between 200 and 300 °C has been reported previously[7] where Hg vapor was introduced into a horizontal reactor cell with Et_2Te and H_2 carrier gas. Illumination of a CdTe or InSb substrate with a high pressure Hg arc lamp resulted in HgTe deposition via a proposed $Hg(^3P_1)$ photosensitization reaction with Et_2Te. However, the preferred Cd metal-organic source, dimethyl-cadmium (Me_2Cd) can undergo a strong vapor phase photochemical reaction with the consequence in extreme cases of homogeneous vapor phase nucleation.[8] For epitaxial crystal growth it is necessary to avoid these vapor reactions and to promote surface photochemical reactions. The growth of HgTe by Hg photosensitization is a surface reaction, probably due to surface excitation of chemisorbed Hg as a result of a shift in the $^3P_1$ absorption line. Strong absorption in a narrow band around 253.7 nm by Hg in the vapor ($> 10^{-2}$ atm) will prevent radiation reaching the substrate, hence the Hg vapor acts as a filter. However, radiation from the Hg arc lamp emitted at wavelengths on either side of this absorption line will reach the substrate and participate in surface photochemical reactions.

II. CONSIDERATIONS IN THE GROWTH OF CdTe AND CMT

The method of surface photosensitization cannot be simply extended to the growth of CdTe and CMT because of the problem of vapor phase reactions. This problem is more severe than when only cadmium is being deposited. The probability of the occurrence of homogeneous nucleation depends on the supersaturation of Cd and Te which in turn depends on the difference between the actual vapor phase concentration and the equilibrium vapor pressure. The excess chemical potential for nucleation can be expressed as

$$\Delta\mu = RT \ln(p_v/p_e), \quad (1)$$

where p_v is the partial pressure in the vapor, p_e the equilibrium vapor pressure, R the gas constant, and T the vapor temperature in Kelvin. The actual vapor pressure of Cd will have as an upper limit the pressure of Me_2Cd which is in the region of 10^{-3} to 10^{-4} atm. If the absorption cross section at 254 nm is 4×10^{-17} cm^2 [9,10] and assuming 1 W cm^{-2} of UV power from the lamp, the likely vapor pressure of Cd will be in the range 3×10^{-6}–5×10^{-7} atm. At 250 °C the equilibrium vapor pressure over Cd is $\sim10^{-5}$ atm but over CdTe (under congruent evaporation conditions) it is $\sim10^{-12}$ atm. Using Eq. (1) for nucleation of CdTe gives a value for $\Delta\mu$ in the range 15.6–13.7 kcal mol^{-1}, which indicates that CdTe may nucleate, even though, under these conditions, pure Cd may not. The photodecomposition of Cd and Te alkyls individually would lead to high supersaturations of Cd and Te vapors with respect to CdTe. If the alkyls form an adduct,[11] photodecomposition with the loss of CH_3 and C_2H_5 radicals would automatically leave CdTe molecules. Vapor phase nucleation could then proceed rapidly due to high Cd and Te or CdTe supersaturations. It is the need to suppress vapor phase nucleation that requires a surface selective reaction.

The calculation of vapor phase concentrations and supersaturation assumes that every Me_2Cd molecule or adduct which absorbs a photon will dissociate to release Cd or CdTe, respectively. However, the reverse reaction could considerably reduce these concentrations and avoid homogeneous nucleation. It is proposed that by replacing the reactive H_2 carrier gas with an inert gas such as He, the CH_3 and C_2H_5 radicals will have an opportunity to recombine with a partially dissociated metal-organic or with monatomic Cd or CdTe molecules. Another reaction which will be occurring in the presence of H_2 is the generation of monatomic H by the very efficient photosensitization reaction with Hg ($^3P_1$)[12]:

$$H_2 + Hg^* \rightarrow Hg + 2H. \quad (2)$$

Any collisions between the monatomic H and metal-organic molecules would result in thermal decomposition, for example:

$$2H + (CH_3)_2Cd \xrightarrow{250\,^\circ C} 2CH_4 + Cd. \quad (3)$$

The enthalpy change for this reaction is ~ -139 kcal/mol and is clearly a very favorable thermal reaction. This reaction path would increase Cd concentrations above those estimated for the purely photochemical reactions.

III. EXPERIMENTAL

Epitaxial growth experiments were carried out in a horizontal flow system operating at one atmosphere total pressure. The reactor cell is shown diagrammatically in Fig. 1 for HgTe growth. The reactor cell diameter was 6 cm and the Hg reservoir zone divided into two so that a pure stream of carrier gas could flow over the section of wall illuminated with UV and prevent deposition. The metal-organics flowed over the Hg reservoir and mixed with the Hg vapor before passing over the substrate.

The substrates were either CdTe or InSb and heated by an infrared lamp controlled by a Eurotherm temperature controller with a reference thermocouple situated in the graphite holder. The CdTe substrates were prepared by polishing on a chemomechanical polisher with 2% Br methanol sclution followed by solvent rinses and a final rinse in deionized water. The InSb substrates were supplied as polished by Mining and Chemical Products and subsequently etched in 25 : 4 : 1, lactic acid, nitric acid, HF, and finally rinsed in deionized water, before being loaded into the reactor.

All gas flows were regulated by mass flow controllers. The hydrogen supply was purified by Pd/Ag membranes and the helium supply was passed through a molecular sieve which reduced the water vapor content to below 1 ppm. The metal-organics used were electronic grade diethyl-telluride (Et_2Te) and dimethyl-cadmium (Me_2Cd) supplied by Alfa Products.

The UV source was a 3-kW-mercury arc lamp with a water cooled, silica jacket, all supplied by Illumination Industries. The lamp was mounted in an elliptic reflector focusing to a 0.5-cm-wide stripe on the substrate.

IV. RESULTS AND DISCUSSION

A. Growth of HgTe

The effects of using He as a carrier gas were studied by growing HgTe using Hg photosensitization under similar conditions to those described elsewhere.[7,13] Figure 2 shows a plot of growth rates vs substrate temperature using H_2 and

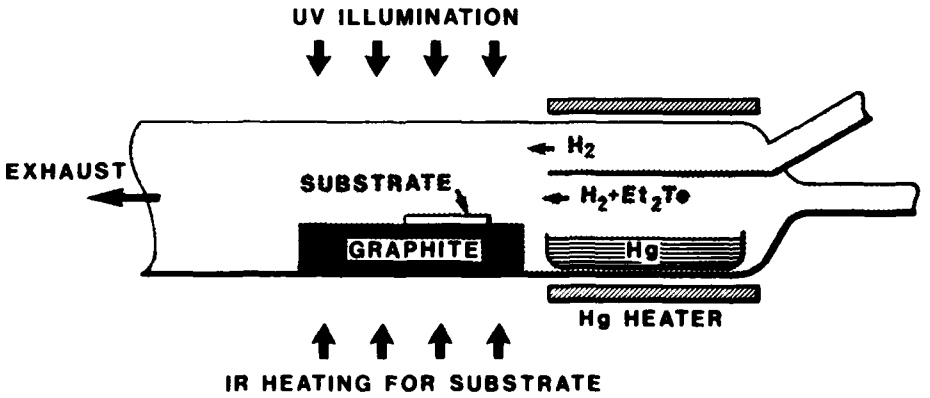

FIG. 1. Reactor cell for UV photolytic deposition. The configuration shown here is for HgTe growth by Hg photosensitization using H_2 carrier gas with Et_2Te and Hg vapor.

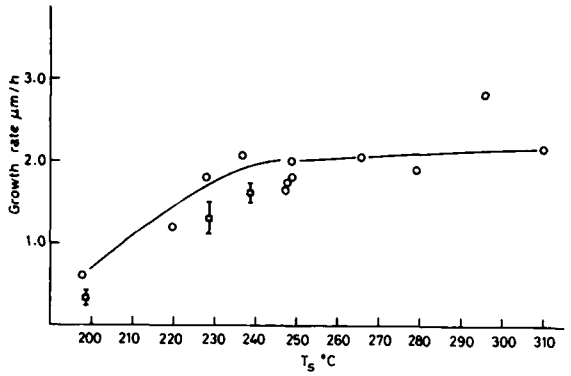

FIG. 2. Plot of HgTe growth rate vs substrate temperature T_s °C for H_2 carrier gas (○), and He carrier gas (□). The other growth conditions were $P_{Hg} > 3 \times 10^{-2}$ atm, $P_{Et_2Te} = 5.9 \times 10^{-3}$ atm and substrates were InSb-oriented (100).

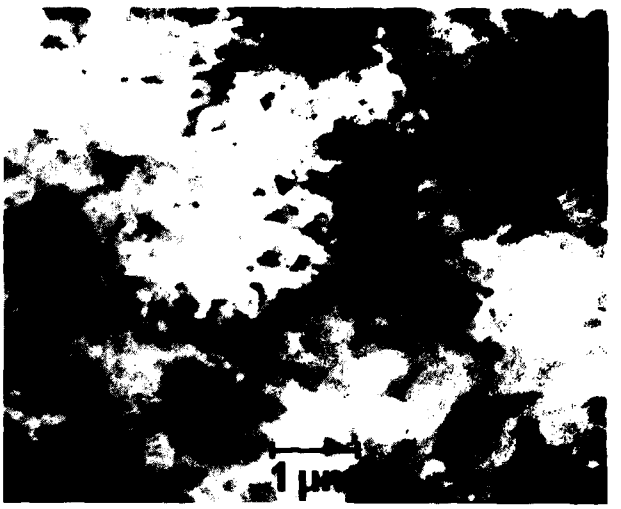

(a)

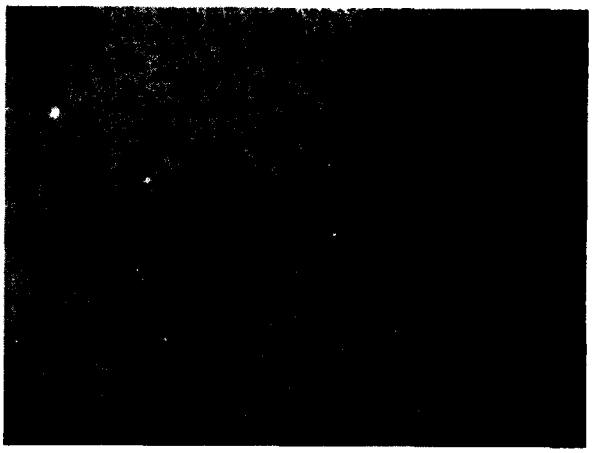

(b)

FIG. 3. (a) SEM micrograph of CMT deposited using H_2 carrier gas, $x \sim 0.5$ showing a porous polycrystalline structure (b) SEM micrograph of a CMT epitaxial layer, $x = 0.33$ after using He carrier gas.

He carrier gases. Both show the same decrease in growth rate below 240 °C. This has been attributed to surface kinetics which limit the growth rate at these lower temperatures. Layers grown in He were of similar quality to layers grown in H_2, but their growth rates were marginally lower.

Two important statements can be made about these results. Firstly, the presence of free alkyl radicals, at the concentrations being generated in the absence of H_2, do not have a significant etching effect on the surface or inhibit the surface decomposition of Et_2Te. This is indicative of a surface catalyzed reaction between C_2H_5 radicals to form C_4H_{10} and is a mechanism for bringing about a surface selective reaction for the deposition of CdTe and CMT. Secondly, although the photosensitization dissociation of H_2 should be competitive with the dissociation of Et_2Te, the surface reaction is not significantly affected by the presence of H_2. This statement is consistent with a view that a surface complex could form between Hg and Et_2Te, before excitation of Hg by UV.

B. Growth of CMT

Two similar deposition experiments were carried out at 250 °C with Me_2Cd added to the reactant gas stream but one experiment used H_2 and the other He carrier gases. The two micrographs in Fig. 3 show the difference in deposition using the two carrier gases. For H_2 carrier gas, the surface appears black and consists of a fragile network of submicron-sized particles of CMT which have formed in the vapor and fallen to the surface, as can be seen in Fig. 3(a). By contrast, Fig. 3(b) shows a flat surface with a very slight ripple, although to the eye it appears as a mirror surface. This layer was 1.3 μm thick and was grown onto a (110)-oriented CdTe substrate. An x-ray diffraction trace for the (220) reflections is shown in Fig. 4 and shows that this layer is epitaxial. The $k_{\alpha 1}$ and $k_{\alpha 2}$ reflections from CMT are clearly resolved and a weaker $k_{\alpha 1}$ reflection from the CdTe substrate can also be seen. Using a lattice parameter for CdTe of 6.4829 Å, the lattice parameter of the CMT layer can be calculated and gives a value of 6.466 Å which is reasonable for CMT $x \sim 0.3$.

The dramatic change in the deposition brought about by a change in carrier gas can only be due to a reduction in the Cd and Te vapor pressures over the substrate, but the exact photochemical process is complicated and can only be speculated on at this stage. The stability of the vapor over the substrate is kinetic and relies on a continual generation of free radicals to offset the photodissociation of the metal-organic vapor. This process is sufficient to maintain low vapor pressures of Cd and Te in a region of the vapor where a balance is maintained between these vapor pressures and the partial pressures of CH_3 and C_2H_5. Once stable organics such as C_2H_5 and C_4H_{10} are formed the process is irreversible as they are thermally stable and are unlikely to photodissociate at these UV wavelengths. So, it is important that a flow system is used as the vapor nucleation of CdTe and CMT is only delayed by the enhanced free radical concentration. If the free radical concentration is reduced, such as in regions of low UV intensity on either side of the focused beam, Cd and Te atoms diffusing from the region of high intensity will be free to nucleate in the vapor. This effect is observed for CMT deposition where epitaxial growth occurs only within the focus of the UV lamp; and on either side the deposit is similar

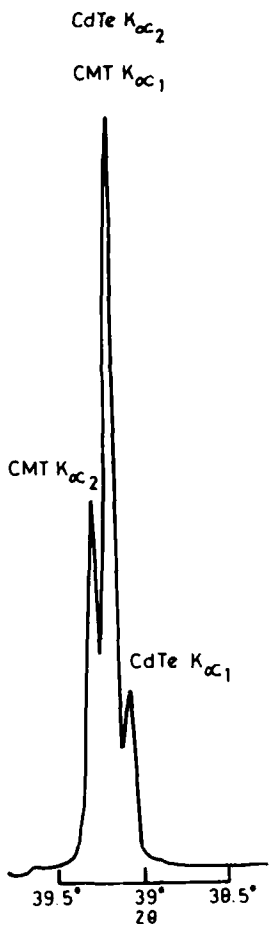

FIG. 4. X-ray diffraction peaks for the (220) reflections from 1.3-μm-thick CMT layer on a CdTe substrate. Cu K_α radiation was used and the positions of the $K_{\alpha 1}$ and $K_{\alpha 2}$ reflections for CMT and CdTe are indicated.

to the vapor nucleated dust observed with H_2 transport. The problem of build up of Cd and Te within the focused region is less severe and epitaxial growth can readily be achieved for 3 to 4 cm downstream.

C. Growth rate dependence on orientation

For HgTe grown by photosensitization, the dependence of growth rate on substrate orientation has been studied in detail.[7] The results indicate that surface kinetics may dominate the epitaxial growth rate, irrespective of transport conditions. A survey was carried out of the CMT growth rates on three orientations of CdTe substrates. The results for growth rate and composition (measured by energy dispersive x-ray microanalysis, EDX) are shown in Table I, together with the corresponding orientations for HgTe growth. The CMT growth rates follow the same trend in behavior as the HgTe growth rates, much lower on (111)*A* than on (100) and (110). However, there are some interesting differences between CMT and HgTe. HgTe growth rates were very similar on (100) and (110) but CMT has a significantly higher growth rate on (110) than on (100). It is possible that for HgTe growth, transport is a significant factor limiting the growth rate on these orientations and slower surface kinetics on CMT makes the variation due to orientation more apparent. It can be seen in Table I that the growth rate on (111)*A* for CMT is significantly higher than for HgTe, reversing the trend of lower CMT growth rates for (100) and (110). The composition also shows interesting differences with a higher Cd content on (100), compared with (110); again this would be expected if the growth is controlled by surface kinetics. Possible steps in the surface chemistry which may be rate limiting are

(a) Hg-Et_2Te complex formation;
(b) reaction of radicals on the surface;
(c) desorption of radicals or stable organic molecules.

TABLE I. Growth rates of HgTe and $Cd_xHg_{1-x}Te$ on different orientations of CdTe substrate, for $T_s = 250$ °C and $P_{Et_2Te} = 4.5$ Torr.

Run no.	Orientation	Growth rate (μm/h)	Composition x
21	(100)1° →(110)	1.9	0
96	(100)2° →(110)	1.2	0.21
20	(110)	1.8	0
96	(110)	1.5	0.15
24	(111)*A*	0.1	0
96	(111)*A*	0.6	...

D. SIMS analysis of HgTe and CMT

Secondary ion mass spectrometry (SIMS) sputter depth profiles were obtained for the major elements, Cd, Hg, and Te; and for impurities. The major element profiles were obtained using an oxygen primary ion beam in a Cameca 3F IMS, and are shown for a 1.3-μm-thick layer, grown at 250 °C in Fig. 5. The ^{125}Te signal is almost constant through the layer and substrate, just showing a small change at the interface. The ^{111}Cd and ^{200}Hg signals are constant in the epitaxial layer, showing an abrupt change at the interface with ^{111}Cd increasing to the CdTe value and ^{200}Hg decreasing by three decades. To examine the interface abruptness

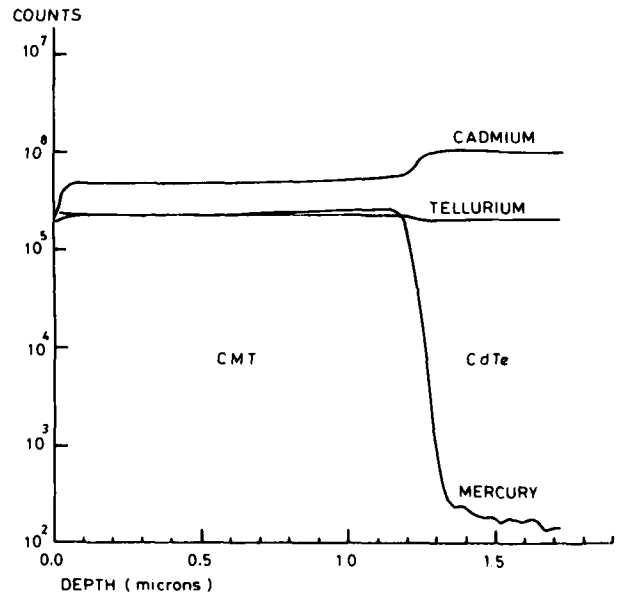

FIG. 5. SIMS depth profiles for ^{111}Cd, ^{125}Te, and ^{200}Hg through a 1.3-μm-thick CMT layer ($x = 0.33$) on a CdTe substrate.

more carefully, a greater density of sample points was obtained by only profiling for ^{200}Hg which is shown in Fig. 6. The interface, shown by the decrease in ^{200}Hg signal is less than 400 Å wide. This assumes that there is no contribution from any surface roughness which would replicate on the sputtered interface or from any cumulative roughening which cannot be estimated at this stage. This interface width is an order of magnitude narrower than CMT/CdTe interfaces grown by thermal-MOVPE at 410 °C. It may be less but the resolution of the instrument, in this measurement, may not be good enough to allow accurate determination of such small dimensions.

The presence of organic products in the growth cell raises the possibility of carbon incorporation in the epitaxial layer due to breakdown of these organic products on the surface. It appears from low temperature growth of GaAs that this risk actually increases at lower temperatures due to slower desorption.[14] A fu ther consideration with He carrier gas is that the radical lifetime is likely to be longer than when H_2 is present to form methane and ethane with the radical products. SIMS profiles were obtained for ^{12}C, using the caesium ion gun, in HgTe layers grown using H_2 and He carrier gases and through a CMT layer. Profiles for the two HgTe layers are shown in Fig. 7. The calibrations used for carbon are for CMT ($x = 0.2$) but are expected to be similar for HgTe. The levels in the InSb matrix cannot however be determined from this analysis. The peaks at the HgTe/InSb interface are thought to be genuine and arise from contamination on the substrate surface before loading in the reactor cell.[15] It can also be noted that the level of carbon rises towards the surface of the HgTe layers. In the bulk of the layers the carbon level is just detectable giving a mean value of 30 ppm in the layer grown with hydrogen and less than 20 ppm for the layer grown with helium. Clearly the helium does not have an adverse effect on carbon incorporation and large amounts of carbon are not observed although there

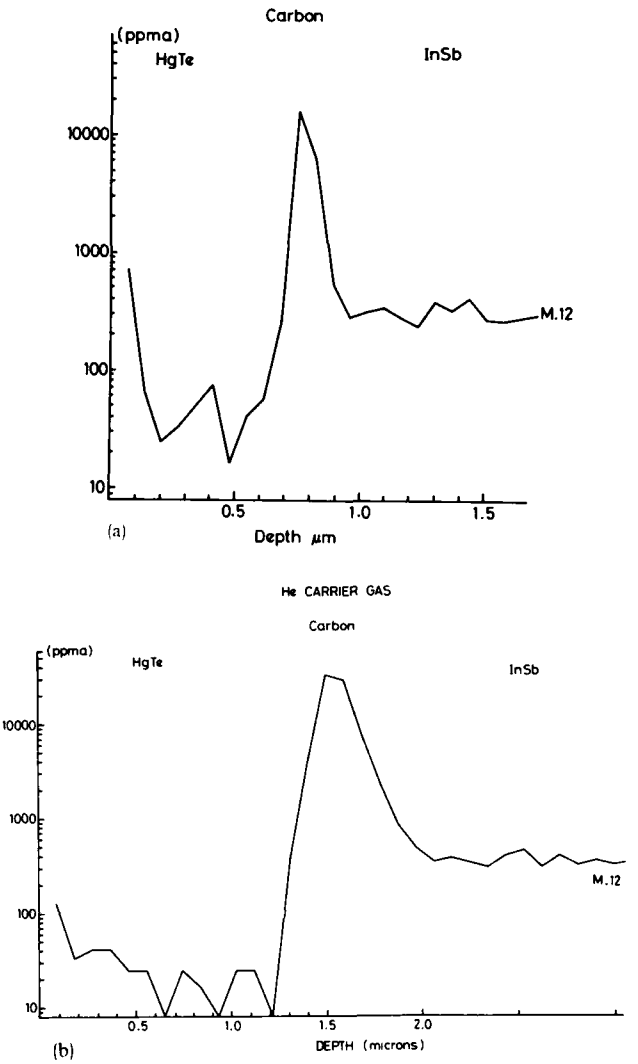

FIG. 7. SIMS depth profile for ^{12}C in HgTe layers on InSb substrates, grown at 240 °C for (a) H_2 carrier (b) He carrier.

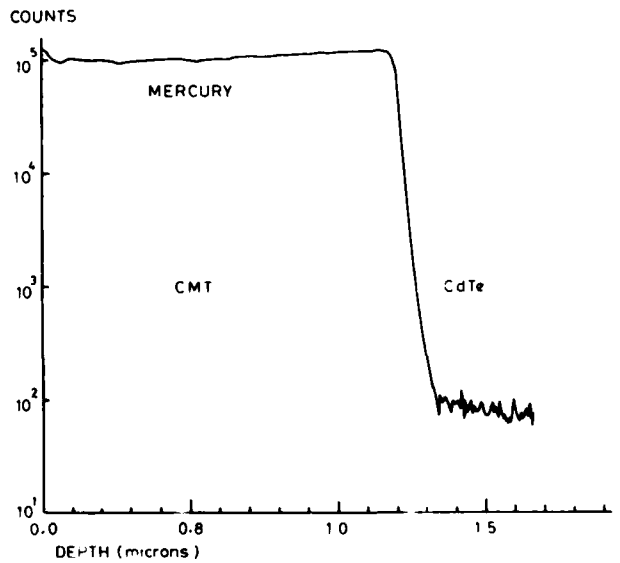

FIG. 6. SIMS depth profile for ^{200}Hg through a 1.3-μm-thick CMT layer, showing an abrupt interface.

may be some problem with low levels of contamination in both layers.

The ^{12}C depth profile for a CMT layer on InSb substrate is shown in Fig. 8. This profile shows the same features (of high interface and surface concentrations) as the HgTe layers. The carbon sensitivity is better in CMT than in HgTe but gives a similar level (of 40 ppm) to the HgTe layers. There is some tailing of the interface peak into the layer and there is the possibility of thicker layers having lower carbon levels in the bulk of the layer than this measurement indicates. The high carbon levels on the InSb substrate surface shows the need for *in situ* etching to clean the surface before growth. Unfortunately, thermal cleaning leaves a nonstoichiometric surface[12] which structurally degrades the interface. Further studies are being carried out on layers grown onto CdTe substrates where suitable thermal cleaning is possible.[16]

V. CONCLUSIONS

A new photo-MOVPE technique for low temperature epitaxial growth has been described. Factors affecting the crys-

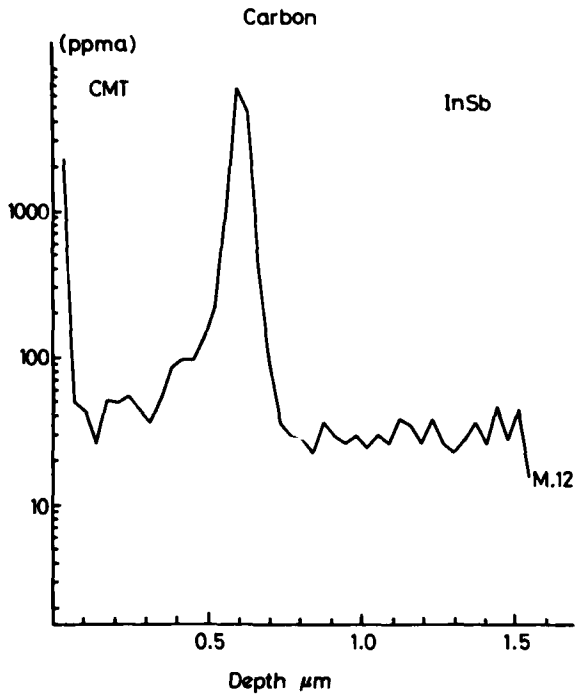

FIG. 8. SIMS depth profiles for ^{12}C in a CMT layer on an InSb substrate, grown at 240 °C.

tal growth of HgTe and CMT at low temperatures have been considered and conditions for their photochemical deposition discussed. Significant vapor pressures of Cd and Te must be avoided in order to prevent homogeneous nucleation of CdTe and CMT and surface photochemical reactions must be encouraged. HgTe has been grown epitaxially at temperatures in the range 200–300 °C by a surface photosensitization reaction using H_2 and He as carrier gases.

Me_2Cd can react strongly in the vapor with UV and also photodecompose Et_2Te, probably via an adduct reaction with Me_2Cd. This vapor phase reaction is suppressed when He carrier gas is used, thereby avoiding homogeneous nucleation of CdTe and CMT, but allowing surface reactions to promote epitaxial growth. These surface photochemical reactions can include Hg photosensitization and photon absorption in the adsorbed metal-organic layer.

High quality CMT and HgTe epitaxial layers have been grown by photo-MOVPE, over the entire composition range, using helium carrier gas to suppress homogeneous nucleation. HgTe growth rates are similar using either H_2 or He. The CMT/CdTe interface width as grown at 250 °C is less than 400 Å, an order of magnitude improvement compared with thermal-MOVPE at 410 °C. SIMS analysis shows that using He does not increase carbon incorporation and that carbon levels of 20–50 ppm in the layer may be associated with high carbon levels at the layer/InSb interface.

Further work is being carried out on determining the electrical quality of these epitaxial layers and on the growth of heterojunctions on CMT/CdTe.

ACKNOWLEDGMENTS

The authors wish to thank Mr. C. A. Jones for the growth of CdTe substrates and gratefully acknowledge the skilled assistance of Mrs. J. Clements.

[1]S. J. C. Irvine and J. B. Mullin, J. Cryst. Growth **55**, 107 (1981).
[2]J. B. Mullin and S. J. C. Irvine, J. Vac. Sci. Technol. **21**, 178 (1982).
[3]S. J. C. Irvine, J. Tunnicliffe, and J. B. Mullin, J. Cryst. Growth **65**, 479 (1983).
[4]J. P. Faurie, A. Million, and J. Piaguet, J. Cryst. Growth **59**, 10 (1982).
[5]J. P. Faurie and A. Million, Appl. Phys. Lett. **41**, 264 (1982).
[6]J. P. Faurie, A. Million, R. Boch, and J. L. Tissot, J. Vac. Sci. Technol. A **1** 1593 (1983).
[7]S. J. C. Irvine, J. B. Mullin, and J. Tunnicliffe, J. Cryst. Growth **68**, 188 (1984).
[8]D. J. Ehrlich, R. M. Osgood, Jr., and T. F. Deutsch, IEEE J. Quantum Electron. **16**, 1233 (1980).
[9]C. J. Chen and R. M. Osgood, Chem. Phys. Lett. **98**, 363 (1983).
[10]S. J. C. Irvine, J. B. Mullin, D. J. Robbins, and J. L. Glasper, Mater. Res. Soc. Symp. Proc. **29**, 253 (1984).
[11]J. B. Mullin, S. J. C. Irvine, and D. J. Ashen, J. Cryst. Growth **55**, 92 (1981).
[12]H. E. Gunning, J. M. Campbell, H. S. Sandhu and O. P. Strausz, J. Am. Chem. Soc. **95**, 746 (1973).
[13]S. J. C. Irvine, J. B. Mullin, and J. Tunnicliffe, Chem. Phys. **39**, 234 (1984).
[14]H. Beneking, Chem. Phys. **39**, 188 (1984).
[15]J. Tunnicliffe, G. W. Blackmore, S. J. C. Irvine, J. B. Mullin, and R. Holland, Mater. Lett. **2**, 393 (1984).
[16]J. G. Werthen, J. P. Haring, A. L. Fahrenbrach, and R. H. Bube, J. Appl. Phys. **54**, 5982 (1983).

Mechanisms of metallo-organic vapor phase epitaxy and routes to a ultraviolet-assisted process

J. Haigh
British Telecom Research Laboratories, Martlesham Heath, Ipswich IP5 7RE, United Kingdom

(Received 15 February 1985; accepted 18 April 1985)

Ultraviolet irradiation during deposition has been reported to improve the morphology and increase the growth rate of GaAs epitaxial layers produced by metallo-organic vapor phase epitaxy. In order to optimize and control these effects for technological applications it is necessary to understand the mechanisms of metallo-organic vapor phase epitaxy (MOVPE). This paper reviews the current state of knowledge relevant to the UV intervention in InP growth. Preliminary experiments on the effect of UV in this system suggest that it may be increasing the mobility of the adsorbed reactant species.

I. INTRODUCTION

The MOVPE process for epitaxial growth of III–V compounds can be formally represented by the general equation

$$R_3M + PnH_3 \rightarrow MPn + 3RH.$$

Here R is an alkyl group, M a Group III metal, and Pn (pnictide) a Group V metalloid. When this pyrolysis reaction is carried out in the presence of a suitable substrate and at a high enough temperature, the III–V compound deposits in a crystalline form in an epitaxial relationship with the substrate. The mechanism of the reaction is attracting attention because of the growing general importance of MOVPE and the need to expand and extend its utility. In particular there is a growing requirement to be able to rapidly change the deposition rate and the composition in order to produce, respectively, localization of growth on small areas of the substrate, and very thin (below 100 Å) layers, in structures for optoelectronic applications.

The reaction is carried out by flowing the reactants at typical concentrations of 10^{-6}–10^{-4} mol/l in a carrier gas over a heated substrate crystal. The total pressure may be around 100 Torr[1] or around 760 Torr[2] and flow speed a few cm/s, so that flow is in the laminar regime.

The thermodynamic free energy change on reaction is highly negative, and the possible component reactions

$$R_3M \rightarrow M + \text{hydrocarbons}$$
$$PnH_3 \rightarrow Pn + 3/2\ H_2$$

may potentially occur either in the gas phase or on the solid surface, and over a range of temperatures which may extend down almost to room temperature. However, the fact that a sizable fraction of the reactants pyrolyze on the substrate suggests a preference for heterogeneous reaction, and hence the kinetics are complex. Furthermore, because the flow is laminar, the reacting species diffuse through a boundary layer to reach the substrate, and at different points in this layer the velocity, composition, and temperature are different. Thus the rates of the gas phase reactions vary from point to point in the layer. Stringfellow[3] has recently examined the thermodynamic aspects of the process and has commented on the complex interplay of boundary-layer diffusion and gas-phase and surface reaction kinetics.

Recently it was shown that Group III alkyls could be photolyzed to relatively carbon-free metals, using 200–300 nm UV radiation.[4] AsH_3 and PH_3 also absorb in this spectral region[5] (although they do not readily photolyze to the elements), so that UV irradiation potentially provides an alternative source of energy for the decomposition processes. As an additional component to the MOVPE process, UV offers several advantages. One of these is the possibility of spatial confinement of deposition, even down to small dimensions, since UV laser beams can be reduced to diameters well below 1 μm. Another is the modulation of growth rates. Confirming an earlier report by Frolov,[6] Pütz and co-workers[7] have recently shown that a 257 nm radiation flux slightly enhances the MOVPE growth rate of GaAs when applied at or slightly below what would normally be the optimum growth temperatures, and produces a great improvement in surface morphology. Donnelly and co-workers[8] have formed indium-phosphorus layers of variable composition using UV to photolyze the species Me_3In and Me_3P at room temperature. Intuitively it is clear that epitaxy can only occur if the substrate temperature is high enough to allow the atomic species generated by the pyrolyses to take up their correct lattice positions, and temperatures in excess of 400 °C are probably needed to allow epitaxial ordering to proceed at a useful rate. At these temperatures pyrolysis, at least of the Group III sources, proceeds at appreciable rates, so that epitaxial deposition by photolysis alone may not be a practical proposition. Thus the successful development of UV-stimulated MOVPE requires control of the balance of pyrolysis and photolysis: it seems likely that this will be achieved by a combination of careful attention to the hydrodynamics of reactor design and by an increased understanding of the mechanisms of the pyrolysis and photolysis.

This contribution will consist firstly of a brief review of recent work relevant to the developments outlined above. Secondly, initial results on the UV-stimulated growth of epitaxial InP will be presented and discussed.

 0734-211X/85/051456-04$01.00

II. MECHANISTICS OF MOVPE

A. The kinetics of the pyrolysis reactions

Jacko and Price examined the pyrolyses of gallium[9] and indium[10] trimethyls over a range of temperatures and showed that the reactions occurred in three stages, corresponding to the sequential removal of methyl groups. The sequence for the indium reaction is

$$(CH_3)_3\,In \rightarrow (CH_3)_2\,In' \rightarrow (CH_3)In'' \rightarrow In.$$

The removal of the third methyl group from indium trimethyl was appreciably slower than the removal of the first two, indicating that the species CH_3In represents an "island of stability" during the pyrolysis sequence. (A tendency towards stability of the univalent state is found elsewhere in indium chemistry.[11]) The rates of loss of the first and third methyl groups were influenced by the nature of the reactor wall, being faster when this (glass) wall was free of deposit. By suppressing the wall reaction these workers were able to calculate gas-phase kinetic constants: the values of these indicate that a substantial fraction of the Group III alkyl undergoes partial or complete pyrolysis in the MOVPE boundary layer. It is not clear however, which, if any, of these decomposition products participate in the growth. It should also be stressed that the fact that the reaction sequence given above can yield gas-phase kinetic constants does not necessarily imply that gas-phase metal atoms are generated, even momentarily: a heterogeneous reaction on suspended microparticles or droplets could yield the same kinetic behavior.

Haigh and O'Brien[12] examined the dependence of the rate of pyrolysis on the nature of surfaces in the reactor. The fraction of material pyrolyzed when a gas stream flowed through a heated tube was greater in the presence of a packing of glass, relative to a packing consisting of an equal area of InP wafers. In the presence of the latter packing, a species that they tentatively identified as $(CH_3)In$ was inferred from the UV spectrum of the product stream from the tube. In other work[13] they reported the use of atomic absorption spectrometry to show that no-gas phase In atoms were present during the pyrolysis. They concluded that only heterogeneous final stage decomposition (on suspended particles or on the packing, substrate or reactor wall) was possible:

$$(CH_3)In \rightarrow CH_3^{\cdot} + In,$$

and that this decomposition was slower on InP than on the glass surfaces. This reaction may thus be rate limiting in MOVPE under some conditions.

Stringfellow,[1] used a similar technique for the pyrolysis of PH_3 in the presence of GaP surfaces. In contrast to the result for the Group III alkyls there was a strong enhancement in rate, relative to a ground quartz surface. A comparison of the absolute rates of pyrolysis of Group III and Group V species on InP would obviously be instructive.

Turning to the kinetics of the overall MOVPE reactions Reep and Ghandhi[14] found three regions in GaAs growth where the slope of the log(growth rate) $-$ 1/ (temperature) curve took distinctly different values. In particular they found a transition at 600 °C from reaction-rate-limited behavior to gas-phase diffusional limited behavior. In the former, lower temperature regime the growth rate saturates at certain limiting values of the partial pressures of both reactants (gallium trimethyl and arsine), indicating that the decomposition of both these species can be rate limiting. Pütz and co-workers[7] confirmed this observation and showed that in the case of the Group III species the saturation could be postponed (moved to higher partial pressures)—and higher growth rates thereby rendered possible—by UV irradiation. By further arguments they concluded that the rate-limiting step that was being affected by the 257 nm (Hg lamp) UV light was located at the surface, and they suggested that it was either desorption of the hydrocarbon reaction product, or surface migration of the reactant. In addition they noted that UV light improved the surface morphology of the layer in both the diffusion-limited and reaction kinetic-limited growth regimes.

B. Gas-phase diffusion

Leys and Veenvliet[15] showed that in a standard MOVPE apparatus with gas flow along a heated horizontally placed susceptor, operated in the diffusion-limited regime as described above, the growth rate showed the behavior expected from laminar-flow hydrodynamics—that is, diffusion through a parabolic boundary layer.[16] Koppitz and coworkers[17] showed that this boundary layer changed in the expected manner when N_2 was substituted for H_2 as the carrier gas.

In the diffusion-limited regime the growth rate varies slowly with temperature and is linear with partial pressure of the Group III alkyl over a wide range, thus allowing good control. The diffusion-limited regime is chosen for practical epitaxy partly for this reason. One approach to the use of UV that might therefore suggest itself would be to modulate the concentration of radical reactant species in the boundary layer. Since, as is clear from the work reviewed above, part of the pyrolysis takes place in the boundary layer, a modulation of the epilayer composition (in the case of alloy growth) and/or of the deposition rate would be expected to result. However, gaseous diffusion is rather too slow (typical diffusion coefficients are around 1 $cm^2\,s^{-1}$) to allow such modulation of the boundary layer composition to be effective practically as a means of rapid modulation of the epitaxial composition, unless the gas phase is very dilute and growth very slow. The fact that the UV enhancements observed by Pütz can be attributed fairly confidently to surface reaction effects is therefore an encouraging development, since in principle surface concentrations can be modulated much more rapidly.

III. EXPERIMENTAL

We report on some preliminary observations on the effect of UV irradiation on MOVPE deposition of InP. An apparatus previously described[18] was used. This is an atmospheric-pressure system, incorporating facilities to transport indium trimethyl as a complex with phosphorus triethyl, and the only modification made in this work was to incorporate a rectangular section reactor tube with a UV-transparent Spectrosil-grade window in the top of the reactor. A 200–400 nm UV flux of a few W was supplied by a high pressure xenon arc lamp and passed through a 1-cm-thick water filter

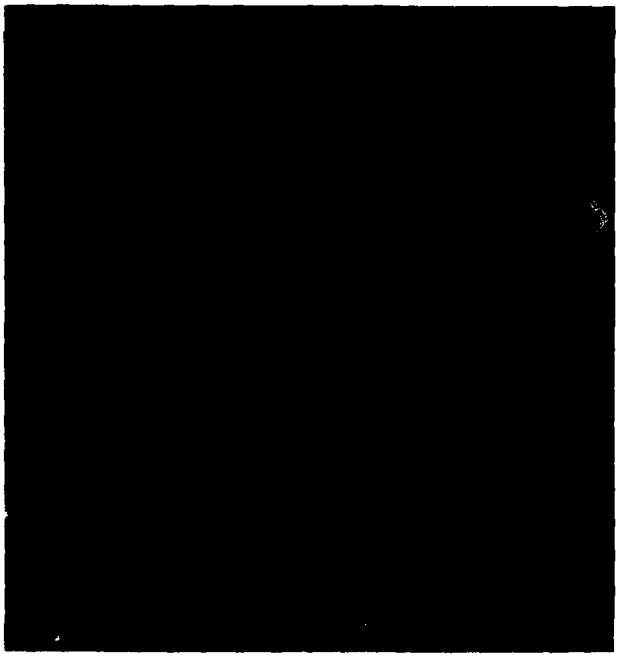

FIG. 1. Surface morphology of an InP layer deposited without UV irradiation showing relatively few rounded regions of enhanced growth. Nomarski optical micrograph, covering a region approximately 100 μm $\times$ 100 μm.

to remove the infrared component. The flux was distributed over about 4 cm^2 of the susceptor surface.

Deposition experiments were carried out at 550 °C with the following reactant concentrations: indium trimethyl 5×10^{-6} mol/*l*, phosphine 10^{-5} mol/*l*, phosphorus triethyl 5×10^{-6} mol/*l*. The carrier gas was palladium-diffused hydrogen at 1 atm pressure. The flow rate was about 2.5 *l*/min. At these pressures and taking the published UV absorption coefficients[5,19] it is calculated that nearly all the UV flux, even in the most heavily attenuated spectral region, reached the substrate.

FIG. 2. InP layer deposited with UV irradiation, showing large numbers of rounded regions of enhanced growth.

A sulfur-doped InP substrate, (100) orientation, was divided and adjacent pieces (placed in the same position on the graphite susceptor) were used for pairs of experiments with and without UV. The time of exposure to reactant vapor was 15 min. Some fogging of the Spectrosil window occurred in this time and the UV flux was thereby diminished.

Figures 1 and 2 show deposition, respectively, without and with UV irradiation. Electrochemical profile plotting shows that the growth features are superimposed on continuous layers which are 0.5–0.6 μm thick in both cases. In Fig. 1 the features are smooth-sided elliptical hillocks about 0.2–0.5 μm high. Such features are commonly found in small numbers when a relatively low temperature is chosen for deposition. In contrast Fig. 2 shows in addition to these hillocks many smaller features about 0.1 μm high. These features are also elliptical, but with some faceting, and like the larger features are oriented with the 110 direction in the substrate surface. Some are distributed inhomogeneously along scratches or in other locations that may be damaged, but others occur in apparently undamaged areas.

The observation that UV produces no observable change (greater than about 10%–20%) in the overall growth rate suggests that to this extent it is not influencing the steps in the process which are rate controlling at 550 °C. Pütz and coworkers, in the work on GaAs previously discussed, similarly did not find large effects of UV exposure on growth rate even under the conditions where the morphological effects were most striking. It seems probable therefore that the intervention of the UV is in the surface migration and nucleation stage. Growth around defects is often energetically favorable; and so if sufficient surface mobility exists, and surface kinetics are rate controlling, excess growth around such defects will be observed. An alternative possibility is that UV lowers the activation energy for nucleation at the defects. The mechanism by which UV produces either of these changes might be either interaction directly with the substrate (bond breaking) or generation of more labile metallo-organic fragments from the gaseous precursors. Further work is necessary to resolve these possibilities.

IV. CONCLUSIONS

The MOVPE process is complex, having gas-phase pyrolysis, surface adsorption, surface migration, and product (hydrocarbon) elimination stages. The kinetics indicate that the adsorbed species are metal-containing radical products of the partial gas-phase pyrolysis, so that elimination of hydrocarbon fragments from the surface must take place. UV light fluxes can modulate the crystal quality, and in GaAs at least also the growth rate: UV appears to enhance either surface mobility of intermediate reaction species, or nucleation at favorable sites, or desorption of the hydrocarbon reaction products. These effects suggest technologically interesting applications for UV-enhanced MOVPE.

ACKNOWLEDGMENTS

Acknowledgment is made to the Director of Research, British Telecom, for permission to publish this work.

[1]J. P. Duchemin, M. Bonnet, F. Koelsch, and D. Huyghe, J. Electrochem. Soc. **126**, 1134 (1979).
[2]S. J. Bass, J. Cryst. Growth **31**, 172 (1975).
[3]G. B. Stringfellow, J. Cryst. Growth **68**, 111 (1984).
[4]M. R. Aylett and J. Haigh, in *Laser Diagnostics and Photochemical Processing for Semiconductor Devices*, edited by R. M. Osgood, S. R. J. Brueck, and H. R. Schlossberg (North–Holland, New York, 1983), p. 177.
[5]M. Halmann, J. Chem. Soc. **1963**, 2853.
[6]I. A. Frolov, B. L. Druz', P. B. Boldyrevskii, and E. B. Sokolov, Izv. Akad. Nauk SSSR Neorg. Mater. **13**, 906 (1977).
[7]N. Pütz, H. Heinecke, E. Veuhoff, G. Arens, M. Heyen, and P. Balk, J. Cryst. Growth **68**, 194 (1984).
[8]V. M. Donnelly, in *Laser Chemical Processing of Semiconductor Devices*, edited by F. A. Houle, T. F. Deutsch, and R. M. Osgood (Materials Research Society, Pittsburgh, PA 1984), p. 15.
[9]M. G. Jacko and S. J. W. Price, Can. J. Chem. **41**, 1560 (1963).
[10]M. G. Jacko and S. J. W. Price, Can. J. Chem. **42**, 1198 (1964).
[11]See, for example, F. A. Cotton and G. Wilkinson, *Advanced Inorganic Chemistry* (Wiley–Interscience, London, 1966).
[12]J. Haigh and S. O'Brien, J. Cryst. Growth **68**, 550 (1984).
[13]J. Haigh and S. O'Brien, J. Cryst. Growth **67**, 75 (1984).
[14]D. H. Reep and S. K. Ghandhi, J. Electrochem. Soc. **130**, 675 (1983).
[15]M. R. Leys and H. Veenvliet, J. Cryst. Growth **55**, 145 (1981).
[16]See, for example, *Modern Developments in Fluid Dynamics Vol. I*, edited by S. Goldstein (Dover, New York, 1965).
[17]M. Koppitz, O. Vestavik, W. Pletschen, A. Mircea, M. Heyen, and W. Richter, J. Cryst. Growth **68**, 136 (1984).
[18]R. H. Moss and J. S. Evans. J. Cryst. Growth **55**, 129 (1981).
[19]J. Haigh, J. Mater. Sci. **18**, 1072 (1983).

AD-A170 797 PROCEEDINGS OF THE TOPICAL MEETING ON THE MICROPHYSICS OF SURFACES BEAMS A..(U) OPTICAL SOCIETY OF AMERICA WASHINGTON D C J W QUINN 10 DEC 85 AFOSR-TR-86-0469 2/3

UNCLASSIFIED AFOSR-85-0018 F/G 7/4 NL

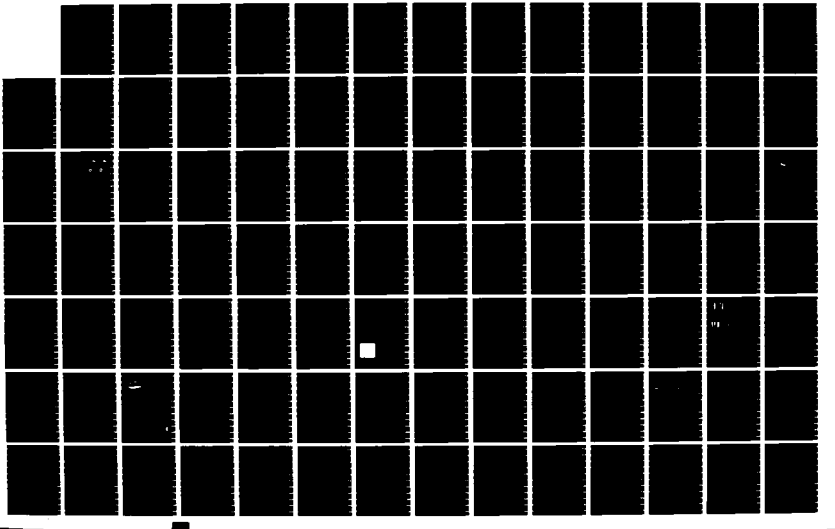

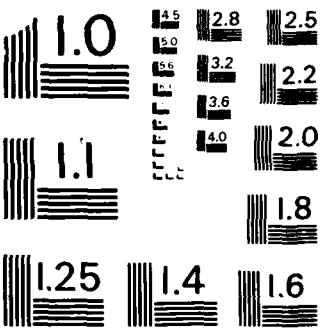

Surface photochemical phenomena in laser chemical vapor deposition

G. S. Higashi and L. J. Rothberg
AT&T Bell Laboratories, Murray Hill, New Jersey 07974

(Received 18 March 1985; accepted 21 May 1985)

The role of surface adsorbate photochemistry in laser assisted Al film growth by photodecomposition of trimethylaluminum is investigated using a pulsed optoacoustic apparatus. The technique permits *in situ* measurements of the vibrational spectra of surface adsorbates on single crystal sapphire even under the ambient pressures typical of laser chemical vapor deposition. We characterize the initial sapphire surface and follow the nucleation and growth of photodeposited films to obtain a microscopic understanding of the growth mechanism. We show that high quantum yield nonthermal photodesorption of methyl groups from growth surfaces occurs with 193 nm irradiation and can be used to produce Al films of higher quality. Features of the vibrational spectra are shown to be correlated with macroscopic properties of metallic films grown under the same conditions and can be used to identify and evaluate the parameters important to high quality film growth.

I. INTRODUCTION

Scientific and technological interest in surface photochemistry has stimulated many recent experiments.[1-3] One area where light-induced adsorbate chemistry has been postulated as an important process is in laser chemical vapor deposition from organometallics. In particular, observations of metal film localization by preirradiation of a surface in vacuum[4] and of surface enhanced photodissociation[5,6] suggest an important role for the surface adsorbates in film nucleation. Some experiments, however, indicate that the bulk of deposition can be explained completely by gas phase photodecomposition of the organometallics.[7,8]

A more detailed investigation of surface processes is hampered by the lack of a surface sensitive tool which is capable of probing absorbate structure and composition while remaining unimpeded by the presence of the ambient organometallic vapor. We have adapted a pulsed optoacoustic technique[9] to monitor vibrational spectra of adsorbates on infrared transparent substrates.[8] Our apparatus has submonolayer sensitivity to surface species containing C–H or O–H bonds *even under several Torr of vapor.*

In the present paper we use the optoacoustic surface spectra to study surface photochemistry and its role in laser chemical vapor deposition (CVD) of aluminum from trimethylaluminum (TMA). We report a direct observation of high quantum yield nonthermal photodissociation of organometallic species adsorbed to single crystal sapphire induced by 193-nm laser radiation. This has potential implications for the quality of Al film growth by laser CVD and for the ability to laser "write" spatially localized metallic features. In view of this, we have investigated the surface during *in situ* CVD of Al films via 193 nm photodecomposition of TMA. The results of these experiments are contrasted with analogous experiments using 248-nm radiation both in terms of the microscopic details of the growth surfaces and in terms of the resulting film properties. It is also found that deposition temperature has dramatic effects on both the surface spectra and the properties of macroscopic films.

II. EXPERIMENTAL

A brief description of our apparatus follows and a more detailed account will be presented elsewhere.[10] The source of tunable infrared radiation is a Nd^{+3} : YAG pumped pulsed dye laser (620–660 nm with DCM dye) which is Raman shifted in high pressure H_2 gas to obtain third Stokes radiation between 2.7 and 3.4 μm. At the maximum ($\sim$ 2.9 μm) we obtain about 300 μJ per pulse, dropping to about 50 μJ at the ends of the quoted wavelength range. This radiation is focused at near normal incidence onto a sapphire substrate to which a piezoceramic transducer is bonded. The transducer and substrate are mounted on electrical feedthroughs in a stainless-steel metal gasket sealed chamber with base pressure of 10^{-8} Torr.

Absorption of the light by the sample results in thermal expansion which creates acoustic waves. These expansions and compressions are translated into oscillatory voltages by the piezoelectric transducer and amplified. The resulting waveforms are filtered, sampled by a boxcar integrator, and divided by the light intensity to obtain normalized spectra and to correct for pulse-to-pulse laser fluctuations. The signal-to-noise ratio is approximately unity for 10 nJ of absorbed energy per pulse before signal averaging.

The sapphire is solvent degreased with trichloroethane, acetone, and methanol and then acid etched prior to use. The etch used is the "piranha" etch (15% H_2O_2, 35% H_2O, and 50% H_2SO_4) and after being rinsed in deionized water, the sample is dried in N_2 and inserted into the vacuum chamber. The trimethylaluminum used was purchased from Alfa Ventron and the ultraviolet (UV) radiation is obtained from an excimer laser which delivers 10-ns pulses at 248 or 193 nm.

III. RESULTS AND DISCUSSION

After evacuation and overnight baking at 140 °C, the infrared optoacoustic spectrum of the sample looks like that of Fig. 1(a). The sharp peaks between 3200 and 3500 cm^{-1} are bulk absorptions of the sapphire. They are unmodified by chemical treatments of the surface and vary from wafer to

 0734-211X/85/051460-04$01.00

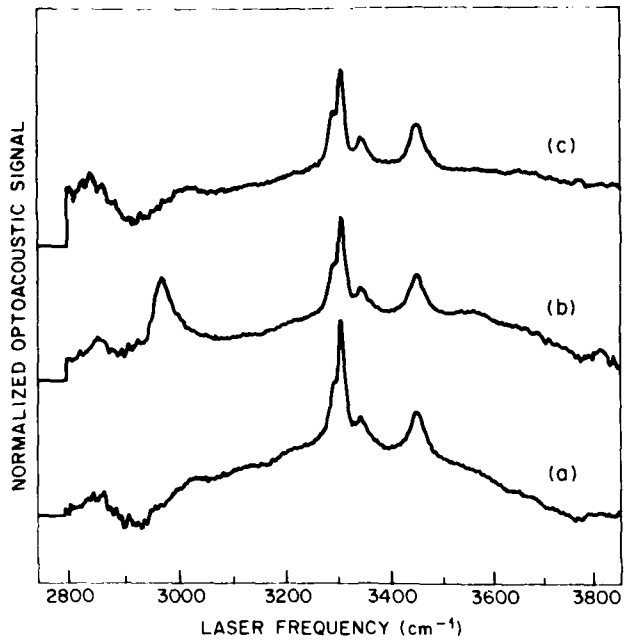

FIG. 1. Effect of 193-nm irradiation in vacuum on $Al(CH_3)_3$ complexes adsorbed to sapphire. (a) Acid etched and baked sapphire surface. (b) After repetitive flushing and dosing with TMA at 250 mTorr and evacuation. (c) After 18 000 laser pulses at 193 nm 15 mJ/cm^2 fluence.

wafer. The broad underlying absorption between 3000 and 3600 cm^{-1} is due to adsorbed hydrogen-bonded OH groups. We estimate the coverage shown to be about a monolayer by performing an adsorption isotherm and associating the knee in the optoacoustic signal intensity versus pressure curve with a monolayer. The spectral shape of these hydrogen-bonded OH groups is similar to those observed on porous glasses[11,12] and that observed for liquid water. By looking at the infrared spectrum near 3000 cm^{-1}, we see that this surface is relatively free of C–H bonds. The slight rise in the spectrum below 2850 cm^{-1} is due to light being scattered into the piezoelectric transducer. It should be noted that irradiation of this surface at 193 nm has no effect,[13] not surprising since neither sapphire nor OH absorb appreciably at this wavelength.

Following repeated TMA dosing at 250 mTorr and evacuation of the chamber (5 cycles), trace 1(b) describes the surface. Two changes in the surface spectrum are evident; the O-H signal intensity decreases slightly ($\sim$ 20%) and a feature appears in the C-H stretching region of the spectrum ($\sim$ 3000 cm^{-1}). The vapors of TMA and H_2O are known to react violently to form aluminum oxides and methane. It is therefore curious that only a small fraction of the surface hydroxyl groups have reacted away even for these large TMA exposures. Similar observations have been made for hydrogen-bonded O-H groups on the porous glasses.[11] The feature observed at $\sim$ 2960 cm^{-1} can be clearly identified as the asymmetric C-H stretching vibration of a methyl group bonded to an Al atom by both its spectral position[14] and its reactivity on exposure to vapors of H_2O. Note that the corresponding symmetric stretching vibration ($\sim$ 50 cm^{-1} lower in frequency) ordinarily present in gas phase TMA in nearly equal intensity is absent. Although we have ascertained that this effect is not due to a preferential orientation of the surface adsorbates by performing a polarization experiment, the origin of this phenomenon is not understood at this time.

The methyl coverage in Fig. 1(b) is estimated to be a monolayer by observing a knee in the adsorption isotherm taken using optoacoustic signal intensity vs ambient TMA pressure in our apparatus. This is not a rigorous procedure since we infer that at least some of the TMA reacts with adsorbed OH. The signal level of Fig. 1(b) for the C-H stretching mode absorption also corresponds approximately to the absorbance one would calculate for a monolayer of methyl groups. There is, in any case, considerable variation in the amount of organometallic adsorption which occurs that depends on sample history. Whether this is an effect of surface chemistry or the result of changing surface morphology is currently under study.

The result of irradiating this surface in vacuum at 193 nm is shown in Fig. 1(c). This illumination leads to a drastic reduction in surface methyl content and is accompanied by the removal of the curvature in the spectrum between 3000 and 3700 cm^{-1} which corresponds to the disappearance of surface OH groups. At the same time, a broad background absorption appears which spans our spectral range. We interpret these observations as follows: First, the incident UV radiation dissociates the organometallic adsorbates and causes the methyl groups to desorb. The reactive unsaturated Al getters the surface OH and excess Al diffuses and coalesces into clusters of sufficient size to have "metallic" optical properties.

Studies of surface phase photodissociation are motivated by both technological and fundamental interest in laser-induced electronic chemistry of adsorbates. Direct observations of photodissociation of surface adsorbates have recently been reported by Bourdon *et al.*,[15] and also by Foord and Jackman,[16] for the CH_3Br on LiF(100) and $Fe(CO)_5$ on Si(111) systems, respectively. As in the above studies, the photostimulated adsorbate reaction we observe is nonthermal and probably occurs in a rapidly dissociative excited state before energy is dissipated by relaxation into the substrate. The nonthermal nature of this photoinitiated adsorbate reaction was demonstrated experimentally by performing surface irradiations at two drastically different fluences. The same methyl decreases are observed at a fluence per pulse of 10 mJ/cm^2 as at 0.1 mJ/cm^2 if one compensates for the difference in fluence by using 100 times as many excimer laser pulses at the lower fluence. This observation not only shows that the process is linear but that the process must also be nonthermal. The pulsed temperature rise is calculated to be less than 5 °C even at the highest fluences we use, providing additional evidence that the process is nonthermal.

It is important to point out that although the process is linear, the decrease in the surface methyl content with excimer laser irradiation at 193 nm is nonexponential. That is to say, it becomes increasingly harder to remove successive methyl units from the surface. This may be because we have several adsorbed organometallic species initially or because each successive methyl group is more difficult to desorb even

from a single molecular species. Kinetic and/or bond orientation effects also cannot be ruled out since our initial surfaces are disordered. While the nonexponential removal of surface methyl groups means the assignment of photodissociation cross sections and quantum yields are not strictly meaningful, we can say that the initial yields we calculate are near unity if we assume the surface absorption cross section at 193 nm to be the same as for gas phase TMA ($\sim 2\times10^{-17}$ cm^2).

Having observed efficient photodecomposition of our organoaluminum adsorbate, it is interesting to ask whether macroscopic films can be deposited via photolysis of these chemisorbed layers alone. Repeated cycles of TMA surface exposures followed by vacuum illumination at 193 nm results in continued metallic absorption growth with virtually no growth in the hydrocarbon region of the spectrum. Under these conditions film growth is entirely dominated by surface adsorbate photodecomposition and suggests the feasibility of growing highly localized high quality Al films.

Obtaining high quality photodeposited Al films has been a long standing problem and only one group has been successful so far.[17] In a previous experiment[8] we demonstrated that, under typically used growth conditions, the degree of methyl contamination of the films photodeposited using 248 nm light was very high. In the present study, since we observe methyl desorption from our surfaces leading to films which are relatively free of hydrocarbon contaminants, it is instructive to observe our growth surfaces using light at 193 nm under conventional growth conditions.

The results of these *in situ* studies of our growth surfaces are shown in Fig. 2. The bottom spectrum [Fig. 2(a)] represents our initial surface after exposure to TMA. Note that the spectrum differs from that of Fig. 1(b) in that the methyl region exhibits two peaks which are much weaker than the single peak of Fig. 1(b), and that the O-H absorption is also significantly reduced. The strength of the peaks is correlated with substrate history, the least used samples exhibiting the largest peaks. The appearance of two peaks (both the symmetric and asymmetric C-H stretching modes) on TMA dosing of our surfaces is rare but we illustrate it here to show that there is significant sample-to-sample variation we do not yet understand. Nonetheless, the results of surface illumination at 193 nm in the presence of TMA vapor remain essentially unaffected by the initial surface.

Figures 2(b) and 2(c) represent surfaces having been illuminated by successively higher doses of 193 nm radiation under 100 mTorr of TMA. Growth of the metallic background is observed, again coincident with the disappearance of the hydrogen-bonded O-H absorption, but the films are badly methyl contaminated. Thus even high quantum efficiency methyl desorption does not compete effectively with organoaluminum adsorption with 100 mTorr ambient TMA.

The question of whether methyl contaminants can now be removed by vacuum illumination is addressed by the experiment of Fig. 2(d). The result of a 193-nm surface irradiation with 10^5 pulses at 10 mJ/cm^2 is striking. Not only can one remove methyl contaminants by this procedure but, as seen in the spectrum, one also increases the metallic background

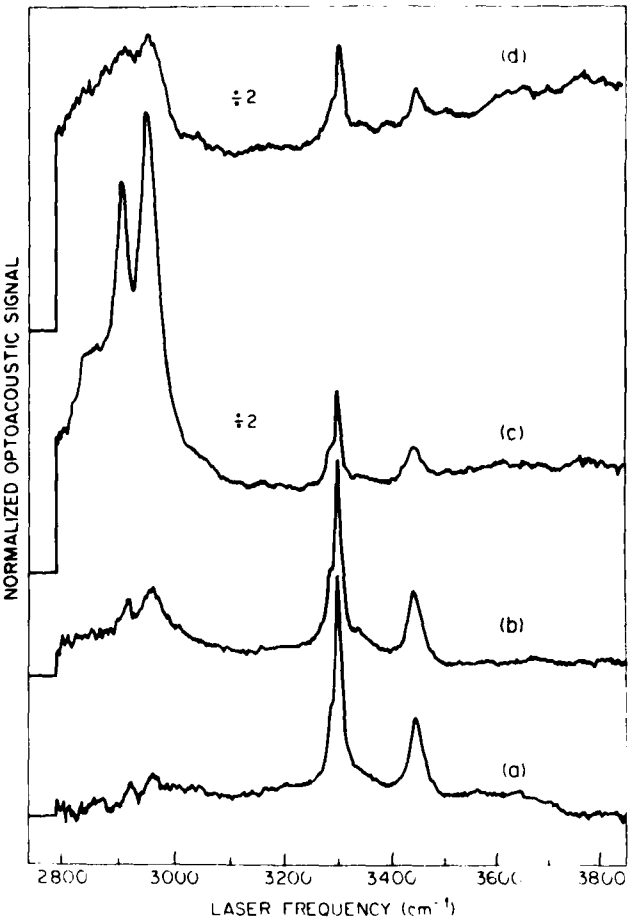

FIG. 2. *In situ* spectra of growth surfaces during 193-nm irradiation in ambient TMA. (a) TMA dosed surface in vacuum. (b) After 1000 laser pulses at 193 nm with 0.3 mJ/cm^2 fluence under 100 mTorr TMA. (c) After 10 000 laser pulses at 193 nm with 0.3 mJ/cm^2 fluence under 100 mTorr TMA. (d) After 100 000 more laser pulses at 193 nm with 10 mJ/cm^2 fluence in vacuum.

absorption. The enhanced metallic optical properties due to film densification cannot only be seen using our photoacoustic technique, but can be seen by eye. Clearly, methyl contaminants are incorporated into the film since they help to satisfy Al atom bond requirements, but they block the formation of a true metallic matrix. Removing these contaminants via photolytically driven methyl desorption allows Al atoms/clusters to coalesce and form films of enhanced metallic properties. Our *in situ* growth studies at 248 nm[8] showed that surface irradiation under vacuum was ineffective at removing methyl contaminants. In that case, no changes occur in the magnitude of the broad metallic absorption. Given these observations it is easy to understand why high quality Al films have been so difficult to laser deposit. $Al(CH_3)_x$ contamination is a severe problem at both 193 and at 248 nm, and results in a porous metallic/organometallic matrix exhibiting poor conductivity.

We have observed that film quality is improved by growth at higher temperatures. Several factors may contribute to this including changes in surface mobility, contaminant adhesion and activation barriers to clustering. In addition, the efficiency of TMA photolysis may be substantially altered

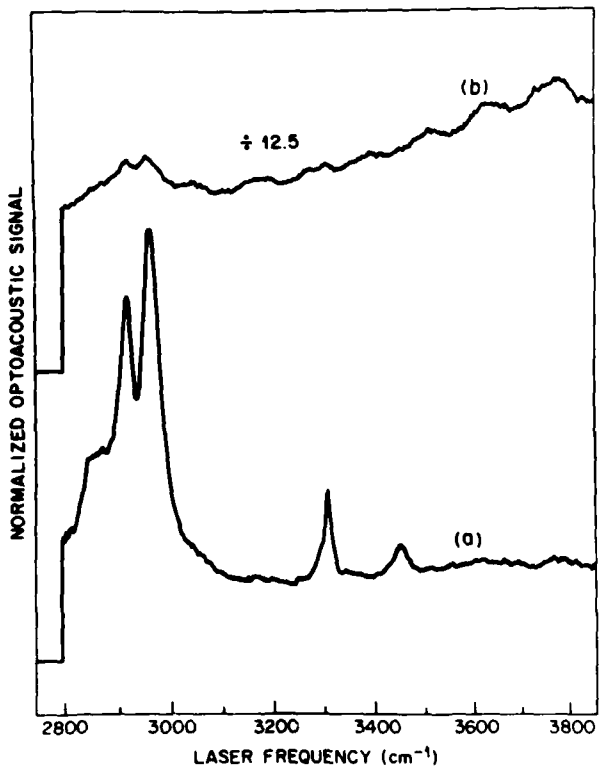

FIG. 3. Effects on temperature on metallic film growth. (a) After 10 000 laser pulses at 193 nm with 0.3 mJ/cm^2 fluence under 100 mTorr [see Fig. 2(c)]. (b) After 10 000 laser pulses at 193 nm with 0.35 mJ/cm^2 fluence under 100 mTorr at 140 °C (after evacuation).

when it becomes predominantly a monomer at higher temperatures (>100 °C).[18] We have, therefore, compared growth surfaces at room temperature to those at elevated chamber temperature. Figure 3(a) is the spectrum of Fig. 2(c) replotted for reference. Figure 3(b) shows the result of irradiation under the same TMA pressure (100 mTorr) with an equal number of photons at 193 nm, but now at 140 °C. In contrast to the room temperature growth, the metallic absorption dominates the methyl contaminant absorption.[19] Many mechanisms can in principle give rise to improved properties at higher temperature and it is difficult to ascertain their relative importance. It is likely, however, that surface mobility plays a crucial role in the metallic growth process since coalescence must be important in producing high quality films.

IV. SUMMARY

We have applied pulsed optoacoustic spectroscopy to measure infrared absorption of surface adsorbates. The sensitivity of the technique allows us to observe nonthermal photodissociation of monolayer coverages of organometallic adsorbates on single crystal sapphire. The high quantum yield photostimulated methyl desorption allows one to envision surface adsorbate dominated photochemical growth of high quality spatially localized films. A unique property of the optoacoustic measurement is that it retains its surface specificity under ambient vapor. It can therefore be used *in situ* to monitor growth by laser chemical vapor deposition. We have recorded vibrational spectra of growth surfaces during Al deposition from photodecomposition of TMA and find that under commonly used growth conditions films show a severe degree of methyl contamination. Our spectra show that the level of contamination can be reduced by illuminating the surface in vacuum or by raising the growth temperature. We observe independently that these treatments also have beneficial effects on macroscopic electrical and optical film properties.

[1] D. J. Ehrlich, R. M. Osgood, and T. F. Deutsch, IEEE J. Quantum Electron **QE-16**, 1233 (1980).
[2] D. J. Ehrlich and J. Y. Tsao, J. Vac. Sci. Technol. B **1**, 969 (1983).
[3] T. J. Chuang, Surf. Sci. Rep. **3**, 1 (1983).
[4] D. J. Ehrlich, R. M. Osgood, Jr., and T. F. Deutsch, Appl. Phys. Lett. **38**, 946 (1981).
[5] C. J. Chen and R. M. Osgood, Jr., Phys. Rev. Lett. **50**, 1705 (1983).
[6] G. M. Goncher and C. B. Harris, J. Chem. Phys. **77**, 3767 (1982).
[7] T. H. Wood, J. C. White, and B. A. Thacker, Appl. Phys. Lett. **42**, 408 (1983).
[8] G. S. Higashi, L. J. Rothberg, and C. G. Fleming, Chem. Phys. Lett. **115**, 167 (1985).
[9] C. K. N. Patel and A. C. Tam, Rev. Mod. Phys. **53**, 517 (1981).
[10] G. S. Higashi and L. J. Rothberg, Appl. Phys. Lett. (submitted).
[11] D. J. C. Yates, G. W. Dembinski, W. R. Kroll, and J. J. Elliott, J. Phys. Chem. **73**, 911 (1969).
[12] R. J. Peglar, F. H. Hambleton, and J. A. Hockey, J. Catal. **20**, 309 (1971).
[13] There is, however, some effect on the intensity of the peaks associated with bulk sapphire absorption.
[14] Our quoted dye laser frequencies are approximately 20 cm^{-1} too high as deduced by a comparison of our gas phase infrared absorption spectrum of TMA with A. P. Gray, Can. J. Chem. **41**, 1511 (1963).
[15] E. B. D. Bourdon, J. P. Cowin, I. Harrison, J. C. Polanyi, J. Segner, C. D. Stanners, and P. A. Young, J. Phys. Chem. **88**, 6100 (1984).
[16] J. S. Foord and R. B. Jackman, Chem. Phys. Lett. **112**, 190 (1984).
[17] R. Solanki, W. H. Ritchie, and G. J. Collins Appl. Phys. Lett. **43**, 454 (1983).
[18] R. J. O'Brien and G. A. Ozin, J. Chem. Soc. A **9**, 1136 (1971).
[19] The slow periodic variation in the signal has to do with periodic fluctuations in the infrared laser intensity with wavelength which are not completely normalized out by our boxcar integrator.

Surface studies by optical second harmonic generation: An overview

Y. R. Shen
Department of Physics, University of California, Berkeley, California 94720
Materials and Molecular Research Division, Lawrence Berkeley Laboratory, Berkeley, California 94720

(Received 18 March 1985; accepted 21 May 1985)

Optical second harmonic generation for surface and interface studies is briefly reviewed, with numerous examples illustrating how powerful and versatile this new surface analytical technique can be.

It has recently been established that optical second harmonic generation (SHG) can be an effective tool for surface and interface studies.[1] The technique has the advantages of being relatively simple, nondetrimental, and capable of remote sensing. It has a submonolayer sensitivity, and can be used to probe *in situ* surface ordering and symmetry as well as molecular arrangement and orientation at any interface between two media with inversion symmetry. Being a process of nearly instantaneous response, SHG is also potentially useful for studies of surface reactions and dynamics.

The basic principle behind the idea of employing SHG for surface studies is fairly simple.[2] In a medium with inversion symmetry, SHG is forbidden in the bulk under the electric-dipole approximation, but the opposite is always true in a surface layer, which, by definition, is centroasymmetric. Thus, intrinsically, SHG is a highly surface-specific process in media with inversion symmetry.

Any viable surface tool should have a sensitivity that can detect at least a molecular monolayer. That SHG is indeed so sensitive can easily be seen from an estimate using the solution of Maxwell equations for SHG from a molecular monolayer with a surface density of 10^{15} molecules/cm^2 and a second-order nonlinear polarizability of 10^{-30} esu/molecule.[2] The second harmonic (SH) signal is as large as 10^4 photons/pulse if a pump laser pulse with a pulsewidth of 10 ns and an energy of 20 mJ at 1.06 μm focused to 0.2 cm^2 is used. Such a signal is readily detectable.

Surface SHG from media with inversion symmetry was a subject of extensive investigation in the 60's.[3-9] Emphasis was on the understanding of the surface nonlinear optical process itself and the origins of surface nonlinearities. Unfortunately, in most cases with metals and semiconductors the surfaces under investigation were not carefully prepared, and the results were often not very conclusive. In a few cases where the surfaces were better defined, the theoretical understanding was not advanced enough to render the results useful. Thus, although the submonolayer sensitivity of SHG was recognized in a few cases, little attempt was made to develop SHG into a viable surface tool.

The renaissance of surface SHG came somewhat accidentally in 1980, when surface-enhanced Raman scattering attracted increasing attention in the physics community.[10] Controversy existed over whether the unusually strong surface enhancement on some metals arose from the surface local-field enhancement or from the molecule-metal interaction. It was realized that if surface local-field enhancement is the dominant mechanism, then SHG from a roughened metal surface should also exhibit a strong surface enhancement. In this case, adsorbed molecules are not needed, and hence the molecule-metal interaction can be eliminated. Indeed, a surface enhancement of 10^4 for SHG from a roughened Ag surface was observed experimentally.[11]

It was then obvious that with such a large surface enhancement, SHG from a submonolayer of adsorbed molecules at a roughened metal surface can be easily detected, and it can be used to probe molecular adsorption and desorption at a metal electrode in an electrolytic cell.[12-14] This provides a new tool for electrochemical studies. The very fast response of the technique allows time-dependent measurements of molecular adsorption and desorption at an electrode.[15] The double-charge layer existing at the electrode/electrolyte interface can also have an effect on SHG. This is most easily seen at a smooth electrode surface. The field of the double-charge layer leads to a field-induced SH signal which varies with the bias potential on the electrode.[16,17] In the case where the SH signal arising directly from the adsorbed molecules or ions is negligible, the result of SHG versus the bias potential can be used to deduce the dc field strength in the double-charge layer, and the corresponding ionic charges adsorbed at the electrode.[18,19]

From the surface science point of view, the capability of SHG to detect a submonolayer of adsorbed molecules on a smooth surface is more interesting because the surface under investigation can then be better characterized. We consider two cases here: one with an induced nonlinearity due to molecular adsorption dominated by the nonlinearity of the adsorbed molecules, and the other with an induced nonlinearity dominated by the molecule-substrate interaction.[2] We discuss the two cases separately below.

In the first case, SHG can be used to probe the symmetry of molecular arrangement on the substrate by simply observing the variation of the SH signal as a function of sample rotation about its surface normal. For example, an SH signal independent of the azimuthal rotation often implies an isotropic arrangement in the two-dimensional space, although an n-fold symmetry with $n \geqslant 4$ is also possible. This has been demonstrated in a number of cases with molecules adsorbed at air/solid,[20,21] liquid/solid,[21] and air/liquid interfaces.[22] SHG can also be used to deduce information about the orientation of molecules at an interface based on the following simple idea. If the local-field correction on the adsorbed molecules is negligible, then the macroscopic nonlinear susceptibility $\chi^{(2)}_{ijk}$ is related to the microscopic nonlinear polarizability $\alpha^{(2)}_{\xi\eta\zeta}$ by a simple coordinate transformation[2]

$$\chi^{(2)}_{ijk} = N \langle G^{\xi\eta\zeta}_{ijk}(\Omega) \rangle \alpha^{(2)}_{\xi\eta\zeta}, \tag{1}$$

 0734-211X/85/051464-03$01.00

where $G_{ijk}^{\xi\eta\zeta}(\Omega)$ describes the transformation from the molecular coordinates (ξ,η,ζ) to the lab coordinates (i,j,k) for a molecule whose orientation is specified by Ω, and $\langle\rangle$ denotes the average over the orientational distribution of the N molecules per cm^2. From Eq. (1), it is seen that if $\alpha_{\xi\eta\zeta}^{(2)}$ are known (or in some cases, if a particular element of $\tilde{\alpha}^{(2)}$ dominates), and if $x_{ijk}^{(2)}$ can be measured using various polarization combinations, then $\langle G_{ijk}(\Omega)\rangle$ can be determined and an average molecular orientation can be deduced. Such measurements of molecular orientation have been performed on molecules at air/solid,[20,21] liquid/solid,[21] and air/liquid[22] interfaces. In the latte ase, the technique was used to study how the orientation of surfactant molecules varies with the surface molecular density.

If the molecular orientation is independent of the surface molecular density so that $x_{ijk}^{(2)}$ is directly proportional to N, the SHG can be used to obtain adsorption isotherms for adsorbants. Adsorption of paranitrobenzoic acid (PNBA) at an ethanol/fused quartz interface is an example.[21] By varying the concentration of PNBA in ethanol and measuring SHG from PNBA adsorbed at the ethanol/quartz interface, the adsorption isotherm can be deduced. From the SH signal corresponding to a saturated monolayer coverage, the second-order nonlinear polarizability averaged over the molecular orientation can also be obtained.

Spectroscopic studies of adsorbed molecules by SHG are possible with a tunable laser source. As an example, the $S_0 \rightarrow S_2$ electronic transitions of some rhodamine dye molecules adsorbed to fused quartz have been measured by SHG via resonant enhancement.[20] Vibrational spectroscopy of adsorbed molecules by SHG can in principle be carried out with a tunable infrared laser. It is unfortunately limited by the insensitivity of the available infrared photodetectors. As a variation of the technique, sum frequency generation, from mixing of IR and visible laser inputs, instead of SHG appears to be promising for surface vibrational spectroscopy.[23]

We now turn to the case where the adsorbate-substrate interaction dominates the induced surface nonlinearity. This generally happens when the adsorbates are atoms or small molecules. It has been found that SHG is also useful for probing these kinds of adsorbates. For illustration a number of experiments have been performed to study atomic and diatomic molecular adsorption on well-characterized metal and semiconductor surfaces in ultrahigh vacuum.[24-28] It was shown that when a clean Rh(111) surface was exposed to oxygen or CO, the SH signal from the Rh surface dropped sharply, and approached a constant as the adsorbates formed a saturated monolayer monitored by the low energy electron diffraction (LEED).[24] That SHG has a submonolayer sensitivity to detect oxygen and CO on Rh(111) is therefore obvious. In the case of CO, it was found that SHG was also site specific, i.e., it would respond to molecules adsorbed at different sites on the surface.[24] Because of the different molecule-substrate interactions, the nonlinearities for molecules adsorbed at different sites are necessarily different.

The SH signal from a surface as a function of exposure (in Langmuir units) can be used to study the adsorption kinetics.[24] In the case of oxygen on Rh(111), for example, the result was found to agree well with the prediction of a simple Langmuir kinetic model. From the theoretical fit with experiment, the sticking coefficient of oxygen on Rh(111) and the induced nonlinearity per adsorbed oxygen could be deduced. The same Langmuir model also describes the adsorption of CO on Ni(100) and Cu(111).[27] Knowing how the SH signal varies with surface coverage, the SHG technique can be used to directly measure the surface density of molecules. This was demonstrated in a recent work comparing the results of thermal desorption spectroscopy (TDS) of CO on Ni(100) and Cu(111) with those of SHG.[27] In TDS, CO molecules desorbed from the surface by thermal heating were monitored by a mass spectrometer as a function of temperature. From an integration of the thermal desorption curves, the surface densities of molecules left on the surfaces could be calculated. They appeared to be in excellent agreement with those obtained from the SHG measurements. SHG as a technique to monitor surface coverage has, however, the advantage of having a time response much faster than the conventional surface tools. It therefore has the potential of being a viable method for dynamic studies of molecular adsorption and desorption.

The SH signal from a metal surface generally decreases upon adsorption of oxygen and CO. This is presumably because the surface nonlinearity of a metal is dominated by the nearly free electrons at the metal surface, and is reduced by the partial localization of such electrons upon adsorption of electron acceptors such as oxygen and CO. One would then expect that adsorption of electron donors on a metal surface should strongly enhance the surface nonlinearity. This was indeed observed when alkali atoms were adsorbed on Rh(111).[28] The measured SH signal as a function of surface coverage of alkali atoms, however, showed rather complicated behavior. In particular, the results obtained with 1.06 μm and 0.532 μm laser excitations were quite different, and the signal increase due to alkali adsorption at low surface coverages, observed with the 1.06 μm excitation, was much stronger than that expected from the free-electron model. These results can only be understood by taking transitions between hybridized adsorbate-metal states into full consideration and realizing that they change continuously with surface coverage.[29] Thus, surface SHG may also become a viable technique for studying hybridized electronic states of adsorbates on a substrate. In the same experiment, it was also found that the SH signal from the alkali-covered Rh surface approached a constant when the surface coverage reached above two hexagonal-close-packed layers. This indicated that the surface nonlinearity was completely dominated by the two top alkali monolayers. The result is therefore a clear manifestation of the surface specificity of SHG.

Surface SHG can also be used to probe adsorbates on Si and Ge. The submonolayer sensitivity of the technique was first noticed by Chen *et al.*[8] In more recent experiments, SHG was used to monitor oxidation of clean Si(111) surfaces in ultrahigh vacuum.[25,26] Upon adsorption of oxygen and Pd, the SH signal dropped sharply and approached a constant at nearly a monolayer coverage. The adsorption appeared to follow the Langmuir kinetic. At high temperatures, oxide multilayers were formed at the surface, but the

SH signal did not change very appreciably. This shows that SHG applied to homopolar semiconductor surfaces is also highly surface specific. The result can be qualitatively understood as follows. It is known that dangling bonds exist on clean Si surfaces. These bonds are highly nonlinear because of the very asymmetric charge distribution on the bonds. They are therefore responsible for the large surface nonlinearity of Si. Upon adsorption of oxygen or Pd, the dangling bonds are quenched and the surface nonlinearity is reduced.

SHG can also be used to probe the ordering and structural symmetry of a bare surface. As we mentioned earlier, the SH signal as a function of sample rotation about the surface normal (or equivalently, rotation of beam polarizations about the surface normal) is expected to reflect the structural symmetry of a surface layer. This was demonstrated in the studies of Si(111) surfaces. The threefold symmetry of a 1×1 Si(111) surface could be readily identified.[30] In a recent experiment, SHG was used to study the symmetry of reconstructed Si(111) surfaces.[26] The 2×1 reconstruction of a freshly cleaved surface exhibited a clear twofold symmetry with a single mirror plane along the $[2\bar{1}1]$ direction in agreement with the π-bonded chain model. After annealing, the 2×1 surface was transformed to a 7×7 surface, and the change from a twofold symmetry to a threefold symmetry was easily detected by SHG. The fast response of SHG also allowed real-time monitoring of the phase transformation from the 2×1 surface to the 7×7 surface induced by annealing.

Melting of a solid surface can also be probed by SHG, since the nonlinearities of crystalline and liquid surfaces are necessarily different. The nearly instantaneous response of SHG suggests that the technique is ideal for real-time monitoring of laser-induced melting of a surface. This was demonstrated in the study of a Si(111) surface.[31] Upon melting, the threefold symmetry of the (111) surface reflected in the SH signal disappeared. It was found, using picosecond pump and probe pulses, that the entire melting process occurred in less than 3 ps. SHG was also used to probe laser-induced melting of GaAs surfaces.[32,33] The result indicated that the induced melting also occurred in less than 2 ps.

The many experiments we have discussed here are examples of how powerful and versatile SHG as a surface tool can be. Yet the application of SHG to surface studies is still in the infant stage. It is quite obvious that SHG as a surface spectroscopy technique should be further developed. Resonant SHG with a tunable laser source could provide a technique with sufficient selectivity to distinguish different molecular adsorbates. With ultrashort laser pulses, SHG has the prospect of becoming an effective tool for surface dynamic studies in the subpicosecond regime. That SHG can then be used for *in situ* probing of catalytical reactions and dynamics is undoubtedly most exciting. On the theoretical side, there are also many questions yet to be answered. Theoretical understanding of the microscopic origins of surface nonlinearities is clearly most important. The surface local-field problem has been treated classically,[34] but a more rigorous quantum-mechanical solution is needed.

Acknowledgment: This work was supported by the Director, Office of Energy Research, Office of Basic Energy Sciences, Materials Sciences Division of the U. S. Department of Energy under Contract No. DE-AC03-76F00098.

[1]See, for example, the review article by Y. R. Shen, in *New Laser and Optical Investigations of Chemistry and Structure at Interfaces*, edited by R. B. Hall and A. B. Ellis (Verlag Chemie, Berlin) (to be published).
[2]Y. R. Shen, *The Principles of Nonlinear Optics* (Wiley, New York, 1984), Chap. 25.
[3]F. Brown, R. E. Parks, and A. M. Sleeper, Phys. Rev. Lett. **14**, 1029 (1965); F. Brown and R. E. Parks, Phys. Rev. Lett. **16**, 507 (1966); F. Brown and M. Matsuoka, Phys. Rev. **185**, (1969).
[4]N. Bloembergen, R. K. Chang, and C. H. Lee, Phys. Rev. Lett. **16**, 986 (1966); N. Bloembergen, R. K. Chang, S. S. Jha, and C. H. Lee, Phys Rev. **174**, 813 (1968).
[5]S. S. Jha, Phys. Rev. Lett. **15**, 412 (1965); Phys. Rev. **140**, 2020 (1965).
[6]C. C. Wang and A. N. Duminski, Phys. Rev. Lett. **20**, 668 (1968); C. C. Wang, Phys. Rev. **178**, 1457 (1969).
[7]J. Rudnick and E. A. Stern, Phys. Rev. B **4**, 4274 (1971).
[8]C. S. Wang, J. M. Chen, and J. R. Bower, Opt. Commun. **8**, 275 (1973); J. M. Chen, J. R. Bower, C. S. Wang, and C. H. Lee, Opt. Commun. **9**, 132 (1973); J. M. Chen, J. R. Bower, and C. S. Wang, Jpn. J. Appl. Phys. Suppl. **2**, Pt. 2, 711 (1974).
[9]H. Sonnenberg and H. Heffner, J. Opt. Soc. Am. **58**, 209 (1968).
[10]See, for example, *Surface-Enhanced Raman Scattering*, edited by R. K. Chang and T. E. Furtak (Plenum, New York, 1982).
[11]C. K. Chen, A. R. B. de Castro, and Y. R. Shen, Phys. Rev. Lett. **46**, 145 (1981).
[12]C. K. Chen, T. F. Heinz, D. Ricard, and Y. R. Shen, Phys. Rev. Lett. **46**, 1010 (1981); Chem. Phys. Lett. **83**, 455 (1981); Phys. Rev. B **27**, 1965 (1983).
[13]D. V. Murphy, K. U. Von Raben, T. T. Chen, J. F. Owen, and R. K. Chang, Surf. Sci. **124**, 529 (1983).
[14]G. L. Richmond, Chem. Phys. Lett. **106**, 26 (1984); Surf. Sci. **147**, 115 (1984).
[15]T. F. Heinz, C. K. Chen, D. Ricard, and Y. R. Shen, Chem. Phys. Lett. **83**, 180 (1981).
[16]C. H. Lee, R. K. Chang, and N. Bloembergen, Phys. Rev. Lett. **18**, 167 (1967).
[17]Y. R. Shen, C. K. Chen, T. F. Heinz, and D. Ricard, in *Laser Spectroscopy V*, edited by A. R. W. McKellar, T. Oka, and B. P. Stoicheff (Springer, Berlin, 1981), p. 412.
[18]R. M. Corn, M. Romagnoli, M. D. Levenson, and M. Philpott, Chem. Phys. Lett. **106**, 30 (1984).
[19]G. R. Richmond, Chem. Phys. Lett. **110**, 571 (1984).
[20]T. F. Heinz, C. K. Chen, D. Ricard, and Y. R. Shen, Phys. Rev. Lett. **48**, 478 (1982).
[21]T. F. Heinz, H. W. K. Tom, and Y. R. Shen, Phys. Rev. A **28**, 1883 (1983).
[22]Th. Rasing, Y. R. Shen, M. W. Kim, P. Valint, and J. Bock, Phys. Rev. A **31**, 537 (1985).
[23]H. W. K. Tom, Ph.D. thesis, University of California, Berkeley, 1984 (unpublished).
[24]H. W. K. Tom, C. M. Mate, X. D. Zhu, J. E. Crowell, T. F. Heinz, G. Somorjai, and Y. R. Shen, Phys. Rev. Lett. **52**, 348 (1984).
[25]H. W. K. Tom, X. D. Zhu, Y. R. Shen, and G. A. Somorjai, in *Proceedings of the XVII International Conference on the Physics of Semiconductors, San Francisco, California* (Springer, Berlin, 1984), p. 99.
[26]T. F. Heinz, M. M. T. Loy, and W. A. Thompson, Phys. Rev. Lett. **54**, 63 (1985); also paper WA2-1 in Topical Meeting on Microphysics of Surfaces, Beams, and Adsorbates, Santa Fe, NM, February 1985.
[27]X. D. Zhu, Y. R. Shen, and R. Carr, Surf. Sci. (to be published).
[28]H. W. K. Tom, C. M. Mate, X. D. Zhu, J. E. Crowell, Y. R. Shen, and G. A. Somorjai, Surf. Sci. (to be published).
[29]N. D. Lang and A. R. Williams, Phys. Rev. Lett. **37**, 212 (1976).
[30]H. W. K. Tom, T. F. Heinz, and Y. R. Shen, Phys. Rev. Lett. **51**, 1983 (1983).
[31]C. V. Shank, R. Yen, and C. Hirlimann, Phys. Rev. Lett. **51**, 900 (1983).
[32]S. A. Akhmanov, N. I. Koroteev, G. A. Paitun, I. L. Shumay, M. F. Guljaudinov, and E. I. Shtyrkov, Opt. Commun. **47**, 202 (1983).
[33]A. M. Malvezzi, J. M. Liu, and N. Bloembergen, Appl. Phys. Lett. **45**, 1019 (1984).
[34]P. Ye and Y. R. Shen, Phys. Rev. B **28**, 4288 (1983).

Study of symmetry and disordering of Si(111)-7×7 surfaces by optical second harmonic generation

T. F. Heinz, M. M. T. Loy, and W. A. Thompson
IBM T. J. Watson Research Center, Yorktown Heights, New York 10598

(Received 15 February 1985; accepted 18 April 1985)

A detailed study of the polarization dependences of the second-harmonic generation process from clean Si(111)-7×7 surfaces is presented and analyzed in terms of the symmetry properties of the surface. Results from real-time, *in situ* measurements on disordering of the Si(111)-7×7 surface by oxidation and Ar^+ ion bombardment are also reported.

I. INTRODUCTION

The process of optical second-harmonic generation (SHG) from a centrosymmetric medium has been found to be highly sensitive to the character of its surface on an atomic level. This behavior arises from the fact that SHG is (electric-dipole) forbidden within the bulk of a centrosymmetric material, but is allowed in the surface region where the inversion symmetry is broken. Indeed, fractional monolayers of atomic[1,2] and molecular[2] adsorbates can be detected readily by SHG measurements. The SH technique has already proved useful for studying the spectroscopy[3] and orientation[4] of adsorbed molecules. Recently, we have demonstrated that the technique can also be applied to probe the symmetry of ordered crystalline surfaces through the polarization dependences of the surface SHG process.[5] For the case of clean Si(111) surfaces, the SH signals from the 2×1 and 7×7 reconstructions could be distinguished from one another and analyzed in terms of their differing symmetry properties. In this paper, we present a detailed discussion of the polarization dependences of the SHG process for the Si(111)-7×7 surface and report new results on the disordering of this surface induced by bombardment with energetic Ar^+ ions. From our real-time measurements of the SH signal, we are able to infer a value for the average area of the surface disordered by each incoming ion. Data are also reported for the oxidation of the Si(111)-7×7 surface.[6]

II. EXPERIMENTAL

The Si(111)-7×7 surfaces were prepared and studied in a standard ion-pumped ultrahigh vacuum chamber at a base pressure of $\sim 5\times10^{-11}$ Torr. The surfaces were obtained by cleaving *in situ* a high purity silicon bar (doped with boron at 10^{15} cm^{-3}) along the $[2\bar{1}\bar{1}]$ direction. The 7×7 reconstruction resulted from a heating cycle bringing the sample to ~600 °C. Low-energy electron diffraction and Auger electron spectroscopy were applied to verify the surface structure and cleanliness of the samples. The pump radiation for the SH measurements was supplied by a *Q*-switched Nd : YAlG laser operating at 1.06 μm and producing 8 ns pulses at a 10-Hz repetition rate. The laser radiation was directed at normal incidence onto the sample surface, where the beam was lightly focused to a diameter of ~1 mm. The laser energy was always maintained sufficiently low to avoid any photoinduced changes in the surface. For a pump pulse of ~10 mJ energy, the reflected SH radiation typically consisted of $\gtrsim 10^3$ photons. The SH signal was detected with a photomultiplier and gated electronics after being isolated spectrally by means of color filters and a monochromator.

III. WELL-ORDERED Si(111)-7×7 SURFACES

For the Si(111)-7×7 surface, the SH intensity has been recorded as a function of the orientation of the linearly polarized pump electric field vector. The data for the intensity of the SH output polarized along the two orthogonal $[2\bar{1}\bar{1}]$ and $[01\bar{1}]$ surface crystal axes have been presented previously.[5] In Fig. 1 we display the corresponding SH electric-field amplitude for the same two independent directions. The magni-

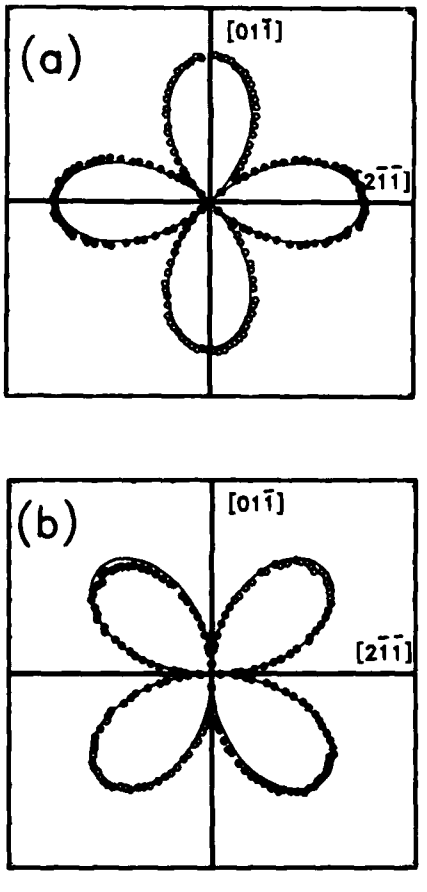

FIG. 1. SH electric field as a function of the angular orientation of the linearly polarized pump electric-field vector for a clean Si(111)-7×7 surface. The field amplitudes polarized along (a) the $[2\bar{1}\bar{1}]$ (x) direction and (b) the $[01\bar{1}]$ (y) direction. Open and filled points correspond to sign changes in the experimental data. The solid curves represent theoretical predictions for the magnitude of the SH electric field under $3m$ symmetry.

 0734-211X/85/051467-04$01.00

tude of the electric-field components is determined directly from the measured SH intensity, but the relative phase between them is not specified. To determine this relative phase, we examined data collected for the SH intensity with the output polarizer oriented midway between the two orthogonal axes, i.e., along the $[10\bar{1}]$ direction. From these data, we found that the SH electric field was linearly polarized. The changes in the relative phase of the two components indicated in Fig. 1 correspond to a smooth variation in the polarization of the SH radiation as the pump polarization is rotated. The open and filled points in the figure correspond to 180° phase differences in the electric-field amplitude.

The data in Fig. 1 completely characterize the SH electric field for any given polarizations of the pump laser. Consequently, we can transform these results into plots of the SH electric field components lying parallel and perpendicular to the polarization vector of the pump beam. This formulation of the experimental data reflects more directly the symmetry of the surface, since the curves can be viewed as having been obtained either by a rotation of the input and output polarizers with a sample fixed in space or, equivalently, by a rotation of the sample about its surface normal with fixed polarizers. Figure 2(a) displays the SH electric field polarized parallel to the pump polarization; Figure 2(b) corresponds to the orthogonal component of the SH field.

We now turn to the analysis of the polarization dependences of Figs. 1 and 2. We should first note that the SH signal for our experimental conditions appears to be dominated by the surface contribution. The effect of the symmetry-allowed higher-order (magnetic-dipole and electric-quadrupole) terms is insignificant. This statement is justified by the results for the oxidation of the silicon surface discussed below. In order to analyze the form of the surface contribution to the SH signal, we introduce the third-rank surface nonlinear susceptibility tensor $\vec{\vec{\chi}}_s^{(2)}$ relating the induced nonlinear dipole moment per unit area and the pump electric-field vector in the surface layer:

$$\mathbf{P}_s^{\mathrm{NLS}}(2\omega) = \vec{\vec{\chi}}_s^{(2)} : \mathbf{E}(\omega)\,\mathbf{E}(\omega). \tag{1}$$

This relation takes account of the entire nonlinear source (NLS) polarization in the surface layer and does not presuppose that only the electric-dipole terms in a multipole expansion are important. Formal expressions for $\vec{\vec{\chi}}_s^{(2)}$ can be derived from second-order perturbation theory, and a complete equation for the amplitude of the electric field of the reflected SH beam can be obtained by solving the wave equation for the specified nonlinear source term. Here we shall restrict our attention to the polarization dependences of the SHG process, which reflect the tensor properties of $\vec{\vec{\chi}}_s^{(2)}$ and, hence, the symmetry properties of the surface. The strength of the radiated SH field polarized along the direction $\hat{e}(2\omega)$ is given by

$$\mathbf{E}(2\omega)\cdot\hat{e}(2\omega) = C\,\hat{e}(2\omega)\cdot\vec{\vec{\chi}}_s^{(2)} : \hat{e}(\omega)\hat{e}(\omega), \tag{2}$$

where $\hat{e}(\omega)$ is the polarization vector of the pump electric field and C is a constant independent of the input and output polarization vectors. For a specified form of the surface nonlinear susceptibility tensor, this equation permits one to predict any desired polarization dependence.

The data in Fig. 2 suggest immediately that the Si(111)-7×7 surface possesses a threefold rotational symmetry about its surface normal. The presence of the null values in Fig. 2(a) indicates additional symmetries in the Si(111)-7×7 surface. For the input and output polarizations parallel to one another, the SHG process will be forbidden if this common direction lies perpendicular to a mirror plane. This situation is effectively a one-dimensional form of inversion symmetry. Examining Fig. 2(a), we find a mirror plane parallel to the $[2\bar{1}\bar{1}]$ crystal axis and two other mirror planes at $\theta = \pm 120°$. Thus, the full symmetry of the Si(111)-7×7 surface appears to be $3m$, just as would be the case for the ideal, unreconstructed Si(111) surface. Under $3m$ symmetry $\vec{\vec{\chi}}_s^{(2)}$ has only a single independent, nonvanishing element: $[\chi_s^{(2)}]_{xxx} = -[\chi_s^{(2)}]_{xyy} = -[\chi_s^{(2)}]_{yxy}$, where x and y correspond, respectively, to the $[2\bar{1}\bar{1}]$ and $[01\bar{1}]$ directions in the crystal surface.

With the form of $\vec{\vec{\chi}}_s^{(2)}$ appropriate for $3m$ symmetry, we can apply Eq. (2) to derive expressions for the radiated SH electric field. For the x and y components, we obtain

$$\begin{aligned} E_x &= C\,[\chi_s^{(2)}]_{xxx}\cos 2\theta, \\ E_y &= -C\,[\chi_s^{(2)}]_{xxx}\sin 2\theta, \end{aligned} \tag{3}$$

where the angle θ denotes the orientation of the pump polarization with respect to the $[2\bar{1}\bar{1}]$ axis (increasing towards the $[0\bar{1}\bar{1}]$ axis). The corresponding relations for the electric-field amplitudes parallel and perpendicular to the pump polariza-

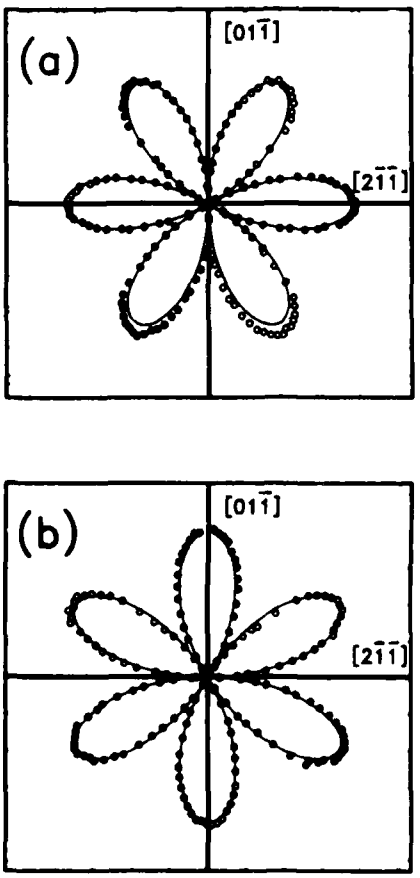

FIG. 2. As in Fig. 1, but with the SH electric field resolved along directions (a) parallel and (b) perpendicular to the pump electric-field vector.

tion are

$$E_{\parallel} = C\,[\chi_{\parallel}^{(2)}]_{\parallel\parallel\parallel}\cos 3\theta,$$

$$E_{\perp} = -C\,[\chi_{\parallel}^{(2)}]_{\parallel\parallel\parallel}\sin 3\theta. \quad (4)$$

Here the polarization vector defining the parallel direction lies at an angle θ with respect to the $[2\bar{1}\bar{1}]$ axis; the vector for the perpendicular direction makes an angle of $\theta + 90°$. One immediate result of Eq. (3) or Eq. (4) is the lack of any dependence in the total SH intensity (taking both polarizations together) on the pump polarization. For normally incident excitation on a surface with $3m$ symmetry, anisotropy can only be observed if the direction, rather than just the magnitude, of the radiated SH electric field is detected.

The solid lines in Figs. 1 and 2 represent the magnitude of the SH electric field predicted by Eqs. (3) and (4), respectively. The constant C has been adjusted to match the overall scale. The relative changes in sign in the electric-field amplitude (not shown) coincide with the experimental results. Good overall agreement is seen between the experimental data and the theoretical curves for $3m$ symmetry. As discussed above, the lack of SH signal for certain orientations in Fig. 2(a) indicates the presence of mirror planes. In order to verify more closely the existence of the mirror planes, we have performed direct measurement of the SH signal with parallel input and output polarizers oriented along and at $\pm$ 120° from the $[01\bar{1}]$ axis. In this manner, we were able to place an upper bound of 3×10^{-4} on the intensity of these symmetry-forbidden signals compared with the symmetry-allowed signal obtained by removing the output polarizer. These results provide a rather sensitive check on the presence of three mirror planes. It should be noted that both resonant and nonresonant transitions can contribute to SHG and, consequently, a vanishing of the SH signal cannot be attributed to fortuitous symmetries of a particular state involved in the nonlinear process.[7]

It is instructive to compare linear and nonlinear optical measurements from a surface with $3m$ symmetry. As we have seen, the SHG process, described by a third-rank susceptibility tensor, reflects the anisotropic character of the surface. On the other hand, the linear response, characterized by a second-rank tensor, will be isotropic under $3m$ symmetry. Thus, only the nonlinear optical process permits one to distinguish between $3m$ and higher (e.g., isotropic) symmetry.

IV. DISORDERED Si(111)-7 × 7 SURFACES

Before considering the question of the disordering of Si(111)-7 × 7 surfaces, let us note a distinctive feature of the SHG process. For pump radiation striking the surface of a centrosymmetric medium at normal incidence, SH radiation from the surface is allowed only in the presence of ordering. This general result follows from symmetry arguments. For normally incident excitation, the electric field of the pump lies in the plane of the surface and only the component of the induced SH polarization in this same plane can contribute to the reflected SH radiation. Thus, the SHG process can occur only if there are nonzero components of the surface nonlinear susceptibility tensor with all three indices corresponding to directions in the surface plane. In the case of a surface with isotropic symmetry (or inversion symmetry in the plane), these components must all vanish. Hence, surface SH radiation for our experimental geometry is correlated with the presence of ordering in the surface plane. More specifically, for measurements of the SH intensity with parallel input and output polarizers, the signal is associated with the lack of mirror symmetry normal to the chosen direction of polarization.

We now present SH measurements on the oxidation and ion bombardment of Si(111)-7×7 surfaces. We were able to collect the data *in situ* and in real time, since the surface SHG technique can be applied in the presence of a gas and provides a sufficiently favorable signal-to-noise ratio to follow changes on the time scale of seconds. In the measurements discussed below, the input and output polarizations lay along the $[2\bar{1}\bar{1}]$ direction, which is not perpendicular to any mirror plane of the Si(111)-7×7 surface.

First we report on the room-temperature oxidation of the Si(111)-7×7 surface. In this experiment, the clean Si(111)-7×7 surface was exposed to research grade oxygen at a pressure of 10^{-6} Torr. This led to a smooth fall in the SH signal to a very low level (Fig. 3). The decay in the SH radiation[8] occurred for an exposure of ~100 L, which is sufficient to allow adsorption of roughly a monolayer of oxygen.[9] This result clearly shows that the surface contribution to the SH signal for the clean Si(111)-7×7 surface dominates that from the bulk for our experimental conditions. The decrease in the SHG efficiency can be attributed to the loss of long range ordering in the surface known to accompany the oxidation process.[9] In addition to the change in symmetry, the SH susceptibility for the partially ordered surface may be diminished by an upward shift in the energy of the surface states as the dangling Si bonds are joined with oxygen atoms, causing the transitions between surface states in the SHG process to be further from resonance.

Ion bombardment of the silicon sample provides an interesting case for monitoring disordering. In this process, the change in the chemical composition of the surface is minor, but the change in the structure is pronounced. Figure 4 displays the SH intensity as a function of exposure to Ar^+ ions. The 5-keV ions struck the silicon sample at 45° from the surface normal with a flux of $2\times10^{11}/cm^2$ s measured in the surface plane. The theoretical fit in the figure was construct-

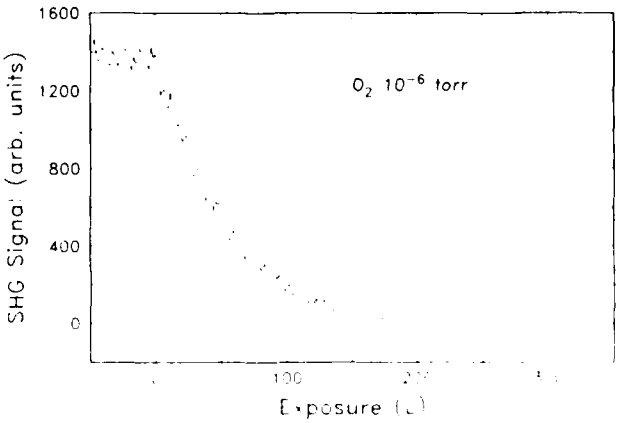

FIG. 3. SH intensity from a Si(111)-7 × 7 surface during exposure to oxygen.

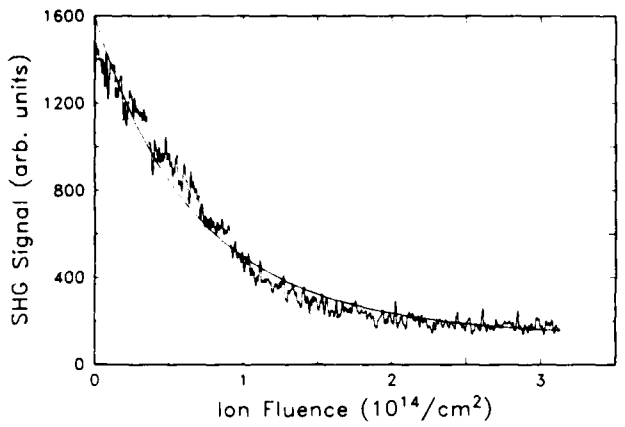

FIG. 4. SH intensity from a Si(111)-7 × 7 surface measured during bombardment with 5-keV Ar^+ ions. The solid line represents the theoretical fit discussed in the text.

ed by assuming a surface nonlinear susceptibility that fell exponentially with increasing exposure, dropping to a small constant value associated with residual ordering. On the basis of this simple analysis, we can infer a value for the average effective area disordered by each incoming ion. From the parameters of the fit, we find this average area to be 105 Å^2.

A comparison of the effective area disordered by each ion with the corresponding sputtering yield helps to give a picture of the effect of the energetic ions. From the literature,[10] we find that the sputtering yield of the 5-keV Ar^+ ions is ~ 1.5. Thus, an average area of ~ 70 Å^2 is disordered for each ejected atom. This large area indicates that the ion bombardment process disorders many more atoms in the surface layer of the crystal than it ejects. Such behavior can be seen clearly in dynamical simulations of the ion bombardment process.[11]

V. CONCLUSION

The surface second-harmonic technique appears to be a sensitive probe of the symmetry of the ordering of the top atomic layers of a surface. The method is particularly well suited for identifying planes of mirror symmetry, which can be related to nulls in the surface SH signal. In the present work, this notion was applied in a precise measurement of mirror planes in the ideal Si(111)-7 × 7 structure. SH measurements of the development of effective mirror planes also served to monitor disordering of the Si(111)-7 × 7 surface induced by oxidation and ion bombardment. The capability of this method for performing real-time, *in situ* studies should be helpful in attacking a variety of problems involving structural changes of surfaces during the course of reactions.

This work was supported in part by the Office of Naval Research.

[1] J.M. Chen, J.R. Bower, C.S. Wang, and C.H. Lee, Opt. Commun. **9**, 132 (1973).
[2] H. W. K. Tom *et al.*, Phys. Rev. Lett. **52**, 348 (1984), and references therein.
[3] T.F. Heinz, C. K. Chen, D. Ricard, and Y.R. Shen, Phys. Rev. Lett. **48**, 478 (1982).
[4] T.F. Heinz, H.W.K. Tom, and Y.R. Shen, Phys. Rev. A **28**, 1883 (1983).
[5] T.F. Heinz, M.M.T. Loy, and W.A. Thompson, Phys. Rev. Lett. **54**, 63 (1985).
[6] For SHG measurements of oxidized silicon samples under ambient conditions, see H.W.K. Tom, T.F. Heinz, and Y.R. Shen, Phys. Rev. Lett. **51**, 1983 (1983), and references therein.
[7] The $3m$ symmetry of the Si(111)-7 × 7 surface is supported, with varying degrees of precision, by other surface probes, including low-energy electron diffraction, ion scattering, and scanning tunneling microscopy.
[8] In repeated trials of the oxidation measurements, we observed a variation in the rate of decay of the SH signal as a function of oxygen exposure. This behavior is presumably associated with differences in the surface defect density or low levels of surface contamination, both of which can strongly affect the oxidation process.
[9] B. Carriere and J. P. Deville, Surf. Sci. **80**, 278 (1979), and references therein.
[10] S. T. Kang, R. Shimizu, and T. Okutani, Jpn. J. Appl. Phys. **18**, 1717 (1979).
[11] See, for example, R. P. Webb and D. E. Harrison, Jr., Phys. Rev. Lett. **50**, 1478 (1983).

Time-resolved vibrational energy relaxation of surface adsorbates

E. J. Heilweil,[a] M. P. Casassa,[a] R. R. Cavanagh, and J. C. Stephenson
Center for Chemical Physics, Molecular Spectroscopy Division, National Bureau of Standards, Gaithersburg, Maryland 20899

(Received 18 March 1985; accepted 21 May 1985)

Time-resolved measurements of picosecond vibrational population decay of chemisorbed species (OH, OD, BOH, NH_2, and OCH_3) on high surface area colloidal silica at room temperature have been performed. The influence of solvents on OH relaxation and the variation in observed relaxation rates are discussed in terms of the vibrational level structure and surface coordination of each adsorbate.

I. INTRODUCTION

Many chemical and physical processes that occur at solid surfaces may be better understood from the measurement of energy flow within adsorbate and substrate vibrational modes. The dissipation and redistribution of chemical bond energy during chemical reactions at surfaces provides one notable example. Manifestations of surface energy transfer also include radiative heating, combustion, reactive etching, and corrosion.

An understanding of the mechanisms and kinetics of vibrational energy transfer in molecular systems is directly attainable by performing time-resolved experiments that monitor populations in particular vibrational modes. While such measurements have been conducted for gas and liquid phase[1] systems, there have been no previous reports of measurements of vibrational energy relaxation in chemical bonds of surface species. Additionally, for molecules in the condensed phase (liquid or solid) or on a surface, the pertinent time scale lies in the picosecond domain.[2] With the advent of ultrashort optical pulse technology,[3] it is now possible to directly measure the kinetics of energy decay of vibrational modes in condensed-phase molecular systems. In order to answer questions associated with vibrational energy transfer at surfaces, we have performed time-resolved measurements to obtain the vibrational relaxation dynamics of molecules adsorbed on high surface area metal oxides.[4-7] Results for a variety of chemisorbed surface species ($-OH$, $-OD$, $-BOH$, $-NH_2$, and $-OCH_3$)[7] on colloidal silica (SiO_2) in several chemical environments are summarized here.

II. EXPERIMENTAL

An infrared pump/probe method using tunable picosecond pulses has been used to measure the vibrational population decay rates (T_1^{-1}) of ground electronic state $v = 1$ vibrational modes. The experimental apparatus[8] has been discussed at length in a previous paper.[5] Briefly a 10 Hz Nd : YAG laser is used to pump an optical parametric amplifier (OPA) to generate tunable infrared pulses. Typically, 35-mJ pulses of 1.06-μm radiation are used to pump the three $LiNbO_3$ crystals of the OPA. An intense ($\sim 250\ \mu$J, ~ 20 ps FWHM) infrared pulse is first used to excite population to the $v = 1$ level of a specific fundamental stretching mode in the sample. Due to anharmonicity, the excited state does not absorb at this frequency so the pulse partially bleaches the sample absorption. As the population relaxes, the transient increase in sample transmission (T) returns to its steady-state value (T_0). The transmission of a second weaker IR pulse as a function of time after the pump pulse passes through the sample is therefore a measure of the $v = 1$ T_1 lifetime.

The technique described above is applicable to samples which transmit IR radiation and contain enough surface species to produce a significant transmission change (typically $T_0 \cong 50\%$ and $T_{max} \cong 55\%$). Such samples include, for example, molecules adsorbed on colloidal particles suspended in solvents[4,5] or pressed as disks in vacuum.[6] For the adsorbates on silica discussed here, straightforward chemical modification of the surface hydroxyl groups is performed to produce a desired optical density (~ 0.3) for the adsorbate modes of interest.[7]

III. RESULTS AND DISCUSSION

Our initial measurements were conducted on the surface hydroxyl group ($-OH$) bound to fumed colloidal silica (120-Å-diam particles with 200 m^2/g surface area) dispersed in liquid CCl_4 at room temperature.[4] Such samples exhibit strong infrared absorptions in the 3000–4000 cm^{-1} region which arise from the isolated SiOH group (3691 cm^{-1}, width 50 cm^{-1} FWHM) and molecular physisorbed water (~ 3400 cm^{-1}). This adsorbed water can be removed by heating in vacuum.

The surface hydroxyl $v = 0 \rightarrow 1$ transition was excited with a resonant IR pulse which transferred about 10% of the population to the $v = 1$ level. The exponential decay (first order kinetics) of the quantity $\ln(T/T_0)$ vs delay time, between probe and pump pulses gives the characteristic time constant (T_1) for vibrational relaxation. It was found that the $v = 1$ population for isolated surface OH groups on dried silica in CCl_4 decays exponentially with a characteristic lifetime of $T_1 \cong 150$ ps, or roughly 10^4 vibrational periods.[4] Data obtained for a dried silica disk in a saturated atmosphere of CCl_4 are identical to those obtained for silica dispersed in liquid CCl_4.[6]

Measurements of the OH($v = 1$) decay for a dried silica disk in vacuum[5,6] yielded the data shown in Fig. 1(a). In this case, the observed relaxation time is found to be larger than for silica contacted with CCl_4. We note again that both relaxation times (T_1 vacuum $= 194 \pm 12$ ps; T_1 CCl_4 $= 154 \pm 16$ ps) are long compared to the vibrational period

(10^{-14} s) and that the presence of CCl_4 enhances the OH relaxation rate.

In the absence of solvent the vibrational relaxation rate is probably controlled by coupling to vibrational modes (in the range 700–1100 cm^{-1}) of the silica-OH system.[5] This mechanism is easily visualized in terms of the vibrational level structure of a single SiO_4H unit. The SiO_4 tetrahedron has nine vibrational modes in the range 400–1100 cm^{-1}. The coordinated hydrogen atom adds two more modes (torsion and bending) in this range, in addition to the high frequency OH-stretching mode. While these low frequency motions are mechanically coupled to the excited motion, the energy gaps for V–V energy transfer are large, requiring multiple quantum ($\Delta V \cong 4$) transitions. It is, therefore, not surprising that the vibrational excitation persists for 2×10^4 vibrational periods.

We have shown that two other conceivable relaxation mechanisms, (1) resonant energy exchange (Förster energy transfer) to nearby OH groups, and (2) dielectric damping are unimportant.[5] Decay by the Förster mechanism has a different functional form than that observed. Both Förster and dielectric damping models also predict relatively slow rates which have the opposite dependence on index of refraction (vacuum vs CCl_4) than the observed rates.

The presence of CCl_4 leads to an enhancement of the relaxation rate of 1.4×10^9 s^{-1}. We suspect that CCl_4-OH collisions, which occur at a rate of $\sim 10^{12}$ s^{-1}, enhance the surface-hydroxyl V–V rate. Energy transfer to the substrate is more likely to occur than energy transfer to the CCl_4 vibrations since the latter rate, based on extrapolated liquid and gas phase results, is expected to be much slower than the experimentally observed rate.

The linewidth of the surface hydroxyl stretching fundamental in vacuum is 8 cm^{-1} (FWHM).[6] The observation of surface vibrational linewidths which exceed the resolution available in optical experiments are numerous and well documented. For the OH/SiO_2 system, the observed width is significantly greater than would be expected if vibrational energy relaxation alone determined the intrinsic absorption width; a 204 ps lifetime corresponds to a homogeneously broadened linewidth of only 0.026 cm^{-1}. The 8 cm^{-1} width is, therefore, attributed to other broadening mechanisms such as pure dephasing or inhomogeneous broadening. In fact, the 3749 cm^{-1} surface hydroxyl band exhibits a slight asymmetry which is indicative of inhomogeneous broadening. The comparison of the relaxation rates observed directly and inferred from the infrared spectrum serves to emphasize the importance of direct measurements of vibrational decay of adsorbed molecules. In this example, the rate inferred from the linewidth is grossly misleading.

The above experiments measured only the $v = 1$ T_1 lifetime of the highly anharmonic OH oscillator on the silica surface. They did *not* directly ascertain where the energy flows or by what mechanism(s). Further studies of OH on silica with coadsorbates and in various organic solvents have therefore been performed.[5] It was found that the OH($v = 1$) T_1 lifetime *decreases* as the highest solvent fundamental vibrational mode frequencies approach the 3700 cm^{-1} OH frequency. This is particularly evident for CH-stretch (~ 3000 cm^{-1}) containing molecules such as CH_2Cl_2 and C_6H_6 where $T_1 = 102 \pm 20$ and 87 ± 30 ps, respectively. In the presence of adsorbed H_2O, which possesses a broad, partially overlapping OH absorption with SiOH, T_1 reduces even further to ~ 56 ps. In this case, direct V–V transfer from the surface OH to adsorbed water by a Förster mechanism may participate in the deactivation process.

Further insight into vibrational energy transfer at surfaces may be gained by studying other species bound to the silica substrate. In this way the potential accepting modes of the bulk material (e.g., vibrational modes or phonons) remain unchanged while the adsorbate local modes and adsorbate-substrate coupling are modified. To investigate this situation, additional measurements of the $-SiOD$, $-SiNH_2$, and $-SiOCH_3$ species and of BCl_3 modified silica ($-BOH$) have been performed.[7] T_1 measurements for these adsorbates have revealed that the dominant relaxation pathway is most likely through local vibrational modes of the adjacent surface subunit (the SiO_4 tetrahedron).

The simplest substitution for the OH group is isotopic exchange to OD. Upon exposure of silica to room temperature vapor pressure of D_2O, roughly 67% of the surface OH groups were exchanged to yield surface OD species which absorb at 2750 cm^{-1}. Measurements of the OD relaxation on dried silica disks in vacuum produced T_1 lifetimes comparable to the corresponding SiOH system.[9] Decay of the lower frequency OD oscillator into the substrate was expected to require fewer quantum transitions than for OH (i.e., $\Delta V \geqslant 3$ for lattice modes vs $\Delta V \geqslant 4$) and result in a faster decay rate. This result was not observed, however. A possible explanation is that the hydroxyl decay may be strongly coupled to such motions as the Si-OH bend or Si-OH torsion.

The hydroxyl T_1 lifetime for BOH modified silica (at ~ 3700 cm^{-1}) in vacuum [see Fig. 1(b)] or CCl_4 is found to be ~ 70 ps. Since the boron atom mass and coordination to the surface oxygens is different from silicon, changes in the local site bending and stretching frequencies must occur. This surface modification is also found to substantially alter the relaxation lifetime of the surface OH species.

Finally, we briefly address the T_1 decays of silica $-NH_2$ and $-OCH_3$ adsorbates.[7] Both NH-stretching modes of $-NH_2$ (at 3420 and 3500 cm^{-1}) were found to saturate to the same extent ($\Delta T/T \sim 5\%$) although time-resolved measurements produced instrumental pulse width limited decays [see Fig. 1(c)]. While precise T_1 values could not be deduced from these results, the two modes apparently have comparable lifetimes on the order of several picoseconds ($\leqslant 20$ ps). Attempts to saturate the CH-stretching transitions of $-OCH_3$ were unsuccessful, however. This may arise because of complex adsorbate vibrational level coupling (Fermi resonances),[10] low molecular absorption cross sections, or extremely rapid vibrational energy decay. The results for adsorbates on SiO_2 indicate that increasing the adsorbate vibrational level structure and complexity leads to more rapid vibrational energy relaxation at the silica interface.

The existing evidence for the role of the low frequency SiO_4H modes in dissipating the vibrationally excited OH oscillators is tentative. It is clearly important to further test the validity of the postulated mechanism. Theories of nonra-

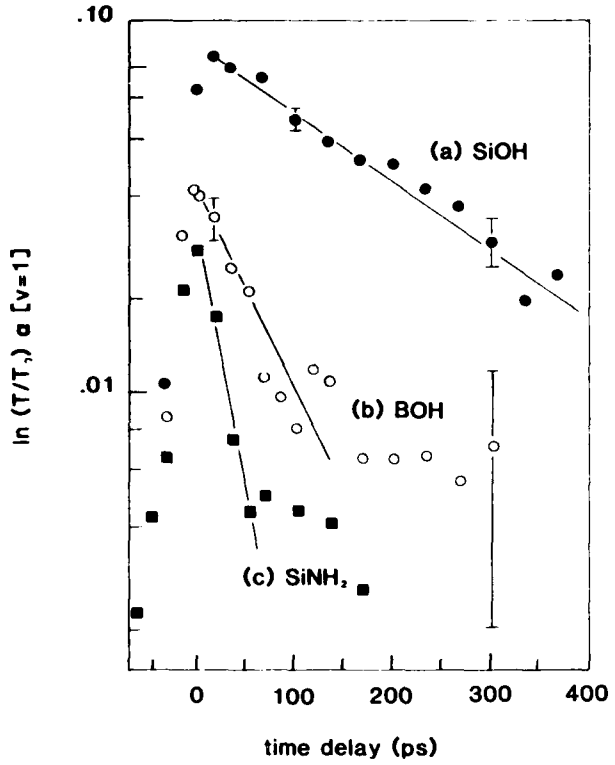

FIG. 1. Experimental vibrational population ($v = 1$) decays at room temperature for adsorbate modes on colloidal (~ 150 Å diameter) silica particles: (a) OH stretch at 3749 cm^{-1} of SiOH on dried pressed disk in vacuum, $T_1 = 194 \pm 12$ ps, (b) OH stretch at 3705 cm^{-1} of BOH on dried BCl_3-modified silica disk, $T_1 \approx 70$ ps, and (c) NH stretches at 3420 and 3500 cm^{-1} of NH_3-modified silica in CCl_4 exhibiting measurable saturation, but pulse width limited decays, ($T_1 \lesssim 20$ ps).

diative relaxation make definite predictions about the temperature dependence of T_1 for such a multiphonon process. We are currently testing this model by studying the temperature dependence of the OH and OD vibrational relaxation rate as a function of sample temperature between 80 and 1000 K.[9] These *surface* measurements can then be compared to results for the OH impurity in *bulk* fused silica which indicate that the OH quantum decays to four lattice vibrations.[11]

IV. CONCLUSIONS

Direct time-resolved picosecond infrared saturation and ground state recovery measurements of the vibrational population decay for $-OH$, $-OD$, $-BOH$, $-NH_2$, and $-OCH_3$ adsorbates on room temperature silica have been conducted. T_1 lifetimes for these systems in vacuum and in contact with several organic solvents range from several picoseconds for $-NH_2$ to 200 ps for $-OH$ in vacuum. Solvent interactions always increase the rate of vibrational energy relaxation.

The measured T_1 values demonstrate that the spectral linewidths (e.g., IR and Raman) for these surface vibrations are too large by factors of 200 to 2000 to be caused solely by T_1 uncertainty broadening.

While the precise mechanism for surface vibrational relaxation of these systems is unclear at present, it appears that the presently known T_1 lifetimes for surface species on silica may have chemical importance. It can be argued that vibrational energy, which can apparently remain localized for periods longer than typical times for molecular reorientation or reactant diffusion, may become available for surface reaction. This concept demands further study of more complex adsorbate-substrate systems which exhibit important chemical dynamics.

This research was supported in part by the Air Force Office of Scientific Research.

[a] NRC/NBS Postdoctoral Fellow.

[1] J. Chesnoy and G. M. Gale, Ann. Phys. Fr. **9**, 893 (1984).
[2] A. Laubereau and W. Kaiser, Rev. Mod. Phys. **50**, 607 (1978).
[3] *Ultrafast Phenomena IV*, edited by D. H. Auston and K. B. Eisenthal, (Springer, New York, 1984).
[4] E. J. Heilweil, M. P. Casassa, R. R. Cavanagh, and J. C. Stephenson, J. Chem. Phys. **81**, 2856 (1984).
[5] E. J. Heilweil, M. P. Casassa, R. R. Cavanagh, and J. C. Stephenson, J. Chem. Phys. **82**, 5216 (1985).
[6] M. P. Casassa, E. J. Heilweil, J. C. Stephenson, and R. R. Cavanagh, J. Vac. Sci. Technol. A **3**, 1655 (1985).
[7] E. J. Heilweil, M. P. Casassa, R. R. Cavanagh, and J. C. Stephenson, SPIE Proc. **533**, 15 (1985).
[8] Certain commercial equipment, instruments, or materials are identified in this paper in order to adequately specify the experimental procedure. In no case does such identification imply recommendation or endorsement by the National Bureau of Standards, nor does it imply that the materials or equipment identified are necessarily the best available for the purpose.
[9] M. P. Casassa, E. J. Heilweil, R. R. Cavanagh, and J. C. Stephenson, Phys. Rev. Lett. (submitted).
[10] A. Fendt, S. F. Fischer, and W. Kaiser, Chem. Phys. **57**, 55 (1981).
[11] E. J. Heilweil, M. P. Casassa, R. R. Cavanagh, and J. C. Stephenson, Chem. Phys. Lett. **117**, 185 (1985).

Angular, velocity, rotational, and electronic distributions of vibrationally elastically scattered NO($v = 1$) from LiF(100)

J. Misewich, H. Zacharias, and M. M. T. Loy
IBM Thomas Watson Research Center, Yorktown Heights, New York 10598

(Received 15 February 1985; accepted 7 May 1985)

Infrared laser excitation has been utilized to excite part of a molecular beam of NO to a single well-defined quantum state, NO($v = 1, J = 3/2, \Omega = 1/2$), which is scattered from a cleaved LiF(100) surface. Laser spectroscopic detection techniques then allow the determination of rotational and electronic distributions as well as state-specific angular and velocity distributions for scattering from a single initial vibrational-rotational state.

I. INTRODUCTION

In order to extract information about the nature of an interaction potential from scattering experiments, ideally one would allow the collision partners to interact under well-defined conditions and investigate cross sections for all final scattering channels. Studies of atomic beam scattering from solid surfaces under ultrahigh vacuum (UHV) conditions approach this ideal and have yielded valuable information on surface structure[1] (diffractive scattering), surface phonons[2] (inelastic scattering), and the properties of the gas-surface interaction potential[3] (e.g., rare gas scattering). The case of molecular beam scattering is more complex since there are now internal degrees of freedom to characterize. Recent experiments on the scattering of nitrogen from Ag(001)[4] and nitrogen and methane from Pt(111)[5] have measured the angular and velocity distributions of the scattered molecules but could not determine the internal energy distributions. Several groups have introduced laser spectroscopic techniques to study the internal energy distributions of molecules scattered from surfaces[6-8] and interesting effects such as rotational rainbows and alignment of rotational angular momentum have been observed. These experiments however have been confined to the scattering of an incident beam of molecules with internal energy distributed over the lowest few rotational states of the ground vibrational level. In order to broaden the scope of the investigations, we have applied state specific laser spectroscopic techniques to define the incident molecular beam internal energy characteristics as well as the scattered beam internal energy characteristics, thereby approaching the ideal of well-defined scattering conditions more closely. The experiments presented here are part of a continuing effort in our laboratory to study the interaction of a molecular beam of vibrationally excited molecules with surfaces.[9,15]

In our experiments a molecular beam is crossed at right angles by pulsed tunable infrared laser radiation to excite part of the beam to a single vibrational-rotational state. This excited molecular beam is then scattered from a well-defined single crystal surface in a UHV chamber. State-specific multiple photon ionization using a tunable ultraviolet laser source is used to characterize the molecular beam both before and after scattering by positioning the ultraviolet (UV) laser beam to intersect either the incident or the scattered molecular beam, respectively. Scanning the UV laser frequency allows the determination of the rotational and electronic distributions of the probed molecules. State-specific angular and velocity distributions are obtained by setting the probe laser frequency to detect a well-defined state. Angular distributions are produced by rotating the intersection of the probe laser beam with the scattering plane. Measurements of velocity distributions are possible because of the short duration of the exciting laser pulse and are done by scanning the delay between the exciting and probe lasers. In this paper we have extended our studies to perform state-to-state scattering experiments of vibrationally excited NO from cleaved LiF(100) surfaces.

II. EXPERIMENTAL

The vacuum system used in this experiment has been described previously.[9] Here we just indicate the principal features. A pulsed [600 full-width at half maximum (FWHM)] supersonic beam of 10% NO seeded in He (total backing pressure 450 Torr) provides a rotationally cold NO molecular beam. The molecular beam is crossed at right angles by tunable infrared radiation ($\lambda \sim 5.3\,\mu$) produced by difference frequency mixing in a lithium iodate crystal of ~ 590 nm output from a Quanta Ray Nd : YAG pumped dye laser and part of the 532 nm second harmonic of the Nd : YAG fundamental. The infrared (IR) laser is tuned to the R_{11} ($J'' = 1/2$) line at 1876.076 cm^{-1} to populate a single rotational state ($v' = 1, J' = 3/2, \Omega' = 1/2$). Infrared pulse energies were approximately 5–10 μJ at a bandwidth of about 0.4 cm^{-1}. The IR beam was slightly focused to a beam waist of about 1 mm and was polarized perpendicular to the molecular beam. Timing between the beam valve and the IR excitation pulse was set so that the laser excited the pulse 230 μs after the start of the molecular beam pulse to ensure homogeneous supersonic flow conditions.

Resonantly enhanced ionization via the $A \leftarrow X$ γ(0-0) and γ(1-1) bands was used to detect the NO with state specificity. The tunable UV laser radiation was produced by frequency doubling the output of a XeCl excimer pumped dye laser in a potassium pentaborate crystal. UV pulse energies of approximately 30 μJ with a bandwidth of about 0.4 cm^{-1} were obtained. The UV beam crossed the molecular beam at right angles and was polarized parallel to the molecular beam. The UV was also focused and could be moved over a variety of radii and angles about the scattering sample surface. Ion-

 0734-211X/85/051474-05$01.00

ized NO molecules were detected using a Johnston MM-1 multiplier.

LiF(100) surfaces were prepared for this experiment by making a fresh cleave just prior to pumpdown of the vacuum system. In a secondary ion mass spectrometer (SIMS) investigation of air- and vacuum-cleaved LiF surfaces, Estel *et al.*[10] have shown that LiF surfaces cleaved in air and then mounted in a vacuum system and pumped down exhibit only contaminations far below the monolayer regime. All results presented here were reproducible on separate cleaves.

The high temporal resolution of our laser excitation and detection system allows us to obtain velocity information on incident and scattered vibrationally excited molecules. Time-of-flight (TOF) spectra for a certain probe laser position are taken by varying the delay between the infrared excitation laser and the UV probe laser using a digital delay generator. A direct measure of the flow velocity of vibrationally excited molecules for either the incident or scattered beams is then obtained by taking such TOF spectra at two probe laser positions a measured distance apart. Molecular beam velocity analysis using laser spectroscopic techniques offer some advantages over conventional chopped beam/mass spectroscopic techniques. Because the excitation laser pulse is only a few ns long, the incident pulse of vibrationally excited molecules is very short ($\sim 2\,\mu$s FWHM 5 mm before scattering) without having to use high speed mechanical choppers. Also, the ionization length is detemined by the focusing of the probe laser beam and is much smaller than electron impact ionizing lengths. Finally, the laser spectroscopic TOF technique is state selective.

Angular distributions for a specific scattered vibration-rotational state are obtained by moving the probe laser beam, which can be done without opening the vacuum system. The polarization of the probe laser beam is always at a constant angle with respect to the surface normal (45°). Care is taken in choosing the UV frequency to be one in which there is no overlap of lines from other branches or bands so that only a single vibrational-rotational state is in fact probed.

Rotational distributions are obtained by scanning the UV laser frequency. An IBM Series/1 computer scans the laser and records ionization signal and laser normalization channels.

III. RESULTS

A. Incident beam characteristics

Supersonic expansion of NO seeded in helium produces a nonequilibrium rotational distribution over molecules in the incident molecular beam that cannot be completely characterized by a single rotational temperature, however, about 95% of the population is concentrated in the lowest few rotational levels and their population can be described by a rotational temperature of about 8.5 K.[11] The infrared laser pulse excites a small part of the incident beam 230 μs after the start of the 600 μs molecular beam pulse. The infrared pulse only excites molecules initially in the $v = 0$, $J = 1/2$ level of the $^2\Pi_{1/2}$ electronic state. In this manner, a short pulse of NO ($v = 1$, $J = 1.5$, $\Omega = 1/2$) is produced on top of a 600 μs background pulse of NO $v = 0$ distributed over the lowest few J states. TOF data on the incident beam shows that the $v = 1$ pulse width is about 2 μs FWHM at the surface. Since the infrared excitation pulse is a few ns in duration, the microsecond time scale of the experiment is determined by overlap of the laser and molecular beams and the velocity distribution over molecules in the supersonic expansion. By taking TOF spectra at two different positions along the incident beam, the incident flow velocity was determined to be 1.42×10^5 cm/s, i.e., the incident beam translational energy is 310 meV. Since the incident angle was $\theta = 45°$, the normal energy ($E_n = E_i \cos^2\theta$) is then 155 meV.

Figure 1 is a UV laser frequency scan of the incident beam taken in the region of the γ(1-1) band. The four lines all originate in NO($v'' = 1$, $J'' = 1/2$, $\Omega'' = 1/2$) and represent the four branches: P_{11}, ($Q_{11} + P_{21}$), ($R_{11} + Q_{21}$) and R_{21}. Since there are no collisions in the molecular beam there are no lines from other rotational levels. It is important to note that lines originating from background NO molecules rather than from molecules which were vibrationally excited by the infrared laser pulse can be distinguished by their very different time scales.

The infrared laser is focused to a size smaller than the molecular beam. Thus even though the molecular beam diameter as determined by expansion and collimation geometry is approximately 2 mm FWHM, the pulse of vibrationally excited molecules is only 1 mm FWHM which was measured by moving the probe laser beam transversely to the incident molecular beam. This improves the resolution we can obtain when measuring scattered angular distributions.

In summary, our effective incident molecular beam pulse is a 1 mm diam 2 μs FWHM pulse of molecules in a specific vibrationally excited state, NO ($v = 1$, $J = 3/2$, $\Omega = 1/2$), incident at $\theta = 45°$ with an incident translational energy $E_i = 310$ meV ($E_n = 155$ meV) on top of a 600 μs $v = 0$ pulse distributed over the lowest few rotational states and both spin-orbit components.

B. Scattered beam results

In Fig. 2, a TOF spectrum for the scattered beam is presented. In this example, the ultraviolet laser frequency is set

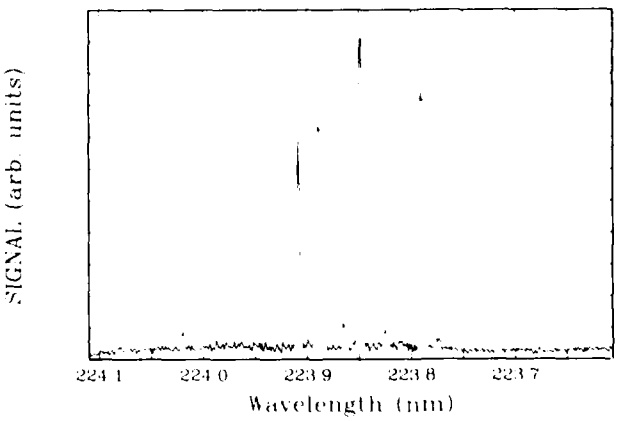

FIG. 1. Incident beam ionization spectrum showing the 4 line spectrum expected for NO ($v = 1$, $J = 3/2$, $\Omega = 1/2$).

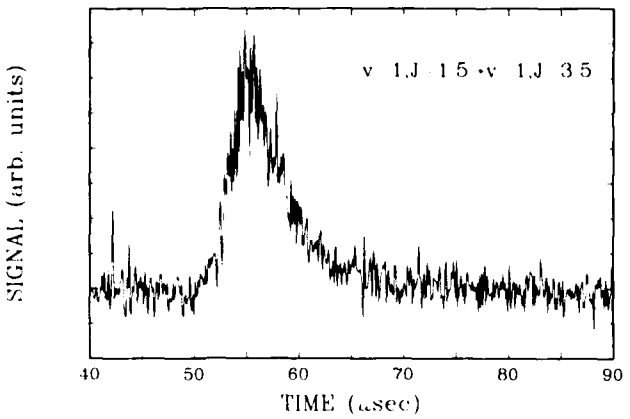

FIG. 2. Scattered beam TOF spectrum for molecules scattered from ($v = 1$, $J = 1.5$) in the incident beam to ($v = 1$, $J = 3.5$) after collision with the surface.

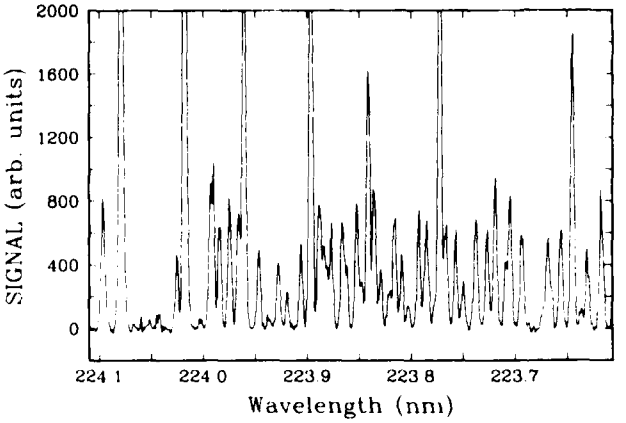

FIG. 4. Multiphoton ionization spectrum of scattered molecules in the region of the $\gamma(1\text{-}1)$ bandheads taken with the infrared laser on.

so that the probe laser detects only NO molecules in ($v = 1$, $J = 3.5$, $\Omega = 1/2$). Figure 3 is a scattered beam TOF spectrum taken under the same conditions as Fig. 2 except that here the UV probe laser frequency is tuned to detect only NO molecules in ($v = 1$, $J = 20.5$, $\Omega = 1/2$), which shows the same behavior as Fig. 2. The detection angle was 45° (i.e., specular direction). A broadening of the incident 2 μs FWHM pulse is observed. There is a small background ionization signal of NO $v = 1$ but this signal is 600 μs long whereas the NO ($v = 1$) that appears due to survival of the initially vibrationally excited NO has a time dependence of only a few μs. TOF spectra were taken for a variety of final J from 1.5 to 20.5, but the results were indistinguishable from those presented above. TOF taken at two different radii for a scattering angle of 45° were used to determine the final translational energy of 190 meV.

Angular distributions showed a narrow (~40° FWHM) nearly specular peak characteristic of direct inelastic scattering. Just as for the velocity data, angular distributions taken for final state J between 1.5 and 15.5 were indistinguishable.

A portion of the scattered NO spectrum taken with the IR laser on is illustrated in Fig. 4. The delay between the lasers was set to correspond to the maximum in the TOF spectrum for this probe laser position and the scattering angle was 45°. Figure 5 is a spectral scan over the same region and under the same conditions except that now the IR laser was blocked. The large lines correspond to the $v = 0$ high J states and have the same size in both spectra. Figure 5 illustrates that we are seeing some $v = 1$ in the scattered beam even in the absence of infrared laser excitation of the incident beam. These lines have the same 600 μs time scale as the molecular beam pulse and appear only as a constant signal which changes the baseline level in the TOF spectra. There are two potential sources for the vibrationally excited molecules that are observed when the infrared excitation laser is blocked: residual vibrationally excited molecules in the incident molecular beam after the supersonic expansion and vibrationally excited molecules produced from the collision of $v = 0$ molecules with the surface. Both sources seem to contribute to the signal we observe. A more detailed investigation of this is currently underway in our laboratory to separate the individual contributions.

From the ultraviolet multiphoton ionization spectra, the rotational distribution for $v = 1 \rightarrow v = 1$ NO scattering shown in Fig. 6 was determined. To be sure that we were observing the distribution for those that are produced by

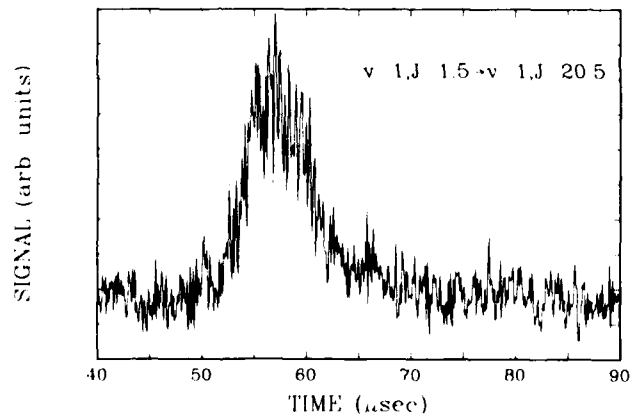

FIG. 3. Scattered beam TOF spectrum for molecules scattered from ($v = 1$, $J = 1.5$) in the incident beam to ($v = 1$, $J = 20.5$) after collision with the surface.

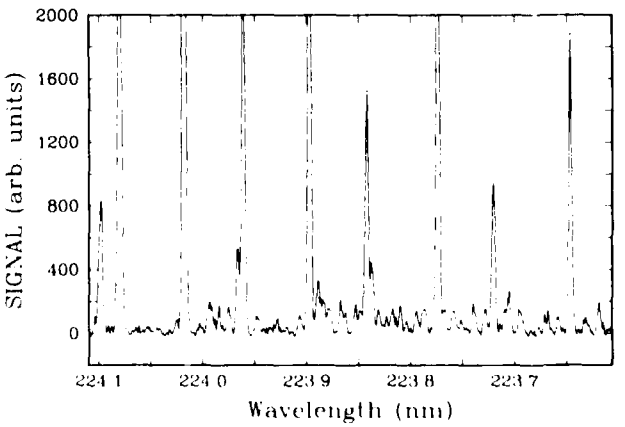

FIG. 5. Multiphoton ionization spectrum of scattered molecules in the region of the $\gamma(1\text{-}1)$ bandheads taken with the infrared laser off.

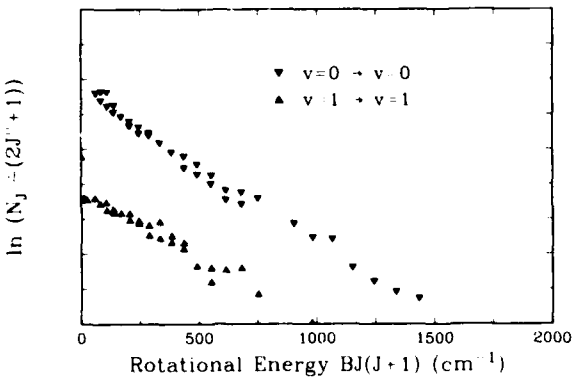

FIG. 6. Rotational distributions for molecules scattered from $v = 0$ to $v = 0$ and for molecules scattered from $v = 1$ to $v = 1$.

infrared laser excitation, the background $v = 1$ peaks were subtracted out by taking the difference between spectra taken with the IR laser on and spectra taken with the IR laser off. The rotational population could be described quite well by a Boltzmann distribution with a temperature of 345 K $\pm$ 35 K. Also plotted in Fig. 6 are the rotational populations for $v = 0 \rightarrow v = 0$ scattering that we obtained from an ultraviolet multiphoton spectrum taken in the region of the $\gamma(0\text{-}0)$ band. It is observed that this distribution can also be described by a Boltzmann distribution at about the same temperature. Rotational distributions in the $^2\Pi_{3/2}$ spin-orbit electronic state gave the same rotational temperature as the $^2\Pi_{1/2}$ distributions.

A comparison of rotational lines originating in the $^2\Pi_{1/2}$ spin-orbit electronic state and lines originating in the $^2\Pi_{3/2}$ state allow the determination of the relative populations of the two states. An electronic temperature of 200 K $\pm$ 50 K was found for both $v = 0 \rightarrow v = 0$ and $v = 1 \rightarrow v = 1$ scattering.

IV. DISCUSSION

These experiments have shown that rotational and electronic energy distributions for $v = 1 \rightarrow v = 1$ and $v = 0 \rightarrow v = 0$ scattering are indistinguishable to within our experimental error. Also, preliminary analysis of the $v = 1$ spectra obtained with the infrared laser off (Fig. 5) indicates approximately the same rotational temperature for $v = 0 \rightarrow v = 1$ scattering. However, this should not be taken to imply anything about the rotational distribution of those molecules that are deactivated at the surface, i.e., $v = 1 \rightarrow v = 0$ scattering. In fact, a theoretical work by Bawagan and co-workers[12] suggested that the dominant role for vibrational deactivation involves transfer of energy from vibration to high J rotational levels of $v = 0$.

Another interesting result is the independence of angular and velocity data on J for $J \leqslant 20.5$. The effect of having rotational degrees of freedom in beam scattering experiments has recently been investigated by several groups. Angular and velocity distributions have been obtained for the scattering of molecular beams of nitrogen from Ag(001)[4] and Pt(111)[5]. Both groups compared their data to the scattering of Ar under similar conditions. Janda *et al.*[5] observed that the nitrogen scattering angular and velocity distributions from Pt(111) were very similar to the Ar distributions. Muhlhausen *et al.*[4] reported both experimental studies of nitrogen and argon scattering from Ag(001) and stochastic trajectory simulations. Experimentally, they found the angular distributions for argon and nitrogen to be identical. Stochastic trajectory simulations were carried out for nitrogen and for "spherical nitrogen" (i.e., the same interaction potential as they used for nitrogen but with the orientational anisotropy removed). In these calculations, the angular and velocity distributions were only slightly affected by the introduction of orientational anisotropy. These simulations do not imply that rotational energy transfer is inefficient. On the contrary, when substantial orientational anisotropy was introduced there was significant rotational energy transfer but the angular distributions were not changed significantly. The implication of both groups is that rotational energy transfer does not appreciably affect angular and velocity distributions. The authors point out, however, that there is a possible complication in comparing the experimental data for argon and nitrogen. Because of the larger mass of argon, it is possible that argon is more efficient at exciting phonons than nitrogen and so the effect of greater phonon excitation for argon might have balanced the rotational energy transfer that is possible only with nitrogen. Our experiments directly show that rotational energy transfer does not significantly affect angular and velocity distributions for final $J \leqslant 20.5$.

V. CONCLUSIONS

In summary, NO ($v = 1$, $J = 3/2$, $\Omega = 1/2$) molecules scatter from freshly cleaved LiF(100) surfaces into a narrow nearly specular lobe characteristic of direct inelastic scattering. The surviving $v = 1$ molecules are distributed over both spin-orbit components ($T_{\text{elec}} = 200$ K) and many J ($T_{\text{rot}} = 345$ K) and the magnitude of both the normal and parallel components of momentum are decreased by about 30% by the collision. Rotational and electronic distributions for $v = 1 \rightarrow v = 1$ scattering are found to be identical to those for $v = 0 \rightarrow v = 0$ scattering. Also, state-specific laser spectroscopic TOF spectra have directly shown that the angular and velocity distributions of scattered molecules are insensitive to rotational energy transfer for $J \leqslant 20.5$.

We are currently calculating the vibrational energy survival probability by integration of the rotational, electronic, spatial, and temporal distributions of the vibrationally elastically scattered molecules and comparing this with the incident beam spatial and temporal distribution.[15] This calculation, in conjunction with data on scattering with other incident translational energies, will enable us to make a detailed comparison with recent calculations of Lucchese and Tully[13] for the same system. Also, it will enable a comparison with recent gas-surface vibrational relaxation experiments carried out with static gas samples and polycrystalline surfaces[14] where an overall deactivation probability could be determined, but the detailed dynamics could not be investigated.

ACKNOWLEDGMENTS

This work was supported in part by the Office of Naval Research.

[1]G. Boato, P. Cantini, and L. Mattera, Surf. Sci. **55**, 141 (1976).
[2]R. B. Doak and J. P. Toennies, Surf. Sci. **117**, 1 (1982).
[3]W. H. Weinberg and R. P. Merrill, J. Chem. Phys. **56**, 2881 (1972).
[4]C. W. Muhlhausen, J. A. Serri, J. C. Tully, G. E. Becker, and M. J. Cardillo, Isr. J. Chem. **22**, 315 (1982).
[5]K. C. Janda, J. E. Hurst, J. Cowin, L. Wharton, and D. J. Auerbach, Surf. Sci. **130**, 395 (1983).
[6]A. W. Kleyn, A. C. Luntz, and D. J. Auerbach, Phys. Rev. Lett. **47**, 1169 (1981).
[7]J. Segner *et al.*, Surf. Sci. **131**, 273 (1983).
[8]G. D. Kubiak, J. E. Hurst, H. G. Rennagel, G. M. McClelland, and R. N. Zare, J. Chem. Phys. **79**, 5163 (1983).
[9]H. Zacharias, M. M. T. Loy, and P. A. Roland, Phys. Rev. Lett. **49**, 1790 (1982).
[10]J. Estel, H. Hoinkes, H. Kaarmann, H. Nahr, H. Wilsch, Surf. Sci. **54**, 393 (1976).
[11]H. Zacharias, M. M. T. Loy, P. A. Roland, and A. S. Sudbo, J. Chem. Phys. **81**, 3148 (1984).
[12]A. O. Bawagan, L. H. Beard, R. B. Gerber, and D. J. Kouri, Chem. Phys. Lett. **84**, 339 (1981).
[13]R. R. Lucchese and J. C. Tully, J. Chem. Phys. **80**, 3451 (1984).
[14]J. Misewich, C. N. Plum, G. Blyholder, P. L. Houston, and R. P. Merrill, J. Chem. Phys. **78**, 4245 (1983).
[15]J. Misewich, H. Zacharias, and M. M. T. Loy (to be published).

CO on Ni[100]: Stark effect and electroreflectance vibrational spectroscopy

David K. Lambert
Physics Department, General Motors Research Laboratories, Warren, Michigan 48090-9055

(Received 18 March 1985; accepted 21 May 1985)

Electroreflectance vibrational spectroscopy (EVS) has been used to study the stretch vibrational mode of CO on Ni[100] at 300 K. The Stark tuning rate of terminally bonded CO is measured to be 1.3×10^{-6} cm^{-1}/(V/cm), acting to decrease frequency as the electric field out of the surface is increased. The present measurement is in close agreement with the Stark tuning rates for CO on Ni[100] and on Pt in an aqueous electrolyte. In addition to the Stark effect, another signal source is observed that is tentatively identified with an electric-field-induced change in the angle some CO molecules have with respect to the surface normal. Recent advances in the EVS measurement technique are also described.

I. INTRODUCTION

Electroreflectance vibrational spectroscopy[1-3] (EVS) is an infrared technique in which derivative vibrational spectra of adsorbed molecules are obtained by modulating their vibrational frequency with an electric field. In this paper an EVS study of CO on Ni[100] and a measurement of its Stark tuning rate are reported.

The EVS optical source is a tunable diode laser. This is possible since EVS has zero background—if no reflectivity change occurs with a change in electric field, then no signal is observed. The poor intensity reproducibility of diode lasers when tuned over the wide wavelength range necessary to study adsorbed molecules precludes their use with most infrared vibrational spectroscopy techniques where a large background signal must be subtracted. Advantages of using diode lasers include low fluctuation of light output ($\Delta I/I$ as low as 2×10^{-8} Hz$^{-1/2}$ has been observed[3] at a 100-kHz modulation frequency), the output power can be focused to a diffraction-limited spot, and frequency resolution can be as good as 10^{-6} cm^{-1}. In the present experiment the diode laser is tuned by changing the heat sink temperature and the current through the laser in steps so that measurements occur at fixed wavelengths. In this way spectra are obtained covering several hundred cm^{-1} with the lasing frequency at each point determined to a precision of 10^{-2} cm^{-1} with a wavemeter. The actual resolution is determined by the spacing of points at which there are measurements.

In addition to vibrational spectroscopy applications, EVS also provides a unique way to study the interaction between an applied electric field and molecules at surfaces. Large, local static electric fields, on the order of 10^7 V/cm, are present at surfaces. Changes in the local static electric field caused by adding coadsorbates can cause significant shifts in vibrational frequencies of adsorbed molecules.[4] The vibrational Stark effect has also been observed for molecules adsorbed at an electrode–electrolyte interface, both by electrochemical modulation infrared spectroscopy[5,6] (EMIRS) and by surface-enhanced Raman spectroscopy[7-9] (SERS). Here the large local electric field in the Helmholtz layer has been observed to cause the vibrational frequency to change tens of cm^{-1} as the potential between the electrode and electrolyte is varied, although in most cases spectral changes are dominated by changes in the quantity of various adsorbed species with potential. Measurement of the Stark tuning rate with EVS of molecules on a well-characterized surface allows one to infer the local electric field causing a frequency shift observed with EMIRS or SERS and thus check models of the electrode–electrolyte interface.[10]

Ultimately, it is hoped, EVS will find use as a routine surface chemistry technique. It should be possible to use EVS to study chemisorbed molecules on surfaces at atmospheric pressure and above. To be useful for such applications, however, the spectra of well characterized surfaces with known adsorbates must first be understood. The Ni[100] surface with CO is a system that has been extensively studied with infrared, electron energy loss spectroscopy (EELS), and other surface analysis techniques. Also, since infrared spectra of CO on Ni[100] are available, a Stark tuning rate can be inferred from EVS measurements.

II. EXPERIMENT

The EVS spectra reported here were obtained using a measurement system described[3] previously. Some modifications have been made to increase the accuracy and reduce the time required to take measurements. A computer interfaced wave meter has been integrated into the optical system, which is used to verify single-frequency laser operation and to measure lasing frequency to $\pm10^{-2}$ cm^{-1} with a 0.8 s repetition rate. The laser heat sink temperature has been brought under computer control by using a voltage calibrator to control the set point of an appropriate temperature controller. Also a quartz fixture has been added to the 9.5-mm-diam spherical counter electrode used to apply the electric field to the sample surface. The quartz fixture acts as a three-point support to maintain a 0.37 mm sample-to-electrode distance.

The Ni[100] crystal was mounted on a manipulator in a UHV system with 5×10^{-10} Torr base pressure. Cycles of ion bombardment, oxygen dosing, and heating to 800 °C were used to prepare a clean surface as measured *in situ* by an Auger spectrometer. As a final cleaning step the surface was dosed with 1 L of CO at 300 K, heated to 400 °C for 5 min, and allowed to slowly cool back to 300 K. After cooling, 2 keV normal incidence Auger showed only sulfur (S) as an impurity above the noise. The ratio of the derivative 152 eV S peak to the 848 eV Ni peak was 0.05. On the basis of the relative cross sections[11] of S and Ni at 3 keV, the fraction of S in the sampling volume is estimated to be 2%. It should be noted that since thermal desorption spectra[12] of CO on

 0734-211X/85/051479-05$01.00

Ni[100] show desorption peaking at 430 °C, some CO probably remained on the surface after heating, even though it was not detected with Auger spectroscopy. Also, about 1 h elapsed between the time the sample was heated and the time spectra began to be taken, so some CO adsorption would be expected from residual gas in the UHV system.

The EVS spectra in Fig. 1 were obtained by first stepping the laser through a predetermined set of operating conditions (some of which result in no laser output, so offsets in the detection electronics can be subtracted) while 2.4×10^{3} V_{rms} at 100 kHz was applied between the counterelectrode and the Ni crystal. After each step in laser operating condition there was a wait of 250 ms followed by a 750 ms integration of the signal from the infrared detector synchronous with the 100 kHz modulation frequency. Next, the Ni surface was dosed with 10 L of CO by opening a leak valve to the UHV system. The sample was not moved during dosing. The laser was again stepped through the predetermined set of operating conditions while measuring the signal synchronous with the modulation as before. The high voltage ac was then turned off and a mechanical light chopper turned on. Again the laser was stepped through the predetermined set of operating conditions while measuring signal synchronous with the chopper. By using a 30-ms-lockin time constant and digitizing the output more rapidly during each integration, we were able to also determine the standard deviation of measurements at each laser frequency. To compute the rms intensity modulation ΔI at the detector divided by the intensity I at the detector, offsets determined by measurement with laser off are subtracted, and the two sets of measurements are ratioed (and multiplied by the appropriate factor). The quantity $\Delta I/I$ with $\pm 1\sigma$ error bars is plotted in Fig. 1 for both the undosed and dosed surface. Points with error bars greater than a fixed value are not plotted.

For synchronous detection at the electric field modulation frequency the lockin amplifier phase was set so that the ac potential of the counterelectrode relative to the Ni surface, when passed through the detector bias network to mimic the detector output, gives an in-phase, negative signal. An increase in optical power incident on the detector causes a negative voltage change to appear across the bias network. Hence an increase in electric field directed out of the Ni surface corresponds to positive $\Delta I/I$. In arriving at this result the assumption is made that detector output voltage has the same phase relationship at 100 kHz as at dc. In support of this assumption, the amplitude response has been verified to be flat to within 5% for frequencies to 100 kHz and the detector has negligible reactive impedance at 100 kHz.

The optical system used to focus light from the tunable diode laser onto the Ni[100] surface at 86° angle of incidence used only reflective elements, except for a CaF_2 window through which light centers the UHV system. A 2.5-cm-diam off-axis parabola with 63.5-cm focal length focuses light on the surface. As part of the alignment, a plane mirror after the final off-axis parabola is used to place the focal point outside the UHV system. There the intensity on a $50\times50\,\mu m$ detector is maximized to obtain a nearly diffraction limited spot size. Alignment of the focal point on the sample includes the use of a He-Ne tracer beam. Maximization of the detected infrared signal is also necessary because the CaF_2 window index of refraction varies with wavelength.

III. DISCUSSION

Vibrational spectra of CO on Ni[100] for 1800 to 2100 cm^{-1} have previously been obtained with both EELS[13-18] and infrared spectroscopy.[19-24] All studies at temperatures near 300 K find a peak at about 2050 cm^{-1} due to the CO stretch mode of terminally bonded CO, the frequency of which increases with coverage. Some studies also find evidence for infrared absorption in the 1800–2000 cm^{-1} region that is attributed to bridge bonded CO not oriented along the surface normal.[17,19,24] Structure in this frequency range has been observed to be strongly dependent on exactly how the surface is prepared.[17,24] In one case[24] when the surface was prepared so no infrared absorption was observed in this frequency range, the integrated absorption of the terminally bonded CO stretch peak was observed to increase by a factor of 4.9 relative to the same coverage when the structure is observed. Photoemission experiments, however, have been interpreted to indicate that CO on Ni[100] adsorbs along the surface normal,[25-28] except at low temperatures with coadsorbates present.[29]

In the EVS spectra in Fig. 1(b) of Ni[100] dosed with 10 L of CO, the derivative of an absorption peak at 2033 cm^{-1} is clearly observed. For the undosed surface there is evidence for a much weaker peak at about 2010 cm^{-1}. The EVS spectra of Figs. 1(a) and 1(b) were integrated with respect to optical frequency and a linear function between the first and last point subtracted from each to give the results plotted in Fig. 1(c). For the undosed and dosed surfaces the linear function corresponds to a $\Delta I/I$ offset of -2.92×10^{-7} and 7.70×10^{-6}, respectively. If the EVS spectra were proportional to the derivative of infrared absorption as previous theory has indicated, then no such offsets would be observed unless there were a large compensating EVS signal out of the spectral range observed. The existence of such large compensating EVS signal is unlikely. The offset does not arise from an instrumental problem unrelated to light modulation by the sample since, if the sample is bypassed optically, zero EVS signal is found. In a previous study[2] of CO on Ni[110] the $\Delta I/I$ offset was only 5×10^{-8} and the integrated spectrum was clearly proportional to the derivative of infrared absorption. One possible source of the offset is mechanical vibrations transmitted through the quartz fixture separating the sample and counter electrode, which was not present in the earlier study. This is also unlikely, since there is a large increase in the offset with CO adsorption. A more probable explanation is that it is related to the previously observed infrared absorption in the 1800–2000 cm^{-1} range with CO on Ni[100]. If this absorption is due to CO bonded at an angle with respect to the surface normal, a change in applied field could change the angle and thereby modulate both the infrared absorption by the CO and the amount of infrared transmitted through the surface to be absorbed in the Ni substrate.

Regardless of the source of the offset, the area under the

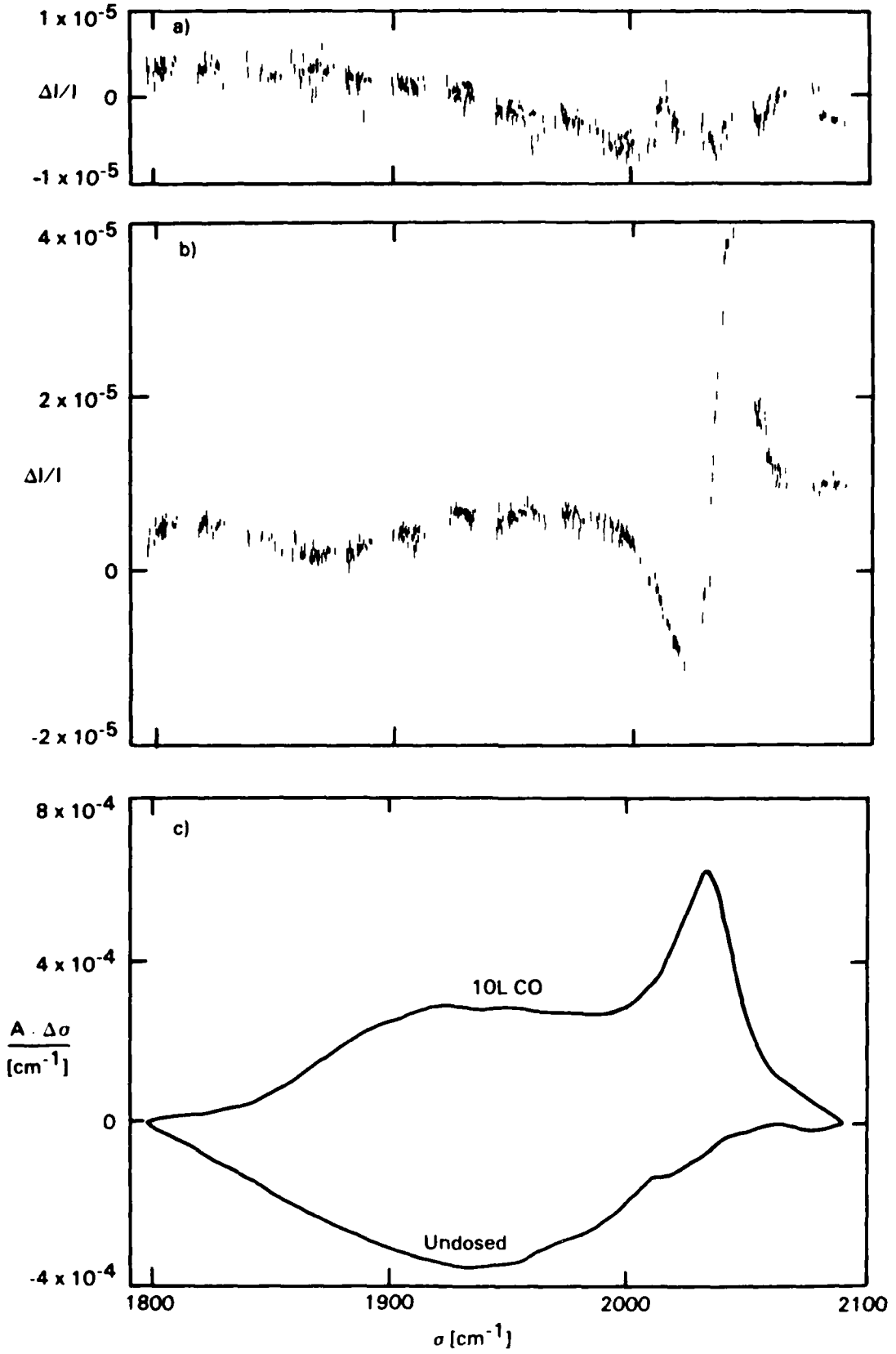

FIG. 1. (a) EVS spectra of Ni[100] surface at 300 K (b) and same surface dosed with 10 L of CO. Also (c), the result of integrating the EVS spectra in (a) and (b) after subtracting $\Delta I/I$ of -2.92×10^{-5} and 7.70×10^{-6} from the spectra of the undosed and dosed surfaces, respectively. The vertical scale for each plot should be multiplied by a factor of 1.3.

terminally bonded peak in the integrated EVS spectra may still be used to determine the Stark tuning rate of molecules that give rise to the peak by comparison with the area under the corresponding infrared absorption peak. In a previous investigation, Fedyk and Dignam[19,21] observed the terminally bonded peak for Ni[100] dosed with 10 L of CO at 80° angle of incidence. The area under the absorption peak they observed is 1.4×10^{-1} cm^{-1}. At the angle of incidence used in the present experiment (86°), the area would be expected to increase[30] by a factor of 1.74. Integrating the area under the peak in the integrated EVS spectrum for the dosed surface in Fig. 1(c) from 1975 to 2075 cm^{-1}, a cross section of 2.0×10^{-2} cm^{-2} is found. Hence the rms frequency modulation of the molecules giving rise to the peak is 8.2×10^{-2} cm^{-1}. The rms electric field, averaged over the surface weighted by incident intensity, is 6.3×10^{4} V/cm. Hence the measured Stark tuning rate is 1.3×10^{-6} cm^{-1}/(V/cm).

The errors in the measurement are primarily systematic due to uncertainty as to the equivalence of the integrated infrared absorption between the surface studied here and that studied[19,21] by Fedyk and Dignam. The terminally bonded CO peak in their spectrum occurs at 2080 cm^{-1} as opposed to 2030 cm^{-1} here, indicating their surface may have been less clean. It is also possible the surface CO coverage was less for the present measurement, since line of sight dosing was not used. An estimate of the likely inaccuracy due to such differences is 30%, but it should be realized that differences by as much as a factor 5 are observed,[24] as mentioned previously. The sign of the Stark tuning rate is such that increasing applied electric field directed out of the surface corresponds to a negative change in vibrational frequency.

For comparison with previous measurements, the Stark tuning rate for CO on Ni[110] was measured[2] to be 1.1×10^{-6} cm^{-1}/(V/cm), and the Stark tuning rate for CO on a Pt electrode in an aqueous electrolyte was deduced[10] to be 1.0×10^{-6} cm^{-1}/(V/cm) from EMIRS measurements and the Stern model. The direction of the Stark tuning rate was not determined for CO on Ni[110]. The direction of the Stark tuning rate for CO on a Pt electrode[5,6] is the same as observed here.

The vibrational Stark effect of adsorbed molecules has been described theoretically both in terms of the interaction between the applied field and the dipole moment of the adsorbed molecule,[10,31] and in terms of field-induced charge transfer between the surface and a molecular bond.[32,33] Only the first approach has been able to predict the Stark tuning rate from other experimental measurements without the use of adjustable parameters. Close agreement is found[10] between the Stark tuning rate measured and predicted for CO on Ni[110]. In terms of the dipole moment description of the Stark effect of CO, the magnitude is determined primarily by the dynamic dipole moment M_1. The infrared cross section is proportional to M_1^2. The cross section for CO on Ni[110] is about a factor 5 greater than for CO on Ni[100] that exhibits infrared absorption in the 1800–2000 cm^{-1} range. This suggests that on such a surface most of the CO is in a less infrared active state, as would be the case if it was bonded at an angle not perpendicular to the surface.

IV. SUMMARY

We have measured the Stark tuning rate of terminally bonded CO on Ni[100] to be 1.3×10^{-6} cm^{-1}/(V/cm), with a sign that results in a decrease in frequency as the electric field out of the surface is increased. The present measurement is in close agreement with a previous measurement of the Stark tuning rate of CO on Ni[100] and with the Stark tuning rate of CO on Pt as seen with EMIRS. The electroreflectance signal is found to result only partly from the vibrational Stark effect. There is some evidence that part of the CO molecules are tilted with respect to the surface normal. Electric-field-induced change in the tilt angle is suggested as an explanation for the additional electroreflectance signal.

ACKNOWLEDGMENTS

I would like to thank C. B. Murphy for technical assistance, D. L. Partin and C. R. Thrush for the diode laser, T. W. Capehart for loan of the Ni crystal and other help, and W. J. Evans and R. E. Teets for help in building the wavemeter.

[1] D. K. Lambert, U.S. Patent No. 4 446 719 (8 May 1984).
[2] D. K. Lambert, Phys. Rev. Lett. **50**, 2106 (1983).
[3] D. K. Lambert, Proc. SPIE **438**, 158 (1983).
[4] S. Efrima and H. Metiu, Surf. Sci. **109**, 109 (1981).
[5] K. Kunimatsu, J. Electroanal. Chem. **145**, 219 (1983).
[6] B. Beden, A. Bewick, and C. Lamy, J. Electroanal. Chem. **148**, 147 (1983).
[7] S. Venkatesan, G. Erdheim, J. R. Lombardi, and R. L. Birke, Surf. Sci. **101**, 387 (1980).
[8] R. Kotz and E. Yeager, J. Electroanal. Chem. **123**, 335 (1981).
[9] J. Billman and A. Otto, Surf. Sci. **138**, 1 (1984).
[10] D. K. Lambert, Solid State Commun. **51**, 297 (1984).
[11] L. E. Davis, N. C. MacDonald, P. W. Palmberg, G. E. Riach, and R. E. Weber, *Handbook of Auger Electron Spectroscopy* (Physical Electronics, Eden Prairie, MN, 1978).
[12] R. J. Madix, S. B. Lee, and M. Thornburg, J. Vac. Sci. Technol. A **1**, 1254 (1983).
[13] J. C. Bertolini and B. Tardy, Surf. Sci. **102**, 131 (1981).
[14] S. Andersson, Solid State Commun. **21**, 75 (1977).
[15] S. Andersson and J. W. Davenport, Solid State Commun. **28**, 677 (1978).
[16] S. Andersson, in *Proceedings of the 7th International Vacuum Congress and 3rd International Conference on Solid Surfaces*, edited by R. Dobrozemsky, F. Rudenauer, F. P. Viehbock, and A. Breth, Vienna, 1977, Vol. 2, pp. 1019–1022.
[17] G. E. Mitchell, J. L. Gland, and J. M. White, Surf. Sci. **131**, 167 (1983).
[18] J. L. Gland, R. J. Madix, R. W. McCabe, and C. DeMaggio, Surf. Sci. **143**, 46 (1984).
[19] M. J. Dignam, in *Vibrations at Surfaces*, edited by R. Caudano, J.-M Gilles, and A. A. Lucus (Plenum, New York, 1982), pp. 265–288.
[20] F. L. Baudais, A. J. Borschke, J. D. Fekyk, and M. J. Dignam, Surf. Sci. **100**, 210 (1980).
[21] J. Fedyk and M. J. Dignam, in *Vibrational Spectroscopies for Adsorbed Species*, edited by A. T. Bell and M. L. Hair (American Chemical Society, Washington, D.C., 1980), pp. 75–97.
[22] J. D. Fedyk, P. Mahaffy, and M. J. Dignam, Surf. Sci. **89**, 404 (1979).
[23] S. Chiang, R. G. Tobin, and P. L. Richards, J. Vac. Sci. Technol. A **2**, 1069 (1984).
[24] R. G. Tobin, S. Chiang, P. A. Thiel, and P. L. Richards, Surf. Sci. **140**, 393 (1984).
[25] C. L. Allyn, T. Gustafsson, and E. W. Plummer, Chem. Phys. Lett. **47**, 127 (1977).

[26]C. L. Allyn, T. Gustafsson, and E. W. Plummer, Solid State Commun. **28**, 85 (1978).
[27]M. Passler, A. Ignatiev, F. Jona, D. W. Jepsen, and P. M. Marcus, Phys. Rev. Lett. **43**, 360 (1979).
[28]S. Andersson and J. B. Pendry, Phys. Rev. Lett. **43**, 363 (1979).
[29]E. Tornqvist, T. Gustafsson, and E. W. Plummer, Bull. Am. Phys. Soc. **28**, 471 (1983).
[40]R. B. Bailey, Ph.D. thesis, University of California Lawrence Berkeley Laboratory Report No. LBL-8482, 1978 (unpublished), p. 24.
[41]J. E. Gready, G. B. Backskay, and N. S. Hush, Chem. Phys. **24**, 333 (1977).
[42]A. B. Anderson, R. Kotz, and E. Yeager, Chem. Phys. Lett. **82**, 130 (1981).
[43]S. Holloway and J. K. Norskov, J. Electroanal. Chem. **161**, 193 (1984).

Excitation and ionization at surfaces: CO on metals

Ph. Avouris
IBM Watson Research Center, Yorktown Heights, New York 10598

P. S. Bagus
IBM Research Laboratory, San Jose, California 95193

A. R. Rossi
Department of Chemistry, University of Connecticut, Storrs, Connecticut 96268

(Received 15 February 1985; accepted 11 April 1985)

We discuss the energetics, electronic structure, and stability of neutral excited and ionic states of adsorbates on metals using CO as a prototype. By *ab initio* cluster calculations we show that two types of negative ion states, bonding and antibonding, exist. We then show that the valence 4σ, $5\sigma \rightarrow 2\pi^*$ excitations of chemisorbed CO are essentially unshifted from their free CO positions, while a charge-transfer excitation appears at $\sim$5–7 eV. Intra-adsorbate polarization effects are shown to be responsible for the spectral shifts of the corresponding core (C1*s*, O1*s*$\rightarrow 2\pi^*$) excitations. The relation between screened positive ion states and neutral excited states is discussed. Finally, the connection between the above spectroscopic results and photon- or electron-stimulated desorption is examined.

I. INTRODUCTION

There is a growing interest in understanding the microscopic mechanisms by which photon or energetic particle (electron, ion)-beams interact with solid surfaces and adsorbate layers. This interest is a result primarily of the increasing use of material-modification technologies based on such interactions, but there is also significant basic scientific interest on this subject.[1] The first step in the energy deposition by energetic photon or electron beams involves neutral excitations or ionizations. Therefore, to understand the beam-surface interaction we need to understand first the nature and energetics of the quantum states of the clean surface or adsorbate layer.

Here, we will concentrate on adsorbate layers, carbon monoxide chemisorbed on metals, in particular. CO has long been a prototype system in chemisorption studies and there is a fairly good understanding of the nature of the chemisorption bond in the ground state. CO binds with the C end, and the CO axis is perpendicular to the surface. The bonding of CO on transition metals is a result of two interactions: (a) a charge donation from the 5σ orbital (essentially a long pair on the C atom) of CO to metal, and (b) a charge backdonation from the metal to the antibonding $2\pi^*$ orbital of CO.[2] The latter interaction provides the larger contribution to bonding.[3] The bonding and energy of the excited and ionic states of chemisorbed CO are more poorly understood. Several studies of the neutral excited states using electron energy loss spectroscopy (EELS) have been reported over the years,[4] but there is significant disagreement regarding their assignment. The bonding of the negative ion states of chemisorbed CO is largely unknown and only a few experimental inverse photoemission (IPE) studies have been reported.[5]

We will first consider the results of cluster calculations on the bonding and energetics of the negative ion states of CO/Cu(100), and use these results to interpret the IPE studies. We will then consider experimental and theoretical results on the valence excitations of CO on Cu, and Ni, and show why previous assignments of these excitations are unsatisfactory. The importance of many-particle interactions in the description of excited states is demonstrated by cluster calculations on the core excitations of CO/Cu(100), and by comparison with experiments on CO/Ni(111).[6] Finally, the positive ion states of chemisorbed CO are considered and the relation between charge-transfer-screened positive ion states and neutral excited states is explored. The behavior of the neutral excited and ionized states in photon- and electron-stimulated desorption is discussed.

II. COMPUTATIONAL AND EXPERIMENTAL DETAILS

Due to the limited space, we will only provide some essential information regarding the computations and experiment. Briefly, self-consistent field (SCF) calculations have been performed on a series of Cu clusters: CuCO, Cu_5(1, 4)CO, Cu_9(5, 4)CO, and Cu_{13}(9, 4)CO to model the on-top binding site of CO on Cu(100). The SCF orbitals were expanded in a set of contracted Gaussian-type orbital (CGTO) basis functions. For C and O, the 9*s*, 5*p* primitive set was contracted to 4*s*, 3*p* CGTO's. All the electrons of the Cu atom directly bonded to CO were included in the calculation in the form of a 14*s*, 11*p*, 6*d* primitive set contracted to 8*s*, 6*p*, 4*d*. The electrons of the other environmental Cu atoms were treated with a pseudopotential and only one electron per atom (the 4*s*) was explicitly included.[7] More detailed discussions on the core excited and negative ion states will be published elsewhere.[8,9] The EELS techniques used to obtain the spectra of solid and chemisorbed CO shown in Fig. 2 are completely analogous to those described in Ref. 10.

III. VIRTUAL LEVELS AND NEGATIVE IONS

Most discussions of the virtual levels of chemisorbed CO are based on a single particle model in which the $2\pi^*$ level of free CO is allowed to interact with the occupied *d* band of the metal to give a filled, metal-like bonding orbital, and an emp-

 0734-211X/85/051484-06$01.00

ty, CO(2π)-like, antibonding orbital.[2] On the basis of this simple local interaction scheme it has been suggested that the $2\pi^*$-like virtual level of chemisorbed CO will be pushed to a higher energy than the $2\pi^*$ level of free CO, and therefore the electron affinity of chemisorbed CO is even more negative than that of free CO. The same assumption is made in single particle descriptions of the valence excitations of chemisorbed CO, and as a result strong blue shifts of these excitations, with respect to their free CO counterparts, have been proposed.[4] The scheme has been criticized on the basis that it neglects the involvement of the metal s, p_π conduction band electrons both filled and unfilled, in the interaction and hybridization with the CO $2\pi^*$ level.[11] For the ground state, cluster studies[12] of CO on Cu give evidence that both the metal d_π and $4sp_\pi$ take part in the back donation to CO $2\pi^*$, the major interunit charge transfer bonding effect. In the negative ion states formed by inverse photoemission processes, strong CO $2\pi^*$ hydridization with $4p_\pi$ metal states is expected because of the large unoccupied conduction band density of states in the vicinity of the CO $2\pi^*$ level. To obtain a qualitative understanding of the importance of the various interactions on the energies of the negative ion states of chemisorbed CO, we have performed SCF calculations on Cu_xCO^- clusters with $x = 1, 5, 9$ and 13.

In all clusters, we find that there are two kinds of virtual orbitals with significant amounts of CO ($2\pi^*$) character, not just one as predicted by the $d_\pi - 2\pi^*$ interaction scheme. These are relatively closely spaced levels with those at lower energy being metal–CO ($2\pi^*$) bonding and those at higher energy anti-bonding. As an example in Fig. 1 (top) we show an orbital plot of the bonding level for Cu_5CO^- which shows clearly its $2\pi^*$ character. Although it can be seen that this level has both bonding and antibonding regions, the overall Cu–C overlap population is bonding. There is a significant metal contribution to this level which ranges (gross populations) from ~16% in $CuCO^-$ to ~38% in $Cu_{13}CO^-$. The metal contribution is primarily valence $4p$ and $4s$ (see Fig. 1) with only a small $3d$ contribution. The higher-lying antibonding level, on the other hand, is predominantly (70%–90%) metal. These conclusions are expressed by the orbital correlation diagram shown at the bottom of Fig. 1. Occupation of the bonding level gives rise to a strongly bound negative ion state with respect to the separated metal + CO system. Thus, for example, we find that while CuCO is unbound at the SCF level,[12] the $CuCO^-$ ($2\pi_h^*$) is bound by almost 2 eV. This strong bonding is the result of two factors: (a) a CO^- ($2\pi_h^*$)→metal ($4p_\pi$) charge donation, the reverse of metal ($3d_\pi$)→CO($2\pi^*$) "backdonation" which is important for the bonding of neutral CO, and (b) the electrostatic polarization of the metal by the CO^-. This electrostatic polarization can be viewed as the metal forming positive image charge due to the presence of a largely anionic CO. We find that in the negative ion the normal $d_\pi, sp_\pi \rightarrow 2\pi^*$ donation is reduced by the negative charge on the CO.

The qualitative result of the strong interaction of the CO($2\pi^*$) with the metal p_π levels giving bonding and antibonding levels is directly transferable to the real CO/metal system. However, with respect to the energetics of the negative ion states, we can only define trends since the clusters are too small to adequately represent the metallic conduction band. In addition, it is known that an explicit account of correlation effects is needed for the accurate calculation of electron affinities. The Δ SCF values of the electronegativities for electron capture at the $2\pi^*$ bonding level vary from −0.2 eV ($CuCO^-$) to +0.2 eV ($Cu_{13}CO^-$). Thus, we see that the electron affinity of coordinated CO is higher than that of free CO, and in the case of $Cu_{13}CO^-$ where the cluster is large enough so that it begins to give some representation of the Cu(100) conduction band, it becomes positive (+0.2 eV). We also find that the separation between the two lowest electronegativity values decreases with increasing cluster size, from 2 eV ($CuCO^-$) to 1.2 eV ($Cu_{13}CO^-$).

There have been two inverse photoemission studies of CO on Cu surfaces. In the first case, a disordered CO layer on Cu(110) was investigated and a broad asymmetric resonance was observed peaked at ~1.1 eV below E_{vac}.[5b] A more recent study involves an ordered CO/Cu(100) system.[13] Our cluster simulations are most appropriate in this case where CO is bound in an on-top site of Cu(100) surface. In this study,[13] two peaks separated by ~1 eV for normal incidence electrons and centered at ~1.1 eV below E_{vac} were resolved. Experiments[14] have eliminated occupation of different sites or lateral interactions as the cause of the splitting. The calculations described above strongly suggest that the observed two peaks in the inverse photoemission spectrum of CO/Cu(100) represent electron capture in a bonding and antibonding level, respectively.

Our calculated values of the electron affinity are expected to be low because the cluster size is too small to give an

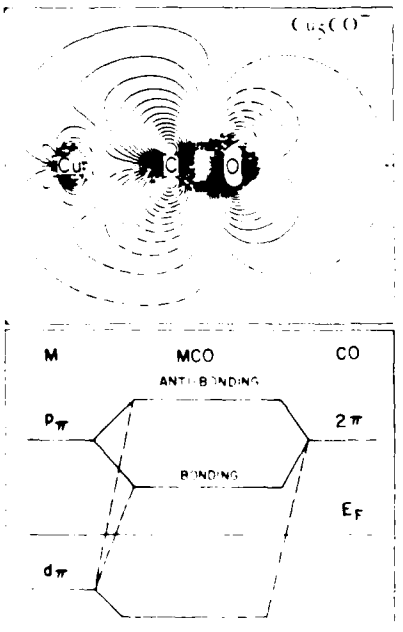

FIG. 1. Top: Orbital contour plot of the lowest energy π-level of Cu_5CO^-. It can be seen that this level is primarily (~80%) CO $2\pi^*$ like; it is bonding with respect to the Cu–CO bond, and that the metal contribution is primarily (~80%) $4p$. Bottom: Schematic molecular representation of the metal–CO $2\pi^*$ interaction. Large contributions to an MCO orbital are shown by solid lines and small contributions by dotted lines.

adequate description of the metallic conduction band or to provide the full polarization, image charge, stabilization of the negative ion. On the other hand, the splitting between the bonding and antibonding states is more sensitive to local bonding interactions and already in $Cu_{13}CO$ the splitting is essentially that of CO/Cu(100).

IV. NEUTRAL AND CHARGE-TRANSFER ELECTRONIC EXCITATIONS

Next, we consider the subject of neutral valence (4σ, $5\sigma \rightarrow 2\pi^*$) and core (C1$s$, O1$s \rightarrow 2\pi^*$) electronic excitations. The assignment of the electronic excitations of chemisorbed CO and of other adsorbates has been the subject of considerable debate. Unlike the spectra of free molecules, the electronic spectra of adsorbates are broad and featureless, providing few clues regarding their origin. In Fig. 2, we show high-resolution low-energy EELS spectra of solid CO, weakly chemisorbed ($\Delta H \sim 0.6$ eV[14]) CO on Cu, and strongly chemisorbed ($\Delta H \sim 1.3$ eV[14]) CO on Ni. The two structured bands at ~ 6 and ~ 8.5 eV in solid CO are due to the

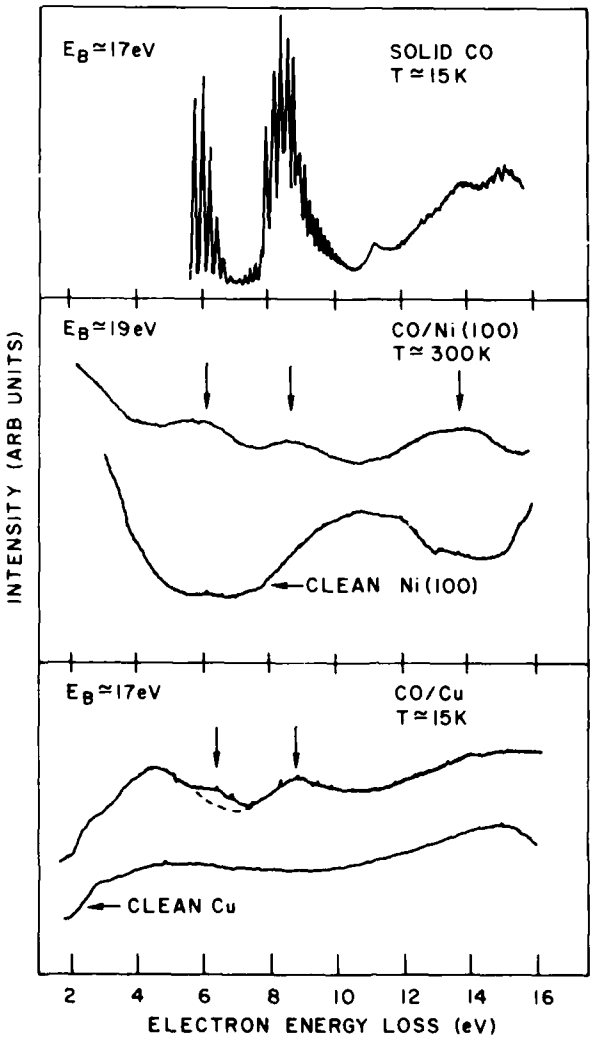

FIG. 2. Electron energy loss spectra of (a) solid CO at 15 K (top), (b) monolayer CO on Ni(100) at 300 K (middle), and (c) monolayer CO on Cu at 15 K (bottom).

$^1\Sigma^+(\ldots 1\pi^4 5\sigma^2) \rightarrow {}^{3,1}\Pi(\ldots 1\pi^4 5\sigma^1 2\pi^{*1})$ valence transitions, respectively.[15] The spectrum of gaseous CO above ~ 11 eV shows a series of highly structured transitions to Rydberg states.[15] All these Rydberg transitions are strongly perturbed and broadened in the solid, giving rise to a weak band at ~ 11.2 eV and an onset-like absorption starting at ~ 13 eV. The broad peak at ~ 13.8 eV in the spectrum of the solid is most likely due to the $^1\Sigma^+ \rightarrow {}^1\Pi(\ldots 4\sigma^1 1\pi^4 5\sigma^2 2\pi^{*1})$ valence excitation which is placed at ~ 13.3 eV in the gas phase.[15] Finally, the 5σ ionization of gaseous CO has a vertical IP$\simeq$14 eV.

The spectra of chemisorbed CO look remarkably similar to those of solid CO. In both CO/Cu and CO/Ni, two broad bands only slightly shifted from the positions of the $^1\Sigma^+ \rightarrow {}^{3,1}\Pi(5\sigma^1, 2\pi^{*1})$ excitations of the solid are observed.[10] At higher energies (13–14 eV) another broad excitation is again observed (weak in the case of CO/Cu). The similarity between the spectra of solid and chemisorbed CO raises the possibility of a common origin of the respective excitations. In most spectral studies, however, the energetic similarity of the excitations of free and chemisorbed CO has been considered to be purely coincidental.[4] The excitation process in chemisorbed CO has been viewed in terms of one-electron level models and the excitation energy often taken to be equal to the difference in orbital energies of the upper and lower orbitals involved in the transition. Thus, based on the ~ 3 eV stabilization of the 5σ level upon chemisorption suggested by valence photoemission[14] and blue shift on the $2\pi^*$ level upon chemisorption predicted by the $d_\pi \rightarrow 2\pi^*$ interaction model (see previous discussion on negative ions), the intra-adsorbate $5\sigma \rightarrow 2\pi^*$ excitation was placed at 13–14 eV, i.e., in the region of the third absorption band of chemisorbed CO (Fig. 2). The two low energy bands in most studies were considered to be due to $d_\pi \rightarrow 2\pi^*$ and $d_\sigma \rightarrow 2\pi^*$ charge transfer transitions.[4] However, this assignment neglects the possibility of large shifts in the $2\pi^*$ orbital energy because of hybridization and interaction with the metal, primarily conduction σ and π levels. From the discussion of the negative ion states, we have shown that this hybridization is reasonably large. A very crude measure of the changes in the transition energies can be made by examining the changes in the occupied 5σ and virtual 2π orbital energies, E_i's, between free CO and the linear CuCO cluster. There is, as noted previously,[16] a large shift of $E_{5\sigma}$ to a more negative value by ~ 3.6 eV. However, the lowest π virtual orbital of CuCO with substantial CO $2\pi^*$ character has a large (45%) mixture of Cu $4p_\pi$; the E of this orbital is 2.6 eV smaller than $E^*_{2\pi}$ of free CO. The consequence is that $E_{2\pi} - E_{5\sigma}$ is smaller by only 1 eV for free CO than for CuCO. Analogously, $E_{2\pi} - E_{4\sigma}$ has similar values for CuCO and CO; the CuCO value is actually smaller, red shifted, than that for CO by 1 eV. The estimate of a transition energy by an orbital energy difference neglects many important factors and it should not be used quantitatively. It does, however, provide strong evidence that a large blue shift of the valence 5σ and $4\sigma \rightarrow 2\pi^*$ excitations upon adsorption should not be expected. The inadequacies of previously proposed assignments of the electronic excitations of chemisorbed CO become even more apparent when one attempts to describe the excitations not at

the single particle level but more correctly, at the state level. In this case, a Born–Haber cycle shows that the excitation energy of the chemisorbed adsorbate is given by the sum of the gas phase excitation energy, plus the difference of the adsorbate–substrate interaction (adsorption) energy in the ground and excited states of the adsorbate. If the $5\sigma \rightarrow 2\pi^*$ excitation of chemisorbed CO is placed at 13–14 eV, then this excitation will be 4–5 eV repulsive at the Franck–Condon geometry. Thus, in a photon-stimulated desorption (PSD) or electron-stimulated desorption (ESD) experiment, emission of very fast neutral CO should be observed at an energy threshold $\simeq$13–14 eV. While an increase in CO emission is observed at $\sim$15 eV (see discussion on positive ions). a threshold or peak for neutral CO emission has been observed at lower energies, at $\sim$10 eV for CO/Ru(001)[17] and at $\sim$9 eV for CO/W(110).[18] Very recent measurements of the kinetic energy distribution of CO desorbed from Ru(001) have yielded most probable $E_{kin} < 0.4$ eV.[19] *Thus, the above experimental results and theoretical expectations do not support the assignment of the 13–14 eV bands as $5\sigma \rightarrow 2\pi^*$ excitations.* We also argued above that the $4\sigma \rightarrow 2\pi^*$ excited state will have an excitation energy not too different from that of ground state CO. Thus, the 13–14 eV band in the spectra of chemisorbed CO (Fig. 2) is likely to have contributions from both the $4\sigma \rightarrow 2\pi^*$ neutral and $5\sigma^2 \rightarrow 5\sigma^1 + e$ ionization transitions.

Let us now consider possible charge-transfer excitations for chemisorbed CO. Recent Penning and inverse photoemission spectroscopy results allow us to predict the energy of such excitations. Thus, Penning studies of CO/Ni(111)[20] show a level with a binding energy of $\sim$2 eV below E_F. This level was assigned as due to a partially filled $2\pi^*$ orbital[20] and our calculations suggest emission from a predominantly sp_π bonding orbital. The electron affinity of CO/Ni(111) was measured to be about $+3$ eV.[5a] Therefore, a $sp_\pi \rightarrow 2\pi^*$ charge-transfer excitation in CO/Ni(111) should have an excitation energy of $\sim$5 eV. The charge-transfer excitation has a transition dipole normal to the surface and thus it should be unscreened and dipole allowed. The 5–7 eV band in the EEL spectrum of CO/Ni(100) in Fig. 2 should contain such a charge-transfer excitation.

Excitation of a sp_π/d_π (bonding)$\rightarrow 2\pi^*$ (antibonding) charge transfer state is expected to lead to neutral CO desorption (the CO^- autoionization lifetime is $< 10^{-14}$ s). A 4–5 eV threshold for CO desorption has indeed been reported in ESD studies of CO/W.[21] We should note, however, that there is an ambiguity in the interpretation of ESD experiments. This ambiguity results from the unknown final state of the exciting electron. If the final state of 5-eV electron is the vacuum level then only the charge-transfer state can be excited. If, however, the electron ends up at the Fermi level of the metal, then the transferred energy is 5 eV plus the metal work function ($\sim$5 eV), i.e., $\sim$10 eV, so that the higher energy side of the intra-adsorbate $5\sigma \rightarrow 2\pi^*$ state is excited. The appearance of a threshold at $\sim$5 eV and of a broad peak at $\sim$9 eV in the ESD spectra of CO/W(110)[18] suggests that perhaps both excitations can lead to CO desorption.

To obtain a better idea of the many electron effects which need to be considered for the understanding of electronic excitations at surfaces, and to provide a more critical comparison of excitation and inverse photoemission spectroscopies, we now will focus on the C1*s* and O1*s*$\rightarrow 2\pi^*$ core excitations of chemisorbed CO. The nonbonding character of the core orbitals simplifies the picture and allows for a clearer understanding of the physics involved.

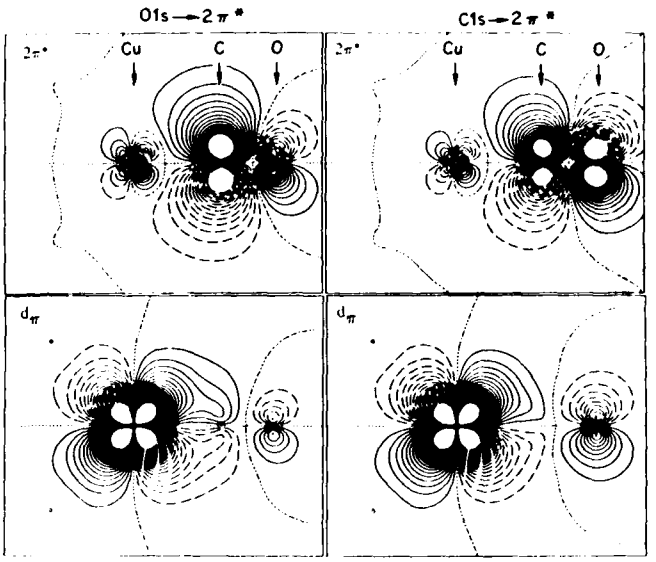

FIG. 3. Orbital contour plots of the bonding (primarily d_π) and antibonding (primarily $2\pi^*$) 2π levels of the O1*s*$\rightarrow 2\pi^*$ and C1*s*$\rightarrow 2\pi^*$ core-excited states of Cu_5CO. There are two important points to be noted. (a) In the O1*s*$\rightarrow 2\pi^*$ state, the $2\pi^*$ amplitude is highest on the C atom, which leads to stronger coupling to the metal. In the C1*s*$\rightarrow 2\pi^*$ state, the amplitude is more evenly distributed among the C and O atoms. (b) The presence of the core hole increases the binding energy of the $2\pi^*$ level which now interacts more strongly with the 3*d* levels (contrast with the negative ion state in Fig. 1).

In a recent high resolution synchrotron study of the core excitations of CO/Ni(111),[6] it was found that the O1*s*$\rightarrow 2\pi^*$ and C1*s*$\rightarrow 2\pi^*$ excitations are correspondingly red shifted and blue shifted (if the first moment of the asymmetric band is used) with respect to the corresponding excitations of free CO. These shifts imply that the O1*s*$\rightarrow 2\pi^*$ excited state CO is more strongly bound to the surface than ground state CO, while CO in the C1*s*$\rightarrow 2\pi^*$ state is more weakly bound. Since the core states are not directly involved in bonding, the observed changes reflect the renormalization of the energy levels resulting from the creation of the core hole.

Our SCF calculations on the core excitations of Cu_5CO provide a clear physical picture.[8] In Figure 3, we show the calculated potential energy curves and excitation energies. Both excited states are bound and the order of interaction (adsorption) energies is $E_{int}(O1s, 2\pi^*) > E_{int}$(ground state) $> E_{int}(C1s, 2\pi^*)$, in agreement with the synchrontron results.[16] In Fig. 4, we show orbital contours of the $2\pi^*$ levels populated by the excited electron in the two core excited states. There are two important points to observe: (a) the relative amplitude of the $2\pi^*$ orbital on the C and O atoms is different in the two excited states, and (b) the metal contribution to the hybridized $2\pi^*$ orbital is different in the core-excited states and in the negative ion state (see Fig. 1). The explanation of the first observation is quite simple. In free CO, the $2\pi^*$ orbital is distributed $\sim$75% on C and $\sim$25%

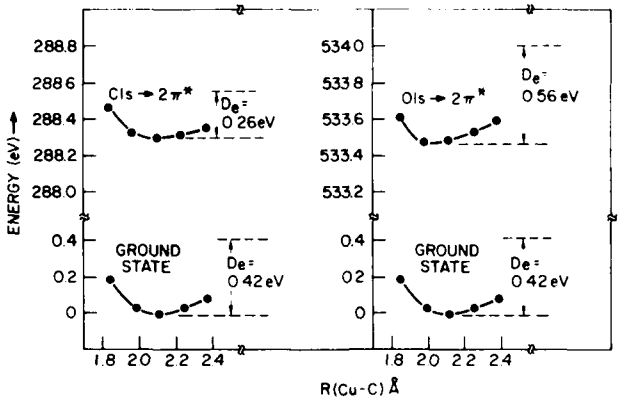

FIG. 4. Potential energy curves for the ground, and C1*s* and O1*s*→$2\pi^*$ core-excited states of Cu_5CO. The order of interaction (M–CO* dissociation) energies is $D_e(O1s, 2\pi^*) > D_e(G.S) > D_e(C1s, 2\pi^*)$.

on O; the creation of a O1*s* hole polarizes the electronic system so that the 1π orbital becomes heavily localized on the O end of the molecule. Thus, the orthogonal $2\pi^*$ orbital must be localized on the C end. This polarization results in increased $d_\pi \rightarrow 2\pi^*$ donation due to the increased $d_\pi - \pi^*$ overlap (see Fig. 4). Thus, the O1*s*→$2\pi^*$ state is more strongly bound than the ground state. The opposite is true for the C1*s*→$2\pi^*$ state. The creation of the C1s hole leads to nearly equal effective nuclear charges seen by the valence electrons. Thus, both 1π and $2\pi^*$ are fairly evenly distributed between C and O, and the interaction energy is reduced.

The second point can be accounted for by considering the energetics of the $2\pi^*$ level. In the negative ion, the affinity level is at 3–4 eV above E_F and involves a strong mixture of $2\pi^*$ and the unoccupied metallic 4*p* levels. In the core-excited state, the electron–hole interaction pulls the $2\pi^*$ level down and localizes it on the CO unit; it is now below E_F and the $3d - 2\pi^*$ interaction is increased. *Thus, $d_\pi \rightarrow 2\pi^*$ charge donation provides the main bonding interation in the excited (and ground state) molecule, while $2\pi^* \rightarrow p_\pi$ donation is the dominant interaction in the negative ion.* It is worth repeating again that not only the energy and but also the electronic distribution in the $2\pi^*$ level depends critically on the state of the molecule.

Up to this point, we have concentrated on spin allowed singlet–singlet excitations. Optically forbidden singlet-triplet surface excitations, however, can be detected readily by low energy electron scattering techniques[10,22]; see for example the $^3(5\sigma \rightarrow 2\pi^*)$ excitation of solid CO in Fig. 2. The exchange scattering cross section peaks for incident electron energies (E_i) near the excitation threshold, and decreases fast as E_i is farther increased. Thus, spectra obtained as high E_i would only reveal allowed excitations. The energy separation ($\Delta E_{s,t}$) between singlet and triplet states arising from the same orbital configuration is due to the interaction of electrons with the same spin. At the SCF level, $\Delta E_{s,t}$ is given by $2K(\phi_i, \phi_j)$, where K is the exchange integral for an electron in orbital i and the other in j. Thus, the singlet–triplet splitting is larger, the larger the spatial overlap of ϕ_i and ϕ_j. Upon chemisorption, the mixing of adsorbate and substrate states delocalizes the free molecule orbitals. As a result, we expect $\Delta E_{s,t}$ to decrease upon chemisorption.[8] (Note that no change in $\Delta E_{s,t}$ was observed upon physisorption).[22] In fact, the measurement of $\Delta E_{s,t}$ could possibly be used as a yardstick for the measurement of the extent of delocalization due to chemisorption. In free CO (Fig. 2), $\Delta E_{s,t} \sim 2$ eV and, therefore, the ~6 eV peak in the spectrum of CO/Cu, a weak chemisorption case, most probably contains the $^3(5\sigma \rightarrow 2\pi^*)$ transition.[10] However, CO is not the best system to use to study the triplet excitations since the expected excitation energies to the charge-transfer and triplet neutral states are similar.

V. POSITIVE IONS

We close our discussion by considering very briefly the interaction of CO^+ ions with metal surfaces. A Born–Haber cycle shows that the energy, E^+_{int}, required to desorb an ion from the surface is given by $E^+_{int} = IP(g) - IP(s) + E^*_{int}$. In general, for core- and valence-hole (4σ, 1π) ions, IP(*g*) > IP(*s*); therefore, these ions are bound. Existing experimental data suggest that 5σ-hole ions are unbound. In ESD experiments, desorption thresholds for CO^+ are observed at ~15 eV.[23] The desorption of CO^+ must be due to transitions from the Franck–Condon region of the ground state to the repulsive 5σ valence-hole state. Neutral CO emission is also enhanced at the same threshold, but more likely this is simply due to the partial neutralization of the desorbing CO^+.

The reduction of the ionization potential in the adsorbed phase is the result of efficient screening of the positive charge. In the case of CO, the screening mechanism is believed to involve charge transfer from the metal to the $2\pi^*$ orbital of the ion.[24] Thus, the screened ionic state should be very similar to a neutral excited state. Our calculations[8] on the screened core hole and neutral excited states find no significant differences between the two electronic structures. Thus, we expect that the binding energy of a level measured by photoemission and referenced to the Fermi level of the substrate should be approximately equal to the transition energy to the corresponding neutral excited state. This behavior is confirmed by the experimental data on CO on Ni(100)[25] and Ni(111).[6] The screening of valence-ion states has also been suggested to proceed via charge transfer to the $2\pi^*$ level.[24] The 5σ binding energies (with respect to E_F) for CO on transition metals are in the range 8–9 eV.[14] Our assignment of the 8–9 eV EELS band to the $5\sigma \rightarrow 2\pi^*$ neutral excitation is in harmony with the charge-transfer screening model.

In conclusion, we believe that we have provided a self-consistent picture of the electronic structure of chemisorbed CO in its excited and ionic states which is in agreement with the results of photoemission, inverse photoemission, excitation, and desorption spectroscopies.

[1]See other articles in these proceedings and also T. J. Chuang, Surf. Sci. Rep. 3, 1 (1983); and Desorption Induced by Electronic Transitions, edited by N. H. Tolk, M. M. Traum, J. C. Tully, and T. E. Madey, *Springer Series in Chemical Physics* (Springer, Berlin, 1983).

[2]See for example, *The Nature of the Surface Chemical Bond*, edited by T. N.

Rhodin and G. Ertl (North–Holland, New York, 1979).
[3]P. S. Bagus, K. Hermann, and C. W. Bauschlicher, J. Chem. Phys. **80**, 4378 (1984).
[4]For recent reviews of the literature see Ph. Avouris and J. E. Demuth, Annu. Rev. Phys. Chem. **34**, 49 (1984); Ph. Avouris, N. J. DiNardo, and J. E. Demuth, J. Chem. Phys. **80**, 491 (1984); S. Ishi and Y. Ohno, Surf. Sci. **139**, L219 (1984); H. J. Freund, W. Spiess, H. Behner, G. Wedler, C. M. Kao, and R. P. Messmer (to be published).
[5](a) Th. Fauster and F. J. Himpsel, Phys. Rev. B **27**, 1390 (1984); (b) J. Rogozik, H. Scheidt, V. Dose, K. C. Prince, and A. M. Bradshaw, Surf. Sci. **145**, L481 (1984); (c) P. D. Johnson, D. A. Wesner, J. W. Davenport and N. V. Smith, Phys. Rev. B **30**, 4860 (1984).
[6]Y. Jugnet, F. J. Himpsel, Ph. Avouris, and E. E. Koch, Phys. Rev. Lett. **53**, 198 (1984).
[7]P. S. Bagus, C. W. Bauschlicher, C. J. Nelin, B. C. Laskowski, and M. Seel, J. Chem. Phys. **81**, 3594 (1984).
[8]P. S. Bagus, A. R. Rossi, and Ph. Avouris, Phys. Rev. B **31**, 1722 (1985).
[9]P. S. Bagus, K. Hermann, Ph. Avouris, A. R. Rossi, and K. C. Prince, Chem. Phys. Lett. (in press).
[10]Ph. Avouris, N. J. DiNardo, and J. E. Demuth, J. Chem. Phys. **80**, 491 (1984).
[11]Ph. Avouris, in *Dynamics on Surfaces*, edited by B. Pullman *et al.* (Reidel, Dordrecht, 1984); Ph. Avouris and J. E. Demuth, Surf. Sci. (in press).
[12]P. S. Bagus, C. J. Nelin, and C. W. Bauschlicher, J. Vac. Sci. Technol. A **2**, 905 (1984).
[13]J. Rogozik, V. Dose, K. C. Prince, A. M. Bradshaw, P. S. Bagus, K. Hermann, and Ph. Avouris, Phys. Rev. Lett. (submitted).
[14]See for example, E. W. Plummer, and W. Eberhardt, Adv. Chem. Phys. **46**, 49 (1982).
[15]F. P. Huber and G. Herzberg, *Molecular Spectra and Molecular Structure* (Van Nostrand–Reinhold, New York, 1979).
[16]P. S. Bagus and K. Hermann, Appl. Surf. Sci. (to be published).
[17]P. Feulner, R. Treichler, and D. Menzel, Phys. Rev. B **24**, 7427 (1981).
[18]J. Rubio, J. M. Lopez-Sancho, and M. P. Lopez-Sancho, J. Vac. Sci. Technol. **20**, 217 (1982).
[19]P. Feulner, D. Menzel, H. J. Kreuzer, and Z. W. Gortel, Phys. Rev. Lett. **53**, 671 (1984).
[20]F. Bozso, J. Arias, J. T. Yates, R. M. Martin, and H. Metiu, Chem. Lett. **94**, 243 (1983).
[21]D. Menzel, Ber. Bunsenges. Phys. Chem. **72**, 591 (1968).
[22]Ph. Avouris and J. E. Demuth, J. Chem. Phys. **75**, 4783 (1981); Ph. Avouris, D. Schmeisser, and J. E. Demuth, J. Chem. Phys. **79**, 488 (1983).
[23]D. Menzel, J. Vac. Sci. Technol. **20**, 538 (1982).
[24]See, for example, S. Krause, C. Mariani, K. C. Prince, and K. Horn, Surf. Sci. **138**, 305 (1984), and references cited therein.
[25]J. Stohr and R. Jaeger, Phys. Rev. B **26**, 4111 (1982).

Laser investigation of the dynamics of molecule–surface interaction: Rotational and translational energy of scattered molecules

J. Häger and H. Walther
Max-Planck-Institut für Quantenoptik and Sektion Physik der Universität München, D-8046 Garching, Federal Republic of Germany

(Received 18 March 1985; accepted 28 May 1985)

Combining molecule surface scattering with state-selective laser-induced fluorescence and laser resonance ionization the internal energy distributions and state- and angular-resolved velocity distributions of surface-scattered NO molecules have been measured. In the experiments a supersonic NO beam was scattered from graphite and platinum surfaces. The parameters being varied were surface temperature and average velocity of the incoming molecular beam. The NO/Pt system shows a trapping/desorption behavior for all surface temperatures and a full rotational accommodation at low and only incomplete rotational accommodation at high temperatures. In the case of the weakly inelastic scattering of NO/graphite a similar behavior of the rotational energy of the scattered molecules was observed. The angle- and state-resolved velocity distributions show at low surface temperatures the coexistence of a quasispecular and an isotropic part. The diffusively scattered NO molecules gain rotational energy, but transfer much more translational energy to the surface, so that the energy balance is considerably negative. For the specularly scattered molecules energy loss and gain are balanced at low surface temperatures. With increasing temperatures the scattered molecules may gain translational energy, but the rotational energy stays constant, resulting under certain conditions in an energy transfer from the surface to the scattered molecules.

I. INTRODUCTION

The scattering of molecular beams from well-characterized solid state surfaces has long been recognized as an important method to investigate the dynamics of the molecule-surface interaction.[1] Most information has been obtained from angular and velocity distribution measurements, giving a complete insight into the dynamics as long as only atoms are involved in the scattering process. For molecules, however, additional knowledge of the change of the internal energy distribution is necessary. It has been demonstrated recently that this latter information can be obtained using the technique of laser-induced fluorescence.[2–10] For this purpose the scattered or also the incoming molecular beam is excited by the light of a frequency tunable laser and the fluorescence spectrum recorded as a function of the laser wavelength. The population number of the rotational or vibrational levels of the molecules can then be deduced from the intensities of the spectra. Using laser diagnostics further information can be obtained on the angle- and state-resolved velocity distributions: the resonant excitation of the molecule allows us to observe the resonantly enhanced ionization; thus time-of-flight measurements become possible leading to the determination of the velocity distribution. The laser measurements thus yield complete description of the dynamics of the molecule-surface interaction.

Laser investigations of the molecule-surface scattering were performed in our laboratory for some time. In the following paper, our investigations of the scattering of NO molecules from clean and precovered Pt(111) and graphite surfaces will be reviewed.

II. EXPERIMENTAL

An ultrahigh vacuum (UHV) chamber with a pulsed or optionally continuous molecular beam was developed for measuring the angular, rotational, and velocity distributions of surface-scattered NO molecules. The molecular beam is generated by a nozzle-skimmer device within a three-stage differentially pumped system. The beam can be seeded with different rare gases to change the translational energy of the molecules. The molecules that enter the UHV chamber through a 1.5-mm aperture are scattered from the solid surface located in the center of the scattering chamber with a background pressure of 2×10^{-10} mbar. The surface is mounted on the rotatable axis of a manipulator and can be cooled with liquid nitrogen or heated via its tantalum support leads. For angular distribution measurements, a quadrupole mass spectrometer can be rotated around the surface. For the measurement of the rotational distribution of NO molecules the frequency doubled radiation of a tunable excimer-pumped dye laser (226 nm) enters the scattering chamber through a Brewster window. The laser pulses are synchronized with the molecular beam pulses. The laser beam can be adjusted in such a way that it crosses, and thus analyzes, either the incoming molecular beam or the molecules scattered from the surface. The fluorescence light is collected on the cathode of a photomultiplier. The intensities of the fluorescence spectra recorded as function of the laser wavelength contain the information on the population of the different rotational states of the NO molecules.

In a slightly modified experimental arrangement (Fig. 1) the velocity of the scattered molecules can be analyzed by

 0734-211X/85/051490-08$01.00

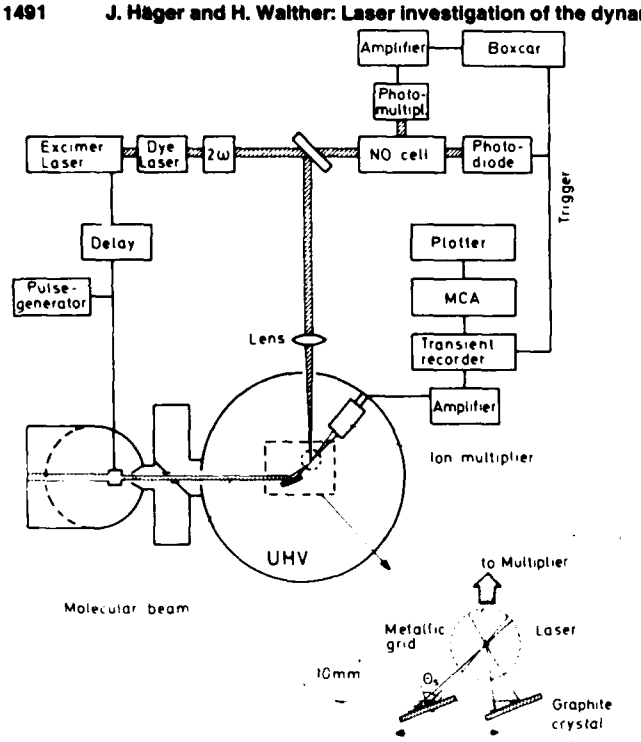

FIG. 1. Experimental setup for the measurement of state and angle-selective velocity distributions.

resonantly enhanced two-photon ionization as described in the following. A cylindrical cage 17 mm in diameter and 6 mm in height made of metal wire mesh at ground potential was set in front of the sample (axis of the cylinder is perpendicular to the scattering plane). The frequency doubled dye laser beam propagated along the cage axis. The NO molecules in a particular energy state are ionized by a two-photon transition via intermediate $X(^2\Pi) \rightarrow A(^2\Sigma)$ resonant excitation: the ions produced have the same velocity as the parent molecules, their velocity distribution can therefore be analyzed using time-of-flight measurements. As soon as the molecular ions emerge from the cage, they are accelerated towards the multiplier and detected. The time-of-flight spectrum of the ions can be recorded with a multichannel analyzer. In test experiments it was verified that both the time of flight of the ions outside the cage and the fringe field effects inside the cage are of no significant influence on the results. Consequently, the observed spectrum was the unperturbed time-of-flight spectrum of the state-selected scattered molecules, from which the velocity distribution of the molecules could then be deduced.

The scattering angle θ_s of the molecules is determined by the relative position of the cage with respect to the sample. Changing the position of the sample in the direction of the molecular beam (Fig. 1) leads to a detection of molecules scattered under different angles. With the given experimental setup scattering angles between 2° and 64° can be covered for an incidence angle $\theta_i = 70°$.

The NO molecules were scattered from the surface of a cleaved pyrolytic graphite crystal, from a carbon-covered Pt surface, or from a clean Pt(111) surface. The graphite crystal consisted of microcrystals with highly oriented basal planes and a mosaic spread of $0.4° \pm 0.1°$ (Union Carbide, grade ZYA).

Due to spin-orbit interaction NO exhibits two electronic states ($^2\Pi_{1/2}$ and $^2\Pi_{3/2}$) separated by 123 cm^{-1}. This offers the additional possibility to probe the redistribution of internal energy to different electronic states.

III. EXPERIMENTS AND RESULTS

The adiabatic expansion of the NO molecular beam in the nozzle causes an increase of the average velocity of the molecules and, simultaneously, a strong reduction of the rotational temperature and the velocity spread. The molecules of the beam had an average velocity of ~750 m/s, a velocity spread full width at half-maximum (FWHM) of ~140 m/s and a rotational population distribution corresponding to a Boltzmann distribution of 35 K.[2] The beam hit the surface at selectable incidence angles between 30° and 70°.

An important parameter in scattering experiments is the depth of the molecule-surface potential. Therefore, the investigations were performed with two systems [NO/graphite and NO/Pt(111)] showing potential depths of 0.1 and 1.4 eV, respectively. Since the deep NO/Pt potential leads to a long residence time of the NO molecules the use of a continuous molecular beam was necessary to guarantee steady state conditions during the measurements. For the NO/graphite system, on the other hand, the NO molecules have a residence time which is short compared to the duration of the molecular beam pulses (~5 ms FWHM). In this case, either the pulsed or the continuous beam source could be used for the measurements.

A. Angular and rotational distributions of NO/Pt(111)

If a clean Pt(111) surface is exposed to NO molecules, they will undergo nonactivated chemisorption. The resulting buildup of an equilibrium coverage with NO molecules on the Pt surface depends on the molecular flux and the surface residence time. Under the given experimental conditions and for low surface temperatures T_s the molecules are scattered from a Pt surface substantially covered with NO molecules ($T_s \lesssim 300$ K), while at $T_s \gtrsim 450$ K the interaction with the clean Pt(111) surface will dominate.

The angular distributions of NO molecules scattered from a Pt(111) surface at temperatures between 250 and 600 K are presented in Fig. 2. The data were derived directly from the rotatable mass spectrometer signals corresponding to the density of the particles. To obtain the molecular flux, the results have to be corrected for the particle velocities. In the case of the NO/Pt system the angular dependence of the velocity is expected to be small, therefore the figure represents quite accurately the angular distribution of the flux.

The results displayed on Fig. 2 show cosine distributions slightly distorted in the direction of specular reflection.[2c] From these results and the long residence time of the molecules it can be concluded that most of the particles leave the surface with their mean translational energy accommodated to the surface temperature. This conclusion is supported by a direct determination of the velocity distributions of the desorbing NO molecules through time-of-flight measure-

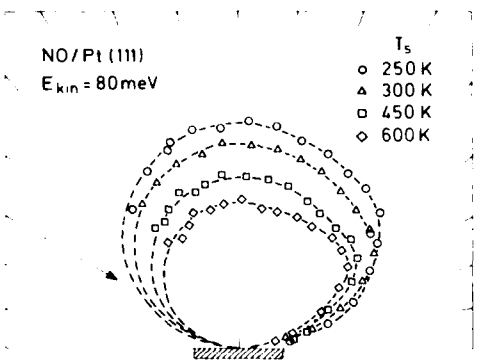

FIG. 2. Angular distributions of NO molecules scattered from a Pt(111) surface at different surface temperatures. [The slight enhancement of the intensity over the cosine distribution near the specular direction is caused by a small fraction (10%) of the particles scattered through a direct inelastic channel.]

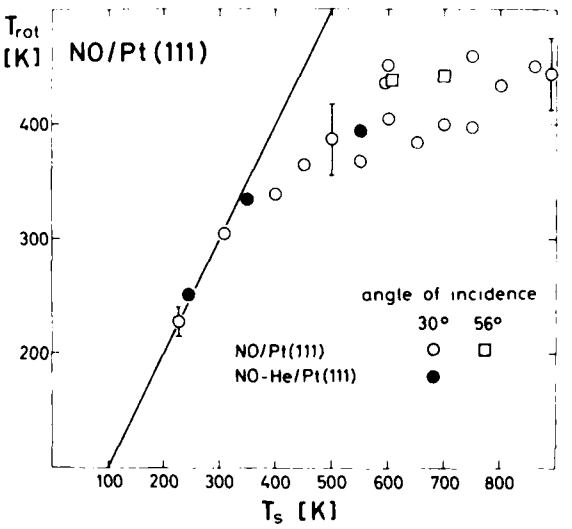

FIG. 3. Rotational temperature T_{rot} vs surface temperature T_s for NO molecules scattered from a Pt(111) surface. The results characterized by open symbols were obtained at $E_{kin} = 80$ meV, and those with solid symbols were obtained at $E_{kin} = 200$ meV (seeded beam). The straight line corresponds to full rotational accommodation to the surface temperature [see also Ref. 2(c)].

ments.[5c] Thus, scattering from both the clean- and NO-covered Pt(111) surface is dominated by trapping/desorption processes.

The chemisorbed NO molecules are characterized by a mean surface residence time which was determined directly by modulating the incoming continuous beam and measuring the phase shift of the outgoing beam pulses with respect to the ones of the incoming beam. The values obtained for T_s between 400 and 600 K were extrapolated to higher values. The results for the residence times range from about 3 s at $T_s = 400$ K to 5×10^{-7} s at $T_s = 800$ K.[2c] With increasing coverage (decreasing temperature) the heat of adsorption decreases continuously; simultaneously the fraction of molecules leaving the surface from the precursor potential increases. In the temperature range between 300 and 400 K the trapping/desorption processes at the clean- and the NO-covered Pt surfaces occur with comparable probabilities.

Below $T_s \leqslant 300$ K trapping/desorption is determined by the precursor potential, i.e., by the interaction of the incoming NO molecules with already adsorbed particles. The lifetime in the precursor state in the relevant temperature range was too short to be measured by modulated beam techniques. Since the interaction will be essentially of the van der Waals or weak dipole–dipole type, the depth of the attractive potential well will not exceed about 10 KJ/mol.

In the experiment the laser-induced fluorescence of the NO molecules was measured in the $^2\Sigma \leftarrow {}^2\Pi(0\text{-}0)$ transition before and after the scattering process. The obtained fluorescence line intensities $I_{J'J''}$ allow the calculation of the relative population densities $N_{J''}$ of the ground-state rotational levels according to

$$I_{J'J''} \sim S_{J'J''} N_{J''}/(2J'' + 1),$$

where $S_{J'J''}$ are the Hönl–London factors of the transition.

The rotational state distribution obtained in this way could in all cases be fitted to Boltzmann distributions yielding a rotational temperature T_{rot}.[2] In addition, it was found that the populations of both electronic states $^2\Pi_{1/2}$ and $^2\Pi_{3/2}$ could be described by the same T_{rot}. Even the overall population ratio $N(^2\Pi_{1/2}) : N(^2\Pi_{3/2})$ is given by $\exp(-\Delta E/kT_{rot})$, where ΔE is the fine-structure splitting.

The variation of T_{rot} with the surface temperature T_s is shown in Fig. 3 for the Pt(111) surface. In the range of desorption from the NO-covered surface, i.e., for $T_s < 300$ K, $T_{rot} = T_s$ is observed. Above $T_s = 350$ K the rotational temperature begins to deviate from T_s. Within the temperature range characteristic for desorption from the chemisorbed state ($\geqslant 450$ K), T_{rot} increases only slightly with T_s. For example, the rotational temperature is only (440 ± 20) K at $T_s = 800$ K. These findings are in agreement with the conclusions of Ref. 4 that NO molecules thermally desorbing from a Ru surface exhibit a considerably lower rotational temperature than that expected for complete thermal accommodation with the surface. (This latter experiment, however, could only be performed at a single value of T_s.)

Changing the translational energy of the primary molecules from 80 to about 200 meV was without measurable effect on the resulting rotational distribution as shown in Fig. 3. The fact that the rotational distribution is independent of the incoming translational energy has to be expected for molecules which had intermediately been trapped at the clean Pt(111) surface and thus lost their "memory" of their primary momentum.

The different orientation of the dipole oscillator for the Q branch transitions as compared with the R and P branches enables one to detect a rotational polarization of the scattered molecules. Experiments with polarized laser light failed to reveal a preferential orientation of the rotational axis.

B. Angular and rotational distributions of NO/graphite

Angular distributions of NO molecules scattered from the graphite surface are shown in Fig. 4. The data were again derived directly from the rotatable mass spectrometer sig-

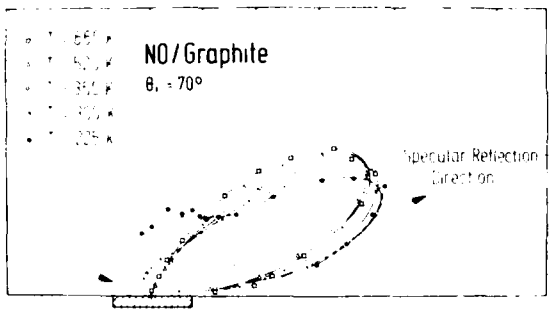

FIG. 4. Angular distributions (normalized mass spectrometer signals) of NO molecules scattered from a graphite surface at different temperatures T_s (angle of incidence $\theta_i = 70°$).

nals and therefore represent the density of the particles. The average velocities of the particles show an angular dependence as will be discussed later; however, this fact does not change the essential features of the distributions shown on Fig. 4.

It is obvious that the distributions are generally composed of a quasispecular or lobular part peaked at a scattering angle θ_s significantly less than the specular reflection angle and a diffusive scattering or cosine distribution part at low T_s. With increasing surface temperatures the diffusive part decreases relative to the specular part; simultaneously the specular lobe is shifted to smaller scattering angles. This can be interpreted as a weakly inelastic scattering process with an increasing trapping/desorption contribution for decreasing temperatures. This behavior is well correlated with the behavior of the velocity distributions of the scattered NO molecules, as will be discussed later.

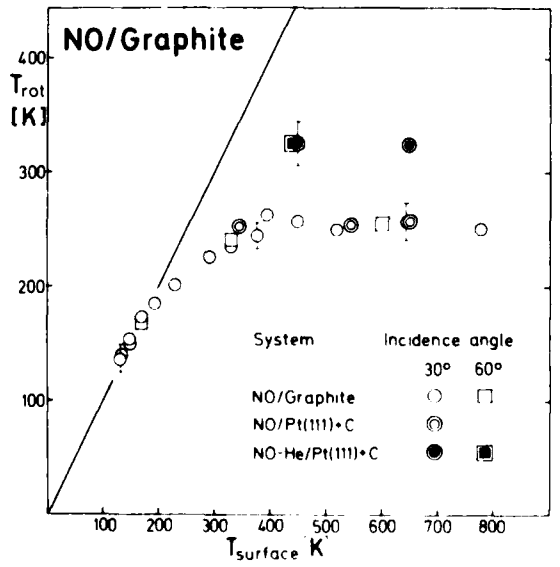

FIG. 5. Scattering of NO molecules from a pyrographite crystal and a carbon covered Pt(111) surface. The rotational temperature of the scattered molecules is plotted vs the surface temperature for two different incidence angles and translational energies of the incoming particles. The results characterized by open symbols were obtained at E_{kin} 80 meV, solid symbols at E_{kin} 200 meV (seeded beam). The straight line symbolizes full rotational accommodation [see also Ref. 2(c)].

As in the case of Pt scattering, the rotational distributions exhibit Boltzmann-like behavior also with respect to both electronic states. Thus, the rotational population of the scattered NO molecules can again be characterized by a rotational temperature T_{rot}.

The dependence of T_{rot} on the surface temperature for the NO/graphite system is shown in Fig. 5. The solid line corresponds to complete accommodation of the rotational degree of freedom to the surface temperature. While the experimental points follow this line closely up to a surface temperature of about 170 K, they deviate at higher temperatures. At T_s higher than 350 K, T_{rot} approaches a constant value of about 250 K. The results characterized by open symbols were obtained at an incoming energy of about 80 meV; increasing the average kinetic energy of the incoming NO molecules to about 200 meV (NO seeded in He) led to a somewhat higher rotational temperature (solid points).

Most of the rotational distributions were measured for NO molecules with an incidence angle of 30°. In this case, molecules predominantly in the specular direction were analyzed. Nearly the same rotational temperatures were obtained at a second incidence angle of 60°, where mainly molecules in surface normal direction were investigated. Because of the bad angular resolution of the measurement a clear distinction between the fluorescence signal of diffusively and specularly scattered particles, and therefore between their respective rotational temperatures, was not possible. Later we will see, however, that the effective rotational temperature is slightly different for diffusively and quasispecularly scattered molecules.

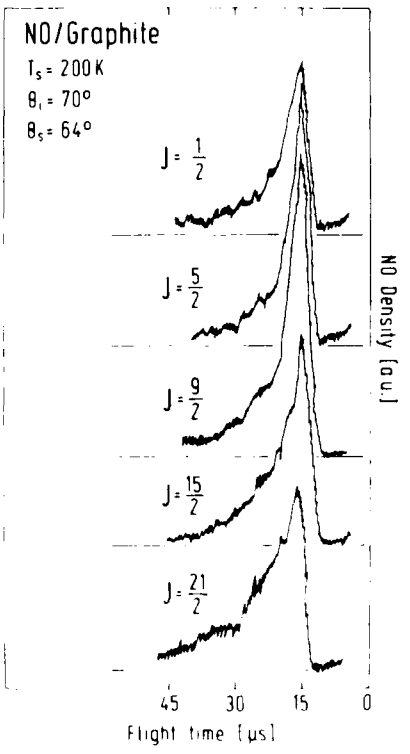

FIG. 6. Time-of-flight spectra of NO molecules in different rotational states, scattered from a 200 K graphite surface with a scattering angle of 64° (incidence angle 70°).

C. Velocity distributions of NO/graphite

A part of the scattered molecules cross the focused laser beam inside the cage. The laser is tuned to a rotational transition and thus ionizes molecules with a specific rotational state and with a specific scattering angle. Since the translational energy is conserved during photoionization the time-of-flight spectra of the ions correspond directly to the velocity distributions of the parent neutral molecules. Examples of time-of-flight spectra are shown in Fig. 6. NO molecules with an incidence angle of 70° were scattered from a 200 K graphite surface with a scattering angle of 64°, i.e., into the maximum of the angular distribution. The spectra show the flight time of molecules in different rotational states (from $J = 1/2$ to $J = 21/2$) corresponding to a rotational energy between 1 and 200 cm^{-1}, respectively. As can be seen the spectra are nearly independent of the rotational states and are composed of a very high quasispecular peak of very fast molecules and a longer tail resulting from diffusively scattered particles with slower velocities. It is obvious that the states with higher rotational quantum numbers have a stronger diffusive part than the low J states which is characteristic for all scattering angles.

With increasing surface temperature also the average velocity of the specularly scattered molecules is increasing. In addition, the scattering angle of the lobular maximum decreases. Molecules in specular direction show a velocity distribution similar to the one of the incoming molecules but with a temperature dependent average velocity. For an experimental geometry (incidence angle 70°, scattering angle fixed at 64°) a peak velocity of 650 m/s was measured at a surface temperature of 200 K, 685 m/s at $T_s = 300$ K, 710 m/s at $T_s = 470$ K, and 730 m/s at $T_s = 660$ K, these values have to be compared to 750 m/s for the peak velocity of the incoming beam.

The results described in the last paragraph suggest an extended investigation of the angular dependence of the time-of-flight spectra. The results of these measurements are shown in Fig. 7 for angles from $\theta_s = 2°$ to $\theta_s = 64°$. In this case the scattered molecules are in the $J = 9/2$ rotational state and are scattered from the 200 K graphite surface with the incidence angle kept at 70°. The time-of-flight spectra

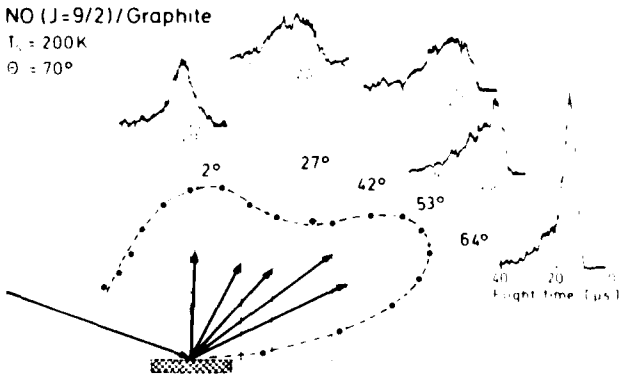

FIG. 7. Time-of-flight spectra of NO molecules in the $J = 9/2$ rotational state scattered into different scattering angles. The spectra are plotted together with a 200 K angular distribution.

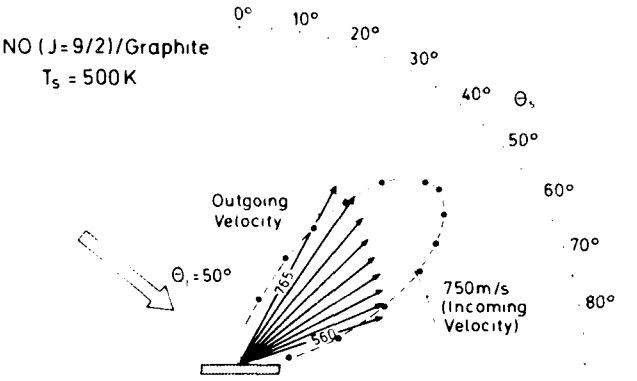

FIG. 8. Angular dependence of the peak velocity of NO molecules scattered from a 500 K graphite surface at an incidence angle of 50°. The peak velocities, represented by arrows, are shown with the corresponding angular distribution and the incoming velocity.

show that the part of the quasispecularly scattered molecules decreases with decreasing scattering angle as expected, and the diffusive part increases. It is obvious that the flight time in the normal direction is much longer than in the specular direction, but the widths of both distributions are comparable with the width of the incoming velocity distribution (the relative velocity spread, however, increases from 20% to 40%). This behavior was also measured for other rotational states, but as pointed out earlier, the diffusive part is larger for states with higher rotational quantum numbers. This means that the diffusively scattered molecules gain more rotational energy during the scattering process. The diffusive and specular parts of the scattered molecules can be characterized by two different rotational temperatures. For $T_s = 200$ K, the quasispecularly reflected part (evaluated at $\theta_s = 64°$) has a rotational temperature $T^{qs}_{rot} = 180 \pm 20$ K, and the diffusive scattering part (evaluated at $\theta_s = 2°$) has $T^{d}_{rot} = 230 \pm 30$ K. The latter appears to be larger than T_s, but this could be the result of experimental inaccuracy. In any case, it is clear that $T^{d}_{rot} > T^{qs}_{rot}$. Similar measurements at $T_s = 250$ K and $T_s = 300$ K yielded $T^{qs}_{rot} = 190$ K, $T^{d}_{rot} = 250$ K and $T^{qs}_{rot} = 250$ K, $T^{d}_{rot} = 250$ K, respectively.

As discussed above the diffusively scattered part of the molecules disappears at high surface temperatures and only a quasispecular part remains. The measured time-of-flight spectra are similar to the spectra in Fig. 6; the peak velocities, however, depend on the scattering angles. This is demonstrated in Fig. 8. To obtain this result, molecules in the $J = 9/2$ rotational state were probed after scattering from the 500 K graphite surface with an incidence angle of 50°. In the figure the peak velocities of the scattered molecules are represented by the length of the arrows. It is obvious that the velocity increases with decreasing scattering angle. For a scattering angle of 72° we find a velocity of 560 m/s, for an angle of 28° a velocity of 765 m/s, compared with an incoming peak velocity of 750 m/s. The velocity of the molecules scattered in the specular direction was 670 m/s.

For an incidence angle of 70° and a surface temperature of 470 K we found a behavior similar to that in Fig. 8, but with a significantly higher average velocity of the scattered particles: 710 m/s at $\theta_s = 64°$, 770 m/s at $\theta_s = 59°$, 820 m/s at

$\theta_s = 53°$, and 850 m/s at $\theta_s = 48°$. This shows that the velocities of the scattered molecules strongly depend on the incidence angle. This is further confirmed by measurements in which the scattered molecules are always probed at the angle where the angular distribution has its maximum. For a surface temperature of 500 K one obtains a peak velocity of 610 m/s for an angle of incidence of 35°, a velocity of 650 m/s for 45°, 700 m/s for 60°, and 730 m/s for 70°. In addition, the peak velocities of the scattered particles vary around the above values when the scattering angle is changed, this being similar to the behavior shown in Fig. 8. It is characteristic of specularly scattered molecules that the peak velocities observed in the direction of the maximum of the angular distribution increase with increasing surface temperature and increasing incidence angle.

In order to obtain information on the momentum transfer to the solid, it is interesting to consider the behavior of the normal and tangential components of the peak velocities of the scattered molecules. It is obvious from Fig. 8 that the normal components increase, whereas the tangential components decrease with decreasing scattering angle. In Fig. 9 the velocity changes in the normal and tangential directions are plotted versus the scattering angle θ_s. The data correspond to the results of Fig. 8. Particles scattered into an angle lower than 40° gain normal velocity, while particles with larger scattering angles show a momentum loss in the normal direction. The tangential components, on the other hand, show a loss relative to the incoming tangential velocity for all scattering angles; the loss increases as the scattering angles decrease.

IV. DISCUSSION

In the following section the results obtained in the scattering experiments are summarized and possible explanations given. In the present situation only the main phenomena can be described; more subtle effects can only be recognized when a more quantitative treatment of the scattering process is available. We start the discussion by summarizing the results for the angular distributions.

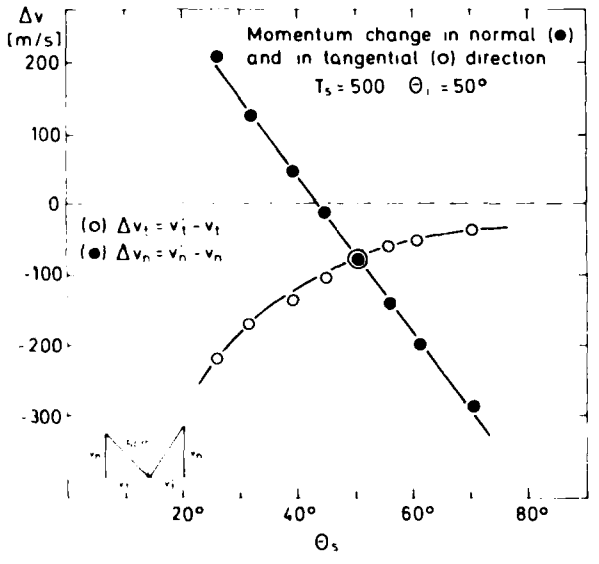

FIG. 9. Change of normal and tangential momenta as a function of the scattering angle θ_s (evaluated with the data plotted in Fig. 8).

A. Angular distribution

Scattering from a Pt(111) surface shows mainly diffusive trapping/desorption scattering; a very small portion of specular reflection is observed in the region where NO is scattered from a NO-covered Pt(111) surface.

Scattering from a graphite surface shows broad lobes of specular reflection and a small diffusive part. With decreasing temperature, the diffusive part increases while the specular part decreases: at low surface temperatures the molecules undergo partly trapping/desorption and partly quasielastic scattering, whereas quasielastic scattering is predominant at high T_s.

B. Rotational distribution

The rotational energy distributions of both electronic ground states show Boltzmann-like behavior and can be characterized by a temperature T_{rot} as well as the overall population of the two electronic states $^2\Pi_{1/2}$ and $^2\Pi_{3/2}$.

For both scattering mechanisms (inelastic for graphite and trapping/desorption for Pt) T_{rot} is equal to T_s at low T_s; at higher surface temperatures, however, T_{rot} is smaller than T_s and slightly increases as T_s increases. T_{rot} was never observed to exceed T_s.

In the case of NO/graphite scattering, the rotational temperature reaches a limiting value which depends on the translational energy of the incoming particles.

Diffusively scattered molecules exhibit a slightly higher T_{rot} than the specularly scattered particles.

C. Velocity distribution

Scattering from the clean Pt(111) surface results in a complete velocity accommodation with a final velocity distribution which can be characterized by the surface temperature.[5c]

Scattering from the graphite surface leads to velocity distributions nearly independent of the rotational state of the scattered particles, also for varying θ_s. At low surface temperatures there are two scattering channels: one corresponds to quasispecularly reflected molecules with a velocity slightly slower than the incoming velocity and a width slightly larger than that of the incoming velocity distribution; the other corresponds to diffusively scattered particles with a much slower velocity. The peak velocity of the quasispecularly scattered molecules increases with increasing T_s, increasing θ_i, and with decreasing θ_s.

The experimental observations must be attributed to the following processes on the surfaces:

In the case of a nearly pure adsorption/desorption process [NO/ Pt(111) at low temperature], the molecules impacting on the NO-covered surface will lose sufficient energy to the solid to be trapped in the attractive "precursor" potential well for a certain residence time. During this time in a shallow physisorption potential the particles may move freely across the surface and exchange energy with the solid through frequent collisions, leading to complete accommo-

dation of the translational and internal energies to the surface temperature; the subsequent desorption occurs in a mainly isotropic distribution.

Incomplete rotational accommodation together with complete velocity accommodation were found after desorption from the chemisorption potential of the clean Pt(111) surface. In this case the NO molecules are in fixed "head-on" positions on the Pt surface and can only undergo movements about an axis along the surface normal. The average rotational energy of such a molecule is $kT_s/2$. A sudden switch off of the binding to the surface would lead to a free rotor with an average internal energy of $2\times kT_{rot}/2$, which means—on the assumption of an unchanged particle energy—that $T_{rot} < T_s$. These simple considerations have led to a theoretical treatment of the desorption behavior of molecules, (yielding $T_{rot} < T_s$) and, under certain conditions, Boltzmann-like distributions, where of course T_{rot} has nothing in common with a thermal equilibrium temperature.[12,13]

In the experiment with the graphite surface a small portion of the scattered molecules indicates an adsorption/desorption process, but the major fraction of the molecules is specularly scattered and, even at very low surface temperatures, the angular distributions show a strong specular contribution (Fig. 4). Nevertheless, one has to assume that at low T_s the average residence time in the shallow NO/graphite potential is long enough to lead to complete rotational accommodation, but not long enough for translational accommodation. This holds for both the diffusively and the specularly scattered particles.

For high surface temperatures the situation seems more complicated. Here we observe Boltzmann-like rotational distributions, but no rotational accommodation to the surface temperature. We observe that the incoming translational energy influences the final rotational temperature of the scattered molecules. But this influence is small: Increasing the incoming translational energy by a factor of 2.5 leads to an increase of T_{rot} of about 25%. Furthermore, the amount of the translational energy change is independent of the final rotational state of the scattered molecules. It seems that during the short interaction time with the surface a part of the translational energy of the molecule is redistributed to the internal degrees of freedom, resulting in a probability distribution for the rotational population which can be described by a Boltzmann distribution. Again T_{rot} has to be understood as a parameter for the description of the population distribution and has nothing in common with an equilibrium temperature. A higher incoming translational energy should then result in a somewhat larger rotational energy. This corresponds to our observations according to Fig. 5.

With increasing surface temperature, increasing incidence angle, and decreasing scattering angle the translational energy of the scattered molecules increases, which indicates interaction of the translational degree of freedom with the phonons of the graphite crystal. There is no influence on the rotational degree of freedom, because the rotational temperature stays nearly constant independently of the surface temperature. These effects suggest a decoupling of the rotational and translational degree of freedom during the interaction process.

A closer look at the results of the velocity measurements can provide more useful information on the molecular energy and momentum exchange with the graphite surface. But the translational (not the rotational) energy of the scattered particles is strongly dependent on the incidence angle, so that the energy balance can only be discussed for a fixed experimental geometry. For an incidence angle of 70° and low surface temperatures the rotational energy gained by the quasispecularly scattered molecules is actually comparable with their translational energy loss. At $T_s = 200$ K, the average rotational energy gain per scattered molecule is ~ 100 cm^{-1}, while the translational energy loss (averaged over the angle variation of the specular velocities) is 170 cm^{-1}. (The average internal energy gain per scattered molecule is 130 cm^{-1}, taking excitation of the $^2\Pi_{3/2}$ state of NO into account.) For the diffusively scattered molecules, the translational energy loss per molecule is in the range of 500 cm^{-1} at $T_s = 200$ K, which is much larger than the internal energy gain per molecule in the scattering process. The large amount of energy deposition by the diffusively scattered molecules in the solid (~ 380 cm per molecule) is in principle characteristic of a trapping/desorption process. However, the mean velocity of the diffusively scattered molecules is larger than that expected for molecules desorbed from a surface at $T_s = 200$ K and, in addition, the velocity distribution ($\theta_s = 2°$ in Fig. 7) is much narrower than the Maxwellian distribution at 200 K. Thus, the diffusive scattering part cannot derive from an equilibrium trapping/desorption process, but is more likely the result of a transitional trapping/desorption process where the molecule interacts with the surface but does not completely come to rest. The interaction time is much shorter than the time required to reach complete thermal equilibrium between the molecules and the surface. This is analogous to the case of gas-phase molecular collisions through a transitional bound state. The residence time at this low surface temperature is long enough for complete accommodation of the internal degrees of freedom, but apparently not long enough for translational accommodation of the diffusively scattered particles.

The quasispecular scattering, especially at higher surface temperature, is believed to be a single-collision process. Here, the molecule-surface interaction time is so short that accommodation of the velocity distribution to the surface temperature seems impossible. The energy transfer to the molecular rotational degree of freedom, however, is still quite efficient.

The velocity variation in the specular lobe reflects the interaction of the NO molecules with the surface phonons, especially in the normal direction. Molecules with a loss of normal velocity were found at large scattering angles and molecules with a gain were found at small angles. In addition, the decreasing outgoing velocity with decreasing incidence angle indicates a loss of normal velocity due to increasing momentum transfer to the surface. Furthermore, the particles experience a loss of their tangential components so that molecules with a larger loss were found at small scattering angles. This behavior of the tangential velocity must be attributed to molecule-surface interaction which allows the molecules to impart to the solid a net average momentum

along the surface. This, however, would be contrary to the assumptions of the hard cube model.[14] Nevertheless, the translational energy exchange in the normal direction between the molecules and the surface should be more or less determined by this hard cube model. There is an active momentum transfer between the surface and molecules in the normal direction, as manifested by the variation of the normal velocity in the specular lobe and the shift of this lobe to smaller scattering angles; however, only at a sufficiently high surface temperature can the molecules gain a net translational energy from the surface in the quasispecular direction.

Summarizing the results on the overall energy balance for the NO/ graphite system with 70° incidence angle, we find that the diffusively scattered NO molecules gain some rotational energy, but transfer much more translational energy to the surface, so that the energy balance is considerably negative. For the specularly scattered molecules, the energy loss and gain are nearly balanced at low surface temperatures, but with increasing T_s the translational energy of the scattered molecules increases while the rotational energy stays constant, resulting in a substantial energy transfer from the surface to the scattered NO molecules.

ACKNOWLEDGMENTS

The authors would like to thank Professor G. Ertl and his group for the fruitful collaboration in the beginning of this work. Furthermore, we thank Professor Y. R. Shen for the help with the time-of-flight measurements and for many discussions.

[1]See, for example, F. O. Goodman and H. Y. Wachman, *Dynamics of Gas Surface Scattering* (Academic, New York, 1976).
[2](a)F. Frenkel, J. Häger, W. Krieger, H. Walther, C. T. Campbell, G. Ertl, H. Kuipers, and J. Segner, Phys. Rev. Lett. **46,** 152 (1981); (b) F. Frenkel, J. Häger, W. Krieger, H. Walther, G. Ertl, J. Segner, and W. Vielhaber, Chem. Phys. Lett. **90,** 225 (1982); (c) J. Segner, H. Robota, W. Vielhaber, G. Ertl, F. Frenkel, J. Häger, W. Krieger, and H. Walther, Surf. Sci. **131,** 273 (1983); (d) J. Häger, Y. R. Shen, and H. Walther, Phys. Rev. A **31,** 1962 (1985).
[3](a) J. E. Hurst, L. Wharton, K. C. Janda, and D. J. Auerbach, J. Chem. Phys. **78,** 1559 (1983); (b) A. W. Kleyn, A. C. Luntz, and D. J. Auerbach, Phys. Rev. Lett. **47,** 1169 (1981); (c) A. W. Kleyn, A. C. Luntz, and D. J. Auerbach, Surf. Sci. **117,** 33 (1982).
[4](a) R. R. Cavanagh and D. S. King, Phys. Rev. Lett. **47,** 1829 (1981); (b) D. S. King and R. R. Cavanagh, J. Chem. Phys. **76,** 5634 (1982).
[5](a) M. Asscher, W. L. Guthrie, T. H. Lin, and G. A. Somorjai, Phys. Rev. Lett. **49,** 76 (1982); (b) H. Asscher, W. L. Guthrie, T. H. Lin, and G. A. Somorjai, J. Chem. Phys. **78,** 6992 (1983); (c) W. L. Guthrie, T. H. Lin, S. T. Ceyer, and G. A. Somorjai, J. Chem. Phys. **76,** 6398 (1982).
[6](a) G. M. McClelland, G. D. Kubiak, H. G. Rennagel, and R. N. Zare, Phys. Rev. Lett. **46,** 831 (1981); (b) G. D. Kubiak, J. E. Hurst, Jr., H. G. Rennagel, G. M. McClelland, and R. N. Zare, J. Chem. Phys. **79,** 5163 (1983).
[7]H. Zacharias, M. M. T. Loy, and P. A. Roland, Phys. Rev. Lett. **49,** 1790 (1982).
[8]J. S. Hayden and G. J. Diebold, J. Chem. Phys. **77,** 4767 (1982).
[9](a) J. W. Hepburn, F. J. Northrup, G. L. Ogram, J. C. Polanyi, and J. H. Williamson, Chem. Phys. Lett. **85,** 127 (1982); (b) D. Ettinger, K. Honma, M. Keil, and J. C. Polanyi, Chem. Phys. Lett. **87,** 413 (1981).
[10]J. B. Cross and J. B. Lurie, Chem. Phys. Lett. **100,** 174 (1983).
[11]D. A. Mantell, Y. F. Maa, S. B. Ryaly, G. L. Haller, and J. B. Fenn, J. Chem. Phys. **78,** 6338 (1983).
[12]J. W. Gadzuk, U. Landman, E. J. Kuster, C. L. Cleveland, and R. N. Barnett, Phys. Rev. Lett. **49,** 426 (1982).
[13]S. E. Bialkowski, J. Chem. Phys. **78,** 600 (1983).
[14](a) R. N. Logan and R. E. Stickney, J. Chem. Phys. **44,** 195 (1966); (b) W. L. Nichols and J. H. Weare, J. Chem. Phys. **63,** 379 (1975).

Above-bandgap optical anisotropies in cubic semiconductors: A visible–near ultraviolet probe of surfaces[a)]

D. E. Aspnes
Bell Communications Research, Inc., Murray Hill, New Jersey 07974

(Received 18 March 1985; accepted 21 May 1985)

I describe some results of the first systematic study of above-bandgap optical anisotropies in cubic semiconductors. The anisotropies are large, of the order of 1% of the relative reflectance differences for light polarized along orthogonal principal axes of the dielectric tensor of the anisotropic phase. Extrinsic contributions arising from anisotropic surface films, physisorbed molecules, and chemisorption-induced changes in the electronic polarizability of the outermost plane of substrate atoms are identified. The line shapes of these reflectance-difference (RD) spectra provide the first critical test of models proposed to describe intrinsic contributions to the optical anisotropies of these materials. The dominant intrinsic contribution is shown to be a surface (interface) many-body effect due to the reduced screening of the surface atoms as a result of the termination of the bulk lattice. A secondary intrinsic contribution from the influence of spatial dispersion on interband energy gaps in the one-electron band structure is also observed. The identification of the intrinsic contributions allows the surface contributions to be obtained. The results show that interface state effects in this spectral range are minimized by oxidation for (110) Si and Ge.

I. INTRODUCTION

Optical anisotropies of electronic origin have been important for distinguishing surface- from bulk-related optical processes in the below-bandgap absorptance[1] and reflectance[2] spectra of semiconductors and in the reflectance[3,4] and ellipsometric[5–8] spectra of metals. The approach takes advantage of crystal symmetry by suppressing by subtraction the dominant, but unwanted, nominally isotropic contribution from the bulk. A similar symmetry related suppression of bulk phenomena underlies the recent interest in second harmonic generation as a probe of surface properties of inversion-symmetric systems.[9] While bulk optical anisotropies are not strictly forbidden for linear processes in cubic materials, the $\sim 10\,000:1$ rejection ratio deduced from the $\sim 4\%$ below-bandgap relative reflectance anisotropy recently measured[2] for the bandgap surface state on the 2×1 cleaved (111)Si surface and the $\sim 4\times 10^{-6}$ below-bandgap relative reflectance anisotropy calculated from the $\sim 10^{-5}$ refractive index differences measured for (110)Si[10] and GaAs[11] implies that optical anisotropies should also be very useful for studying above-bandgap surface electronic properties of cubic semiconductors.

Surprisingly, except for a single exploratory spectrum reported nearly 20 years ago for (110)Si,[12] this area of research has been completely neglected. The present work was initially motivated by a search for microscopic etchant-induced (111)A facets on (001)GaAs surfaces. These facets are expected to occur under certain conditions, and since they would all be aligned parallel to $\langle 1\bar{1}0\rangle$, a measurable anisotropy in the apparent dielectric properties of this material should result. Initial spectroellipsometric measurements[13] indeed revealed a $\sim 1\%$ anisotropy, but further investigation showed that this anisotropy persisted even for (001)GaAs surfaces that were nominally flat. Therefore, a more fundamental mechanism was clearly operative. Further investigation showed that these optical anisotropies were quite general, appearing not only for (001) surfaces of GaAs but also for (001) surfaces of other III–V compound semiconductors and for (110) surfaces of these and Group IV semiconductors as well.

Here, I describe some results of the first systematic study of these anisotropies. I show that they are surprisingly rich, with contributions arising not only from microscopic surface roughness but also from other extrinsic effects such as the presence of surface films or physisorbed molecules and chemisorption-induced changes in the electronic polarizability of the outermost plane of substrate atoms. Intrinsic effects unrelated to the specific condition of the surface are observed as well. A key feature of these data is that their spectral line shapes provide the first critical test of the various models that have been proposed to describe intrinsic contributions to the optical anisotropies of these materials. These data show that the primary intrinsic contribution is due to a surface many-body effect arising from the reduced screening experienced by atoms in the surface region because the bulk lattice has been terminated. This surface many-body effect, recently predicted in surface local-field form by Mochán and Barrera,[14] is limited to the outer few atomic planes and should lead to interesting optical phenomena at surfaces and interfaces in general. A secondary intrinsic contribution is shown to arise from the influence of spatial dispersion on the effective energy gaps of the one-electron band structure. With the intrinsic line shapes established, it follows that the oxidized, rather than oxide-stripped, (110)Si and Ge surfaces are those for which interface state contributions to the optical anisotropy are minimized.

II. EXPERIMENT

The data reported here were obtained by spectrophotometry using the optical configuration shown in Fig. 1. Linearly polarized light was reflected at near-normal incidence ($\phi = 10°$, p-polarization) from the specular surface of a rotat-

 0734-211X/85/051498-09$01.00

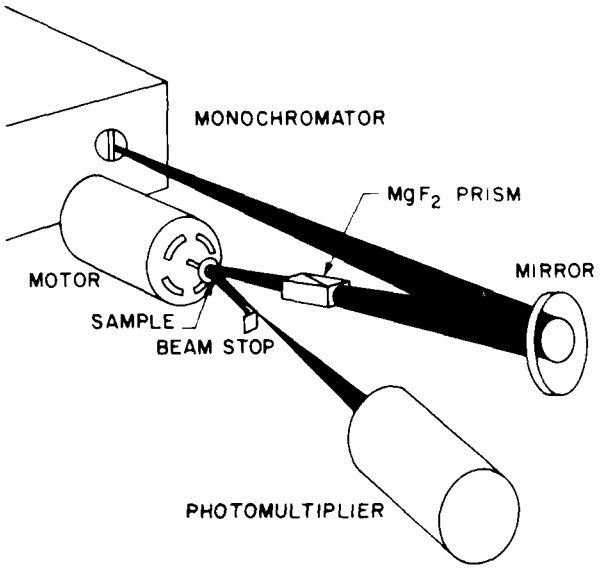

FIG. 1. Optical diagram of the RD spectrometer.

ing sample and the anisotropy determined by phase sensitively detecting the second harmonic of the mechanical rotation frequency in the reflected beam. The motor was frequency stabilized at 50 Hz, and an optical encoder provided the reference signal for the phase-sensitive detector. The optical system consisted of a 75 W short-arc Xe lamp, a 1 m single-grating Czerny–Turner monochromator, a MgF_2 beam-splitting polarizer, and a 5 cm diam end-on photomultiplier with an extended S-20 response. The average anode current of the photomultiplier was regulated to obtain reflectance-difference (RD) spectra $(R_\sigma - R_\tau)/R$ directly, where the subscripts σ and τ refer to the principal orthogonal axes of the anisotropic bulk and/or surface phases, and R is the average value $(R_\sigma + R_\tau)/2$. Note that $(R_\sigma - R_\tau)/R$ is just the normalized peak-to-peak value of the sinusoidal component of the detected beam.

Surfaces were prepared by methods described previously,[15] and were maintained in a dry N_2 atmosphere to minimize surface contamination. The photomultiplier output was monitored by an oscilloscope to ensure that no scratches, pits, or other macroscopic asperities affected the sinusoidal component of the reflected beam. Optical measurements that involve sample motion are particularly sensitive to macroscopic imperfections that scatter light.[16] In the present experiment, such motion-related artifacts produce essentially wavelength-independent offsets in the detected signal. These effects were minimized by defocusing the incident beam to a circular area about 5 mm in diameter at the sample, and aligning the samples to yield minimal beam motion at the photomultiplier. Overall system performance was equivalent to that of a good modulation spectrometer, yielding a scatter of the order of $\pm 3\times 10^{-5}$ for 0.6 s-per-point averaging as indicated by the data in Fig. 2.

III. THEORY

The phenomenological optical description of RD spectra is straightforward because the observed anisotropies, while large enough for easy measurement, are still small enough to allow them to be treated to first order in the optical functions. The formal expressions can be derived without approximation using the systematic approach of Yeh.[17] These expressions show that the azimuthal dependence of the detected intensity should be sinusoidal, as observed. Alternatively, reflectance differences for bulk processes can be described by the basic equation of modulation spectroscopy,[18] where to first order in $\epsilon_{\sigma\sigma} - \epsilon_{\tau\tau}$

$$\frac{R_\sigma - R_\tau}{R} = \mathrm{Re}\left(\frac{2n_a(\epsilon_{\sigma\sigma} - \epsilon_{\tau\tau})}{n_s(\epsilon_s - \epsilon_a)}\right), \tag{1}$$

where $\epsilon_{\sigma\sigma}$ and $\epsilon_{\tau\tau}$ are the components of the bulk dielectric tensor along σ and τ, respectively, ϵ_s and $n_s = \epsilon_s^{1/2}$ are the average dielectric function and refractive index of the bulk, and n_a is the index of refraction of the ambient. If the anisotropy originates in the surface region or from a film present on the surface, the reflectance differences can be described to first order in d/λ by the three-phase model:[19]

$$\frac{R_\sigma - R_\tau}{R} = \frac{8\pi d n_a}{\lambda}\,\mathrm{Im}\left(\frac{\epsilon_{\sigma\sigma} - \epsilon_{\tau\tau}}{\epsilon_s - \epsilon_a}\right), \tag{2}$$

where $\epsilon_{\sigma\sigma}$ and $\epsilon_{\tau\tau}$ now refer to the surface or thin-film phase, d is the effective thickness of the phase, and λ is the wavelength of light.

For cubic materials, the bulk dielectric tensor can be expanded as[20]

$$\epsilon_{ij} = \epsilon\delta_{ij} + \gamma_{ijk}V_k - \gamma_{ijkl}V_kV_l, \tag{3}$$

where the third-rank component has the form γ_{xyz} and is allowed only for materials lacking inversion symmetry, and the nonvanishing fourth-rank components have the form γ_{xxxx}, γ_{xxyy}, and γ_{xyxy}. The vectors V_i represent, e.g., a space-charge electric field or the wave vector of light. In the former case the γ describe electro-optic phenomena and in the latter case spatial dispersion. For space charge fields and

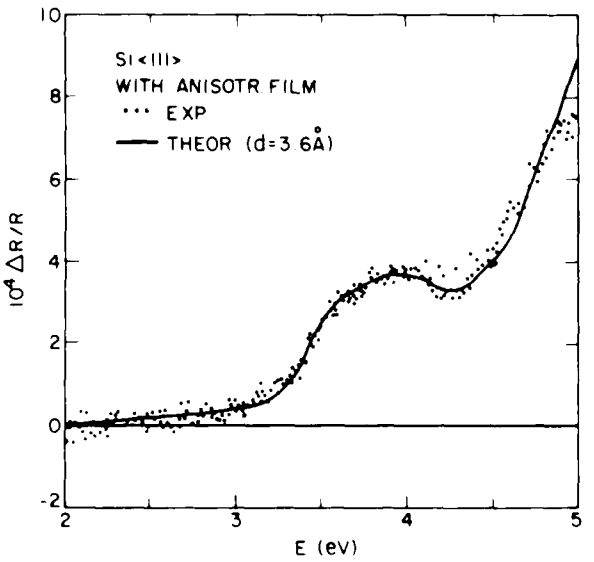

FIG. 2. Points: RD data for a (111)Si wafer covered with a transparent, microstructurally anisotropic film. Line: spectrum calculated from Eq. (4) as described in the text.

for propagation normal to the surface, the principal axes are $\langle 110\rangle$ and $\langle 1\bar{1}0\rangle$ for (001) surfaces and $\langle 1\bar{1}0\rangle$ and $\langle 001\rangle$ for (110) surfaces. No azimuthally dependent contributions arise for (111) surface orientations.

IV. RESULTS AND DISCUSSION

A. Extrinsic effects

I consider first the RD spectrum given in Fig. 2, which was obtained for a (111)Si wafer with a carrier concentration of $n = 2\times 10^{14}$ cm^{-3} and with an anisotropic film (fingerprint) present on its surface. Because no contribution can arise from the bulk, the spectrum should be described by Eq. (2). If the film is modeled as a series of parallel lines of rectangular cross section with dimensions small compared to λ, then its dielectric properties can be calculated by effective medium theory and the observed spectrum is predicted to be given by

$$\frac{R_\parallel - R_\perp}{R} = \frac{8\pi d n_a}{\lambda} f_o f_a \,\mathrm{Im}\left[\frac{(\epsilon_o - \epsilon_a)^2}{(f_a\,\epsilon_o + f_o\,\epsilon_a)(\epsilon_s - \epsilon_a)}\right]. \tag{4}$$

Here, the subscripts $\parallel$ and $\perp$ refer to the orientation of the polarization vector with respect to the lines, ϵ_o and ϵ_a are the dielectric functions of the line and ambient phases, and f_o and f_a, $f_o + f_a = 1$ are the relative fractions (surface areas) of the line and ambient phases, respectively. Different microstructures yield expressions of similar form but with different prefactors. If the material is transparent and shows negligible dispersion, then Eq. (4) has the form of the substrate loss function scaled by $1/\lambda$. The solid line in Fig. 2 was calculated from Eq. (4) using known bulk dielectric function data for Si[21] and using $f_o = f_a = 0.5$, $\epsilon_a = 1$, $\epsilon_o = 2.25$, and $d = 3.6$ Å, and is seen to give an excellent representation of the data. Therefore, an extrinsic mechanism has been identified explicitly.

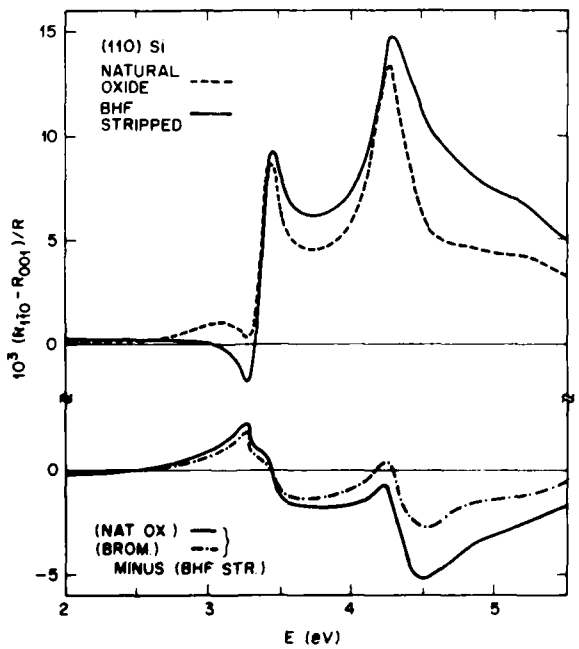

FIG. 3. Top: RD spectra for a naturally oxidized (110)Si surface and for the same surface after the oxide was stripped with buffered HF (BHF). Bottom, solid line: change resulting when the stripped surface is allowed to oxidize in air. Bottom, dot-dashed line: similar change, when the stripped surface is exposed to Br_2 in methanol.

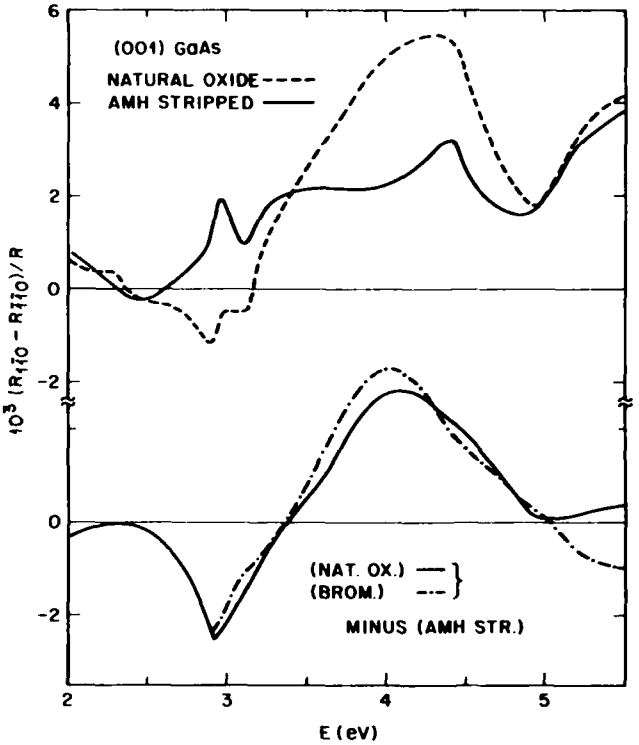

FIG. 4. As Fig. 3, but for (001)GaAs.

Microscopically rough surfaces, for which $\epsilon_o = \epsilon_s$, represent another application of Eq. (4). If $|\epsilon_s| \gg \epsilon_a$, then a first-order expansion in ϵ_a/ϵ_s shows that the same line shape is again obtained.

If the overlayer is optically absorbing, its dielectric properties affect RD spectra in a nontrivial way. Figure 3 shows RD spectra obtained for a naturally oxidized (110)Si wafer with a carrier concentration $n = 2\times 10^{14}$ cm^{-3} and for the same wafer with the oxide removed by buffered HF (BHF). The orientation of the crystallographic axes in the plane of the surface was established by anisotropic etching procedures.[22] The reflectance difference is small below the direct-transition threshold at 3.4 eV but reaches a maximum of nearly 1.5% at the 4.3 eV E_2 peak in ϵ_2. The change observed with oxidation is reversible, with the oxidized-surface spectrum being recovered if the stripped surface is allowed to reoxidize naturally in air. The change resulting from oxidizing the stripped surface is shown explicitly at the bottom. Also shown is the change obtained by exposing the stripped surface to a 3 vol. % solution of Br_2 in methanol. By the usual surface physics arguments, these changes are due to surface effects, i.e., these changes are extrinsic effects due to changes in the electronic polarizability of the outermost atomic plane(s) that result from different chemical ways of terminating the bulk lattice. The similarity of the changes induced by Br_2 or O_2 implies either that the relevant surface

electronic polarizability is relatively unaffected by the specific oxidant used to terminate the (110) surface, or that O_2 oxidation is promoted by Br_2. Changes in space charge electric fields, which may occur with chemical treatment, can be eliminated as a major contributor to these data because a comparison to electroreflectance spectra of Si[23] shows that the line shapes of the observed RD changes are far too broad and their magnitudes too large to be explained by this effect.

Figure 4 shows similar spectra for a (001)GaAs wafer with a carrier concentration of $n = 2\times10^{17}$ cm^{-3}. These spectra are of third-rank rather than fourth-rank origin, and have smaller amplitudes than those of Fig. 3. However, as with (110)Si the changes observed by allowing the AMH (1 : 1 NH_4OH:H_2O)-stripped surface to oxidize naturally in air or by forcing oxidation with Br_2 in methanol are again similar, indicating that either the specific identity of the oxidant is unimportant or that Br_2 promotes O_2 oxidation. The presence of several different mechanisms giving rise to these spectra is clearly evident from the differences in lineshapes, for example in the complete absence of the E_1 and $E_1 + \Delta_1$ splitting in the RD change spectra at the bottom, although the structure is quite prominent in the direct RD spectra at the top. Again, a comparison of these data to both linear and quadratic electroreflectance spectra for GaAs[24,25] shows that these RD lineshapes do not contain major contributions from space-charge-field effects.

Figure 5 shows equivalent data for a (110)Ge wafer with a carrier concentration of $n = 3\times10^{16}$ cm^{-3}. The overall RD line shapes are similar to those seen for (110)Si, but virtually no change is observed if the H_2O-stripped surface is allowed to oxidize naturally in air. Thus while H_2O readily dissolves GeO_2, it evidently fails to remove oxygen bonded to the outermost (110) plane of Ge atoms. The effect of exposing the H_2O-stripped surface to Br_2 in methanol is also quite different to that seen in Figs. 3 and 4, with changes occurring only in the 2.0–3.5 eV region of the spectrum.

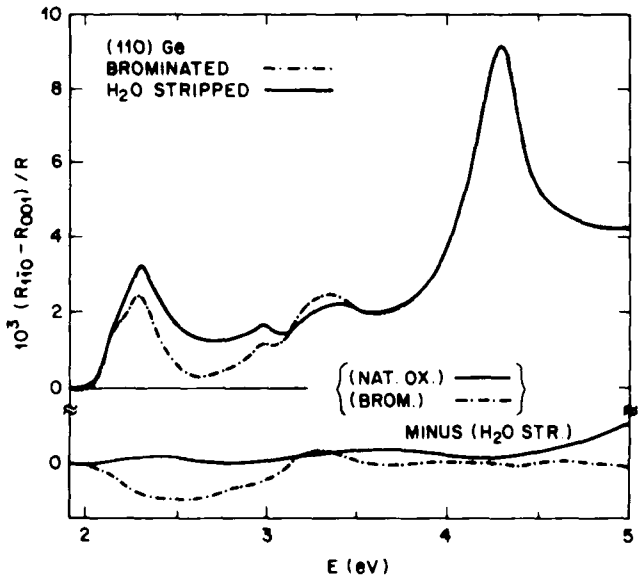

FIG. 5. As Fig. 3, but for (110)Ge. The RD spectrum for the naturally oxidized surface is virtually identical to that for the (110) surface stripped with H_2O and is not shown explicitly.

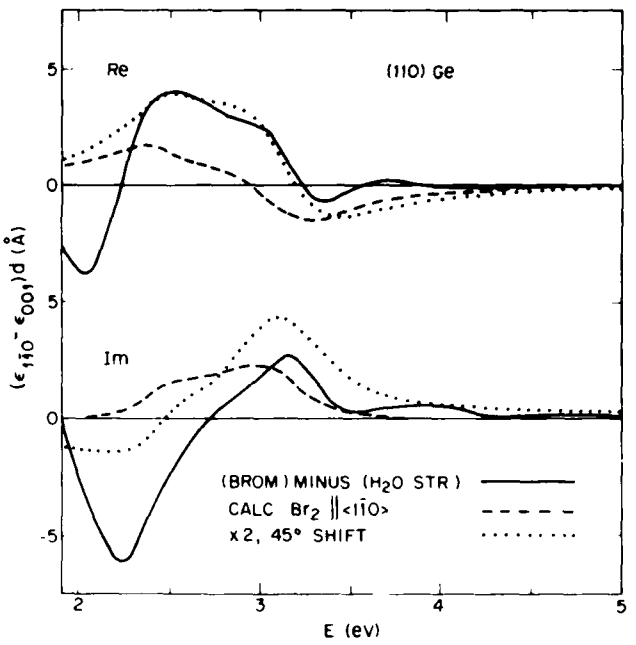

FIG. 6. Solid lines: adsorbate dielectric function difference $(\epsilon_{1\bar{1}0} - \epsilon_{001})\,d$ calculated from the brominated-surface data at the bottom of Fig. 5. Dashed lines: dielectric function spectrum for a monolayer of molecular Br_2 calculated from the gas-phase extinction data of Ref. 26 assuming complete orientation of the Br_2 molecular axes parallel to $\langle 1\bar{1}0\rangle$. Dotted lines: molecular Br_2 spectra shown two times larger and phase shifted 45° to illustrate optical structure more clearly.

The fact that bromination causes changes only over this energy range is suggestive, because it coincides with the range of optical absorption in gaseous Br_2,[26] thereby implying that Br is physisorbed on the H_2O-stripped (110)Ge surface in molecular form. To investigate this possibility further, a Kramers–Kronig analysis was performed on these data and Eq. (2) was used to directly calculate the real and imaginary parts of $(\epsilon_{1\bar{1}0} - \epsilon_{001})\,d$, the difference between adsorbate dielectric responses along $\langle 1\bar{1}0\rangle$ and $\langle 001\rangle$, respectively, scaled by the layer thickness d. The results are shown as the solid lines in Fig. 6. The equivalent spectrum for Br_2, calculated from gas-phase extinction data[26] assuming an areal density of 1 Br_2 molecule per surface Ge (which corresponds approximately to the bulk density of solid Br_2) and complete orientation of the Br_2 molecules along $\langle 1\bar{1}0\rangle$, is also shown, Structure corresponding to the dominant $B^3\Pi(0_u^+)\leftarrow X^1\Sigma_g^+$ and $^1\Pi(1_u)\leftarrow X^1\Sigma_g^+$ transitions at 2.5 and 3.0 eV, respectively, in the unperturbed Br_2 molecule[27] is clearly seen in the RD data. If the equivalent Br_2 spectrum is doubled in amplitude and expressed as the linear combination $\epsilon_1' + i\epsilon_2' = (\epsilon_1 + i\epsilon_2)(1+i)/\sqrt{2}$, the agreement with the RD spectrum is striking. Thus the identity of the physisorbed layer as molecular Br_2 appears established.

The implications of the results deserve further comment. The observation of a molecular Br_2 response on the H_2O-stripped (110)Ge surface is further evidence for a residual oxide, since Br_2 does not attack either oxidized semiconductors or semiconductor oxides. The observation of a molecu-

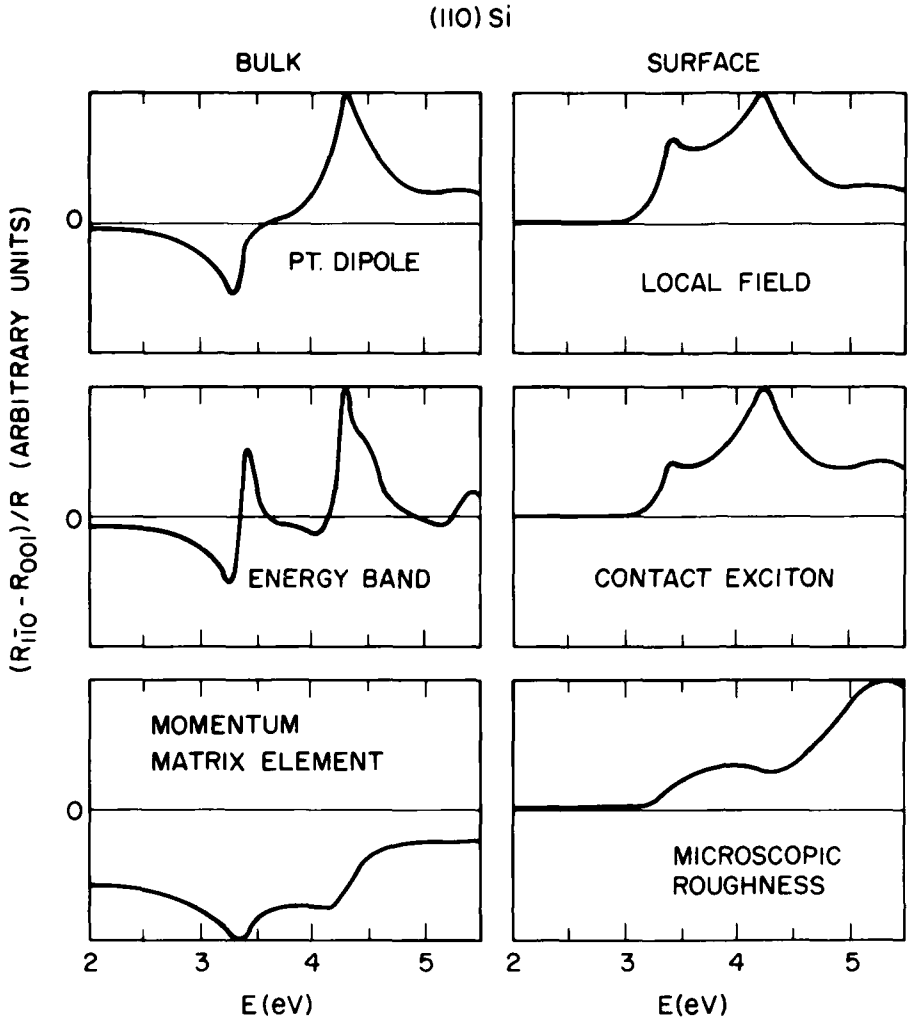

FIG. 7. RD line shapes for (110)Si predicted by various models. Bulk models are shown at left and surface models at right. Details are given in the text.

lar Br_2 response in a reflectance *difference* spectrum implies that the Br_2 is physisorbed with a preferred orientation with respect to the crystalline substrate. Since the absorption cross section for this $\pi_g - \sigma_u$ transition vanishes for light polarized perpendicular to the molecular axis, the sign of the RD change spectrum shows that the preferred orientation is that with the molecular axis parallel to $\langle 1\bar{1}0 \rangle$. Thus the residual oxide cannot be thick enough to destroy bulk registry, i.e., the outer Ge atoms are probably terminated by bonds to single oxygen atoms with the oxygen not penetrating in significant amounts below the outer Ge plane. By extension, the results also imply that BHF and AMH effectively remove most or all surface oxygen from (110)Si and (001)GaAs, respectively.

While the identity of the physisorbed Br_2 layer on H_2O-stripped (110)Ge appears to be established, several difficulties remain. The anomalous strength of the spectrum and the necessity of an *ad hoc*, linear combination to achieve the best line shape agreement are not understood, particularly since independent spectroellipsometric measurements seem to rule out the possibility of several monolayers of Br_2. The explanation may lie with the surface local fields[14] that contribute significantly to the intrinsic RD line shapes, as will be discussed in the next section.

B. Intrinsic effects

In this section I discuss intrinsic mechanisms and identify the origins of the "background" RD spectra of (110)Si and Ge, as shown in Figs. 3 and 5, respectively. The RD lineshapes are very similar overall to the imaginary parts of the respective bulk dielectric functions[21] except that the critical point structures are exaggerated. Thus as a first approximation, mechanisms that yield RD spectra proportional to Im (ϵ_s) and $d\epsilon_s/dE$ should be anticipated. These data will be used to provide the first critical test of theories that have been proposed to describe optical anisotropy in cubic materials.

The line shapes predicted for (110)Si by these theories are shown in normalized form in Fig. 7. The functional dependences themselves are given explicitly in Table I. I have everywhere set $\epsilon_a = 1$, and in some cases have assumed that $|\epsilon_s| \gg \epsilon_a$ to simplify the form of the resulting expressions. The mechanisms considered are, in turn:

1. Bulk local field effects; Lorentz point dipole approximation

The application of an external electric field E_{ext} generates electric dipoles on an atomic scale in any medium. The field at any given dipole is a superposition of the applied field and

TABLE I. Predicted energy dependences of RD spectra $(R_{1\bar{1}0} - R_{001})/R$ for (110) surfaces of cubic crystals. Parameter definitions and original references are given in the text.

Bulk (spatial dispersion)	Surface
Point dipole: $-0.22\frac{8\pi a_0^2 E^2}{(hc)^2}\,\mathrm{Re}\,[n_s(\epsilon_s-1)]$	Local field: $\frac{\sqrt{2}}{8}\frac{a_0 E}{hc}\left[\sum_j(\Delta\beta_j^{1\bar{1}0}-\Delta\beta_j^{001})\right]\mathrm{Im}\,(\epsilon_s)$
Energy band: $-\frac{E^2}{6M_T c^2}\,\mathrm{Re}\left(\frac{1}{n_s}\frac{\epsilon_s}{\epsilon_s-1}\frac{d\epsilon_s}{dE}\right)$	Contact exciton: $\frac{8\pi d E^3}{hc}\,\mathrm{Im}[(\Delta\tilde{g}_{1\bar{1}0}-\Delta\tilde{g}_{001})(\epsilon_s-1)]$
Momentum matrix element: $-\frac{p^2}{6M^2 c^2}\,\mathrm{Re}(n_s)$	Surface films: $\frac{8\pi dE}{hc}\,\mathrm{Im}\left(\frac{\epsilon_{\sigma\sigma}-\epsilon_{\tau\tau}}{\epsilon_s-1}\right)$

the fields of the other induced dipoles. For a lattice of points of polarizability α, the local field $\mathbf{e}(\mathbf{r})$ at any point $\mathbf{r}$ can be written

$$\mathbf{e}(\mathbf{r}) = \mathbf{E}_{\mathrm{ext}} + \sum_{\mathbf{R}_n} \mathbf{e}_{\mathrm{dip}}(\mathbf{r} - \mathbf{R}_n), \tag{5}$$

where the $\mathbf{R}_n$ are the lattice vectors and $\mathbf{e}_{\mathrm{dip}}(\mathbf{r})$ is the standard expression[28] for the electric field at $\mathbf{r}$ due to a dipole $\mathbf{p}$ located at $\mathbf{r} = \mathbf{0}$. Since $\mathbf{p} = \alpha\mathbf{e}(\mathbf{0})$, Eq. (5) is a self-consistency relation with a solution of the general form

$$\mathbf{e}(\mathbf{0}) = \frac{\mathbf{E}_{\mathrm{ext}}}{1 - \beta\alpha/a_0^3}, \tag{6}$$

where β is a number given by the lattice sum of Eq. (5) evaluated with the origin $\mathbf{r} = \mathbf{0}$ chosen at any arbitrary lattice site $\mathbf{R}_n$ and normalized to α and the volume a_0^3 of the unit cell (cubic symmetry is assumed). The dielectric function for this model can be evaluated by averaging the microscopic field $\mathbf{e}(\mathbf{r})$ and polarizability $\mathbf{p}(\mathbf{r}) = \sum_{\mathbf{R}_n} \mathbf{p}\delta(\mathbf{r} - \mathbf{R}_n)$ by standard methods.[29] The result is

$$(\epsilon_s - 1) = \frac{4\pi n\alpha}{1 - \frac{4\pi}{3}n\alpha - \frac{\beta\alpha}{a_0^3}}, \tag{7}$$

where n is the density of dipoles (lattice points). For simple cubic lattices $\beta = 0$ and Eq. (7) reduces to the usual Lorentz–Lorenz expression.[30]

However, β does not vanish in general for systems of lower symmetry such as molecules absorbed on a surface,[31] for random distributions of polarizable points,[32,33] or for finite wavelengths[34] for which $\mathbf{e}(\mathbf{R}_n) = e^{i\mathbf{q}\cdot\mathbf{R}_n}\mathbf{e}(\mathbf{0})$, where $\mathbf{q}$ is the wave vector of the light in the medium. When substituted in Eq. (1), the Lorentz expression[34] yields the function in the upper left corner of Table I and the line shape in the upper left corner of Fig. 7.

It is clear that this theory fails to reproduce the observed energy dependence, in particular for energies below the 3.4 eV E_1 critical point. This is not surprising, since point-lattice models are not expected to provide as accurate a description of the bulk dielectric properties of semiconductors as energy band models.

2. Spatial dispersion; one-electron approximation

In the semiclassical band picture, the $\mathbf{q}$-dependent dielectric function can be written[35]

$$\epsilon_s = 1 + \frac{4\pi e^2}{V}\sum_{\mathrm{states}}\langle v, \mathbf{k}|\mathbf{x}e^{-i\mathbf{q}\cdot\mathbf{r}}|c, \mathbf{k}+\mathbf{q}\rangle \times \frac{1}{E_c(\mathbf{k}+\mathbf{q}) - E_v(\mathbf{k}) - E - i\Gamma} \times \langle c, \mathbf{k}+\mathbf{q}|\mathbf{x}e^{i\mathbf{q}\cdot\mathbf{r}}|v, \mathbf{k}\rangle, \tag{8}$$

where v and c represent the valence and conduction bands, respectively, V is the crystal volume, and Γ is the broadening parameter. Finite values of $\mathbf{q}$ therefore modify the momentum matrix element and—if the conceptually useful vertical-transition picture is to be retained—shift the conduction band with respect to the valence band. This reciprocal-space displacement effectively increases the valence-conduction band separation by an amount proportional to $\mathbf{q}^2$,[36] and thus the spectrum resulting from the energy denominator is functionally equivalent to that encountered in first-derivative modulation spectroscopy except that the line shape is scaled by $\mathbf{q}^2 \sim E^2\epsilon_s$.

Both bulk energy-band (BEB) and momentum-matrix element contributions have been evaluated by Yu and Cardona[37] for the fundamental absorption edge of GaAs. I consider here the four equivalent ⟨111⟩ critical points giving rise to the E_1 structures at 3.4 and 2.1 eV in Figs. 3 and 5, respectively. A straightforward calculation assuming three-dimensional simple parabolic bands with the usual momentum selection rules yields for the energy-band contribution the result given in Table I and the line shape shown in Fig. 7. Here, $M_T = m_{ct} + m_{vt}$ is the sum of the transverse effective masses of the valence and conduction bands. The sign and numerical value of the prefactor depend not only on the symmetry of the critical points but also on the order of the singularity. If a two-dimensional model density of states with a momentum-space cutoff in the third dimension had been assumed, the expression would have vanished identically. Thus these data can also be viewed as a test of the two-dimensional nature of the E_1 transitions.

Because the effective masses and selection rules differ with critical point, the energy-band expression derived for the E_1

structure is not expected to describe the RD spectra in the vicinity of the 4.2 eV E_2 features in Figs. 3 and 5. However, the first-derivative functional form is general. Consequently, the energy band mechanism satisfies one of the qualitative criteria needed to describe the intrinsic contributions to the RD spectra.

The momentum matrix element contribution can be evaluated by $\mathbf{k}\cdot\mathbf{p}$ perturbation theory.[37] The result is also given in Table I and Fig. 7 for $\langle 111\rangle$ critical points, where $P \cong 2\pi/a_0$ is the momentum matrix element. This mechanism fails badly with respect to sign, magnitude, and line shape, and is not considered further.

3. Surface effects

As mentioned in connection with Eq. (7), local fields at lattice sites will not necessarily cancel if lattice sums are restricted, as for example by the existence of a surface. This effect was recently shown by Mochán and Barrera[14] to produce in principle a large anisotropy in the optical properties of cubic crystals with (110) surfaces. To calculate the expected line shape, Eq. (7) can be written

$$\epsilon_s + \Delta\epsilon_s^{\sigma\sigma} - 1 = \frac{4\pi n\alpha}{1 - \frac{4\pi}{3}n\alpha - \frac{\beta\alpha}{a_0^3} - \frac{\Delta\beta_j^{\sigma\sigma}\alpha}{a_0^3}}, \qquad (9)$$

where $\Delta\epsilon_s^{\sigma\sigma}$ represent the corrections to the dielectric function and lattice sum, respectively, for the layer j and polarization direction σ. If the $\Delta\beta_j^{\sigma\sigma}$ (and the corresponding $\Delta\beta^{\tau\tau}$) are small, the first-order expansion of Eq. (9) can be substituted in Eq. (2) to yield the surface local field (SLF) expression given in Table I and the normalized line shapes shown in Fig. 7. I have approximately evaluated the prefactor in Table I for a (110) surface of an f_{cc} lattice, for which $n = 4/a_0^3$ and $d = \sqrt{2}\,a_0/4$. Note that $\beta = 4\pi/3$ for the f_{cc} lattice, i.e., the local field contribution is equal to that obtained by averaging over dipole fields for this configuration.

In fact, only two assumptions are necessary for obtaining the Im (ϵ_s) functional form. These are (1) that the anisotropy arises from a *surface* phenomenon, so that Eq. (2) applies, and (2) that ϵ_s has the functional form

$$\epsilon_s = \epsilon_{s0} + \epsilon_{s0}\, g\epsilon_s\,, \qquad (10)$$

where ϵ_{s0} is a "bare" or "one-electron" dielectric response and g is an interaction or "screening" parameter with anisotropic corrections $\Delta g^{\sigma\sigma}$ in the vicinity of the surface. For example, in Eq. (9) ϵ_{s0} is $4\pi n\alpha$ and $\Delta_g^{\sigma\sigma}$ is $\Delta\beta^{\sigma\sigma}/(4\pi n a_0^3)$. But Eq. (10) can also be derived under rather general conditions[38] by applying the resolvent operation to the Dyson equation, which describes many-body corrections to the one electron approximation.[39] The existence of these many-body corrections to the optical spectra of semiconductors has been well documented in the literature.[39,40,41] Thus the Im(ϵ_s) RD response is more general than the Mochán–Barrera derivation would imply, and the observation of the Im (ϵ_s) component in RD spectra is direct evidence for the existence of *surface* many-body effects.

If the electron-hole Coulomb interaction is represented approximately by a δ function, Eq. (10) follows directly with $g = E^2\tilde{g}$, where $\tilde{g}$ is the contact-exciton interaction parameter.[39] The resulting line shape and functional representation for the surface contact exciton (SCE) model are given in Fig. 7 and Table I, respectively, and differ from the surface local field contribution by a scaling factor of E^2. This similarity is not surprising, since both mechanisms are manifestations of many-body screening effects. Consequently, a clear-cut distinction between the two may not be possible.

For completeness, the line shape and functional form of the RD contribution from an anisotropic transparent surface film is also given in Table I and Fig. 7.

From an inspection of Fig. 7 and Table I it is clear that the dominant contributions to the intrinsic or background RD spectra come from the bulk energy band and surface local field and/or surface contact exciton effects. Figures 8 and 9 show best-fit representation of the oxidized-surface RD spectrum of Fig. 3 and the H_2O-stripped RD spectrum of Fig. 5 for (110)Si and Ge, respectively. The spectra are divided into two ranges centered about the E_1 and E_2 transitions. Two best-fit curves are shown in each case, corresponding to linear combinations of the bulk energy band and surface local-field contributions, and of the bulk energy band and surface contact exciton contributions, respectively. Separate weighting factors were used for each constituent in each half.

The justification of different weighting factors for the first-derivative energy band contribution follows from the fact that different critical points are involved. The justification of separate weighting factors for the local-field and contact-exciton contributions is more subtle, since the corrections $\Delta\beta$ and $\Delta\tilde{g}$ do not contain any explicit energy dependences. However, an energy dependence can be expected to arise for $\Delta\beta$ if a more realistic local-field model is used to describe the semiconductor, where the electronic charge is distributed over the unit cell rather than being concentrated at lattice points. Since local field effects decrease as charge distributions become more uniformly distributed,

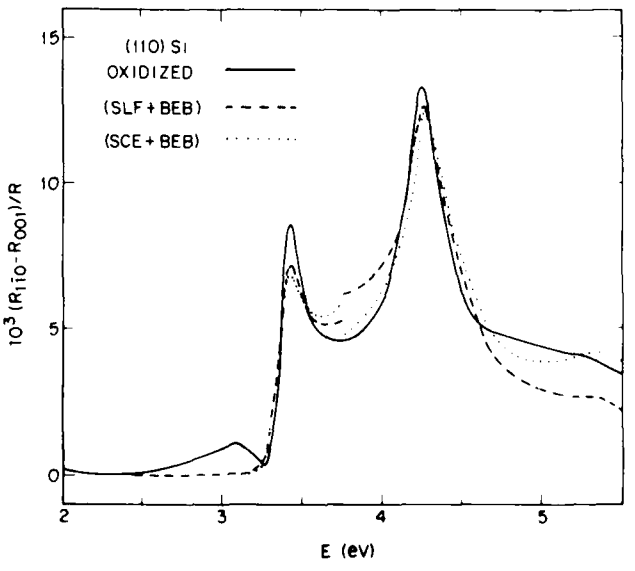

FIG. 8. Comparison of experimental and best-fit intrinsic RD line shapes for the oxidized (110)Si surface. Solid line: data. Dashed line: linear combination of surface local field and bulk energy band models. Dotted line: linear combination of surface contact exciton and bulk energy band models.

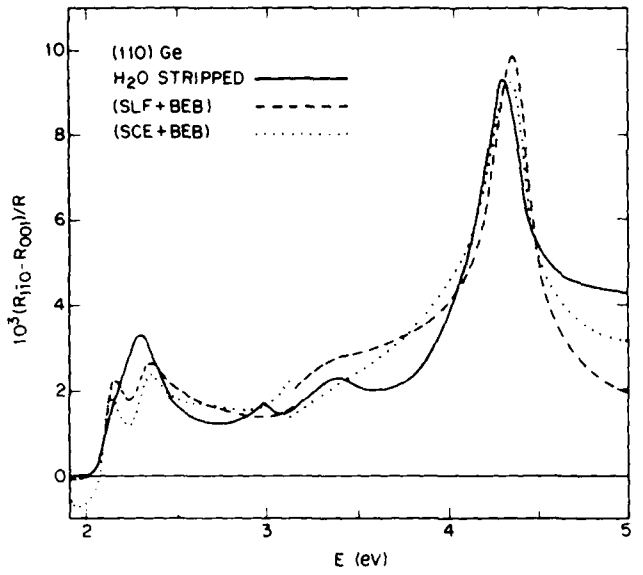

FIG. 9. As Fig. 8, but for (110)Ge.

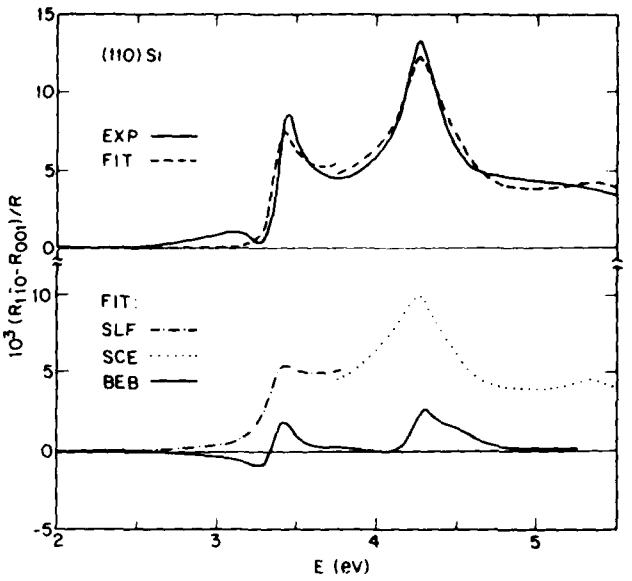

FIG. 10. Top: best-fit comparisons of the oxidized (110)Si surface, from Fig. 8. Bottom: intrinsic contributions shown separately.

and since the real-space distribution of the electronic wave functions depends on their energy and momentum, some energy dependence of $\Delta\beta$ can be anticipated. Likewise, since the strength of the electron-hole interaction depends on the overlap of the electron and hole wave functions, a weak energy dependence can also be expected for $\Delta\tilde{g}$.

Figures 8 and 9 show that the major spectral dependences of these RD data are well represented by these contributions, with the local field and contact exciton models providing somewhat better fits in the E_1 and E_2 spectral regions, respectively. The near-equivalence of the two models is not surprising, since as discussed above, both are approximate representations of surface many-body screening effects and differ only by a scaling factor E^2. In fact, the distinction in the E_2 spectral range is only possible at the limits of the fitting range. The overall agreement is sufficiently good to indicate that the major contributions have been correctly identified, but not good enough to allow the claim of complete success. This could have been anticipated because the line shapes corresponding to the chemically induced changes in the electronic polarizability of the surface bonds have no analog in Fig. 7, would not necessarily be expected to be dominated by bulk-related features, and have not been considered in the above discussion.

The best-fit contributions are shown individually in Figs. 10 and 11. These show that about 1/3 of the intrinsic contribution comes from the bulk energy band mechanism and 2/3 from surface many-body screening effects. The magnitudes obtained in the E_1 spectral regions can be compared to the predictions of the respective models. The results show that the surface local field model overestimates the experimentally determined amplitudes by factors of 10 and 11 for Si and Ge, respectively, and the energy band model underestimates the determined amplitudes by factors of 7 and 9. These discrepancies are at least in the expected direction; the former because local field effects are overestimated by assuming that the polarizable species are points whereas the diamond structure has a relatively extended two-atom basis in the unit cell, and the latter because the one-electron approximation consistently underestimates oscillator strengths of actual critical point transitions.

Figure 8 shows that the best approximation to the intrinsic (110)Si line shape is provided by the oxidized, not stripped, surface. This shows that surface-state effects are reduced by oxidation in this spectral range. Consequently, the RD change spectrum at the bottom of Fig. 3 is the line shape characteristic of states on this surface. Since the RD

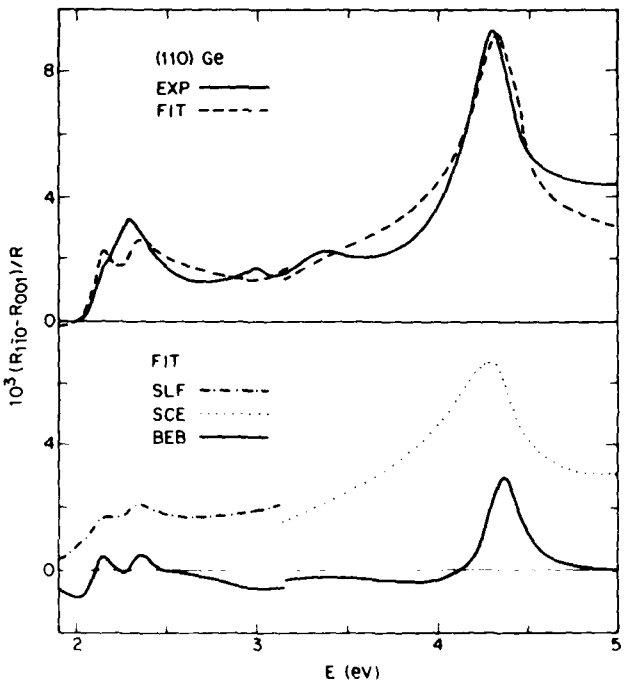

FIG. 11. As Fig. 10, but for (110)Ge.

The laser can also be frequency tripled to generate 355 nm light with less pulse energy. The N_2 laser (Molectron) can produce 2 mJ per pulse at 337 nm with 10 ns pulse duration and 30 Hz pulse rate. An XeCl excimer laser can provide 500 mJ per pulse at 308 nm with 20 ns pulse width and a maximum of 25 Hz repetition rate. UV transmitting quartz lenses and windows are used in the experiments.

III. RESULTS AND DISCUSSION

A. Spontaneous etching systems

As discussed by Winters, *et al.*,[11] spontaneous etching is defined to mean the process whereby neutral species (including radicals) in the absence of energetic radiation can interact with a solid surface to produce volatile products. Many of these reactions occur at or near room temperature. For instance, XeF_2 can spontaneously etch Si, Ta, Mo, Ti, and W.[12] At high gas pressure, F_2 can etch Si[13] and Cl_2 can etch Al.[14] The interaction of XeF_2 with Si in the presence[3,4,6] and in the absence[12,15,16] of photon radiation has been quite extensively studied in recent years. In this section, we present new results on Al-Cl_2 reaction enhanced by UV laser radiation. Without external radiation, spontaneous etching usually results in isotropic etching of solid materials.

When a clean Al is exposed to Cl_2, chemisorption readily takes place as detected by the decrease of the frequency (f) of an Al-quartz-crystal microbalance (Al-QCM). The dissociative chemisorption behavior at low pressure range ($\leqslant 10^{-5}$ Torr) has been investigated by Smith.[17] Above the gas pressure $P \geqslant 10^{-2}$ Torr, we observe a spontaneous etching of the Al film from the frequency response of the Al-QCM. Figure 1(a) shows the initial chemisorption phase causing f to decrease followed by the spontaneous etching causing f to increase at $P = 10^{-2}$ Torr. A N_2 laser at 337 nm irradiated on the Al surface can greatly enhance the etch rate. For example at this pressure, the UV laser-enhanced etch rate at the laser fluence $F = 0.12$ J/cm^2 (10 ns pulse width, 30 Hz pulse rate) is more than a factor of 15 higher than the spontaneous etch rate [Fig. 1(b)]. The etch rate enhanced by the laser increases as P is increased to 0.1 Torr [Fig. 1(c)]. Under the excitation condition, the etch rate is determined to be about 20 000 Å/min, i.e., about 11 Å/pulse. The etching behavior is also studied with a XeCl excimer laser. Figure 2 shows the frequency response of an Al-QCM exposed to Cl_2 at $P = 1$ Torr and the laser at $F = 0.30$ J/cm^2 (20 ns pulse width). The observed etch rate at 10 Hz pulse rate is about 300 Å/s, i.e., 30 Å/pulse. In the absence of Cl_2 gas, no etching, i.e., phys-

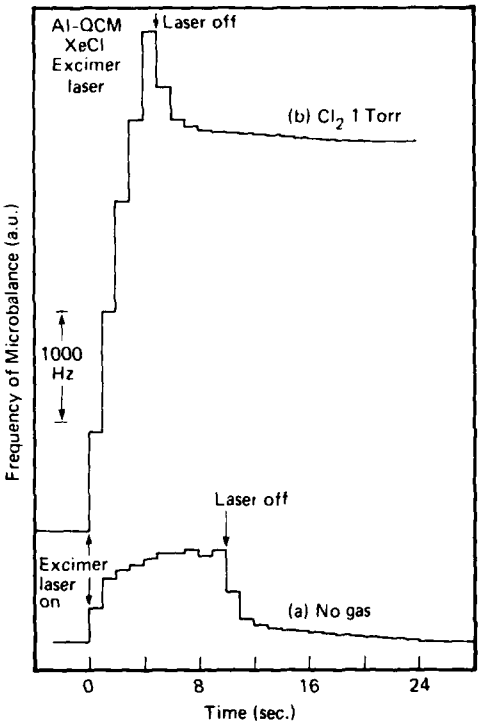

FIG. 2. Frequency responses of an Al-QCM: (a) excited by a XeCl laser at 0.30 J/cm^2, 10 Hz pulse rate, without gas and (b) same condition with Cl_2 at $P = 1$ Torr.

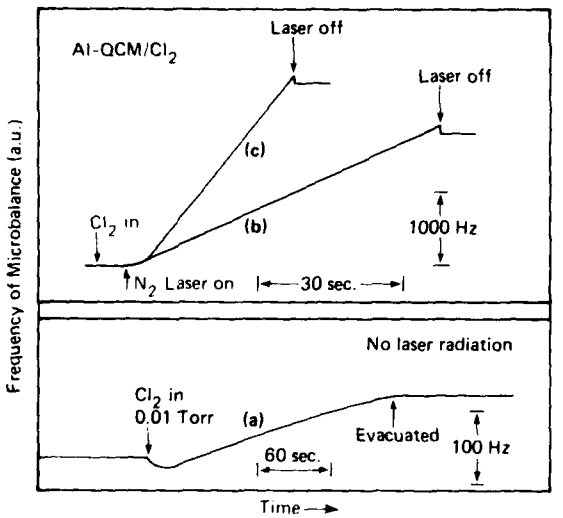

FIG. 1. Frequency responses of an Al-QCM: (a) exposed to Cl_2 at 10^{-2} Torr, (b) excited by a N_2 laser at 0.12 J/cm^2, 30 Hz pulse rate and $P = 10^{-2}$ Torr, and (c) excited by a N_2 laser and $P = 0.1$ Torr.

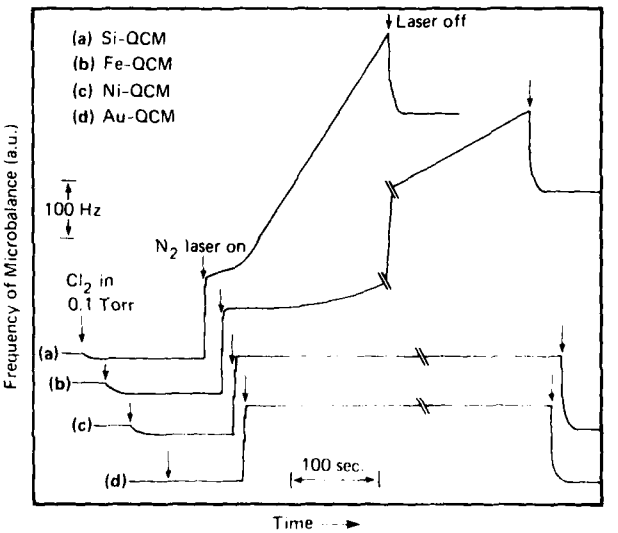

FIG. 3. QCM frequency responses show the chemisorption and the N_2 laser-induced etching behavior for some Cl_2-solid systems.

TABLE I. Relative etch rates observed in chemical etching of solids induced by a N_2 laser at 0.12 J/cm, 30 Hz pulse rate, and Cl_2 pressure at $P = 0.1$ Torr. Except Si(111) crystals, all solids listed here are prepared as films on QCM or quartz substrates.

Al	20 000 Å/min	Si film	1 600 Å/min	Ni	< 10 Å/min
Ag	500	n-Si(111) (0.1 Ω)	1 130	$Ni_{80}Fe_{20}$	120
Mo	1 000	p-Si(111) (0.1 Ω)	800	$Ni_{47}Fe_{53}$	350
W	240			$Ni_{20}Fe_{80}$	640
Au	< 10			Fe	850

ical ablation, of the Al film is detected under our irradiation conditions [Fig. 2(a)]. Since Cl_2 strongly absorbs photons near 300 nm, a rather short optical path length (~ 2.5 cm) is used in these experiments to reduce the effect of optical attenuation in the gas phase.

It is clear from the experimental results that chlorine can readily chemisorb on an Al surface and spontaneous etching can occur at $P \geqslant 10^{-2}$ Torr. We find that spontaneous etching is not always observed if the Al surface is contaminated. Under a steady state condition, the thickness of the chlorinated surface layer is likely to be about 30 Å which can be removed by a laser pulse at $F = 0.25$ J/cm^2 or higher. Since the laser-enhanced Al etch rate, depending on the laser fluence and pulse repetition rate, can be two orders of magnitude higher than the spontaneous etch rate at 25 °C, anisotropic etching of Al by Cl_2 gas can be achieved with laser beams. This is indeed observed. The etched features induced by the UV lasers are very clean and the walls are steep apparently suitable for practical applications.

B. Passive reaction systems

When a solid is exposed to halogen gases, the surface reaction often stops after forming a relatively thin passive surface layer which impedes further reaction. Among the three classes of heterogeneous systems that we discuss here, this type of reaction is by far the most prevailing behavior. The interaction of chlorine with Si, Ni, Fe, Mo, W, and Au clearly belongs to this class with the Au-Cl_2 reaction being the weakest among these solids. The typical chemisorption behavior as observed with QCM's as a function of Cl_2 exposure for some of these materials is shown in Fig. 3. Some of the etching reactions induced by a N_2 laser irradiation on solid surfaces are also displayed. The relative etch rates of these solids along with Al and Ag (to be further discussed below) at $P = 0.1$ Torr and $F = 0.12$ J/cm^2 (30 Hz pulse rate) are summarized in Table I. As discussed above, a very high etch rate is observed for Al films. Relatively high rates are detected for Si films, Si(111) (0.1 Ω, *n*- or *p*-type), Mo, and Fe. No or negligible etching is found for Au and Ni. To some extent, the laser-induced etch rates seem to be directly related to the volatilities of solid chloride compounds. For instance, $AlCl_3$, $SiCl_4$, $MoCl_5$, and $FeCl_3$ have relatively high vapor pressures at $T \leqslant 200$ °C,[18] which can be easily reached by a pulsed laser radiation on the solids. The chlorides of Ni and Ag at the same temperature are essentially nonvolatile. The notable exception to this etch rate-volatility correlation is tungsten. While the boiling points of WCl_5 and WCl_6 are relatively low (about 300 °C) and their vapor pressures are high even at $T = 200$ °C,[18] the etch rate of W by Cl_2 is very low. In fact, the optical (e.g., reflectivity) and thermal properties (e.g., heat capacity and thermal conductivity) of W and Mo are so similar that the surface temperatures raised by the UV pulses should be about the same. It is thus somewhat surprising to observe that the W etch rate can be a factor of 4 lower than Mo under our Cl_2 exposure and laser excitation conditions. From these results, it is clear that while the volatility of the reaction product is certainly an important factor in affecting the etch rate, other factors such as surface reactivity and photochemistry involving specific products formed in the reaction can be just as or even more important in determining the etching kinetics. At the present time, the laser-induced etching behavior for a given gas-solid system, even for such simple gas as Cl_2, is still not easily predictable from our limited knowledge in surface photochemistry. It should be further pointed out that for this class of chemical systems, laser-induced etching involves the formation and removal of a surface layer with the thickness usually of about 30 Å or less. This is the maximum etching yield per laser pulse due to the chemical effect along, i.e., not including the

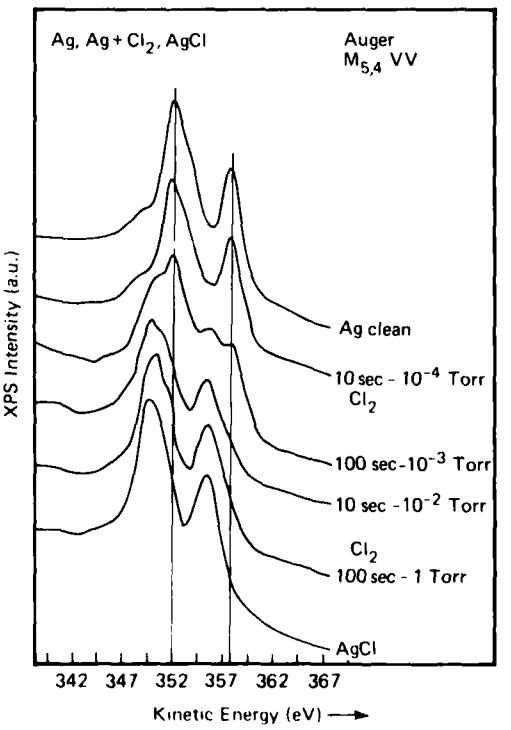

FIG. 4. X-ray induced $M_{4,5}VV$ Auger spectra of a clean Ag, Ag exposed to Cl_2, and a solid AgCl.

effect of physical ablation by laser pulses at very high laser intensities. Also, because Cl_2 can often readily adsorb dissociatively on metal and semiconductor surfaces, photodissociation of Cl_2 molecules in the gas phase usually is not an essential process for chemical etching to take place. Enhancement of etch rates due to Cl_2 photolysis is, however, observed in some cases.

In addition to pure Ni and Fe films, we have also investigated the etching reaction on Ni-Fe alloy surfaces. Although the etch rate for Ni induced by the N_2 laser at 12 MW/cm^2 and $P = 0.1$ Torr is negligible, the etch rate of the alloy increases with the Fe concentration as shown in Table I. Apparently the chemical etching of Fe whose rate is about two orders of magnitude higher than Ni has enhanced the Ni etching in the alloy system. Without such Fe-associated etching enhancement, the surface of the solid would be enriched with Ni and the etch rate of the alloy would be greatly reduced. We are carrying out further studies of the alloy system with XPS and AES in order to better understand the differential etching behavior of binary materials.

C. Diffusive reaction systems

Ag represents a class of solids which strongly react with Cl_2 so that chlorine not only chemisorbs on the surface but also diffuses into the bulk of the material. The interaction of Cl_2 with Ag surfaces in the low exposure range has been extensively studied by several groups.[19,20] Cl_2 can dissociatively adsorb on Ag with an initial sticking probability of about 0.5 and this value drops to about 0.01 above a monolayer surface coverage. In addition to chemisorption, a partial silver halide (AgCl) formation has been detected. We have studied the Ag-Cl_2 reaction in the pressure range between 10^{-4} and 10 Torr, and the exposure time between 10 and 1000 s. The x-ray induced $M_{4,5}VV$ Auger spectra as shown in Fig. 4 exhibit a chemical shift of about 2 eV indicating the formation of AgCl in the surface region. Coexistence of metallic Ag and AgCl is found in the chlorinated surface layer even for Cl_2 exposures as high as 1 Torr-100 s. Namely, Ag is always enriched with respect to Cl for exposures $\leqslant 10^8$ L. The surface Cl concentration (averaged over the sampling depth of the photoelectrons, i.e., ≈ 15 Å) can be determined quantitatively from the XPS intensity analyses of the Ag($3d$) and Cl($2p$) emission peaks (Fig. 5). The XPS spectrometer is calibrated with a solid AgCl sample and an excellent agreement with the calculated photoionization cross sections[21] of the two core level peaks is found. Figure 6 shows the average Cl surface concentration x with respect to Ag as a function of Cl_2 pressure exposed for various times. The chlorinated surface layer may be described with an average stoichiometry of $AgCl_x$ with $x < 1$. Only at much higher Cl_2 exposures, e.g., 10 Torr-1000 s, stoichiometry AgCl ($x = 1.0$) formation is observed with XPS.

The Cl penetration behavior is studied with both QCM and Auger depth profiling (ADP) along with Ar^+-ion bombardment. Typical responses of an Ag-QCM exposed to Cl_2 are shown in Fig. 7. The decrease of the QCM frequency $\Delta f = -220$ Hz at 10^8 L exposure (1 Torr-100 s) corresponds to an equivalent amount of 45 monolayers of Cl being adsorbed in the surface region of the metal. Since Cl is not

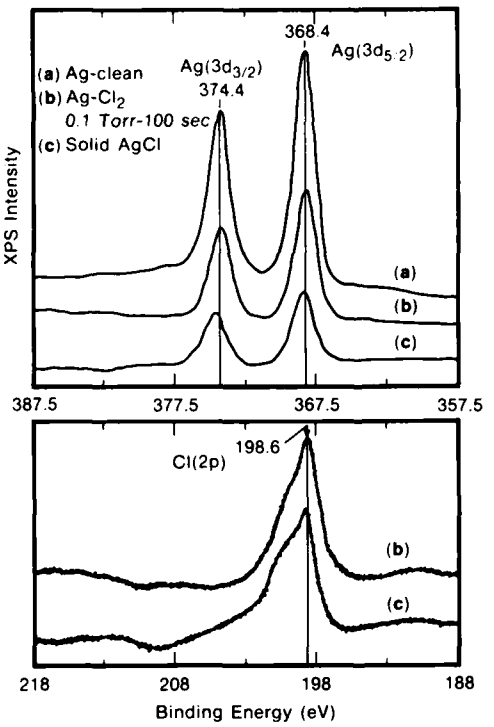

FIG. 5. XPS spectra of Ag(3d) and Cl(2p) of an Ag film exposed to Cl_2: (a) clean Ag surface, (b) exposed to Cl_2 at 0.1 Torr for 100 s and (c) a solid AgCl for comparison.

evenly distributed as a uniform AgCl layer as determined by XPS, the actual Cl penetration depth can easily reach 200 Å or more into the Ag lattice. This depth distribution is examined by ADP and the results are shown in Fig. 8. Clearly at low exposures, the Cl concentration (x) on the surface is low and it decreases rapidly as a function of depth. Whereas at high exposures, x can be close to 1 and a layer with constant Cl concentration is found [Fig. 8(c)]. The tails of the depth profiles are due mainly to intrinsic Cl diffusion (or more correctly Ag diffusion) and to a small extent to the ion-bombardment-induced effects such as surface compositional mixing and roughening. Ion-induced chemical change is a pronounced effect on solid AgCl and chlorinated Ag sur-

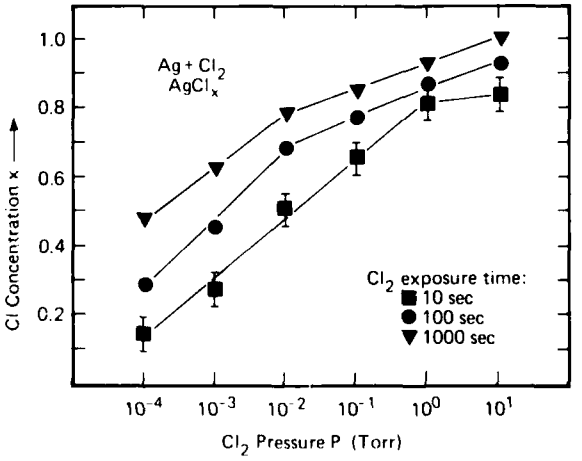

FIG. 6. Average surface Cl concentration x as in $AgCl_x$ on an Ag surface exposed to Cl_2 under various exposure conditions.

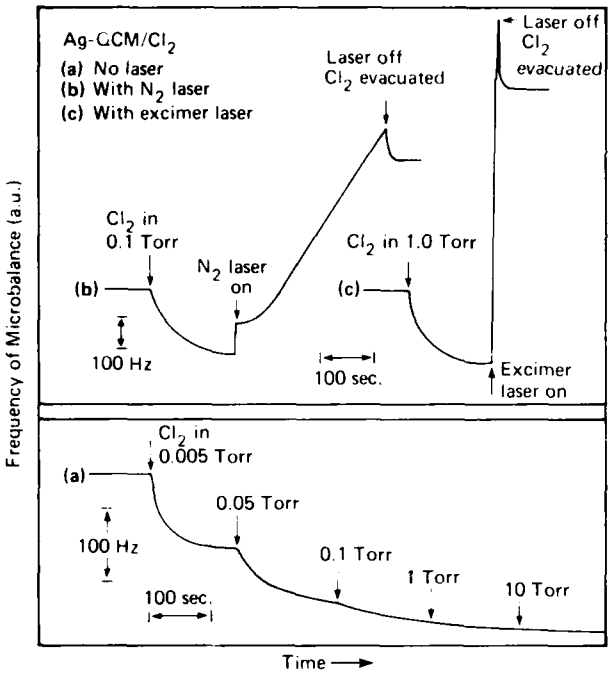

FIG. 7. Frequency responses of an Ag-QCM: (a) exposed to Cl_2 up to 10 Torr for 100 s, (b) excited by a N_2 laser (0.12 J/cm^2, 30 Hz) at $P = 0.1$ Torr, and (c) excited by a XeCl laser (0.30 J/cm^2, 10 Hz) at $P = 1.0$ Torr for 10 s.

faces. We have extensively investigated these effects and found that not only Ar^+-ions but also x-ray (used in XPS) and e-beam (used in AES) radiation can cause AgCl to be reduced to metallic Ag in the surface region. Photodecomposition of AgCl by x-ray irradiation was also observed by Sharma, *et al.*[22] Thus in the XPS, AES, and ADP analyses we have to take the radiation-induced effects into account. Details of this study will be published elsewhere.[23] It suffices to mention here that as displayed in Fig. 8, Cl indeed can penetrate quite deeply ($\gtrsim 200$ Å) into the bulk of Ag.

In spite of the incomplete surface chlorination (i.e., the surface is enriched with Ag), exposure of the surface to a UV or visible laser can result in efficient etching of the metal. Figures 7(b) and 7(c) show the responses of an Ag-QCM exposed to Cl_2 at 0.1 Torr excited by a N_2 laser at 12 MW/cm^2 and an XeCl laser at 15 MW/cm^2 and $P = 1.0$ Torr, respectively. Between 10^{-3} and 1 Torr, the laser-induced etch rate increases with pressure. Efficient etching is also obtained with 532 and 355 nm light pulses generated from a Q-switched Nd : YAG laser even under relatively low Cl_2 exposure conditions. Using a mass spectrometer in the time-of-flight (TOF) mode, we can detect Ag, Cl, and AgCl species desorbed by the laser pulses at $F \geqslant 0.3$ J/cm^2 from the Cl_2-exposed surfaces (1200 L at 2×10^{-6} Torr). Figure 9 shows the typical TOF spectra obtained with 532 nm pulses at 0.49 J/cm^2. The kinetic energies of the desorbed particles determined from the TOF spectra are 0.1, 2.9, and 4.7 eV, respectively, for Cl, Ag, and AgCl. Clearly their translational "temperatures" are not uniform and are much higher (some more than a factor of 50) than the estimated surface temperature raised by the laser-induced heating. When the laser fluence is raised to 0.7 J/cm^2, a small amount of genuine Ag^+ ions are detected without using the ionizer of the mass spectrometer. At $F = 1.3$ J/cm^2, only ionic Ag^+ and Cl^+ species are observed along with visible emission from the surface. The etching and desorption behavior induced by 355 nm light pulses is very similar to the excitation at 532 nm. For a clean Ag without Cl_2 exposure, atom and ion desorption is observed only at very high laser fluences (> 0.8 J/cm^2), and it always occurs along with a slightly bluish luminescence from the surface. Figure 9(b) shows the TOF spectra of Ag and Ag^+ species from a clean Ag irradiated by 532 nm light pulses at 1.13 J/cm^2. The prominent ionic emission and the characteristic visible luminescence strongly indicate the formation of plasma at the metal surface. Such emission of photons and charged particles has been

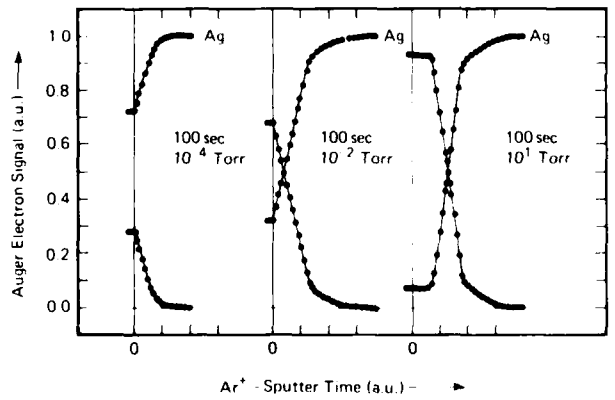

FIG. 8. Auger depth profiling showing the Cl and Ag signals as a function of sputtering time by Ar^+-ions on Ag surfaces exposed to Cl_2 under various exposure conditions.

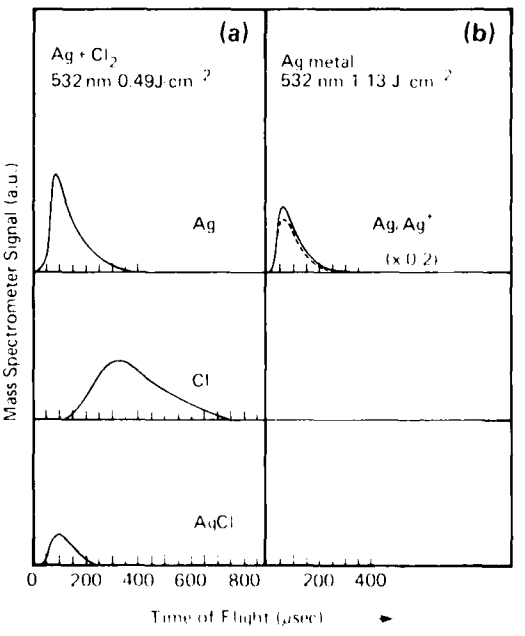

FIG. 9. Time-of-flight (TOF) mass spectrometer signals from (a) a chlorinated Ag surface (1200 L of Cl_2 at 2×10^{-6} Torr) and (b) a clean Ag surface, both irradiated by 532 nm laser pulses at different fluences. The dashed curve in (b) indicates the signal for genuine Ag^+ ions detected without using the ionizer of the mass spectrometer.

observed on a number of metal systems under high power laser radiation.[7]

Our results show that the photoetching behavior of a chlorinated Ag surface is very different from that of a metallic Ag. It is certainly not a thermal evaporation process of the surface AgCl species. The desorption products in AgCl thermal evaporation experiments showed a very different product distribution.[24] Furthermore, the high kinetic energies and the nonuniform energy distributions for the laser desorbed atomic and molecular species simply cannot be explained by the laser-induced surface heating effects. For $Ag-Cl_2$, the incident UV and visible photons are primarily absorbed by the metallic Ag within the top 400 Å of the solid. Although a partial formation of AgCl is found on the chlorinated surface and Cl penetrates quite deeply into the Ag lattice, optical absorption by the surface AgCl is quite small. A solid AgCl is practically transparent above 500 and at 355 nm its absorption coefficient is two orders of magnitude less than that of Ag.[25] Yet, we have observed very similar photon radiation effects between 355 and 532 nm light pulses. It should be pointed out that while the nonthermal radiation effects apparently play an important role in photoetching of gas-metal systems, the precise mechanism of the etching and desorption process is still unknown. It appears that for some metal systems, photogeneration of electron-hole pairs due to excitation of valence electrons in the halogenated surface could lead to breaking of surface bonds. Indeed, for molecular adsorbates evidence has been found[26,27] for a photon-stimulated-desorption (PSD) process, where a photon can excite a valence electron of the adsorbate-surface complex to an antibonding state, resulting in the repature of the surface bond and photodesorption along a repulsive surface potential. This PSD process could lead to kinetic energies in the eV range. According to this description originally proposed by Menzel, Gomer, and Redhead,[26,27] the kinetic energies may be different for various desorption products, because different potentials and bonding–antibonding states may be involved in the PSD process. Our observed desorption product and kinetic energy distributions seem to exhibit such PSD characteristics. Whether or not a PSD process similar to the MGR desorption model could indeed be important in the laser-induced chemical etching of solids remains to be clearly elucidated. Our results nevertheless illustrate the importance of electronic excitation effects involved in the surface etching of materials induced or enhanced by lasers.

ACKNOWLEDGMENTS

The authors wish to thank J. Goitia for his assistance with the experiments and E. E. Marinero for his contribution to part of the $Ag-Cl_2$ work.

[a] Present address: Institut für Physikalische Chemie der Universität München, Sophienstrasse 11, D-8000 München 2, West Germany.

[1] T. J. Chuang, J. Vac. Sci. Technol. **21**, 798 (1982); Mater. Res. Soc. Proc. **17**, 45 (1983); **29**, 185 (1984).
[2] D. J. Ehrlich and J. Y. Tsao, J. Vac. Sci. Technol. B **1**, 969 (1983).
[3] T. J. Chuang, J. Chem. Phys. **74**, 1461 (1981).
[4] F. A. Houle, J. Chem. Phys. **79**, 4237 (1983); **80**, 4851 (1984).
[5] M. Sekine, H. Okano, and Y. Horriike, in *Proceedings of the 5th Symposium on Dry Processes*, Tokyo, Japan, 1983 (Institute of Electrical Engineers of Japan, Tokyo, 1983), p. 97.
[6] T. J. Chuang, I. Hussla, and W. Sesselmann, in *Laser Processing and Diagnostics*, edited by D. Bäuerle (Springer, Heidelberg, 1984), p. 300.
[7] J. F. Ready, *Effects of High-Power Laser Radiation* (Academic, New York, 1971).
[8] See, e.g., P. C. Townsend, in *Sputtering in Particle Bombardment II*, edited by R. Behrisch (Springer, Heidelberg, 1983), p. 147.
[9] N. Itoh and T. Nakayama, Phys. Lett. A **92**, 471 (1982); T. Nakayama and N. Itoh, Radiat. Eff. Lett. **67**, 129 (1982).
[10] T. J. Chuang, J. Chem. Phys. **72**, 6303 (1980); **74**, 1453 (1981).
[11] H. F. Winters, J. W. Coburn, and T. J. Chuang, J. Vac. Sci. Technol. B **1**, 469 (1983).
[12] H. F. Winters and J. W. Coburn, Appl. Phys. Lett. **34**, 70 (1979).
[13] J. A. Mucha, V. M. Donnelly, D. L. Flamm, and L. M. Webb, J. Phys. Chem. **85**, 3529 (1981).
[14] D. L. Smith and P. G. Saviano, J. Vac. Sci. Technol. **21**, 768 (1982); also, H. F. Winters, J. Vac. Sci. Technol. B **3**, 9 (1985).
[15] (a) Y. Y. Tu, T. J. Chuang, and H. F. Winters, Phys. Rev. B **23**, 823 (1981); (b) H. F. Winters and F. A. Houle, J. Appl. Phys. **54**, 1218 (1983).
[16] (a) T. J. Chuang, J. Appl. Phys. **51**, 2614 (1980); (b) F. R. McFeely, J. F. Morar, N. D. Shinn, G. Landgren, and F. J. Himpsel, Phys. Rev. B **30**, 764 (1984).
[17] T. Smith, Surf. Sci. **32**, 527 (1972).
[18] O. Kubaschewski and C. B. Alcock, *Metallurgical Thermochemistry*, 5th ed. (Pergamon, New York, 1979), p. 358.
[19] See, e.g., Y. Y. Tu and J. M. Blakely, Surf. Sci. **85**, 276 (1979); M. Kitson and R. M. Lambert, Surf Sci. **100**, 368 (1980).
[20] M. Bowker and K. C. Waugh, Surf Sci. **134**, 639 (1983).
[21] J. H. Scofield, J. Electron Spectrosc. Relat. Phenom. **8**, 129 (1976).
[22] J. Sharma, P. Dibona, and D. A. Wiegand, Appl. Surf. Sci. **11/12**, 420 (1982).
[23] W. Sesselmann and T. J. Chuang (to be published).
[24] L. C. Wagner and R. T. Grimley, J. Phys. Chem. **76**, 2819 (1972).
[25] F. C. Brown, J. Phys. Chem. **66**, 2368 (1962); H. Kanzaki and S. Sakuragi, Photogr. Sci. Eng. **17**, 69 (1973).
[26] D. Menzel and R. Gomer, J. Chem. Phys. **41**, 3311 (1964); also, D. Menzel, J. Vac. Sci. Technol. **20**, 538 (1982).
[27] P. A. Redhead, Can. J. Phys. **42**, 886 (1964).

Mechanistic studies of the decomposition of trimethylaluminum on heated surfaces

D. W. Squire,[a] C. S. Dulcey,[b] and M. C. Lin
Chemistry Division, Naval Research Laboratory, Washington, D. C. 20375-5000

(Received 18 March 1985; accepted 21 May 1985)

The decomposition of trimethylaluminum (TMA) on copper, aluminum, quartz, and gallium arsenide substrates has been studied as a function of substrate temperature from 550–900 K under low pressure conditions. Detection of gaseous products was carried out by laser multiphoton ionization mass spectrometry (MPI/MS) for methyl radical and aluminum species and electron impact mass spectrometry (EI/MS) for stable species. The methyl radical was the sole gaseous reaction product observed above these substrates, with an apparent activation energy for production of 13 ± 2 kcal/mol. Neither ethane nor methane was observed at the low pressures employed in these experiments, with either helium or hydrogen as carrier gases. A mechanism is proposed to explain these results.

I. INTRODUCTION

Organometallic chemical vapor deposition (OMCVD) is an increasingly important semiconductor processing technique, and is a subject of considerable current research interest.[1–6] In OMCVD, metal alkyls and hydrides are mixed in a carrier gas (H_2, N_2, or noble gas) and flowed into a reactor, where they deposit a metal layer on a high temperature substrate. Most studies of OMCVD have concentrated on properties of the deposited surface and the stable end products, ignoring reactive intermediates necessary for a detailed understanding of mechanism. Detection of the reactive intermediates has been hampered by the operating pressures of practical CVD reactors (about 1 atm). The principal gaseous products observed are the alkanes corresponding to hydrogenation or recombination of the alkyls attached to the source metal.

The relative importance of gas phase vs surface reactions and the role of free radicals in the OMCVD process are not well understood. The standard models proposed for CVD have been surface reactions occurring by Langmuir-Hinshelwood (adsorbed state) mechanisms.[1–5] Recently, however, Breiland and Ho have detected Si_2 in the gas phase during the deposition of silicon from silane, suggesting a more prominent role for gas phase reactions.[6]

As an example of possible operative mechanisms, consider gallium arsenide deposition from trialkylgallium and arsine. The observed gaseous organic products may result from the surface reactions

$$GaR_x(a) + AsH_y(a) \rightarrow RH(g) + GaR_{x-1}(a) + AsH_{y-1}(a),$$

$$GaR_x(a) \rightarrow R_2(g) + GaR_{x-2}(a),$$

or from alkyl radicals in the gas phase via the reactions

$$R\cdot(g) + AsH_y(g) \rightarrow RH(g) + AsH_{y-1}(g),$$

$$R\cdot(g) + R\cdot(g) \rightarrow R_2(g),$$

where $x, y \leq 3$, a = adsorbed, and the alkyl radical $R\cdot(g)$ is a desorbed surface reaction product. To distinguish between these channels, it is necessary to examine the reaction on a heated surface under low pressure ($< 10^{-5}$ Torr) conditions. This pressure regime diminishes certain high density effects (secondary reactions, flow and boundary effects, etc.) and allows a clearer understanding of the primary mechanism, which can then be extended to model higher pressure results.

In our experiments, we have studied the thermal decomposition of trimethylaluminum (TMA) on heated substrates at low pressures.[7] The current interest in GaAlAs semiconductor manufacturing makes the TMA/GaAs system an obvious candidate for study. Detection of the reaction products was done by resonance enhanced multiphoton ionization (REMPI)[8–10] and electron impact (EI) mass spectrometry. The use of MPI allowed selective detection of the (nonfluorescing) methyl radical and the alkylaluminum compounds with the high sensitivity of ion detection.[8–10] Electron impact allowed us to monitor methane and ethane, or any other relatively stable molecule which does not fluoresce or photoionize in the wavelength region employed in these experiments.

The decomposition of TMA was studied on a variety of substrates chosen to distinguish possible mechanisms. Both helium and hydrogen were employed as carrier gases to investigate the possible role of hydrogen in the deposition process. We find that TMA decomposition on heated substrates produces only the methyl radical as the initial gaseous product. Neither methane nor ethane production was observed using electron ionization within the detectivity of our mass spectrometer under the experimental conditions employed.

II. EXPERIMENTAL

A schematic of the apparatus used in these experiments is shown in Fig. 1. The system is a modified version of that previously used for MPI spectroscopy of free radicals.[8–10] Briefly, TMA diluted in H_2 or He was bled through an orifice onto a heated surface held 45 deg to both the gas flow and the axis of a quadrupole mass spectrometer (extranuclear). In the mass spectrometer, products passing through a skimmer were ionized and mass analyzed. Ionization was achieved by either electron impact or MPI (multiphoton ionization). With MPI, ions were generated in the focal volume of a pulsed laser. Following mass selection, these ions were

 0734-211X/85/051513-07$01.00

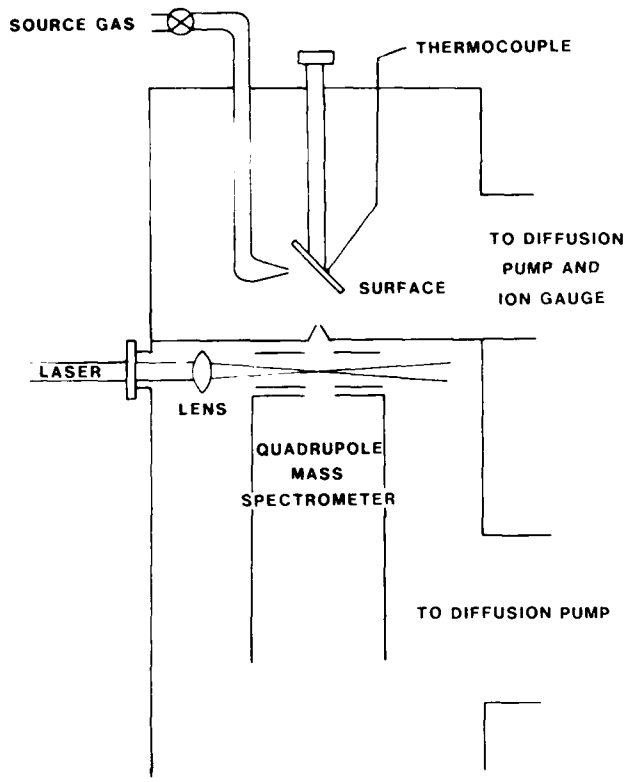

FIG. 1. Schematic of the apparatus used in these experiments. For a full discussion see experimental section.

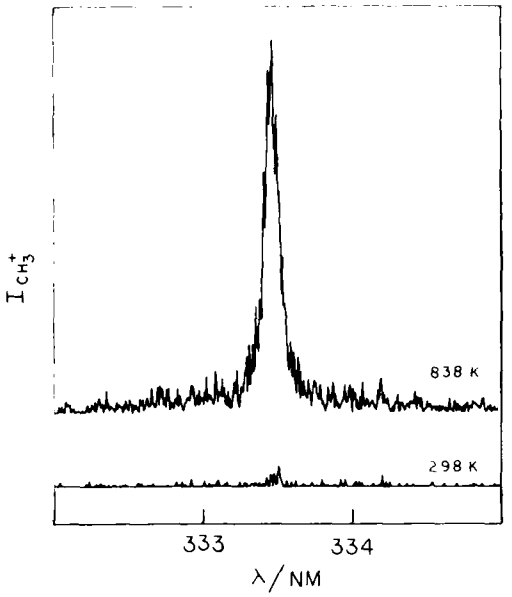

FIG. 2. Methyl signal as a function of wavelength at surface temperatures of 298 and 838 K. Ionization was achieved by two photon resonance via the $3p\ ^2A_2$ Rydberg state. No resonance peak was noted at m/z 12 and 27 in this frequency region.

detected, amplified, sampled, and signal averaged. Ions generated by electron impact were monitored on an oscilloscope.

The TMA dilution was prepared by passing helium or hydrogen at ~1000 Torr through a LN_2-cooled molecular sieve and then bubbling it through TMA. The latter was held at temperatures between 273-290 K, which maintained the vapor pressure at a maximum of ~1 Torr. The dilution ratio was, therefore, at least 1000 : 1 at all times. The gas mixture was then bled onto the surface to achieve an ambient pressure rise of 2.0×10^{-6} Torr. At the surface, which was 10 mm from the orifice, the maximum TMA partial pressure was believed to be on the order of 10^{-8} Torr. It was necessary to maintain these pressures and dilutions because high TMA concentration caused degradation of the performance of the electron multiplier used for ion detection.

Surfaces used were copper, aluminum, quartz, and GaAs. With the exception of aluminum, for which household (low purity) foil was used, these substrates were of high purity. Standard cleaning techniques were employed before these substrates were introduced into the vacuum system.

In the ionization region of the mass spectrometer, 25 mm from the surface beneath the skimmer (3 mm diam), reaction products and deflected reactants were ionized, either by 50 eV electrons or the frequency doubled output of a Nd : YAG pumped dye laser. The laser pulses were focused with a 38-mm focal length quartz lens into the ionization region. Typically, 200-300 laser pulses (333.4 nm) were used to ionize the methyl radical. Two photons are required to resonantly excite the $3p\ ^2A_2''$ Rydberg transition and a third required for ionization.[10] Ionized products were then mass selected and detected. About 400 laser shots were averaged per amu at a fixed wavelength, and ~800 per nm at a fixed mass.

III. RESULTS

The first studies were of TMA (in a helium carrier) decomposing on a copper surface. Typical experimental results of laser ionization are shown in Figs. 2 and 3. Figure 2 displays

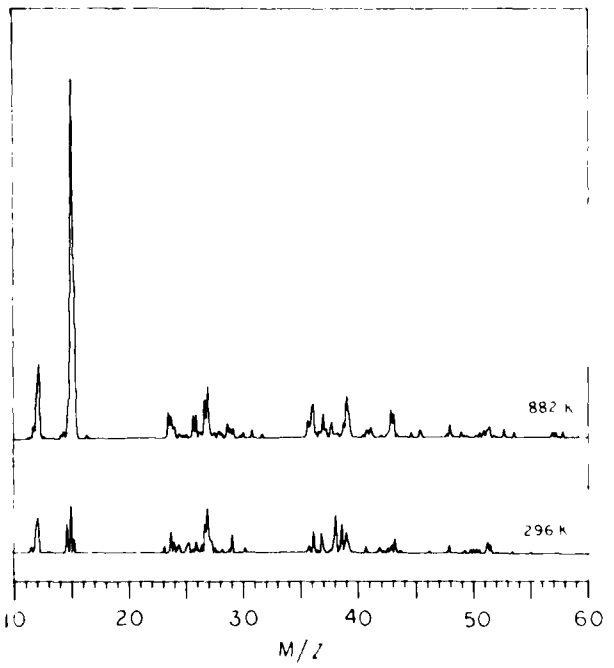

FIG. 3. REMPI mass spectra at 333.4 nm with surface temperatures of 298 and 882 K. Higher masses are insignificant. Masses other than m/z 12, 15, and 27 are believed to be generated from background.

the methyl radical signal as a function of wavelength for the copper substrate maintained at room temperature and at an elevated (840 K) temperature, showing the dependence of the methyl signal on substrate temperature. No sharp resonances were noted for other masses in the same wavelength region.

Figure 3 shows typical mass spectra obtained with the copper substrate at room temperature and at 880 K. Both spectra were taken at a laser wavelength of 333.4 nm, the peak of the transition observed in Fig. 2. Masses 12, 15, and 27 are the only masses appearing in these spectra that can be unambiguously assigned to TMA decomposition. Other mass signals are believed to arise from nonresonant ionization of background gases. The origin of mass 12 is unclear, but it has no consistent temperature dependence. Mitchell and Hackett have shown that laser irradiation of TMA between 390 and 475 nm leads to dissociation of TMA and MPI of the aluminum atom (mass 27).[11] Mass 15 is the mass peak that shows the strongest dependence on temperature. It should be noted that all mass peaks other than m/z 15 and m/z 27 disappeared when the TMA partial pressure in the reaction chamber was raised.

To verify the monomolecular character of the decomposition reaction, the pressure dependence of the methyl radical MPI signal was studied. The results are shown in Fig. 4, for TMA in helium (TMA-He) striking a gallium arsenide surface at two different temperatures. The linear dependence indicates the absence of surface saturation and secondary reactions under the conditions employed.

At room temperature, TMA exists primarily as the dimer $Al_2(CH_3)_6$. In order to establish that the production of methyl radicals does not depend on the surface dimer dissociation reaction

$$Al_2(CH_3)_6 + S \rightarrow 2Al(CH_3)_3(a)$$

which has a ΔH° of 20 kcal/mol,[12] the TMA inlet tube was heated to 360 K to dissociate the dimer before it struck the surface. The heating had no effect on the CH_3 signal relative to that seen with a room temperature inlet. Thus, the dimer does not appear to play an active role in the deposition.

In the initial experiments, the copper surface employed allowed higher temperatures (900 K) for a more accurate activation energy measurement for methyl radical production. GaAs experiments were limited to 750 K, the point at which arsenic desorption begins. Aluminum and quartz substrates were also investigated. The former was used as a surface composed of the depositing metal, aluminum, to investigate the source of the m/z 27 signal rise observed at elevated temperatures. The latter was employed as a nonconducting, nonmetallic crystal (to test a proposed mechanism).

Figures 5–8 show the dependence of the methyl signal on substrate temperature for four combinations of diluent gases and substrate materials. Figure 5 shows the methyl signal as a function of substrate temperature for TMA-He striking a copper surface. Six experimental runs are included in the figure. To compensate for small variations in operating conditions, data from the six independent runs were normalized to each other at 700 K. Two of the six data sets plotted here were taken with the substrate temperature declining following experimental sets recorded as temperature increased. For metallic surfaces, apparent activation energies for methyl radical production were found to be consistently larger for data taken as the substrate temperature declined.

To investigate the role of carrier gas in the reaction, He was replaced with H_2 as the carrier gas; the dependence of methyl signal on substrate temperature is shown in Fig. 6. The results in Fig. 6 can be superimposed on those presented in Fig. 5.

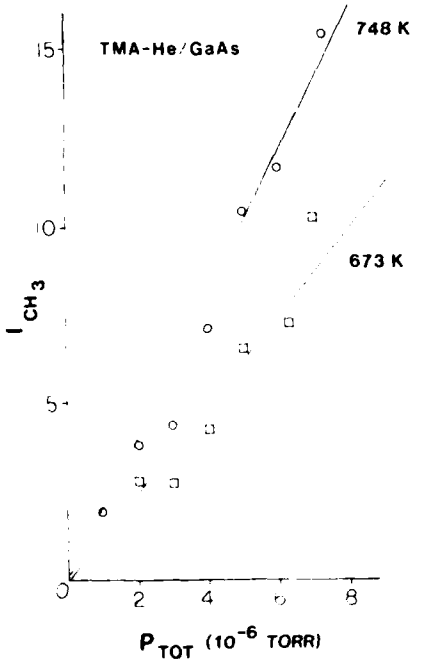

FIG. 4. Methyl signal as a function of TMA-He pressure for two temperatures on a GaAs surface showing the linear dependence.

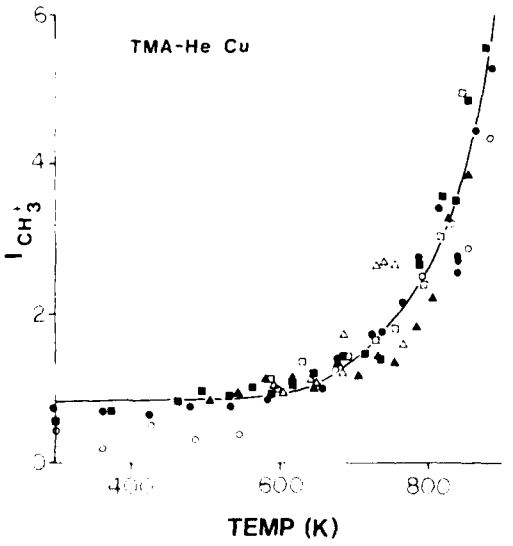

FIG. 5. Methyl signal as a function of surface temperature for TMA in a helium carrier gas striking a copper surface. Data from six experimental runs are presented, normalized at 700 K. In this and subsequent figures, the intensity scales are arbitrary and the solid lines are least squares fits of the data to the form $I = A\exp(-B/RT) + C$. The value of B derived from this analysis is 15 kcal/mol.

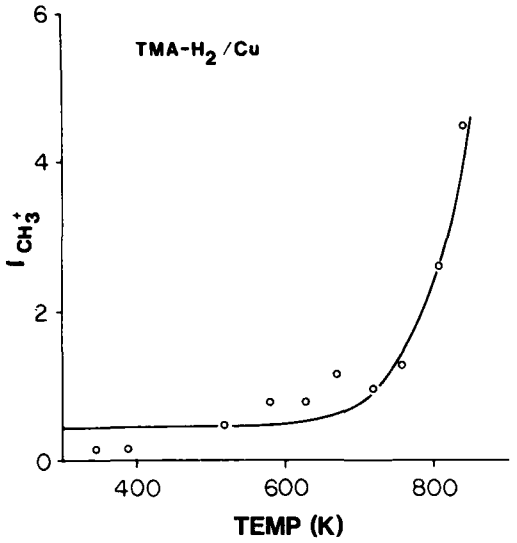

FIG. 6. Methyl signal plotted against surface temperature for TMA in a hydrogen carrier gas striking a copper surface. These data are superimposable on the helium carrier results.

Figure 7 shows a similar plot [$I(CH_3^+)$ vs substrate temperature] for the aluminum surface. This surface was studied in an attempt to examine the possibility of aluminum evaporation to account for the observed m/z 27 at high temperatures (see Fig. 11 and discussion below). The methyl signal as a function of temperature was essentially the same and could be superimposed on Fig. 5.

The results of TMA decomposition on a gallium arsenide surface are shown in Fig. 8. Again, the methyl signal (mass 15) varied with substrate temperature in a manner similar to the other surfaces up to 750 K. This experiment was repeated using hydrogen carrier with the same results.

Methane and ethane are present as impurities in TMA. Despite repeated purification of the TMA sample, constant methane and (much smaller) ethane signals were observed

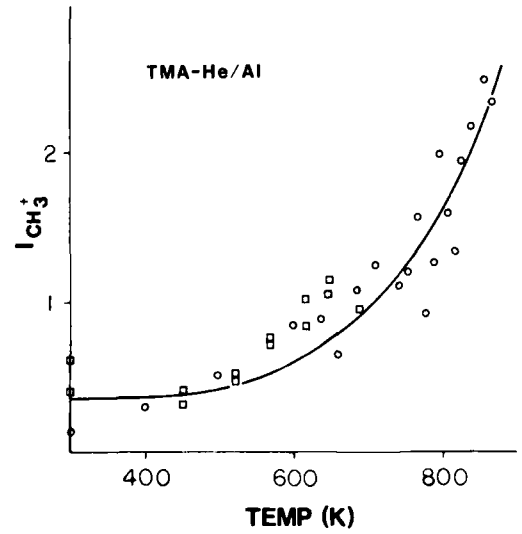

FIG. 7. Methyl signal generated from TMA seeded in helium striking an aluminum surface plotted against the surface temperature. These results are superimposable on the TMA-He/Cu results of Fig. 5.

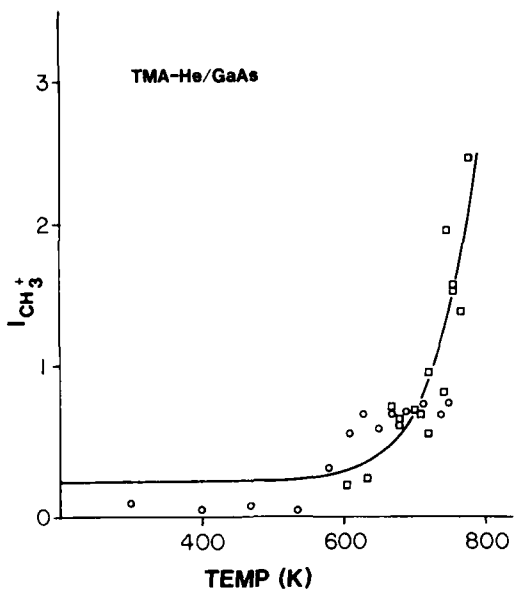

FIG. 8. Methyl REMPI signal for TMA seeded in helium striking a GaAs surface plotted against the surface temperature. The data can be superimposed on the results shown in Fig. 5.

using electron ionization at room temperature. These signals were monitored as a function of substrate temperature to determine if any methane or ethane was produced in TMA decomposition. The low levels of methane and ethane (m/z 16 and 30) signals observed had no dependence on substrate temperature for any combination of carrier gas and substrate. To test the sensitivity of our mass spectrometer using electron ionization, a sample of ethane diluted in helium 1 : 1000 was introduced into the system through the TMA inlet. An ambient pressure rise of 2.0×10^{-6} Torr produced a twenty to fortyfold increase in m/z 30 EI signal over background levels, depending on electron multiplier gain. Accordingly, a 3%–5% conversion of TMA into ethane, a more probable surface reaction product than methane on these surfaces, could be readily detected.

An Arrhenius plot of all the results presented in Figs. 5–8 is shown in Fig. 9, with all data separately corrected for background methyl signal below 500 K. This plot covering 600–900 K gives an apparent activation energy $E_a \pm 2\sigma = 13 \pm 2$ kcal/mol for methyl radical production from the thermal decomposition of TMA on heated substrates at low pressures. The fact that all results are superimposable within experimental error indicates that the reaction mechanism on metals and semiconductors was independent of the nature of the substrate.

The number of methyl groups remaining on the surface following the decomposition reaction and the methyl desorption is unknown. An $Al/Al(CH_3)_x$ ($x < 3$) surface layer develops during deposition; the remaining surface methyls will eventually separate from the aluminum layer by desorption, migration or decomposition but on a time scale long compared to the initial deposition step. In the absence of direct surface analysis, a temperature jump experiment was carried out to verify the presence of surface methyls. The surface was first reacted at 600 K for 15 min and then the TMA and carrier gas were turned off, pumped away and the

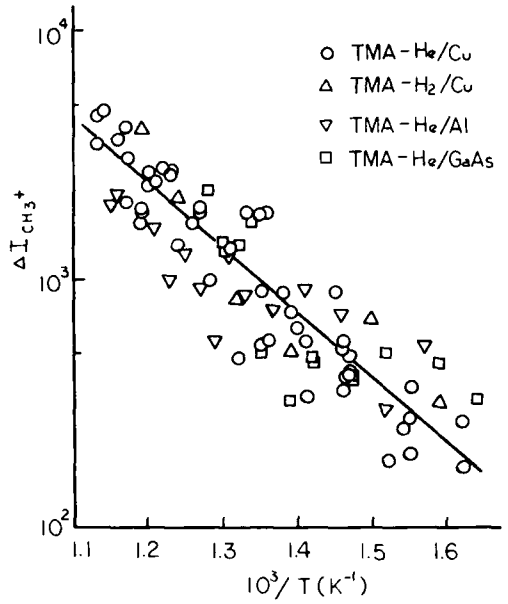

FIG. 9. Arrhenius plot of all methyl REMPI data from copper, GaAs, and aluminum substrates (all data corrected for baseline shifts separately). The slope of the line gives an apparent activation energy for methyl radical production to be 13 ± 2 kcal/mol (the error given is two standard deviations).

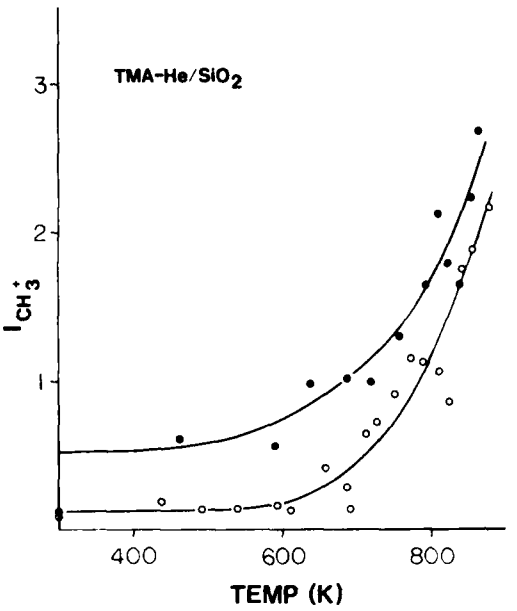

FIG. 10. Methyl signal as a function of substrate temperature for TMA seeded in helium impinging on a quartz substrate. Open circles are data taken with the substrate rising in temperature; filled circles were taken with the substrate dropping in temperature.

surface temperature was rapidly increased to 800 K. A small but real surge in methyl signal was observed immediately following the jump, indicating the presence of surface methyls.

In order to test our proposed mechanism (see Sec. IV), the reaction on a nonconducting quartz substrate was studied. In Fig. 10, methyl radical production as a function of surface temperature is shown for TMA decomposition on the quartz substrate. Although these data are qualitatively similar to those shown in Fig. 5, they are different in one important aspect—the activation energy determined as the substrate temperature rose was greater than that determined when surface temperature subsequently declined. Further comments on this interesting observation will be made later.

Aluminum (m/z 27) was routinely monitored in the above experiments as a measure of the unreacted TMA concentration. The results were unexpected. Figure 11 shows the aluminum signal (m/z 27) as a function of substrate temperature observed during the decomposition of TMA on copper and gallium arsenide substrates. The relatively low apparent activation energies from these data (~ 20 kcal/mol) in comparison with the heat of vaporization of aluminum (77 kcal/mol[13]) suggests that the m/z 27 signal does not derive from the ionization of Al atoms by MPI. To verify this supposition, an aluminum surface was heated in the absence of TMA to see if aluminum desorption occurs at these temperatures. The signal was found to be far too low to explain the behavior shown in Fig. 11.

IV. DISCUSSION

The primary gaseous product of TMA decomposition on heated surfaces at low pressures is the methyl radical. The apparent activation energy for its production (13 ± 2 kcal/mol) was found to be independent of surface type or carrier gas. Methane or ethane products were not detected within the sensitivity of our present electron-impact mass spectrometer. This result implies that radical hydrogenation or recombination takes place as a secondary gas-phase reaction and not as part of the thermal decomposition of TMA on surfaces.

The bond strength of the aluminum-carbon bond in TMA is believed to be in the range of 50–60 kcal/mol. The surprisingly low apparent activation energy observed for methyl

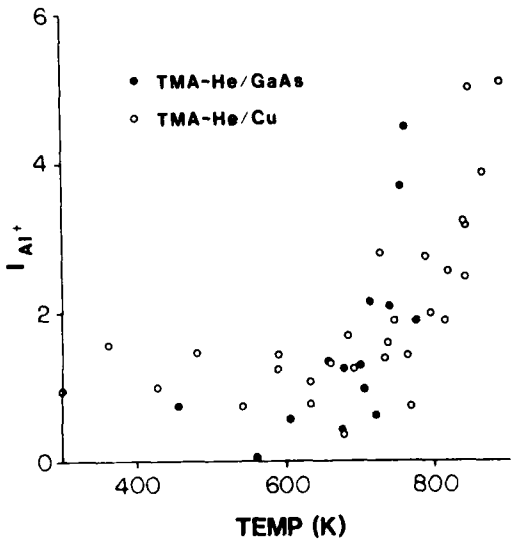

FIG. 11. Aluminum (m/z 27) MPI signal as a function of surface temperature arising from TMA-He impinging on Cu and GaAs surfaces. A least-squares Arrhenius fit of these data give apparent E_a's for aluminum production of ~ 20 kcal/mol.

radical production (13 ± 2 kcal/mol) may be due to the formation of a new Al–Al surface bond

$$(CH_3)_3Al + :Al(s) \rightarrow (CH_3)_{3-x}Al\text{–}Al(s) + xCH_3.$$

This bond formation could release enough energy to weaken at least one Al–C bond, leading to the observed methyl signal dependence on surface temperature. TMA is known to be highly reactive due to its electron deficient Al atom,[14] which spontaneously reacts with electron donors.

The increased apparent activation energy for methyl production observed when temperature decreases requires explanation. After reaction at elevated temperatures for an extended period of time, products other than aluminum may build up on the surface. The rate at which these products decompose and desorb may limit further deposition. That some such products exist on the surface was shown by the temperature jump experiment described previously. The higher activation energy for methyl production determined while the substrate temperature was lowered may be caused by surface methyls blocking reaction sites or binding electrons. The above mechanism for the decomposition reaction is supported by the results of the experiments using quartz as a substrate. On a nonconducting surface such as quartz, the production of methyl radical should initially be very slow, due to the absence of surface electrons to form a bond with TMA. A very low methyl signal level would be observed arising from thermal decomposition, with the surface simply acting as a passive heat source. The deposition reaction should proceed via the proposed mechanism when enough aluminum is present on the surface to form a thin layer. This hypothesis is consistent with the observed activation energy which was higher as the quartz substrate temperature rose than that determined as it fell (Fig. 10).

Hydrogen carrier is postulated as an active reagent in the surface hydrogenation of methyl radicals by some CVD models.[1-5] The helium carrier was replaced by hydrogen to test this hypothesis. With hydrogen, no changes were observed in methyl signal, methyl temperature dependence, or methane or ethane abundance. Accordingly, hydrogen does not play an active role in the *surface* reaction.

The rise in the aluminum signal at high temperatures is dependent on the presence of TMA and has too low an activation energy to be accounted for by aluminum vaporization from the surface. Aluminum desorption does occur at these temperatures but at a slow rate ($\Delta H^\circ = 77$ kcal/mol). Laser ionization of both aluminum and TMA produces m/z 27.[11] By inference, the Al^+ signal could arise from all $Al(CH_3)_x$ ($0 \leqslant x \leqslant 3$). The observed high temperature aluminum signal may derive from $Al(CH_3)_x$ ($x = 1$ or 2) desorbing from the surface. This possibility will be tested in the near future.

V. CONCLUDING REMARKS

The unique feature of these experiments is the use of MPI to detect methyl radical reaction products. The advantages of MPI as a probe are significant relative to other detection techniques. MPI combines the sensitivity of mass spectrometry with the state selectivity of laser spectroscopy permitting both accurate determination of products and measurement of internal energy.

In the present experiment, the pressure of helium in the ionization region of the mass spectrometer was found to be $\sim 10^{-6}$ Torr. If TMA maintained its (minimum) dilution of 1 : 1000, the partial pressure of TMA in the ionization region would be at most 10^{-9} Torr. If each molecule produced three methyl radicals in the deposition process, the density of methyl radicals would be 3×10^{-9} Torr or 10^7 molecules cm^{-3}. Since the observed methyl radical signal was usually over 1000 counts and sometimes over 10 000, this indicates a sensitivity limit for methyl radical detection of 10^4 molecules cm^{-3}.

Using this sensitive technique of REMPI, the direct reaction product of trimethylaluminum decomposition on heated surfaces at low pressures was found to be the methyl radical, with an apparent energy of 13 ± 2 kcal/mol. This result can be explained most easily by the interaction of TMA aluminum atom with a surface metal atom to form a bond, aiding the cleavage of one or more $Al\text{–}CH_3$ bonds. This mechanism, however, requires the presence of a metallic layer on the surface which can donate the electrons required to bond the electrophilic aluminum in TMA. If no such metallic layer is present, as in the case of quartz, the deposition reaction cannot readily take place until a thin aluminum film is pyrolytically formed on the surface to accelerate the deposition reaction.

The ethane and methane products commonly seen in OMCVD reactors were not observed using any substrate at any temperature in the present experiments. This suggests that both products are the result of secondary gas phase reactions; for example,

$$CH_3 \cdot (g) + AsH_3(g) \rightarrow CH_4(g) + \cdot AsH_2(g),$$

$$CH_3 \cdot (g) + CH_3 \cdot (g) \rightarrow C_2H_6(g).$$

This is quite likely in view of the observed low activation energy for CH_3 production. The enhanced, but still weak, aluminum signal seen at elevated surface temperatures is attributed to the desorption of $Al(CH_3)_x$ ($x = 1$ or 2).

The present work employs REMPI and EI to elucidate the mechanism of metal alkyl decomposition on solid substrates in the absence of metal hydrides. Metal hydrides may affect the rates of metal deposition, methyl radical production, and alkylaluminum desorption via surface reactions such as

$$GaCH_3(a) + AsH(a) \rightarrow CH_4(g) + GaAs(a),$$

which has been proposed as the rate-limiting step in GaAs deposition by Reep and Ghandhi.[5] A REMPI/EI study of metal alkyl/metal hydride mixtures should provide the information necessary to determine the importance of such reactions in OMCVD processes.

[a] NRC/NRL Cooperative Research Associate (1984–present).
[b] GeoCenters, Inc., 320 Needham Street, Newton Upper Falls, MA 02164.

[1] G. B. Stringfellow, J. Cryst. Growth **68**, 111 (1984).
[2] P. D. Dapkus, Annu. Rev. Mater. Sci. **12**, 243 (1982).
[3] G. B. Stringfellow, Annu. Rev. Mater. Sci. **8**, 73 (1978).
[4] D. W. Kisker and D. A. Stevenson, J. Electron. Mater. **12**, 459 (1983).
[5] D. H. Reep and S. K. Ghandhi, J. Electrochem. Soc. **130**, 675 (1983).
[6] P. Ho and W. G. Breiland, Appl. Phys. Lett. **44**, 51 (1984).
[7] D. W. Squire, C. S. Dulcey, and M. C. Lin, Chem. Phys. Lett. **116**, 525 (1985).

[8]T. G. DiGiuseppe, J. W. Hudgens, and M. C. Lin, Chem. Phys. Lett. **82**, 267 (1981).
[9]T. G. DiGiuseppe, J. W. Hudgens, and M. C. Lin, J. Phys. Chem. **86**, 36 (1982).
[10]J. W. Hudgens, T. G. DiGiuseppe, and M. C. Lin, J. Chem. Phys. **79**, 571 (1983).
[11]S. A. Mitchell and P. A. Hackett, J. Phys. Chem. **79**, 4815 (1983).
[12]C. H. Hendrickson and D. P. Eynam, Inorg. Chem. **6**, 1461 (1967).
[13]M. Kh. Karapet 'yants and M. L. Karapet 'yants, *Thermodynamic Constants of Inorganic and Organic Compounds*, translated by J. Schmorak (Ann Arbor–Humphrey Science, Ann Arbor, 1970), p. 6.
[14]See, for example, G. Bruno and J. B. Honeycutt, *The Use of Aluminum Alkyls in Organic Synthesis*, and its subsequent supplements, (Ethyl Corp., Baton Rouge, LA, 1969, 1973, 1979).

Infrared laser-induced photodesorption and ultraviolet laser-induced thermal desorption of methylfluoride and carbon monoxide from polycrystalline copper

Ingo Hussla[a] and R. Viswanathan[b]
Chemistry Department, Northwestern University, Evanston, Illinois 60201

(Received 18 March 1985; accepted 21 May 1985)

Preliminary results of CO_2 laser-induced photodesorption and KrF excimer laser-induced thermal desorption of methylfluoride from mixtures with carbon monoxide coadsorbed on polycrystalline copper surfaces are reported. The data indicate that selective desorption of CH_3F in the presence of CO-coadsorbate is feasible by thermal desorption using a KrF pulse laser, due to differences in absorbed laser power density desorption threshold of the coadsorbate components. Photodesorption of CH_3F is accomplished by vibrational excitation of the ν_3 mode of adsorbed CH_3F, while simultaneous desorption of CO is not observed.

I. INTRODUCTION

Laser-induced thermal desorption (LITD) and laser-induced photodesorption (LIPD) have emerged as new and versatile techniques[1] in the investigation of the dynamics of desorption processes occurring at the gas–solid interface. Although both the LITD and LIPD techniques utilize a pulsed laser beam to deposit energy into the gas–solid interface and thereby cause desorption of adsorbates, the mechanisms of the absorbed laser energy transfer are different.

In IR-LIPD the laser radiation is resonantly absorbed by internal vibrational modes of the adsorbate and is rapidly degraded into thermal energy, making the final desorption process independent of the initial resonant excitation mechanism. This process has been termed *resonant heating*[2,3] or *indirect heating*.[1,4] Experiments have been performed using IR-LIPD to separate coadsorbates. Recently, equal amounts (within 25% accuracy) of the two isotopes NH_3 and ND_3 have been photodesorbed from coadsorbed 1:1 mixtures of NH_3 and ND_3 at two or more monolayer coverages. In other words, any enhanced molecular selective effect has been found to be smaller than 25%[5–7] in this case. On the other hand, successful separation of CH_3F/C_2H_6 mixtures from NaCl substrates by CO_2-LIPD has been reported.[8,9] In the latter case the coadsorbate components differ not only in their infrared absorption frequencies, but also in their heats of adsorption. IR-LIPD has been carried out with ionic crystals,[4–6,8,9,10–20] semiconductors,[4] and metals[5,6,19,21–26] as substrates. SF_6,[4,10] CH_3F,[8,9,11–18,23] pyridine,[4,19–22] and NH_3[5–7,24–26] have been used as adsorbates.

In LITD, the laser radiation is absorbed by the substrate, which causes heating with rates in the order of $(10^8–10^{12})$ K s^{-1} (depending on the laser pulse duration). Surface phonons can couple into the surface adsorbate bound states resulting in breaking of the surface bond, when a certain laser power density threshold is reached. Applying too high a laser power density can cause an alteration of the surface structure which is clearly indicated by nonreproducible pulse-to-pulse desorption yields. Early experiments in LITD were carried out by Levine *et al.*[27] in 1968. The systems CO-Pd,[28] H_2-stainless steel,[29] H_2-W,[30] D_2-W,[30] CO-Fe(110),[31] CO-Cu(polycrystal),[32] and CO-Cu(100)[33,34] have been studied under ultrahigh vacuum (UHV)-controlled conditions. Recently, LITD has been successfully used to determine isotope concentrations of NH_3 and ND_3 in mixtures coadsorbed on copper and silver substrates.[5–7]

Time-of-flight (TOF) mass spectrometry has been used in LITD and LIPD in order to detect the molecular desorbing species. In addition to the data on the desorption yield, information on the desorption dynamics has been obtained by fitting the TOF signals to Maxwell–Boltzmann (MB) distributions, thus providing information about translational temperatures and equilibrium desorption characteristics.[35] Because of problems encountered with high speed amplification of the small mass spectrometer ion current and spurious effects due to wall scattering of laser light, very few *real-time* desorption signals have been reported in the literature.

The present work describes preliminary results of an experimental investigation of the desorption dynamics in a coadsorbate/metal adsorption system, CH_3F/CO-Cu(polycrystal), utilizing *both* the LITD and LIPD techniques. Real-time TOF signals are reported and analyzed in order to shed more light on the nature of the laser-adsorbate-surface interaction. Absorbed laser power densities for desorption were measured simultaneously with the occurrence of the desorption events. The results for the mixed CH_3F/CO-Cu system demonstrate the feasibility of selective laser-induced desorption of one of the adsorbates when two or more adsorbates are simultaneously present on the surface at low coverage.

II. EXPERIMENTAL

The experiments were carried out under UHV (system base pressure 3×10^{-10} mbar) in an apparatus that has been described in detail elsewhere.[34] CH_3F (Matheson, Research Grade) and CO were adsorbed on a clean polycrystalline copper surface at 105 K. Due to a high residual partial pressure of CO in the UHV system, it was found that CH_3F and CO were always present in the residual gas when CH_3F was admitted. The ratio of the mixture (about 1:1) was constant for days and was regularly checked during the experiment. The copper polycrystal (OFHC, prepared from a copper gas-

 0734-211X/85/051520-05$01.00

ket) was cleaned by oxygen treatment and Ar^+ sputtering, followed by annealing. A quadrupole mass analyzer (UTI 100C) operating in time-of-flight mode (TOF distance 22 cm) was used to detect the flux of desorbing molecules, and the amplified signal (rise time 3 μs) was digitized and signal averaged using a Nicolet 1170 signal averager with a 100 MHz digitizer (Biomation 8100) at its front end. The data acquisition system was triggered by the actual laser beam via a photodetector signal. A discriminator device was employed in the TOF path to ensure that only molecules that did not undergo wall collisions are detected by the mass spectrometer, in order to obtain real-time spectra. The salient features of the apparatus and experiments are described below.

A. UV-LITD apparatus

Laser-induced thermal desorption was accomplished by the use of pulses (15 ns FWHM, 250 mJ/pulse maximum energy) from an excimer laser (Lamda Physik EMG 101) operating at the KrF wavelength of 248 nm in the UV. As shown in the right-hand portion of Fig. 1, the focused UV-laser beam enters and leaves the UHV system at a 45° angle with respect to the Cu surface normal, i.e., the detection angle of the desorbing species was 0° (surface normal). Absorbed laser power density is measured on a pulse-to-pulse basis (Scientech thermopile output to op-amp amplifier[36]) *simultaneously* with the desorption event. More details are given in the caption of Fig. 1. The UV-LITD technique utilized has been described in detail in a previous publication.[34] The main features in which our technique differs from others are (i) we use a constant backing exposure of the adsorptive, (ii) the laser-induced thermal desorption mass signal is sampled repetitively, (iii) the laser surface spot is much smaller than the sample crystal, and (iv) the excimer laser beam used has been shown to possess two-dimensional uniformity in its intensity distribution.

B. IR-LIPD apparatus

The experimental setup described in Ref. 34 had to be modified in order to carry out CO_2-laser induced photodesorption. The arrangement is shown schematically in the left-hand portion of Fig. 1. Both IR-LIPD and UV-LITD can be carried out simultaneously. The copper sample position shown is that for IR-LIPD. The CO_2-TEA-laser pulse (50 ns FWHM, 1 J/pulse maximum energy) is steered into the chamber through the barium fluoride window W3 (transparent between 150 nm and 12 μm), using gold front-surface mirrors M3 and M4. The pulse energy can be suitably attenuated using a gas-cell variable attenuator A.[37] The operating wavelength of the CO_2 laser is monitored by spectrum analyzer B (Optical Engineering). The laser beam is incident over an approximately 4 mm^2 area of the copper surface, at an angle of 67.5° to the surface normal, and exits through window W2 after being reflected off the copper surface. It must be noted that the angle of incidence of the laser beam on the surface is near the optimum value predicted for effective laser coupling to a perpendicular adsorption site.[38] The incident laser beam can be either *s* or *p* polarized by inserting a home-built polarizer C, constructed using gold mirrors (Edmund Scientific Company, New Jersey), into the optical path. This polarizer can handle the high power laser beam without the need for frequent replacement. The incident and reflected laser pulse energies were monitored on a pulse-to-pulse basis using beam splitters in conjunction with pyroelectric detectors LP (Laser Precision Model RJ-7200). Thus, accurate numbers for the laser energy *absorbed* by the copper surface could be determined. The detection angle for the molecular desorbing species is 22.5°. The actual LIPD experimental procedure is similar to that described above and in Ref. 34 for LITD. The infrared laser-induced desorption experiment was done over a range of wavelengths accessible with the CO_2 laser in order to detect the effect of vibrational excitation of the ν_3 mode of CH_3F by the laser.

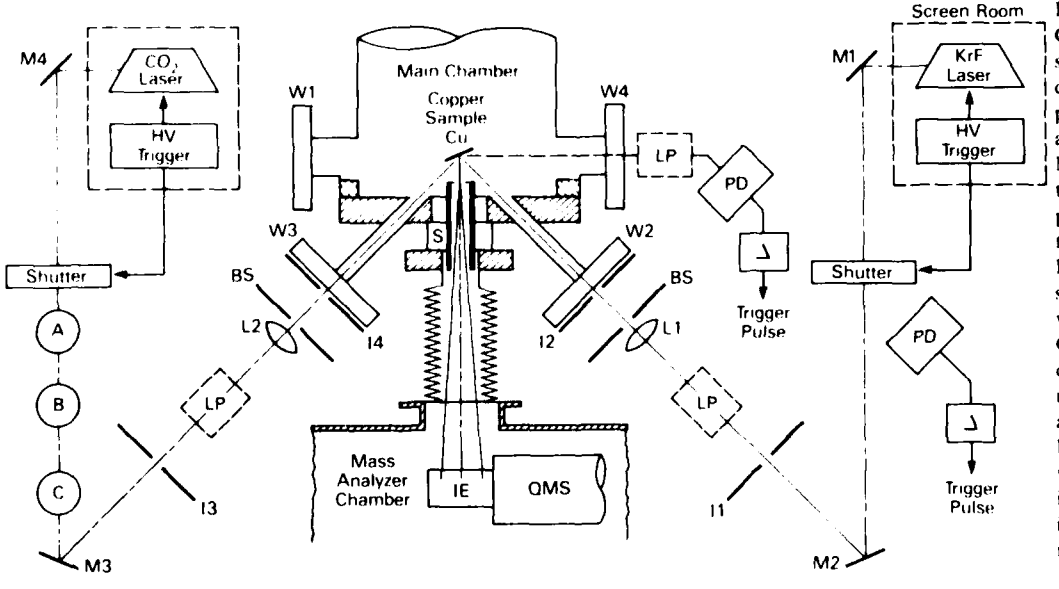

FIG. 1. Apparatus for tandem CO_2 laser-induced photodesorption and KrF laser-induced thermal desorption experiments is depicted. Explanation of symbols: M1, M2-aluminum mirrors; PD-trigger detector (for UV-LITD photodiode, for IR-LIPD photon drag detector); I1, M2, M3, M4-irises; BS-backscattering stop; W1, W2, W3, W4-BaF_2 windows; L1-quartz lens; L2-CaF_2 lens; Cu-copper polycrystal mounted on a sample manipulator; A-IR-attenuation gas cell; B-spectrum analyzer; C-polarizing mirror device; S-double slit discriminator; IE-electron impact ionizer; QMS-quadrupole mass analyzer.

III. RESULTS AND DISCUSSION

A. UV-LITD of CH_3F and CO from Cu(polycrystalline)

Time-of-flight signals of CH_3F and CO desorbed thermally by KrF excimer laser pulses with peak absorbed power densities of 7 and 12 MW/cm^2 are shown in the oscilloscope traces of Fig. 2. The experiments were carried out at a constant total backing pressure of 5×10^{-7} mbar. The ratio of the mass spectrometer ion currents measured at amu 28 (CO) and amu 34 (CH_3F) in the gas phase was 1.14. Methylfluoride desorption, monitored at amu 34, is shown in Fig. 2(a) and 2(b), while Fig. 2(c) and 2(d) represent desorption signals for CO, monitored at amu 28. Each of the signals shown is the average of 32 desorption events, obtained using a constant time interval of 40 s between consecutive laser pulses by means of a low repetition rate shutter device.[39] Methylfluoride desorption was clearly discernible at absorbed peak laser power densities in the range of 7–9 MW/cm^2 [see Fig. 2(b)]. However, no desorption of CO was observed under identical conditions [see Fig. 2(d)]. Graphs of the UV excimer laser-induced desorption yields of CH_3F and CO, plotted as a function of the peak absorbed laser power density, are shown in Fig. 3. The data establish that the laser power density thresholds for thermal desorption of CH_3F and CO are different. Furthermore, the data show that *selective* laser-induced thermal desorption of CH_3F in the presence of CO coadsorbate occurs at peak absorbed laser power densities in the range 5–7 MW/cm^2. The laser power density thresholds for desorption are estimated to be 5 and 7 MW/cm^2 for CH_3F and CO, respectively, from extrapolation of the graphs in Fig. 3. Heats of adsorption of CH_3F and CO in the mixed CH_3F/CO-Cu system have not been measured. However, the lower absorbed laser power density threshold for CH_3F indicates that the heat of adsorption of CH_3F is lower than that of CO, assuming that there is no

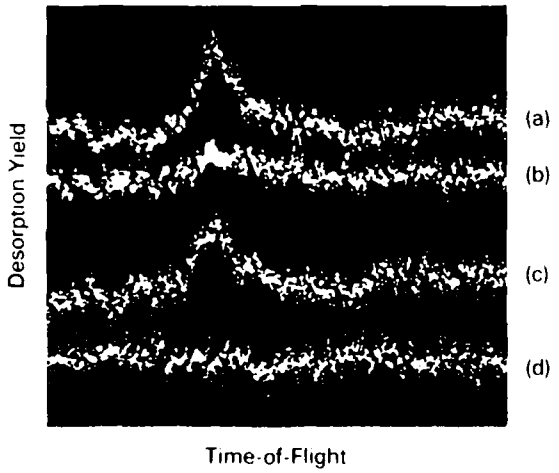

FIG. 2. Time-of-flight signals for UV-LITD of CH_3F and CO from polycrystalline copper surfaces at 105 K shown for two different absorbed laser power densities. 32 desorption events were signal averaged at a backing pressure of 5×10^{-7} mbar. Exposure time of 1.14:1 mixture of CO and CH_3F was 40 s. (a) CH_3F at 12 MW/cm^2, (b) CH_3F at 7 MW/cm^2, (c) CO at 12 MW/cm^2, (d) CO at 7 MW/cm^2.

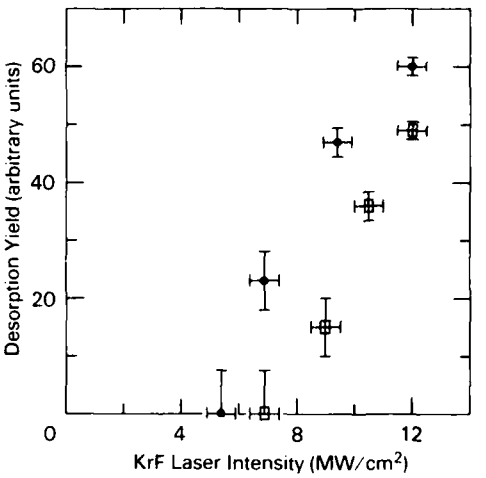

FIG. 3. Absorbed KrF-laser power density dependence of the UV-LITD yield of CH_3F and CO desorbing from CO/CH_3F-Cu(polycrystal) at 105 K.

significant difference in the preexponential factors of the desorption rates for the two molecules. A comparison of the data shown in Fig. 3 with the LITD data for the pure CO-Cu system[33] indicates that the threshold value for LITD of CO is not changed by the coadsorbate and that the coverage of CO in the experiments reported here is low ($\theta<0.5$), due to the substrate temperature of 105 K. The heat of adsorption of pure CO on Cu(100) is known to be about 70 kJ/mol for $\theta<0.1$ and 56 kJ/mol for $\theta=0.5$.[40] An adsorption energy of 46 kJ/mol was recently reported for CH_3F adsorbed on NaCl.[18] Both species (CH_3F and CO) are desorbed by LITD at laser power densities above threshold in the range between 9 and 12 MW/cm^2.

Figure 4 shows least square fits of the TOF signals of both species to a Maxwell–Boltzmann distribution. Translational temperatures T_d for desorbing molecules obtained from these fits range from 240 to 260 K. The CO translational temperatures appear to be higher than the CH_3F translational temperatures. In conventional temperature programmed desorption (TPD), different desorption temperatures T_p (i.e., the surface temperatures T_s of maximum desorption rates) are related to differences in the heats of adsorption. For our heating rate $\beta>10^{10}$ K s^{-1}, the kinetic parameters predict a peak desorption rate $T_p=510$ K for CO; this calculated T_p is twice the observed value of T_d. Similar results were obtained in the case of the pure adsorption system CO-Cu(100),[33,34] the observed translational temperatures always being lower than values predicted by a Frenkel–Arrhenius-type analysis at all coverages and laser power densities applied. The velocity distributions for LITD normal to the surface are Maxwell–Boltzmann. The implication of these results is that the translational degrees of freedom are not in complete equilibrium with the copper surface heat bath during LITD.[33] Recent calculations[41] on LITD of NO from LiF(100) using the stochastic trajectory technique, as well as LITD measurements[42] in the system Xe-Cu(film), where no energy transfer in internal degrees of freedom can take place, support this conclusion. In the present work, we would like to emphasize that the observed translational temperatures of CO are not influenced by the coadsorbate and

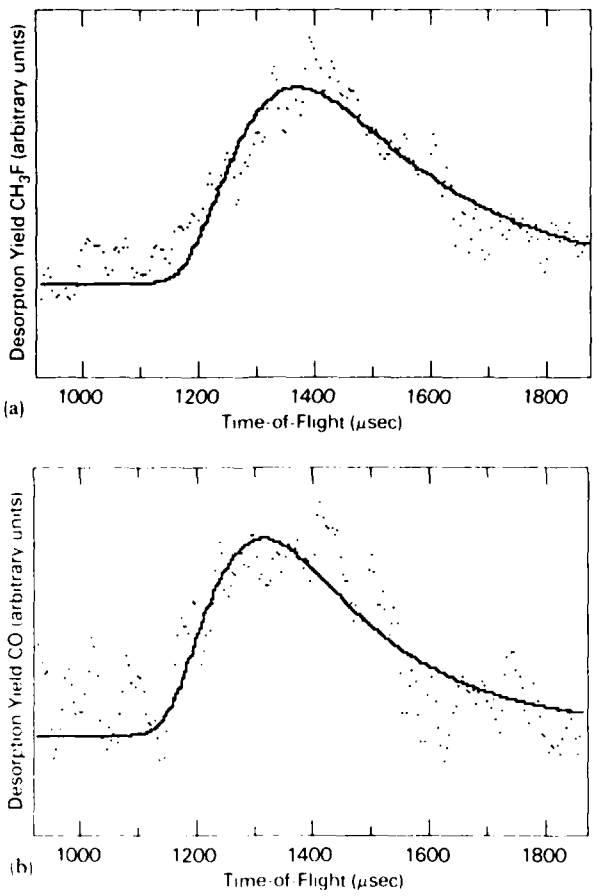

FIG. 4. Maxwell-Boltzmann fits of TOF signals of CH_3F and CO desorbed by UV-LITD from CH_3F/CO-Cu(polycrystal) at 105 K. Absorbed laser power density 12 MW/cm^2. (a) CH_3F, translational temperature T_d = 244 K. (b) CO, translational temperature T_d = 251 K.

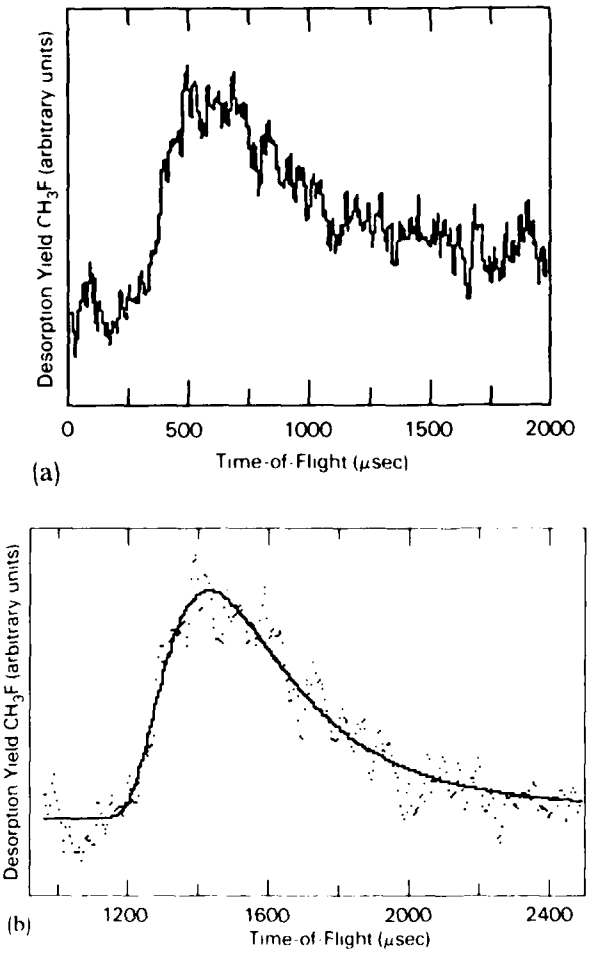

FIG. 5. (a) TOF signal for IR-LIPD of CH_3F from CH_3F/CO-Cu(polycrystal) at 105 K, at an absorbed laser power density of 0.55 MW/cm^2. (b) Maxwell-Boltzmann fit for (a), T_d = 190 K.

are close to the values observed in the pure system CO-Cu(100). Furthermore, there is a difference between the translational temperatures of CO and CH_3F, presumably due to a difference in the heats of adsorption.

B. IR-LIPD of CH_3F in the system CH_3F/CO-Cu

The CO_2 laser-induced photo desorption experiments were carried out under conditions analogous to the excimer-laser LITD case. Figure 5 shows a typical TOF spectrum of CH_3F desorbed by CO_2 laser pulses at 950 cm^{-1} and a peak absorbed laser power density of approximately 0.55 MW/cm^2. No enhancement of the desorption yield was observed when the incident peak laser power density was increased. No desorption of CO was observed at a peak absorbed laser power density of (4 ± 1) MW/cm^2, which actually requires an incident laser power density of 100 MW/cm^2. Copper has a high reflectivity in the 10 μm region (96 ± 2%, measured experimentally in the present work) as opposed to its low reflectivity at 248 nm region (85 ± 2)% (measured). Thus, the CO_2 laser is not effective in direct heating of the copper substrate and in causing thermal desorption, even at incident peak laser power densities in the neighborhood of 100 MW/cm^2. Resonant heating of CH_3F does not result in desorption of coadsorbed CO at the given low coverage. The results indicate that the CH_3F is desorbed due to a coupling of the laser energy into the ν_3 vibrational mode of the molecule, rather than through direct heating of the copper substrate. This conclusion is also substantiated by the observation that CO desorption does not occur, even when the laser power density is increased by a factor of 4 over the value (0.55 MW/cm^2) used in the CH_3F photodesorption experiments (see our LITD findings in Fig. 3). It must be noted that no dramatic frequency dependence of the desorption yield was observed when the CO_2 laser was scanned through the range of 1060–930 cm^{-1}. This is not surprising if one considers the fact that CH_3F forms several different adsorption phases. Such phases have been detected by infrared spectroscopy in the system CH_3F-NaCl[43]. Additionally, the use of a polycrystalline copper substrate may produce multiple adsorption sites, resulting in a broad infrared absorption spectrum for adsorbed CH_3F. The TOF spectra have rather poor signal-to-noise ratios, presumably due to very small coverages of CH_3F on the surface. However, the results do show that selective desorption of CH_3F in the presence of CO coadsorbate is feasible via a photodesorption technique at submonolayer coverages.

The translational temperature of CH_3F photodesorbed from the copper surface using CO_2 laser peak absorbed pow-

er densities of approximately 0.55 MW/cm^2 is 190 K. This temperature is lower than in the LITD case where desorption was detected at a 0° detection angle. However, it is higher than the substrate temperature of 105 K. Only limited data on real-time measurements of translational temperatures in photodesorption experiments are available in the literature for comparison with the observed translational temperatures in the present work. A T_d value of 17 K has been reported for CH_3F desorbed from NaCl(film), however, the authors have pointed out that slow electronics may have altered the measurements.[15,18] On the other hand, a translational temperature which is close to the substrate temperature has been reported for NH_3 photodesorbed from Cu(100).[5-7] We believe that from the standpoint of ion current amplification we have measured real-time spectra[34] with a true translational momentum distribution and that more attention should be paid towards obtaining such real-time spectra with high speed electronics in future experiments.

IV. CONCLUSIONS

The feasibility of selective desorption of CH_3F coadsorbed with CO at low coverages on a polycrystalline copper surface has been demonstrated, using both LITD and LIPD. In the case of LITD, low KrF laser peak power densities were employed and separation was achieved utilizing the difference in the laser power density thresholds of LITD for CO and CH_3F. This clearly shows an analogy to conventional thermal desorption spectroscopy (TDS), where subtle differences in adsorption energies of adsorbates result in discernible peaks in the TDS spectra. In the case of LIPD, selective desorption of CH_3F from coadsorbate was obtained by coupling laser energy into the ν_3 vibrational mode of adsorbed CH_3F. Here the absorbed laser power density needed for inducing desorption is much lower than in the case of LITD.

ACKNOWLEDGMENTS

We would like to thank Professor Eric Weitz, Professor Peter Stair, and the Office of Naval Research for support of this work under ONR Contract No. N00014-79-C-0794. One of us (I.H.) would like to thank the Deutsche Forschungsgemeinschaft for granting a fellowship. Special thanks to D. R. Burgess, Jr., for providing the Maxwell–Boltzmann computer fit programs. Helpful discussions with Dr. T. J. Chuang, Professor Dr. J. Heidberg, Professor Dr. H.-J. Kreuzer and Professor Dr. G. Wedler are gratefully acknowledged.

[a] Present address: IBM Research Laboratory, San Jose, California 95193.
[b] Present address: Chemistry Department, Beloit College, Beloit, Wisconsin 53511.

[1] T. J. Chuang, Surf. Sci. Rep. **3**, 1 (1983).
[2] Z. W. Gortel, H.-J. Kreuzer, P. Piercy, and R. Teshima, Phys. Rev. B **27**, 5066 (1983).
[3] Z. W. Gortel, H.-J. Kreuzer, P. Piercy, and R. Teshima, Phys. Rev. B **28**, 2119 (1983).
[4] T. J. Chuang, J. Electron Spectrosc. Relat. Phenom. **29**, 125 (1983).
[5] T. J. Chuang and I. Hussla, in *Dynamics on Surfaces*, edited by B. Pullman, J. Jortner, A. Nitzan, and B. Gerber (Reidel, Dordrecht, 1984), p. 313.
[6] T. J. Chuang, H. Seki, and I. Hussla, Surf. Sci. **158**, 525 (1985).
[7] I. Hussla, H. Seki, T. J. Chuang, Z. Gortel, H.-J. Kreuzer, and P. Piercy, Phys. Rev. B (in press).
[8] J. Heidberg and I. Hussla, J. Electron Spectrosc. Relat. Phenom. **29**, 105 (1983).
[9] J. Heidberg and I. Hussla, Appl. Phys. B **29**, 184 (1983).
[10] J. Heidberg, H. Stein, A. Nestmann, E. Hoefs, and I. Hussla, *Materials Research Society Proceedings*, edited by S. D. Ferris, H. J. Leamy, and J. M. Poate (American Institute of Physics, New York, 1979), p. 49.
[11] J. Heidberg, H. Stein, E. Riehl, and A. Nestmann, Z. Phys. Chem. Neue Folge **121**, 145 (1980).
[12] J. Heidberg, H. Stein, and E. Riehl, in *Vibrations at Surfaces*, edited by R. Caudano, J. M. Gilles, and A. A. Lucas (Plenum, New York, 1982), p. 17.
[13] J. Heidberg, H. Stein, and E. Riehl, Phys. Rev. Lett. **49**, 666 (1982).
[14] J. Heidberg, H. Stein, and E. Riehl, Surf. Sci. **126**, 183 (1983).
[15] J. Heidberg, H. Stein, E. Reihl, I. Hussla, in *Surface Studies with Lasers*, edited by F. R. Aussenegg, A. Leitner, and M. E. Lippitsch (Springer, Berlin, 1983), p. 226.
[16] J. Heidberg, in *Materials Research Society Proceedings*, edited by A. Wayne Johnson and D. J. Ehrlich (North–Holland, Amsterdam, 1984), p. 333.
[17] J. Heidberg, H. Stein, Z. Szilàgi, D. Hoge, and H. Weiss, in *Dynamics on Surfaces*, edited by B. Pullman, J. Jortner, A. Nitzan, and B. Gerber (Reidel, Dordrecht, 1984), p. 329.
[18] J. Heidberg, H. Stein, E. Riehl, Z. Szilàgyi and H. Weiss, Surf. Sci. (in press).
[19] T. J. Chuang and F. A. Houle, J. Vac. Sci. Technol. **20**, 603 (1982).
[20] T. J. Chuang, J. Chem. Phys. **76**, 3828 (1982).
[21] T. J. Chuang and H. Seki, Phys. Rev. Lett. **49**, 382 (1982).
[22] H. Seki and T. J. Chuang, Solid State Comm. **44**, 473 (1983).
[23] I. Hussla, R. Viswanathan, D. R. Burgess, Jr., P. C. Stair, and E. Weitz, *Abstracts of the 29th IUPAC Congress, Cologne, Federal Republic of Germany, 1983* (Gessellschaft Deutscher Chemiker, Cologne, 1983), p. 413.
[24] I. Hussla and T. J. Chuang, Ber. Bunsenges. Phys. Chem. (in press).
[25] I. Hussla and T. J. Chuang, *Materials Research Society Proceedings*, edited by A. Wayne Johnson and D. J. Ehrlich, (North–Holland, Amsterdam, 1984), p. 341.
[26] T. J. Chuang and I. Hussla, Phys. Rev. Lett. **52**, 2045 (1984).
[27] L. P. Levine, J. F. Ready, and E. Bernal, J. Appl. Phys. **38**, 331 (1967); also IEEE J. Quantum Electron. **QE-4**, 18 (1968).
[28] G. Ertl and M. Neumann, Z. Naturforsch. Teil A **27**, 1607 (1972).
[29] H. Hartwig, P. Mioduszewski, and A. Pospieszczyk, J. Nucl. Mater. **76**, 625 (1978).
[30] J. P. Cowin, D. J. Auerbach, C. Becker, and L. Wharton, Surf. Sci. **78**, 545 (1978).
[31] G. Wedler and H. Ruhmann, Surf. Sci. **121**, 464 (1982).
[32] R. Viswanathan, D. R. Burgess, Jr., P. C. Stair, and E. Weitz, J. Electron Spectrosc. Relat. Phenom. **29**, 111 (1983).
[33] D. R. Burgess, Jr., R. Viswanathan, I. Hussla, P. C. Stair, and E. Weitz, J. Chem. Phys. **79**, 5200 (1983).
[34] D. R. Burgess, Jr., I. Hussla, H. Viswanathan, P. C. Stair, and E. Weitz, Rev. Sci. Instrum. **55**, 1771 (1984).
[35] Z. W. Gortel and H.-J. Kreuzer, Phys. Rev. B **29**, 6926 (1984).
[36] R. Viswanathan and I. Hussla (to be published).
[37] T. G. Roberts, Rev. Sci. Instrum. **47**, 59 (1976).
[38] R. G. Greenler, J. Vac. Sci. Technol. **12**, 1410 (1975).
[39] R. Viswanathan and I. Hussla, Rev. Sci. Instrum. **56**, 1468 (1985).
[40] J. C. Tracy, J. Chem. Phys. **56**, 2748 (1979).
[41] R. R. Lucchese and J. C. Tully, J. Chem. Phys. **81**, 6313 (1984).
[42] I. Hussla, H. Coufal, F. Träger, and T. J. Chuang, Can. J. Phys. (in press).
[43] J. Heidberg, I. Hussla, and Z. Szilàgyi, J. Electron Spectrosc. Relat. Phenom. **30**, 53 (1983).

Quantum model of dephasing-enhanced laser desorption: Master equation approach

Jui-teng Lin
Laser Physics Branch, Optical Sciences Division, Naval Research Laboratory, Washington, D.C. 20375
Xi-Yi Huang and Thomas F. George
Department of Chemistry, University of Rochester, Rochester, New York 14627

(Received 18 March 1985; accepted 21 May 1985)

A new model for laser-induced desorption is proposed based on a master equation for the photon population in a closely coupled subsystem involving the relevant degrees of freedom. The validity of approximations such as the Born and Markovian approximations is discussed in terms of the laser pulse duration and multiple time scales of the adspecies-surface system. The desorption rate is numerically calculated from the photon population and the threshold number of photons absorbed by the adspecies. The effects of anharmonicity, dephasing and laser detuning on the desorption rate are examined. The mechanism of dephasing and the possible direct and indirect desorption channels are discussed.

I. INTRODUCTION

Laser-stimulated surface processes (LSSP) have been investigated during the past several years, due both to their academic interest and industrial potential. Recent progress in experimental[1] and theoretical[2,3] studies and in applications[4] of LSSP has been reported. Laser excitation and/or desorption of adspecies have been investigated theoretically by a variety of techniques, including harmonic,[5] anharmonic[6] and Morse[7,8] potential models, and master equation approaches,[7-16] where attention has been focused on the excitation of the active mode and the population of its vibrational states. The desorption rate is usually overestimated by the harmonic model,[5] whereas it is underestimated by the one-dimensional Morse potential model.[7,8]

In the present paper, we propose a new model in which all the degrees of freedom of a closely coupled subsystem (including the active mode of the adspecies) are treated on an equal footing. The desorption rate is calculated from the photon population and the threshold number of photons absorbed by the adspecies as a whole, rather than from the average excitation of the active mode. In Sec. II, the generalized master equation is developed within the Born approximation, and a reduced master (rate) equation including the anharmonicity of the adspecies surface potential is investigated within the Markovian approximation. Numerical results are shown in Sec. III, where dephasing-enhanced desorption is suggested. In Sec. IV, the mechanism of dephasing and a variety of desorption channels are discussed.

II. MASTER EQUATION

Let us first define our model system, which is particularly appropriate for admolecules with very fast intramolecular relaxation. In the frequency domain, the total adspecies-surface system is divided into two subsystems, S_1 and S_2, where S_1 consists of the active mode (A) and the strongly coupled modes (B) within the adspecies, and S_2 consists of the remaining lower frequency modes serving as a heat bath (see Fig. 1). From the concept of the energy-gap law, we expect intramode relaxation within S_1 to be much faster than intersystem relaxation, i.e., $\gamma_{AB}, \gamma_{BB} \gg \gamma_{BC}, \gamma_{AC}$, where γ_{ij}^{-1} is the relaxation time between the i and j modes. When the system is irradiated by a laser field, S_1 will be excited through the active mode and its coupling to the B modes. The excitation rate of S_1, after a short time of γ_{AB}^{-1}, is proportional to the absorption cross section of the active mode. We can therefore express the interaction between the laser field and S_1 as

$$H_{SF}(t) = V(t)(a^\dagger + a), \tag{1}$$

where $V(t) \propto \gamma_{AB}\mu' E(t)\cos(\omega t)$ is proportional to the derivative of the active-mode dipole moment (μ'), the coupling factor between A and B (γ_{AB}), and the laser field amplitude [$E(t)$] with a frequency ω which is near resonant to that of the active mode. $a^\dagger$ and a are the ladder operators for S_1 defined in photon space, i.e., $a^\dagger|n\rangle = \sqrt{n+1}\,|n+1\rangle$, where $|n\rangle$ is a basis function for S_1 as a whole, rather than for just the active

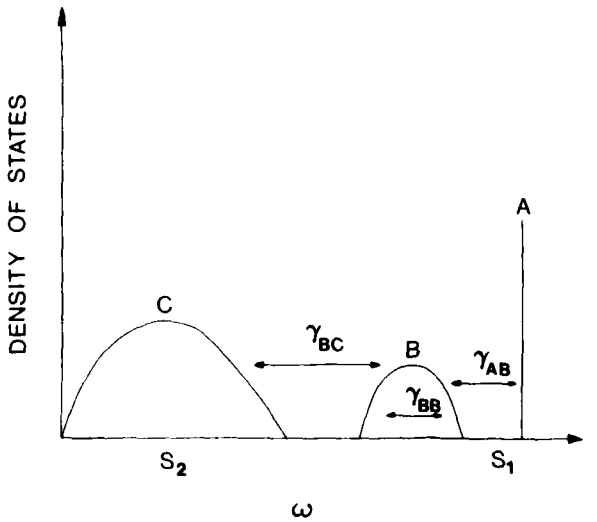

FIG. 1. Schematic diagram for the frequency spectrum of the total system $S_1 + S_2$, where S_1 = A + B, with the corresponding relaxation factors indicated.

 0734-211X/85/051525-04$01.00

mode which reaches steady state in the time γ_{AB}^{-1}.

The vibrational Hamiltonian of the system is

$$H = H_{S_1} + H_{S_2} + H_S + H_{SF}(t), \tag{2}$$

where H_S couples S_1 and S_2 (it is generally time independent). The density matrix for the total system obeys the Liouville equation[16]

$$\frac{d\rho}{dt} = -\frac{i}{\hbar}[H,\rho] \equiv -\frac{i}{\hbar}(L_{S_1} + L_{S_2} + L_S + L_{SF})\rho. \tag{3}$$

Within the Born approximation $(L_{S_1} + L_{S_2} + L_S \simeq L_{S_1} + L_{S_2})$ and for Markovian processes where the characteristic time of the heat bath (S_2) is much shorter than other time scales of the system, the S_2 variables may be eliminated. We can then work with a reduced density matrix $\bar{\rho} \equiv \mathrm{Tr}_B(\rho)$, which obeys the equation

$$\frac{d\bar{\rho}}{dt} = -\frac{i}{\hbar}(L_{S_1} + L_0 - iL_1 + L_{SF})\bar{\rho}, \tag{4}$$

where the effects of the interaction between S_1 and S_2, L_S, are now reduced to a constant frequency shift (L_0) and a damping factor (L_1). We now introduce the Markovian approximation for the relaxation associated with L_S (assumed to be time independent), but retain memory effects due to the off-diagonal matrix elements associated with the laser excitation. For a Hamiltonian such as given by Eq. (1), we obtain a generalized master equation for the diagonal matrix element $[P_n \equiv (\mathrm{Tr}_B\rho)_{nn}]$ as[9] (detailed discussions of the generalized master equation are avialable in the literature[16-18])

$$\frac{dP_n}{dt} = \gamma_1[(n+1)P_n - nP_n] + \int_0^t dt'\{W_{n,n+1}(t-t')[P_{n+1}(t') - P_n(t')] + W_{n,n-1}(t-t')[P_{n-1}(t') - P_n(t')]\}, \tag{5}$$

with the time-dependent photon absorption/emission rates given by

$$W_{n,n-1}(\tau) = 2(n+1)\Omega(t)\Omega(t')e^{-\Gamma\tau}\cos(\Delta_{n-1}\tau), \tag{6}$$

$$W_{n,n+1}(\tau) = 2n\Omega(t)\Omega(t')e^{-\Gamma\tau}\cos(\Delta_n\tau). \tag{7}$$

Here, $\Omega(t) = V(t)/\cos(\omega t)$; $\tau = t - t'$; $\Delta_m = \omega_{mn} - \omega = \Delta - 2\epsilon m$, where ω_{mn} is the transition frequency between levels m and n, $\Delta = \omega_{10} - \omega$ is the laser detuning with respect to the fundamental frequency ω_{10}, and ϵ is the anharmonicity; $\Gamma = \gamma_1/2 + \gamma_2$ is the total damping associated with the off-diagonal matrix elements, where γ_1 and γ_2 denote the energy and (pure) dephasing factors, respectively. We have used the rotating-wave approximation and the dipole transition for the n dependence of $W_{m,n}$ (such that $m = n \pm 1$) for absorption $(n < n)$ and emission $(m > n)$. Note that P_n is the probability of the adspecies as a whole (S_1 subsystem) absorbing n photons, in which the active-mode state is given by its steady-state excitation, i.e., $n_A(\mathrm{s.s}) = \gamma_{AB}\sigma I/\hbar\omega$, where σ is the steady-state absorption cross section.

For a very short laser pulse with duration $t_p \lesssim \Gamma^{-1}$, the transient solution of Eq. (5) contains the memory effects of the population function, and the Markovian approximation may not be applied to this time-dependent excitation. We shall, instead, focus on the case of a long pulse excitation, e.g., a CO_2 laser pulse with $t_p \approx 10$ ns which is much longer than the dephasing time Γ^{-1}, such that the population function $P_n(t)$ and $\Omega(t)$ are slowly varying and may be factored out of the integrals in Eq. (5). Employing this adiabatic, Markovian approximation, the transition rates $W_{m,n}$ have no memory effects, although they are still time dependent due to the laser temporal profile $E(t)$, and a simpler master equation is then obtained[9,16]:

$$\frac{dP_n}{dt} = \gamma_1[(n+1)P_{n+1} - nP_n] + 2\Gamma\Omega^2(t)\left\{\frac{n(P_{n-1} - P_n)}{[\Delta - 2\epsilon(n-1)]^2 + \Gamma^2} + \frac{(n+1)(P_{n+1} - P_n)}{(\Delta - 2\epsilon n)^2 + \Gamma^2}\right\}. \tag{8}$$

Several features of this equation are (i) the absorption cross section for the adspecies (S_1 subsystem) is saturated at a higher photon population due to the anharmonicity, (ii) the first two terms describe the actual energy flow from S_1 to the surface (S_2), (iii) the pure dephasing factor (γ_2) changes only the intramolecular phase without changing the energy populations, (iv) the multiphonon relaxation factor (γ_1) is generally strongly temperature dependent and is a strongly decreasing function of the energy gap between S_1 and S_2, and (v) the remaining terms containing the factor Γ indicate that the effect of the applied field is always intimately related to the phase dissipation or broadening mechanisms.

Equation (8) may be referred to as the usual rate equation in which no memory effects are preserved either in the relaxation or the excitation process. For weaker dephasing systems subject to a short pulse excitation, the "most general" form of the generalized master equation is given by Eq. (5) in which the relaxation terms are replaced by[18]

$$\frac{2}{\hbar^2}\mathrm{Re}\sum_m\int_0^t dt'\langle H'_S(t)H'_S(t')\rangle \times [P_m(t') - P_n(t')]e^{[i(\omega_{mn} + \Gamma_{mn})(t-t')]}, \tag{9}$$

where $\Gamma_{mn} = (\gamma_m + \gamma_n)/2 + \gamma_2$ is the total surface-induced damping. Furthermore, for a short-pulsed laser with high intensity, the Born approximation may not be valid. Improvements can be made by performing a trace over the photon (laser)-dressed states of the heat bath (S_2). For the case of strong coupling between S_1 and S_2, H'_S may not be used as a perturbation, and again the Born approximation is questionable. To go beyond this, we may carry out a unitary transformation on S_1 with subsequent laser interaction with the phonon (surface)-dressed states.[2] These improvements allow for both multiphonon (relaxation) and multiphoton (excitation) processes. The absorption cross section for the S_1 subsystem, for example, will be related to the laser intensity by a power law $\sigma \propto I^n$ for n-photon processes. We also note that a nonlinear power law, $\sigma \propto I^m$ with $m < 1$ is also possible by anharmonic saturation.[3]

III. DESORPTION RATE

For a first-order desorption process, the rate constant is related to the inverse of the mean first-passage time $(\bar{t})$ and is given by[19]

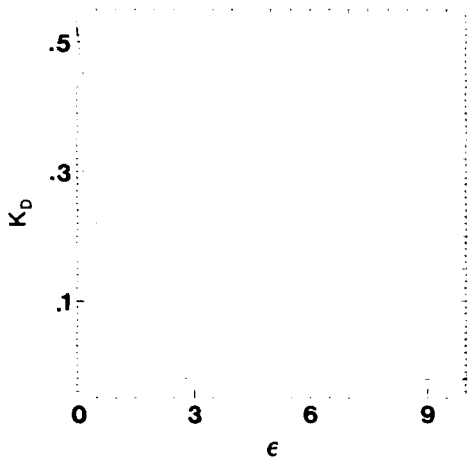

FIG. 2. Anharmonicity (ϵ) dependence of the desorption rate K_D in arbitrary units. The parameters used are $(\gamma_1, \gamma_2, \Omega_0, \Delta) = (0.1, 2.0, 0.1, 0.0)$, with a laser pulse duration of $t_p = 10$ ns, where $\Omega(t) = \Omega_0 \sin^2(\pi t/t_p)$. $\gamma_1, \gamma_2, \Omega_0$, and Δ are in the unit of 10^{11} s^{-1}, and $n^* = 3$ has been used in Eq. (10).

$$K_D = \frac{1}{\bar{t}} = \left[\sum_{n=0}^{n^*} \int_0^\infty dt\, P_n(t)\right]^{-1}, \tag{10}$$

where n^* is the desorption threshold number of photons absorbed by the adspecies. Numerical results are shown in Figs. 2 and 3. From Fig. 2 we see that the desorption rate is a strongly decreasing function of the anharmonicity. Dephasing-enhanced desorption is seen in Fig. 3, where an optimal value at $\gamma_2 \simeq 1.8$ is found for a maximal desorption rate. This is realized by the fact that the dephasing tends to compensate for anharmonicity "bottleneck" effects. An enhancement factor of about 3 is possible if we tune the dephasing to the optimal value of $\gamma_2 \simeq 1.8$, in comparison with $\gamma_2 = 4$. We note that the dephasing-enhanced effects caused by the nonlinear behavior are absent in a harmonic model, were K_D is always a decreasing function of γ_2.

In Fig. 4 we show the time evolution of the desorption probability, defined by

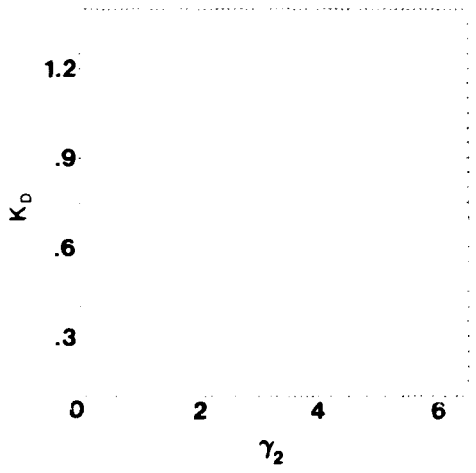

FIG. 3. Phase-relaxation (γ_2) dependence of K_D. The parameters used are $(\gamma_1, \Omega_0, \epsilon, \Delta, t_p) = (0.5, 0.1, 1.3, 10)$. The envelope function of the laser pulse is the same as in Fig. 2.

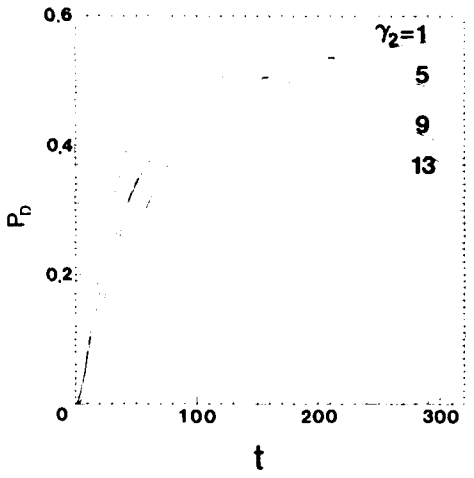

FIG. 4. Time dependence of the desorption probability $P_D(t)$, where $n^* = 3$ has been used in this calculation. A cw laser field has been assumed, and the other parameters are $(\gamma_1, \Omega_0, \epsilon, \Delta) = (0.01, 0.1, 1.5, 3.0)$.

$$P_D(t) = \sum_{n=n^*}^{\infty} P_n(t). \tag{11}$$

Again, we see the nonlinear behavior of the dephasing effects. For a fixed time (say $t = 100$ units) P_D increases when γ_2 increases from 1 to 5, but it decreases at higher values of γ_2.

IV. DISCUSSION

A. Mechanism of dephasing

As indicated in the previous section, the dephasing factor changes only the phase of the excited subsystem S_1 without changing its energy populations. In the language of gas-phase scattering theory, this can be referred to as an "elastic" scattering process. In the presence of a laser field, dephasing can be viewed as energy transfer from the excited subsystem to a "virtual" state of the field and back to the original excited state. Within the adspecies/surface system itself, the dephasing is due to one or more of the following[6,20,21]: (i) dephasing of the active dipole of the adspecies (or dephasing of the laser field itself), (ii) fluctuation of the conformation of the adspecies due to the thermal energy provided by either the initial surface temperature or laser-heating effects, (iii) librational and rotational relaxation within the vibrational manifold of the excited S_1 subsystem, (iv) intramolecular mode–mode coupling within S_1 and intermolecular coupling between S_1 and S_2, (v) lateral motion or migration-induced elastic collisions between adspecies and with the substrate surface, and (vi) surface phonon-dispersion-induced level broadening of the vibrational manifold.

We note that the dephasing factor γ_2 introduced in Sec. II is formally derived from the Liouville equation within the Markovian approximation, where the laser field amplitude is assumed to be generated by a coherent source. However, the field itself may often be only partially coherent and hence will cause additional dephasing of the excited subsystem. To demonstrate this mathematically, we start with the reduced density matrix equation of motion for

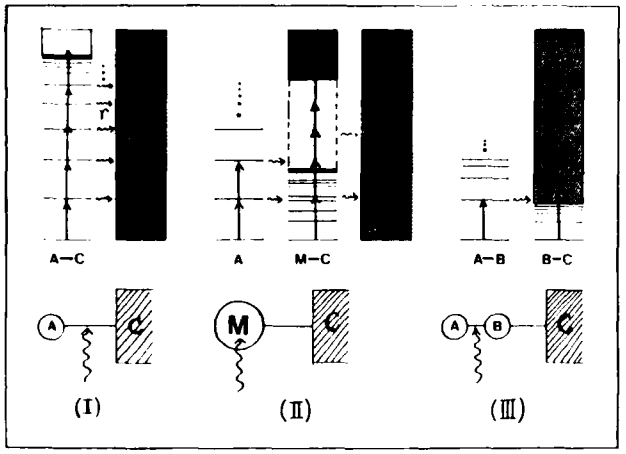

(a)

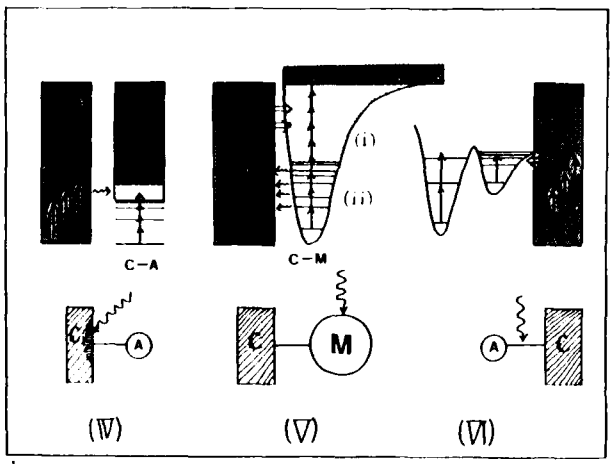

(b)

FIG. 5. Schematic diagrams of adspecies-surface systems and the associated energy levels, where A, B, and M represent the adspecies (adatom or admolecule), C represents the substrate (or bath modes), and the laser radiation is indicated by the wiggly lines. Several types of desorption channels are illustrated: (i) direct desorption via active-mode excitation, (ii) direct desorption via the quasicontinuum, (iii) indirect desorption via tunneling, (iv) indirect desorption via substrate heating, (v) phonon-assisted desorption, and (vi) indirect desorption via dynamics.

$$P_{mn} = [\mathrm{Tr}_B \rho]_{mn}, \quad m \neq n,$$

$$\frac{dP_{mn}}{dt} = -i[\omega_{mn} + \bar{\omega}(t)]P_{mn}, \tag{12}$$

where we have introduced a stochastic frequency shift of the system $[\bar{\omega}(t)]$, caused by the partially coherent behavior of the laser field. By assuming a "white noise," $[\langle \omega(t) \rangle = 0]$, and a Markovian correlation $[\langle \bar{\omega}(t)\bar{\omega}(t') \rangle = \bar{\gamma}_2 \delta(t - t')]$ we obtain an ensemble-averaged (over the stochastic variable) equation

$$\left\langle \frac{dP_{mn}}{dt} \right\rangle = -[i\omega_{mn} + (\Gamma_{mn} + \bar{\gamma}_2)]\langle P_{mn} \rangle, \tag{13}$$

where $\bar{\gamma}_2$ is the laser-induced dephasing.[21]

B. Mechanism of desorption

The desorption mechanism, which may involve several channels, depending on the nature of the adspecies (e.g., physisorbed or chemisorbed, adatom or admolecule, and the potential of the adbond), and the associated energy levels of the system are shown in Fig. 5. The desorption may result from direct laser excitation or indirect energy transfer processes. The details of the desorption channels from Type I to Type VI have been discussed previously.[3,4] As a concluding remark, we note that a complete description of laser-induced desorption should at least include the competing processes, e.g., migration-induced desorption and readsorption after the mean first-passage time. Furthermore, for systems with more than one active mode, desorption may occur via a two-stage process: the initial stage of absorbing n^* photons followed by thermal phonon-assisted and/or V–V energy transfer among the excited active modes. This type of process is under investigation in our laboratories.

ACKNOWLEDGMENTS

This research was supported in part by the Office of Naval Research and the Air Force Office of Scientific Research (AFSC), United States Air Force, under Grant No. AFOSR-82-0046. The United States Government is authorized to reproduce and distribute reprints for governmental purposes notwithstanding any copyright notation hereon. TFG acknowledges the Camille and Henry Dreyfus Foundation for a Teacher-Scholar Award (1975–86).

[1] T. J. Chuang, Surf. Sci. Rep. **3**, 1 (1983).
[2] T. F. George, J. Lin, A. C. Beri, and W. C. Murphy, Prog. Surf. Sci. **16**, 139 (1984).
[3] J. Lin, M. Hutchinson, and T. F. George, in *Advances in Multi-Photon Processes and Spectroscopy*, edited by S. H. Lin (World Scientific, Singapore, 1984), Vol. 1, pp. 105–237.
[4] J. Lin, W. C. Murphy, and T. F. George, Ind. Eng. Chem. Prod. Res. Dev. **23**, 334 (1984).
[5] M. S. Slutsky and T. F. George, Chem. Phys. Lett. **57**, 474 (1978); J. Chem. Phys. **70**, 1231 (1979).
[6] J. Lin and T. F. George, J. Chem. Phys. **72**, 2554 (1980); **78**, 5197 (1983).
[7] C. Jedrzejek, K. F. Freed, S. Efrima, and H. Metiu, Surf. Sci. **109**, 191 (1981).
[8] Z. W. Gortel, H. J. Kreuzer, P. Piercy, and R. Teshima, Phys. Rev. B **27**, 5066 (1983); H. J. Kreuzer and Z. W. Gortel, *ibid.* **29**, 6926 (1984).
[9] J. Lin and T. F. George, Surf. Sci. **115**, 569 (1982).
[10] J. Lin and T. F. George, Chem. Phys. Lett. **66**, 5 (1979).
[11] A. C. Beri and T. F. George, J. Chem. Phys. **78**, 4288 (1983).
[12] A. C. Beri and T. F. George, J. Chem. Phys. **83**, 2482 (1985).
[13] A. C. Beri and T. F. George, J. Vac. Sci. Technol. B **3**, 1529 (1985).
[14] B. Fain and S. H. Lin, Surf. Sci. **147**, 497 (1984).
[15] G. S. Wu, B. Fain, A. R. Ziv, and S. H. Lin, Surf. Sci. **147**, 537 (1984).
[16] X. Y. Huang, T. F. George, J. M. Yuan, and L. M. Narducci, J. Phys. Chem. **88**, 5772 (1984); X. Y. Huang, T. F. George, and J. M. Yuan, J. Opt. Soc. Am. B **2**, 985 (1985).
[17] W. H. Louisell, *Quantum Statistical Properties of Radiation* (Wiley, New York, 1973), Chap. 6.
[18] S. H. Lin and H. Eyring, Proc. Natl. Acad. Sci. USA **78**, 2013 (1978).
[19] E. W. Montroll and K. E. Shuler, Adv. Chem. Phys. **1**, 361 (1958).
[20] X. Y. Huang, J. Lin, and T. F. George, J. Chem. Phys. **80**, 893 (1984); X. Y. Huang and T. F. George, *ibid.* **88**, 4801 (1984).
[21] X. Y. Huang, J. D. Cresser, and J. H. Eberly, J. Opt. Soc. Am. B (in press).

Laser-stimulated vibrational excitation of an adspecies studied by a generalized master equation: Neutral atomic hydrogen on hydrated KCl(001)

A. C. Beri and Thomas F. George
Department of Chemistry, University of Rochester, Rochester, New York 14627

(Received 18 March 1985; accepted 21 May 1985)

Vibrational energy transfer between an IR laser, a solid surface, and an adatom is studied by a genralized master equation which includes memory effects. Numerical problems associated with the temporally delocalized memory kernel are overcome by introducing the isomnesic approximation. Results obtained for time scales ranging from 2 ps to 2 μs for $H(H_2O)/KCl(001)$ show that effective vibrational excitation is possible with low-power lasers (1 W/cm^2) in spite of fast phonon relaxation. Detailed time evolution of the system is seen to differ radically from that predicted by Markovian theories, even for fairly long time scales.

I. INTRODUCTION

Developments in the experimental study of clean, well-characterized solid surfaces and surface processes such as scattering, adsorption, desorption, and migration in the presence of laser radiation have resulted in important technological applications (e.g., laser-assisted vapor deposition of microcircuits). The underlying dynamics of these heterogeneous systems is a many-body problem involving the elementary excitations of the solid and its surface (such as phonons, electrons, and plasmons) the degrees of freedom of the adsorbed species or gas molecules, and those of the laser.[1,2] The excitation process can be considered as direct laser pumping of the substrate leading to a primarily nonselective thermal effect, or a pumping of the adsorbed species, which can be selective in the sense that only a single degree of freedom is excited by the laser. The resulting energy absorption and the dissipation involving all other degrees of freedom govern the overall chemical process.[3–8]

In this work, the vibrational excitation of a prototype system, viz. the adsorptive bond (adbond) between an atom and a surface is studied. This system is not in the same category as those in which internal vibrational modes of an adsorbed molecule are excited, with subsequent energy transfer to the adbond.[7,9] It is substantially simpler, in view of the aim of this work, which is to investigate the mechanisms involved in IR laser-stimulated surface processes (LSSP) using a treatment which is as close to first principles as possible. One of the fundamental questions addressed is whether a low-power laser, because of its coherence, can deposit large amounts of energy into a specific mode of a system (such as an adbond) which is coupled to energy sinks, such as phonons, which are not infinite. Early classical treatments[10] of the problem and phenomenological quantum treatments[4,5] provided conflicting answers to this question. Recently, more fundamental studies[8] have suggested that extremely high laser powers would be needed to effectively desorb an adspecies. However, our preliminary work[11] showed that a very small degree of detuning between the laser and energy levels of the system excluded the possibility of long-term energy absorption. The reason for this behavior is seen to be the oscillatory nature of the laser energy absorption "rate" (actually, the memory kernel) for the adbond, with a frequency related to the detuning, typically a small percentage of the laser frequency itself, viz. $\sim 10^{10}$–10^{11} s^{-1}. Thus, for processes lasting over a few hundred picoseconds, substantial cancellations in the overall absorption can be expected, and only a very high-power laser would be able to compete with the loss of energy from the adbond to phonons through relaxation effects. In view of this, the systems chosen here have little or no detuning, viz. systems with one bound-to-bound transition exactly resonant with the laser frequency and another very close to or equal to the Debye frequency of the solid. This represents an ideal situation which emphasizes the coherent nature of laser radiation.

The widely varying temporal behavior of dynamical systems far from equilibrium is well established. From a fundamental point of view, theoretical treatments of such systems depend crucially on the time scales being considered. The most common long-time limit, for example, allows a description of energy transfer in terms of average relaxation rates in the Markovian approximation, where approach to equilibrium is assumed to be monotonic. Non-Markovian behavior is asumed to last for extremely short times compared to typical relaxation times of the system. The forces are considered to be random, with a very short correlation time. Resonant excitation with a low-power laser does not satisfy these conditions, and one should expect non-Markovian behavior to persist for times that increase with decrease in laser power. Whether the two approaches lead to the same steady state is also open to question.

Non-Markovian effects are conveniently treated by using a generalized master equation (GME) to describe the time evolution of the adbond (the "relevant" system) with the laser and phonon fields as two uncoupled irrelevant systems (reservoirs).[12–14] The Liouville equation for such a system is conveniently solved by using the Zwanzig projection-operator technique[12] and results in a set of coupled integrodifferential equations for the occupation probabilities P_S of states $|S\rangle$ of the adbond[14]:

$$\dot{P}_S(t) = \sum_{S' \neq S} \int_0^t dt' \left[K_{SS'}(t-t')P_{S'}(t') - K_{S'S}(t-t')P_S(t') \right], \quad (1)$$

 0734-211X/85/051529-05$01.00

where the memory kernels $K_{SS'}$ include contributions due to the phonon field $K^{(p)}$ and the radiation field $K^{(r)}$:

$$K_{SS'}(t) = K^{(p)}_{SS'}(t) + K^{(r)}_{SS'}(t) . \tag{2}$$

Using a one-dimensional lattice and a Debye model to describe the lattice vibrations, we have obtained $K^{(p)}_{SS'}$ in a closed form which involves a summation over all lattice positions l and number of phonons n independently.[11,15] The former is due to a summation of pair potentials between the adatom and the lattice atoms, while the latter results from an expansion of $\exp[y_{ll'}(t)]$ in a Taylor series, where $y_{ll'}(t)$ is the lattice displacement correlation function

$$y_{ll'}(t) = \langle\langle u_l(t) u_{l'} \rangle\rangle . \tag{3}$$

Using techniques described elsewhere,[11] $y_{ll'}(t)$ can be obtained in closed form as

$$y_{ll'}(t) = \mathscr{R}_{ll'}(t) + i\,\mathscr{I}_{ll'}(t) , \tag{4}$$

where $\mathscr{R}_{ll'}$ and $\mathscr{I}_{ll'}$ involve products of polynomials in t and $\cos(\omega_D t)$ or $\sin(\omega_D t)$, and ω_D is the Debye frequency. The phonon part of the memory kernel can then be written in terms of all the system parameters as follows:

$$K^{(p)}_{SS'}(t) = A_p \sum_n (B_p)^n \sum_{ll'} \sum_{\mu\mu'} (\mu\mu')^n \times \lambda_{ll'\mu\mu'}(S \leftarrow S') [\tilde{\mathscr{C}}_{nll'}(t) \cos(\omega_{SS'} t) + \tilde{\mathscr{S}}_{nll'}(t) \sin(\omega_{SS'} t)] . \tag{5}$$

Here

$$A_p = 8(D^{(0)}_e/\hbar)^2 , \tag{6}$$

$$B_p = 6\gamma^{(0)} k_b T)^2/m_S \hbar\omega_D^3 , \tag{7}$$

$$\tilde{\mathscr{C}}_{nll'}(t) = \sum_{j_e = 0,2,4,\ldots} \frac{(-1)^{(j_o-1)/2}}{j_e!(n-j_o)!} \mathscr{R}^{n-j_e}_{ll'}(t) \mathscr{I}^{j_e}_{ll'}(t) , \tag{8}$$

$$\tilde{\mathscr{S}}_{nll'}(t) = \sum_{j_o = 1,3,5,\ldots} \frac{(-1)^{(j_o-1)/2}}{j_o!(n-j_o)!} \mathscr{R}^{n-j_o}_{ll'}(t) \mathscr{I}^{j_o}_{ll'}(t) , \tag{9}$$

$$\max(j_e, j_o) \leqslant n . \tag{10}$$

B_p is a smallness parameter which dictates, in part, the convergence properties of the expansion in number of phonons n. It is of the order of 0.02 for common temperatures T and common Debye frequencies (k_B is the Boltzmann constant and m_s the mass of a lattice atom). μ and μ' take on the values 1 and 2. The supermatrix λ involves powers of $\exp(a)$ and $\exp(\langle\langle u^2 \rangle\rangle)$ and the matrix elements

$$E^{(\mu)}_{SS'} = \langle S | e^{\mu(z - z^{(0)}_0)} | S' \rangle , \tag{11}$$

where a is the lattice constant, u is the lattice displacement operator, and z is the distance of the adatom from the equilibrium position of the outermost lattice atom. The frequencies $\omega_{SS'}$ correspond to transitions between levels $|S\rangle$ and $|S'\rangle$ of the adbond represented by a Morse potential with depth $D^{(0)}_e$, equilibrium distance $z^{(0)}_0$, and exponent $\beta^{(0)}$.

The radiation part $K^{(r)}_{SS'}$ of the memory kernel is given by

$$K^{(r)}_{SS'}(t) = A_r z_{S''S} z_{SS'} \cos(\omega_L - |\omega_{SS'}|)t , \tag{12}$$

where $z_{SS'} = \langle S | z | S' \rangle$. The amplitude $A_r = (Ie_0^2/\epsilon_0 c\hbar^2)$ is proportional to the laser frequency I and the square of the charge separation e_0 between the adspecies and the surface.

The complicated form of $\mathscr{R}_{ll'}$ and $\mathscr{I}_{ll'}$ precludes analytic solution of the GME. Numerical solution is made difficult by the presence of high frequencies in $K^{(p)}_{SS'}$ and the large difference in the magnitudes of A_r ($\sim 10^{17}$ s^{-2} for a 1 W/cm^2 laser) and A_p ($\sim 10^{29}$ s^{-2} for $D^{(0)}_e = 0.1$ eV). One can only solve the *exact* GME for a few periods of oscillation of $K_{SS'}$, which amount to a few picoseconds.

Examination of a typical phonon kernel (Fig. 1) shows that it has substantial amplitude only for times of the order of a Debye period τ_D, representative of phonon correlation times. The laser kernel, on the other hand, has constant amplitude for the case $\omega_L = \omega_{SS'}$ for a given pair of levels (S,S'). For times larger than τ_D, the integrated effect due to $K^{(p)}_{SS'}$ will be unchanging because of cancellations, whereas that due to $K^{(r)}_{SS'}$ will be cumulative. We have recently demonstrated this effect[11] using the exact GME (with very high laser power in order for the effect to manifest itself in the very short time for which solution was possible), and predicted, via extrapolation arguments, that effective pumping of the adbond with a low-power laser would be possible if the long-time regime could be examined. We present here an actual calculation of this long-time behavior using low-power lasers, and find that the average adbond energy, given by

$$\mathscr{E}(t) = \sum_S \mathscr{E}_S P_S(t) , \tag{13}$$

where $\mathscr{E}_S$ are eigenvalues of the zeroth order adbond Hamiltonian, rises rapidly after an initial loss to the phonon field, and exhibits a decidedly non-Markovian pattern throughout.

The approximations required for the long-time treatment are described in Sec. II. The resulting probability and energy profiles are presented in Sec. III, where comparison is made with the exact results (for a short-time scale) and with a Markovian limit.

II. THE ISOMNESIC (CONSTANT-MEMORY) APPROXIMATION

We begin with the assertion that the physically important situation is one where the laser frequency and the Debye

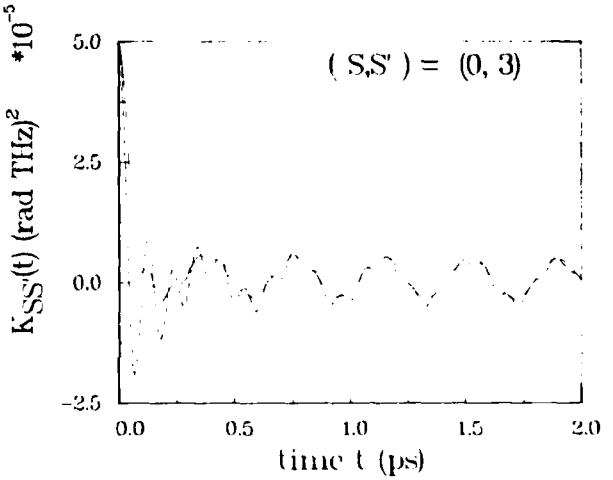

FIG. 1. Memory kernels $k^{(r)}_{SS'}(t)$ for $(S,S') = (0,3)$. Solid line: 3 → 0; dotted line: 0 → 3.

frequency equal different transition frequencies $\omega_{SS'}$ of the adbond.[11] For this case $K^{(r)}_{SS'}$ becomes a constant $k_{SS'}$ (from the term with $|\omega_{SS'}| = \omega_L$) plus oscillating terms which we ignore in the sense of the rotating-wave approximation.[16] The phonon term $[K^{(p)}_{SS'}(t)]$ has a complicated behavior typified by $K^{(p)}_{03}(t)$ in Fig. 1, but we note that it has appreciable magnitude for times $\leqslant 2$ ps, and almost vanishes subsequently. If the mesh size of our theoretical experiment is no less than 2 ps, we can treat $K^{(p)}_{SS'}(t)$ as a delta function, so that, from Eq. (2)

$$K_{SS'}(t) = \Omega_{SS'}\delta(t) + k_{SS'}\,, \tag{14}$$

where

$$\Omega_{SS'} = \int_0^\infty dt\, K^{(p)}_{SS'}(t)\,. \tag{15}$$

In Eq. (14), the first term, originating from the coupling of the adbond to the phonons, is the amnesic or Markovian term, and would lead, in the absence of the laser term, to the elimination of all memory effects. The second term, due to the resonant laser coupling, is the isomnesic non-Markovian term, and represents a *constant memory effect* all the way back to $t = 0$.

The subsequent treatment is simplified by defining "diagonal" elements Ω_{SS} as

$$\Omega_{SS} = -\sum_{S' \neq S} \Omega_{SS'} \tag{16}$$

and similarly for k_{SS}, and by introducing the vector notation $\mathbf{P}(t) \equiv [P_S(t)]$ and matrix notation $\mathbf{\Omega} = \{\Omega_{SS'}\}$, $\mathsf{k} \equiv \{k_{SS'}\}$, etc. The exact GME may be written as

$$\dot{\mathbf{P}} = \int_0^t dt'\, \mathsf{K}(t-t')\cdot\mathbf{P}(t')\,; \tag{17}$$

in the isomnesic approximation (IA) it becomes

$$\dot{\mathbf{P}} = \mathsf{k}\cdot\int_0^t dt'\, \mathbf{P}(t')\mathbf{\Omega}\cdot\mathbf{P}(t)\,. \tag{18}$$

Formally this can be solved without any further approximations. Differentiating both sides of Eq. (18) we get the second-order differential equation

$$\ddot{\mathbf{P}} = \mathsf{k}\cdot\mathbf{P}(t) + \mathbf{\Omega}\cdot\mathbf{P}(t)\,, \tag{19}$$

whose Laplace transform,

$$\mathsf{M}(s)\cdot\mathbf{P}(s) = \mathbf{T}(s)\,, \tag{20}$$

where

$$\mathsf{M}(s) \equiv \mathsf{k} + s\mathbf{\Omega} - s^2\Delta\,, \tag{21}$$

$$\mathbf{T}(s) \equiv -s\mathbf{P}(0)\,, \tag{22}$$

and $\mathbf{P}(s)$ is the Laplace transform of $\mathbf{P}(t)$, is easily inverted using the Heaviside expansion theorem.

While this effectively eliminates the non-Markovian bottleneck, it is instructive to generate solutions of a Markovian version of this class of problems. To do this, we have to make provisions for localizing $K^{(r)}_{SS'}$ in time. This brings to the fore the pervasive issue of time scales in dynamical many-body systems, our specific questions being the relative degree of localization ascribable to $K^{(p)}_{SS'}$ and $K^{(r)}_{SS'}$. If the laser radiation is localized as a pulse, it can still extend over a period of time much longer than the extent of $K^{(p)}_{SS'}(t)$. In other words, the delta function representing $K^{(p)}_{SS'}(t)$ may be quite different from the delta function representing $K^{(r)}_{SS'}(t)$, and the former may in fact not really be considered as localized with respect to the latter. With these provisos in mind, we can proceed to write the Markovian version of Eqs. (14), (17), (19), and (20):

$$\mathsf{K}(t) = (\mathbf{\Omega} + \mathsf{f})\delta(t)\,, \tag{23}$$

$$\dot{\mathbf{P}}(t) = \mathsf{W}\cdot\mathbf{P}(t)\,, \tag{24}$$

$$\mathsf{J}(s)\cdot\mathbf{P}(s) = \mathbf{U}\,, \tag{25}$$

where

$$\mathsf{f} = \mathsf{k}\tau\,, \tag{26}$$

$$\mathsf{W} = \mathbf{\Omega} + \mathsf{f}\,, \tag{27}$$

$$\mathsf{J}(s) = (\mathbf{\Omega} + \mathsf{f} - s\Delta)\,, \tag{28}$$

$$\mathbf{U} = -\mathbf{P}(0)\,, \tag{29}$$

and τ represents the actual extent of the laser signal or a variable time parameter. Equation (24) is the well-known Pauli master equation (PME).

III. RESULTS OF THE EXACT, ISOMNESIC, and MARKOVIAN APPROXIMATIONS

The formalism of Sec. I and II was applied to the system $H(H_2O)/KCl(001)$, the primary reasons for choosing which are the shallow adsorption potential well and the small number of bound states (seven) it generates.[17] In Fig. 2 the results of the IA and the exact GME are compared for the system of Refs. 11 and 15. The two are identical for $H(H_2O)/KCl$, and are not shown. While this is a short-time-scale comparison, the closeness of the two leads us to expect the long-time IA results to be reliable. The Markovian approximation, on the other hand, cannot provide an unambiguous comparison because of the large variations in the results for different values of τ (shown in Fig. 3). All subsequent figures, therefore, present our IA results.

Figure 4 is a composite display of the function $\mathscr{E}(t)$ obtained from results of Eq. (28) for six ranges of time differing by factors of 10 and for a laser intensity $I = 1$ W/cm^2. It is seen that in going from a picosecond time range to a microsecond time range, the behavior of the system changes dramatically. The early behavior is dominated by fast energy transfer to phonon modes, completely overwhelming the

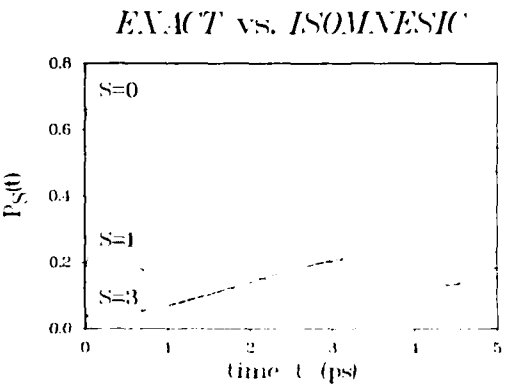

FIG. 2. Probability profiles for system of Refs. 11 and 15 obtained by solving the exact GME (solid line) and the isomnesic GME (dashed line).

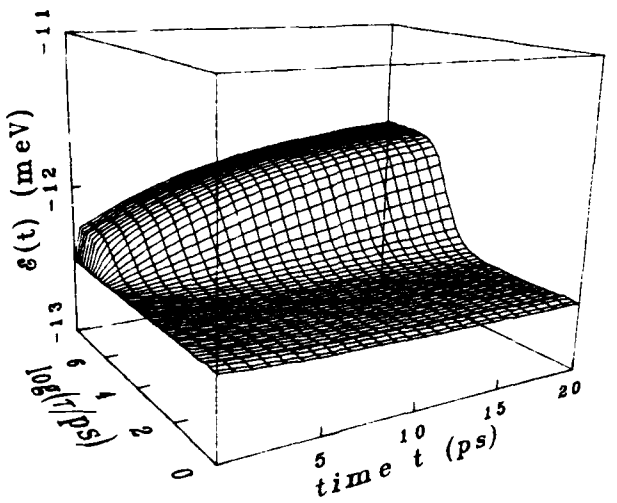

FIG. 3. Average adbond energy $\mathscr{E}(t)$ obtained within the Markovian approximation for a range of values of the parameter τ.

slow laser pumping. The monotonic decay is representative of relaxation phenomena. For the 100 ps range, a false steady state seems to have been reached, but is in fact only an artifact of the large difference between A_r and A_p. The adbond energy starts to increase in the ns range, again suggesting a possible steady state. However, this is a transitional period during which the relative importance of the phonon terms and the laser terms starts to change. The latter, in fact, originate from a probability profile of the form $(Ae^{\alpha t}\cos\beta t - \beta^{\alpha t}\sin\beta t)$, where $\alpha + i\beta$ are complex roots of

$$\det \mathsf{M}(s) = 0\,, \tag{30}$$

and $A + iB$ are complex coefficients obtained from $\mathsf{M}(s)$ and $\mathsf{T}(s)$.

The phonon terms come from real roots and are therefore nonoscillatory. The magnitudes of the exponents α in the laser part of the solution are much smaller than corresponding exponents in the phonon term. This is responsible for the radically different nature of $\mathscr{E}(t)$ in the different time regimes. Thus, the seemingly monotonic rise in $\mathscr{E}(t)$ apparent in the 10 ns regime is seen to be only the early segment of a cycle which becomes evident in the 100 ns results and beyond. The frequency of this oscillation is seen to be $k_0^{1/2}$, where k_0 is the amplitude of the laser kernel $k_{SS'}$, and is essentially the Rabi frequency for the pair of levels resonant with the laser.

While the frequency of the long-term oscillations of $P(t)$ and $\mathscr{E}(t)$ depends only on the laser term, being proportional to the square root of the intensity, the rate of onset of this behavior depends on α which varies linearly as k_0 and inversely as the amplitude Ω_0 of the phonon kernel. Thus, increasing the laser power from 1 to 25 W/cm^2 advances the onset time for the oscillatory state while increasing the frequency by a factor of 5 (as displayed in Fig. 5).

Physically, the results of Figs. 4 and 5 can be interpreted in terms of desorption rates. Thus, the time required for $|A|e^{\alpha t}$ and $|B|e^{\alpha t}$ to become large enough so that the amplitude of $E(t)$ in the oscillatory regime is substantially larger than the $(t = 0)$ equilibrium Boltzmann value, is a reasonable measure of the desorption time to within an order of magnitude. This time is estimated by $\tau_D = \alpha^{-1}$. For our case,

$$\tau_D^{-1} = \alpha \approx 0.5\,\frac{k_0}{\Omega_0} \approx (10^4\, w)\mathrm{s}^{-1}\,, \tag{31}$$

where w is laser power in W/cm^2. Thus, for a 1 W/cm^2 laser, a hydrogen atom will stay adsorbed on the KCl(H_2O) surface for $\sim 10^{-4}$ s on the average before desorbing, or at least becoming very highly excited. The data mentioned here is for $T = 150$ K.

It must be pointed out that a number of mechanisms whereby the desorption cross section could be modified are not included. Spontaneous decay, phase relaxation, phonon–phonon interaction, and electron-hole pair creation are some of the ones being considered in extensions of this work. As a result, the sharp transitions assumed here will be broadened by a detuning-type effect, and estimates of the desorption rate presented above will have to be modified. However, the selectivity represented by the dominant T_1 energy-transfer process will be retained.

For a complete study of desorption, transitions to the continuum must be included, and at the outset it is difficult to predict which levels will be most important. Work in this

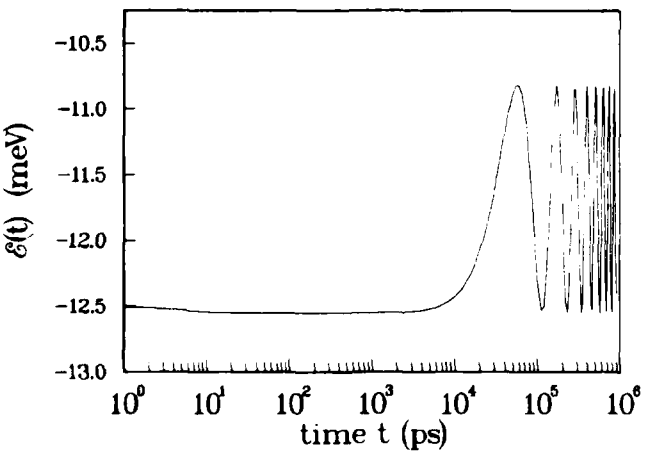

FIG. 4. $\mathscr{E}(t)$ obtained by using the isomnesic approximation for time scales ranging from ps to μs, for laser intensity $I = 1$ W/cm^2.

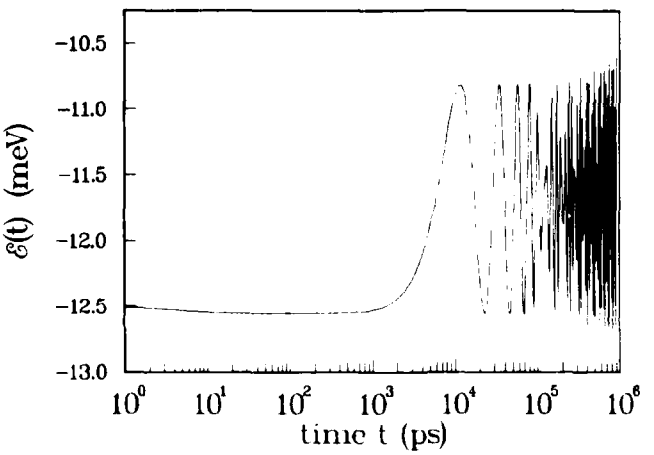

FIG. 5. Same as Fig. 4 for $I = 25$ W/cm^2.

direction is in progress, and represents a departure from the first-principles approach in the inclusion of the bound-to-continuum transitions. This, as well as a complete first-principles treatment of vibrational LSSP including desorption, will be presented in the near future.

ACKNOWLEDGMENTS

This work was supported in part by the Office of Naval Research and the Air Force Office of Scientific Research (AFSC), United States Air Force, under Grant No. AFOSR-82-0046. The United States Government is authorized to reproduce and distribute reprints for governmental purposes notwithstanding any copyright notation hereon. TFG acknowledges the Camille and Henry Dreyfus Foundation for a Teacher–Scholar Award (1974–86).

[1]T. F. George, A. C. Beri, K. S. Lam, and J. Lin, in *Laser Applications*, edited by J. F. Ready and R. K. Erf (Academic, New York, 1984), pp. 69–127.
[2]T. F. George, J. Lin, A. C. Beri, and W. C. Murphy, Prog. Surf. Sci. **16**, 139 (1984).
[3]T. J. Chuang, Surf. Sci. Rep. **3**, 1 (1983).
[4]J. Lin and T. F. George, J. Chem. Phys. **72**, 2554 (1980); J. Lin and T. F. George, Phys. Rev. B **24**, 64 (1981).
[5]J. Lin, A. C. Beri, M. Hutchinson, W. C. Murphy, and T. F. George, Phys. Lett. A **79**, 233 (1980).
[6]A. C. Beri and T. F. George, J. Chem. Phys. **78**, 4288 (1983).
[7]H. J. Kreuzer and D. N. Lowy, Chem. Phys. Lett. **78**, 50 (1981); D. Lucas and G. E. Ewing, Chem. Phys. **58**, 385 (1981); Z. W. Gortel, H. J. Kreuzer, P. Piercy, and R. Teshima, Phys. Rev. B **27**, 5066 (1983); **28**, 2119 (1983).
[8]C. Jedrzejek, K. F. Freed, S. Efrima, and H. Metiu, Surf. Sci. **109**, 191 (1981).
[9]T. J. Chuang and H. Seki, Phys. Rev. Lett. **49**, 382 (1982); T. J. Chuang, J. Chem. Phys. **76**, 3828 (1982).
[10]W. C. Murphy and T. F. George, Surf. Sci. **102**, L46 (1981).
[11]A. C. Beri and T. F. George, J. Chem. Phys. **83**, 2482 (1985).
[12]R. W. Zwanzig, in *Lectures in Theoretical Physics*, edited by W. E. Brittin, B. W. Downs, and J. Downs (Interscience, New York, 1961), Vol. III, p. 106ff.
[13]F. Haake, in *Springer Tracts in Modern Physics*, edited by G. Höhler (Springer, Berlin, 1973), p. 98ff.
[14]C. Jedrzejek, K. F. Freed, E. Hood, and H. Metiu, J. Chem. Phys. **79**, 2436 (1983).
[15]A. C. Beri and T. F. George (unpublished).
[16]W. H. Louisell, *Quantum Statistical Properties of Radiation* (Wiley, New York, 1973), Chap. 6.
[17]H. Frank, H. Hoinkes, and H. Wilsch, Surf. Sci. **63**, 121 (1977).

Photochemical deposition of Sn for use in molecular beam epitaxy of GaAs

Steven P. Kowalczyk and D. L. Miller
Rockwell International Corporation, Microelectronics Research and Development Center, Thousand Oaks, California 91360

(Received 18 March 1985; accepted 28 May 1985)

The suitability of several Sn-containing molecules (tetramethyltin, tetrabutyltin, dibutyltin dibromide, and stannic chloride) as gas phase sources of Sn for use in molecular beam epitaxy of GaAs was evaluated. *In situ* Auger electron spectroscopy showed that the Sn molecules absorbed at approximately the monolayer level at room temperature on GaAs (001) epilayer surfaces and pyrolytically decomposed before desorption. Capacitance–voltage and secondary ion mass spectrometry profiles demonstrated that the pyrolytic Sn deposits incorporated as an *n*-type dopant into newly regrown GaAs epilayers. Sn films were ultraviolet (UV) photolytically deposited on GaAs from each of these Sn-containing molecules and characterized by x-ray photoelectron spectroscopy.

I. INTRODUCTION

Ultraviolet (UV) initiated microchemistry has recently emerged as a potential new tool in microfabrication for solid state electronic applications.[1–4] The employment of such a technique offers attractive new possibilities for microelectronic processing. Much of the recent research has centered on delineated deposition of metal films by laser UV photolysis of gaseous metal-containing compounds.[5–15] The effort in this area has been successful in highlighting the capability of photodeposition and has begun to illuminate some of the fundamental processes involved. One intriguing possibility for semiconductor device processing that this capability opens up is that of selected area (i.e., lateral area) doping of semiconductors. In particular, we are interested here in developing *in situ* selected area doping within molecular beam epitaxy (MBE) technology.

The purpose of the work reported here is the investigation of the possibility of selected area Sn doping in GaAs MBE. There are several attractive features in such a combination. The selected area doping scheme proposed here involves UV photolysis. As applied to GaAs, it consists of five steps (Fig. 1):

(1) Growth of a GaAs MBE epilayer (buffer layer) on an atomically clean and crystallographically ordered GaAs (001) substrate.
(2) Adsorption of approximately one monolayer of the dopant atom (Sn) containing molecules on the epilayer surface.
(3) UV irradiation of selected areas of the epilayer to produce photolytic decomposition of the dopant molecule, resulting in the dopant atom on the selected areas of the epilayers of the surface and the adsorbed molecules remaining on the unirradiated portions of the epilayer.
(4) Thermal desorption of the nondecomposed physisorbed molecules, while the more strongly bound atoms remain on the surface.
(5) Regrowth of GaAs and incorporation of dopant atoms in the selected areas of the new GaAs epilayer.

However, before such a fabrication process can be imple-

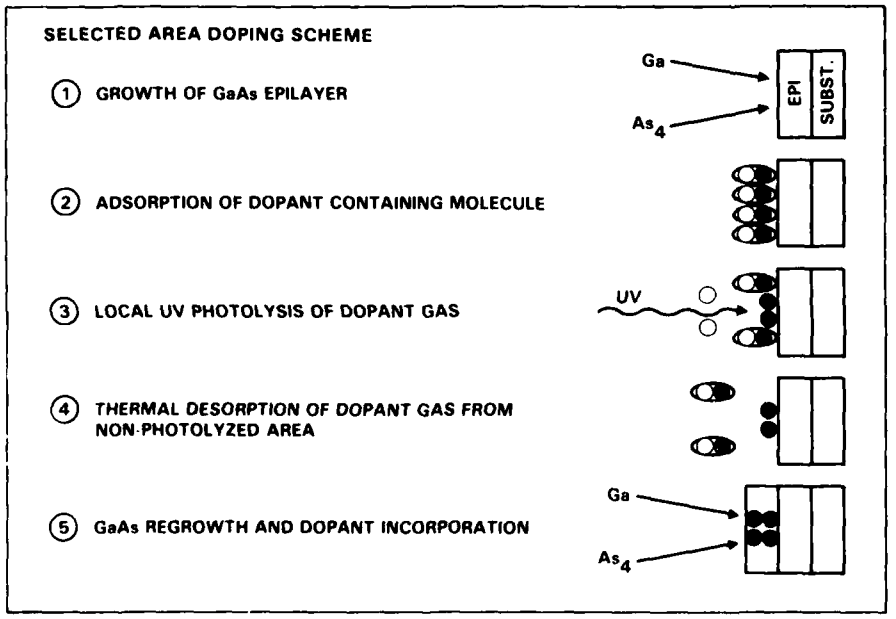

FIG. 1. Five steps of the proposed *in situ* selected area doping scheme for MBE GaAs.

 0734-211X/85/051534-05$01.00

mented, many fundamental aspects associated with the basic mechanism of each of the above steps must be clarified. In this paper, we present the results of our initial studies of steps (2)–(5). The adsorption [step (2)] and desorption [step (4)] of Sn-containing molecules on GaAs (001) surfaces was studied by means of *in situ* Auger electron spectroscopy (AES). UV photolytic deposition [step (3)] of Sn films on GaAs (001) was studied separately by *ex situ* experiments using x-ray photoelectron spectroscopy (XPS) for characterization of the photodeposited Sn films. Sn incorporation [step (5)] was studied by means of secondary ion mass spectrometry (SIMS) and electrolytic capacitance–voltage (C–V) profiling techniques.

II. EXPERIMENTAL ASPECTS

The MBE growths utilized a multichambered, cryopumped, LN shrouded, homebuilt MBE apparatus. The MBE system consists of three chambers: a load-lock chamber, an antechamber primarily for degassing of substrates, and a growth chamber equipped with a cylindrical mirror analyzer for Auger electron spectroscopy (AES), a reflection electron diffraction (RED) system, and a quadrupole mass spectrometer. The sample can be moved between all three chambers while maintaining ultrahigh vacuum ($< 10^{-9}$ Torr). The MBE open crucible cell sources, which are mounted vertically, are filled with elemental As and Ga for production of As_4 and Ga beams. With growth rates of $\sim 1\,\mu$m/h, standard MBE growth temperatures and As_4/Ga flux ratios, unintentional doping levels in the 5×10^{14}–5×10^{15} atoms/cm^3 range were normally achieved. For these experiments, a manifold for handling and purification by means of freeze-thaw cycles of the Sn-containing molecules was built and attached to the antechamber of the MBE system through a ultrahigh vacuum (UHV) leak valve.

The substrates were pieces of GaAs (001) (n^+ and semi-insulating) wafers which had been polished and given a standard solvent degrease and chemical etch. After mounting on a Mo substrate holder with In, the substrates were spun etched with H_2O:H_2O_2:NH_4OH (10:1:1) and blown dry with N_2. The substrates were immediately loaded into the MBE system, pumped and transferred to the antechamber, where they were degassed and then transferred to the growth chamber, where they were thermally cleaned in an As_4 flux. Epilayer growth then commenced on an As-stabilized surface.

Sn is a n-type dopant for MBE GaAs,[16–19] which is particularly good for the proposed selected area doping scheme because it incorporates in MBE GaAs by a surface accumulation mechanism.[17] Thus, one can deposit a small amount of Sn on a GaAs surface and upon regrowth of GaAs, the Sn incorporates into the newly grown epilayer. The compounds investigated as Sn sources in these experiments were tetramethyltin $(CH_3)_4Sn$ (TMT), tetrabutyltin $(C_4H_9)_4Sn$ (TBT), dibutyltin dibromide $(C_4H_9)_2SnBr_2$ (DBTB), and stannic chloride ($SnCl_4$). All of these compounds are high vapor pressure liquids at room temperature.[20] TMT and $SnCl_4$ exposures were performed at their room temperature equilibrium vapor pressures, while the TBT and DBTB exposures were performed at their 100 °C equilibrium vapor pressures.

The adsorption/desorption experiments were performed by placing a freshly grown epilayer at room temperature in the preparation chamber (base pressure $\sim 1\times10^{-9}$ Torr) and exposing the epilayers to the Sn compound vapor pressure for between 15–30 min. The surfaces were then examined by AES in the growth chamber. The temperature was ramped in ~50–100 °C steps up to approximately the growth temperature of ~580 °C and the desorption/pyrolysis characteristics were followed by *in situ* AES measurements. At the conclusion of the desorption measurements, a new undoped epilayer of GaAs was grown and Sn incorporation was studied by electrolytic C–V[21] and SIMS profiling.[22]

UV photolysis experiments were performed in separate experiments. GaAs (001) wafers were etched with a 4:1:1 H_2SO_4:H_2O_2:H_2O solution, quenched in deionized H_2O and dried in a N_2 flow. Such a procedure produces a layer containing Ga_2O_3/As_2O_3, approximately 15 Å thick on the surface.[23] The wafer was placed in a quartz ampoule containing several drops of the liquid Sn compound and the ampoule was then sealed. This procedure was performed in a N_2 ambient in a glovebag. The sample was exposed to UV irradiation from either a high pressure Xe arc lamp (500 W) or an array of five low pressure Hg lamps (5 W each). The main Hg

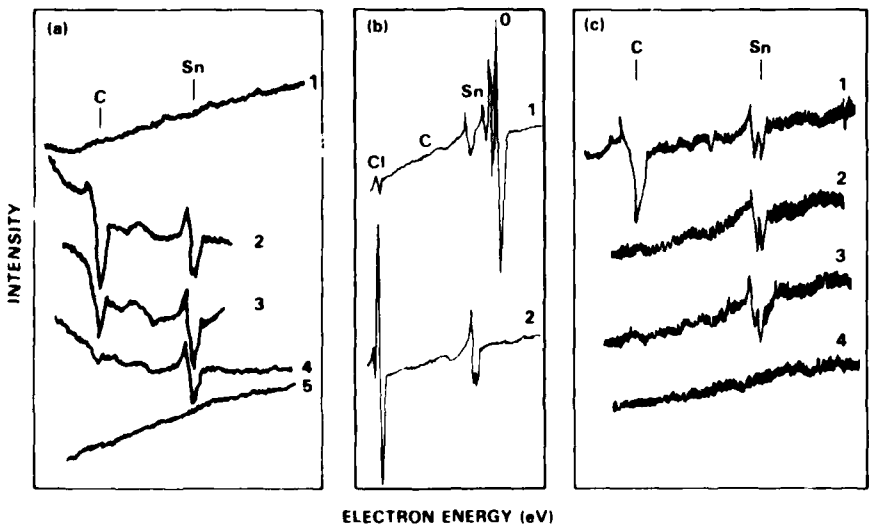

FIG. 2. AES spectra for the adsorption/desorption experiments of several Sn molecules on GaAs (001): (a) tetramethyltin, (1) fresh MBE-grown GaAs epilayer, (2) room temperature adsorption of TMT, (3) heated to 270 °C, (4) heated to 570 °C, and (5) MBE regrowth; (b) stannic chloride, (1) adsorption of $SnCl_4$ on an oxide surface, and (2) adsorption on a clean epilayer; (c) tetrabutyltin, (1) room temperature adsorption of TBT, (2) heated to 270 °C, (3) heated to 600 °C, and (4) MBE regrowth.

lines are at 2537 and 1849 Å. For convenience of analysis, broad areas were exposed, since the main area of interest in these experiments is in Sn deposition properties, and pattern delineation has been amply demonstrated for a number of metals in other laboratories. After UV photolysis of the Sn-containing compounds, the sample was transferred to an XPS system via air and the surface was analyzed. The XPS system which was used is a Hewlett–Packard HP5950A electron spectrometer with a monochromatized Al$K\alpha$ ($h\nu = 1486.6$ eV) x-ray source.

III. RESULTS AND DISCUSSION

A. Tetramethyltin

Exposure of fresh GaAs (001) epilayers to TMT resulted in approximately a monolayer of TMT being adsorbed. The TMT adsorption had no effect on the As/Ga ratio observed with AES, suggesting physisorption. All adsorption experiments with TMT showed significant oxygen contamination despite performing up to six freeze/thaw purification cycles prior to adsorption. Figure 2 shows AES spectra in the carbon and Sn region for TMT adsorption/desorption, and Fig. 3 summarizes some of the data for the AES lines of Sn, C, Ga, and As as a function of temperature. The main conclusion is that TMT starts to pyrolytically decompose around 200 °C and is completely decomposed by 600 °C. This results in a Sn film with a small amount of residual carbon contamination. The unintentional oxygen contamination was not observed above ~450–500 °C. Since the TMT pyrolyzes before it can desorb, it can be ruled out as a source for selected area doping. When GaAs is regrown over a surface in which TMT has been pyrolytically decomposed, Sn is incorporated across the entire surface as a n-type dopant, as shown by the C–V analysis in Fig. 4. The C–V profile shows the expected exponential profile. SIMS analysis (Fig. 4) shows a similar Sn profile and also shows a large sharp carbon and much smaller oxygen buildup at the regrowth interface.

UV photolysis of TMT in sealed ampoules using either Xe or Hg radiation produced a metallic-looking film on the GaAs surface. XPS analysis showed the GaAs to be covered by Sn, but with significant carbon and oxygen contamination, which is not surprising due to non-UHV ambient in the ampoules. Upon heating the sample in the 200–450 °C range, carbon was removed while the oxygen remained, suggesting

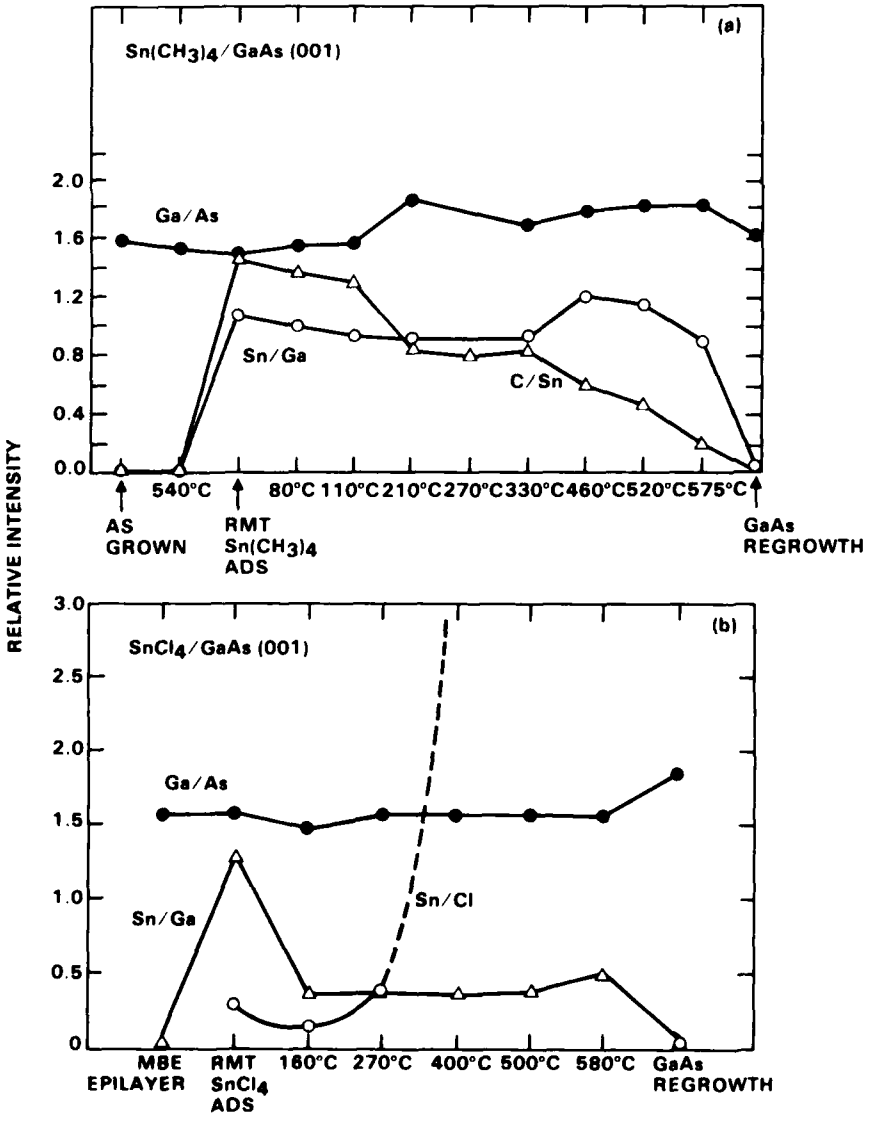

FIG. 3. Relative AES intensity ratios for TMT and $SnCl_4$ on GaAs (001) as a function of thermal treatment.

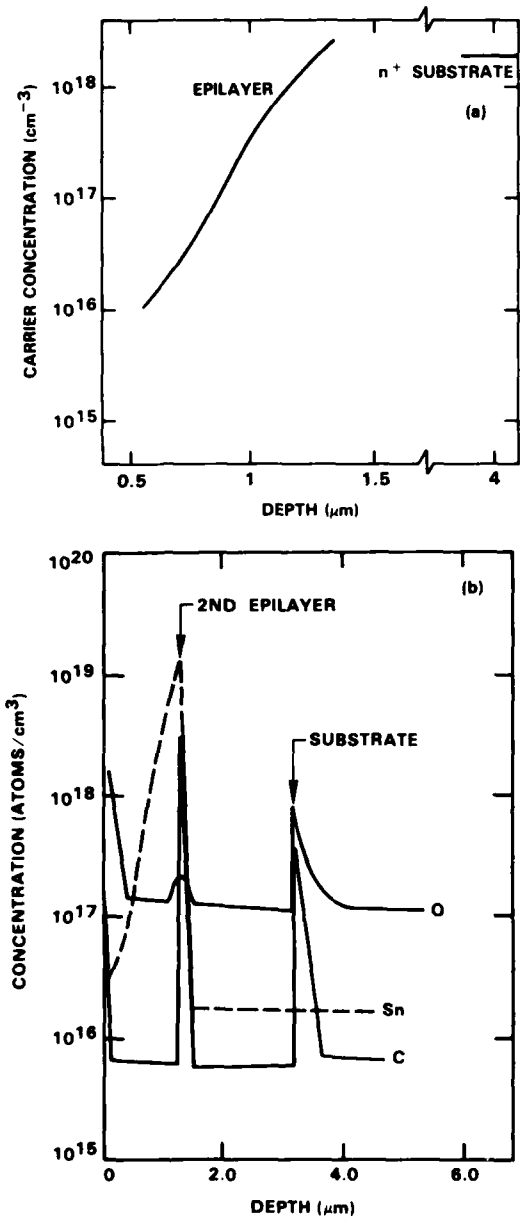

FIG. 4. (a) C–V profile and (b) SIMS carbon, oxygen, and Sn profile through an epilayer which had Sn incorporated from pyrolytic decomposition of TMT on GaAs, followed by MBE regrowth after the decomposition.

that the carbon was mainly adsorbed on the surface as a monolayer of TMT and/or carbon contamination from the air transfer to the XPS system, while the oxygen was in the Sn film, perhaps due to the Sn photolytically reacting with the residual oxygen in the quartz ampoule. Experiments involving sputter profiling would be helpful for further clarification of these two points.

B. Tetrabutyltin

Tetrabutyltin also adsorbed at the monolayer level on GaAs (001). It adsorbed without any oxygen contamination. AES spectra are shown in Fig. 2. TBT was completely pyrolyzed by 270 °C with no residual carbon contamination. UV photolysis in a sealed ampoule with Hg radiation resulted in a Sn film which had much less oxygen contamination than in the case of TMT.

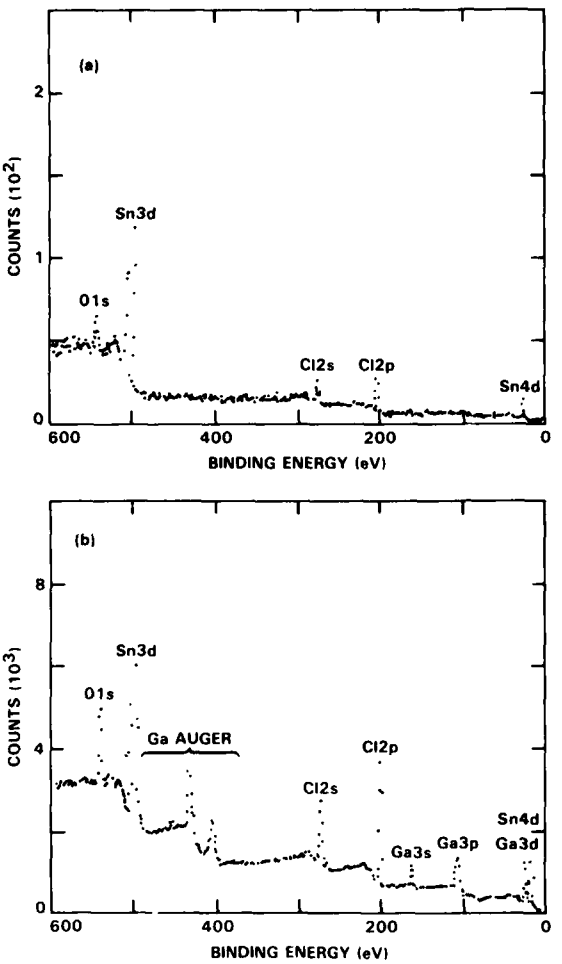

FIG. 5. XPS spectra for films from UV photolytic deposition from $SnCl_4$: (a) thick film and (b) thin film.

C. Dibutyltin dibromide

A brief screening experiment with DBTB was performed. DBTB adsorbed, but similar to the above organometallic compounds, it pyrolytically decomposed, thus ruling it out as a selected area dopant source. Also, under UV irradiation with a Hg lamp, it produced a Sn film.

D. Stannic chloride

Stannic chloride was the only inorganic compound evaluated in this investigation. $SnCl_4$ adsorbed at approximately the monolayer level as determined by AES. Its desorption characteristics are shown in Fig. 3. It partially desorbs, but eventually decomposes with no Cl observed at the surface. C–V profiles after regrowth showed that Sn did incorporate into the GaAs material as a dopant, as expected.

One $SnCl_4$ adsorption was done on a GaAs surface which had been thermally cleaned at a temperature which was not high enough to desorb the Ga oxide. Adsorption on this Ga oxide surface (Fig. 2) resulted in Sn, but little Cl on the surface, especially when compared with adsorption on the clean surface. One explanation could be that the $SnCl_4$ reacted with the Ga oxide to produce Sn oxide with liberation of Cl_2.

UV photolysis was done in a sealed ampoule using Hg lamp irradiation. This produced a thick film which con-

tained Sn, Cl, a little oxygen, and no carbon (Fig. 5). In another experiment, a thin film of ~30 Å was deposited, such that the substrate core levels could be seen by XPS (Fig. 5). It is known that the surface treatment given the sample yields about equal amounts of As and Ga within the XPS sampling depth.[23] However, for the sample which had undergone UV photolytic deposition of Sn, the Ga/As ratio was ~30:1. This suggests that at the interface, UV photolytic etching may have occurred. The UV photolysis may have decomposed $SnCl_4$ into excited Sn atoms and radical Cl_2 species with the chlorine species etching the surface, producing volatile As chlorides and nonvolatile Ga chlorides.

IV. CONCLUSIONS

The main results of this study are (1) MBE GaAs can be doped with Sn from a vapor phase source, (2) Sn films can be UV photolytically deposited from all four of the Sn compounds investigated in this work, (3) each of the Sn molecules adsorbed on GaAs (001) surfaces at room temperature, (4) each compound pyrolytically decomposed before desorbing, and (5) there appear to be complicated interface interactions occurring on adsorption, desorption, and pyrolysis of these Sn-containing molecules on GaAs surfaces, which must be understood before practical application can be undertaken. Because the pyrolytic decomposition resulted in Sn films over the entire epilayer surface, none of the Sn compounds thus far investigated were found to be suitable for use in the proposed selected area doping scheme.

The key to further development of this proposed selected area doping process would be to find a Sn molecule which desorbs before it pyrolytically decomposes (i.e., one with stronger Sn–ligand bonding), but which is still very weakly physisorbed to GaAs (001). Other approaches to selective area doping may be possible. We have recently performed preliminary adsorption/desorption experiments on an As overlayer on GaAs, where it appears that the Sn molecule (DBTB) is more weakly adsorbed to the amorphous As surface than to the GaAs(001) surface. This suggests a selected area doping process that consists of making an As cap,[24] patterning the cap (e.g., by laser or electron beam desorption), adsorption of the desired Sn molecule, and thermal treatment (~580 °C) which in the As capped areas results in clean GaAs via desorption of As and Sn molecules, and in the uncapped area results in metallic Sn via pyrolytic decomposition of the Sn molecule. GaAs regrowth would produce Sn doping in the selected areas. This approach is actually a hybrid of the method investigated in this paper and a previously proposed method[25] which involved As capping. This new approach would surmount the problem encountered here due to pyrolysis; it would, in fact, use pyrolytic decomposition to advantage and avoid the limitation due to the metallic Sn desorption mechanisms from As[26] in the earlier As cap technique. We are investigating this new approach in more detail.

ACKNOWLEDGMENTS

This work was supported by the Army Research Office, Research Triangle Park, N. C. The help of Dr. K. Hess in handling of organometallic compounds and of L. A. Wood for substrate preparation are greatly appreciated.

[1] D. J. Ehrlich, R. M. Osgood, and T. F. Deutsch, IEEE J. Quantum Electron. **QE-16**, 1233 (1980).
[2] R. M. Osgood, Annu. Rev. Phys. Chem. **34**, 77 (1983).
[3] D. J. Ehrlich and J. Y. Tsao, J. Vac. Sci. Technol. B **1**, 969 (1983).
[4] M. W. Jones, L. J. Rigby, and D. Ryan, Nature **212**, 177 (1966).
[5] T. F. Deutsch, D. J. Ehrlich, and R. M. Osgood, Appl. Phys. Lett. **35**, 175 (1979).
[6] D. J. Ehrlich and R. M. Osgood, Chem. Phys. Lett. **79**, 381 (1981).
[7] R. D. Coombe and F. J. Wodarczyk, Appl. Phys. Lett. **37**, 846 (1980).
[8] J. G. Eden, J. E. Greene, J. F. Osmundsen, D. Lubben, C. C. Abele, S. Gorbatkin, and H. D. Desai, Mater. Res. Soc. Symp. Proc. **17**, 185 (1983).
[9] Y. Rytz-Froidevaux, R. P. Salathé, H. H. Gilgen, and H. P. Weber, Appl. Phys. A **27**, 133 (1982).
[10] P. K. Boyer, C. A. Moore, R. Solanki, W. K. Ritchie, G. A. Roche, and G. J. Collins, Proc. SPIE **385**, 120 (1983).
[11] P. J. Love, R. T. Loda, R. A. Rosenberg, A. K. Green, and V. Rehn, Proc. SPIE **459**, 25 (1984).
[12] J. Y. Tsao and D. J. Ehrlich, J. Cryst. Growth **68**, 176 (1984).
[13] J. S. Foord and R. B. Jackman, Chem. Phys. Lett. **112**, 190 (1984).
[14] W. Krüter, D. Bäuerle, and F. Fimberger, Appl. Phys. A **31**, 13 (1983).
[15] C. J. Chen and R. M. Osgood, Appl. Phys. A **31**, 171 (1983).
[16] J. J. Harris, D. E. Ashenford, C. T. Foxon, P. J. Dobson, and B. A. Joyce, Appl. Phys. A **33**, 87 (1984).
[17] C. E. C. Wood and B. A. Joyce, J. Appl. Phys. **49**, 4854 (1978).
[18] A. Rockett, T. J. Drummond, J. E. Greene, and H. Morkoç, J. Appl. Phys. **53**, 7085 (1982).
[19] F. Alexandre, C. Raisin, M. I. Abdalla, A. Brenac, and J. M. Masson, J. Appl. Phys. **51**, 4296 (1981).
[20] Materials were obtained from Alfa Products, Danvers, Mass., as high purity liquids.
[21] Polaron Instruments semiconductor profile plotter. See, for example, T. Ambridge and M.M. Faktor, J. Appl. Electrochem. **5**, 319 (1975).
[22] SIMS analysis was performed at Charles Evans and Associates, San Mateo, Calif.
[23] R. W. Grant, S. P. Kowalczyk, J. R. Waldrop, and W. A. Hill, in *Proceedings of the International Conference on the Physics of MOS Insulators*, edited by G. Lucovsky, S. T. Pantelides, and F. L. Galeener (Pergamon, New York, 1980), p. 202.
[24] S. P. Kowalczyk, D. L. Miller, J. R. Waldrop, P. G. Newman, and R. W. Grant, J. Vac. Sci. Technol. **19**, 255 (1981).
[25] D. L. Miller, U.S. Patent No. 447 901 92.
[26] N. J. Kawai, T. Nakagawa, T. Kojima, and K. Ohta, in Proceedings of the 3rd International Conference on MBE, San Francisco, 1984, p. 7.

Large modification of the surface-enhanced Raman scattering of pyridine on Ag surfaces by Pd submonolayers

T. Lopez-Rios and Y. Gao
Laboratoire d'Optique des Solides, U.A. CNRS 781, Université P. et M. Curie 4, Place Jussieu 75230 Paris Cédex 05, France

(Received 18 March 1985; accepted 21 May 1985)

We report on a large decrease of surface-enhanced Raman scattering (SERS) of pyridine on cold and island Ag films due to Pd submonolayers. In contradistinction, it is shown that very thin (~ 1 monolayer) Ag deposits give rise to SERS unobserved before the Ag deposition. Auger and reflectivity measurements are also presented.

I. INTRODUCTION

It is almost clear today that the enhancement of electromagnetic fields at a rough surface is a necessary condition to SERS. Many experimental observations show a link between SERS and the optical characteristics of the surfaces. For instance SERS, Rayleigh scattering, and optical absorption present identical variations with the thickness of discontinuous films[1] and the SERS excitation spectra peak at the same frequency as optical absorption of rough surfaces[2,3] or of colloidal particles.[4] Experiments with molecules, spaced from the metal surface by low Raman cross section layers, show that Raman enhancement is long ranged as expected for an electromagnetic effect.[5] Beside these well established facts indicating that SERS is due to a field amplification at the surface, valuable electromagnetic models are unable to unambiguously explain some striking results. Let us recall some of them here. SERS is not observed for methane, ethane, and propane physisorbed on quenched Ag films at 11 K.[6] Another surprising observation is the irreversible decrease of the enhancement factor when Ag electrodes are polarized in the nonfaradic region at more cathodic potentials than the potential of zero charge.[7,8] Moreover, SERS studies of electrodes show that underpotential deposition of Tl and Pb irreversibly suppress SERS[9] and that several species present at the electrode could compete in the Raman enhancement.[10] These results, among others, show that the chemical bonding of the molecule to the surface is an important parameter of SERS.

In our laboratory we are, at present, investigating the influence on SERS of very thin metal deposits on Ag surfaces under ultrahigh vacuum (UHV) conditions. In this way we hope to estimate how important the chemical contribution is to SERS. We have already shown that Al submonolayers give rise to some frequency shift and intensity decrease of the pyridine lines, the out-of-plane modes being less modified than the vibration in the pyridine plane.[11] We have already observed[12] that Pd adsorbates produce a very pronounced quenching of SERS of pyridine on Ag surfaces and that very thin Ag deposits (< 1 monolayer) partially restore the SERS suppressed by the Pd atoms. We report now on supplementary experiments on such effect and we discuss, on the basis of optical experiments, the limits of a possible explanation by a broadening of the surface electromagnetic resonances by the Pd overlayers.

II. EXPERIMENTAL

The experiments were performed in an ultrahigh vacuum system equipped with a LEED-Auger spectrometer.[13] A spectrophotometer attached to the vacuum chamber allows the reflectivity and differential reflectivity measurements.[13,14] A collecting optic inside the vacuum chamber allows the SERS investigations. A 164 Spectra Physics Ar^+ laser, providing the 5145 Å line with a power of 300 mW on the sample, was used for the present experiments. The exciting light was p polarized and the scattered light was collected disregarding the eigenstates of polarization. The monochromator (Jobin–Yvon MRD1) slits were adjusted for a resolution of 4 cm^{-1}. Experimental details are given elsewhere.[11]

The sample was either cold Ag films 10^3 Å thick quenched on a polished glass substrate at 120 K, or Ag island films deposited on glass at room temperature. A double crucible evaporation system, with a 5 MHz Sloan oscillating quartz thickness monitor allowed an accurate control of the metal deposits. Pd and Ag coverages could be monitored with a precision of about 0.03 monolayers.

III. RESULTS AND DISCUSSION

A. Reduction of SERS by Pd adsorbates

In first type of experiments, cold Ag films (10^3 Å thick) were exposed to pyridine and subsequently covered by different amounts of Pd. Figure 1(a) shows the SERS spectrum for such a cold film exposed to 3 L uncorrected langmuirs (1 $L = 10^{-6}$ Torr s) of pyridine. This exposure corresponds to a pyridine coverage of about 1/3 monolayer, as determined from Auger and optical measurements in agreement with reported experiments.[15] The wave numbers of the main pyridine lines are indicated on Fig. 1 (in all figures in this paper the Raman spectra were arbitrarily placed on the vertical axis). The spectra for subsequent Pd overlayers (0.7 Å and 1.5 Å thick) deposited on the sample at 120 K, previously exposed to pyridine, are given in Figs. 1(b) and 1(c). Pd overlayers produce a drastic decrease of the intensity and a broadening of the pyridine lines. A Pd overlayer 0.70 Å thick, reduces by 10 the intensity of the ν_1 (1006 cm^{-1}) ring breathing mode and by about eight the area under the peak, while the pyridine lines are nearly suppressed for a Pd layer 1.5 Å thick. Probably some pyridine is desorbed by the impinging Pd atoms but this should not be an important contri-

 0734-211X/85/051539-04$01.00

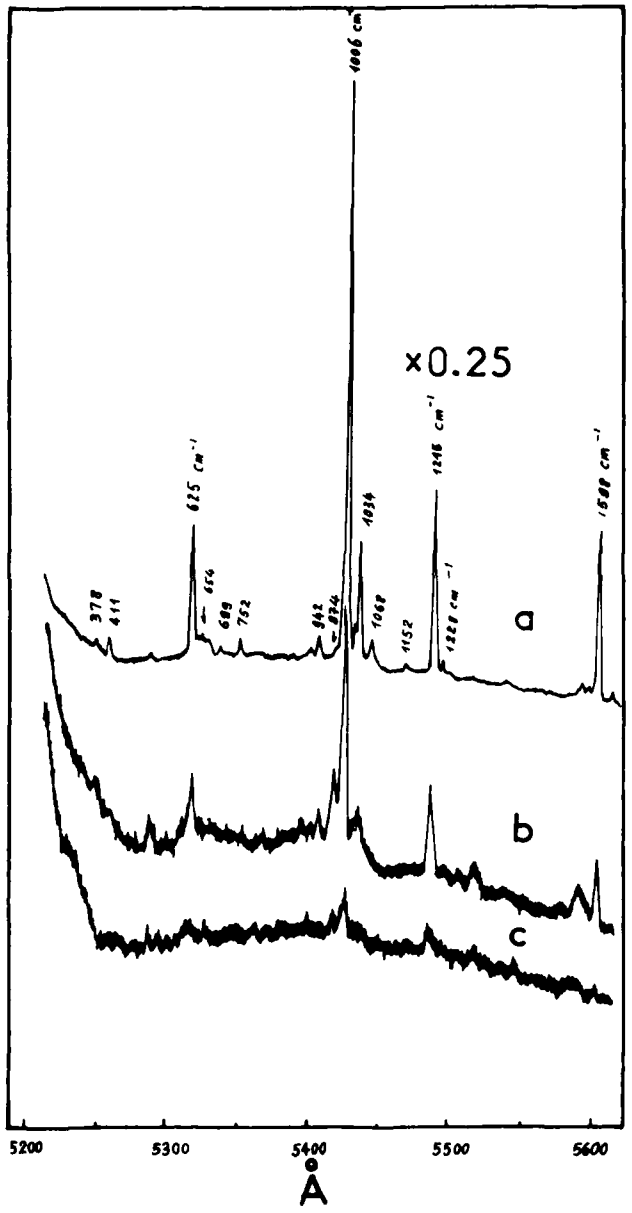

FIG. 1. SERS spectra for a "cold" film exposed to (a) 3 L of pyridine after the deposition of Pd layers (b) 0.7 Å and (c) 1.5 Å thick.

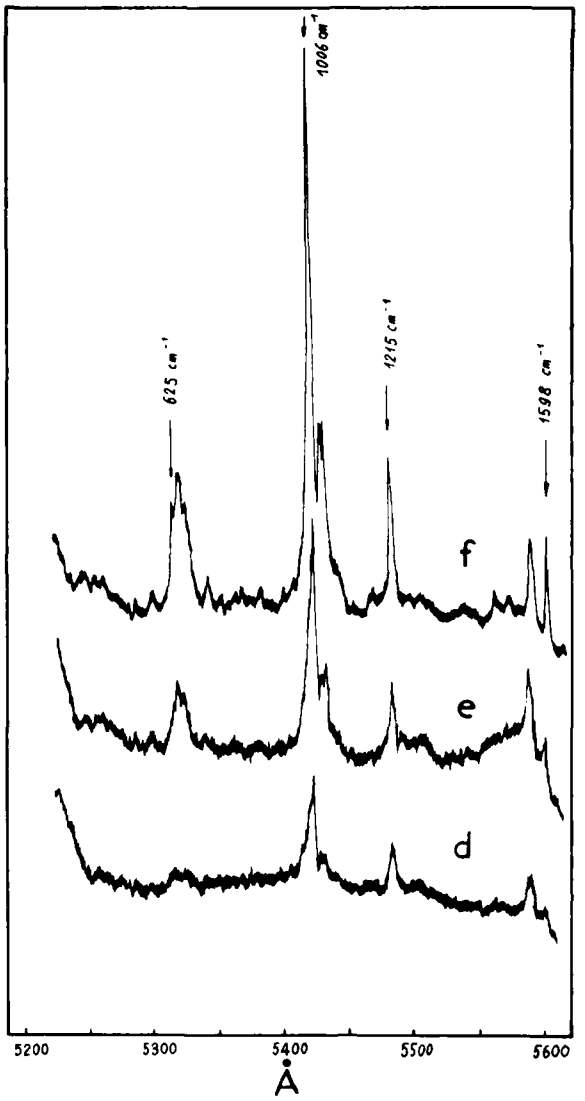

FIG. 2. SERS spectra when the sample [Fig. 1(c)] is (d) reexposed to 3 L of pyridine and for (e) subsequent Ag deposits 1.4 A, and (f) 2.9 A thick.

bution to the observed effect. The spectrum d in Fig. 2 corresponding to the sample reexposed to 3 L of pyridine clearly indicates that SERS activity was irreversibly lost with the Pd overlayers. Later on we will show that, on the contrary, very thin Ag deposits produce an increase of SERS. Concerning possible pyridine desorption, we can expect similar effects for impinging Pd or Ag atoms. In conclusion we can definitely admit that pyridine desorption is not the observed effect in our experiments.

B. Increase of SERS by Ag adsorbates

Figures 2(e) and 2(f) show the increase of SERS of the sample 2(d) by silver layers 1.4 and 2.9 Å thick. After the reduction of SERS by Pd submonolayers, subsequent Ag deposits appreciably increase the SERS intensity [Figs. 2(e) and 2(f)]. The spectral positions of the four main lines of pyridine of Fig. 1 are indicated by arrows on Fig. 2. The observed broadening of the lines can be due to pyridine bonded to different surface atoms (Pd and Ag) leading to a different shift of the Raman lines. We found that the intensity of the B2 out-of-plane mode of pyridine ν_{22} (973 cm^{-1}) is only weakly reduced by the Pd layers. The ratio of the intensity of the in-plane breathing mode ν_1 (1006 cm^{-1}) to the intensity of this mode ν_{22} (973 cm^{-1}) is about 36 in Fig. 1(a) and 4 with a Pd overlayer 0.7 Å thick [Fig. 1(b)]. We also observe a peak of unknown origin at 1544 cm^{-1}.

Identical results were obtained when the substrate was an island film instead of a cold film. We have also checked that a quenching by Pd overlayers and reenhancement by Ag atoms occurs when Pd is deposited prior to pyridine exposures. Figure 3(a) displays the spectrum for an Ag island film mass thickness 60 Å, prepared at room temperature, then cooled to 120 K and covered at this temperature by 4.6 A of

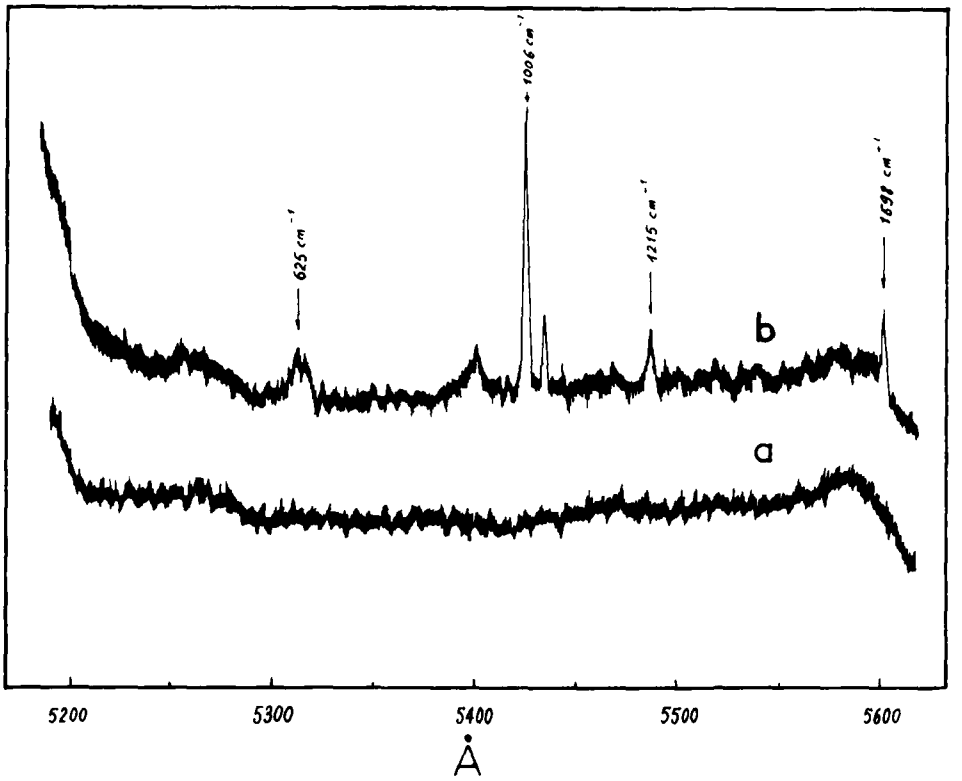

FIG. 3. (a) Spectrum for an island film of mean thickness of 60 Å, produced at room temperature, after cooled to 120 K and covered at this temperature by 4.6 Å of Pd and immediately afterwards exposed to 3 L of pyridine. (b) Spectrum for a subsequent deposit of 4.1 Å of Ag.

Pd (~2 monolayers), and immediately afterwards exposed to 3 L of pyridine. A subsequent deposit of 4.1 Å of Ag produces a nice appearance of the usual SERS lines of pyridine [Fig. 3(b)].

For a quenched Ag film (700 Å thick), we have followed the intensity of the main Ag (356 eV) and Pd (330 eV) Auger peaks as a function of the increasing thickness of the Pd deposits. Figure 4 shows the peak-to-peak Auger signals versus Pd coverages for the first derivative spectrum. The intensity is given in arbitrary units and the scale is different for each peak. We have found that Pd grows on Ag monolayer by monolayer and that, even for such poorly crystallized films, a slope break characteristic of the completion of the first monolayer is clearly shown for 2.38 Å of Pd. Concerning the problem at hand, Fig. 4 indicates that Pd adsorbates should not modify the macroscopic structure of the sample and that a possible clustering of Pd at atomic faults should be of microscopic dimensions.

C. Reflectivity measurements

It is most important to know whether our results can be understood on the frame of electromagnetic models. Murray[16] has shown that Raman scattering of cyanide species, adsorbed on Ag island films, decreases in intensity with increasing thickness of Au overlayers and she explained this result by considering an electrostatic model of Ag ellipsoids coated with Au overlayers. Roughly speaking, gold coatings damp the plasma resonances of the ellipsoidal particles and, in consequence, the electromagnetic field at the surface.[17,18] We believe that in our case, such a model, at least considering a macroscopic description of electromagnetic fields at the surface of the particles, cannot completely explain our results but only a small fraction of the observed decrease of SERS. Our conviction is based on the fact that the electric fields inside the particles are proportional to the optical absorption. Boundary conditions imply a straightforward relation between the fields outside the particles and the inner fields. In conclusion, a large decrease of field enhancements should be accompanied by a noticeable modification of optical absorption. For instance, for a silver sphere of 100 Å radius, a Pd overlayer 1 Å thick reduces the intensity of the external fields by a factor of 2.4 and the optical absorption by 1.6 at the resonance (3.5 eV).

We have measured the square of the reflectivity for p-polarized light at an incidence of 55° for a cold Ag film 1000 Å thick (R_0) for the same film covered by Pd overlayers 2.3

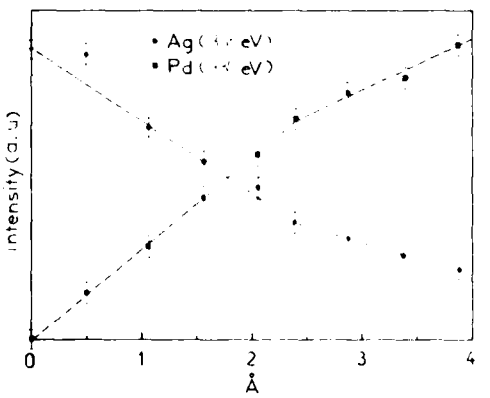

FIG. 4. Amplitude of the Auger peak of Pd and Ag vs the Pd coverage determined by a calibrated quartz microbalance.

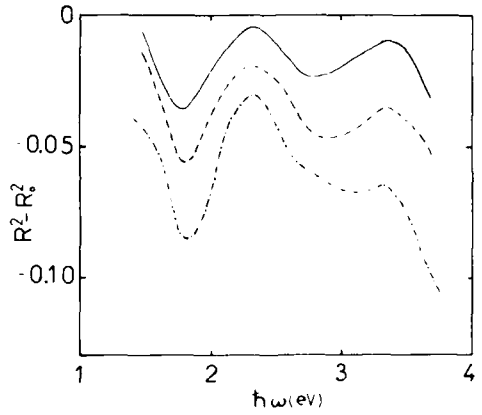

FIG. 5. $R^2 - R_0^2$ vs photon energy for a cold film 10^4 Å thick at 120 K. R_0 is the reflectivity for the clean Ag surface and R for the surface with adsorbates; Pd layers 2.3 Å (continuous line) and 4.6 Å (dashed line) thick and subsequent exposure to 7 L of pyridine (dotted dashed line). The light was p-polarized and the incidence was 55°.

and 4.6 Å thick and for a subsequent exposure of 7 L of pyridine (R^2). Figure 5 displays R^2–R_0^2 versus the energy of light. We have R^2–$R_0^2 \simeq 2R_0\Delta R$, where $\Delta R = R - R_0$ is the reflectivity change induced by the adsorbates. We see that the reflectivity changes produced by 1 Pd monolayer are smaller than 2%. On the contrary, the supplementary optical absorption of cold films, attributed to electromagnetic resonances, is greater than 20%[14,19–21] and still clearly observed in our experiments after the Pd deposition.

Two optical absorptions are clearly observed on Fig. 5; one at 1.85 eV and another one at ~3 eV. Identical results were obtained by Lopez-Rios *et al.* for Al and Cu adsorbates.[3] Similar observations were reported by Garoff *et al.*[22] and Glass *et al.*[23] for several dye molecules on island films. Such an absorption found independent of the nature of the surface atoms is, in our opinion, indicative of the spectral distribution of the electromagnetic field intensity at the surface. It should be noticed that the abnormal optical absorption of quenched Ag films is centered at 2.5 eV, whereas the absorption induced by the surface layers has a minimum. This point, not well understood by us, cannot be explained with simple models of isolated particles. Particle interaction rises with supplementary optical absorption and large fields between particles[24] and should probably be taken into account for a realistic description of rough surfaces employed in the present experiments.

IV. CONCLUSIONS

We have shown that submonolayer metal coverages can induce large modifications of the Raman enhancements. Our experiments in ultrahigh vacuum corroborate the important observation of a quenching of SERS at electrodes by some underpotentially deposited metal. We also show that very thin Ag layers can produce large increase of SERS. We definitely show that surfaces with identical macroscopic roughness can present very different Raman enhancements. We conclude that our results cannot be fully understood on the basis of electromagnetic resonances of isolated particles.

ACKNOWLEDGMENT

We thank Dr. Kai Ming Ho for stimulating discussions about optical absorption resonances on quenched Ag films.

[1] J. G. Bergman, D. S. Chemla, P. F. Liao, A. M. Glass, A. Pinczuk, R. M. Hart, and D. H. Olson, Opt. Lett. **6**, 33 (1981).
[2] A. Girlando, J. G. Gordon II, D. Heitmann, M. R. Philpott, H. Seki, and J. D. Swalen, Surf. Sci. **101**, 417 (1980).
[3] T. Lopez-Rios, Y. Borensztein, and G. Vuye, J. Phys. C **44**, 10 (1983).
[4] J. A. Creighton, in *Surface Enhanced Raman Scattering*, edited by R. K. Chang and T. E. Furtak (Plenum, New York, 1982), p. 315.
[5] C. A. Murray, in Ref. 4, p. 203.
[6] D. P. Dilella and M. Moskovits, J. Phys. Chem. **85**, 2042 (1981).
[7] J. F. Owen, T. T. Chen, R. K. Chang, and B. L. Laube, Surf. Sci. **131**, 195 (1983).
[8] R. K. Chang and B. L. Laube, CRC Crit. Rev. Solid State Sci. **12**, 1 (1984).
[9] J. Watanabe, N. Yanagihara, K. Honda, B. Pettinger, and L. Moerl, Chem. Phys. Lett. **96**, 649 (1983).
[10] T. E. Furtak and D. Roy, Phys. Rev. Lett. **104**, 59 (1983).
[11] T. Lopez-Rios, Y. Gao, and G. Vuye, Chem. Phys. Lett. **111**, 249 (1984).
[12] Y. Gao and T. Lopez-Rios, Phys. Rev. Lett. **53**, 2583 (1984).
[13] T. Lopez-Rios and G. Vuye, J. Phys. E **15**, 456 (1982).
[14] T. Lopez-Rios, Y. Borensztein, and G. Vuye, Phys. Rev. B **30**, 659 (1984).
[15] I. Pockrand, Chem. Phys. Lett. **92**, 509 (1982).
[16] C. A. Murray, J. Electron Spectrosc. Relat. Phenom. **29**, 371 (1983).
[17] R. R. Bilboul, Br. J. Appl. Phys. **2**, 921 (1969).
[18] M. Kerker, *Scattering of Light and Other Electromagnetic Radiation* (Academic, New York, 1969).
[19] O. Hunderi and M. P. Myers, J. Phys. F **3**, 683 (1973).
[20] P. M. McBreen and M. Moskovits, J. Appl. Phys. **54**, 329 (1983).
[21] A. Otto, I. Pockrand, J. Billmann, and C. Pettenkofer, in Ref. 4, p. 147.
[22] S. Garoff, D. A. Weitz, J. J. Gramila, and C. D. Hanson, Opt. Lett. **6**, 245 (1981).
[23] A. M. Glass, P. F. Liao, J. G. Bergman, and D. H. Olson, Opt. Lett. **5**, 368 (1981).
[24] P. K. Aravid, A. Nitzan, and H. Metiu, Surf. Sci. **110**, 189 (1981).

Doppler shift laser fluorescence spectroscopy of sputtered and evaporated atoms under Ar^+ bombardment

W. Husinsky, I. Girgis, and G. Betz
Institut für Allgemeine Physik, Technische Universität Wien, Karlsplatz 13, A-1040 Wien, Austria

(Received 15 February 1985; accepted 11 April 1985)

The temperature dependence of the sputtering yield and velocity distribution of sputtered neutral Ca and Cr atoms has been studied by Doppler shift laser fluorescence spectroscopy (DSLFS) for 15-keV-Ar^+ ion bombardment.These investigations have been performed in the search for thermal spike effects and radiation-enhanced sublimation in sputtering at elevated temperatures. Ca targets have been studied up to about 270 °C and Cr targets up to 750 °C. The shapes of the velocity distributions do not change in the respective temperature ranges for both target materials. Furthermore, the absolute yield of sputtered neutral ground state atoms does not increase with temperature.This indicates that no radiation-enhanced thermal contribution is of relevant importance. Moreover, we can explain the velocity distributions in both cases by the linear cascade theory of sputtering. The thermal contribution due to thermal evaporation increases drastically above 230 °C for Ca and 550 °C for Cr. In both cases the corresponding velocity distribution can be fitted by a Boltzmann distribution.

I. INTRODUCTION

Recently there has been a lot of discussion, whether sputtering from thermal elastic-collision spikes[1,2] can be observed at elevated temperatures for bombardment with heavy ions as Ar^+ in the keV energy range. Effects attributed to sputtering from thermal elastic-collision spikes at elevated target temperatures under these conditions have been reported by Nelson[3] and Ahmad *et al.*[4] In these papers drastically increased sputtering yields for different metals (Au, Al, and Cu) at elevated target temperatures for 30-keV-Xe^+ and Ar^+ bombardment have been reported. In these experiments the target temperatures used can be best characterized by the vapor pressure of the respective material. Measurements have been performed up to temperatures corresponding to approximately a few times 10^{-10} bar vapor pressure. Furthermore, an increasing low energy contribution in the time-of-flight velocity spectrum has been observed[4] and attributed to sputtering by thermal spikes for Ar^+ and Xe^+ bombardment of polycrystalline gold targets. On the other hand, contradicting results have been obtained by Besocke *et al.*[5] and Hofer *et al.*[6] No increased sputtering yields for silver targets have been observed in their experiments neither for 10-keV-Argon and Xenon ion bombardment nor for 45-keV-heavy ion and molecular ion bombardment at high target temperatures. Furthermore, very interesting results have been recently obtained for high temperature sputtering of carbon.[7–9] Increasing sputtering yields by factors 10–20 have been found for carbon above 1100 K due to radiation enhanced sublimation. The energy distribution of these additionally released particles is clearly thermal.[7] Radiation-enhanced sublimation is also established for sputtering of alkali halides.[10] Furthermore, we have found evidence of radiation-enhanced evaporation for sputtering of Na at elevated temperatures.[11] For Na it is not easy to decide whether this effect is rather due to Na metal or Na oxide, however.

DSLFS with cw dye lasers[10–12] offers an excellent tool to tackle the problematic described above. It allows to measure the velocity distribution of sputtered particles with a high accuracy and therefore, to distinguish between thermal and other contributions to the velocity spectrum. Of great advantage also is the selectivity in respect to the atomic species and the electronic state. And most important in the particular case, by chopping the ion beam and using a lock-in technique for detecting the fluorescence signal, a perfect discrimination between thermally evaporated atoms and atoms released by radiation-induced processes can be achieved.

Therefore, we have measured the velocity spectra of sputtered Ca and Cr ground state atoms for target temperatures between room temperature and 270 °C for Ca and 750 °C for Cr under 15-keV Argon ion bombardment.

II. EXPERIMENTAL

The DSLFS spectrometer used is identical with the one described in other papers.[13,14] The angle of incidence of the ion beam was 50°. The sputtered particle beam was defined by a diaphragm 2.5 cm away from the target surface with a diameter of 3 mm. The angle was 55° to the target normal in the forward direction. The interaction volume with the laser beam was 5 cm in front of the target. In addition to the setup described there, the target could be heated by an ohmic thermo-coax wire up to about 800 °C. The target temperature could be measured by a thermocouple. In addition, the target temperatures for elevated temperatures could be determined from the maximum of the velocity distribution of evaporated atoms. Both temperature measurements were in good agreement. The 15-keV mass-separated Ar^+ ion beam was periodically deflected by capacitor plates and a lock-in technique applied. During ion bombardment the residual gas pressure in the chamber was below 3×10^{-8} mbar.

Both, Ca and Cr have strong resonance transitions from the electronic ground state. Ca has been excited at 422.6 nm ($A_{12}=2.1\times10^8$ s^{-1}) and Cr at 425.4 nm ($A_{12}=0.3\times10^8$ s^{-1}). The 699-21 ring dye laser has been operated with a Stilben 3 dye. Both transition lines represent ideal two level

 0734-211X/85/051543-03$01.00

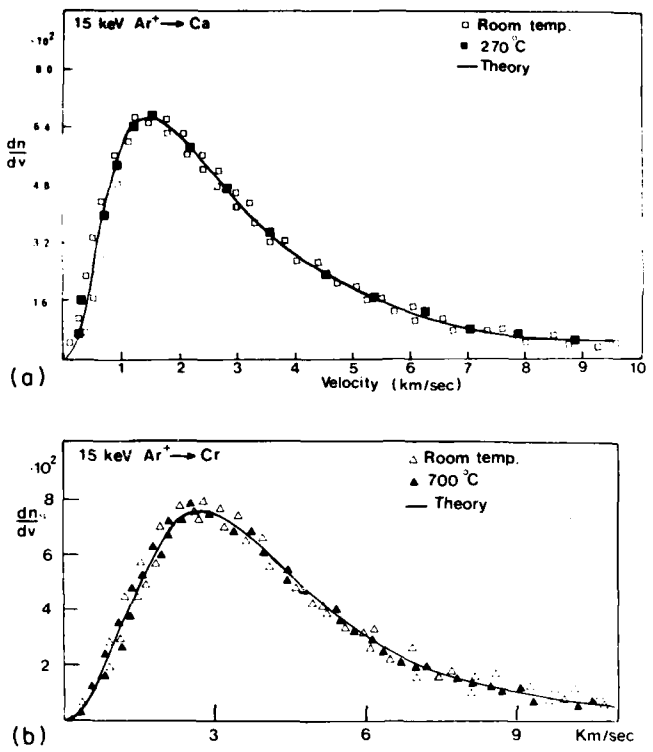

FIG. 1. Velocity distributions of sputtered neutral ground state atoms at room temperature and elevated temperatures (a) Ca and (b) Cr. No measurable difference in the shape of the velocity distributions could be observed between room temperature and high temperature sputtering. The measured spectra are compared with the theoretical distribution [Eq. (1) in the main text] due to elastic collision sputtering.

systems. In this case the measured fluorescence signal is directly proportional to the number density distribution dn/dv over the entire velocity range.[12]

III. RESULTS

The velocity distributions of sputtered Ca and Cr ground state atoms at room temperature are shown in Fig. 1. In both cases linear cascades dominate the sputtering process. The number density velocity distribution $dn_{sp}(v)/dv$, according to the Sigmund theory, can be written in the form

$$dn_{sp}(v)/dv = v^2/(v^2 + v_b^2)^3, \tag{1}$$

where v_b is the velocity corresponding to the surface binding

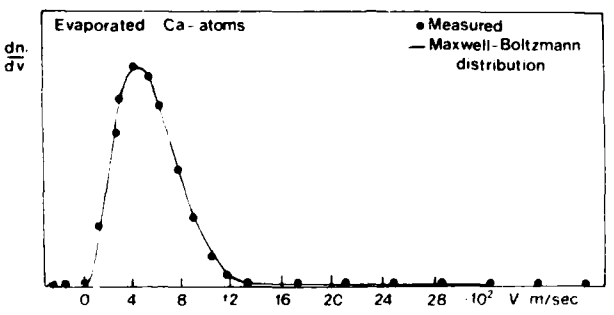

FIG. 2. Velocity distribution of evaporated Ca atoms at 270 °C. The measured spectrum is fitted with the Maxwell-Boltzmann distribution (2).

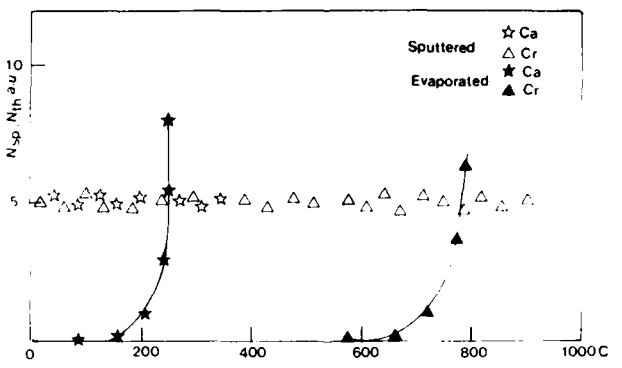

FIG. 3. Number density N_{sp} of sputtered and N_{th} of evaporated Ca and Cr atoms in arbitrary units as a function of the target temperature.

energy E_b. The fit of the measured distributions with the theoretical distribution (1) is shown in Fig. 1 and is very good. From the best fit an E_b of 1.3 eV for Ca was obtained. This value is on good agreement with the heat of sublimation of Ca. For Cr the E_b values obtained varied between 2 and 4 eV depending on the target treatment.[14] The heat of sublimation of Cr is tabulated with 4.3 eV. The deviations of the measured E_b values for Cr are definitely not within the experimental error and have been discussed in Ref. 14. The target temperature was slowly increased to approximately 280 °C for Ca and 750 °C for Cr targets and decreased to room temperature in several repetitive cycles. Velocity spectra have been recorded during these cycles. Examples of velocity distributions at elevated temperatures are also shown in Fig.1 and are in fact identical with the distributions obtained at room temperature.

At this point one remark is necessary. Great care has to be taken in respect to the target composition before starting the temperature cycles. If the target has been originally contaminated by oxygen or carbon, the heating procedure under simultaneous ion bombardment will remove most of the oxygen and carbon layers.[14] Because of the extreme sensitivity of the velocity distribution and the neutral ground state densities to surface oxidation[13,14] in particular, the heating of the target might result in changes of the shape of the velocity distribution and also the sputtered neutral atom densities if the target has been originally contaminated.

In addition we have recorded velocity distributions of evaporated atoms without ion bombardment but otherwise identical conditions. For Ca a sizable amount of evaporated atoms has been found for target temperatures above 150 °C. For Cr the thermal evaporation started between 650 and 700 °C. The velocity distribution of these evaporated atoms can be fitted with high accuracy by a Maxwell–Boltzmann distribution

$$dn_{th}(v)/dv = v^2 \exp(-v^2/x^2), \tag{2}$$

where

$$x = \sqrt{2kT/m} \tag{3}$$

is the most probable velocity and m the mass of the atoms, as shown in Fig. 2. The target temperatures obtained from these spectra agree very well with the temperatures measured with a thermocouple.

The densities for Cr and Ca atoms removed from the tar-

get due to sputtering and due to evaporation are shown in Fig. 3 as a function of the target temperature.

IV. CONCLUSIONS

DSLFS measurements of the sputtered neutral particle flux from Ca and Cr targets show that for argon ions, medium energy bombardment of these materials no thermal spike contributions and no thermal-enhanced radiation exist. The melting point of Ca is 839 °C and of Cr is 1857 °C. The vapor pressure of Ca and Cr is 10^{-10} bar at 314 °C and 902 °C, respectively. The results shown in Fig. 3 clearly show that the sputtering yield for neutral ground state atoms remains constant over the entire temperature range. Evaporation of neutral atoms starts slightly below temperatures corresponding to a vapor pressure of the material of 10^{-10} bar. At temperatures corresponding to a vapor pressure of 10^{-10} bar particle release due to evaporation is already the dominant contribution.

Our results are in good agreement with the results by Besocke *et al.*,[5] who also observed no thermal spike effects for 8 keV Ar^+ bombardment of Ag. Similar to our experiments thermal evaporation was found to dominate particle removal from the surface at temperatures where the vapor pressure of the material exceeds 10^{-10} bar. As any nonlinear or high-density cascade effects should be clearly visible in the energy distribution of the ejected particles, we conclude that at least for medium mass, medium-energy sputtering such effects do not exist and cannot be provoked by a temperature increase of the target. Even at temperatures where particle ejection due to thermal evaporation dominates, the cascade is not influenced by it. This can of course be easily understood, as the energy per lattice atom during evaporation is much smaller than the typical energy of an atom in the collision cascade, which might eventually lead to sputtering.

In conclusion, we can say that that radiation-enhanced evaporation has been clearly identified to be a contributing factor to the particle release for materials where interstitial-vacancy pairs are created by the incoming ions. Examples are alkali halides[10,15] and graphite.[9] On the other hand no radiation-enhanced evaporation or spike effects could be identified in the velocity spectra of metals, with the one possible exemption for Na.

ACKNOWLEDGMENT

This work was supported by the Austrian "Fonds zur Förderung der wissenschaftlichen Forschung" under project No. 4547.

[1]P. Sigmund and C. Claussen, in *Proceedings of the Symposium on Sputtering*, Perchtoldsdorf, Austria, edited by P. Varga, G. Betz, and F. Viehböck (1980).
[2]D. A. Thompson, in *Proceedings of the Symposium on Sputtering*, Perchtoldsdorf, Austria, edited by P. Varga, G. Betz, and F. Viehböck (1980).
[3]R. S. Nelson, Philos. Mag. **11**, 291 (1965).
[4]S. Ahmad, B. W. Farmery, and M. W. Thompson, Nucl. Instrum. Methods **170**, 327 (1980).
[5]K. Besocke, S. Berger, W. O. Hofer, and U. Littmark, Radiat. Eff. **66**, 35 (1982).
[6]W. O. Hofer, K. Besocke, and B. Stritzker, Appl. Phys. A **30**, 83 (1983).
[7]E. Vietzke, K. Flaskamp, M. Hennes, and V. Philipps, Nucl. Instrum. Methods Phys. Res. B **2**, 617 (1984).
[8]J. B. Roberto and R. Behrisch, J. Nucl. Mater. **128&129**, 764 (1984).
[9]J. Roth, J. Bohdansky, and J. B. Roberto, J. Nucl. Mater. **128&129**, 534 (1984).
[10]W. Husinsky and R. Bruckmüller, Surf. Sci. **80**, 637 (1979).
[11]W. Husinsky, R. Bruckmüller, and P. Blum, Nucl. Instrum. Methods **170**, 287 (1980).
[12]W. Husinsky, J. Vac. Sci. Technol. B **3**, 1546 (1985).
[13]W. Husinsky, G. Betz, and I. Girgis, J. Vac. Sci. Technol. A **2**, 689 (1984).
[14]W. Husinsky, G. Betz, I. Girgis, F. Viehböck, and H. Bay, J. Nucl. Mater. **128&129**, 577 (1984).
[15]J. P. Biersack and E. Santner, Nucl. Instrum. Methods. **198**, 29 (1982).

The application of Doppler shift laser fluorescence spectroscopy for the detection and energy analysis of particles evolving from surfaces

Wolfgang Husinsky
Institut für Allgemeine Physik, Technische Universität Wien, Karlsplatz 13, A-1040 Wien, Austria

(Received 15 February 1985; accepted 11 April 1985)

Doppler shift laser fluorescence spectroscopy (DSLFS) has been developed in the last few years as a powerful tool to measure densities and energy distributions of neutral particles. Its main application described in this paper is the study of particles ejected from surfaces under impact of atoms, ions or electrons. Complications and controversies in the interpretation of DSLFS spectra will be discussed. The major achievements and applications of the method over the last few years will be presented. One of the most important results has been a deeper insight into the composition of the particle fluxes ejected from surfaces under ion beam bombardment in respect to the degree of surface oxidation. This has been possible due to the fact that DSLFS enables us to measure the densities and energy distributions of neutral particles in specific electronic states. As a direct consequence, a large amount of information on sputtered excited atoms has recently been obtained by DSLFS.

I. INTRODUCTION

About 10 years ago, the development of tunable dye lasers offered a challenging new aspect for the detection of neutral particles using laser induced fluorescence (LIF). In addition, the extremely small bandwidth of dye lasers, in particular single mode cw dye lasers with only a few MHz linewidth made it possible to utilize the Doppler effect for measuring the velocity distribution of neutral particles (DSLFS).

Although the dye laser has revolutionized the field of spectroscopy since it became commercially available,[1-3] the idea of using lasers had been rather new among scientists working in the field of particle-solid interactions. Nonetheless, the potential and the simplicity of LIF and DSLFS was apparent and a few groups started to develop these methods around 1975. Detection of neutral atoms sputtered from surfaces under ion beam bombardment was of special interest, because most of the released particles are known to be neutral. Two groups pioneered in developing DSLFS spectrometers for measuring sputtered fluxes of neutral atoms.[5-8] More recently, several other groups have also been using DSLFS very successfully for measuring sputtered neutral fluxes,[9,10] detecting desorbed particles,[11] and investigating impurity fluxes in the plasma wall region of fusion machines.[12-16]

The aim of this paper is to describe the technique of DSLFS and to summarize the major achievements of this method as applied in the field of particle-solid interaction. Emphasis will be given on results of our group in Vienna achieved during the last two years. Furthermore, we will discuss the major difficulties connected with the use of DSLFS, which in some cases could lead to a conflicting interpretation of the results, in spite of how simple and straightforward the method might look at first sight.

Finally it should be noted that recently the method of multiphoton resonance ionization spectroscopy has been developed and successfully applied in the field of particle solid interactions. This method can be regarded as a second generation of LIF.[17,18]

II. STATE OF THE ART OF LIF AND DSLFS

A. Experimental method

LIF is based on the resonance excitation of the particles to be investigated by intense laser radiation. The particles are excited to an upper level and decay to lower levels by spontaneous emission which can be detected very efficiently. The combination of intense small bandwidth laser radiation, extremely high resonance excitation cross sections of 10^{-9} cm^2 and efficient photon detection systems[4] results in an extremely high detection sensitivity of LIF. In fact, densities of less than 100 particles/cm^3 could be measured by LIF.[4] A detailed description of the advantages of LIF in comparison to other methods for neutral particle detection can be found elsewhere.[4,19,20]

In addition to LIF, DSLFS makes use of the Doppler-shifted excitation of particles with a nonzero velocity component in the direction of the laser beam. For an atom traveling with a velocity v directed at an angle to the laser beam, its excitation frequency is shifted by an amount of $\Delta\nu$

$$\Delta\nu = v/c \cdot \nu_0 \cos\theta, \tag{1}$$

where ν_0 is the unshifted resonance frequency of the atoms. By tuning the laser over the Doppler profile of these atoms and simultaneous recording of the resulting fluorescence signal the velocity spectrum will directly be obtained. Because of the extremely small bandwidth of the laser, the fluorescence light can be detected without frequency selection. Thus the need of high resolution spectrometers in the detection optic used in conventional spectroscopy, which cause large intensity losses, is eliminated.

B. Laser systems and resolution

Taking a closer look at existing DSLFS spectrometers one has then to distinguish according to the laser type involved. Many DSLFS spectrometers use pulsed dye laser.[9,15] Recently excimer laser pumped dye laser systems have become dominant among these systems. The advantage of using a

 0734-211X/85/051546-14$01.00

pulsed system is evident. The output power of these lasers is high. The visible frequency range can be covered by different dyes. At these high output powers, frequency doubling can be used very efficiently. Thus even the UV frequency range between approximately 200–350 nm can be covered. This is very important, since many atoms possess resonance transitions in this frequency range. However, due to the short pulse time of typically a few ns, the bandwidth of these lasers is Fourier limited. Typically, bandwidths down to several hundred MHz can be achieved. This limits the application of pulsed laser systems to velocity measurements of thermal particles where Doppler shifts in the MHz range can be expected.[4,5,21] Pulsed DSLFS spectrometers have found a wide application for impurity diagnostics in fusion devices.[12–16]

DSLFS spectrometers with frequency stabilized, single mode, tunable cw dye lasers can achieve velocity resolutions down to a few m/s. In most cases their resolution is only limited by the particle beam divergence.[4,6] However, due to the lack of pump lasers, cw dye laser can only be operated from 410 to 700 nm using various dyes and, moreover, frequency doubling is rather difficult.[22] DSLFS spectrometers with cw dye lasers have found their major area of application, where an exact measurement of the velocity distribution is of interest. From the shape of the velocity distribution the different mechanisms contributing to the particle ejection may be deduced.[5,11,21,23]

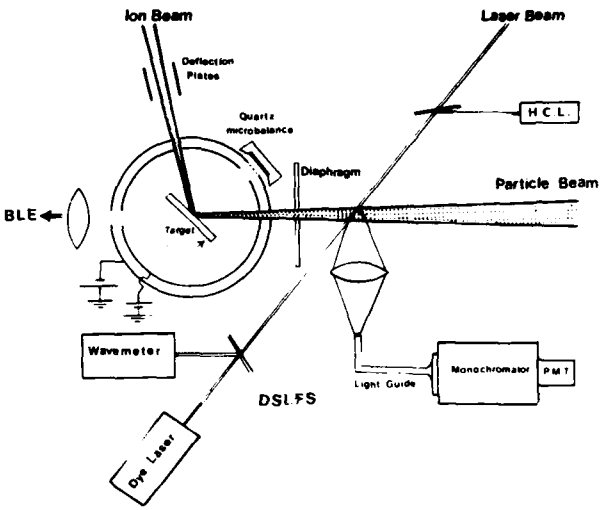

FIG. 1. Schematic diagram of a high-resolution DSLFS spectrometer. The laser spectrometer consists of a 20-W Innova argon ion laser and a 699-21 stabilized ring dye laser system. A hollow cathode lamp can be used for monitoring the exact zero position of transition lines. A mass analyzed ion beam from a duoplasmatron ion source is used for bombarding the target, which can be rotated and is surrounded by two cylindrical shields. Small holes in the cylindrical shield define a sputtered beam direction. The intersection of the laser beam with the particle beam occurs approximately 5 cm from the target surface. Further additional experimental equipment allows to measure the light emission during ion bombardment (BLE) and to collect sputtered particles on a quartz microbalance.

C. Different excitation geometries

We must distinguish two philosophies with respect to the geometrical arrangement used in present-day DSLFS spectrometers. In a typical arrangement, the sputtered particles are excited very close to the target surface.[23] Using this geometry the particle detection sensitivity is very high, due to the large solid angle involved. On the other hand, in this way one sacrifices one of the greatest advantages of DSLFS: the fluorescence signal is now not proportional to the number of particles within the velocity interval corresponding to the laser bandwidth. Instead, the experimental geometry has to be taken into account, because particles move into the observation volume from different directions.[9,24,25] A different approach is shown in Fig. 1, where the particle trajectories are well defined by a system of diaphragms. In this case the particles are excited by the laser beam in a small intersection volume, typically a few cm away from the target in the atomic beam. This geometry offers either the possibility to perform Doppler-free[3] spectroscopy by exciting the atoms at 90° with respect to the particle beam or to excite the atomic beam at many different angles. In this case the measured fluorescence spectrum directly resembles the velocity distribution of particles ejected in the direction defined by diaphragms. As a compromise between maximal Doppler shift for particle and laser beam being collinear with the particle beam and possible experimental realizations an angle between 30° and 45° is usually chosen. However, in this geometry the solid angle is rather small and the fluorescence signals are lower than in the first case.[5,26] The setup shown in Fig. 1 is commonly used for high resolution DSLFS experiments with a cw dye laser. Especially if the atoms under investigation can be excited in a two level scheme, the intensity loss due to the small solid angle can be compensated for by using lock-in techniques and integrating the fluorescence signal over an extended time.

III. SOME PROBLEMS REGARDING THE INTERPRETATION OF DSLFS SPECTRA

A. Saturation, interaction time, and line broadening

Excitation of moving neutral particles by laser radiation has advantageous features compared to excitation by other means, e.g., electrons. The excitation cross section is high and, even more important, independent of the particle velocity. Furthermore, the excitation is extremely selective in respect to atomic species and electronic states. With cw dye lasers bandwidths of 1 MHz can be achieved. This yields a velocity resolution of a few m/s. This is sufficient to resolve velocity distributions of thermal particles. The direct proportionality between velocity and excitation frequency shift allows, in general, a straightforward interpretation of the spectra. There are, however, several complications, which have been discussed in the literature and have caused some controversies.[9,23,25,27–29] The main sources for complications are (a) the usually small intersection area between laser beam and particle beam resulting in transit time broadening, (b) the high power densities of lasers, resulting in power broadening of the transition lines, (c) saturation effects,[30] (d) nonideal spectral properties of laser as, for instance, time-dependent jitter,[25] (e) the short duration of the laser pulse resulting in transit time broadening, and (f) the limited observation volume.

All these effects may influence the LIF and DSLFS spec-

tra. Whether the influence is negligible or not must be decided for each experimental setup independently. Using a pulsed dye laser will generally involve a quite considerable power broadening up to several GHz.[9] On the other hand, in a typical cw dye laser setup, as used in our experiments, power broadening due to the laser power in the low MHz range can be expected and, therefore, neglected in practically all sputter experiments.[28] In order to obtain an upper limit for the power broadening in a typical cw dye laser DSLFS spectrometer, we have measured the hyperfine structure of the Na D_2 line in a Doppler-free geometry described earlier with laser power densities up to the maximal output power of the 699-21 ri ıg dye laser. While the hyperfine splitting of the upper level (16,4 MHz, 34 MHz, 58,9 MHz) can be clearly resolved for very low laser power densities of a few mW/cm^2, at maximal power densities of several W/cm^2 only the envelope of the three hyperfine lines is observed, indicating a power broadening of the order of 50 MHz. Although the actu.: power broadening has to be decided on a system to system basis, the value obtained for Na represents a realistic limit for what can be expected in cw experiments.

A very sensitive parameter is the interaction time between the laser field and the atoms. It is limited by either the flight path of the atoms through the laser beam (cw lasers) or the pulse length of the laser. Particularly in the case of an atomic three level system the transit time and correlated saturation effects become important.[25,29,30] This can be easily understood from the fact that with increasing transit time an enhanced pumping contribution by the wings of the Lorentzian laser profile can be observed.

B. Evaluation of excitation probabilities

A very comprehensive in-depth treatment of these problems has been made by Berres *et al.*[25,29] In the following we will discuss the essential features of their work and evaluate the implications for the experimental results obtained by DSLFS. Furthermore, we will restrict this discussion to cw lasers, although the results can be applied to pulsed lasers in a straightforward manner. Similar calculations and a comparison of applications of pulsed and cw lasers have been published by Wright *et al.*[9,27]

Starting from the rate equations for a two and three level atomic system, respectively, exposed to a monochromatic laser field, Berres *et al.* derive the probability of finding one atom in the excited state. This probability depends on the residence time of the atom in the laser field, the frequency dependent saturation parameter $S(\xi)$ and the life times of the states involved. ξ is a normalized frequency given by

$$\xi = 4\pi(\nu - \nu_0)/\gamma. \tag{2}$$

ν_0 is the central frequency of the Doppler shifted absorption line of the atom, ν the actual laser frequency, and γ the inverse life time of the transition. The saturation parameter $S(\xi)$ can be written in the following form, using the "saturation parameter" [maximal value of $S(\xi)$, which is $S(\xi = 0)$] S_m, the Lorentzian line shape of the transition line and the laser power density ϕ_L:

$$S(\xi) = (4\phi_L/\phi^{\circ}\cdot\gamma)/(1 + \xi^2) = S_m/(1 + \xi^2). \tag{3}$$

The probability of finding the atom in the excited state can be expressed in terms of γ and $S(\xi)$. However, in practical cases we are not interested in the excitation probability of one atom, but in the number of atoms excited by the laser in an ensemble of atoms. Because these atoms are not at rest, their Doppler shift has to be considered. The number of excited atoms n_2 can be directly correlated with the measured fluorescence signal $I(n_2)$. This number n_2 can be expressed in terms of an "excitation function" $F(S_m, \alpha,\theta)$:

$$n_2 = (dn/dv)(\gamma\lambda/2\pi)F(S_m,\alpha,\theta). \tag{4}$$

λ is the laser wavelength and dn/dv the velocity distribution of the number density of the atoms. We limit our discussion to the case, where the trajectories of the atoms are well defined. Otherwise, we would have to use the z component (velocity component in the direction of the laser beam) of the velocity. This complicates the deconvolution of the spectra, but does not influence the problems discussed here. The excitation function $F(S_m,\alpha,\theta)$ is a function of the saturation parameter, the branching ratio α of the upper level and the residence time t of the atom in the laser field. Of more significance than the residence time itself is the ratio θ between the residence time and the life time of the excited state, because it determines the relaxation of the atomic system. In Fig. 2 some examples for excitation functions are given for two and three level systems in dependence on θ. The examples shown refer to atomic systems used in experiments to be described later. From the experimental point of view it is important and remarkable that even in the case of a three level system (Zr, Ca metastable) the probability of finding the system in the excited state is quite considerable even after long residence times. This is caused by increased pumping by the wings of the laser line. Without taking into account these effects one would otherwise expect that in the case of a three level system the excitation probability should drop to zero after all atoms have been pumped over into the third level.

C. Fluorescence signal vs velocity distributions

We will now restrict ourselves to the experimental geometry shown in Fig. 1. In this case the measured fluorescence signal $I(n_2)$ can be correlated with the velocity distribution to be determined by the following equation:

$$I(n_2) = (dn/dv)GA_{2i}V(\gamma\lambda/2\pi)(1/\Theta)\int_0^{\Theta} F(S_m,\alpha,\theta)d\theta. \tag{5}$$

A_{2i} is the spontaneous transition probability for the observed transition from the excited to the lower level. G is the detection efficiency of the system. V is the volume of the intersection region between laser and particle beam. Θ is the θ value corresponding to the transit time of a group of atoms with a given velocity through the interaction region. We can see that in order to obtain the number density velocity distribution the measured fluorescence signal has to be divided by the Q function defined by $Q(S_m,\alpha,\Theta) = 1/\Theta \times \int_0^{\Theta} F(S_m,\alpha,\theta)d\theta$.

The knowledge of $Q(S_m,\alpha,\Theta)$ allows us in principle to correct the measured spectra, and to obtain the velocity distributions by calculating the Q function for each velocity in the spectrum and dividing the fluorescence signal by it. In Fig. 3 the Q functions for the examples of Fig. 2 are given. For a two level system the Q function is constant over a large regime. For most sputter experiments (see Table I) values

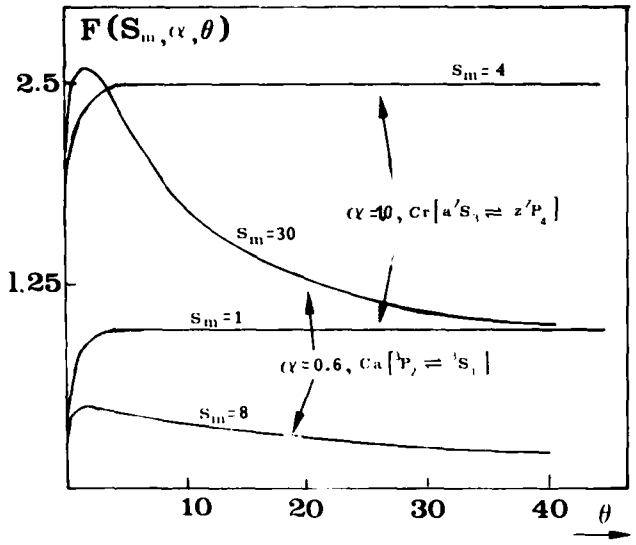

FIG. 2. Excitation function $F(S_m, \alpha, \theta)$ is plotted as a function of θ for different S_m values. Examples for a two level system (Cr, $\alpha = 1$, transition from the ground state a^7S_3) and a three level system (Ca, $\alpha = 0.6$, transition from the metastable $^3P_2$ level) are given.

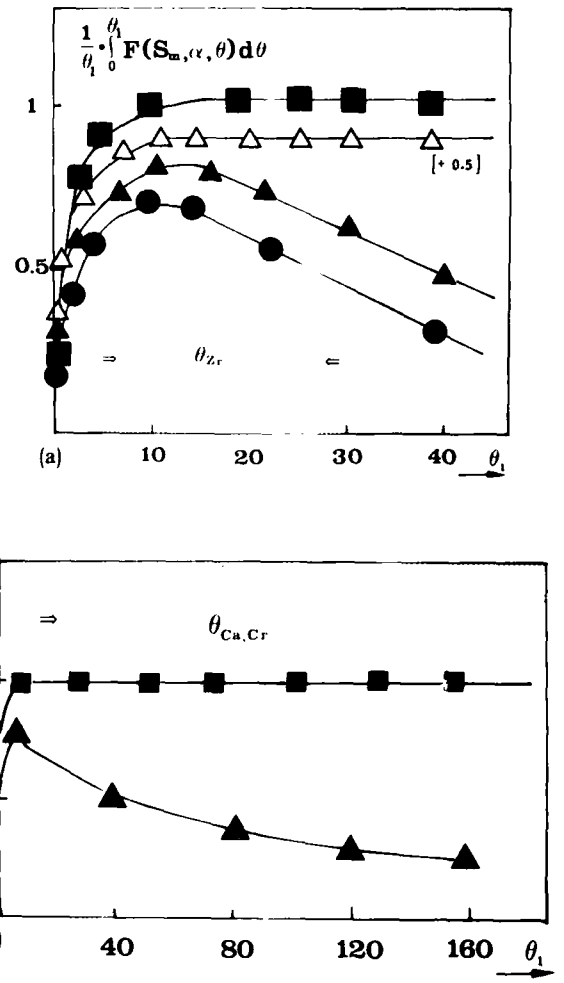

FIG. 3. Relation $Q(S_m, \alpha, \theta_1) = (1/\theta_1)\int_0^{\theta_1} F(S_m, \alpha, \theta)\,d\theta$ is plotted in dependence of θ_1. The function has been calculated for the experimental geometry shown in Fig. 1 with the following parameters: Laser power: 200 mW/cm^2, length of the interaction and observation volume: 0.5 cm. The parameters of the transitions can be found in Table I. The shaded area indicates the regimes of interest for velocity measurements of different sputtered materials (velocities typically between 0.5 and 30 km/s). (a) Regime of small θ_1 values for Cr (open triangles), Ca ground state (full squares), Ca metastable (full triangles) and Zi ground state (full circles). (b) Regime of high θ_1 for Ca ground state (full squares) and Ca metastable (full triangles).

between 20 and 300 are of relevance. Therefore, in this case no correction is needed. The situation is more complicated for a three level system. Again, as in the previous case, for very small Θ values a correction is necessary. But, more important, for intermediate Θ between 10 and 80 a linear decrease of the Q function is observed. In principle this corresponds to a division of the signal by the velocity, which is equivalent to converting a flux distribution into a number density distribution.[4,6] Because the decrease of $Q(S_m, \alpha, \Theta)$ is less steep than $1/\Theta$ (see Fig. 3) in most realistic cases, we cannot speak of a flux nor a density distribution in the case of a three level system. For $\Theta > 80$ the Q function saturates and becomes nearly constant again. Again, this is equivalent to changing into a number density distribution.

As a consequence, for weak atomic transitions ($A_{ik} < 10^7\,s^{-1}$) particular care has to be taken in interpreting the measured spectra. Furthermore, three level systems are more likely to lead to a misinterpretation of the fluorescence spectra due to saturation effects.

Even though the Q function can be calculated and represents a handy tool to correct the spectra, several facts complicate the situation: (a) the exact determination of the residence time is sometimes rather complicated and (b) the effective laser bandwidth and therefore, the S_m value is difficult to determine,[25,29] in particular on a larger time scale due to jitter. Furthermore, it varies from system to system.

IV. VELOCITY DISTRIBUTIONS OF SPUTTERED NEUTRAL GROUND STATE ATOMS

A. Sputtering mechanisms

When energetic particles interact with solid surfaces, various physical processes can be observed, as secondary electron emission, secondary ion emission, radiation damage, and sputtering. The emission of surface or near surface atoms, molecules or ions under particle impact is commonly known as sputtering. The consequences of this phenomenon are widespread and of great importance in different areas. Emission of sputtered target particles can be used for analytical purposes. Secondary ion mass spectroscopy (SIMS) is an important and widely used method. Interaction of plasma particles with the surrounding walls in reactors or fusion devices causes particle release from the walls due to sputtering. If these particles reach the plasma, they will cause energy losses by radiation and consequently plasma cooling.[16,31,32] Furthermore, damage of mechanical parts and walls exposed to the plasma will take place due to sputtering.[33] Another very important area, where sputtering plays an important role, is the field of sputtering deposition of thin films[34] and of sputter-assisted plasma technologies.[35] A de-

TABLE I. Velocities and corresponding values for sputtered atoms. Values θ_1 and θ_2 correspond to a minimum velocity $v_1 = 0.5$ km/s and a maximal velocity $v_2 = 30$ km/s, which are typical for sputtered particles. Examples are given for some atomic species, for which DSLFS results are presented in this paper. The length of the intersection volume between laser beam and atomic beam is 5 mm, in accordance with the experimental setup shown in Fig. 1.

Atomic species	Transition line 1–2	Branching ratio $A_{21}/(A_{21}+A_{23})$	A_{12} (s^{-1})	θ_1 / θ_2
Ca	$^1S_0 - {}^1P_2$	1	2.1×10^8	2000 / 30
Ca	$^1P_2 - {}^3S_1$	0.6	3.5×10^7	500 / 10
Cr	$a^7S - z^7P^0$	1	3.1×10^7	300 / 10
Zr	$a^3F_2 - y^3D^0$	0.14	5×10^5	30 / 1.5

tailed understanding of the sputtering process is, therefore, of great importance.

In order to tackle the problem of understanding the sputtering mechanisms, different physical quantities may be investigated: (a) the sputtering yield, (b) the angular distribution of sputtered particles, (c) the energy or velocity distribution of the sputtered particles, (d) the mass distribution of sputtered particles and (e) the electronic states of the particles leaving the surface. By comparison of the measured quantities with existing theoretical models, the different mechanisms responsible for sputtering may be inferred. For such purposes, DSLFS is an ideal tool, because it can yield information about all the quantities, noted under (a)–(e).

The knowledge of the energy of the sputtered particles is of particular importance, because it allows one to calculate the fluxes of released particles. These results can, e.g., be used to estimate the impurity flux into the plasma core in fusion machines. Furthermore, the energy of the released particles carries a large amount of information about the process responsible for the emission of the particles. Thus the analysis of velocity spectra will enable us to distinguish between different sputtering mechanisms.

Because in many cases most of the sputtered particles are neutral atoms in their electronic ground state,[36] the need to measure the energy distribution of neutral atoms was one of the driving forces to develop DSLFS and LIF.[5,11] In the following we will describe the most prominant results of DSLFS as far as velocity spectra of neutral ground state atoms are concerned.

In this chapter we will restrict the discussion to results obtained for clean surfaces of metals and alkali halides. In a following chapter the more complicated situation of oxidized targets will be discussed. For atomically clean targets more than 90% of the sputtered particles are neutral atoms in the ground state and only a small percentage of ions and excited atoms contributed to the sputtered flux. The sputtering behavior of metals is particularly interesting in regard to plasma-wall-interaction studies. The sputtering behavior of alkali halides involves an interesting combination of different particle release mechanisms.

If a solid target is bombarded by heavy ions of medium energy (keV range), nuclear stopping is dominant and the linear collision cascade theory[37] is applicable. However, deviations from this model are expected for low and high energies as well as for light ion bombardment. Assuming an isotropic cascade and a planar surface potential, the following formula for the number density velocity distribution was deduced by Sigmund[37]:

$$dn_{col}(v)/dv = v^2/(v^2+v_b^2)^{3-2m}, \tag{6}$$

where v_b is the velocity corresponding to the surface binding energy E_b. For metals the surface binding energy is usually assumed identical to the heat of sublimation. Formula (6) is valid for velocities corresponding to energies much below T_{max}, which is the energy transfer in an elastic head on collision. T_{max} is given by

$$T_{max} = 4M_1M_2/(M_1+M_2)^2E_{ion}. \tag{7}$$

m is defined by the power cross section

$$d(T) = CE_{ion}T^{1-m}dT. \tag{8}$$

In sputtering where low energy collisions are dominating, m is expected close to zero.

Nonlinear effects caused by high density cascades[38] have been found experimentally[39] in sputtering yield measurements at bombarding energies around 100 keV. These nonlinear effects are particularly pronounced for heavy bombarding particles, but have also been reported for primary energies in the keV range.[40] They have been explained by the thermal spike concept[38,41] and should also show up in the velocity spectrum of the sputtered particles, delivering a velocity distribution contribution described by

$$dn_{spi}(v)/dv = v^2\exp[mv^2/(2kT_{sp})] \tag{9}$$

with T_{sp} the so called "spike temperature." The spike concept is, however, controversial.[42] Measurements of velocity spectra of sputtered particles should help to clarify the situation.

Another deviation from the cascade model is expected for bombardment with light particles as for instance H, D, and He. For low bombarding energies and even more pronounced for light particle bombardment, anisotropic energy distributions can be expected due to enhanced contributions to the sputtering yield by the first few recoils.

B. Velocity spectra of sputtered ground state atoms

The aim of detailed DSLFS experiments was to examine the validity of the linear collision cascade theory, and deviations from it. In Table II a summary of DSLFS results obtrained from different target materials and bombarding conditions is given. The type of DSLFS spectrometer used is indicated in order to specify the resolution of the particular experiment (see the second chapter).

1. Collision cascade regime

In general, DSLFS velocity spectra of neutral metal atoms sputtered from metal targets by He^+, Ar^+ Kr^+,Xe^+, C^+, and O^+ bombardment at impact energies in the range between 3 and 50 keV show a good agreement with the Sigmund theory [formula (6)].[3,24,26,27,43-46] In Fig. 4, measured

TABLE II. Surface binding energy E_b as obtained from velocity spectra of neutral ground state atoms sputtered from clean (oxygen free) surfaces. The tabulated values for the heat of sublimation U_O are compared with the measured surface binding energy. Bombarding conditions and the type of DSLFS spectrometer used are given. The excitation geometry is indicated as high resolution setup with excitation of the sputtered atoms being accomplished in a well defined beam a few cm apart from the target, or as excitation directly in front of the target.

Atom	E_b(eV)	U_O(eV)	Bombarding conditions	Laser type	Excitation geometry	Ref.
Cr	1.6–2.0	4.2	15 keV Ar^+ ($10\,\mu A/cm^2$)	cw	high resolution	43
	4	4.2	15 keV O^+ ($4\,\mu A/cm^2$)	cw	high resolution	26
Ca	1.3	1.8	15 keV Ar^+ ($10\,\mu A/cm^2$)	cw	high resolution	43
Ba	1.8	1.86	10 keV Ar^+ ($20\,\mu A/cm^2$)	cw	in front of the target	46
Ti	4.6	4.9	1 keV Ar^+ ($2\,mA/cm^2$)	pulsed	in front of the target	44
Zr	8	6.4	8 keV Ar^+ ($2\,mA/cm^2$)	cw	high resolution	24
	4–6	6.4	15 keV Ar^+ ($10\,\mu A/cm^2$)	cw	high resolution	
Fe	4.3	4.3	10 keV Ar^+ ($2\,mA/cm^2$)	pulsed	on front of the target	68

data for Cr, Ca, Fe, and Ti are shown and compared with the Thompson formula (6). The fit of Eq. (6) to the measured spectra yields a value for the fitting parameter E_b. In most cases the E_b values giving the best fit to the measured spectra are in good agreement with the tabulated value for the heat of sublimation of the respective material. However, in some cases[26] deviations have been observed with a tendency to E_b values lower than the heat of sublimation (see Table II).

2. Light-ion, low-energy regime

For light-ion and low-energy bombardment the Sigmund theory is no longer applicable. In this case T_m becomes of the order of the surface binding energy and Eq. (6) is only valid for energies much lower than T_m. In this case a single collision model should be more appropriate to describe the sputtering process.[51] Results of H^+ and D^+ bombardment of Zr,[24,47] Ti,[49] and Fe[50] show a dependence of the velocity spectrum on the ion mass and energy, contrary to the Sigmund theory. For instance, the maximum of the velocity spectrum of Fe shifts from about 2 km/s for 100 eV H^+ bombardment to about 3 km/s for 500 eV H^+ bombardment.[50] Furthermore, at high particle velocities a contribution from direct recoils could be identified for D^+ bombardment. As an example, velocity spectra for light-ion bombardment are given in Fig. 5. Anisotropy effects can be clearly seen for D^+ bombardment of Zr.[15] Experimentally found anisotropy contributions are much more pronounced than such predicted by some theories.[48] In Fig. 5 it can also be seen that for light ion sputtering the maximum of the energy distribution is very sensitive to differences in the angle of ion incidence. This effect is much more pronounced than in cases of ion bombardment for which the collision cascade theory is applicable.

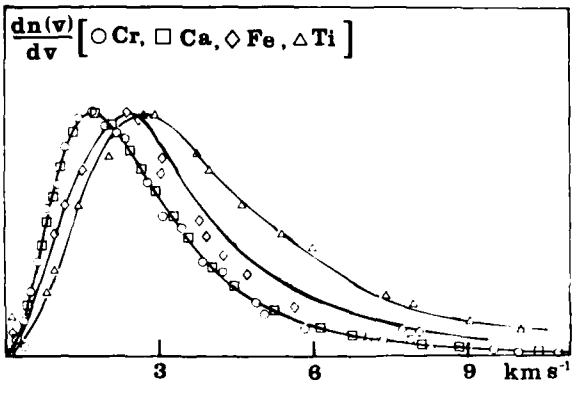

FIG. 4. Velocity distributions of sputtered neutral metal atoms in the ground state under bombarding conditions, where the isotropic, linear collision cascade theory is valid. The spectra shown are for atom emission from clean, oxygen-free surfaces. The full lines indicate the fit by Eq. (6) using E_b as fitting parameter. (Fe from Ref. 68, Ti from Ref. 44.) For more details of the E_b values and experimental details see Table II.

In order to use formula (6) for light-ion sputtering, some corrections have been proposed. Thompson[59] suggested to use the following formula for the velocity distribution

$$dn_{\text{anal}}(v)/dv = KE\,[1-(v^2+v_b^2)/v_m\,]/(v^2+v_b^2)^{1+n}, \quad (10)$$

where v_m is the velocity corresponding to the energy T_m defined in Eq. (7). This distribution exhibits nearly the same behavior as is obtained from the single collision model proposed by Littmark.[51] The distributions obtained experimentally by DSLFS of H^+ bombardment of Fe and Ti can be fitted by Eq. (10) varying the parameter n. The value n as obtained from these measurements changes from about 2 in the cascade regime (where the Sigmund theory is valid) to about 4 for small T_m/E_b values. These high n values, which result in a steeply falling tail of the velocity distribution are on the one hand quite plausible, because one would expect fewer energetic particles in the light-ion low-energy collisions. But on the other hand, the high n value corresponds to a $m > 1$ in Eq. (8), which is in contradiction with the assump-

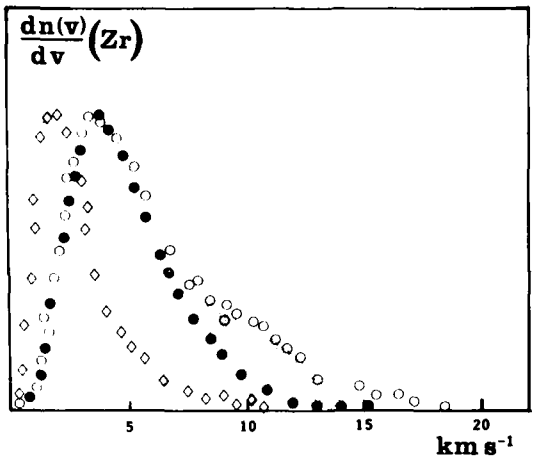

FIG. 5. Velocity distributions of sputtered Zr ground state atoms under 2.5 keV H^+ (full circles) and D^+ bombardment (open circles for oblique ion beam incidence, open squares for normal incidence) (from Ref. 24.) The shaded area indicates anisotropic contributions to the sputtering yield from direct recoils.

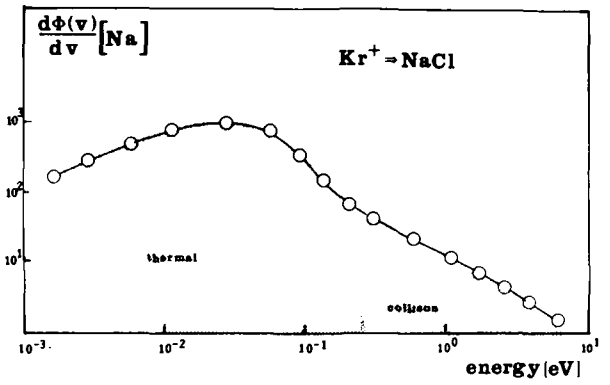

FIG. 6. Logarithmic plot of the velocity flux distribution of Na released from a NaCl target under 20 keV Kr^+ bombardment. A thermal and a high-energy contribution from linear cascades can be clearly identified. The contribution between 0.1 and 1 eV can be explained by a thermal spike contribution. Another explanation might be, that Eq. (6) is incorrect in the low energy regime for alkali halides in particular, and insulators in general.

tions for the power cross section (8). As a consequence, DSLFS velocity spectra obtained for light-ion low-energy bombardment of metals cannot be accurately described by simple analytical models like Eq. (10). Therefore, more detailed measurements and refined models are necessary.

3. Radiation-enhanced evaporation and thermal spikes

The sputtering of alkali halides has proven to be a good test for the abilities of DSLFS.[5,26] In this case elastic as well as inelastic energy losses[52,53] of the primary ions contribute to particle release from the surface. Sputtering can even be observed for electron and photon irradiation.[54,55] Velocity spectra of Na atoms sputtered from NaCl and NaI[19,21] targets allowed identification of principally three different processes leading to Na ejection: (a) collisional sputtering, (b) thermal evaporation, and (c) thermal spike sputtering. An analysis of a DSLFS velocity spectrum of Na emitted from NaCl during 20 keV Kr^+ bombardment is shown in Fig. 6. Processes (a) and (b) can be clearly identified and fitted by the appropriate theoretical distributions. The contribution and existance of thermal spikes might be questionable.[42] However, thermal spikes represent a possibility to explain the deviations in the spectra from formula (6) in the low energy regime. For heavy-ion impact collisional sputtering dominates. Thermal evaporation is the dominant particle release mechanism of Na for light-ion bombardment (He^+).[21] This can be explained by the strong contribution of electronic stopping for light ions, creating defects in the crystal. The deexcitation of these electronic defects eventually results in replacement collisions leading to particle ejection. In such cases usually the halogen atom is ejected. As a consequence, a surface enrichment in Na occurs which finally leads to evaporation of Na atoms. Another possibility is the migration of an interstitial-vacancy pair to the surface where it gets trapped and consequently some atoms gain enough activation energy in order to evaporate.

In the recent paragraph, I have shown that over the last few years DSLFS has been very successful in acquiring useful data which can help to verify existing theories for the sputtering process. However, some of the data have shown, that in many cases (light ion sputtering is only one example) more accurate theories are needed.

V. INVESTIGATIONS OF SPUTTERED EXCITED ATOMS

A. Excitation and ionization during sputtering

Although elastic collisions and linear cascades dominate the sputtering of particles under ion impact and the majority of these particles are consequently neutral and in the electronic ground state, ions and excited particles contribute to some extent to the sputtered flux. Even though the absolute densities of sputtered excited atoms, excited molecules and ion are rather small (for clean targets they make up only a few percent), the implications of their existence are quite considerable. Because these excited particles and ions can be easily detected, surface analysis methods have been developed on the basis of secondary ion detections (SIMS[56–58]) and light emission from sputtered excited species (SCANIR, BILE[60,61]). In spite of the small absolute densities of sputtered ions and excited atoms or molecules, the sensitivity of these methods is very high, because the detection sensitivity for ions and photons is extremely high.

Therefore, particular interest exists in a detailed understanding of the mechanism of excitation and ionization in the sputtering process. The interpretation of SIMS and SCANIR spectra is complicated by many effects. In particular, the strong dependence of the ion and excited atom yields on the surface oxidation causes essential problems for a quantitative analysis. It is a well established fact, that ion and excited particle yields from oxidized surfaces can exceed those from clean surfaces by orders of magnitudes.[58,62,63]

Until the availability of LIF and DSLFS the main experimental method to study sputtered excited particles was the spectroscopy of emitted light of sputtered short lived excited atoms and molecules in front of the target.[63–66]

In this way the population of different excited states during the sputtering process can be obtained. Furthermore, attempts have been made to measure the velocity distribution from the spatial decay of the fluorescence light of different transitions in front of the target.[63–66] From these measurements astonishingly high values for the average energy of sputtered excited atoms reaching from some hundred eV up to several keV, have been obtained.

B. DSLFS measurements of sputtered metastable atoms

Since the development of DSLFS it has been clear, that this method would be unique for investigating the state distribution and the velocity distributions in specific states of sputtered atoms. Due to the low intensities involved, such experiments are, however, much more difficult than those for measuring ground state distributions. As far as investigations of particle-solid interaction processes are concerned, one of the recent great achievements of DSLFS and LIF has been the first direct measurements of velocity distributions of sputtered excited atoms.[10,23,46,68] The results obtained have been rather unexpected and in strong contradiction to the estimates obtained by light emission studies. There is, however, one restriction imposed on DSLFS measurements: the short lifetime of excited states with allowed dipole transitions to lower levels will cause decay very close to the target surface and, therefore, these particles are not accessible for laser excitation. DSLFS is, therefore, restricted to measurements of excited metastable states. However, this restriction is not really a disadvantage, because sputtered metastable atoms should not behave differently from those sputtered in short-lived excited states. This assumption is reasonable, because excitation by photons during sputtering can be excluded and, therefore, no selection rules for the excitation will apply. Furthermore, we have to be aware that the metastable state will accumulate atoms decaying from other excited levels of the same multiplet. The velocity distribution will thus provide an "averaged picture" of atoms sputtered in several excited levels.

DSLFS measurements of the velocity distribution of sputtered metastable atoms have been obtained for two different types of metastable levels: (a) fine structure levels of the electronic ground state [Fig. 7(a), for Zr] and (b) metastable levels lying typically 1–2 eV above the ground state [Fig. 7(b), for Ca]. This classification is useful, because the behavior of these two types of metastable states is quite different as far as sputtering is concerned. Velocity spectra of Zr atoms sputtered in the a^3F_3 (570 cm^{-1} above the a^3F_2 ground state) and a^3F_4 (1240 cm^{-1} above the ground state) states have been reported by Gruen *et al.*[69] and are identical to the ground state velocity distribution of sputtered Zr atoms. On the contrary, the velocity distributions of atoms sputtered in metastable states not belonging to sublevels of the electronic ground state, are in general different from the ground state distributions.[10,23,46,68,70] For the $^3P_2$ metastable level of Ca, which is 1.9 eV above the ground state and is so far the highest excited level investigated by DSLFS,[23] we have observed a maximum in the velocity distribution for the metastable state when compared to the ground state which is higher by a factor of approximately 3.5.[43] Similar values have been observed for Ba,[10,46] Fe,[68] and Ti.[70] In spite of the evident differences between the velocity distributions for sputtered ground state atoms and sputtered excited atoms found by DSLFS, the earlier mentioned high velocity values predicted by light emission studies[64–66] could not be confirmed.[10,23,43]

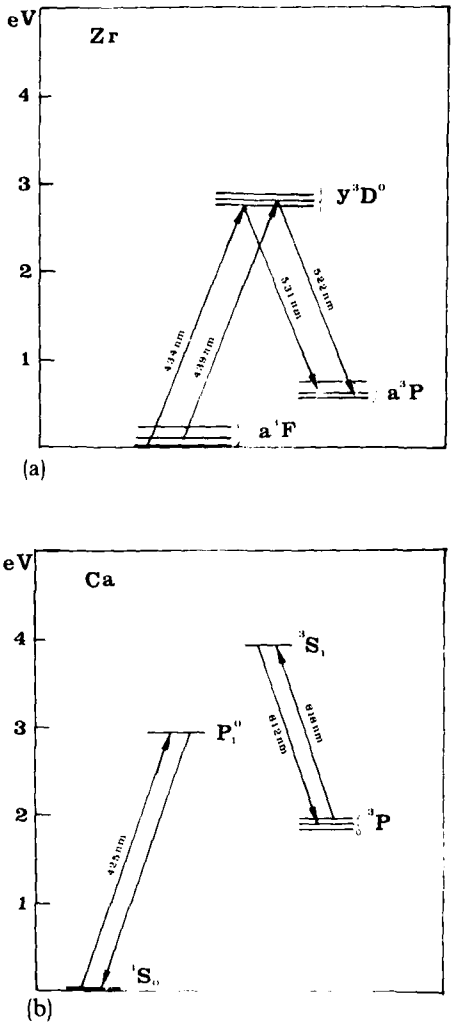

FIG. 7. Partial energy diagram of (a) Zr and (b) Ca showing transitions used in DSLFS experiments for detecting sputtered ground state and metastable atoms.

Table III summarized the quantities obtained from DSLFS measurements of sputtered excited atoms. The E^* values given correspond to the fitting parameter E_b in Eq. (6) and have been obtained by fitting the measured distribution to Eq. (6). A physical meaning of E^* is, however, not given in this case. It is, nonetheless, astonishing that in most cases the measured spectra can be fitted by Eq. (6) quite well, using E_b as a fitting parameter. Corresponding results are shown in Fig. 8.

In addition, another important observation has been made by DSLFS. As expected from what has been known for a long time, the sputtered metastable atom fluxes increase with oxygen adsorbed on the surface by approximately one order of magnitude. However, in good agreement among all

TABLE III. Summary of available DSLFS measurements of the velocity distribution of sputtered metastable atoms. E^* values are obtained by fitting the measured spectra of Eq. (6). E_b values are obtained from DSLFS measurements of the velocity distribution of sputtered ground state atoms.

Atom	E^* (eV)	E_b (eV)	Metastable level	Energy of metastable level (eV)	Ion beam	Ref.
Fe	20	4.3	a^5F	0.86	10 keV Ar^+	68
Ca	13	1.3	$^3P_2$	1.9	7 keV Kr^+	23
Ba	11	1.8	1D	1.4	10 keV Ar^+	46
Ti	16	4.6	a^1D	0.75	1 keV Ar^+	70

measurements reported so far, the shape of the velocity distribution does not change from clean to oxidized targets. This was rather unexpected and in contradiction to theoretical predictions as shown later in this chapter. A critical remark is, however, needed at this point. Because of the very low densities of sputtered excited atoms for clean targets, the measurements are limited by the detection sensitivity and a further enhancement of the sensitivity for experiments with well characterized oxygen free surfaces is needed to reach final conclusions.

C. DSLFS vs light emission results

The disagreement between DSLFS results and light emission studies needs a clarification.[71] If one summarizes the available data from light emission studies and plots the values obtained for the average energies E_m (which can be interpreted as the most probable energy of sputtered excited atoms) as a function of the inverse life time of the upper level of the transition used in the light emission studies, we obtained a linear dependance as shown in Fig. 9. This is, indeed, very surprising, because no influence of the lifetime of the excited state on the energy distribution is expected. The E_m values in Fig. 9 have been obtained from the spatial resolution of the fluorescence light by Dzioba *et al.*[65,66] using a mathematical analysis on the basis of the Sigmund theory (6) and a step function for the probability of finding an atom with kinetic energy E in a particular excited state. In this case the value E_m can be interpreted as a threshold value or the average energy in the energy distribution. In this treatment the influence of cascading from higher excited levels is not included. Cascading will be a particularly serious problem, if the higher excited states are long lived. We have included the contribution from cascading in the treatment. Assuming the partial Grotrian diagram for Ca shown in Fig. 10, we obtained cascade corrected values shown in Table IV[71] for the E_m value deduced from the light emission of the $4p^1P\ 4s^1S$ transition. This demonstrates that the original value of 1510 eV can be considerably reduced to 60 eV for a 50% cascade contribution. Moreover, the value of 60 eV is of the same order of magnitude as the E^* value obtained for the $^3P_2$ level of Ca by DSLFS.

D. Evaluation of different models for excitation

Several different models for the excitation mechanism of atoms and molecules during sputtering have been proposed.[63–66] Each of these models is challenged to explain the increase in excited yield for increasing oxygen coverage of the surface as well as to explain the velocity distributions. Due to the new information on the velocity distribution of sputtered excited atoms obtained by DSLFS, the picture concerning the excitation mechanism has changed to some extent. If in addition the same mechanism is assumed to be responsible for ionization and excitation in the sputtering process, the generally higher ion yields as compared to excit-

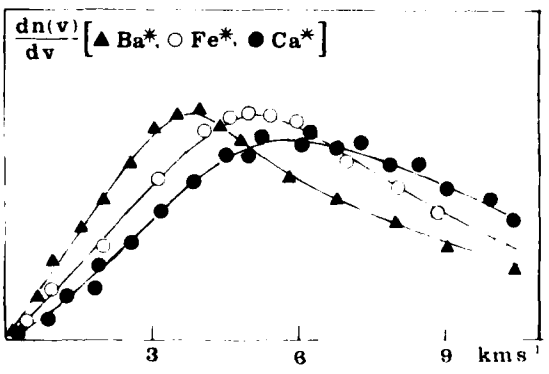

FIG. 8. Velocity spectra of sputtered metastable atoms. The maxima appear at higher velocities than for ground state atoms as shown in Fig. 4. Fits with Eq. (6) (full lines) are rather good, but yield E_b values with no physical meaning (see Table III). (Fe results from Ref. 68 and Ba from Ref. 46).

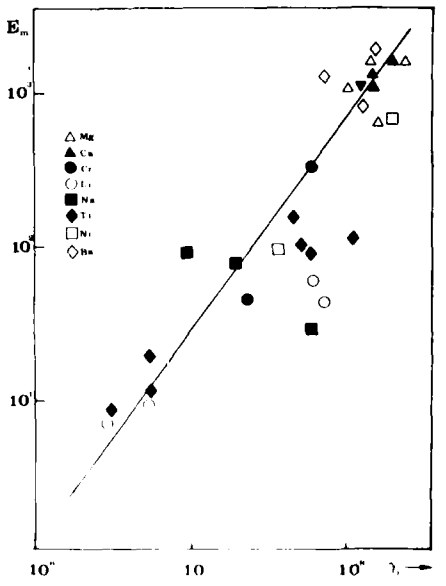

FIG. 9. E_m values obtained from spatially resolved light emission studies plotted as a function of the inverse life time of the upper state of the observed transition (see also Fig. 10).

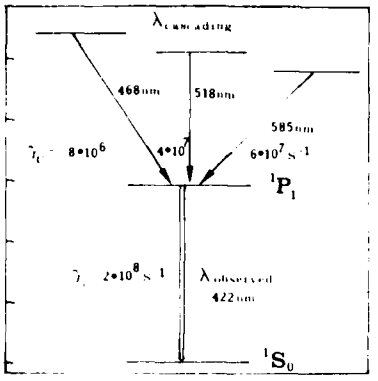

FIG. 10. Partial Grotrian diagram of Ca showing the transition wavelengths and inverse life times of levels influencing light emission studies via the 422 nm transition by cascading.

ed particles have to be explained. A theoretical model for the creation of excited atoms in the sputtering process should of course incorporate all the experimental facts. Due to the complexity of the process several pros and cons to the different approaches will be found and no conclusive answer has yet been discovered.

In principle two different types of models can be distinguished. In the first type the excitation occurs during the last few collisions in the cascade. A survival probability for the excited atom at the surface is introduced, which describes the probability of surviving nonradiative decay close to the target surface.[58,72-74] A different approach is taken by the second type of model. In the model proposed by Williams and Tsong[64] based on an earlier model by Blaise,[67] the creation of excited atoms is explained by the level crossing[75] process for the dissociation of an metal–oxygen quasimolecule leaving the surface. The mechanism is explained in more detail in Fig. 11. During the last collision in the collision cascade process, an atom pair consisting of a substrate metal atom and an adsorbed oxygen atom is ejected with a good chance of forming a quasimolecule. At first this quasimolecule will be compressed and thus move up the repulsive side of the potential curve in Fig. 11. Depending on how far it moves up the potential curve, it can finally end up in one of the possible dissociative levels corresponding to different final combinations of metal, metal-ion, oxygen, and oxygen-ion as shown on the right side of the figure.

This molecular model incorporates in principle all the facts observed in DSLFS measurements: (a) the density of sputtered excited atoms increases with oxygen coverage of the surface, (b) the shape of the velocity distribution is independent of the amount of oxygen on the surface, and (c) the velocity gain of the sputtered excited atoms as compared to ground state atoms by 10–20 eV is reasonably well explained by the potential curves in Fig. 11.

On the other hand, if one uses the other type of model for the excitation in sputtering, in particular one difficulty in the interpretation of DSLFS results arises: The survival probability of the excited atoms at the surface should be influenced by the degree of oxidation; consequently the shape of the velocity distribution should change from clean to oxidized targets simultaneously with the increase of intensity.

VI. INFLUENCE OF SURFACE OXIDATION ON THE COMPOSITION OF THE SPUTTERED FLUX

In previous sections we have shown that the sputtered flux consists predominantly of neutral monoatomic target particles in the electronic ground state, if a clean, oxygen-free surface is bombarded with rare gas ion. This statement is also valid for most other bombarding ions. We have also seen that for oxides and metals with adsorbed oxygen the contribution of excited atoms and ionic particles to the sputtered flux can increase by orders of magnitudes with increasing oxygen coverage on the surface. However, no detailed information is available about the quantitative composition of the sputtered flux. In particular, relatively little has been known about the contribution of neutral atoms in the electronic ground state for different stages of oxidation. A detailed knowledge of the flux composition is, however, needed in all cases where LIF is used for sputtering yield measurements.[76] Moreover, neutral particle detection has been proposed and thought to be superior to ion detection for surface analysis applications. Two reasons can be brought forward to justify

TABLE IV. E_m values for sputtered excited Ca atoms in the $^1P_1^0$ level after cascade correction. The uncorrected value (0% cascading) is taken from Ref. 66.

Contribution of cascading in percent	k (γ_i $k \cdot \gamma_i$)	E_m (eV)
00	...	1510
10	0.5	910
10	0.25	550
10	0.1	210
50	0.25	210
50	0.1	63

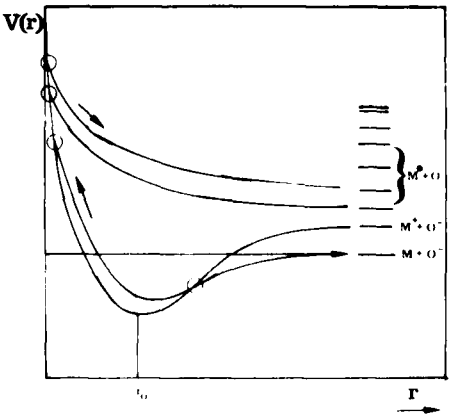

FIG. 11. Potential curves of a metal-oxygen quasimolecule formed in the last step of the collision cascade during sputtering, illustrating a possible mechanism for production of sputtered excited atoms. If enough energy is transferred to the molecule, it might be compressed and consequently moves up the potential curve as indicated in the figure. If level crossing points (open circles) exist, this might result in dissociation of the molecule leading the atoms in excited or ionized states as shown in the right part of the figure. Another possibility for the transition from the binding ground state to the antibonding excited state would be a transformation of vibrational energy into electronic energy via an inverse Franck-Condon transition Ref. 84.

this: (a) the neutral flux is larger by several orders of magnitudes than the ion flux and (b) the extreme dependence on the surface composition was believed to be more serious for the ion yield than for the neutral flux.

A. Dependence of the densities of sputtered ground state atoms on the surface composition

One of the important achievements of DSLFS and LIF in the last two years has been to produce a great deal of new information about the composition of the sputtered particle flux. It came to a great surprise when DSLFS measurements showed, that sputtered neutral Cr atoms can be nearly suppressed for Cr targets with oxygen contamination.[26,43] In fact, if an originally clean Cr is exposed to an oxygen partial pressure of about 10^{-6} mbar under simultaneous Argon ion bombardment (current densities a few $\mu A/cm^2$), the yield of neutral ground state atoms is reduced to 1% of the original amount. Similar results have been found by Dullni[44] for sputtering from Ti and Al, by Gruen *et al.*[18,69] from Ti and by Grischkovsky *et al.* from Ba.[46] Most of these experiments have been performed in the so called dynamic mode. In this case the vacuum chamber is backfilled with oxygen. The ratio between the oxygen partial pressure and the ion beam density will characterize the degree of surface oxidation during ion bombardment. Gruen *et al.* have operated in the so-called static mode, where a defined amount of oxygen is deposited on the surface by exposing it to oxygen. Subsequently, measurements are performed under high vacuum conditions and very low ion current densities.

The most pronounced influence on the sputtered ground state densities has been observed for oxygen adsorbed on the surface. The influence of hydrogen[26,44,70] and nitrogen[44,70] is much less drastic. Hydrogen and nitrogen adsorbed on Cr, Ti, and Al surfaces reduces the sputtered ground state densities by about a factor of 2.

B. Velocity spectra of atoms sputtered from oxidized targets

In addition to the observed drastic intensity decrease, the velocity spectra broaden quite substantially for increasing oxygen partial pressure. For oxygen partial pressures of a few 10^{-6} mbar the maxima of the velocity distributions shift from the values corresponding to the surface binding energy of the clean metal of such resembling that obtained for distributions of sputtered metastable atoms (Fig. 12).

There are two possible sources, which might contribute to the broadening of the velocity spectra under increased oxygen partial pressure:

(a) Dullni[44] proposes a model in which the broadening is explained by changes of the surface binding energy. This explanation is a straight forward consequence, if formula (6) is valid. However, in this case the surface binding energy has to be calculated from the formation enthalpies of the oxides, the recombination energy of O_2 and the sublimation energy of the metal. The sum of these three energies should be the energy parameter E_b in Eq. (6) obtained from the velocity distributions. The existence of different oxides will complicate the calculation of E_b. Averaging over two or more different possible types of oxides, Dullni obtained reasonably good agreement between the measured and calculated E_b values for Ti.

(b) For an oxygen pressure regime where the density of sputtered ground state becomes very small, the amount of sputtered excited and ground state atoms might become of comparable size. In this case the ground state atoms which are excited by the laser in the interaction volume will consist of two types, i.e., such sputtered in the ground state and such sputtered in short-lived excited states but having already decayed into the ground states before reaching the interaction volume. The velocity distributions of these two types will be different as shown above. Hence, the measured spectrum is a superposition of two spectra with different shapes.

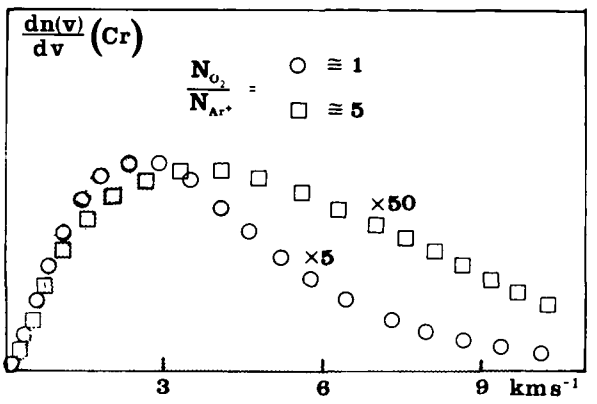

FIG. 12. Velocity spectra of ground state atoms sputtered from oxidized surfaces are broadened compared to those from clean surfaces (shaded area). The yield of ground state atoms decreases drastically for increasing oxidation (by a factor 5 and 50 for the examples shown). Examples for Cr measured in the dynamic mode are given for two different ratios N_{O_2}/N_{Ar^+}. An interpretation of the broadening is given in the text.

C. Composition of the sputtered flux

It would be misleading to identify the behavior of the ground state with the behavior of the total sputtering yield under increasing oxidation of the surface. In order to obtain more detailed information about the quantitative composition of the sputtered flux from both clean and oxidized targets, we have used a combination of different techniques: DSLFS, LIF, BLE, and a quartz microbalance for collection of sputtered particles.

Using Doppler-free LIF, we have measured relative partial sputtering yields of sputtered Ca, Cr, and Zr ground state atoms.[26,78] For Zr targets also Zr atoms sputtered in the lowest lying metastable sublevels of the electronic ground state have been investigated. The experimental results are shown in Fig. 13. In the case of Cr we observed a decrease of the partial sputtering yield by more than a factor of 100, if the oxygen partial pressure is increased up to 10^{-6} mbar. A similar behavior was found for other target species shown in Fig. 13. For Cr we have performed the measurements with two different argon ion current densities, in order to check

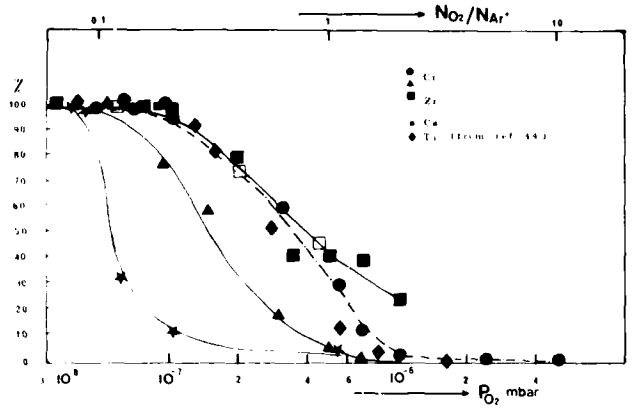

FIG. 13. Dependence of the partial sputtering yield of neutral metal ground state atoms as a function of the surface oxygen coverage as measured by LIF for 15-keV-Ar^+ bombardment (for Ti 1 keV Ar^+, from Ref. 44). As a measure for the surface coverage with oxygen the partial pressure P_{O_2} or the ratio N_{O_2}/N_{Ar^+} between oxygen molecules reaching the surface and the Ar^+ ion beam current density is used. The scale for N_{O_2}/N_{Ar^+} is valid for Zr, Ca, in the case of Cr for Ar^+ ion current I_1 and also for Ti. For the Ti results, however, the ion beam current densities used have been approximately a factor of 10 higher. The figure shows the results for Cr in the ground state for ion currents I_1 (full circles) and $I_2 = I_1/2$ (full triangles), for Zr in the ground state (full squares) and the first excited level of the ground state multiplet (open squares) for Ca atoms in the ground state (stars) and Ti in the ground state. The curves are normalized for the sputtering yield from clean targets to 100%. In spite of the different materials and the different ion current densities (for Ti) the agreement between the different results is very good, if the sputtered neutral atom densities are plotted as a function of N_{O_2}/N_{Ar^+}.

the assumption that the ratio N_{O_2}/N_{Ar^+} between oxygen molecules reaching the target surface and the Ar^+ ion current density is the physical quantity characterizing the oxygen coverage in the dynamic mode.

In summary, we conclude that the sputtering yield of metal atoms in the electronic ground state or in a metastable sublevel of the ground state multiplet decreases very drastically for $N_{O_2}/N_{Ar^+} > 0.5$.

The increase of sputtered metastable atoms for oxidized surfaces has been described in the previous paragraph. For clean targets, it is known that contributions for excited states are well below 1%.[68] From the LIF results presented in Fig. 13 we can conclude that even for high oxygen coverage the absolute contribution by sputtered excited atoms must be very low. If otherwise, we should detect most of the short-lived excited species in the ground state, due to the reasons explained above.

In order to put the partial sputtering yields obtained by DSLFS in the right perspective, we have performed total sputtering yield measurements for the same targets and for the same oxygen partial pressures using a quartz microbalance collector.[26,78] By applying positive and negative voltages, respectively, to two cylinders surrounding the target assembly (see Fig. 1) we could measure the total fluxes of neutral and charged particles to the quartz collector independently. The calibration of the system has been performed by measuring the theoretically and experimentally well known sputtering yield of Cu. Starting from a clean target the sputtering yield for oxidized targets (number of metal atoms removed from the surface per incoming ion) drops by factors between 1.5 and 4 depending on the material. The contribution of ions to the total sputtering yield were found to be 1% for clean and $<25\%$ for oxidized targets.

Summarizing the results obtained with differen. techniques we can obtain a quantitative picture of the composition of the sputtered flux. This is shown for the specific case of Cr sputtering in Fig. 14. The total sputtering yield was found to be in reasonable agreement with the theoretical value. In similarity to lower sputtering yields for oxides compared with pure metals,[77] we also observed a decrease of the partial sputtering yield by a factor of 4 for 1×10^{-6} mbar oxygen partial pressure. For a clean target the contribution of ions and excited atoms to the sputtered flux is negligible, inferring that the majority of sputtered particles are neutral ground state atoms. For oxidized targets, however, the yield of sputtered ground state atoms becomes negligible. Even though an increase by an order of magnitude was observed for short lived excited and metastable atoms with increasing oxygen coverage, their contribution to the total sputtered flux remains rather small. In addition, it was found that Cr sputtered as charged particles (ions or ionized molecules) amounts to about 25% of the total sputtering yield. We thus conclude, that the majority of sputtered Cr leaves the surface as neutral molecules or clusters.

VII. INVESTIGATIONS OF ELECTRON AND PHOTON STIMULATED DESORPTION BY DSLFS

In the last few years, there has been an increasing number of investigations of desorption of particles from surfaces induced by electronic transitions.[80–83] The reasons for this are

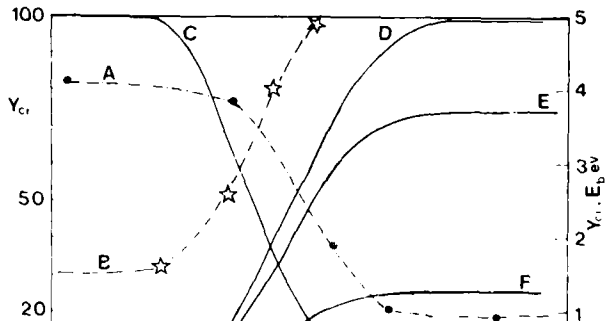

FIG. 14. Composition of the sputtered flux as a function of the oxygen partial pressure for 15-keV-Ar^+ ion bombardment of Cr. Under the given experimental conditions an oxygen partial pressure of about 5×10^{-9} corresponds to a ratio N_{O_2}/N_{Ar^+} of 1. Curve (A) Total sputtering yield of Cr (Y_{Cr}); Curve (B) Measured surface binding energy E_b (eV) [from fit of Eq. (6) to the measured spectral]; Curve (C) Partial yield of Cr atoms sputtered in the ground state given in percent of the total Cr yield; Curve (D) Partial yield of Cr sputtered as ions, neutral or ionized molecules in percent of the total Cr yield; Curve (E) Partial yield for Cr sputtered as neutral molecules in percent of the total Cr yield; Curve (F) Partial yield of Cr sputtered as ions and ionized molecules in percent of the total Cr yield; and Curve (G) Partial yield of sputtered excited Cr atoms in percent of the total Cr yield.

AD-A170 797 PROCEEDINGS OF THE TOPICAL MEETING ON THE MICROPHYSICS OF SURFACES BEAMS A.. (U) OPTICAL SOCIETY OF AMERICA WASHINGTON D C J W QUINN 18 DEC 85 AFOSR-TR-86-0469 3/3

UNCLASSIFIED AFOSR-85-0018 F/G 7/4 NL

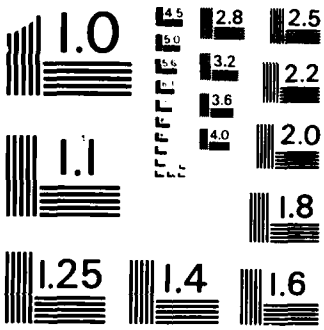

manyfold and caused by the fact that desorption induced by electronic transitions is concerned with the basic questions of physical and chemical surface interactions. Thus information about such quantities as the geometrical structure, the electronic structure, and the dynamics of bond making and breaking can be obtained.

Similar to the sputtering process, most of the desorbed particles are neutral ground state atoms.[11,83] It is, therefore, desirable to develop a powerful tool for measuring the densities and energy distributions of desorbed particles. DSLFS and LIF, as described in the previous sections, can be used to study desorbed particles. In spite of this promising fact, a critical remark is necessary. Traditionally, most of the desorption studies have dealt with oxygen, nitrogen or CO desorbed from metal surfaces. However, oxygen and nitrogen are not accessible with LIF using commercially available lasers, because their resonance lines lie in the vacuum UV. If one wants to use LIF or DSLFS for desorption studies, different target-adsorbate systems, which are accessible to tunable lasers, have to be chosen.

Recently, DSLFS measurements of neutral Na desorbed from NaCl by electron stimulated desorption have been reported by Tolk *et al.*[11] The velocity spectrum of Na desorbed from NaCl shows a nearly thermal velocity distribution. This result is very similar to what we have obtained for He^+ bombardment of NaCl,[21] indicating that the same mechanism (as described in Sec. IV B 3), might be responsible for electron stimulated desorption in this case.

The use of DSLFS in desorption studies is very promising and new information about desorption mechanisms can be expected from DSLFS measurements of desorbed neutral atoms.

VIII. CONCLUSION AND FUTURE PROSPECTS

The methods of LIF and DSLFS have been successfully used over the last few years to study different aspects of particle-solid interaction phenomena. The highly developed technology of tunable dye lasers in combination with the large cross sections for exciting atoms by visible and UV laser radiations results in detection sensitivities for neutral atoms of a few atoms per cm^3 and velocity resolutions better than a few meters per second. The high selectivity of resonance excitation is the basis for the ability of LIF to investigate the state distribution of ejected particles.

The application of LIF and DSLFS for studying the sputtering process has enabled us in many cases to identify the mechanisms responsible for particle ejection. For the first time, velocity distributions of sputtered metastable atoms could be measured and insight into the state distribution of sputtered atoms has been obtained. The detailed information about the composition of the sputtered flux has far-reaching implications for analytical methods in general, and those based on neutral particle detection in particular.

In spite of encouraging results, a lot of questions are still open and will have to be dealt with in the near future. More information about light-ion sputtering is needed to develop satisfactory models in thes regime where the isotropic cascade theory is not valid. A conclusive picture about the excitation mechanism during sputtering has not been reached yet, and further DSLFS measurements concerning this question are needed.

To push the detection sensitivity even further a new method, "multiphoton resonance ionization spectroscopy," has been developed recently.[17,79] It is anticipated to become an excellent method for trace analysis. Since it based on the resonant multiphoton ionization of neutral atoms the similarities to LIF are evident, but detection of ions is, however, more efficient than detection of photons. The application of this method to investigations of particle-solid interaction processes are manyfold and promising.

ACKNOWLEDGMENTS

This work has been made possible by the financial support of the Austrian "Fonds zur Förderung der wissenschaftlichen Forschung" (Project No. 4547). Additional support by the "Hochschuljubiläumsfonds der Stadt Wien" is gratefully acknowledged. The encouragement and support of Professor F. Viehböck was invaluable for the success of this work. In particular, I would like to thank G. Betz for his interest and many helpful discussions. I would also like to thank Professor H. Winter for supplying the ion source and his support.

[1] *Topics in Applied Physics*, edited by F. P. Schäfer (Springer, Berlin, Heidelberg, New York, 1973), Vol. 1.
[2] *Topics in Applied Physics*, edited by H. Walther (Springer, Berlin, Heidelberg, New York, 1976), Vol. 2.
[3] *Topics in Applied Physics*, edited by K. Shimoda (Springer, Berlin, Heidelberg, New York, 1976), Vol. 13.
[4] D. Hammer, E. Benes, P. Blum, and W. Husinsky, Rev. Sci. Instrum. **47**, 1178 (1976).
[5] W. Husinsky, R. Bruckmüller, P. Blum, F. Viehböck and E. Benes, J. Appl. Phys. **48**, 4737 (1977).
[6] W. Husinsky, thesis, TU-Wien, Vienna, Austria, 1977 (unpublished).
[7] A. Elbern, KFA Jülich, FRG, interner Bericht (1977).
[8] A. Elbern, E. Hintz, and B. Schweer, J. Nucl. Mater. **76&77**, 143 (1978).
[9] R. B. Wright, M. J. Pellin, and D. M. Gruen, Surf. Sci. **110**, 151 (1981).
[10] M. L. Yu, D. Grischkowsky, and A. C. Balant, Phys. Rev. Lett. **48**, 427 (1982).
[11] N. H. Tolk, P. Buchsbaum, N. Gershenfeld, J. S. Kraus, R. J. Morris, D. E. Murnick, J. C. Tully, R. Daniels, G. Margaritondo, and N. G. Stoffel, Nucl. Instrum. Methods Phys. Res. B **2**, 457 (1984).
[12] B. Schweer, D. Rusbüldt, E. Hintz, J. B. Roberto, and W. Husinsky, J. Nucl. Mater. **93&94**, 357 (1980).
[13] C. M. Muller, III, D. R. Eames, K. H. Burell, and S. C. Bates, J. Nucl. Mater. **112&118**, 56 (1982).
[14] E. Dullni, E. Hintz, J. B. Roberto, R. J. Colchin, and R. K. Richards, J. Nucl. Mater. **112&118**, 61 (1982).
[15] H. L. Bay and B. Schweer, J. Nucl. Mater. **128&129**, 257 (1984).
[16] W. Husinsky, J. Vac. Sci. Technol. **18**, 1054 (1981).
[17] F. M. Kimock, J. P. Baxter, and N. Winograd, Surf. Sci. **124**, L41 (1983).
[18] D. M. Gruen, A. R. Krauss, and M. J. Pellin, in Proceedings of the Workshop on Synergistic Effects in Sputtering, Nagoya, Japan (1984).
[19] W. Husinsky, R. Bruckmuller, and P. Blum, Nucl. Instrum. Methods **170**, 287 (1980).
[20] D. Hammer, Vacuum **28**, 107 (1978).
[21] W. Husinsky and R. Bruckmuller, Surf. Sci. **80**, 637.
[22] L. Woeste, in Advances in Laser Spectroscopy, edited by F. T. Arecchi and F. Strumia, *NATO ASI Series*, Series B: Physics, 1983, Vol. 95.
[23] W. Husinsky, G. Betz, and I. Girgis, Phys. Rev. Lett. **50**, 1689 (1983).
[24] W. Berres and H. L. Bay, Appl. Phys. A **33**, 235 (1984).
[25] W. Berres, D. Rusbuldt, E. Hintz, and H. L. Bay, Appl. Phys. B **35**, 83 (1984).

[26]W. Husinsky, G. Betz, I. Girgis, F. Viehböck, and H. Bay, J. Nucl. Mater. **128&129**, 577 (1984).
[27]R. B. Wright, C. E. Young, M. J. Pellin, and D. M. Gruen, J. Vac. Sci. Technol. **20**, 510 (1982).
[28]K. Thomsen, W. Husinsky, and G. Betz, Proceedings SASP 82, Maria Alm, Austria (1982).
[29]W. Berres, thesis, D294 Bochum, FRG (1983).
[30]P. G. Papas, M. M. Burns, D. D. Hinshelwood, M. S. Feld, and D. E. Murnick, Phys. Rev. A **21**, 1955 (1980).
[31]P. Bogen and E. Hintz, Lecture Notes, NATO Advanced Course, Val Morin, Quebec, Canada (1984).
[32]G. M. McCracken and P. E. Scott, Nucl. Fusion **19**, 887 (1979).
[33]J. B. Roberto and R. Behrisch, J. Nucl. Mater. **128&129**, 764 (1984).
[34]R. A. Roy and R. Messier, J. Vac. Sci. Technol. A **2**, 312 (1984).
[35]D. W. Hess, J. Vac. Sci. Technol. A **2**, 244 (1984).
[36]B. Schweer and H. L. Bay, *Proceedings of the 4th Conference on Solid Surfaces*, edited by P. A. Degras and M. Costa (Societe Francaise Vide, Paris, 1980), p. 1349.
[37]P. Sigmund, in *Topics in Applied Physics*, edited by Behrish (Springer, Berlin, 1981), Vol. 47, p. 9.
[38]D. A. Thompson, Radiat. Eff. **56**, 105 (1981).
[39]H. L. Bay, H. H. Andersen, W. O. Hofer, and O. Nielsen, Nucl. Instrum. Methods **132**, 301 (1976).
[40]M. Szymonski, R. S. Bhattacharya, H. Overeijnder, and A. E. de Vries, J. Phys. D **11**, 751 (1978).
[41]P. Sigmund, Appl. Phys. Lett. **25**, 169 (1974).
[42]W. O. Hofer, K. Besocke, and B. Stritzker, Appl. Phys. A **30**, 83 (1983).
[43]W. Husinsky, G. Betz, and I. Girgis, J. Vac. Sci. Technol. A **2**, 689 (1984).
[44]E. Dullni, Nucl. Instrum. Meth. Phys. Res. B **2**, 610 (1984).
[45]R. Bruckmüller, W. Husinsky, and P. Blum, Radiat. Eff. **45**, 199 (1980).
[46]D. Grischowsky, M. Yu, and A. C. Balant, Surf. Sci. **127**, 315 (1983).
[47]H. L. Bay, W. Berres, and E. Hintz, Nucl. Instrum. Method **194**, 555 (1982).
[48]H. L. Bay and W. Berres, Nucl. Instrum. Methods Phys. Res. B **2** (1984).
[49]H. L. Bay, B. Schweer, P. Bogen, and E. Hintz, J. Nucl. Mater. **118&112**, 732 (1982).
[50]H. L. Bay and B. Schweer, in Proceedings of the Symposium on Surface Physics 1985, Obertraun, Austria, edited by G. Betz, W. Husinsky, H. Störi, P. Varga, and F. Viehböck (1985).
[51]U. Littmark and S. Fedder, Nucl. Instrum. Methods **194**, 607 (1982).
[52]D. Pooley, Proc. Phys. Soc. London **87**, 245 (1966).
[53]J. B. Biersack and E. Santner, Nucl. Instrum. Methods **198**, 29 (1982).
[54]P. D. Townsend and P. J. Elliot, Phys. Lett. A **28**, 587 (1969).
[55]P. D. Townsend, R. Browning, D. J. Garlant, J. C. Kelly, A. Mahjoobi, A. J. Michael, and M. Saidoh, Radiat. Eff. **30**, 55 (1976).
[56]M. L. Yu and W. Reuter, J. Appl. Phys. **52**, 1478 (1981).
[57]I. S. Tsong and A. C. McLaren, Anal. Chem. **48**, 699 (1976).
[57]M. L. Yu and W. Reuter, J. Appl. Phys. **52**, 1489 (1981).
[58]P. Williams, Surf. Sci. **90**, 588 (1979).
[59]M. W. Thompson, Philos. Mag. **18**, 377 (1968).
[60]C. W. White, D. L. Sims, and N. H. Tolk, Science **17**, 481 (1972).
[61]G. E. Thomas, Surf. Sci. **90**, 381 (1979).
[62]K. Wittmaack, Surf. Sci. **112**, 168 (1981).
[63]R. J. MacDonald, C. M. Loxton, and P. J. Martin, in Inelastic Particle-Surface Collisions, in *Springer Series in Chemical Physics 17*, edited by E. Taglauer (Springer, Berlin, 1981), p. 224.
[64]I. S. Tsong, in Inelastic Particle-Surface Collisions, *Springer Series in Chemical Physics 17*, edited by E. Taglauer and W. Heiland (1981), p. 258.
[65]S. Dzioba, O. Auciello, and R. Kelly, Radiat. Eff. **45**, 235 (1980).
[66]S. Dzioba and R. Kelly, Surf. Sci. **100**, 119 (1980).
[67]G. Blaise, Surf. Sci. **60**, 65 (1976).
[68]B. Schweer and H. L. Bay, Appl. Phys. **29**, 53 (1982).
[69]D. M. Gruen, M. J. Pellin, C. E. Young, and M. H. Mendelsohn, Phys. Scr. **T6**, 42 (1983).
[70]E. Dullni, thesis, Bochum, FRG (1983).
[71]G. Betz and W. Husinsky, in Proceedings of the Symposium on Atomic and Surface Physics SASP 84, Maria Alm, Austria, edited by F. Howorka and W. Lindinger (1984).
[72]H. D. Hagstrum, Phys. Rev. **96**, 336 (1954).
[73]H. D. Hagstrum, in *Electron and Ion Spectroscopy of Solids*, edited by L. Fiermans, J. Vennik, and W. Dekeyser (Plenum, London, 1978), p. 273.
[74]R. B. Wright and D. M. Gruen, J. Chem. Phys. **72**, 147 (1980).
[75]U. Fano and W. Lichten, Phys. Rev. Lett. **14**, 627 (1965).
[76]E. Hintz, D. Rusbüldt, B. Schweer, J. Bohdansky, J. Roth, and A. P. Martinelli, J. Nucl. Mater. **93&94**, 656 (1980).
[77]G. Betz and G. K. Wehner, in *Topics in Applied Physics 52* (Springer, Berlin, 1983), p. 11.
[78]G. Betz and W. Husinsky, in Proceedings of the Symposium on Surface Physics SSS85, Obertraun, Austria (1985).
[79]M. J. Pellin, C. E. Young, W. F. Calaway, and D. M. Gruen, Surf. Sci. **144**, 619 (1984).
[80]D. Menzel and R. Gomer, J. Chem. Phys. **41**, 3311 (1964).
[81]M. L. Knotek and P. J. Feibelman, Phys. Rev. Lett. **40**, 964 (1978).
[82]T. E. Madey and J. T. Jates, Jr., Surf. Sci. **63**, 203 (1977).
[83]N. H. Tolk, L. C. Feldman, J. S. Kraus, R. J. Morris, M. M. Traum, and J. C. Tully, Phys. Rev. Lett. **46**, 134 (1981).
[84]A. R. Ziv, B. V. King, S. H. Lin, and I. S. Tsong, Nucl. Instrum. Methods in Phys. Res. **218**, 742 (1983).

Laser-driven metal cluster segregation in oxide matrices[a)]

E. E. Marinero, W. Pamler,[b)] M Chen, V. Jipson, and W. Y. Lee
IBM Research Laboratory, San Jose, California 95193

(Received 18 March 1985; accepted 28 May 1985)

We report on metal atom segregation within an oxide matrix as a consequence of absorption of short ($\simeq$12 ns) excimer laser pulses at 249 nm. The segregation phenomenon is investigated by the example of Au-TeO_2 thin films on glass substrates using transient reflectivity and transmissivity techniques as well as ESCA analysis. ESCA depth profiles show drastic modification of the film composition upon laser exposure. Whereas the distribution of Au and TeO_2 is homogeneous for the as-deposited films, the laser-irradiated areas show a total depletion of Au in the surface region exposed to the laser. We interpret this as a laser-driven segregation of TeO_2 to the surface and correspondingly of Au towards the substrate. The time-resolved optical experiments show that the segregation takes place within 30 ns following the laser pulse. The reflectivity and transmissivity changes are characterized by a sharp fluence threshold corresponding to the melting of the film surface.

The interaction of high power laser pulses with strongly absorbing metal and semiconductor solids leads to a variety of effects such as heating, melting, phase transformations, ablation, etc. In recent years these types of laser-induced processes have been widely utilized in pulsed laser annealing,[1] optical storage,[2] and laser quenching experiments.[3] In this contribution we present preliminary results on a new class of phenomena which to date has been barely studied, namely laser-induced segregation in binary systems[4] consisting of metal clusters in oxide matrices. Our report describes the segregation of Au clusters within a tellurium dioxide matrix driven by the absorption of excimer laser photons. A complete mechanistic report is presently under preparation.[5]

Time-resolved optical measurements as well as x-ray photoelectron spectroscopy (ESCA) studies have been utilized to characterize the nature of the segregation process. Although a detailed model for the segregation process has not yet been established, we consider in this report mechanisms that may account for our observations.

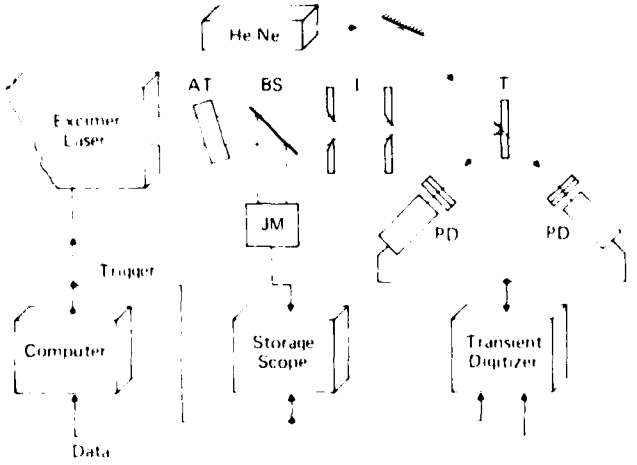

FIG. 1. Experimental setup for the time-resolved reflectivity and transmissivity measurements (AT = attenuator, BS = beam splitter, I = iris, JM = joule meter, PD = photodetector, and T = target).

75-nm-thick Au-TeO_2 films were prepared by coevaporating high-purity (99.999%) Au and TeO_2 in a commercial evaporation system onto glass substrates held at ambient temperature. The sample composition was determined from the individual evaporation rates of Au and TeO_2 ($\simeq$0.6 Å/s) monitored by separate quartz microbalances. A variety of compositions were prepared; however, in this report, we confine ourselves to the following composition of 67% mole fraction Au to TeO_2, we will use in the text the following nomenclature to identify this system: $Au_{67}(TeO_2)_{33}$.

Figure 1 shows the setup used for the time-resolved optical measurements during laser irradiation. A commercial KrF excimer laser (λ = 249 nm, 12 ns pulses) was used to single-shot expose in air the Au-TeO_2 films. Variable energy fluences (0–100 mJ/cm^2) were obtained by sending the excimer laser beam through a dielectric-coated quartz flat attenuator (AT) whose transmissivity depends on the angle of incidence of the laser radiation. The size of the exposed area is determined by the apertures [I(iris)] and has a diameter of 2.5–7 mm . The probe beam is the low-power output (< 1 mW) of a cw He-Ne laser at 632.8 nm . This is fully contained within the excimer laser-irradiated area.

Computer-controlled transient reflectivity and transmissivity experiments during the laser exposure were performed using silicon *PIN* diodes (Hamamatsu S-11 8803) together with a 500-MHz transient digitizer (Tektronix 7912 AD).

Concentration depth profiles of the as-deposited and the laser-irradiated samples were measured by ESCA in conjunction with 1 keV Ar ion sputtering using an HP 5950 spectrometer. The Au4$d_{5/2}$, Te3$d_{5/2}$, and O 1s transitions were recorded as a function of the sputtering time, i.e., depth in the sample. The ESCA intensities were calibrated from the nominal sample composition established during the evaporation. For the laser-irradiated samples, however, the compositions given should be considered only qualitatively as the different sputtering behavior of the altered film structure has not been taken into account.

In Fig. 2 we present a typical transient reflectivity profile in $Au_{67}(TeO_2)_{33}$ obtained by irradiating the sample with a single laser pulse of 30 mJ/cm^2. A permanent reflectivity

 0734-211X/85/051560-03$01.00

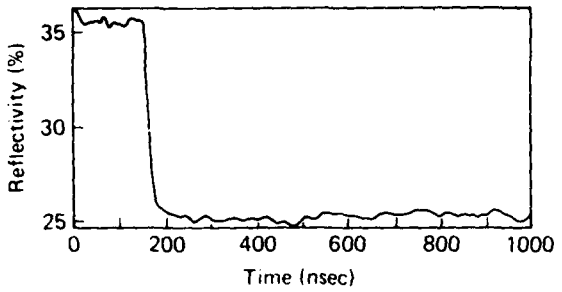

FIG. 2. Transient reflectivity change of a $Au_{67}(TeO_2)_{33}$ sample exposed to a single excimer laser pulse of $\simeq 30$ mJ/cm^2.

change takes place within 30 ns following the laser pulse (the rise time of the photodiode-digitizer combination is < 12 ns). The sample becomes less reflective, and accordingly, the transmissivity increases.

In Fig. 3 the overall reflectivity and transmissivity changes of the films are given as a function of laser fluence. It is clearly seen that the optical changes occur only if the laser energy exceeds a threshold of about 25 mJ/cm^2. With increasing fluence a saturation value is obtained for both reflectivity and transmission change. Ablation becomes evident for fluences > 55 mJ/cm^2.

The ESCA depth profiling measurements confirm that these optical changes are connected to modifications of the film composition and structure. The depth profile of an as-deposited sample (Fig. 4) shows an essentially homogeneous distribution of the film components. The higher oxygen levels at the surface (zero sputtering time) and at the substrate (40 min sputtering time) are caused by surface contamination and interference of the glass substrate oxygen, respectively.

In contrast, the depth profile of the laser-exposed sample (Fig. 5) clearly shows a wide region near the film surface which is depleted in Au and enriched in TeO_2. Partial ablation of Au (in excess of 5 nm) from the surface was ruled out by measuring the thickness profile across the edge of the exposed area by an Alpha-step profilometer. No thickness

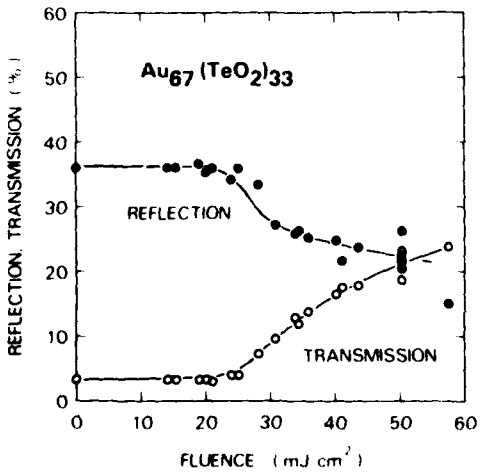

FIG. 3. Reflectance and transmittance as a function of laser fluence. A threshold is clearly observed which is correlated to melting of the film (see text for details).

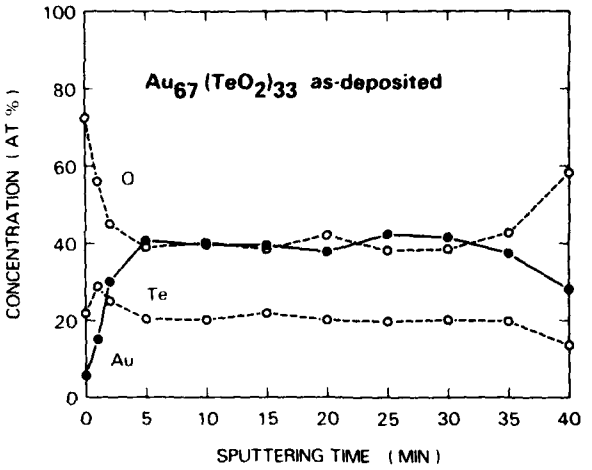

FIG. 4. ESCA depth profile of an as-deposited Au-TeO_2 thin film.

variations could be detected. This indicates that the changes observed in the depth profile are primarily due to a redistribution of the Au and TeO_2 within the film. That the Au as a consequence of laser irradiation segregates to the substrate interface cannot be unambiguously established from the ESCA profiles of Fig. 5. The concentrations given in that figure should be considered only qualitatively as the simple calibrations of the ESCA line intensities using the as-deposited sample as a standard do not take into account the fact that the sputtering rate is possibly different because of the altered composition. This is confirmed in separate experiments in which we have depth-profiled films whose Au content is 80% mole fraction to TeO_2. The calibration of the ESCA line intensities in this case clearly showed that the concentrations reported in Fig. 5 for sputtering times in excess of 15 minutes are too low. In the absence at the present of further microanalysis the segregation of Au to the interface can be inferred only indirectly.

The characteristic time scale involved in the segregation phenomenon here reported ($\simeq 30$ ns) is too short to be accountable by solid state diffusion processes. Typically, to allow solid state diffusion over several tens of nm, time scales

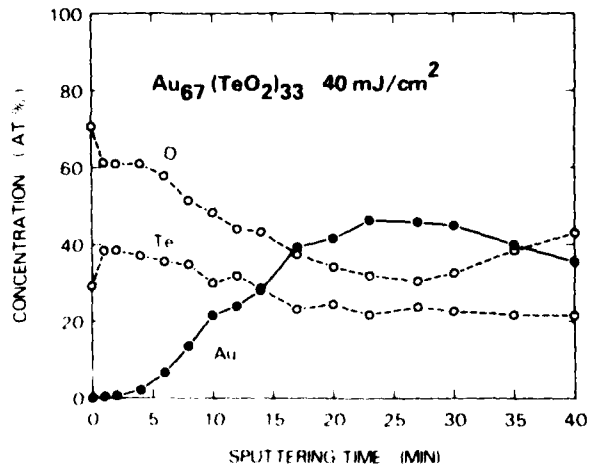

FIG. 5. ESCA depth profile of a Au-TeO_2 sample exposed to a single 249-nm laser pulse of $\simeq 40$ mJ/cm^2.

of seconds and minutes would be needed, depending on the temperature.[6] The observations are, however, consistent with diffusivities in the liquid state. Thus, we propose that the onset of the segregation process, as evidenced by the change in optical characteristics of the films, is correlated to the melting of the Au/TeO_2 mixture. The exact melting point of this binary mixture is not known. However, separate transient reflectivity experiments indicate that pure Au and TeO_2 films melt at fluences of ~ 32 mJ/cm^2. This fluence is $\sim 20\%$ higher than the threshold here reported for the binary mixture. This is not inconsistent as comparison to other Au + X phase diagrams readily shows melting point depression of Au ($T_M = 1336$K). Thus at 25 mJ/cm^2 a temperature rise sufficiently high to melt both Au and TeO_2 is attained.

The exact driving force for the speculated segregation process reported here is presently under investigation. Three possibilities are considered:

(a) Melt front resolidification propagation: Above the segregation threshold one has initially a thin molten layer given by the absorption depth ($\simeq 20$ nm) which propagates towards the substrate and later recedes back to the surface.[1] Hence resolidification begins near the glass-film interface. It is expected that the component with the higher melting point will resolidify first. The net effect is that Au will concentrate at the substrate and TeO_2 at the surface.

(b) Difference in surface energy: This effect predicts segregation of the species with the lowest surface energy.

(c) Soret effect[7]: In this effect the high temperature gradient induced by the absorption of the laser energy in the film surface acts as a driving force for directional atomic diffusion.

Experimental results to be described in Ref. 5 presently favor mechanism (a); however,the participation of either (b) or (c) cannot be excluded completely.

The reflectivity change could arise from either an optical interference phenomenon or, as discussed in Ref. 8 it may be determined by the size and shape of the Au clusters produced by the laser exposure. We are conducting further experiments using cross sectional electron microscopy and optical spectra characterization to find the exact cause of the reflectivity change.

In summary, we have observed in this preliminary study the laser-induced segregation of Au atoms or clusters in a TeO_2 matrix. As a consequence of intense excimer laser exposure, the Au atoms move away from the surface and accumulate near the substrate. The nature of the segregation was investigated using transient optical measurements as well as ESCA depth profiling techniques. We suggest that experiments of this kind will permit a clear understanding of laser-driven diffusion phenomena in condensed phase research.

Acknowledgments: We thank Bill McChesney for preparing the thin films and R. Barton for fruitful discussions.

[a] This report contains material presented at the Topical Meeting on Surfaces, Beams, and Adsorbates, Santa Fe, NM, Feb. 4–6, 1985.

[b] Institut für Angewandte Physik, Universität Regensburg, West Germany.

[1] R. F. Wood and G. E. Giles, Phys. Rev. B **23**, 2923 (1981).
[2] A. E. Bell, Proc. of the Soc. for Inf. Disp. **24**, 17 (1983).
[3] D. M. Follstaedt, in *Laser and Electron Beam Interaction with Solids*, edited by B. R. Appleton and G. K. Celler (North-Holland, New York, 1982), p. 377.
[4] M. A. Bosch, A. H. Dayem, T. R. Harrison, and R. A. Lemons, in *Laser and Electron Beam Interaction with Solids*, edited by B. R. Appleton and G. K. Celler (North-Holland, New York, 1982), p. 431.
[5] W. Pamler, E. E. Marinero, and M. Chen (to be published).
[6] G. L. P. Berning and W. Pamler, Thin Solid Films **116**, 351 (1984).
[7] S. R. deGroot and P. Mazur, *Non-equilibrium Thermodynamics* (North-Holland, Amsterdam, 1962).
[8] J. Perrin, B. Despax, and E. Kay, Phys. Rev. B **32**, 719 (1985).

Atomic-resolution studies of surface dynamics by electron microscopy

David J. Smith[a)]
Center for Solid State Science and Department of Physics, Arizona State University, Tempe, Arizona 85287

(Received 18 March 1985; accepted 28 May 1985)

High resolution electron microscopy (HREM) has been applied to the characterization of surfaces and surface rearrangements using the profile imaging method. This review paper outlines the basic principles of the technique and then surveys the recent atomic-level observations of metal, semiconductor, and oxide particle surfaces. Advantages and possible drawbacks of the technique are briefly discussed.

I. INTRODUCTION

Recent instrumental developments for the high-resolution electron microscope (HREM) have made it possible to obtain localized real-space information about many important materials' properties.[1] The technique of high resolution imaging has recently also been shown to be applicable to the characterization of surfaces in profile and initial studies of semiconductor, gold, and catalyst particle surfaces have been both very interesting *and* highly promising for future detailed study.[2-14] In this paper, the basis of surface profile imaging is first summarized before some of the initial results are reviewed in more detail. These include the direct observation of atomic column motion and surface rearrangements under the local (heating) influence of the incident electron beam. Note that no attempt is made here to review the techniques of reflection electron microscopy (REM) or conventional transmission imaging as applied to the characterization of surfaces. Both techniques—see the recent review by Takayanagi[15]—can supply atomic-level surface information. However, no *dynamic* studies on this scale so far appear to have been made except for those by Isaacson *et al.* using the scanning transmission electron microscope (STEM) (e.g., Ref. 16) which were restricted to the highly specific case of heavy atoms or clusters diffusing over light element substrates.

II. PRINCIPLES OF HIGH-RESOLUTION SURFACE PROFILE IMAGING

A. Resolution

The best possible "point" or "interpretable" resolution (δ) attainable in an HREM depends only on the wavelength (λ) of the incident electron beam and on the value of the spherical aberration coefficient (C_s) of the imaging or objective lens of the microscope, being given by the simple relationship

$$\delta \sim 0.7 C_s^{1/4} \lambda^{3/4}. \quad (1)$$

It is implicit in this expression that extraneous limiting factors such as high voltage and other electrical and mechanical instabilities have been properly overcome or minimized. In recent HREM's, this is the case, so that in order to improve the point resolution it is necessary to go to higher voltages such as 300, 400, or even 1000 kV, since reductions in C_s values are effectively limited by saturation of lens pole-piece materials. The potential improvement in resolution to the scale of atomic dimensions provided the motivation for a number of custom-built "prototype" instruments which were developed during the 1970's, and several commercial "production-line" microscopes are also now available. Some typical C_s, λ, and δ values are shown in Table I.

It is important to appreciate that the minimum value for the so-called "lattice" resolution of a HREM is not relevant to the requirements of surface profile imaging. Very finely spaced lattice fringes, generally well beyond the point resolution limit can be resolved on many microscopes. These fringes mainly reflect the mechanical and instrumental stabilities of the particular microscope but they do not provide any reliable guide to the finest image detail which can be readily interpreted in terms of specimen features. On the other hand, there are certain circumstances wherein it is possible to locate *relative* atomic positions to an accuracy of finer than 10% of the instrumental resolution.[17,18] The major imaging requirement is actually one of statistical definition, rather than resolution *per se*, and surface profile images accordingly are typically recorded at magnifications in excess of 7.5×10^5 times so as to ensure that the signal-to-noise ratio in the final image does not impose any unsuspected artificial restriction. In this way, for example, relaxations of the outermost atomic layers at Au {110} surfaces have been established as being as much as 20%.[18]

B. Imaging conditions

It is not sufficient for surface profile imaging just to have an HREM capable of atomic resolution. A number of other requirements must also be satisfied before the microscopist can trust that the image he has recorded is really a faithful representation of the surface in question. For example, it is necessary in any high-resolution imaging circumstances to record the image within very specific, and restricted, focal ranges if there is to be a direct homomorphic relationship between the image and the atomic arrangements in the sam-

TABLE I. Interpretable resolution for various λ and C_s values.

kV	λ (Å)	C_s (mm)	δ (Å)
100	0.0370	0.7	2.9
200	0.0251	0.8	2.3
400	0.0164	1.0	1.7
600	0.0126	2.0	1.7
1000	0.0087	2.3	1.3

 0734-211X/85/051563-05$01.00

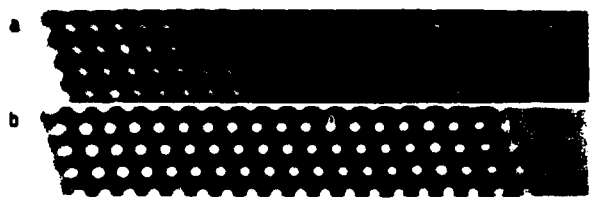

FIG. 1. Simulated surface profile images demonstrating that discrimination between high and low Z materials is possible to a limited extent. Images calculated for a 500-kV microscope (C_s = 2.7 mm) at lens defoci of (a) − 675 Å ("black dot" focus) and (b) − 975 Å ("white dot" focus). Carbon atom columns, along the right surface, appear black in (a) but are smeared out in (b), unlike the gold atom columns which are white in the latter (Ref. 17).

ple. Typically, in small-unit-cell materials, there is a complete reversal of image contrast with focal shifts of no more than a few hundred angstroms (for example, for the {200} reflections of Au at 500 kV, the focal change for reversal is 320 Å). Moreover, the area imaged cannot be too thick or else multiple (dynamical) electron scattering occurs and there is then again no straightforward correlation between the features of the image and that of the sample (for example, for Au, again at 500 kV, the sample thickness should be less than 100 Å).

These general constraints on focus and specimen thickness are applicable to the special case of surface profile imaging. Moreover, imaging of an edge is further complicated by the occurrence of diffraction effects which lead to a Fresnel fringe along the edge with its shape and form depending on among other things the lens defocus, the specimen thickness, and the particular material. Submonolayer coverage of a different material can also have a marked effect on the image appearance. For all these reasons, it is strongly advisable (when embarking on any extensive surface profile imaging exercise) also to carry out image simulations. Indeed, if reliable *quantitative* information is required (for example, about the extent of any surface contraction or relaxation) then simulations should be considered mandatory.[18]

Finally, it is significant that the surface profile image can be sensitive, to some limited extent, to the chemical species at the surface. It has been shown (as demonstrated, for example, in Fig. 1) that the presence of a surface layer of carbon atoms on a gold sample can be determined by altering the objective lens focus from the "black atom" position to the "white atom" position. Both gold and carbon atomic columns at the surface give black image contrast at the former, whereas gold atomic columns appear white at the latter focus but the contrast from the carbon layer is washed out.

C. Specimen preparation

A number of different methods have so far been used in the preparation of samples suitable for surface profile imaging. For the particular examples of small metal particles[5] and oxide crystals,[6] the materials were actually prepared on holey support films with imaging restricted to crystallites which were protruding out from the support and over holes. In this manner, extraneous signal noise from the amorphous support films did not degrade the quality of the surface profile images. A remaining bothersome problem with such small samples is the difficulty of orientating the crystals accurately to the required zone axis projection. Small apertures for selected area diffraction[9] or else focused probes[6,13] have been successfully used, but noneucentricity of the sample holder during the tilting process leads to sideways movement, making it difficult to keep track of the crystal. There is no necessity for a substrate support with bulk ion-thinned semiconductor crystals,[2] or with evaporated semicontinuous metal films,[4,7,8] although precession during tilting maneuvers is still troublesome, and it often turns out that the sample is too thick for useful profile imaging. A further constraint of specimen preparation is that most samples prepared at atmospheric pressure will invariably grow a surface layer of carbonaceous material before insertion into the microscope. It appears, however, that irradiation with a high-intensity electron beam can generally lead to etching away of this layer.[4,5,7–9] Alternatively, as discussed later in more detail, facilities need to be provided for *in situ* crystal cleaving or surface cleaning. Finally, it is worth noting our experience that rearrangements of surface atomic layers or columns are not usually seen until the carbonaceous overlayer is removed.[3,4,7,8]

III. SURFACE PROFILE IMAGING AT ATOMIC RESOLUTION

A. Semiconductors

The technique of surface profile imaging was effectively pioneered by the studies of the semiconducting material cadmium telluride (CdTe) by Sinclair *et al.*[2] This work did not have the benefit of a TV camera and real-time recording facilities, so that dynamic events could only be "followed" by routine photographic recording (exposures separated by ~ 10–15 s). Moreover, the resolution of the 100-kV microscope then available was around 3.5 Å so that "atom-pair" resolution, rather than atomic resolution, was achieved. Nevertheless (as shown in Fig. 2) images taken over a time

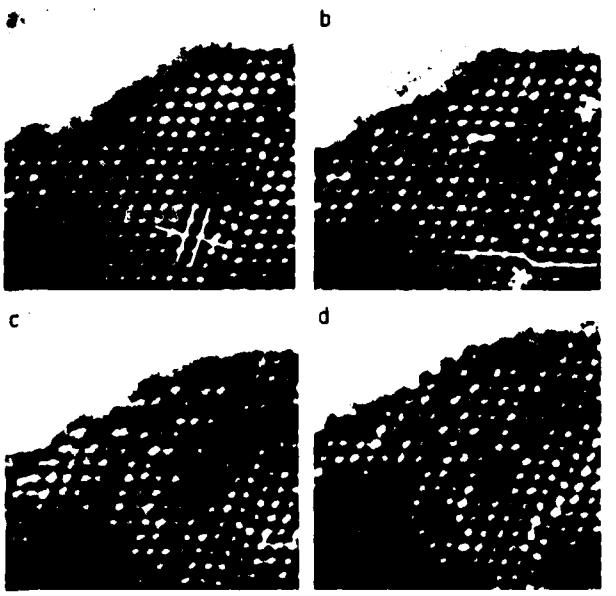

FIG. 2. Series of surface profile images from a sample of CdTe recorded over a period of several minutes. Note the changes in the surface contours (Ref. 2).

interval of several minutes established that atomic-level rearrangements on the CdTe crystal surfaces were occurring. The authors also reported seeing individual image spot jumps on the microscope viewing screen sometimes as often as several times per second, but these could not be separately recorded.

B. Small metal particles and extended metal surfaces

With the improvement in point resolution which results from higher accelerating voltages, it becomes possible to achieve atomic resolution even in cubic-close-packed metals. Marks and Smith[3] were able to demonstrate that surface profile images could be recorded, under favorable circumstances, from small gold and silver particles. Moreover, it was also observed that surface reconstructions also occurred *once* the carbon overlayer on the particles was removed. For example, the gold particle in Fig. 3, which is in a (110) orientation, has a surface atomic configuration locally corresponding to the so-called 2×1 "missing-row" model for the (110) surface. Subsequent detailed analysis also established that the outermost atomic columns on this particle were relaxed outwards by about 20%,[18] a figure which was in reasonable agreement with the results of other techniques.

Comprehensive examinations have since also been made of extended Au surfaces, rather than small particles, as this circumvented the problems of particle stability which normally arose when the carbon was partially etched away. These particular studies have been described in detail elsewhere.[4,7,8] However, it is relevant to note here some of the more significant events which took place, once again only after the overlying carbonaceous layer had been removed by the action of residual water vapor in the microscope column under the (catalyzing) influence of the incident electron beam.

Typical images which contrast the differences between the (111), (110), and (100) surfaces are shown in Figs. 4(a)–4(c), respectively. For the (111) surfaces, it was discovered that an irregular hill-and-valley structure developed, with outward normal expansions of the first atomic layer, typically of ~5%–10%, and both phenomena could be explained in terms of a positive tangential pressure on the clean gold surface.[19] In the case of extended (110) surfaces, it was significant that no extended 2×1 superstructure was observed to develop, although short lengths were sometimes found and even these did not persist for very long due to the continual surface rearrangements taking place. It was interesting that local expansions *and* contractions were observed in images of the (100) surface, and surface defects, believed to be surface Shockley partial dislocations,[20] were also relatively common.

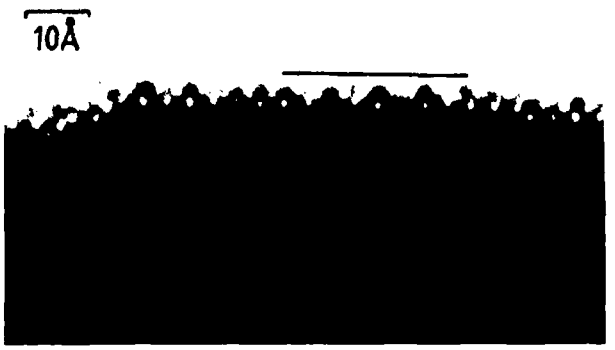

FIG. 3. Surface profile image from a small Au crystal imaged in the (110) projection showing partial reconstruction of the (110) surface into a 2×1 "missing-row" structure (Ref. 3).

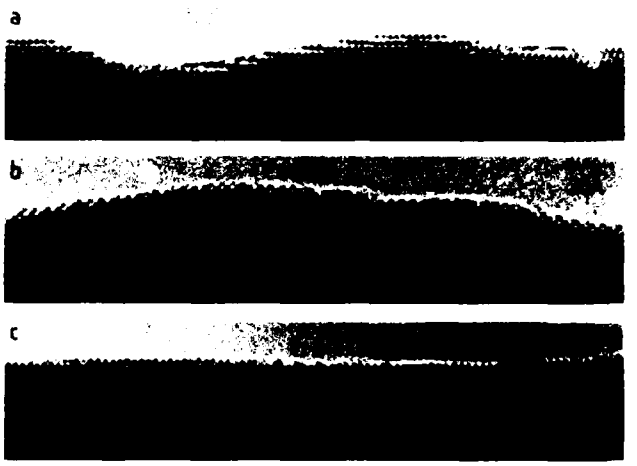

FIG. 4. Comparison of profile images from extended Au surfaces imaged in the 110 projection (a) (111) surface, (b) (110), and (c) (100). Note the hill-and-valley structure in (a) and the surface irregularities arrowed in (c).

C. Oxide catalyst particles

Obvious candidates for detailed examination using the surface profile imaging technique are oxide catalyst particles, particularly from the points of view of determining whether any significant morphological changes occur as a result of catalytic processes or whether the surface morphology can indeed be related to the catalytic behavior. Hutchison and Briscoe[5,9] have chosen initially to study compounds based on the ferrite spinel $ZnCrFeO_4$ and a number of novel and interesting results have already been reported. It was found (as described above for the gold surfaces) that after removal of surface contamination, different surfaces displayed different characteristic features with (111) surfaces, for example, remaining atomically flat, while (110) surfaces developed a prominent hill-and-valley structure. Moreover, following intense electron irradiation, it was usually found that the surface structures were modified, although {111} facets proved relatively stable compared to the reconstructions seen on (100) and (110) surfaces. Following catalytic reactions, further modifications have also been observed and Fig. 5 provides a striking example of how small "rafts," believed to consist of ZnO, develop on the surfaces of the catalyst particles.[9] These initial studies clearly demonstrate the potential of surface profile imaging as an important technique for characterizing catalysts.

IV. DYNAMIC SURFACE REARRANGEMENTS AND DIFFUSION

A particularly noteworthy feature of all surface profile imaging studies so far published is that surface rearrange-

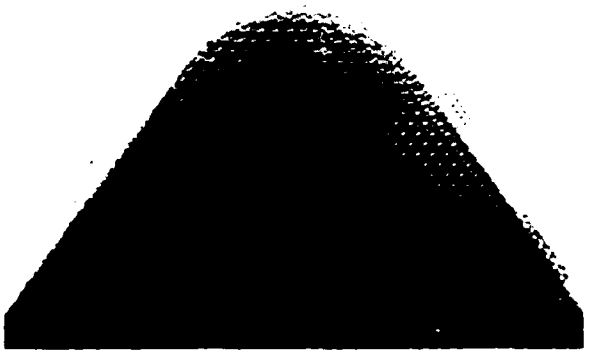

FIG. 5. High resolution profile image from a sample of $ZnFeCrO_4$, after exposure to a catalytic reaction, showing the development of small rafts believed to consist of ZnO (Ref. 9).

ments are described as occurring continually. These events are no doubt due in part to the local heating and/or ionizing effect of the incident electron beam (current densities are typically ~ 10–25 A/cm^2). However, it must be regarded as significant that the dynamic events are apparently only taking place once the carbonaceous overlayers are removed. Moreover, atomic motion at room temperature on many crystal surface faces would be anticipated, given information already available about surface diffusion from other techniques. It is also worth noting that several workers have reported substantial differences in the dynamic behavior which depends on the particular crystal face, and this is again to be expected because of different surface-dependent diffusion rates. For all these reasons, it is simply not possible to dismiss these observations of atomic (column) motion as being no more than an amusing curiosity, without practical value, even though the extraction of useful and relevant surface information could still remain a nontrivial exercise.

The modifications of CdTe surfaces observed by Sinclair *et al.*,[2] as described above and shown in Fig. 2, appear to be the first examples of atomic-resolution surface profile images wherein columnar rearrangements ("spot jumps") have been reported as occurring in real time. Smith and Marks[8] have since made a more detailed comparative study of different extended gold surfaces and substantial differences in *dynamic* behavior were noted. For example, on the (110) surfaces, it was found that there was generally little change in the overall surface profile over extended observation periods even though local rearrangements were continually taking place. Figure 6 shows two successive images of a macroscopically rough (110) surface and the atomic column movement between exposures is readily apparent (arrowed). Unfortunately, such images can only be regarded as circumstantial, rather than uncategorical, evidence for "column hopping," i.e., coordinated atomic movement, as has previously been reported in field ion microscopy studies of surface diffusion.[20] For (100) surfaces, it was again interesting that extensive rearrangements did not occur except in the presence of surface ledges when (as shown in Fig. 7) a net migration in the direction of the "lower" side of the ledge was usually observed. This preferential surface diffusion has been interpreted in terms of the surface steps acting as asymmetric potential barriers to the diffusion process: this is almost certainly too simple minded and the directional diffusion is more likely to be due to the surfaces not being at equilibrium.

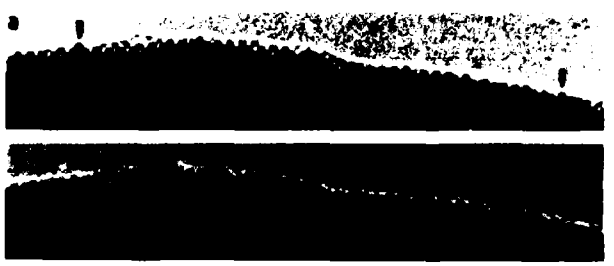

FIG. 6. Successive exposures (time difference ~ 15 s) from an area of extended Au (110) surface showing the movement of gold atomic columns (arrowed) (Ref. 7).

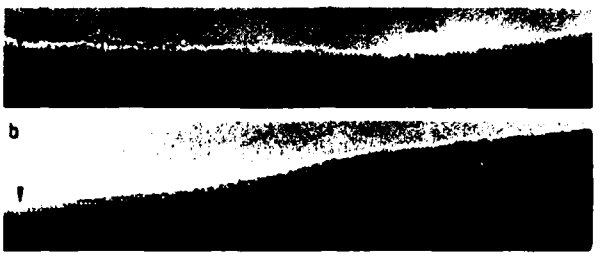

FIG. 7. Profile images from an extended Au (100) surface recorded with a time difference of about 30 min and showing substantial sideways migration of atomic columns.

High-quality on-line TV viewing and recording facilities have recently become available and these have been used to good advantage in the latest studies of dynamic events using the surface profile imaging technique. Bovin and co-workers have been able to document the growth process, row by row, of small gold crystals[10,11] and the formation and behavior of "atomic clouds" outside Au particle surfaces has been observed.[11,12] Iijima and Ichihashi have described[13] the real-time motion of surface atoms on various faces of small gold clusters, in particular observing that the {111} surfaces appeared stable, without atomic movement, and this was explained in terms of the low {111} surface energy.

V. DISCUSSION

As a specialized application of HREM, the technique of surface profile imaging is still in its infancy, as will be evident from the publication dates of the references listed. Nevertheless, it is already apparent that the technique can provide unique details about surfaces which are currently unobtainable by other means. For example, while other bulk characterization techniques such as low energy electron diffraction (LEED) can provide accurate *average* information about surface reconstructions, details of local inhomogeneities are simply unobtainable and it is certainly not possible to follow directly any surface modifications or reordering processes. Surface profile imaging has these capabilities and, moreover, it allows the influence of surface features, such as steps or terraces, on these processes to be observed. Since it gives a transverse cross sectional view of the bulk material, the technique is especially useful for establishing any changes

and/or shifts of the surface layer, and deeper layers, relative to the bulk lattice.

Notwithstanding these attractions, it must be admitted that, at its present state of development, high-resolution profile imaging is not also without shortcomings. Observations have generally been made in the relatively poor vacuums (in surface science terms) of the conventional electron microscope, and it is virtually certain that the surfaces observed were not entirely free of contaminants, nor were they in states of equilibrium with respect to surface diffusional rearrangements. Considerable energy is doubtless imparted to the surfaces by the incident beam and this will have two main effects. Local heating (to an unknown temperature) will occur and any weakly bound species at the surface is likely to be desorbed. This beam-induced desorption will almost certainly preclude high-resolution investigations of many catalytically interesting systems. It should also be appreciated that, since the profile image represents a projection of the surface, it is insensitive both to height variations and to the specific nature of any inclined surface features.

Finally, this short review can be concluded on an optimistic note. As well as the UHV HREM already in operation at Tokyo Institute of Technology,[22] several developmental projects are currently under way, in a number of laboratories spread around the world, aimed at constructing high-resolution microscopes with truly ultrahigh vacuum conditions (i.e., $\sim 10^{-10}$ Torr) at the specimen level. Surface cleaning is generally to be provided in an adjacent (interlocked) treatment chamber. Moreover, the provision of heating facilities on the specimen cartridge itself will make it possible to study a range of surface reconstructions in metals, semiconductors, and oxides which are known to occur at elevated temperatures. There is no doubt that, over the next few years, the profile imaging technique will produce a variety of results which are both interesting and also highly significant in advancing our knowledge and understanding of surface phenomena.

ACKNOWLEDGMENTS

The study of gold surfaces was undertaken in collaboration with Dr. L. D. Marks, using the Cambridge University High Resolution Electron Microscope supported by the Science and Engineering Research Council (U.K.). The author is grateful to Dr. L. D. Marks, Dr. R. Sinclair, and Dr. J. L. Hutchison for supplying Figs. 1, 2, and 5 respectively.

* Address for correspondence: Dr. D. J. Smith, Center for Solid State Science, Arizona State University, Tempe, AZ 85287.

[1] D. J. Smith, Helv. Phys. Acta **56**, 463 (1983).
[2] R. Sinclair, T. Yamashita, and F. A. Ponce, Nature **290**, 386 (1981).
[3] L. D. Marks and D. J. Smith, Nature **303**, 316 (1983).
[4] L. D. Marks and D. J. Smith, Surf. Sci. **143**, 495 (1984).
[5] N. A. Briscoe and J. L. Hutchison, Inst. Phys. Conf. Ser. **68**, 249 (1984).
[6] S. Iijima, Jpn. J. Appl. Phys. **23**, L347 (1984).
[7] D. J. Smith and L. D. Marks, Ultramicroscopy **16**, 101 (1985).
[8] D. J. Smith and L. D. Marks, Mater. Res. Symp. Proc. **41**, 129 (1985).
[9] J. L. Hutchison and N. A. Briscoe, Ultramicroscopy (in press).
[10] L. R. Wallenberg, J.-O. Bovin, and G. Schmid, Surf. Sci. (in press).
[11] J.-O. Bovin, and L. R. Wallenberg, Ultramicroscopy (in press).
[12] J.-O. Bovin, L. R. Wallenberg, and D. J. Smith, Nature (in press).
[13] S. Iijima and T. Ichihashi, Jpn. J. Appl. Phys. **24**, L125 (1985).
[14] S. Iijima and M. Ichikawa, J. Catal. (in press).
[15] K. Takayanagi, J. Microsc. (Oxford) **136**, 287 (1984).
[16] M. S. Isaacson, J. Langmore, N. W. Parker, D. Kopf, and M. Utlaut, Ultramicroscopy **1**, 359 (1976).
[17] W. O. Saxton and D. J. Smith, Ultramicroscopy (in press).
[18] L. D. Marks, Surf. Sci. **139**, 281 (1984).
[19] L. D. Marks, V. Heine, and D. J. Smith, Phys. Rev. Lett. **52**, 656 (1984).
[20] L. D. Marks and D. J. Smith, Surf. Sci. **157**, L 367 (1985).
[21] H. P. Bonzel, CRC Crit. Rev. Solid State Mater. Sci. **6**, 171 (1976).
[22] K. Yagi, K. Takayanagi, K. Kobayashi, and S. Nagakura, in *Proceedings of the 7th International Conference on the High Voltage Electron Microscope*, edited by R. M. Fisher, R. Gronsky, and K. M. Westmacott (Lawrence Berkeley Laboratory, Berkeley, CA, 1983), pp. 11–14.

AUTHOR INDEX

To papers presented at the Topical Meeting on the Microphysics of Surfaces, Beams, and Adsorbates

Unclassified

SECURITY CLASSIFICATION OF THIS PAGE

AD-A170 797

REPORT DOCUMENTATIC

1a. REPORT SECURITY CLASSIFICATION: Unclassified	1b. RESTRICTIVE MARKINGS: n/a
2a. SECURITY CLASSIFICATION AUTHORITY	3. DISTRIBUTION/AVAILABILITY OF REPORT: Approved for public release; Distribution unlimited
2b. DECLASSIFICATION/DOWNGRADING SCHEDULE	
4. PERFORMING ORGANIZATION REPORT NUMBER(S)	5. MONITORING ORGANIZATION REPORT NUMBER(S): AFOSR-TR-86-0469
6a. NAME OF PERFORMING ORGANIZATION: Optical Society of America; 6b. OFFICE SYMBOL (If applicable):	7a. NAME OF MONITORING ORGANIZATION: AFOSR/NC
6c. ADDRESS (City, State and ZIP Code): 1816 Jefferson Place, N.W. Washington, D.C. 20036	7b. ADDRESS (City, State and ZIP Code): Bldg. 410 Bolling AFB D.C. 20332
8a. NAME OF FUNDING/SPONSORING ORGANIZATION: AFOSR; 8b. OFFICE SYMBOL (If applicable): NC	9. PROCUREMENT INSTRUMENT IDENTIFICATION NUMBER: AFOSR-85-0018
8c. ADDRESS (City, State and ZIP Code): Bldg. 410 Bolling AFB 20332	10. SOURCE OF FUNDING NOS.

PROGRAM ELEMENT NO.	PROJECT NO.	TASK NO.	WORK UNIT NO.
61102F	2303	A2	

11. TITLE (Include Security Classification): Proceedings of the Topical Meeting on the Microphysics of Surfaces, Beams, and Adsorbates

12. PERSONAL AUTHOR(S): Quinn, Jarus W.

13a. TYPE OF REPORT	13b. TIME COVERED	14. DATE OF REPORT (Yr., Mo., Day)	15. PAGE COUNT
Final	FROM 01 Nov 84 TO 18 Dec85	85 12 18	329

16. SUPPLEMENTARY NOTATION

17 COSATI CODES			18. SUBJECT TERMS (Continue on reverse if necessary and identify by block number)
FIELD	GROUP	SUB. GR.	

19. ABSTRACT (Continue on reverse if necessary and identify by block number)

The Topical Meeting on Microphysics of Surfaces, Beams, and Adsorbates was organized within the interdisciplinary area of molecule/surface interactions induced, or studied, by laser-and ion-beam techniques. Especially emphasized was the molecular physics and electro-magnetism of beam-activated chemical reactions for applications in fabrication of semiconductor devices, in photocatalysis, and in optical recording. Emphasis was on the laser spectroscopy of molecular-collision and reaction processes on surfaces, new sensitive or high-resolution spectroscopies for studies of adsorbates, and optical methods applied to surface characterization.

20. DISTRIBUTION/AVAILABILITY OF ABSTRACT	21. ABSTRACT SECURITY CLASSIFICATION
UNCLASSIFIED/UNLIMITED ☒ SAME AS RPT. ☒ DTIC USERS ☐	Unclassified

22a. NAME OF RESPONSIBLE INDIVIDUAL	22b. TELEPHONE NUMBER (Include Area Code)	22c. OFFICE SYMBOL
Francis J. Wodarczyk	767-4963	NC

DD FORM 1473, 83 APR EDITION OF 1 JAN 73 IS OBSOLETE

Unclassified

SECURITY CLASSIFICATION OF THIS PAGE

END

DTIC

9-86